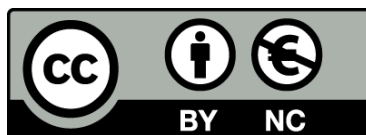




UNIVERSITAT<sub>DE</sub>  
BARCELONA

## Enzyme Powered Nanomotors Towards Biomedical Applications

Ana Cândida Hortelão



Aquesta tesi doctoral està subjecta a la llicència **Reconeixement- NoComercial 4.0. Espanya de Creative Commons**.

Esta tesis doctoral está sujeta a la licencia **Reconocimiento - NoComercial 4.0. España de Creative Commons**.

This doctoral thesis is licensed under the **Creative Commons Attribution-NonCommercial 4.0. Spain License**.





Thesis Doctoral

# **Enzyme Powered Nanomotors Towards Biomedical Applications**

Ana Cândida Hortelão

*Directors:*

Prof. Samuel Sánchez Ordóñez and Dr. Tania Patiño Padial



UNIVERSITAT DE  
BARCELONA

# Enzyme Powered Nanomotors Towards Biomedical Applications

*Memoria presentada para optar al grado de Doctora por la Universitat de Barcelona*

Programa de Doctorado en Nanociencias

Autor: Ana Cândida Hortelão

*Directores:*

Prof. Dr. Samuel Sánchez Ordóñez, Dr. Tania Patiño Padial

*Tutor:* Prof. Dr. Josep Samitier Martí



UNIVERSITAT DE  
BARCELONA

*To my mom,  
for all my achievements are hers too.*

*To my dad,  
my curiosity for science began with you.*



*“What is a scientist after all?  
It is a curious man looking through a keyhole,  
the keyhole of nature, trying to know what's going on.”*

Jacques Cousteau





# Contents

<b>Contents</b>	<b>I</b>
<b>Acknowledgments</b>	<b>III</b>
<b>Funding Sources</b>	<b>V</b>
<b>List of Abbreviations</b>	<b>VII</b>
<b>List of Figures</b>	<b>VIII</b>
<b>Abstract</b>	<b>X</b>
<b>Resumen</b>	<b>XII</b>
<b>Chapter 1. Introduction</b>	
1.1. From Nanotechnology to Nanomedicine	1
1.2. Nanomedicine: Progress and Challenges	4
1.3. Synthetic nano- and micromotors: a motile alternative to improve nanomedicine	5
<i>1.3.1. Biohybrid Motors</i>	6
<i>1.3.2. Externally Powered Nano- and Micromotors</i>	8
<i>1.3.3. Chemically Powered Nano- and Micromotors</i>	13
<i>1.3.4. Enzyme-powered nano- and micromotors</i>	16
1.4. Potential Biomedical Applications of Nano- and Micromotors	20
<i>1.4.1. Active Transport and Delivery of Cargos</i>	20
<i>1.4.2. Microsurgery and Enhanced Penetration of Cells or Tissues</i>	22
1.5. From one to many: collective behavior of synthetic motors	23
<i>1.5.1. In Vitro Evaluation of the Collective Behavior of Nano- and Micromotors</i>	23
<i>Taxis</i>	23
<i>Assembly, clustering and swarming</i>	24
<i>1.5.2. Ex vivo and in vivo Imaging and Evaluation of Swarms' Functionalities</i>	27
<b>Chapter 2. Objectives</b>	<b>33</b>
<b>Chapter 3. Enzyme-Powered Nanobots Enhance Anticancer Drug Delivery</b>	<b>37</b>
<b>Chapter 4. Targeting 3D Bladder Cancer Spheroids with Urease-Powered Nanomotors</b>	<b>51</b>
<b>Chapter 5. Swarming behavior and in vivo monitoring of enzymatic nanomotors within the bladder</b>	<b>65</b>
<b>Chapter 6. LipoBots: using liposomal vesicles as protective shell of urease-based nanomotors</b>	<b>81</b>
<b>Chapter 7. General Discussion</b>	<b>93</b>

<b>Chapter 8. Conclusion and Outlook</b>	<b>101</b>
<b>Chapter 9. References</b>	<b>105</b>
<b>Chapter 10. Annexes</b>	<b>125</b>

# Acknowledgments

Reaching this milestone in my career would not have been possible without the support of many people, for the best journeys in life are always the ones we get to share with other people. When I first arrived to the Smart Nano-Bio-Devices group, doing cutting-edge research seemed as much exciting as daunting, but being surrounded by a team of brilliant people made all the difficulties fade into learning and success.

No one achieves milestones alone, and it is of the utmost importance to have people who believe in your abilities in your corner. On this, I was most fortunate to have Samuel Sanchez believing enough in me to take a chance as my PhD advisor. His incredibly high standards for research quality and hawk eyes for detail pushed me to always be the best possible version of my scientific self. I will forever cherish the memories of the late-night sprints to finish a manuscript, and his ever-lasting willingness to spend time discussing ideas and results. Samuel always gave me the freedom to pursue ideas, and made the impossible possible so that I would have the best conditions to do research. His focus on people and on the fun-side of science are, without a doubt, one of the reasons why the group has such a strong sense of comradery and friendship.

When Tania Patiño joined the group and became my co-advisor, her friendly attitude and uplifting personality made it extremely easy to work with her. Our hours on end fighting together with the DLS at the sound of Queen, the road trips in the first retreat and to the Basque Country, the discussions on how to improve manuscripts and responses are moments that I will never forget and always recall with a smile on my face. Through this journey towards a PhD, Tania has given me a lot of her time and patience, navigating with me through so many ideas, experiments and data and for that I will forever be thankful.

I was incredibly lucky to share my time as PhD student with amazing people that today I get to call friends. Jaideep and Jemish, always encouraging, relentlessly supportive, they lifted me in tough times and gave me so many good memories. Rafa and Xavi the best office mates one could ask for, thank you for the discussions, laughs and conversations that quickly descended into madness. Diana and Maria, the kindest people I've known, equally ready to lend a helping hand or have a break for merienda, you brightened my days with your cheerful souls. Ángel brought many moments of fun, with his wonderful and quirky interjections. Agostino, Paul, Katherine, and Albert's contributions to the group dynamics undoubtedly improved my work.

During this time, I was fortunate to work closely with many people, including Ma Xing, to whom I am thankful for the time taken to teach me when I started; and Lei Wang, who was kind enough to share projects and ideas with me. I was privileged to guide incredible students, like Rafa C., Tania, and recently Meritxell, Noelia and *peque* Ferran, from whom I might have learnt much more than what I taught. You were all unfailingly inspiring, and your joyful positivity definitely had an impact on me.

Lastly, and perhaps most importantly, I want to thank my family for their unrestricted support, unfading understanding, and especially for the freedom to chase whatever dream is in the pipeline. In particular, I thank my mom: I owe the core of who I am to you, and so, this is thesis is also yours.



# Funding Sources





# List of Abbreviations

Mononuclear phagocytic system	MPS
Extracellular Matrix	ECM
Ribonucleic Acid	RNA
Reynolds number	<i>Re</i>
Ultraviolet	UV
Generally Regarded as Safe	GRAS
Food and Drug Administration	FDA
Metal-organic frameworks	MOF
Clustered Regularly Interspaced Short Palindromic Repeats	CRISPR
Green Fluorescent Protein	GFP
Gastrointestinal Tract	GI
Photoacoustic Computed Tomography	PACT
Magnetic Resonance Imaging	MRI
Gold Nanoparticles	AuNPs
Fibroblast Growth Factor Receptor 3	FGFR3
Lipobot-Inside	LB-I
Lipobot-Outside	LB-O



# List of Figures

<b>Figure 1.</b> Evolution of nanomedicine.....	2
<b>Figure 2.</b> Nanomedicines incorporating multifunctionality.....	3
<b>Figure 3.</b> Biological barriers encountered by nanomedicines in vivo .....	4
<b>Figure 4.</b> Biohybrid micromotors .....	7
<b>Figure 5.</b> Light-powered nano- and micromotors .....	10
<b>Figure 6.</b> Nano/ and micromotors powered by external magnetic-, electric- and ultrasound fields. a) Helix-shaped magnetic motor capable of moving through viscoelastic media .....	12
<b>Figure 7.</b> Chemically powered motors propelling through reactions with water. ....	14
<b>Figure 8.</b> Nano- and micromotors powered by inorganic catalysts .....	15
<b>Figure 9.</b> Nano- and micromotors powered by enzymatic catalysis.....	18
<b>Figure 10.</b> Proof-of-concept biomedical applications of nano- and micromotors.....	21
<b>Figure 11.</b> In vitro collective behavior of nano- and micromotors. ....	26
<b>Figure 12.</b> Ex vivo and in vivo imaging and evaluation of of nano- and micromotor swarms and their biomedical applications. ....	28



# Abstract

The advancements in nanotechnology enabled the development of new diagnostic tools and drug delivery systems based on nanosystems, which offer unique features such as large surface area to volume ratio, cargo loading capabilities, increased circulation times, as well as versatility and multifunctionality. Despite this, the majority of nanomedicines do not translate into clinics, in part due to the biological barriers present in the body. Synthetic nano- and micromotors could be an alternative tool in nanomedicine, as the continuous propulsion force and potential to modulate the medium may aid tissue penetration and drug diffusion across biological barriers. Enzyme-powered motors are especially interesting for biomedical applications, owing to their biocompatibility and use of bioavailable substrates as fuel for propulsion.

This thesis aims at exploring the potential applications of urease-powered nanomotors in nanomedicine. In the first work, we evaluated these motors as drug delivery systems. We found that active urease-powered nanomotors showed active motion in phosphate buffer solutions, and enhanced *in vitro* drug release profiles in comparison to passive nanoparticles. In addition, we observed that the motors were more efficient in delivering drug to cancer cells and caused higher toxicity levels, due to the combination of boosted drug release and local increase of pH produced by urea breakdown into ammonia and carbon dioxide.

One of the major goals in nanomedicine is to achieve localized drug action, thus reducing side-effects. A commonly strategy to attain this is the use moieties to target specific diseases. In our second work, we assessed the ability of urease-powered nanomotors to improve the targeting and penetration of spheroids, using an antibody with therapeutic potential. We showed that the combination of active propulsion with targeting led to a significant increase in spheroid penetration, and that this effect caused a decrease in cell proliferation due to the antibody's therapeutic action.

Considering that high concentrations of nanomedicines are required to achieve therapeutic efficiency; in the third work we investigated the collective behavior of urease-powered nanomotors. Apart from optical microscopy, we evaluated the tracked the swarming behavior of the nanomotors using positron emission tomography, which is a technique widely used in clinics, due to its noninvasiveness and ability to provide quantitative information. We showed that the nanomotors were able to overcome hurdles while swimming in confined geometries. We observed that the nanomotors swarming behavior led to enhanced fluid convection and mixing both *in vitro*, and *in vivo* within mice's bladders.

Aiming at conferring protecting abilities to the enzyme-powered nanomotors, in the fourth work, we investigated the use of liposomes as chassis for nanomotors, encapsulating urease within their inner compartment. We demonstrated that the lipidic bilayer provides the enzymatic engines with protection from harsh acidic environments, and that the motility of liposome-based motors can be activated with bile salts.

Altogether, these results demonstrate the potential of enzyme-powered nanomotors as nanomedicine tools, with versatile chassis, as well as capability to enhance drug delivery and tumor penetration. Moreover, their collective dynamics *in vivo*, tracked using medical imaging techniques, represent a step-forward in the journey towards clinical translation.



# Resumen

Recientes avances en nanotecnología han permitido el desarrollo de nuevas herramientas para el diagnóstico de enfermedades y el transporte dirigido de fármacos, ofreciendo propiedades únicas como una gran capacidad de encapsulación de fármacos, el control sobre la biodistribución de estos, versatilidad y multifuncionalidad. A pesar de estos avances, la mayoría de nanomedicinas no consiguen llegar a aplicaciones médicas reales, lo cual es en parte debido a la presencia de barreras biológicas en el organismo que limitan su transporte hacia los tejidos de interés. En este sentido, el desarrollo de nuevos micro- y nanomotores sintéticos, capaces de autopropulsarse y causar cambios locales en el ambiente, podrían ofrecer una alternativa para la nanomedicina, promoviendo una mayor penetración en tejidos de interés y un mejor transporte de fármacos a través de las barreras biológicas. En concreto, los nanomotores autopropulsados por enzimas poseen un alto potencial para aplicaciones biomédicas gracias a su biocompatibilidad y a la posibilidad de usar sustancias presentes en el organismo como combustible.

El objetivo de esta tesis es explorar el potencial de nanomotores, autopropulsados mediante la enzima ureasa, para aplicaciones biomédicas. En el primer trabajo, se evaluó el uso de estos nanomotores como vehículos para el transporte de fármacos anticancerígenos. Se observó que los nanomotores, activos gracias al consumo de urea, eran capaces de moverse en solución salina y su actividad resultó en una mayor liberación de fármaco *in vitro*, en comparación con partículas pasivas. Además, se observó que estos motores poseían una mayor eficiencia para el transporte del fármaco en el interior de células cancerígenas, causando una mayor toxicidad que las partículas pasivas gracias a la combinación de la liberación del fármaco y los cambios en el pH promovidos por la conversión de urea en amoníaco y dióxido de carbono.

El mayor reto al que se enfrenta la nanomedicina actualmente es la consecución del transporte de fármacos dirigido, reduciendo al máximo los efectos secundarios que estos puedan causar en tejidos sanos del organismo. La estrategia más común para conseguir dirigir fármacos a tejidos diana es el uso de biomoléculas capaces de reconocer ciertas células o tejidos, como por ejemplo los anticuerpos. En el segundo trabajo de esta tesis, se diseñaron nanomotores propulsados por ureasa y equipados con un anticuerpo capaz de reconocer células cancerígenas de vejiga, cultivadas en forma de esferoides. Se estudió cómo el movimiento de los nanomotores podía mejorar la capacidad de reconocimiento de estas, donde se demostró que la combinación de nanomotores activos con el anticuerpo, resulta en una mayor eficiencia en la penetración de esferoides de cáncer de vejiga, y que este efecto causaba una mayor inhibición de la proliferación celular, debido a los efectos terapéuticos del anticuerpo.

Considerando el hecho de que se necesita transportar altas concentraciones de nanomedicinas para conseguir efectos terapéuticos, en el tercer trabajo se investigó el comportamiento colectivo de nanomotores propulsados por ureasa. Para ello, a parte del uso de microscopía óptica para analizar el movimiento y el

comportamiento colectivo de los nanomotores, en este trabajo se utilizaron técnicas de imagen molecular basada en emisión de positrones, una técnica no invasiva ampliamente utilizada en ámbitos clínicos, capaz de proporcionar datos cuantitativos. Se observó que los nanomotores eran capaces de superar obstáculos y avanzar a través de espacios confinados con diferentes geometrías, y que su movimiento en forma de enjambres es capaz de generar movimiento de fluidos tanto in vitro como dentro de la vejiga de ratones vivos.

Con el objetivo de proteger la actividad enzimática en ciertos ambientes, como puede ser el estómago, donde el pH ácido podría destruir las enzimas de los nanorobots, en el cuarto trabajo se investigó el uso de liposomas como elemento protector. Se demostró que la bicapa lipídica proporciona protección de las enzimas en ambientes donde el pH es extremadamente ácido, y que el movimiento de estos nanomotores se puede activar mediante el uso de sales biliares, lo que les confiere un alto potencial para aplicaciones en el tratamiento y diagnóstico de enfermedades gastrointestinales.

En conjunto, los resultados presentados en esta tesis doctoral demuestran el potencial del uso de nanomotores autopropulsados mediante enzimas como herramientas biomédicas, ofreciendo versatilidad en su diseño y una alta capacidad para promover el transporte de fármacos y la penetración en tumores. Por último, su movimiento colectivo observado in vivo mediante técnicas de imagen médicas representan un significativo avance en el viaje hacia su aplicación en medicina



# Chapter 1



## Introduction

*“A great discovery does not issue from a scientist’s brain ready-made, like Minerva springing fully armed from Jupiter’s head; it is the fruit of an accumulation of preliminary work”*

*Marie Curie*





## 1.1. From Nanotechnology to Nanomedicine

Biological systems were one of the inspirations that drove Richard P. Feynman to a series of thoughts that culminated on his lecture “Engineering and Science: There’s plenty of room at the bottom”,<sup>1</sup> which was considered the birth of nanotechnology.<sup>2</sup> Advancements in technology led to the emergence of several topics of research, such as nanofabrication,<sup>3</sup> nanomaterials,<sup>4,5</sup> bionanotechnology,<sup>6–8</sup> and ultimately nanomedicine.<sup>9–</sup>  
20

The past decades exhibited a considerable stream in research outputs in the field of nanomedicine (**Figure 1a**).<sup>9–20</sup> Several physical effects at the interface between the molecular and macroscopic worlds were explored,<sup>21,22</sup> leading to new insights for the design of healthcare products. For instance, for diagnostics and imaging, new sensor devices aim to increase sensitivity, reduce production costs and/or measure novel analytes, and nanoparticulated contrast agents are investigated to enhance medical imaging.<sup>23–25</sup> Nanostructured biomaterials are used in the implant industry due to their ability to improve mechanical properties.<sup>26,27</sup> However, one of the sectors that gathers more attention in nanomedicine is the development of new drug delivery systems.<sup>28–31</sup> This is due to the unique features that nanostructured materials offer, namely large surface area to volume ratio,<sup>32–34</sup> cargo loading capabilities,<sup>32–34</sup> increased circulation times,<sup>35,36</sup> and the possibility to integrate multifunctionality into a single particle.<sup>37–41</sup> Particularly, in drug delivery, researchers not only aim at improving the bioavailability and pharmacokinetics of drugs, but also at the development of safe and effective therapy approaches that are lesion-specific, thus having fewer off-target effects.

A myriad of advances were made in the development of new drug delivery systems, stemming from applied research to the approval and commercialization of new products comprising nanotechnology (**Figure 1a**).<sup>42–45</sup> Nanoscale manufacturing, either by building up molecules (bottom-up) or micronizing of materials (top-down), yield a plethora of nanoparticle types with different physical and chemical properties suited for drug delivery systems (**Figure 1b-g**), such as high entrapment efficiency or ease of surface modification. In this sense, liposomes were one of the first nanoparticulate systems to be reported and used as drug carriers.<sup>46–</sup>  
<sup>48</sup> These nanoparticles are fabricated using bottom-up approaches by hydrating phospholipid films, and have been extensively studied in nanomedicine due to their biocompatibility and loading abilities of varied sizes of cargoes, ranging from small drug molecules, to genes and proteins (**Figure 1b**). In fact, Doxil<sup>®</sup> – the first clinically nanomedicine approved – was based on doxorubicin-loaded liposomes.<sup>49</sup> Following this, several other nanomedicines based on liposomes were approved, as the cases of Myocet<sup>®</sup> and Daunosome<sup>®</sup>.<sup>50</sup>

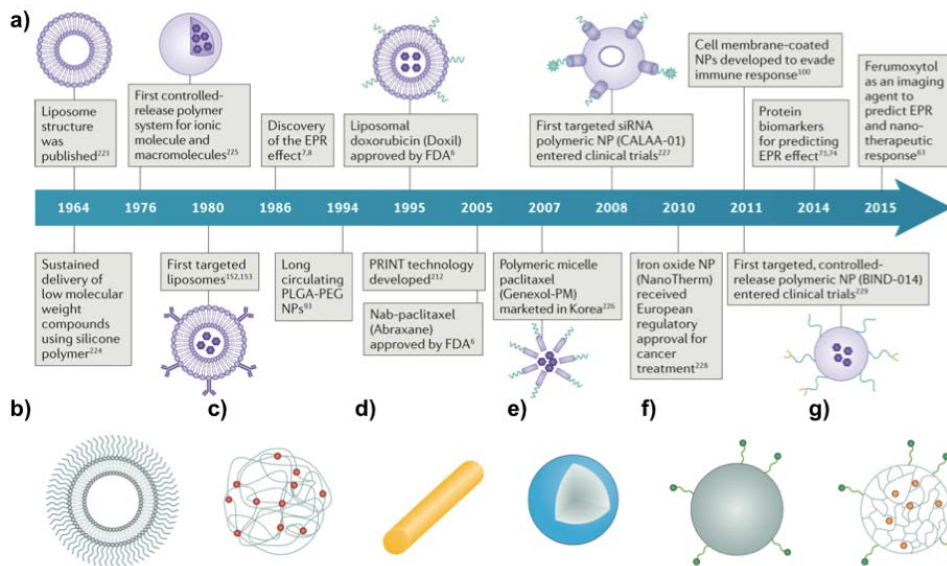


**Figure 1.** Evolution of nanomedicine. a) Chronological outputs of nanomedicine and drug delivery systems from academic research to clinical use, where various types of nanoparticles are used, such as b) stealth liposomes, c) micelles, d) metallic nanorods, e) metallic nanospheres, f) mesoporous silica nanoparticles, and g) polymeric nanoparticles. Adapted from Shi *et al*<sup>10</sup> and Chen *et al*,<sup>51</sup> respectively, with permission from Springer Nature.

Other nano-sized structures, such as metallic nanoparticles, were investigated as drug delivery systems (**Figure 1c-g**).<sup>52–54</sup> For example, iron oxide nanoparticles have been widely studied for photodynamic cancer therapy<sup>55,56</sup> or hyperthermia,<sup>57–59</sup> while silver nanoparticles were explored for their antimicrobial activity.<sup>60–62</sup> Polymers were also used for the fabrication of nano-scaled delivery systems, taking advantage of inherent desirable features such as biodegradability, stability, affinity to drug molecules, etc. to yield functional nanocarriers.<sup>63–65</sup> In addition, researchers emulated the attractive features of liposomes using copolymers to fabricate polymersomes, which are self-assembled hollow capsules with high structural versatility, encapsulation efficiency and stability.<sup>66–69</sup>

Another strategy followed for the development of drug delivery systems was the fabrication of drug nanoconjugates, where drug molecules were attached to polymers or proteins to improve their circulation time and efficacy.<sup>70–73</sup> Drug stability and efficiency issues were also tackled by nanosizing pharmacologically active substances, yielding nanocrystals, which improve the solubility and dissolution rates of poorly soluble compounds.<sup>74,75</sup>

Drug delivery systems based on nanomedicine aim at improving both safety and treatment efficacy. However, nanocarriers' design should be approached considering requirements beyond biocompatibility and drug loading abilities, as for instance, the incorporation of multiple functionalities into a single carrier. Anti-fouling coatings, targeting ligands, as well as co-encapsulation of drugs and diagnostic agents are examples of multifunctionalities that can increase both efficacy and safety of nanomedicines (**Figure 2a**).<sup>37–41</sup> Researchers designed functional nanocarriers for combination therapy, where the co-delivery of drug cocktails aims to achieve better efficacies while reducing side-effects.<sup>76–82</sup> Nanocarriers with triggered drug release abilities were widely investigated as a means to ensure a localized therapeutic effect (**Figure 2b-c**), using molecular gates or stimuli-sensitive coatings to attain this purpose.<sup>83–86</sup> Furthermore, the incorporation of multiple therapy

modes, such as chemo- and thermal therapies, as well as permeating agents in one single carrier has also been explored to increase the efficiency of the nanomedicines (**Figure 2d**).<sup>87–89</sup>

The advancements in nanomaterials synthesis and engineering enabled the development of systems where diagnostics and treatment capabilities are combined to improve clinical outcomes, *i.e.* theranostic systems, which typically consist in single entities that can perform both functions simultaneously.<sup>51,90–93</sup>

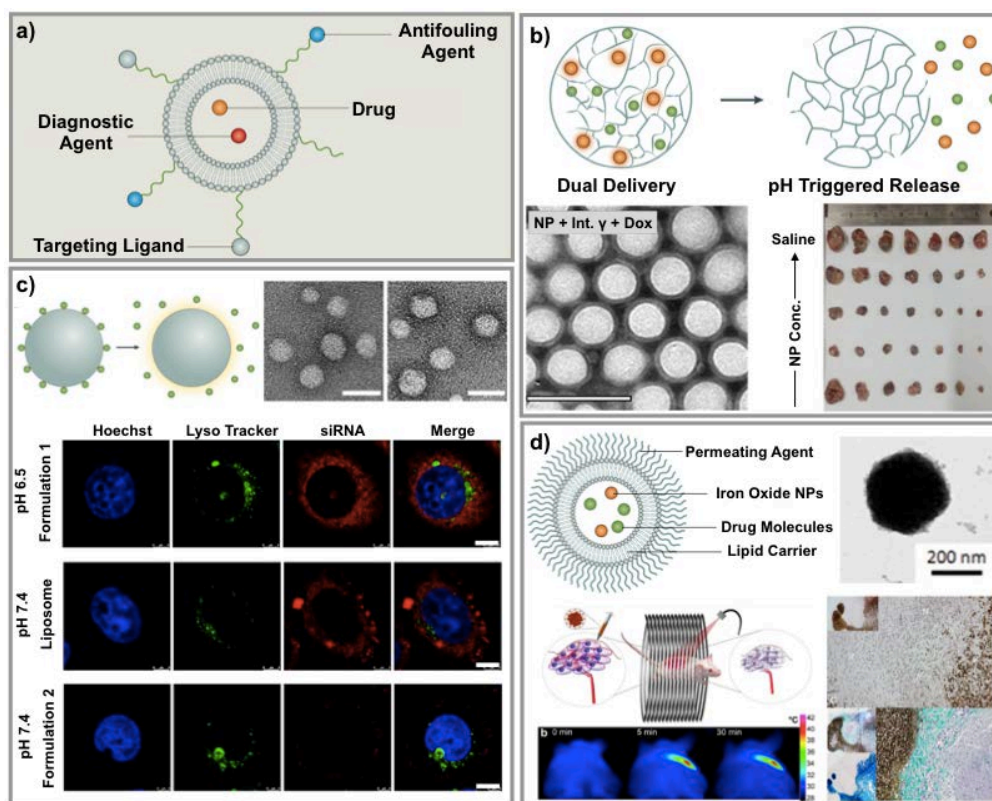


**Figure 2.** Nanomedicines incorporating multifunctionality. a) Design example of multifunctional nanocarrier, adapted from Chen *et al.*<sup>51</sup> b) Co-delivery of several pharmaceuticals by a single nanocarrier and triggered drug release. Adapted from Chen *et al.*<sup>51</sup> and Yin *et al.*<sup>82</sup> c) Drug delivery triggered by environment stimuli, adapted from Chen *et al.*<sup>51</sup> and Zhang *et al.*<sup>86</sup> d) Nanoparticle capable of enhanced permeation, carrying both drugs and iron oxide nanoparticles, which could be used as imaging contrast or to generate reactive oxygen species, adapted from Di Corato *et al.*<sup>94</sup> Adaptations with permissions from the publishers.

Although the field is associated with many possible applications in the clinic, the most striking one is cancer management, such as patient stratification.<sup>91</sup> Another interesting theranostics approach is monitoring the response post-treatment, aiming at achieving rapid prognosis between therapy cycles.<sup>92</sup> In this way, the early and sensitive detection of alterations at molecular level allows necessary adjustments to be made, ensuring the best treatment outcome.

Theranostics were also explored for imaging-guided localized therapy,<sup>88</sup> tumor characterization,<sup>95,96</sup> prediction of tumor-nanocarrier and tumor-drug interactions,<sup>93,97</sup> and even as a source of information for the design of personalized treatments.<sup>98–100</sup>

Altogether, the advances in nanomedicine hold great promise for the establishment of more effective and personalized therapies, with a particular focus on cancer treatment, as this disease continues to be among the most significant healthcare problems globally.

## 1.2. Nanomedicine: Progress and Challenges

Despite the plethora of research outputs concerning nanoparticle-based cancer therapies, to date only a few cancer nanomedicines have been approved.<sup>42,44,45,101</sup> Based on a search on the *clinicaltrials.gov* database using the keywords ‘nanoparticle’ and ‘cancer’ on April 2021, there were 116 active clinical studies on cancer nanomedicines. However, only three new nanomedicine products were approved for clinical use since 2016.<sup>42,45,101</sup> In contrast, the *Web of Science* database shows that over 50.000 research articles including the terms ‘nanomedicine’ and ‘drug delivery’ were published between 2000 and 2020.

This disparity between research outputs, the nanomedicines under clinical investigation and the ones that actually reach regulatory approval indicates the difficulty in the translation of research into clinical use.<sup>10,20,102–104</sup>

Several challenges must be addressed in order to achieve better results in the clinical translation of nanomedicine.<sup>10,105,106</sup> First, key factors such as controlled, reproducible and scalable synthesis of nanomedicines are essential to reduce batch-to-batch variation and thus enable clinical translation. Second, a fundamental understanding of the nanoparticles behavior *in vivo* is an unmet challenge,<sup>105,107</sup> mostly due to the need for the development of tools that enable their imaging and study in biological systems, with a focus on obtaining quantitative data. In fact, a recent meta-analysis study that reviewed the delivery of nanoparticles to tumors surveyed the literature, from 2006 to 2016, and reported that only 0.7% of the administered nanoparticle dose actually reaches the tumor site.<sup>105</sup> This can be due to several reasons, such as the myriad of biological barriers that nanomedicines face *in vivo*,<sup>108</sup> which are not mimicked well enough *in vitro*.

Upon entering the body, nanoparticles will firstly face the mononuclear phagocytic system (MPS) barrier, which is a network of organs such as the spleen, liver and lymph nodes, that have phagocytic cells able to capture the nanoparticles before they reach the target site (**Figure 3a**).<sup>109–112</sup>

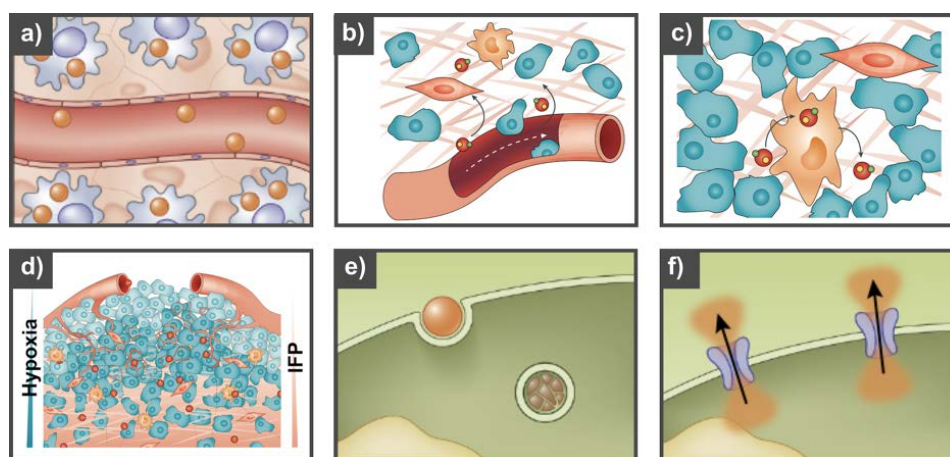


**Figure 3.** Biological barriers encountered by nanomedicines *in vivo*. a) Mononuclear phagocytic system (MPS). b) Physical barriers such as flows, shear forces and geometrical constraints. c) Interstitial fluid pressure arising from the uneven vasculature. d) Complex extracellular matrix surrounding tumor tissue. e) Endosomal trapping of nanomedicines. f) Efflux of delivered drugs due to the action of molecular and ionic pumps, such as multi-drug resistant proteins. Adapted from Blanco *et al*<sup>112</sup> and Chen *et al*,<sup>51</sup> with permission from Springer Nature.

Even if the nanoparticles are engineered to avoid the MPS, *e.g.* with coatings that prolong their circulation lifetime, then they are subjected to other barriers, as is the case of flows and shear forces (**Figure 3b**), which limit both active and passive targeting strategies.<sup>112–114</sup>

Furthermore, when the nanoparticles reach the tumor site, they encounter the hurdles presented by the heterogeneities in the tumor microenvironment, *i.e.* a dense extracellular matrix (ECM) (**Figure 3c**) and high interstitial fluid pressures (**Figure 3d**).<sup>108,112,115</sup> These phenomena, coupled to the accumulation of nanoparticles in the peripheral tumor cells (binding-site barrier effect)<sup>116,117</sup> hinder the penetration of nanomedicines into the tumor, leaving deep-seeded cells untreated. Additionally, to effectively act as drug delivery systems, upon entering the cells, the nanoparticles need to avoid endosomal trapping (**Figure 3e**),<sup>118,119</sup> and ensure that the drug delivery does not suffer from efflux due to the action of molecular and ionic pumps (**Figure 3f**).<sup>120,121</sup>

Apart from the barriers discussed above, nanomedicines face yet other hurdles, such as biofouling. When administered *in vivo*, opsonin proteins present in the nanomedicines' surroundings can bind to their surface and hinder their functionality.<sup>122–126</sup> Moreover, the translation of nanomedicines to clinical use requires that the formulations adhere to high standards of *in vivo* stability, adequate safety *vs.* efficacy ratios, as well as fabrication scalability.<sup>43</sup>

In the past decades, researchers focused on developing nanomedicines able to overcome the physical and chemical barriers that handicap *in vivo* effectiveness.

### 1.3. Synthetic nano- and micromotors: a motile alternative to improve nanomedicine

Active matter, in particular synthetic nano- and micromotors could be an elegant alternative to conventional nanoparticles in the design of nanomedicines, since they could bring a series of advantages, not only due to the driving force provided by propulsion, but also because of their potential to modulate physicochemical properties of the microenvironment, such as pH or viscosity. This could be of special interest to overcome biological barriers, especially cell and tissue penetration, as well as to improve nanomedicines or drug diffusion into tumor regions.

Nano- and micromotors were studied for their ability to perform various proof-of-concept tasks, such as tow multiple cargos,<sup>127–131</sup> drill<sup>132–134</sup> or capture species present on their surroundings.<sup>135–139</sup> These tiny machines were explored as functional and controlled tools for applications across fields such as environmental remediation,<sup>140–144</sup> sensing,<sup>145–147</sup> and in biomedicine.<sup>148–156</sup>

However, nano- and microscale motion is challenging, since at these scales reciprocal work will only result in back-and-forth movements, and non-reciprocal work or time-reversal asymmetry is required to achieve net displacement. Purcell compares nanoscale motion to a human swimming in a pool of honey, *i.e.* motion at low Reynolds number (*Re*) regimes is governed by viscous forces, while macroscale motion (*e.g.* a human swimming in water) is governed by inertial forces (high *Re*).<sup>157</sup> *Re* is a dimensionless number, defined as the ratio of inertial to viscous forces acting on an object in a fluid,

$$Re = \rho V l / \mu = (\text{Inertial Forces}) / (\text{Viscous Forces}), \quad (1)$$



where,  $\rho$  is the density of the fluid,  $V$  and  $l$  are the velocity and the characteristic length of the object, respectively, while  $\mu$  is the viscosity of the fluid.

Researchers investigated different methods to achieve nanoscale motion, by coupling synthetic particles to motile living organisms (*e.g.* bacteria,<sup>158–168</sup> cells,<sup>131,169–179</sup> etc.), or by designing nano- and micromotors capable of converting energy into mechanical work. In this sense, motors can either utilize energy from external inputs,<sup>180–183</sup> such as magnetic,<sup>184–187</sup> light,<sup>188–191</sup> or ultrasound fields,<sup>183,192</sup> or harness free energy from their surroundings and convert it to displacement via chemical reactions.<sup>193–200</sup>

### 1.3.1. Biohybrid Motors

Researchers took advantage of the innate motile abilities of microorganisms and cells to develop self-propelled systems able to accomplish specific tasks. These so-called biohybrid motors focus on the coupling of synthetic materials with motile biological entities, which bear interesting features, such as responsiveness to environmental stimuli (*e.g.*, pH, temperature, or chemical gradients).

Several flagellated biological units were used to power the propulsion of biohybrids. Sperm is a promising candidate, since this type of cells demonstrated powerful propulsion in biological environments, and can exhibit chemo-, thermo- and rheotaxis, which can be advantageous to control the motors directionality. Typically, these biohybrids are fabricated by entrapping single sperm cells within tubular structures. Magdanz *et al* used a rolled-up microtube with magnetic properties to fabricate a sperm-based micromotor, investigating the influence of design parameters on the performance of this biohybrid, such as radius of the microtube and penetration depth of the sperm cells, as well as temperature.<sup>172</sup> Moreover, by taking advantage of sperm motility and the magnetic control, the authors demonstrated separation of selected motors on a microfluidic chip. The same group continued working towards the improvement of sperm micromotors,<sup>179</sup> investigating the effect of the microtubes' length, and studying different biofunctionalizations to improve the coupling efficiency. The authors reported that the addition of caffeine to the medium led to a temporary improvement on the micromotors' velocity.

Researchers hypothesized that such biohybrids could hold potential in the development of alternative fertilization methods, micromanipulation and targeted drug delivery.<sup>131,172,173,177</sup> In this regard, Medina-Sánchez *et al* used metal-coated polymer helices to aid the transport of sperm with deficient motility, thus helping it carry out their natural function.<sup>173</sup> The authors showed the efficient capture, transport and release of live sperm in microfluidic cells that mimicked physiological conditions. In addition, Striggow *et al* entrapped sperm cells on capped microtubes fabricated by using photoresist and lithography, showing that the streamlined shape improved navigation through obstacles, and demonstrating their motility in oviduct fluid (**Figure 4a**).<sup>178</sup> However, the authors point out that for successful applications in biomedicine, further control on directionality towards the target, as well as triggered degradability of the encasing tubes are required. To improve on this issues, Chen *et al* studied the chemotactic behavior of sperm micromotors, showing their ability to detect and respond to external chemical stimuli and swim toward a gradient of egg secretions.<sup>174</sup> The authors also demonstrated that additional control on the propulsion could be achieved by controlling the osmolarity of the solution, pointing the potential of these micromotors as controlled and responsive devices.

Apart from sperm, bacterial cells were also used in the development of biohybrid micromotors. These multiflagellated motile microorganisms are present in several areas of the body. Moreover, like sperm cells, bacteria exhibit chemo- and pH taxis, and in specific cases they can follow oxygen gradients, or sense and align with magnetic fields, which opens possibilities for several biomedical applications. Due to their great diversity, bacteria allow for the fabrication of multiple biohybrid motors, based on spherical particles,<sup>164,165,201</sup> microtubes,<sup>166,168</sup> cells,<sup>202</sup> or even rotors.<sup>163,203</sup>

The earlier works on the use of bacteria to propel microscale spherical particles mostly consisted on the use of multiple bacteria to achieve efficient displacement of the particle cargo.<sup>161,164</sup> For instance, Behkam and Sitti attached several *S. marcescens* to polystyrene microbeads, controlling the motility of the complex through the addition of heavy metal ions (motion off) or ion chelating agents (motion on).<sup>204</sup> Akin *et al* showed the potential of bacterial biohybrids as delivery systems by coupling *L. monocytogenes* bacteria to cargo-loaded nanoparticles (**Figure 4b**).<sup>158</sup> To improve the biohybrid's stability, Park *et al* engineered *S. typhimurium* bacteria to display biotin in the outer membrane proteins, using this as a link to attach several bacteria to microparticles.<sup>159</sup> Similarly, Taherkhani and co-workers loaded a substantial amount of nanoliposomes to the surface of magnetotactic bacteria through carbodiimide chemistry, aiming at designing a self-propelled therapeutic agent with magnetic control.<sup>201</sup>

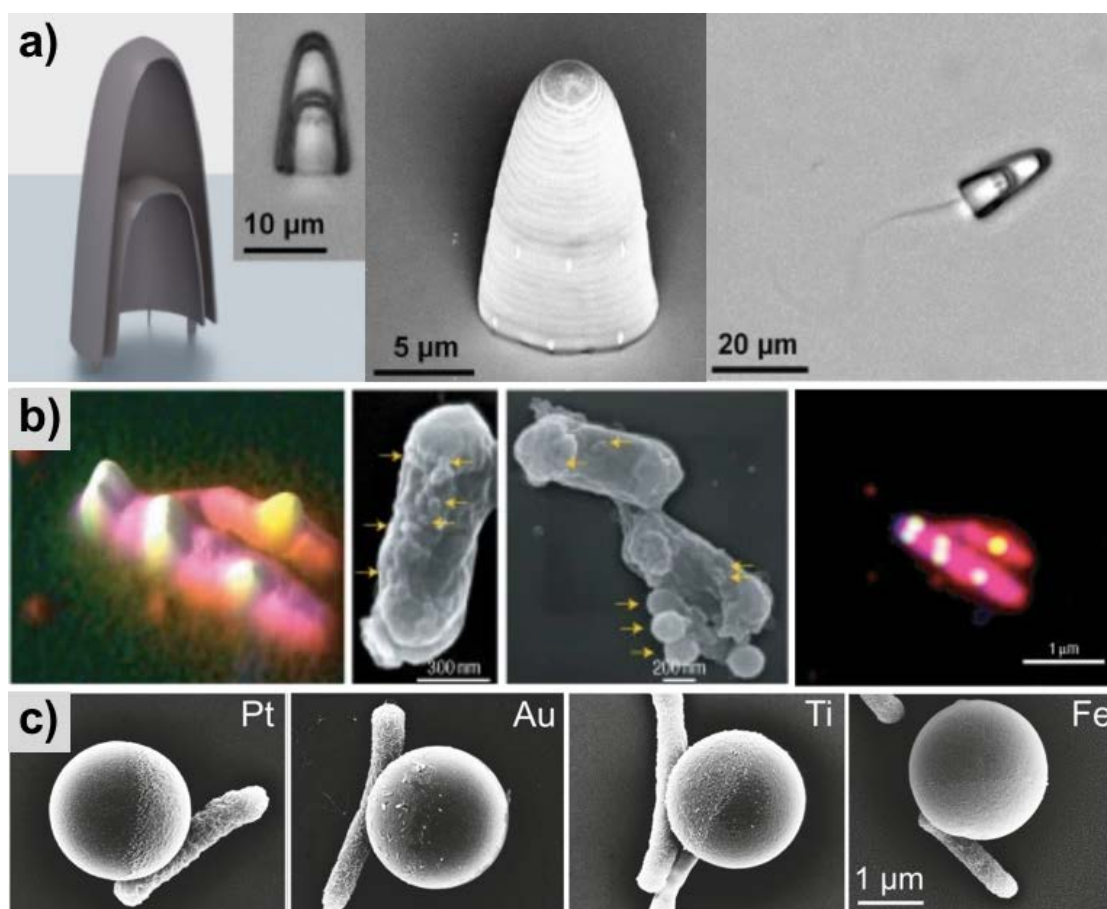


**Figure 4.** Biohybrid micromotors. a) Sperm-powered micromotor based on a streamlined microtube. Adapted from Striggow *et al*,<sup>178</sup> with permission from the publisher. b) Bacterial biohybrids coupled to cargo-loaded nanoparticles. Adapted from Akin *et al*,<sup>158</sup> with permission from the publisher. c) Janus biohybrids powered by *E. coli*. Adapted from Stanton *et al*,<sup>167</sup> with permission from the publisher.



Biohybrids composed of several bacteria lack directionality, since each bacterium exerts force in a different direction. To achieve better control, Zhuang and Sitti investigated the chemotactic behavior of a biohybrid motor driven by several *S. marcescens*. This motor actively moved towards a gradient of L-serine with consistent speed.<sup>161</sup> The same group reported the fabrication of a multifunctional hybrid micromotor, composed by a polyelectrolyte multilayer magnetic microparticle, loaded with a model drug cargo and coupled to *E. coli* bacterium.<sup>162</sup> These motors could be guided via magnetic fields, and exhibited biased directional motion towards aspartate. Researchers also worked into coupling a single bacterium to synthetic entities, paying special attention to the adhesion between the two components of the biohybrids. Stanton *et al* systematically studied the affinity of *E. coli* to different metals, for the fabrication of bacteria-powered micromotors. For this, the authors developed Janus particles, where polystyrene particles were half coated with either Fe, Ti, Au or Pt (**Figure 4c**) and the latter revealed to yield better results compared to the others, indicating that surface hydrophobicity played a key role for bacteria adhesion.<sup>167</sup>

The design of bacteria-powered swimmers could potentially be improved by changing the shape of their synthetic component, since spherical particles induce torque and rotational motion, which in turn reduce net displacement. Stanton and co-workers reported the first biohybrid that did not comprise a spherical chassis. Instead, the authors designed a polydopamine microtube capable of partially entrapping a single bacterium and exhibiting increased unidirectional speed.<sup>168</sup> Stanton *et al* further explored this strategy using magnetotactic bacteria and mesoporous silica microtubes loaded with antibiotics, demonstrating the versatility of chassis used for the development of biohybrids and their potential to dismantle biofilms.<sup>166</sup>

In addition to sperm and bacteria, other motile living organisms, such as algae,<sup>169</sup> monocytes,<sup>170</sup> or neutrophils<sup>176</sup> were also explored as means to power the motion of micro-scaled loads.

### 1.3.2. Externally Powered Nano- and Micromotors

Externally powered nano- and micromotors are fuel-free machines that take up physical inputs for their propulsion. Light irradiation has been extensively studied as a source of energy to power the motion of nano- and micromotors, since it brings advantages as wireless and remote propagation, tunability and reversibility, which allow the light-powered motors to be controlled in a non-invasive manner, with precise spatial and temporal resolution.<sup>205</sup> The nano- and micromotors propelled by light-irradiation must contain a photoactive material in their composition, which can either perform photochemical reactions (photocatalytic), convert the absorbed light into heat (photothermal), or induce isomerization (photochromic). These light-triggered processes lead to the generation of an asymmetric field of products or energy across the motors, which in turn provokes their active motility.

Photochemically powered nano- and micromotors are among the most thoroughly explored in light-propulsion, where photocatalytic reactions give rise to bubble nucleation or generate a gradient of solute, thus pushing the motors forward. In the latter case, the propulsion of micro motors can be based on self-electrophoresis,<sup>206–208</sup> diffusiophoresis,<sup>209–212</sup> or thermophoresis phenomena. Silver chloride was widely explored as a photochemically active material to develop light-powered nano- and micromotors of different shapes and with interesting motility behaviors. The motion patterns of AgCl spherical particles under ultraviolet (UV) light were investigated. The authors showed that these motors could exhibit three different

diffusive dynamics (ballistic propulsion, enhanced diffusion and subdiffusion), as well as active schooling and coupling.<sup>209,213,214</sup> The effect of shape and, therefore, number of active sites on the propulsion of light-powered micromotors based on AgCl was also studied by Simmchen *et al*, where the authors demonstrate that a micro-star shaped motor facilitated motility (**Figure 5a**).<sup>212</sup>

The photocatalytic abilities of titanium dioxide were also probed in the fabrication of motors. In this sense, Hong and co-workers reported on the ability of TiO<sub>2</sub> micromotors to not only propel, but also exhibit expansion-contraction behaviors under UV light. The authors hypothesized that the motility arose from the uneven distribution of chemical species, such as O<sub>2</sub><sup>-</sup>, OH radicals or H<sup>+</sup>.<sup>215</sup> However, this material has a wider absorption spectrum, which allows the use of wavelengths other than the UV region for light-powered propulsion. In this sense, Jang *et al* reported the fabrication of black TiO<sub>2</sub> and Au micromotors capable of propelling under exposure to a broad range of wavelengths (**Figure 5b**).<sup>216</sup> In turn, Wang and co-workers fabricated nanocap-shaped nanomotors based on Au-TiO<sub>2</sub> shells, and showed their motility powered by visible light. The authors attributed the motility to a plasmon resonance effect leading to self-electrophoresis between the two metallic layers of the nanocaps.<sup>217</sup> Similarly, micromotors based on bismuth oxyiodide<sup>218</sup> or copper oxide coated with light-inert materials were also shown to propel under visible light.

The ability of light-powered motors to exhibit taxis was also investigated. Dai *et al* fabricated a nanotree comprising TiO<sub>2</sub> and silica, which upon exposure to light acted as a photocathode and a photoanode, respectively, leading the propulsion of nanotrees (**Figure 5c**). These motors were able to self-align in the direction of light propagation, and exhibit positive or negative phototaxis depending on the surface charge of the silica tail.<sup>208</sup>

Besides photocatalysis, the development of light-powered motors also relies on the use of photothermal materials, where the generation of a temperature gradient across asymmetric particles upon continuous light irradiation leads to displacement of the surrounding fluid, resulting in active motion.<sup>219–224</sup> In this sense, Xuan *et al* reported a Janus mesoporous silica/Au motor, driven by NIR light due to the generation of a net thermophoretic force along the asymmetric motor, which enabled the motor to propel at an ultrafast speed.<sup>223</sup> The generation of thermal gradients along Janus motors was also exploited by Jiang and co-workers,<sup>220</sup> as well as Qian and colleagues,<sup>221</sup> who used Au as photothermal material.

Confined structures, such as tubular cavities, instead of inherently asymmetric particles can also be used to achieve propulsion via generation of temperature gradients. Wu *et al* fabricated a superfast multilayer rocket functionalized with Au in the inner cavity. The rockets propelled upon irradiation with NIR light due to the generation of a high temperature gradient between the inner and outer surfaces, providing the motors with impressive speed (**Figure 5d**).<sup>225</sup> Tubular structures also favor propulsion via bubble-recoil mechanism, since the cavity hinders the diffusion of gases, which then nucleate into bubbles that push the motors forward upon ejection. Mou *et al* exploited this effect to develop a TiO<sub>2</sub> microtubular motor propelled by the photocatalytic decomposition of hydrogen peroxide.<sup>226</sup> By modulating the temperature of the motors, and thus their photocatalytic activity, it is possible to control the bubble release frequency. Similarly, Giudicatti *et al* fabricated a micromotor with tubular shape using roll-up technology, which propelled due to the photocatalytic activity of TiO<sub>2</sub> under UV light.<sup>227</sup> Wu and co-workers evidenced this using a tube-shaped multilayered motor

functionalized with a Au shell and Pt nanoparticles. The authors showed that the motility of the tubular microengines was not observed by simple addition of hydrogen peroxide, but could be switched on with NIR light.<sup>228</sup> Nevertheless, this type of motion mechanism is not entirely fuel free, and makes use of toxic chemicals such as hydrogen peroxide for bubble generation.

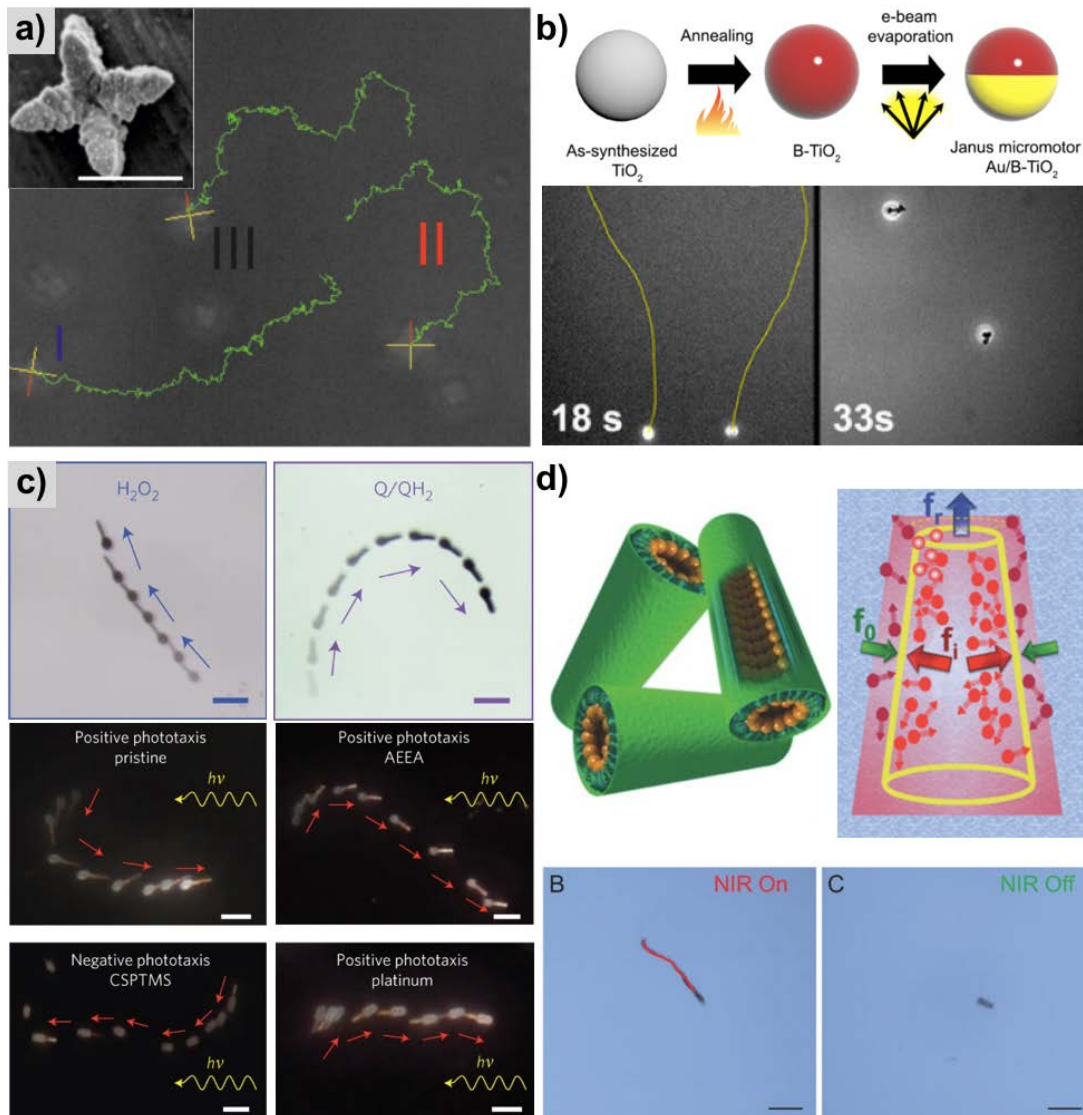


**Figure 5.** Light-powered nano- and micromotors. a) AgCl microstar-shaped motors and their propulsion under UV light. Adapted from Simmchen *et al.*,<sup>212</sup> with permission from the publisher. b) Black TiO<sub>2</sub> Janus nanomotors propelled by visible light. Adapted from Jang *et al.*,<sup>216</sup> with permission from the publisher. c) Light-powered nanotrees exhibiting positive and negative phototaxis. Adapted from Dai *et al.*,<sup>208</sup> with permission from the publisher. d) Light-powered rockets propelled by NIR irradiation. Adapted from Wu *et al.*,<sup>228</sup> with permission from the publisher.

Another external source of power to propel nano- and micromotors are magnetic fields, which do not require high intensity lasers, offer remote guidance abilities, and are minimally affected by the surrounding medium. These motors can either use rotating magnetic fields, where the magnetic induction vector rotates at a fixed frequency in space, provoking a torque in magnetic structures. Zhang *et al* explored this effect to propel and steer artificial bacterial flagella consisting of a spiral rod tail and a soft magnetic head, showing their displacement and control over directionality under homogeneous magnetic fields.<sup>229</sup> Schamel and co-workers

also used magnetic fields to propel a nanosized helix-shaped propeller and study their locomotion through macromolecular meshes of biologically relevant fluids and gels (**Figure 6a**).<sup>230</sup> However, in water or water-like solutions, these nanomotors were unable to overcome thermal fluctuations and display directional motion, as previously predicted through simulations.<sup>231</sup> Other magnetic nano and micromotors actuated using rotating fields were reported, showing their ability to probe hydrodynamic forces such as shear and vorticity,<sup>232</sup> as well as towing different cargos,<sup>232–234</sup> controlled motility in patterned surfaces,<sup>235</sup> and navigation through mucus and tissues.<sup>236–238</sup> Oscillating magnetic fields were also used to power the propulsion of nano- and micromotors of diverse shapes and compositions. For instance, Dreyfus and co-workers reported the fabrication of an artificial flagellum made of a linear chain of colloidal magnetic particles linked by DNA attached to a red blood cell. This flagellum aligned with a uniform magnetic field and upon exposure to an oscillating field exhibited a beating behavior that led to propulsion.<sup>239</sup> Liu *et al* also used oscillating magnetic fields to propel a worm-like wrinkly micromotor composed of iron and nickel (**Figure 6b**).<sup>240</sup> In turn, Li and colleagues reported the fabrication of a magnetic walker - a dimeric micromotor composed of Janus microparticles capable of rolling back and forth in an alternating manner - which could be steered through defined paths.<sup>241</sup>

Alternatively, electric fields can also be used as an external energy source to propel nano- and micromotors.<sup>242–247</sup> In this case, the electric energy is converted to motion, through mechanisms such as the generation of electro-osmotic or electrohydrodynamic flows. Chang *et al* reported a micro-semiconductor diode motor, capable of rectifying current internally which leads to generation of electro-osmotic flows pushing the motor forward (**Figure 6c**).<sup>247</sup> Similarly, Calvo-Marzal and co-workers showed the electric-field powered motility of a semiconductor diode nanowire.<sup>244</sup>

Ni and co-workers took a radically different strategy, designing clusters of colloidal molecules connected through capillarity-assisted particle assembly. These charged particles were able to deform vertical electric fields and drive the induced charge on the electrodes, provoking an electrodynamic flow that led to active motion.<sup>246</sup>

In another approach, Loget and Kuhn presented a new concept for triggered motility, where the applied electric field led to the polarization of the motors, causing redox reactions and gas bubble formation, and thus directional motion and rotation (**Figure 6d**).<sup>245</sup>

Even though progress has been made in powering propulsion recurring to electric fields, these motors may lack controllability and practicality for biomedical applications.

Other alternative actuator of externally powered nano- and micromotors are ultrasound waves, which are widely used in clinics and offer advantages such as speed and deep tissue penetration. Several motors with different shapes and sizes powered by ultrasonic standing waves were developed.<sup>248–252</sup> Wang *et al* reported the design of asymmetrical bimetallic nanorods, comprising Au in the concave end and Ru in the convex end.<sup>250</sup> Upon exposure to ultrasounds, an uneven sound pressure distribution was originated due to the asymmetry of the nanorods structure, which induced their motility. Similarly, Ahmed and colleagues showed the ultrasonic actuation and magnetic steering of a Au-Ni-Ru nanowire in phosphate buffer (**Figure 6e**).<sup>251</sup>



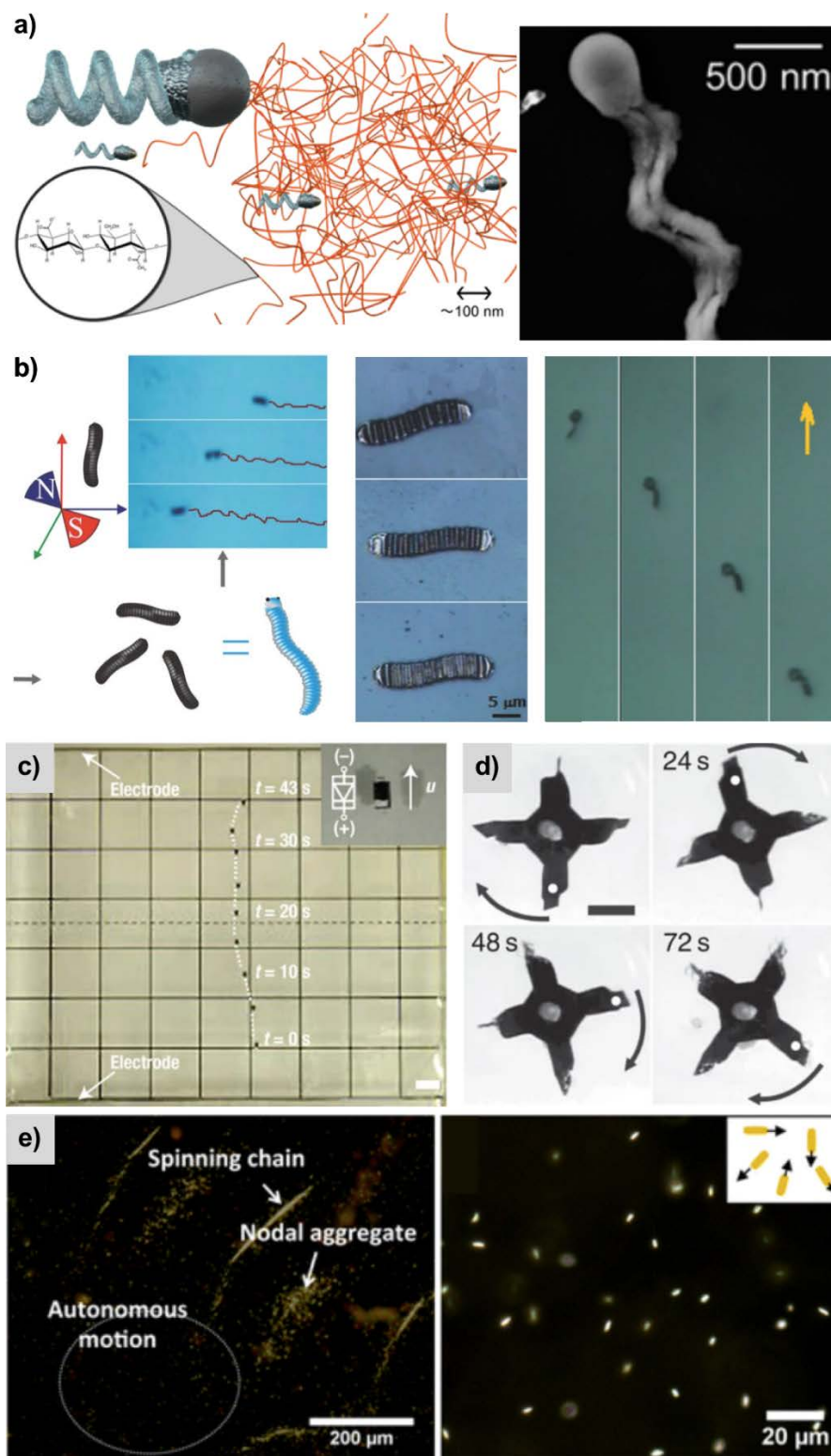


**Figure 6.** Nano/ and micromotors powered by external magnetic-, electric- and ultrasound fields. a) Helix-shaped magnetic motor capable of moving through viscoelastic media. Adapted from Schamel *et al.*,<sup>230</sup> with permission from the publisher. b) Annelid-like magnetic motor moving upon exposure to oscillating magnetic fields. Adapted from Liu *et al.*,<sup>240</sup> with permission from the publisher. c) Semiconductor diode motor powered by electric fields. Adapted from Chang *et al.*,<sup>247</sup> with permission from the publisher. d) Electric-field powered rotation of micro-objects due to redox reactions. Adapted from Loget and Kuhn,<sup>245</sup> with permission from the publisher. e) Ultrasound-powered propulsion of a Au-Ni-Ru nanowire. Adapted from Ahmed *et al.*,<sup>251</sup> with permission from the publisher.

In addition, Wang *et al* developed Au nanorod motors powered by ultrasound and showed their propulsion within living cancer cells.<sup>253</sup> The abilities of ultrasound-powered Au-based nanowires to carry different cargos such as drugs,<sup>248,254</sup> nucleic acids,<sup>255,256</sup> and protein were also demonstrated.<sup>256–258</sup>

In a different approaches, Wu *et al* used red blood cells as a chassis to develop ultrasound powered motors, incorporating iron oxide nanoparticles,<sup>259</sup> and Sabrina *et al* reported the acoustic motility of shape-dependent microspinners.<sup>260</sup>

Acoustic droplet vaporization was also used to propel motors via ultrasound. Kagan *et al* demonstrated this effect loading tubular structures with perfluorocarbon, which upon ultrasound exposure vaporized causing a powerful thrust that propelled the microtubes.<sup>249</sup>

Recently, McNeill *et al* reported the wafer-scale fabrication of motors with variable sizes, propelled via/bubble ejection powered by ultrasonic waves.<sup>261</sup> Ren *et al* fabricated micromotors with 3D steering features and able to propel at low power acoustic force.<sup>262</sup>

### 1.3.3. Chemically Powered Nano- and Micromotors

The use of free chemical energy present in the surrounding environment is an ingenious strategy to power the motion of nano- and micromotors, which avoids the use of burdensome and expensive equipment. This type of motors typically consists of a chassis, which can have a myriad of different shapes and compositions, and/or a material (organic or inorganic) able to react with molecules in the fluid.

The use of inorganic materials to power the propulsion of motors can be divided in two major categories: motors comprising *i)* elements or alloys that react with water, or *ii)* inorganic catalysts.

The first report of a water-driven was microsphere of Al-Ga alloy partially coated with titanium. The exposed alloy hemisphere ejected hydrogen bubbles upon contact with water, providing the micromotor with directional motion at remarkable speed (**Figure 7a**).<sup>263</sup> To avoid toxicity caused by the leaching of Al and Ga species, other elements were also exploited to fabricate water-driven motors. For instance, Gao *et al* presented a Zn-based electro-deposited polyaniline/Zn microrocket, which moved in extremely acidic media due to the redox reactions taking place at the inner Zn cavity.<sup>264</sup> The same group later demonstrated the use of tubular Zn micromotors for combinatorial delivery of cargoes such as silica and Au nanoparticles.<sup>265</sup> Mg is also of considerable interest to power the propulsion of motors, as it can use acid or water to react and generate bubbles, thus enabling the use of the motors in various environments. These motors have been reported to show propulsion in seawater,<sup>266</sup> serum,<sup>267</sup> as well as simulated body fluid and blood plasma.<sup>268</sup>

Even though water-driven motors present several advantages towards the operation in biological media, they typically incorporate noble metals in their composition, which can remain in the body and cause toxic responses. To circumvent this issue, Chen and co-workers investigated different designs of motors based on transient materials (*e.g.* Mg, ZnO, Si, Zn and Fe) and demonstrated their degradability (**Figure 7b**).<sup>269</sup> In turn, Zhou and colleagues, reported the fabrication of a biodegradable poly(aspartic acid)/Fe–Zn microrocket which was able to propel in gastric acid.<sup>270</sup> Calcium carbonate is another example of inorganic material that is highly biocompatible and has been used to fabricate micromotors. Jia and co-workers used CaCO<sub>3</sub> as base material for the development of micromotors that can glide on microtubules with considerable velocities, by converting ADP into ATP via creatine phosphate kinase activity.<sup>271</sup> In another work, Guix *et al* used CaCO<sub>3</sub>

microspheres as both chassis and propulsion engine for the development of micromotors, which were able to propel in acidic environments due to the reaction between the carbonate and the acid in the media (**Figure 7c**).<sup>272</sup>

The propulsion of nano- and micromotors was also achieved using inorganic catalysts. In this sense, the motors were designed incorporating elements capable of catalyzing the decomposition of molecules present in the surrounding medium and converting the resulting energy into net displacement. This type of motors has been widely investigated since their onset with the pioneer works of Whitesides,<sup>273</sup> Sen, Mallouk<sup>274</sup> and Ozin's groups.<sup>275</sup> Even though these pioneer systems presented different propulsion mechanisms, the common thread among these works was the use of hydrogen peroxide as fuel for propulsion.

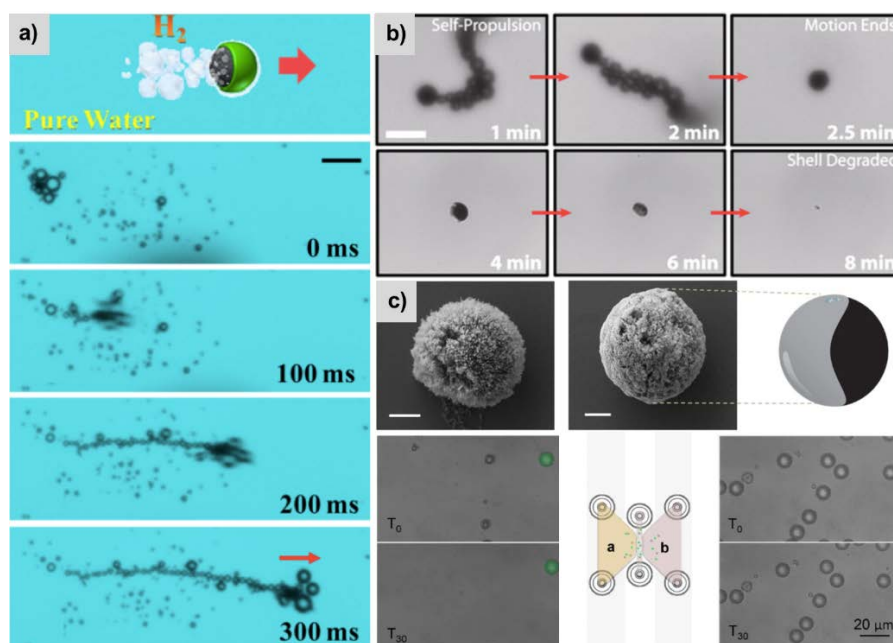


**Figure 7.** Chemically powered motors propelling through reactions with water. a) Al-Ga alloy-based micromotor moving in pure water by bubble ejection. Adapted from Gao *et al.*,<sup>263</sup> with permission from the publisher. b) Transient micromotors that degrade after propelling. Adapted from Chen *et al.*,<sup>269</sup> with permission from the publisher. c) CaCO<sub>3</sub> based motors propelling in acidic media. Adapted from Guix *et al.*,<sup>272</sup> with permission from the publisher.

The most typical inorganic catalyst used to fabricate these motors is Pt, and through the years several shapes and design were reported. Janus nano- and microparticles of different compositions, half coated with Pt, using techniques such as sputtering or electron-beam deposition, were widely used for fundamental studies on active matter due to their simplistic arrangement.<sup>276–288</sup> For instance, Simmchen *et al.* investigated the topographical guidance of Pt-based active Janus colloids (**Figure 8a**),<sup>287</sup> while Volpe and co-workers focused on the motility in patterned environments.<sup>288</sup> Rods and tubular structures, where Pt is asymmetrically distributed towards one end of the rod, or enclosed in the tube inner cavity, were developed using diverse materials.<sup>289–292</sup>

Electrochemical deposition was used to fabricate rod-shaped Pt based motors. In this regard, multiple examples of rod-shaped motors were demonstrated, using Pt in combination with other metals such as Au,<sup>145,293–295</sup> Ru,<sup>295</sup> and Cu.<sup>296</sup>

Laocharoensuk *et al* boosted the speed of bimetallic nanowire motors by combining carbon nanotubes with the Pt catalyst. The authors hypothesized that this combination led to increased electrocatalytic activity towards hydrogen peroxide, and improved internal electron transfer, thus leading to higher speeds.<sup>297</sup> Demirok *et al* also reported the increase in speed of nanowire-shaped nanomotors by using Ag/Au alloys instead of pure Au segments (**Figure 8b**).<sup>298</sup>

Tubular structures were also explored for the development of catalytic motors. For instance, Solovev *et al* reported the fabrication of tubular motors using roll-up technology. These motors propelled due to the catalytic conversion of hydrogen peroxide by the Pt placed in the inner layers of the tubes. In addition, by introducing an Fe thin film into the tubes, the authors were able to control the motors directionality.<sup>299</sup> Solovev *et al* later reported another tubular motor consisting in InGaAs/GaAs/(Cr)Pt fabricated with the same technology, and its application as a nanotool for micromanipulation.<sup>289</sup> Sánchez *et al* took advantage of roll-up technology to develop Ti/Fe/Pt tubular motors, showing their ability to manipulate cells.<sup>300</sup> Later, Parmar *et al* used the same technology to develop Fe/Pt multi-functional motors and explored their use as environmental remediation tools (**Figure 8c**).<sup>292</sup>

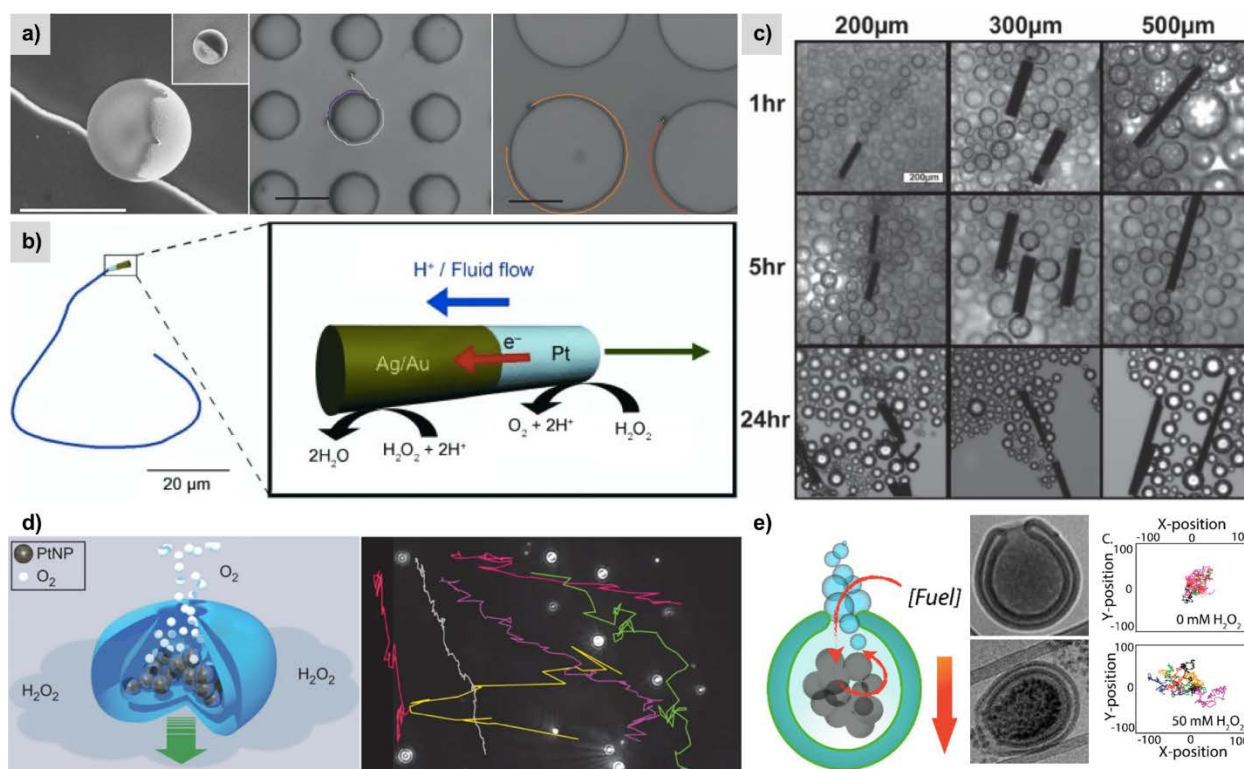


**Figure 8.** Nano- and micromotors powered by inorganic catalysts. a) Silica/Pt-based Janus micromotor guided by topographical pathways. Adapted from Simmchen *et al*,<sup>287</sup> with permission from the publisher. b) Ag-Au alloy nanowire motors propelled by hydrogen peroxide catalysis. Adapted from Demirok *et al*,<sup>298</sup> with permission from the publisher. c) Microtubular motors fabricated by roll-up technology, moving due to catalytic conversion of hydrogen peroxide by Pt. Adapted from Parmar, *et al*,<sup>292</sup> with permission from the publisher. d) Stomatocyte nanomotors containing Pt nanoparticles in the inner cavity. Adapted from Wilson *et al*,<sup>301</sup> with permission from the publisher. e) Stomatocyte nanomotor powered by catalysis of hydrogen peroxide by manganese oxide nanoparticles. Adapted from Pijpers *et al*,<sup>302</sup> with permission from the publisher.



Wu *et al* also explored tubular structures as chassis for Pt-based catalytic motors. The authors used template-assisted layer-by-layer assembly to develop a tubular motor where the inner cavity was functionalized with Pt nanoparticles, leading to motion via ejection of oxygen bubbles.<sup>303</sup>

Vilela *et al* used sequential electrochemical deposition to create a multifunctional microtubular motor, which consisted of multilayers of graphene oxide, nickel, and platinum. The authors showed efficient motility in the presence of hydrogen peroxide, as well as the ability to capture several heavy metals from contaminated water.<sup>139</sup>

Besides spherical, rod and tubular shapes, other configurations were also tested in the design of chemical motors based on inorganic catalysts. Stomatocytes, which are bowl-shaped polymersomes made of block copolymers, can entrap the catalysts within the bowl cavity, allowing the asymmetric release of the reaction products. Wilson *et al* pioneered the use of such geometries as nanomotors. The authors loaded Pt nanoparticles in the stomatocyte cavities and reported their autonomous movement due to the localized release of oxygen and water (**Figure 8d**).<sup>301</sup> The versatility of these structures was also demonstrated, showing temperature modulation of speed,<sup>304</sup> magnetic control over directionality,<sup>305</sup> ability load cargos and exhibit chemotaxis,<sup>306</sup> as well as biodegradability and triggered cargo release.<sup>307–309</sup>

Beyond Pt, other inorganic catalysts were explored to power the propulsion of different nano- and micromotors. Parmar *et al* demonstrated cobalt ferrite cluster micromotors and their ability to degrade antibiotics.<sup>310</sup> In addition, Villa *et al* used manganese oxide to propel mesoporous silica-based microtubular motors, taking advantage of motility and surface functionalities to remove heavy metals and organic pollutants from contaminated waters.<sup>138</sup> Pijpers *et al* fabricated stomatocytes based on biodegradable poly(ethylene glycol)-block-poly(D,L-lactide) block copolymers (**Figure 8e**), and loaded them with manganese oxide nanoparticles, that upon reaction with hydrogen peroxide at very low concentrations led to the bubble-propulsion of the stomatocytes.<sup>302</sup>

#### 1.3.4. Enzyme-powered nano- and micromotors

The use of enzymatic catalysis emerged as an ingenious and biofriendly alternative to inorganic catalysts,<sup>311–313</sup> bringing several advantages, such as the use of *in situ* fuels,<sup>314</sup> capacity to modulate their surrounding environment,<sup>238</sup> and to be tailor-made to specific applications due to the wide variety of enzymes available.

A variety of nano- and micromotors, consisting of different base materials and shapes have been reported thus far.<sup>315–329</sup> Structures based in inorganic materials were investigated for the development of enzyme-powered nano- and micromotors. Sánchez *et al* demonstrated the use of catalase to power the propulsion of rolled-up microtubes via bubble expulsion mechanism in the presence of hydrogen peroxide (**Figure 9a**).<sup>330</sup> However, since catalase requires the use of a toxic substrate, the quest to develop fully biocompatible motor/fuel complexes led to the use of other enzymes.

Silica -based materials, in particular mesoporous silica, offer a wide range of advantages for the fabrication of nano- and micromotors for biomedical applications. This material is well-known and studied, has a high surface area and high cargo loading capacity. Furthermore, silica is reported to present good

biocompatibility and it is General Recognized As Safe (GRAS) by the Food and Drug Administration (FDA).<sup>331</sup> In addition, its easy surface chemistry allows several possibilities of surface modifications, such as conjugation of enzymes, antibodies or cargos. In this sense, Sánchez's group demonstrated the use of different enzyme as engines to power the motion of silica based nano- and microparticles.<sup>316,317,320,324</sup> Ma *et al* showed the enzyme-powered propulsion of mesoporous silica based Janus nanomotors (**Figure 9b**).<sup>324</sup> The authors broke symmetry by depositing silica on one half of the particles, and functionalizing the other half with enzymes, namely urease, catalase or glucose oxidase. The active propulsion of the Janus enzymatic nanomotors in the presence of the specific substrates was characterized by tracking their displacements using optical microscopy, and by DLS. Furthermore, the authors used optical tweezers to measure the force exerted by the motors, revealing a driving force around 60 fN applied on a catalase-powered nanomotor.<sup>324</sup> Moreover, Ma *et al* reported the use of urease as engine to power the propulsion of Janus hollow mesoporous silica microcapsules.<sup>317</sup> The authors showed that the capsule micromotors were able to transport cargoes such as nanoparticles, and their direction of motion could be controlled by a magnetic field due to the Ni element coated on one side of the motors via electron-beam deposition. In addition, Schattling *et al* immobilized catalase and glucose oxidase onto one face of Janus silica particles, and demonstrated their enhanced diffusion (**Figure 9c**).<sup>332</sup>

Apart from silica, materials such as gold nanorods and metal-organic frameworks (MOF) were studied as chassis of enzymatic nanomotors.<sup>318,333</sup> Pavel *et al* and Bunea *et al* tested several enzymes, including glucose oxidase, glutamate oxidase xanthine oxidase, horseradish peroxidase and catalase and achieved propulsion of polypyrrole-gold nanorods.<sup>334,335</sup> The authors observed a substrate-dependent enhanced diffusion of the nanorods and explained it by self-electrophoresis mechanism, based on the bio-electrochemical reactions. Moreover, You and co-workers developed MOF-based nanomotors functionalized with glucose oxidase and catalase and demonstrated their motility in the presence of hydrogen peroxide.<sup>318</sup> The authors exploited the enhanced generation of oxygen radicals upon near-infrared irradiation for photodynamic therapy, showing the potential of these systems in nanomedicine.

The power of enzyme catalysis was also used to achieve the propulsion of several organic structures. For instance, Mano and Heller coupled glucose oxidase and bilirubin oxidase onto a macroscale carbon fiber. This macro-fiber motor moved at the air-liquid interface as a result of the bio-electromechanical power generated by glucose catalysis (**Figure 9d**).<sup>336</sup> In addition, Pantarotto *et al* employed the combination of glucose oxidase and catalase enzymes to propel one-dimensional carbon nanotubes by bubble expulsion mechanism.<sup>337</sup>

Dey *et al* demonstrated the propulsion of polystyrene microparticles powered by urease and catalase. In this case, the authors used biotin-streptavidin linkage to immobilize two individual enzymes, catalase, and urease, onto the surface of the polystyrene particles. Upon investigating the motion of the micromotors by optical microscopy and DLS techniques, the authors hypothesized that a thermal effect due to the exothermic nature of the enzymatic reactions could be the origin of the micromotors self-propulsion.<sup>319</sup>

Polymeric structures were also studied as chassis for nano- and micromotors. Abdelmohsen *et al* loaded a combination of catalase and glucose oxidase into supramolecular stomatocytes. The glucose present in the

fluid was converted into gluconic acid and hydrogen peroxide. The latter was then converted by catalase into water and oxygen, which formed bubbles that were expelled from the small cavity of the bowl-shaped stomatocytes, leading to their active motility (**Figure 9e**).<sup>325</sup>

Nijemeisland and co-workers added an extra level of complexity to multiple enzyme systems and explored the cascade reactions of a chain of enzymes to power the propulsion of stomatocytes. The authors rationally designed an enzymatic network with multiple feedforward loops, comprising horseradish peroxidase, L-Lactate oxidase, hexokinase, and glucose-6-phosphate dehydrogenase. These feedforward loops were activated in the presence of glucose, and their action ultimately led to the production of oxygen bubbles, which were expelled through the cavity of the bowl-shaped stomatocytes providing them propulsion.<sup>338</sup> In another work, Che *et al* developed a stomatocyte with transient behavior mediated by ATP and apyrase. This nanosystem was decorated with polylysine (PLL), and the interaction of PLL with ATP led to the closing of the cavity, while the addition of ATP-consuming apyrase caused its opening (**Figure 9f**).<sup>339</sup>

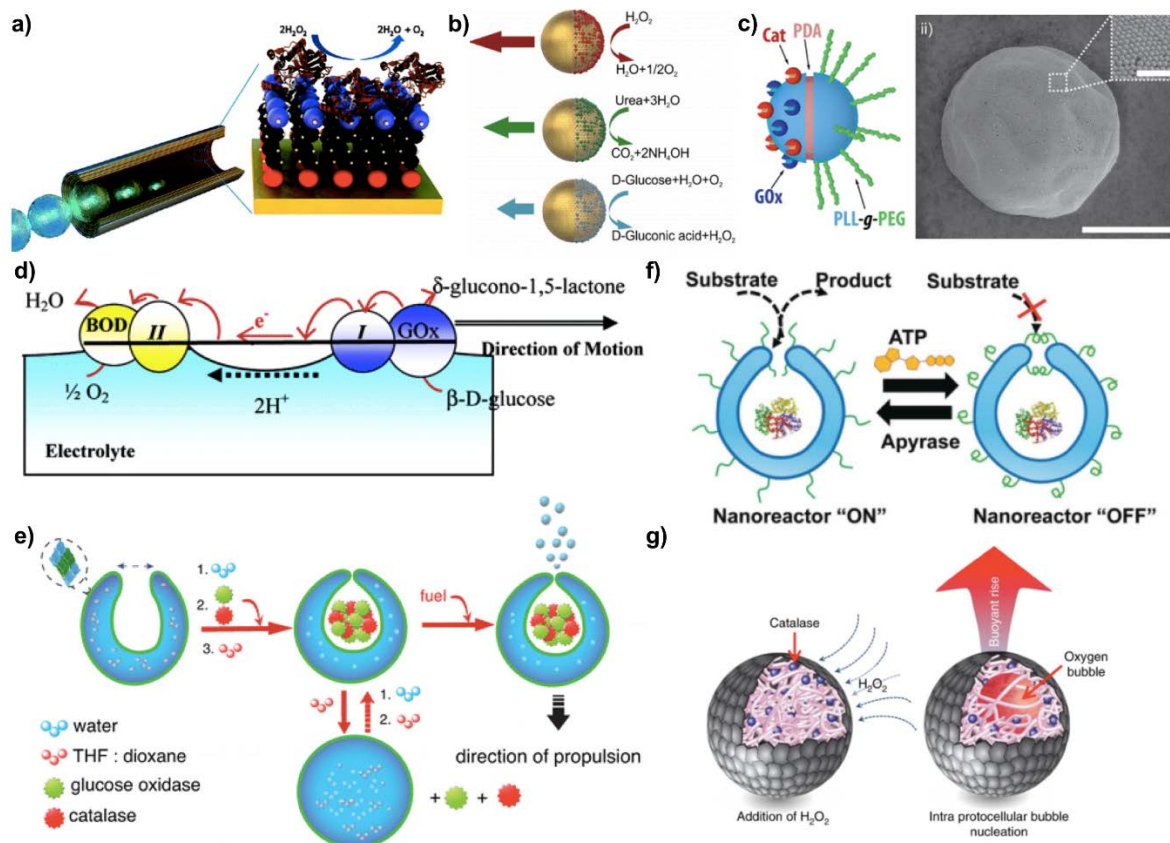


**Figure 9.** Nano- and micromotors powered by enzymatic catalysis. a) Microtubular motor fabricated by roll-up technology and powered by catalase. Adapted from Sanchez *et al*,<sup>330</sup> with permission from the publisher. b) Enzymatic nanomotors based on Janus mesoporous silica nanoparticles. Adapted from Ma *et al*,<sup>324</sup> with permission from the publisher. c) Silica-based Janus nanomotors powered by catalase and glucose oxidase. Adapted from Schattling *et al*,<sup>332</sup> with permission from the publisher. d) Carbon fiber nanomotor powered by bilirubin oxidase and glucose oxidase. Adapted from Mano and Heller,<sup>336</sup> with permission from the publisher. e) Stomatocyte nanomotor powered by glucose oxidase and catalase. Adapted from Abdelmohsen *et al*,<sup>325</sup> with permission from the publisher. f) Stomatocyte motor with transient behavior mediated by apyrase. Adapted from Che *et al*,<sup>339</sup> with permission from the publishers. g) Organoclay-based buoyant motor propelled by the biocatalytic decomposition of hydrogen peroxide. Adapted from Kumar *et al*,<sup>340</sup> with permission from the publishers.

Schattling *et al* also investigated polymeric materials for the fabrication of enzymatic nanomotors. In this work, the authors used PLL/PMA particles and combined them with PtNPs, glucose oxidase enzymes, and trypsin to achieve a double-fueled motor, leading to an enhancement in the diffusivity of the motors.<sup>341</sup>

Other polymer-based structures have been used as chassis for nano- and micromotors. Joseph *et al* reported the design of asymmetric synthetic vesicles, called polymersomes, based on the self-assembly of amphiphilic copolymers in water.<sup>342</sup> These polymersomes encapsulate glucose oxidase and catalase in the inner compartment, which upon the presence of a gradient of glucose lead to the propulsion of the polymersome motors via expulsion of reaction products through the semi-permeable fraction of the vesicle.

Traditional liposomes were also demonstrated as chassis for micromotors. Ghosh *et al* reported the use of transmembrane ATPase to power the propulsion of liposome vesicles, observed using fluorescence correlation spectroscopy.<sup>329</sup> In a subsequent work, Somasundar *et al* reported the positive and negative chemotaxis (displacement toward or further away from the substrate) of enzyme-powered liposome vesicles, using not only ATPase, but also catalase and urease as engines.<sup>328</sup>

Other organic materials were also reported as scaffolds/chassis for the fabrication of enzymatic motors. Kumar *et al* the motility of organoclay-DNA protocells co-encapsulating catalase and glucose oxidase. These structures demonstrated sustained buoyant movement in an oscillatory and vertical manner (**Figure 9g**).<sup>340</sup> In a distinct approach, Li and co-workers developed a tadpole-like molecular bottlebrush nanomotor, propelled by catalase.<sup>343</sup> These motors exhibited propulsion in water and also in a tumor microenvironment gel model containing breast cancer cells, showing promise for biomedical applications. Wu *et al* fabricated catalase-powered Janus capsules composed of poly(styrenesulfonate) sodium salt and poly(allylamine hydrochloride, via template assisted polyelectrolyte layer-by-layer techniques.<sup>344</sup> Following a similar approach, Wu *et al* also developed biodegradable poly-L-lysine/BSA based micro-rockets that propelled due to biocatalytic decomposition of hydrogen peroxide.<sup>345</sup> Furthermore, Tang *et al* used platelets as the chassis for a Janus enzymatic micromotor.<sup>346</sup> The authors showed the potential of the platelet-based urease motors demonstrating their motility in the presence of substrate urea.

The extensive work on the use of enzymes and combinations thereof to function as engines to power the propulsion of nano- and microstructures also led to the interest of the community in unravelling fundamental aspects intimately connected with their motility. For instance, the degree of asymmetry necessary to achieve self-propulsion is still under investigation. The stochastic coating of enzymes onto nano- and microstructures to power their motility was reported.<sup>316,319–321</sup> In this sense, Patiño and co-workers used super-resolution microscopy to explore the stochastic binding of enzymes to motors and the formation of patches to break the symmetry, thus allowing propulsion.<sup>316</sup> Apart from symmetry breaking, other aspects are crucial for the design of enzymatic nano- and micromotors, such as the biocatalytic properties of the enzymes chosen,<sup>320</sup> and the properties of the surrounding medium, as it has been reported that the presence of ionic species in the surrounding medium has a detrimental effect in the motion of catalytic motors.<sup>347–350</sup>

Despite the efforts devoted to investigating the mechanisms underlying synthetic motion at the nano- and microscales, this concept remains unclear. Fundamental studies provide a deeper understanding on the

factors governing catalytic motion, which is paramount for the rational design of enzymatic nano- and micromotors.

In this thesis, the work is focused on the potential biomedical applications of enzyme-powered nanomotors, which do not require external power sources and harness the required energy for propulsion from endogenous bioavailable fuels.

## 1.4. Potential Biomedical Applications of Nano- and Micromotors

Despite its infancy, the field of nano- and micromotors devoted considerable attention to nanomedicine. The research community explored combinations of biocompatible chassis and propulsion sources and demonstrated proof-of-concept biomedical applications of motors taking advantage of their unique capabilities arising from motility, namely aiding in the penetration of complex biological structures,<sup>314,351–353</sup> and performing superior drug delivery compared to traditional passive particles.<sup>306–308,354–356</sup>

### 1.4.1. Active Transport and Delivery of Cargos

In the advent phase of research in nano- and micromotors, their continuous and powerful thrust was explored to achieve towing of multiple cargoes.<sup>128,129,131,357,358</sup> In the early proof-of-concept demonstrations, the cargos chosen were mostly synthetic microparticles or ensembles of micro-objects<sup>291,299,357,359</sup>. For instance, Baraban *et al* used catalytic Janus micromotors to carry both single particles and ensembles of particles.<sup>359</sup> Similarly, Solovev *et al* demonstrated the transport and assembly of micro-objects via magnetic control of catalytic tubular microbots (**Figure 10a**).<sup>299</sup> Moreover, Gao *et al* reported on the self-assembly of Janus micromotors and their capability of transporting ensembles of spheres,<sup>127</sup> while Sanchez *et al* reported the transport of microparticles in flow streams of microfluidic channels.<sup>360</sup> Burdick *et al* also took advantage of microfluidic channels to demonstrate the directional motion and controlled transport of a microparticle.<sup>361</sup>

Apart from transporting synthetic materials, researchers also investigated the ability of nano- and micromotors to deliver biological entities, such as whole cells.<sup>135,173,300,362–364</sup> In this regard, Sanchez *et al* demonstrated the transport of multiple cells through a microfluidic chip, as a proof-of-concept demonstration of the applicability of motors in cell sorting and separation.<sup>300</sup> Aiming at the development of novel assisted-fertilization techniques, Medina-Sanchez *et al* showed the delivery of a non-motile sperm cell through the use of helical micromotors.<sup>173</sup> In regards to diagnostic applications, Balasubramanian *et al* fabricated a catalytic microtube capable of detecting, capturing and transporting circulating tumor cells *in vitro* (**Figure 10b**).<sup>135</sup>

The applicability of nano- and micromotors as active nanovehicles for drug delivery was also investigated. Researchers aimed at taking advantage of the continuous momentum provided by the nano- and micromotors to deliver pharmacological actives, such as nucleic acids,<sup>255,256</sup> proteins,<sup>258</sup> and anticancer drugs.<sup>150,307,365,366</sup> In this sense, Esteban-Fernandez de Avila *et al* used ultrasound/powered motors for the delivery of Caspase-3.<sup>258</sup> Similarly, Hansen-Bruhn *et al* demonstrated direct intracellular delivery of a functional Clustered Regularly Interspaced Short Palindromic Repeats (CRISPR) associated protein/single guide ribonucleic acid (RNA) complex, achieving a highly effective (green fluorescent protein) GFP gene knockout (**Figure 10c**).<sup>256</sup>





Considering that one of the major goals in nanomedicine is to achieve the delivery of drugs while avoiding their off-target effects, researchers also centered their focus on investigating strategies to target the drug-loaded nano- and micromotors to specific sites. In this sense, apart from the use of external guidance, researchers incorporated typical strategies from traditional nanomedicine, using cleavable linkers to trigger release the loaded cargo in response to their surroundings.<sup>308,345,356</sup> For instance, Tu *et al* fabricated doxorubicin-loaded stomatocyte nanomotor, which exhibited triggered drug released due to redox reactions (**Figure 10d**).<sup>308</sup> Moreover, Diez and co-workers developed a glucose-mediated motor for the triggered delivery of insulin. This motor consisted of Au and silica, loaded with insulin, which was release on-command in response to presence of glucose.<sup>257</sup> Llopis-Lorente *et al* and Diez *et al* also investigated the use of molecular gates to avoid drug leaching before entering the target cells, developing motors which apart from efficient propulsion in fluids, were able to perform delivery of drugs in response to endogenous stimuli.<sup>355,356,369</sup> In another strategy, researchers have used peptide moieties to trigger the internalization of the nanomotors.<sup>352,367</sup> In this regard, Alapan *et al* showed the targeted delivery of doxorubicin to breast cancer cells using magnetic microroller robots functionalized with antibodies against the human epidermal growth factor receptor 2 (**Figure 10e**).<sup>367</sup> In turn, Peng and co-workers developed a peptide/functionalized stomatocyte nanomotor to facilitate cellular uptake and thus improve the efficiency of drug delivery.<sup>352</sup>

#### 1.4.2. Microsurgery and Enhanced Penetration of Cells or Tissues

Given the growing interest in the concept of minimally invasive surgery and robot-assisted surgery, researchers also took advantage of the magnitude of the force exerted by the nano- and micromotors propulsion, using these motile structures as microsurgery tools. Xi *et al* developed a sharp-end microtool that enabled drilling and related incision operations of tissues, *ex vivo*.<sup>132</sup> Furthermore, Gultepe *et al* reported a micromotor-assisted biopsy tool, where thermally activated microgrippers are used to excise tissues from porcine bile ducts.<sup>133</sup> Srivastava *et al* fabricated a micromotor capable of drilling into cells due to actuation by magnetic fields.<sup>134</sup> In a similar approach, Vyskočil and co-workers demonstrated a magnetic walker capable of entering cells in a micro-surgery manner, being able to enter a cell and removing a piece of the cytoplasm without inducing damage to the cytoplasmic membrane.<sup>370</sup> Diller and Sitti reported a magnetic micromotor with micro-gripper arms capable of locomotion for precise transport, orientation, and programmable assembly of micro-objects, and hypothesized its potential as a microsurgery tool.<sup>371</sup> In a step-forward for the field, Chatzipirpiridis *et al* fabricated a microtubular magnetic motor capable of performing microsurgery, showing controlled rotation and displacement inside the vitreous humor of a living rabbit eye.<sup>372</sup>

The use of coatings that only allow the activation of the motors in specific locations as a strategy to enhanced penetration and retention of motors in tissues has also been considered. In this regard, Mazur *et al* recently demonstrated an *in vitro* proof-of-concept micromotor activable in the presence of bile salts, which are a part of GI fluids. The PLL micromotor was coated with liposomes, which disintegrated asymmetrically upon presence of bile salts, leaving the PLL exposed to electrolytes and thus giving rise to motility.<sup>373</sup> The concept of motors activable in specific conditions was also investigated *in vivo*. Several works have been reported using either by showing the design of micromotors that activate in specific environments, such as the stomach due to the acidity of the gastric fluid.<sup>368,374,375</sup> An example of this is the work of Gao and co-workers,

who developed tubular micromotors based on Zn and studied their biodistribution, retention in target site, cargo delivery, and toxicity profiles in mice stomachs.<sup>374</sup> Coating the micromotors with enteric films, which only disintegrate in the intestines, is another method to accomplish the delivery of the cargo on the desired location.<sup>368</sup> For instance, Li *et al* coated tubular micromotors powered by magnesium with an enteric polymer, which upon reaching the desired segments of the gastrointestinal tract (GI) would disintegrate and allow the magnesium present in the motor to contact with the aqueous environment of the intestine, leading to motor activation (**Figure 10f**).<sup>368</sup>

### 1.5. From one to many: collective behavior of synthetic motors

In the recent years, the research in nanomedicine made it increasingly evident that in order to achieve satisfactory results, the administered doses of nanomedicines needed to be in the magnitude of trillions of nanoparticles per administration.<sup>17</sup> In the body, the nanomedicines are expected to carry out similar and competitive functions, therefore strategies to amplify the efficiency of nanomedicines were demanded. In this regard, the design of nanocarriers in such ways that they can exhibit collective behavior, instead of acting as single entities has become an increasingly explored method to improve their *in vivo* response.<sup>17,376</sup> The community working on nano- and micromotors and their applications in nanomedicine also took this into account and reported the swarming behavior of motors *in vitro*, *ex vivo* and *in vivo*.

#### 1.5.1. In Vitro Evaluation of the Collective Behavior of Nano- and Micromotors

##### Taxis

The pioneering works on the evaluation of the collective behavior of nano- and micromotors were performed in *in vitro* settings, where the researchers studied the interactions of the motors in response to stimuli on a global scale. For instance, Sen *et al* and Hong *et al* evaluated the ability of motors to exhibit tactic behaviors, such as the movement toward higher hydrogen peroxide concentrations of PtAu rods (**Figure 11a**).<sup>214,377</sup> Baraban *et al* also investigated the chemotactic behavior of both catalytic Janus particles and microjets, using microfluidic channels and gradients of hydrogen peroxide.<sup>378</sup>

The chemotactic behavior of enzyme-powered nano- and micromotors was also investigated by several researchers. For instance, Dey *et al* took advantage of enzyme's ability of exhibit chemotaxis to separate a mix of active and inactive enzymes.<sup>379</sup> Moreover, Zhao *et al* demonstrated that the chemotactic behavior of enzymes could lead to assembly in a enzymatic cascade, which could have potential implications for the study of the organization of metabolic networks within cells.<sup>380</sup> Dey *et al* also investigated the chemotaxis of polystyrene-base enzymatic motors using microfluidic channels, showing the chemotactic migration of both urease- and catalase powered particles.<sup>319</sup> In a similar manner, Somasundar *et al* showed the positive and negative chemotaxis of liposome-based enzymatic motors, denoting the enzyme-catalysis induced positive chemotaxis and solute-phospholipid led to negative chemotaxis of the motors.<sup>328</sup>

The movement toward higher concentrations of the enzymatic substrate was also exploited *in vitro* for the development of micromotors towards localized drug delivery. In this regard, Wang *et al* developed catalase-powered micromotors with chemotactic response to inflammation. The motors reported in this work



carried doxycycline, a drug commonly used in the treatment of periodontal disease and showed directional movement toward macrophages which were stimulated with phorbol esters to release hydrogen peroxide.<sup>314</sup>

### Assembly, clustering and swarming

Taking inspiration from self-organization and swarms in nature (*e.g.*, bacterial colonies or schools of fish), researchers investigated nano- and micromotors' collective phenomena and ability to perform tasks as an ensemble. The interest in complex multi-unit systems of nano- and micromotors has expanded considerably during the last decade, ranging from studies regarding self-assembly of motors into multimers and rotors,<sup>273,381–388</sup> to the design and analysis of more complex behaviors such as clustering,<sup>389–395</sup> aggregation<sup>396–398</sup> and swarming.<sup>209,399–425</sup>

In order to achieve “*quorum* intelligence”, motors must be able to communicate with each other, for example by releasing chemical signals into their surroundings. In this sense, several stimuli were studied as triggers for collective behavior of motile particles, as the case of light irradiation. For instance, Ibele *et al* reported AgCl particles that were not only able to propel upon UV light exposure, but also release ions into the medium. The released ions acted as signals to the neighboring particles, provoking a ‘schooling’ behavior into regions with higher particle concentration. Moreover, the authors also denoted that in a mixture of AgCl motors with non-light sensitive silica particles, the system exhibits a ‘predator-prey’ behavior, where the silica particles actively seek the motors upon UV light irradiation.<sup>209</sup> Similarly, Ibele *et al* made use of the AgCl motors to further study their swarming dynamics, demonstrating that these particles can show both single- and collective oscillations in their motion, while in the presence of hydrogen peroxide and UV light. The authors stated that this behavior arose from the oscillatory, reversible conversion of AgCl to metallic silver at the surface of the motors, which led to the formation of clusters that could engage in collective motility.<sup>399</sup>

*In vitro* collective phenomena were additionally investigated by Palacci *et al* regarding clustering and self-organization stemming from nonequilibrium driving forces. These forces led to the generation of 2D “living crystals”, which were capable of forming, breaking, exploding, and re-forming at another location, due to a competition between propulsion and attractive interactions induced by osmotic and phoretic effects activated by light (**Figure 11b**).<sup>426</sup> Moreover, Hong *et al* studied photocatalytic titanium dioxide micromotors and their ability to generate collective behaviors in the presence of silica particles and UV irradiation. The authors observed that silica particles had a strong tendency to aggregate around the titanium dioxide motors. The exposure to UV light generated microfireworks, due to the expulsion of the silica particles by the titanium dioxide motors. The process showed to be reversible, with multiple cycles of aggregation/generation of microfireworks by switching the UV light on and off (**Figure 11c**). The authors hypothesized that the clustering collective behavior was a result of a sum of multiple mechanisms, namely diffusiophoresis as a result of the differential diffusion of the photocatalytic products, osmotic propulsion due to the uneven solute concentration on different sides of the silica particles, and surface charge interactions originating from the charge separation and redistribution of the titanium dioxide motors due to UV irradiation.<sup>215</sup>

Magnetic fields were widely used for powering the propulsion of nano- and micromotors, and also to trigger the emergence of their collective dynamics. Researchers strived to generate collective behaviors, with high pattern stability and controlled reconfiguration abilities. Yu *et al* reported an ultra-extensible ribbon-like

magnetic swarm, with multimode reconfiguration abilities. These ribbon-like structures were able to merge, split and elongate on demand (**Figure 11d**). Moreover, the swarms could perform controlled navigation and exhibit pattern stability through confined environments. The authors stated that this work could pave the way for applications of swarms in maskless patterning for microfabrication, micromanipulation, as well as for the understanding of complex morphological transformations in living systems.<sup>407</sup>

Xie *et al* also showed magnetic micromotors that were capable of swarming behavior and shape reconfiguration. In this work, the authors use alternating magnetic fields to lead hematite particles into swarms shaped as chains, vortexes, or ribbons. The high degree of control provided by the magnetic field and the ability to reconfigure shape on-demand has great potential to address multitasking requirements or environmental variations expected to be encountered *in vivo* (**Figure 11e**).<sup>413</sup> Similarly, Yigit *et al* demonstrated the collective behavior with well-defined spatial organization, by engineering attractive and repulsive interactions among individual magnetic particles. These magnetic micromotors were able to show dynamic programmable self-assembly into chains and propel in semiplanar surfaces.<sup>414</sup>

These reports hold great potential in nanomedicine, where ridged surfaces are common (*e.g.* stomach and intestinal linings, tumor vasculature, etc), and control over well-defined ensembles could, for example, potentially improve active transport and diffusion of actives. In this regard, Schuerle *et al* used swarms of magnetotactic bacteria to create a living ferrofluid. The authors tested the swarm in a microfluidic model of blood extravasation and tissue penetration, consisting of channels lined with a collagen matrix and showed that collective motility led to enhanced transport of co-delivered nanoparticles into the collagen matrices.<sup>416</sup>

However, systems that rely on magnetic fields face important challenges for nanomedicine applications, primarily due to the fact that magnetic gradients drop off rapidly with distance in respect to the magnet, which limits their applicability to surface tissues.<sup>427–429</sup>

Several authors investigated the collective dynamics of chemically powered nano- and micromotors.<sup>382,430–435</sup> The first works regarding this type of motors concerned their self-organization and coordination of motility in solution.<sup>382,430,435</sup> Gibbs *et al* reported tadpole-like catalytic motors that self-assembled in solution to form dimeric clusters. Moreover, Wang *et al* demonstrated that PtAu nanorods exhibited pairwise interactions in the presence of hydrogen peroxide, where attractive and repulsive forces arose from the catalytically generated electric field, driving the assembly of nanorods doublets or triplets which moved collectively in the same direction. The authors also showed that these motors were able to collect tracer particles at their head or tail, originating close-packed rafts.<sup>382</sup>

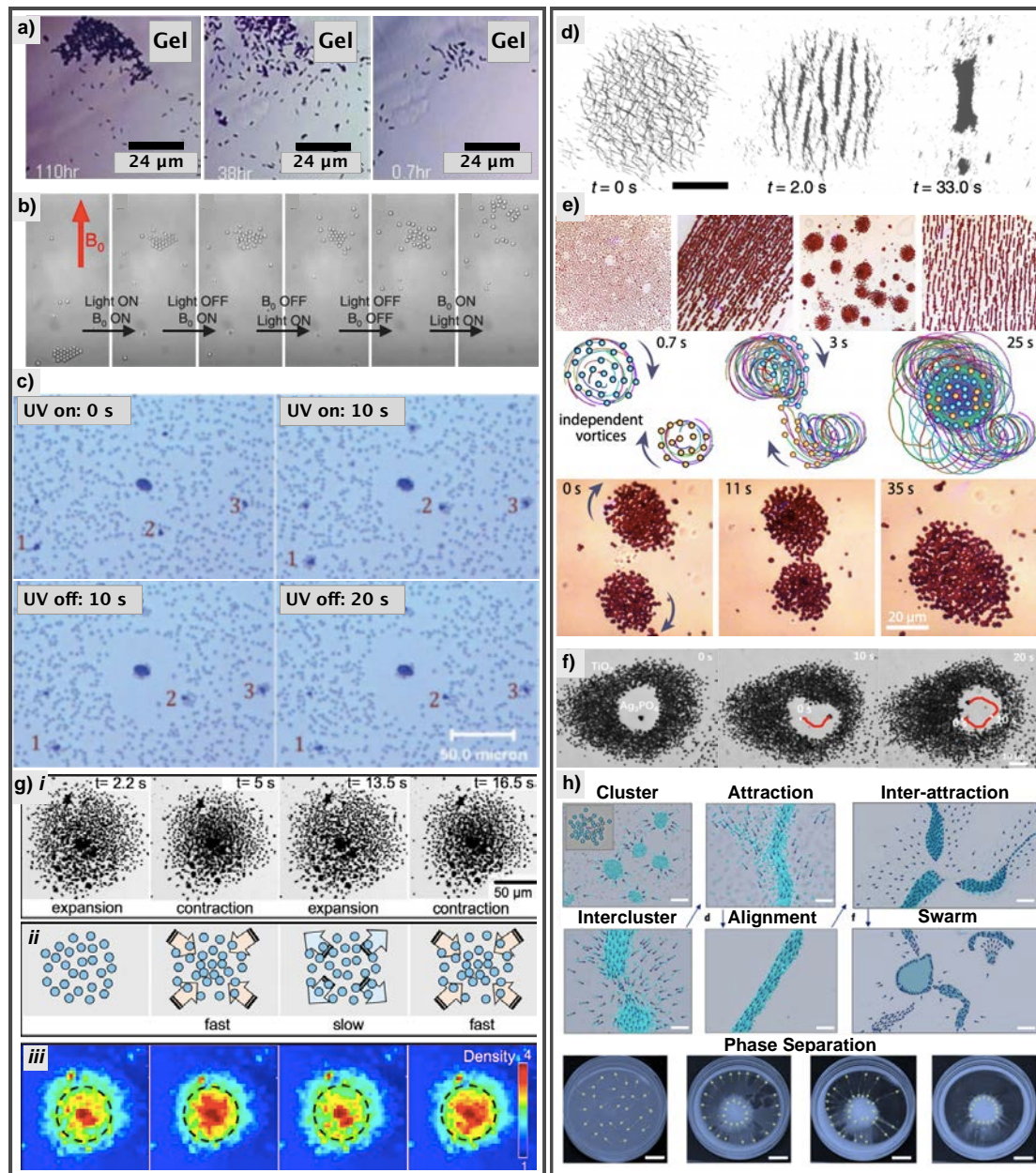


**Figure 11.** *In vitro* collective behavior of nano- and micromotors. a) Chemotaxis of PtAu rods, adapted from Hong *et al.*<sup>377</sup> b) Collective motion of ‘living crystals’, adapted from Palacci *et al.*<sup>426</sup> c) Titanium dioxide-based microfireworks powered by UV light, adapted from Hong *et al.*<sup>215</sup> d) Ribbon-like magnetic swarm and its shape reconfiguration, adapted from Yu *et al.*<sup>407</sup> e) Multimode magnetic swarm, its transformation and locomotion. Adapted from Xie *et al.*<sup>413</sup> f) Predator-prey behavior of micromotors, adapted from Mou *et al.*<sup>432</sup> g) Spontaneous synchronization of micromotor ensembles, adapted from Zhou *et al.*<sup>436</sup> h) Ion-exchange based emergence of swarming behavior of chemically powered motors, adapted from Wu *et al.*<sup>423</sup> Adaptations with permission from the publishers.

Aiming at studying the ability of chemically powered nano- and micromotors to perform cooperative tasks as ensembles, researchers increased the complexity of the systems investigated. In this sense, Zhou *et al* demonstrated the spontaneous synchronization of micromotor ensembles *in vitro* (Figure 11g).<sup>436</sup> The authors exploit Ag Janus micromotors ability to spontaneously synchronize their dynamics as chemically couple oscillators, and show that the contraction/expansion phenomena are highly dependent on inter-particle or inter-

cluster distances. In addition, researchers took inspiration from the predator-prey interactions abundant in nature and designed biomimetic swarms where prey particles are chased by predator particles (**Figure 11f**). For this, Mou *et al* designed a binary system comprising attractive diffusiophoretic particles (prey) and diffusiophoretic repulsive ones (predator), and evaluated the interactions between the two populations, paving the way for micromotor systems capable of carrying out cooperative functions.<sup>432</sup> Shklyaev and co-workers investigated the role of enzymatic micropumps to organize capsules in solution into swarms. In this work, the authors demonstrated that the energy released by the enzymatic pumps can be harness to organize microparticles, leading to the formation of ensembles, which could be used to control the targeted delivery of carriers in microfluidic devices.<sup>431</sup>

The amplification of response through swarming and cooperation of nano- and micromotors holds great potential for the improvement of nanomedicines efficacy. However, these behaviors require motor systems to comprise features such as *quorum* sensing and intelligent consensus decision-making, which must be achieved through inter-motor communication. Wu *et al* devoted efforts on the quest to develop a chemically powered motor swarm capable of inter-unit communication (**Figure 11h**). For this, the authors explored the non-reciprocal ion exchange interactions between ZnO nanorods and sulfonated polystyrene beads, where the chemical “waste” of one acted as the “fuel” for the other. This exchange led to the formation of nanorod-microbead complexes, which could further interact to form hierarchical and dynamic swarms capable of phase segregation and consensus decision-making due to chemical communication, shedding light on the design of adaptable and responsive chemical motor swarms.<sup>423</sup>

### 1.5.2. *Ex Vivo* and *In vivo* Imaging and Evaluation of Swarms' Functionalities

Despite the exciting research on the *in vitro* generation and characterization of nano- and micromotor swarms, their applicability and efficacy in real scenarios is required to advance the development of more efficient active nanomedicines. To achieve that long-standing milestone, researchers turned to *ex vivo* models for the study of swarm behavior, focusing mostly on magnetically powered systems.

Wu *et al* took advantage of helical micromotors ability to move in complex viscous media and explored them as intraocular delivery devices (**Figure 12a**).<sup>237</sup> For this, Wu *et al* coated the helical motors with a slippery perfluorocarbon liquid layer, which allows them to propel in the vitreous humor of the eye. By using rotating magnetic fields, the authors were able to achieve propulsion of the micromotors within porcine eyes *ex vivo*, and image the phenomenon using optical coherence tomography. In similar approach, Yu *et al* demonstrated the active generation and actuation of magnetic micromotor swarms in various fluids (*i.e.*, gastric fluid, plasma and whole blood), as well as through the vitreous humor of bovine specimen *ex vivo* (**Figure 12b**). The swarms could be induced by the magnetic fields or by the surrounding medium and were imaged using medical techniques, namely ultrasound imaging.<sup>437</sup>

In turn, Wang *et al* reported the real-time navigation guidance of a paramagnetic microswarm using ultrasound. This swarm was comprised of magnetite nanoparticles and was generated by exposure to rotating magnetic fields. The authors studied the effect of depth in the imaging of the swarm, as well as the minimum dose required for the precise localization of the swarm *ex vivo*, revealing a maximum depth of *ca.* 8 mm, with a steady-state error of *ca.* 34% of the swarm's body length.<sup>438</sup> Wang *et al* also demonstrated a strategy to



assemble and disassemble magnetic clusters on uneven surfaces, using the bladder of a swine and imaging the process with ultrasound (Figure 12c).<sup>439</sup>

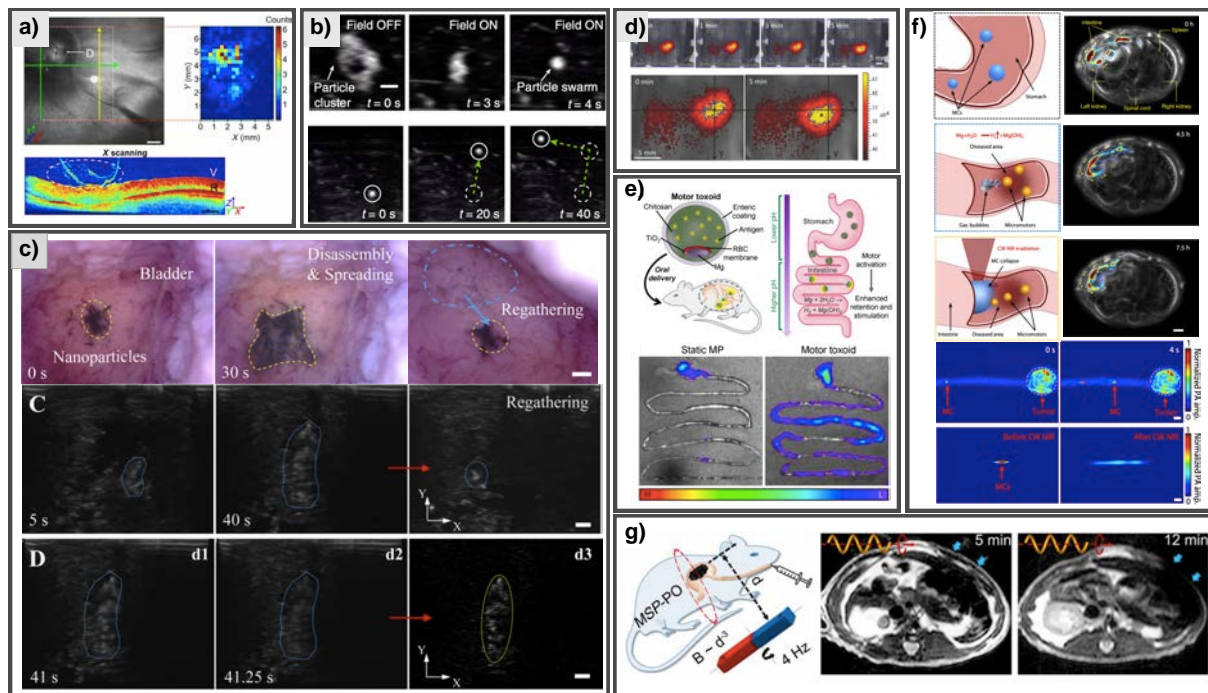


**Figure 12.** *Ex vivo* and *in vivo* imaging and evaluation of nano- and micromotor swarms and their biomedical applications. a) Slippery swarm of micromotors penetrating the vitreous humor of the eye, imaged *ex vivo* using optical coherence tomography. Adapted from Wu *et al.*<sup>237</sup> b) Swarms of micromotors navigating in porcine eyes, imaged using ultrasound. Adapted from Yu *et al.*<sup>437</sup> c) *Ex vivo* imaging of the assembly and disassembly of a magnetic swarm imaged by ultrasound. Adapted from Wang *et al.*<sup>439</sup> d) *In vivo* actuation of a swarm of magnetic motors, imaged by optical fluorescence. Adapted from Servant *et al.*<sup>440</sup> e) Motor toxoid for active delivery of oral vaccination, imaged by optical fluorescence. Adapted from Wei *et al.*<sup>441</sup> f) PACT imaging of micromotors in the GI tract, adapted from Wu *et al.*<sup>442</sup> g) MRI imaging of spirulina-based motor swarms inside a rat's stomach, adapted from Yan *et al.*<sup>443</sup> Adaptations with permission from the publishers.

However, a major milestone in the field is to move nano- and micromotors from *in vitro* or *ex vivo* settings to living organisms, where the precise tracking of motility and validation of *in vitro* proof-of-concept functionalities still has not been widely investigated. In this sense, Chao and co-workers developed a magnetic nanomotor for the acceleration of thrombolysis and tested its efficacy *in vitro*, as well as *in vivo*. The authors demonstrated that the mass transport of tissue plasminogen activator in a microfluidic channel was enhanced by the presence of the motors, and then validated the efficiency of the treatment in a rat embolic model. Nevertheless, in this work, the validation was based on end results – *i.e.* in the efficiency of thrombus removal, and the process was not monitored through imaging.<sup>444</sup>

In another approach, Servant *et al* demonstrated the actuation and *in vivo* imaging of a swarm of magnetic helical micromotors in deep tissues (Figure 12d). The so-called artificial bacterial flagella could be precisely controlled by weak rotating magnetic fields, and their navigation within the peritoneal cavity of a mouse was tracked using whole-body optical fluorescence imaging.<sup>440</sup> Contrarily to the work mentioned above, in this report the author focused on imaging and motility tracking, rather than in the validation of a specific biomedical application of the motors.

Joseph *et al* designed polymersome-based nanomotors aiming at blood-brain barrier crossing. The nanomotors in this work were powered by either glucose oxidase or a combination of glucose oxidase and catalase and exhibited chemotactic response toward a gradient of fuel concentration. The authors demonstrated, using immunofluorescence histology, that active nanomotors augment blood-brain crossing *in vivo*.<sup>342</sup>

The potential of nano- and micromotors as nanomedicines with specific activation in desired locations, namely the gastrointestinal tract, was also investigated *in vivo*.

Apart from the works from Gao,<sup>374</sup> Li<sup>368</sup> and Esteban-Fernández de Ávila *et al*,<sup>375</sup> concerning the localized activation and retention within the GI tract, Wei and co-workers developed a micromotor capable of delivering antigens in the intestine, and showed that propulsion led to enhanced retention and immunogenic response, demonstrating the capabilities of actively-propelling systems as oral vaccination platforms (**Figure 12e**).<sup>441</sup> The common feature throughout the works mentioned is the use of optical fluorescence imaging to evaluate the retention of motors within the target organ after the treatment, without real-time monitoring of motility and collective behavior *in vivo*.

The *in vivo* swarming behavior of micromotors was investigated using medical imaging techniques. In this sense, Wu *et al* reported the development of micro-robotic system for targeted navigation in the intestines (**Figure 12f**), guided by photoacoustic computed tomography (PACT).<sup>442</sup> To achieve stability *in vivo* and navigation in the intestines, the micromotors were encapsulated to resist the stomach. Recurring to the visualization by PACT, the capsules were then disintegrated upon reaching the intestines using near-infrared irradiation. Similarly, Xie *et al* used photoacoustic imaging to track the swarming behavior of magnetic motors *in vitro* and to evaluate their efficacy in the treatment of bacterial infections *in vivo*.<sup>445</sup>

In another approach, Yan *et al* showed the remote control of magnetic microrobots and their applicability for imaging-guided therapy using magnetic resonance imaging (MRI).<sup>443</sup> For this, the researchers used *Spirulina* microalgae as template, and dip-coated it with magnetite, thus enabling its remote control and visualization with MRI (**Figure 12g**), demonstrating it as a potential tool for imaging-guided therapy.

The rapid development of actively propelled nano- and micromotors, as well as the many proof-of-concepts reported show that these tools hold great potential in the nanomedicine field being able to overcome barriers, enhance retention in the target sites and even enable localized treatment guided by medical imaging techniques. Even though researchers have shown several demonstrations of nano- and micromotors abilities, and despite the considerable advantages of the use of enzymes as engines, enzyme-powered nanomotors have been scarcely explored as nanomedicine tools. The work developed on the scope of this thesis is focused on the study of enzymatic nanomotors, with a special focus on urease as engine and the investigation of their potential as active nanomedicines, going from *in vitro* proof-of-concept demonstrations of enhanced drug delivery, cancer targeting in three-dimensional models, as well as chassis versatility, to *in vivo* monitoring of nanomotor swarming behavior using medical imaging techniques



# Chapter 2



## Objectives





Considering the state of the art in the field of nano- and micromotors, the objectives of this thesis were established in order to tackle key aspects on the fabrication of nano- and micromotors for biomedical applications, and on the understanding of paramount interactions between the active carriers and biological systems. These objectives are defined as follows:

- (i) To study the effect of active motion of enzyme-powered nanomotors on drug release and delivery to 2D cell cultures, in comparison to non-motile mesoporous silica nanocarriers.
- (ii) To examine the ability of urease-powered nanomotors to target and penetrate into 3D bladder cancer spheroids.
- (iii) To investigate the motion dynamics and collective behavior of enzymatic nanomotors *in vitro* and *in vivo*, using optical microscopy and medical imaging techniques.
- (iv) To fabricate new enzyme-powered nanomotors with features to protect enzymatic activity from harsh biological environments and trigger motion on-demand.







# Chapter 3



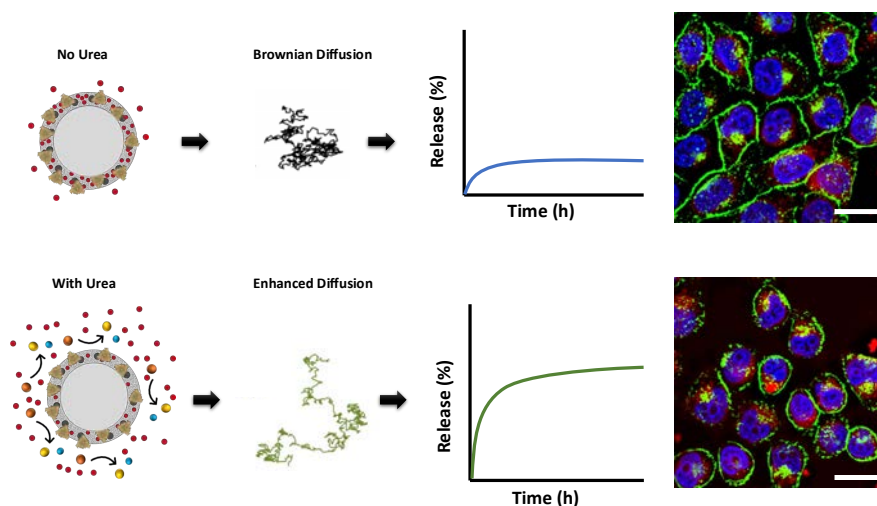
## **Enzyme-Powered Nanobots Enhance Anticancer Drug Delivery**





Nano- and micromotors emerged as an attractive alternative for the development of nanomedicines, since their intrinsic propulsion may help to surpass biological barriers that hinder the *in vivo* efficacy of traditional nanoparticles. In this work, we aimed at assessing the efficacy of enzyme powered nanomotors as **active drug delivery vehicles**. For this, we developed urease-powered nanomotors comprising **doxorubicin anticancer drug loaded** onto the mesoporous silica shell. Mesoporous silica has been widely studied as drug nanocarrier owing to its high cargo loading capacity, controllability in size and shape, and well-known surface chemistry.

Urease-powered nanomotors showed self-propulsion in ionic media and significantly **improved doxorubicin release**, in a urea concentration-dependent manner. We further explored the capabilities of the nanomotors as drug delivery systems by studying their drug delivery efficacy to cells. We found that the synergy between the enhanced drug release and the local increase in pH, caused by urea decomposition into carbon dioxide and ammonia, resulted in **higher cytotoxic effect toward HeLa cells** of the doxorubicin-loaded nanomotors than their passive counterparts.



**Graphical Abstract 1.** Doxorubicin-loaded urease powered nanomotors for enhanced drug release and delivery to HeLa cells.

# Enzyme-Powered Nanobots Enhance Anticancer Drug Delivery

Ana C. Hortelão, Tania Patiño,\* Ariadna Perez-Jiménez, Àngel Blanco, and Samuel Sánchez\*

The use of enzyme catalysis to power micro- and nanomotors exploiting biocompatible fuels has opened new ventures for biomedical applications such as the active transport and delivery of specific drugs to the site of interest. Here, urease-powered nanomotors (nanobots) for doxorubicin (Dox) anticancer drug loading, release, and efficient delivery to cells are presented. These mesoporous silica-based core-shell nanobots are able to self-propel in ionic media, as confirmed by optical tracking and dynamic light scattering analysis. A four-fold increase in drug release is achieved by nanobots after 6 h compared to their passive counterparts. Furthermore, the use of Dox-loaded nanobots presents an enhanced anticancer efficiency toward HeLa cells, which arises from a synergistic effect of the enhanced drug release and the ammonia produced at high concentrations of urea substrate. A higher content of Dox inside HeLa cells is detected after 1, 4, 6, and 24 h incubation with active nanobots compared to passive Dox-loaded nanoparticles. The improvement in drug delivery efficiency achieved by enzyme-powered nanobots may hold potential toward their use in future biomedical applications such as the substrate-triggered release of drugs in target locations.

Traditional drug delivery systems rely on the use of passive nanoparticles (i.e., without propulsion capabilities), which has been reported to have low efficacy.<sup>[2]</sup> In contrast, in the last decade, researchers have developed micro-/nanoparticles able to self-propel in aqueous media, which have potential as novel and active drug delivery vehicles.<sup>[4–9]</sup> Propulsion at the micro-/nanoscale can be achieved by a multitude of approaches, such as the use of ultrasound waves,<sup>[10]</sup> light,<sup>[11,12]</sup> magnetic fields,<sup>[13,14]</sup> by coupling motile cells to particles,<sup>[15–21]</sup> or by catalytic decomposition of a chemical substrate.<sup>[22–25]</sup> Since catalytic micro-/nanomotors were primarily based on the use of toxic fuels, such as hydrogen peroxide<sup>[26–29]</sup> and hydrazine,<sup>[30]</sup> the potential of these synthetic motors in the biomedical field demanded the quest for alternative biocompatible fuel sources. Alternatively, the use of enzymes as biological catalytic

units to power the motion of varied micro-/nanostructures has been reported.<sup>[22,31–37]</sup> Enzyme catalysis presents several advantages as compared to other catalytic motors. For instance, enzymes provide a more versatile library of relevant, bioavailable, and biocompatible substrates to be used as fuels upon demand of the target application.


The self-propulsion abilities of these synthetic motors may bring distinct improvements when compared to passive drug carriers. Namely, self-propulsion provides the vehicles with continuous driving force, aiding their transport across biological tissues.<sup>[5,38]</sup> In addition, upon regulation of the motors' speed, cell targeting and internalization phenomena could be modulated, providing enhanced control and tunability of the drug delivery system.<sup>[39]</sup> Considerable efforts have been applied to the fabrication of micro-/nanomotors that fulfill the requirements for ideal drug delivery vehicles.<sup>[31,32,40–42]</sup> Mesoporous silica, specifically the Mobil Composition of Matter No. 41 (MCM-41) type, is a widely studied material for biomedical applications which is approved for clinical use by the FDA.<sup>[43,44]</sup> Previous research on this type of silica revealed it to be biocompatible, which in addition to its high cargo loading capacity, tunability, and easy surface chemistry make it an optimal chassis for drug delivery vehicles.<sup>[44]</sup> Our group previously demonstrated the self-propulsion of micro- and nanostructures based on MCM-41 silica and their coupling with enzymes to

## 1. Introduction

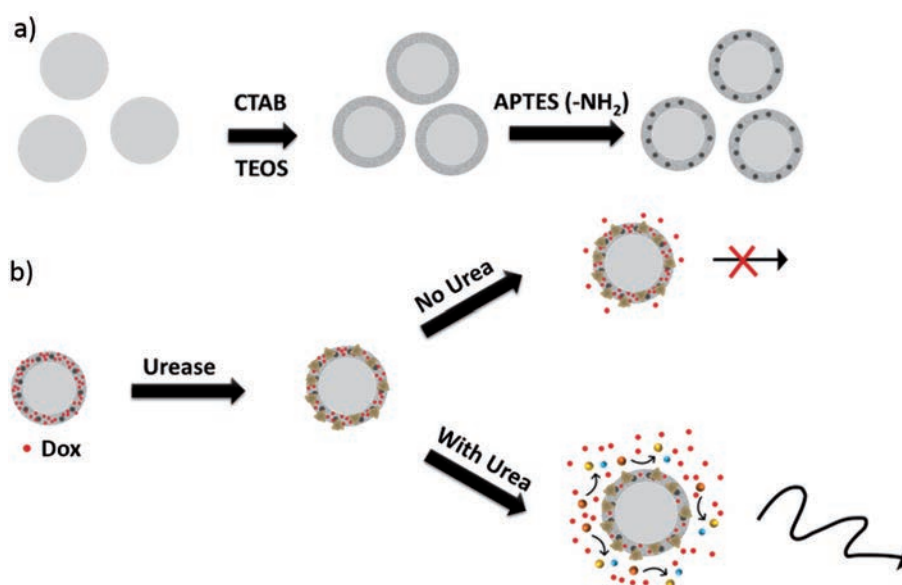
The design of active and smart systems capable of bypassing side effects while increasing drug efficacy is a long-standing challenge in biomedicine and nanotechnology. Such systems require a number of characteristics, namely, biocompatibility, biodegradability, and circulation stability. Furthermore, their maneuvering for full motion control is required to be able to deliver cargo at the defined locations, minimizing undesirable effects in the bystander tissues.<sup>[1–3]</sup>

A. C. Hortelão, Dr. T. Patiño, A. Perez-Jiménez, À. Blanco, Prof. S. Sánchez  
Institute for Bioengineering of Catalonia (IBEC)  
The Barcelona Institute of Science and Technology  
Baldiri Reixac 10-12, 08028 Barcelona, Spain  
E-mail: tpatino@ibecbarcelona.eu; ssanchez@ibecbarcelona.eu

A. C. Hortelão, Dr. T. Patiño, Prof. S. Sánchez  
Max Planck Institute for Intelligent Systems Institution  
Heisenbergstraße 3, 70569 Stuttgart, Germany  
Prof. S. Sánchez  
Institutió Catalana de Recerca i Estudis Avançats (ICREA)  
Pg. Lluís Companys 23, 08010 Barcelona, Spain

 The ORCID identification number(s) for the author(s) of this article can be found under <https://doi.org/10.1002/adfm.201705086>.

DOI: 10.1002/adfm.201705086



**Scheme 1.** Schematic illustration of the fabrication and drug delivery system features of the urease nanobots. a) Fabrication of the nanobot mesoporous structure using cetyltrimethylammonium bromide (CTAB) and tetraethylorthosilicate (TEOS), and further modification with amine groups using 3-aminopropyltriethoxysilane (APTES). b) Loading of doxorubicin (Dox) onto the mesoporous shell, urease attachment and enhanced drug release provoked by self-propulsion due to the presence of urea.

engineer nanomotors powered by the biocatalytic conversion of urea and glucose, aiming at their application in the biomedical field.<sup>[31,32,45,46]</sup> However, the benefits in drug delivery based on active particles compared with passive particles, as well as their motion in physiological media has not been reported yet.

Herein, we present the facile fabrication of enzymatic nanomotors, dubbed nanobots, comprised of a solid silica core and a mesoporous silica shell (Scheme 1a). The shell was coated with urease enzymes which allows to harness chemical energy and convert it into mechanical work even in ionic media (phosphate buffer saline (PBS) buffer solution), an important characteristic for their potential use in biomedical applications. Furthermore, the mesoporous shell provides high loading capacity, enabling the retention of the anticancer water-soluble drug doxorubicin (Dox) (Scheme 1b) and its active transport toward cancer cells. The presence and release of Dox inside the cell is quantified and imaged by fluorescence microscopy.

## 2. Results and Discussion

### 2.1. Synthesis and Characterization of the Urease Nanobots

Solid silica spheres, synthesized using a modified Stöber method,<sup>[47]</sup> were used as core for the fabrication of core-shell mesoporous silica nanoparticles (MSNPs), as depicted in Scheme S1 (Supporting Information). The mesoporous silica shell was grown based on previously reported approaches that provide stability and low aggregation in solution.<sup>[31]</sup> We used cetyltrimethylammonium bromide (CTAB) as porogenic agent and triethanolamine (TEOA) as a base catalyst (see experimental details in the Experimental Section). The MSNPs were

functionalized with 3-aminopropyltriethoxysilane (APTES) to obtain nanoparticles with free amine groups on the surface (MSNP-NH<sub>2</sub>), which were used to covalently attach urease to the nanoparticles using glutaraldehyde (GA) as linker molecule, thus yielding urease nanobots. The fabrication process was characterized by scanning electron microscopy (SEM) and dynamic light scattering (DLS). Figure 1a displays SEM microscopy image of MSNP, revealing the good monodispersity of the MSNPs ( $\varnothing = 344 \pm 3$ , average size  $\pm$  standard error of mean (SE),  $N = 60$ ). DLS analysis of the hydrodynamic radius showed a single population distribution, indicating that the particles were not aggregated, even after their functionalization with APTES. After urease attachment, however, a slightly broader peak than the one detected for the MSNP-NH<sub>2</sub> was observed, indicating a lower monodispersity of the particles in terms of hydrodynamic radius, which could be attributed to enzyme conjugation (Figure 1b, green). Furthermore, we evaluated the evolution of the surface charge upon the modifications of the as-synthesized MSNPs (Figure 1c), denoting negative surface charge for the MSNPs ( $-16.5 \pm 1.4$  mV, average  $\pm$  SE,  $N = 9$ ) and a clear shift to positive surface charge after amine modification ( $43.5 \pm 0.4$  mV, average  $\pm$  SE,  $N = 9$ ). Moreover, we observed a sharp decrease on the positively charged surface after the functionalization with urease enzyme ( $10.3 \pm 1.0$ , average  $\pm$  SE,  $N = 9$ ) (Figure 1c). Since urease has an isoelectric point between 5.0 and 5.2, the observed decrease on the surface charges could be attributed to a successful binding of urease enzyme to the particles.<sup>[48]</sup> The porosity and structure of the nanobots were analyzed by transmission electron microscopy (TEM). We observed a clear core-shell structure (Figure 1d-f), where the nanochannels formed upon CTAB removal can be clearly distinguished (Figure 1f). The presence

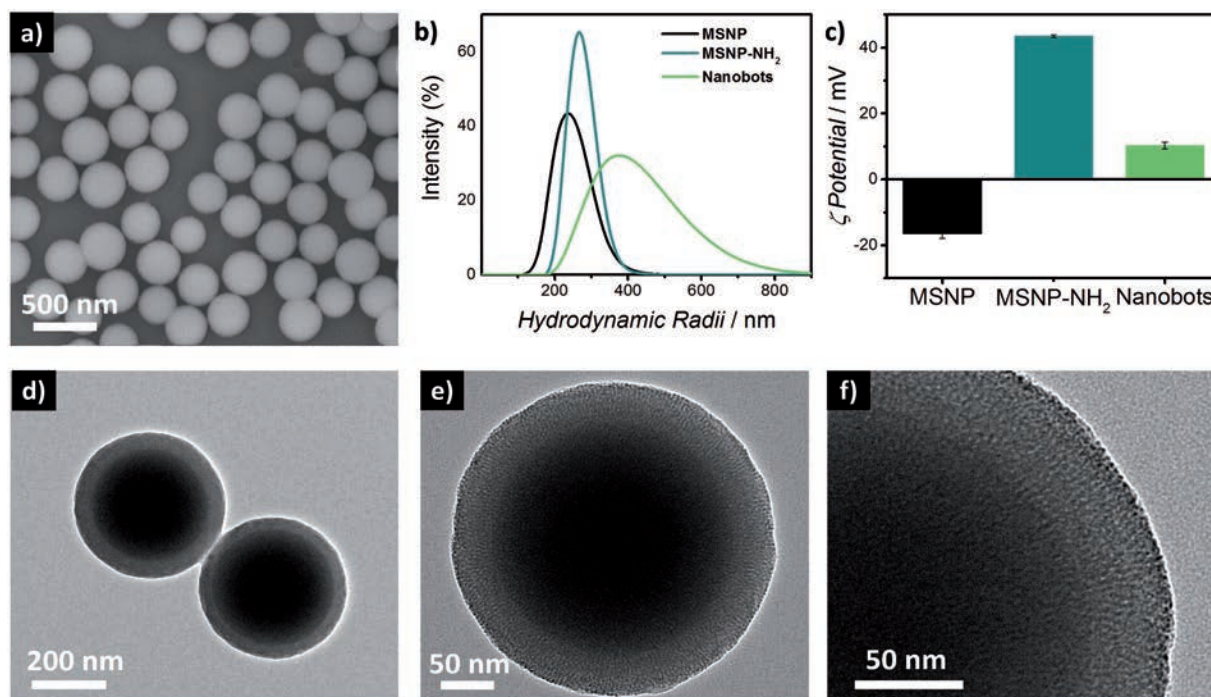


**Figure 1.** Characterization of the mesoporous silica nanoparticles (MSNPs) and further modifications to obtain the mesoporous silica nanoparticles functionalized with urease (nanobots). a) SEM microscopy image of MSNPs. b) Hydrodynamic radii and c) surface charge evolution upon surface modification of the mesoporous silica nanoparticles with amine functional groups and further with urease enzyme. d) TEM microscopy images of MSNP-NH<sub>2</sub>, e) evidencing the core–shell structure, and f) porosity features of the nanoparticles.

of urease enzyme on the particles' surface, as well as the elimination of unbound enzymes was analyzed through the use of a colorimetric kit based on reduction of copper by proteins' peptide bonds (Figure S1, Supporting Information).<sup>[49]</sup>

## 2.2. Motion Behavior of Urease Nanobots

In the presence of urea, the urease bound to the surface of the nanobots catalyzes the decomposition of urea into ammonia and carbon dioxide [(NH<sub>2</sub>)<sub>2</sub>CO + H<sub>2</sub>O → CO<sub>2</sub> + 2NH<sub>3</sub>]. As previous reports have shown, enzymatic catalysis can be used to achieve self-propulsion of micro- and nanostructures with different architectures.<sup>[22,31,34,36,45]</sup> Some nanomotors have been fabricated by inducing structural asymmetries such as the creation of Janus particles<sup>[31,32]</sup> or other asymmetric shapes such as polymeric stomatocytes.<sup>[34]</sup> However, other studies have reported an enhanced diffusion for non-Janus spherical polystyrene particles.<sup>[50]</sup> The actual mechanism of motion for enzymatic motors is still under debate.<sup>[32,33,35,37,50–52]</sup> The self-propelling abilities of the nanobots due to the presence of urea were characterized by optical tracking of the nanobots trajectories under a range of urea concentrations (Figure 2a). The mean-squared displacement (MSD) resulting from the tracked trajectories (Figure 2b) increases linearly with time, which is typical of diffusive motion.<sup>[53]</sup> The effective diffusion coefficient (*D<sub>e</sub>*) was obtained by fitting the MSD curves to Equation (1)

$$\text{MSD}(\Delta t) = 4D_e\Delta t \quad (1)$$

where *D<sub>e</sub>* represents the effective diffusion coefficient and  $\Delta t$  represents the time interval.<sup>[54]</sup>

The calculated effective diffusion coefficients are represented in Figure 2c (blue). We further confirmed these results by analyzing the diffusion coefficients of nanobots in the presence of urea by DLS (Figure 2c, green). In both cases a significant increase in the effective diffusion coefficient was observed at a  $25 \times 10^{-3}$  M urea concentration ( $p < 0.05$ ), which was further increased at  $50 \times 10^{-3}$  M urea, reaching a stabilization. The stabilization of the diffusion coefficient values in the presence of increasing concentrations of urea can be explained by the activity kinetics of urease. We evaluated the activity of the covalently bound urease on the nanobots surface, over the range of urea concentrations studied for motion and we observed that the nanobots present Henri–Michaelis–Menten kinetics (Figure 2d), obeying Equation (2)

$$v = \frac{V_{\max} [S]}{K_m + [S]} \quad (2)$$

where *V<sub>max</sub>* represents the maximum reaction rate, *S* represents the urea concentration, and *K<sub>m</sub>* represents the Henri–Michaelis–Menten constant.<sup>[55]</sup> By fitting our data to the equation, we found that  $K_m = (4.7 \pm 0.5) \times 10^{-3}$  M and  $V_{\max} = 162.1 \pm 1.5$  units mg<sup>-1</sup> of urease, where unit is defined as the amount of enzyme required to generate 1 μmol of ammonia



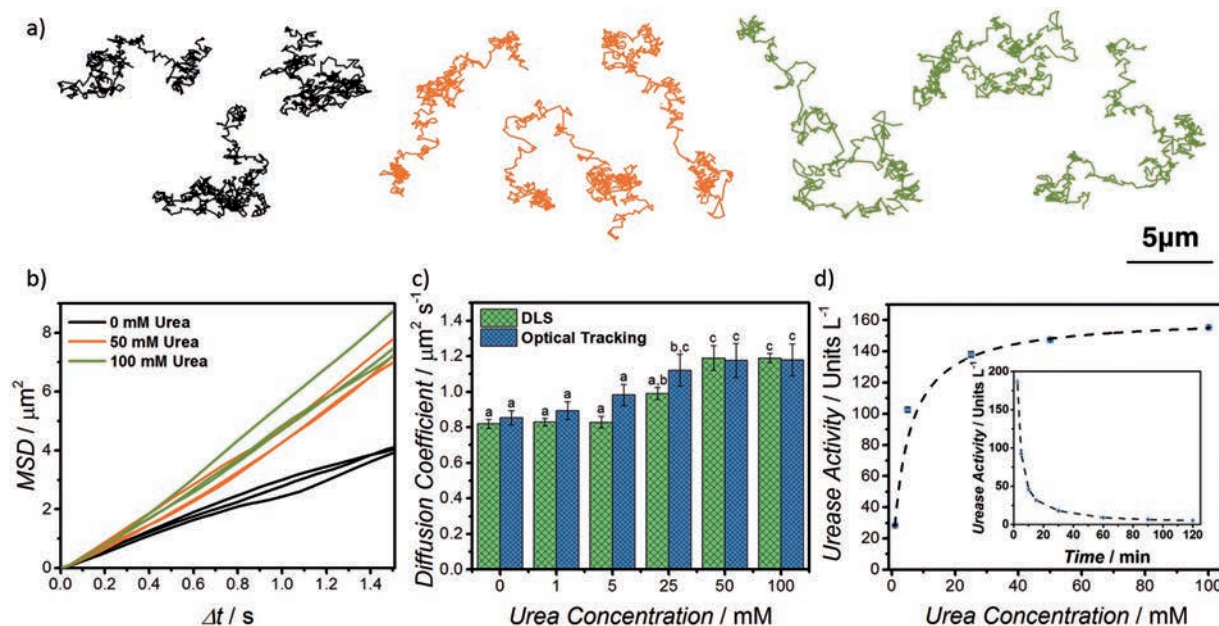


**Figure 2.** Analysis of the motion behavior of urease nanobots. a) Representative tracking trajectories of urease nanobots with different urea concentrations ( $0 \times 10^{-3}$  M, black;  $50 \times 10^{-3}$  M, orange; and  $100 \times 10^{-3}$  M, green) and b) correspondent mean-squared displacement (MSD) plots; c) effective diffusion coefficient obtained by analyzing the MSD (blue) and by DLS (green) of urease nanobots at different urea concentrations ( $n = 20$ , error bars represent SE). Different superscripts denote significant differences among groups with  $p < 0.05$ ; d) enzymatic activity of the urease nanobots at different urea concentrations fitted to Henri-Michaelis-Menten equation (inset: variation of enzymatic activity of the nanobots with time).

per minute, at 37 °C and pH 7.0. These results are in good agreement with values for free enzyme found in literature, indicating that urease activity was not affected by its functionalization onto the particles.<sup>[56]</sup>

We further characterized the activity of urease enzyme present on the nanobots' surface over a period of 120 min, denoting that the enzymatic rate decreases continually with time (inset of Figure 2d), suggesting that the consumption of substrate and generation of products slows the reaction rate over time.

Motivated by the intrinsic presence of salts in physiologically relevant media, we investigated the effect of the

presence of salts in the surrounding medium on the nanobots' diffusion coefficient, using PBS solution (PBS 1x). We observed different diffusion coefficient values between nanobots suspended in water and in PBS (Figure 3a), which could be attributed to changes in electrostatic interactions between motors and neighboring surfaces driven by the presence of salts.<sup>[57]</sup> However, the nanobots displayed enhanced diffusion in both PBS and water solutions in the presence of urea, where an increase in diffusion coefficient of roughly 35% and 60% was detected for water and PBS, respectively (Figure 3b). We also analyzed the nanobots' self-propulsion in ionic media

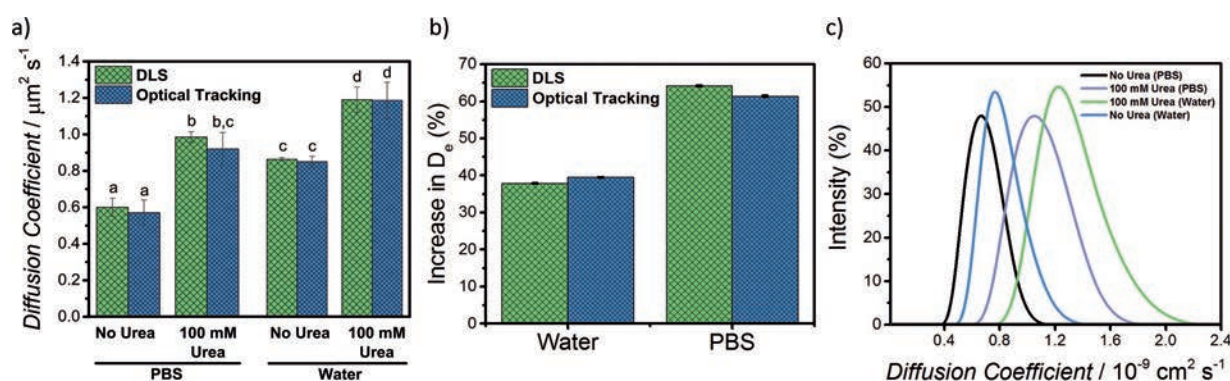


**Figure 3.** Analysis of motion behaviors of urease nanobots in water and ionic media. a) Characterization of the motion profiles of urease-powered nanobots in ionic media (PBS) and in water by optical microscopy and DLS ( $N = 20$ , error bars represent SE). Different superscripts denote significant differences among groups with  $p < 0.05$ . b) Percentage increase in diffusion coefficient in the presence of urea, in water and in PBS; error bars represent the error calculated by propagating the SE obtained in the measurements. c) Diffusion coefficient histogram nanobots in water and PBS obtained by DLS.

by DLS, where a shift on diffusion coefficient is observed (Figure 3c).

### 2.3. Drug Loading and Release Profiles of the Urease Nanobots

We investigated the drug loading and releasing capabilities of nanobots in order to determine whether their enhanced diffusion due to availability of urea relates with enhanced drug release kinetics. First, we investigated the loading capacity of the architecture of the nanobots before and after functionalizing with urease enzyme as drug delivery carrier, using Dox as model drug. Dox is a chemotherapeutic agent which belongs to the family of anthracyclines and antitumor antibiotics, which intercalates between the base pairs in the DNA, preventing replication and thereby arresting the cell cycle.<sup>[58]</sup> We determined nanobots' loading capacity and drug entrapment efficiency, which represent the drug content and the percentage of drug successfully encapsulated in the nanoparticles, respectively, as follows

$$\text{Drug Loading (\%)} = \frac{\text{Mass of Drug Loaded}}{\text{Mass of Nanobots}} \times 100 \quad (3)$$

$$\text{Entrapment Efficiency (\%)} = \frac{\text{Mass of Drug Loaded}}{\text{Total Drug Mass}} \times 100 \quad (4)$$

Despite a slight loss of Dox mass during the washing process required for functionalization with urease, the nanobots retain roughly 10% (w/w) of drug (Figure 4a).

Then, we compared the drug release capabilities of enzymatic nanobots in the presence of increasing concentrations of fuel with their passive counterparts (Figure 4b,c). We observed that the drug release over 24 h increased according to the presence of urea. A positive correlation between the urea concentration and the release profile was found, reaching a saturation at  $50 \times 10^{-3}$  M urea. The amount of Dox released by the nanobots at urea concentrations above  $50 \times 10^{-3}$  M is almost four times higher compared to the one obtained at  $0 \times 10^{-3}$  M urea (Figure 4b). These results are in agreement with the motion analysis, since the saturation of motion was also found to be  $50 \times 10^{-3}$  M of urea. We attribute the enhancement of the drug release from the mesoporous cavities to the increased diffusion of the nanobots in the presence of urea, and to the flow

generated through the surface.<sup>[33,59]</sup> Since we observed that urease activity decreases overtime (Figure 2d), we performed the release experiments collecting aliquots at every time point and replenishing the medium with fresh supply of urea. Thus, the slow release rate between 6 and 24 h, observed for all conditions analyzed, could be explained by the depletion of urea from the medium, as well as by the saturation of the solution with Dox, slowing down the drug release.

To study whether the changes in the Dox release profiles could be affected by the changes in the pH provoked by urease activity, we monitored the pH of the nanobots solution upon the addition of urea. For this, we used PBS adjusted to different pH (5, 6, 9, and 10) as the starting solutions, and the pH was measured every minute upon the addition of urea. We observed that in all cases, the pH changed immediately to 9, indicating the self-buffering properties of the system (Figure S3a, Supporting Information). To assess if the quick change in pH was the reason underlying the enhancement on drug release, we evaluated the release profiles of nanobots in the presence and absence of urea, when placed in buffer solutions at pH 9 (Figure S3b, Supporting Information). We observed that even when the initial solution was stabilized at pH 9, the release of Dox from the urease nanobots was significantly enhanced in the presence of urea, indicating that this phenomenon stems from nanobots' surface activity, regardless of the pH change of the surrounding medium.

### 2.4. Nanobots' Efficacy as Drug Delivery Vehicles

Taking advantage of the enhanced Dox release kinetics from active nanobots, we tested nanobots' biocompatibility and efficacy as drug delivery vehicles to human epithelial cervix adenocarcinoma HeLa cells. Urease-powered nanobots' biocompatibility was evaluated by using the (3-(4,5-dimethylthiazol-2-yl)-2,5-diphenyltetrazolium bromide (MTT) assay, which is a colorimetric method that determines metabolic activity, by assessing the reduction of MTT and formation of formazan crystals by viable cells. The nanobots exhibited biocompatibility (>80% viable cells) up to a concentration of  $0.5 \text{ mg mL}^{-1}$  (Figure 5a, black), where less than 70% of the cells remained viable after the 24 h incubation period. Viability below that value would denote cytotoxicity of nanoparticles, as per the FDA's and ISO's standards.<sup>[60]</sup> When nanobots were loaded with Dox and incubated with cells (even in the absence of urea)

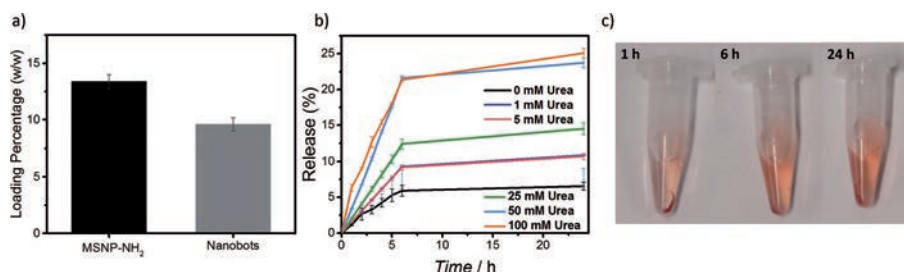


**Figure 4.** Evaluation of MSNP-NH<sub>2</sub> and urease nanobots as drug carriers for Dox. a) Loading capacity of doxorubicin on MSNP-NH<sub>2</sub> and urease nanobots; b) release profiles for Dox from the nanobots in different urea concentrations (*N* = 3, error bars represent SE) and c) release of Dox from nanobots in the presence of  $100 \times 10^{-3}$  M urea.

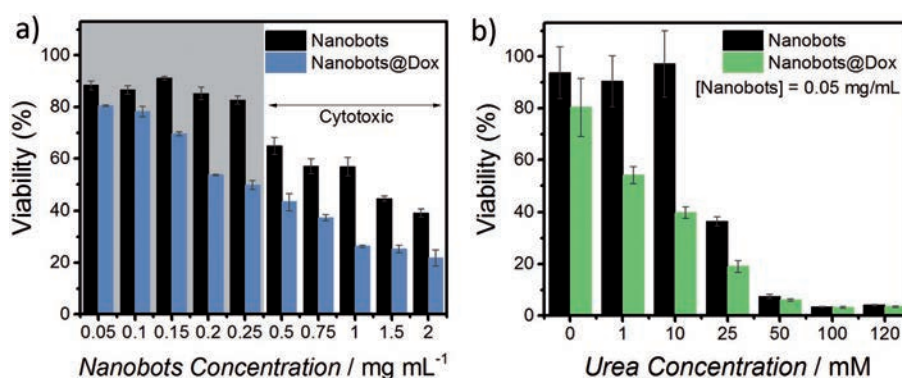


**Figure 5.** Cytotoxicity assays and efficacy testing of the nanobots as drug carriers in the presence and absence of urea. a) Biocompatibility of nanobots (black) up to high concentrations and evaluation of its efficacy as Dox carrier (blue) without urea; b) urea-dependent biocompatibility of the urease nanobots (black) and increased efficacy as Dox delivery vehicles (green) at  $0.05 \text{ mg mL}^{-1}$  ( $N = 3$ , error bars represent SE).

we observed a concentration-dependent toxicity trend, which was significantly higher than non-Dox loaded nanobots in all cases (Figure 5a, blue). A concentration of  $4 \mu\text{g mL}^{-1}$  of free Dox is needed to achieve the IC<sub>50</sub> on HeLa cells after 24 h incubation (Figure S3, Supporting Information). Using core-shell nanoparticles, we detected the IC<sub>50</sub> as  $0.5 \text{ mg mL}^{-1}$  for passive nanobots, whereas only  $0.05 \text{ mg mL}^{-1}$  of active nanobots are required to obtain the same effect. These results indicate that not all the loaded Dox encapsulated in passive nanobots is released or capable of reaching the desired location, i.e., inside the cells. Yet, once urea is present in the medium, a more efficient delivery of Dox to the cells is achieved, which could be attributed to a faster release of drug to the media, increased transport near or inside the cell and increased cell uptake of the nanobots. The exact contribution from each effect needs to be investigated in future works.

Figure 5b (green columns) shows the anticancer effect of Dox-loaded active nanobots, which was attributed to the enhanced release of Dox from active nanobots for increasing concentrations of urea. Moreover, we observed a sharp decrease in cell viability for bare nanobots for concentrations above  $10 \times 10^{-3} \text{ M}$  of urea (Figure 5b, black columns). To investigate the origin of this low viability, we studied the cytotoxic contribution of fuel and products; we evaluated the biocompatibility of urea and ammonia. Urea was found to be biocompatible for concentrations up to  $400 \times 10^{-3} \text{ M}$  (Figure S5a, Supporting Information). Yet, we observed a cytotoxic effect for ammonia concentrations higher than  $50 \times 10^{-3} \text{ M}$  (Figure S5b, Supporting Information), which would correspond to the total conversion of  $25 \times 10^{-3} \text{ M}$  urea.

Altogether, these results indicate that, as a matter of comparison, we obtain the same effect on cells with at least 10 times lower concentration of active nanobots than with passive counterparts. We attribute these results to a synergistic effect of the improved Dox release induced by motion, and the ammonia produced by catalytic decomposition of urea.

As Dox is a fluorescent molecule, we used fluorescence microscopy to monitor its uptake by HeLa cells (Figure 6a). For this, cells were incubated with  $0.05 \text{ mg mL}^{-1}$  of Dox-loaded nanobots, either in the absence or presence of urea ( $10 \times 10^{-3} \text{ M}$ ) during 1, 4, 6, and 24 h, after which the cells

were washed with PBS and labeled with wheat germ agglutinin (WGA–membrane, green) and Hoescht (nuclei, blue). Next, quantitative imaging analysis of the red fluorescence emission within cells (Figure 6b,  $N = 15$ ) was performed, observing that the fluorescence signal increases with time. Moreover, for all the data points analyzed, we observed a higher red fluorescence signal within cell cytoplasm when the nanobots were incubated with urea compared to the control, as depicted in Figure 6b,c (red channel column). These results agree with the findings from the cytotoxicity experiments, where active nanobots lead to an enhanced cytotoxic effect of the drug delivery system.

### 3. Conclusion

In summary, we report urease-modified nanobots, composed of mesoporous silica shell, capable of loading the anticancer drug Dox, presenting enhanced drug release profiles dependent on urea concentration. Furthermore, we demonstrate the nanobots' self-propulsion in ionic media (PBS buffer), which is a crucial ability for its use in biomedical applications. We found that in the presence of urea, the active Dox-loaded nanobots exhibit improved effect on HeLa cells compared to passive carriers, due to a synergistic effect of improved drug release kinetics and ammonia production by the catalytic decomposition of urea. Future work on fuel-dependent targeting and cell uptake, novel triggered release mechanisms and in situ guidance methods, such as the use of pH, thermal, or chemical gradients to attract and guide nanomotors in vitro and in vivo need to be addressed for the development of smart and self-propelled drug delivery vehicles based on enzyme catalysis.

### 4. Experimental Section

**Materials:** Ethanol (EtOH, >99%), methanol (MeOH, >99%), hydrochloric acid (37% in water), ammonium hydroxide (25% in water), tetraethylorthosilicate (TEOS, 99%), TEOA (99%), CTAB (99%), APTES (99%), GA (25% in water), urease (from *Canavalia ensiformis*, Type IX, powder, 50 000–100 000 units g<sup>-1</sup> solid), Urease Activity Kit, doxorubicin hydrochloride (Dox, 99.9%), urea (99.9%), and dimethyl sulfoxide (DMSO, 99.9%) were purchased from Sigma-Aldrich. MTT, PBS, and



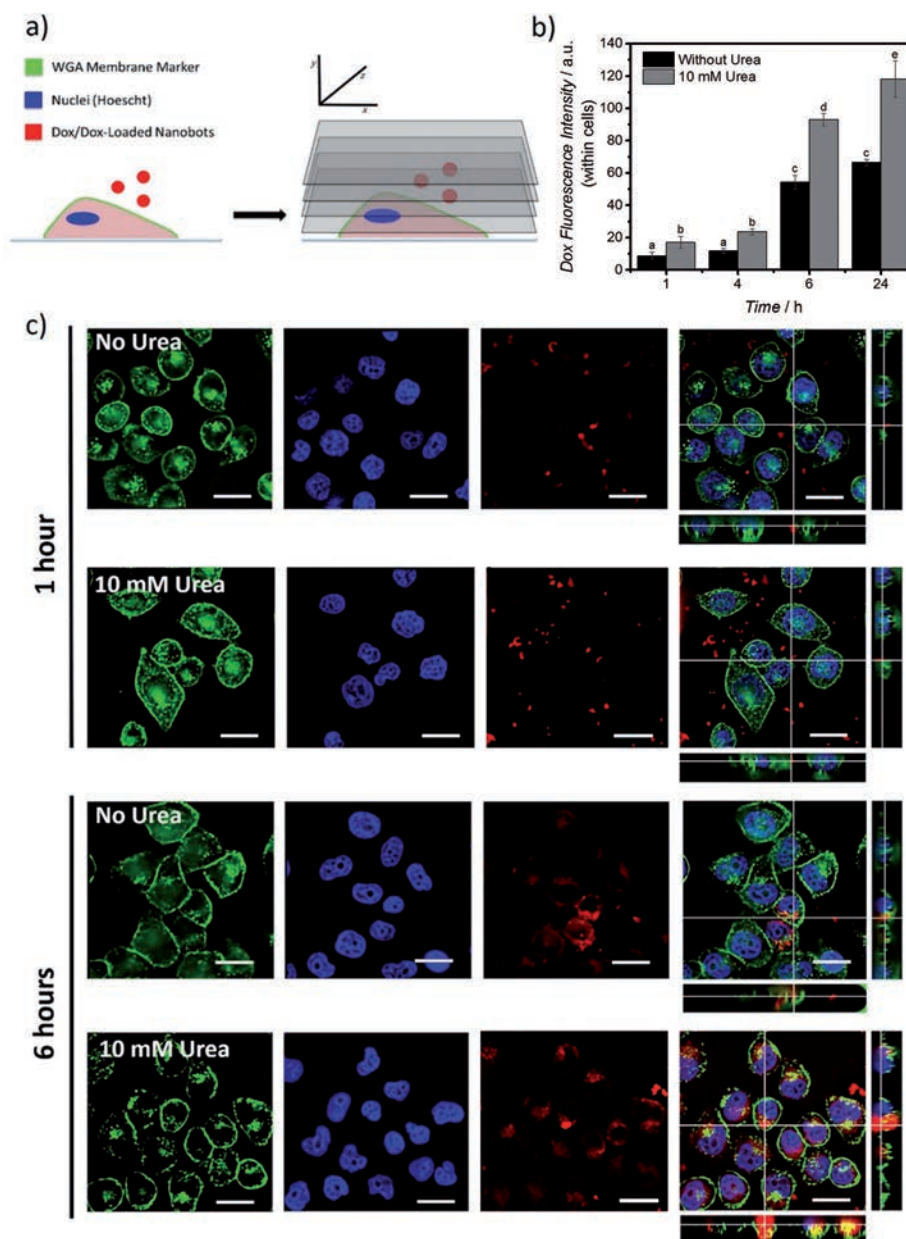


**Figure 6.** Interaction of Dox-loaded urease nanobots with HeLa cells. a) Schematic representing the cell labeling and imaging acquisition; cell membranes were marked with wheat germ agglutinin (WGA, green), and nuclei were marked with Hoescht (blue); red emission comes from Dox. b) Dox fluorescence emission quantification in regions within cells, in the absence (black) and presence of urea (grey) ( $N = 15$ , error bars represent SE), different superscripts denote significant differences among groups with  $p < 0.05$ ; c) fluorescence imaging of HeLa cells and Dox-loaded nanobots ( $0.05 \text{ mg mL}^{-1}$ ). Scale bars are  $20 \mu\text{m}$ .

Dulbecco's Modified Eagle Medium (DMEM) were purchased from Thermo Fischer Scientific.

**Instruments:** TEM images were captured by a JEOL JEM-2100 microscope. SEM images were captured by an FEI NOVA NanoSEM 230 at 5 kV. Hydrodynamic radii and electrophoretic mobility measurements were performed using a Wyatt Möbius coupled with an Atlas cell pressurization system. Absorbance spectra of Dox, protein quantification, and enzymatic activity assays were carried out using an Infinite M200 PRO Multimode Microplate Reader. Optical videos were

acquired using a Leica DMI8 inverted microscope equipped with a  $63\times$  water objective.

**Synthesis of Solid  $\text{SiO}_2$  Spheres:** The solid silica spheres were prepared using the modified Stöber method.<sup>[47]</sup> Briefly, a solution containing EtOH (7 mL), ultrapure water (10 mL), and ammonium hydroxide (2 mL) was stirred for 15 min. After, TEOS (6 mL) was added dropwise and the mixture was kept stirring for 21 h. The formed particles were then collected by centrifugation and washed with EtOH (3 times, 2348 g, 3.5 min). Finally, the spheres were suspended in EtOH and aliquots

(0.5 mL) were collected, centrifuged, air dried, and weighed to determine the concentration of the solid SiO<sub>2</sub> suspension.

**Coating of Mesoporous Silica Shell on Solid SiO<sub>2</sub> Spheres:** Solid silica spheres (60 mg) were suspended in a solution containing water (20 mL), TEOA (40 mg), and CTAB (75 mg). The solution was heated to 80 °C and TEOS (0.125 mL) was added dropwise, while the solution was stirred. The mixture was kept stirring for 2 h, after which it was collected by centrifugation (845 g, 2.5 min) and washed with ultrapure water once. Following, the obtained particles were suspended in a solution of MeOH and HCl (30 mL, 10:0.6) and refluxed at 80 °C for 24 h. Finally, the particles were collected by centrifugation (2.5 min, 845 g) and washed in EtOH (3 times) and ultrapure water (3 times). Aliquots (0.5 mL) were collected, centrifuged, air dried, and weighed to determine the concentration of the suspension.

**Amine Functionalization of MSNP:** The obtained MSNP (2 mg mL<sup>-1</sup>) were then suspended in EtOH:APTES mixture (20:1, v/v) and shaken during 24 h on an end-to-end rotary shaker. After, the particles were collected by centrifugation (845 g, 2.5 min) and washed in 3 times with EtOH and 3 times with water. Aliquots (0.5 mL) were collected, centrifuged, air dried, and weighed to determine the concentration of the suspension.

**Urease Functionalization of MSNP-NH<sub>2</sub>:** MSNP-NH<sub>2</sub> (2 mg) were washed 3 times with PBS 1x. After, the MSNP-NH<sub>2</sub> were suspended in (0.9 mL) PBS and GA (100 µL, 25% in water) was added to the mixture. The mixture was thoroughly vortexed to ensure good dispersion and shaken during 2.5 h on an end-to-end rotary shaker. Then, the particles were collected by centrifugation and washed 3 times with PBS. Afterward, the MSNP-NH<sub>2</sub> activated with GA were suspended in a solution of PBS containing urease (3 mg mL<sup>-1</sup>) and mixed end-to-end on a rotary shaker for 18 h. The resulting urease nanobots were collected by centrifugation (1150 g, 3.5 min) and washed 3 times with PBS.

**Dox Loading in MSNP-NH<sub>2</sub>:** Aliquots of MSNP-NH<sub>2</sub> (1 mg) were suspended in a Dox solution at a concentration of  $1 \times 10^{-3}$  M and vortexed thoroughly to ensure good dispersion. Then, the mixture was incubated during 24 h at room temperature, mixing end-to-end on a rotary shaker. The Dox loaded MSNP-NH<sub>2</sub> were then collected by centrifugation (1150 g, 3.5 min) and washed 3 times with PBS to ensure complete removal of non-loaded drug. The supernatants were kept and analyzed by measuring the absorbance at 480 nm, using an Infinite M200 PRO Multimode Microplate Reader, to determine the drug loading capacity and the entrapment efficiency of the MSNP-NH<sub>2</sub>.

**Dox Loading and Functionalization of MSNP-NH<sub>2</sub>:** To obtain Dox loaded nanobots, first the MSNP-NH<sub>2</sub> (1 mg) are incubated with  $1 \times 10^{-3}$  M solution of Dox (0.5 mL) as mentioned above. After, the particles are washed 3 times with PBS, suspended in PBS (0.9 mL), and GA (100 µL) was added, to follow the protocol for the functionalization of MSNP-NH<sub>2</sub> with urease as mentioned above, yielding Dox-loaded urease nanobots.

**In Vitro Release of Dox from MSNP-NH<sub>2</sub> and Urease Nanobots:** To evaluate the ability of the nanobots to enhance the release of the drug in the presence of urea, Dox-loaded nanobots (2 mg mL<sup>-1</sup>) were dispersed in solutions of PBS without urea and solutions containing different concentrations of urea. To compare the nanobots to the conventional MSNP-NH<sub>2</sub> carrier, Dox loaded MSNP-NH<sub>2</sub> were also placed in PBS. Then, the dispersions were placed on a thermomixer at 37 °C with 300 rpm shaking to avoid sedimentation and aliquots (100 µL) were collected every hour over the course of 6 h and at 24 h, refreshing the medium at every time point. The aliquots were then analyzed by measuring the absorbance at 480 nm, using an Infinite M200 PRO Multimode Microplate Reader, to obtain the cumulative release profile of each system.

**Optical Video Recording of Nanobots and MSD Analysis:** An inverted optical microscope (Leica DMI8) with a 63x water objective was used for the observation and video recording of the nanobots movement. An aqueous solution of nanobots was placed on a glass slide and thoroughly mixed with the solutions of urea at the desired concentrations. Then, the mixture was covered using a cover slip to avoid artifacts caused by the

drifting effect. Videos of 30 s were recorded up to the first 3 min after performing the mixture to ensure that the analysis is performed under the same conditions. The videos were obtained using a Hamamatsu camera at a frame rate of 50 fps, under bright field.

The videos were then analyzed using a Python code to obtain the tracking trajectories. Then, the MSD was calculated using the following

$$\text{MSD}(\Delta t) = \left\langle \left( x_i(t + \Delta t) - x_i(t) \right)^2 \right\rangle, (i=2, \text{ for 2D analysis}) \quad (5)$$

The diffusion coefficient ( $D_e$ ) is afterward obtained by fitting the data to Equation 1, which is valid at small time intervals for small particles with low rotational diffusion.<sup>[53]</sup> The resulting  $D_e$  is obtained by analyzing 20 particles per condition and the error represents SE.

**Enzymatic Activity Evaluation:** The activity of the covalently bound urease on the nanobots surface was evaluated using a commercial kit that determines the concentration ammonia generated by the Berthelot method.<sup>[61]</sup> The nanobots (0.5 mg mL<sup>-1</sup>) were incubated with a range ( $1 \times 10^{-3}$ ,  $5 \times 10^{-3}$ ,  $25 \times 10^{-3}$ ,  $50 \times 10^{-3}$ , and  $100 \times 10^{-3}$  M) of concentrations of urea for 10 min, to study the effect of urea concentration. The enzymatic activity was also investigated over time, by incubating the nanobots (0.5 mg mL<sup>-1</sup>) with the urea solution provided with the kit for varied time periods (2.5–120 min).

**Hydrodynamic Radii and Surface Charge Analysis:** A Wyatt Möbius coupled with an Atlas cell pressurization system was used to obtain the hydrodynamic radii and electrophoretic mobility of the MSNP. The equipment uses a laser with 532 nm wavelength, with a detector angle of 163.5°, performing three scans over an acquisition time of 5 s, acquiring light scattering and electrophoretic mobility data simultaneously. Each measurement was performed at least three times. To analyze the nanobots' movement by DLS, aqueous solutions containing nanobots and the different concentrations of urea were introduced in the DLS. The measurements were repeated to yield 20 data points per condition. The diffusion coefficient is obtained directly from the analysis of the scattering data on the Dynamics software, and the error represented is the SE.

**Nanobots and Dox-Loaded Nanobots Cytotoxicity Assays:** Human epithelial cervix adenocarcinoma HeLa cells were cultured in DMEM supplemented with fetal bovine serum (10%), L-glutamine ( $200 \times 10^{-9}$  M) and penicillin-streptomycin (1%), in a 37 °C and 5% CO<sub>2</sub> atmosphere, and split every 3 d at a 1:4 ratio. For the viability assessment, cells were seeded in 96-well plates at a density of 10 000 cells per well. After 24 h, the cells were incubated with nanobots or Dox-Loaded nanobots at different concentrations for another 24 h. The MTT was performed according to manufacturer's instructions. Briefly, a working solution of MTT ( $12 \times 10^{-3}$  M) was prepared and added to cell culture medium in a ratio of 1:10 and the cells were incubated with it for 4 h. Afterward, the medium was removed and the formazan crystals formed were dissolved using DMSO (50 µL). Absorbance values at 570 nm wavelength were measured using an Infinite M200 PRO Multimode Microplate Reader.

**Nanobots' and Dox-Loaded Nanobots Cytotoxicity Assays:** Human epithelial cervix adenocarcinoma HeLa cells were cultured in DMEM supplemented with Fetal Bovine Serum (10%), L-glutamine ( $200 \times 10^{-9}$  M) and penicillin-streptomycin (1%), in a 37 °C and 5% CO<sub>2</sub> atmosphere, and split every 3 d at a 1:4 ratio. For the viability assessment, cells were seeded in 96-well plates at a density of 10 000 cells per well. After 24 h, the cells were incubated with nanobots (0.05 mg mL<sup>-1</sup>) or Dox-loaded nanobots in the presence of  $1 \times 10^{-3}$ ,  $5 \times 10^{-3}$ ,  $25 \times 10^{-3}$ ,  $50 \times 10^{-3}$ ,  $100 \times 10^{-3}$ , and  $120 \times 10^{-3}$  M of urea for 24 h. The MTT assay was then performed as described above.

**Imaging of HeLa Cells with Dox-Loaded Nanobots:** Human epithelial cervix adenocarcinoma HeLa cells were cultured in DMEM supplemented with fetal bovine serum (10%), L-glutamine ( $200 \times 10^{-9}$  M) and penicillin-streptomycin (1%), in a 37 °C and 5% CO<sub>2</sub> atmosphere, and split every 3 d at a 1:4 ratio. For the viability assessment, cells were seeded in 8-well plates at a density of 15 000

cells per well. After 24 h, the cells were incubated with Dox-loaded nanobots ( $0.05 \text{ mg mL}^{-1}$ ) with urea ( $10 \times 10^{-3} \text{ M}$ ) and without urea for 1, 4, 6, and 24 h. After each incubation period, the cells were washed with PBS and the membranes were labeled with WGA and the nuclei with Hoescht. The cells were imaged in 3D, using an inverted optical microscope (Leica DMI8) equipped with a  $63\times$  water objective and a galvo stage, coupled with filter cubes for Rhodamine, FITC, and DAPI.

## Supporting Information

Supporting Information is available from the Wiley Online Library or from the author.

## Acknowledgements

The research leading to these results received funding from the European Research Council under the European Union's Seventh Framework Program (FP7/20072013)/ERC grant agreement no. 311529 (LT-NRBS). S.S. thanks the Spanish MINECO for grants CTQ2015-68879-R (MICRODIA) and CTQ2015-72471-EXP (Enzwin). A.C.H. thanks MINECO for the Severo Ochoa fellowship and T.P. thanks MINECO for the Juan de la Cierva fellowship. The authors thank A. M-López for developing the Python code for motion analysis. S.S., A.C.H., and T.P. designed the experiments. A.C.H. and T.P. performed the experiments and analyzed the data. A.P.-J. contributed to the execution of cell assays and A.B. participated in the fabrication process. S.S., A.C.H., and T.P. wrote the manuscript. All authors discussed the results and commented on the manuscript.

## Conflict of Interest

The authors declare no conflict of interest.

## Keywords

drug delivery, enzymatic catalysis, nanobots, nanomachines, nanomotors

Received: September 4, 2017

Revised: September 27, 2017

Published online: November 27, 2017

- [1] J. M. Rosenholm, C. Sahlgren, M. Lindén, *Nanoscale* **2010**, *2*, 1870.  
 [2] J. Shi, P. W. Kantoff, R. Wooster, O. C. Farokhzad, *Nat. Rev. Cancer* **2017**, *17*, 20.  
 [3] I. I. Slowing, J. L. Vivero-Escoto, C. Wu, V. S. Lin, *Adv. Drug Delivery Rev.* **2008**, *60*, 1278.  
 [4] L. K. E. A. Abdelmohsen, F. Peng, Y. Tu, D. A. Wilson, *J. Mater. Chem. B* **2014**, *2*, 2395.  
 [5] J. Wang, W. Gao, *ACS Nano* **2012**, *6*, 5745.  
 [6] F. Mou, C. Chen, Q. Zhong, Y. Yin, H. Ma, J. Guan, *ACS Appl. Mater. Interfaces* **2014**, *6*, 9897.  
 [7] X. Ma, K. Hahn, S. Sanchez, *J. Am. Chem. Soc.* **2015**, *137*, 4976.  
 [8] D. Patra, S. Sengupta, W. Duan, H. Zhang, P. Ryan, A. Sen, *Nanoscale* **2013**, *5*, 1273.  
 [9] W. Gao, J. Wang, *Nanoscale* **2014**, *6*, 10486.  
 [10] B. E.-F. de Ávila, C. Angell, F. Soto, M. A. Lopez-Ramirez, D. F. Báez, S. Xie, J. Wang, Y. Chen, *ACS Nano* **2016**, *10*, 4997.  
 [11] R. Dong, Y. Hu, Y. Wu, W. Gao, B. Ren, Q. Wang, Y. Cai, *J. Am. Chem. Soc.* **2017**, *139*, 1722.  
 [12] M. Xuan, Z. Wu, J. Shao, L. Dai, T. Si, Q. He, *J. Am. Chem. Soc.* **2016**, *138*, 6492.  
 [13] X. Chen, M. Hoop, F. Mushtaq, E. Siringil, C. Hu, B. J. Nelson, S. Pané, *Appl. Mater. Today* **2017**, *9*, 37.  
 [14] W. Gao, D. Kagan, O. S. Pak, C. Clawson, S. Campuzano, E. Chuluun-Erdene, E. Shipton, E. E. Fullerton, L. Zhang, E. Lauga, J. Wang, *Small* **2012**, *8*, 460.  
 [15] M. M. Stanton, B.-W. Park, A. Miguel-López, X. Ma, M. Sitti, *Small* **2017**, *13*, 1.  
 [16] M. M. Stanton, B.-W. Park, D. Vilela, K. Bente, D. Faivre, M. Sitti, S. Sanchez, *ACS Nano* **2017**, *11*, 9968.  
 [17] M. M. Stanton, J. Simmchen, X. Ma, A. Miguel-López, S. Sánchez, *Adv. Mater. Interfaces* **2016**, *3*, 1.  
 [18] B. Mostaghaci, O. Yasa, J. Zhuang, M. Sitti, *Adv. Sci.* **2017**, *4*, 1700058.  
 [19] S. Martel, M. Mohammadi, O. Felfoul, Z. Lu, P. Pouponneau, *Int. J. Rob. Res.* **2009**, *28*, 571.  
 [20] R. Di Leonardo, L. Angelani, D. Dell'arciprete, G. Ruocco, V. Iebba, S. Schippa, M. P. Conte, F. Mecarini, F. De Angelis, E. Di Fabrizio, *Proc. Natl. Acad. Sci. USA* **2010**, *107*, 9541.  
 [21] M. Medina-Sánchez, L. Schwarz, A. K. Meyer, F. Hebenstreit, O. G. Schmidt, *Nano Lett.* **2016**, *16*, 555.  
 [22] X. Ma, A. C. Hortelao, T. Patiño, S. Sanchez, *ACS Nano* **2016**, *10*, 9111.  
 [23] J. Katuri, X. Ma, M. M. Stanton, S. Sanchez, *Acc. Chem. Res.* **2016**, *50*, 2.  
 [24] S. Sanchez, L. Soler, J. Katuri, *Angew. Chem., Int. Ed.* **2015**, *54*, 1414.  
 [25] K. K. Dey, A. Sen, *J. Am. Chem. Soc.* **2017**, *139*, 7666.  
 [26] V. Magdanz, G. Stoychev, L. Ionov, S. Sanchez, O. G. Schmidt, *Angew. Chem., Int. Ed.* **2014**, *53*, 2673.  
 [27] A. A. Solovev, W. Xi, D. H. Gracias, S. M. Harazim, C. Deneke, S. Sanchez, O. G. Schmidt, *ACS Nano* **2012**, *6*, 1751.  
 [28] A. A. Solovev, S. Sanchez, M. Pumera, Y. F. Mei, O. G. Schmidt, *Adv. Funct. Mater.* **2010**, *20*, 2430.  
 [29] S. Sanchez, A. A. Solovev, S. Schulze, O. G. Schmidt, *Chem. Commun.* **2011**, *47*, 698.  
 [30] W. Gao, A. Pei, R. Dong, J. Wang, *J. Am. Chem. Soc.* **2014**, *136*, 2276.  
 [31] X. Ma, A. Jannasch, U.-R. Albrecht, K. Hahn, A. Miguel-López, E. Schäffer, S. Sánchez, *Nano Lett.* **2015**, *15*, 7043.  
 [32] X. Ma, X. Wang, K. Hahn, S. Sánchez, *ACS Nano* **2016**, *10*, 3597.  
 [33] X. Ma, A. C. Hortelao, A. Miguel-López, S. Sánchez, *J. Am. Chem. Soc.* **2016**, *138*, 13782.  
 [34] L. K. E. A. Abdelmohsen, M. Nijemeisland, G. M. Pawar, G.-J. A. Janssen, R. J. M. Nolte, J. C. M. van Hest, D. A. Wilson, *ACS Nano* **2016**, *10*, 2652.  
 [35] P. Schattling, B. Thingholm, B. Städler, *Chem. Mater.* **2015**, *27*, 7412.  
 [36] P. S. Schattling, M. A. Ramos-Docampo, V. Salgueiriño, B. Städler, *ACS Nano* **2017**, *11*, 3973.  
 [37] M. Nijemeisland, L. K. E. A. Abdelmohsen, W. T. S. Huck, D. A. Wilson, J. C. M. van Hest, *ACS Cent. Sci.* **2016**, *2*, 843.  
 [38] F. Peng, Y. Tu, A. Adhikari, J. C. J. Hintzen, D. W. P. M. Lowik, D. A. Wilson, *Chem. Commun.* **2016**, *53*, 1088.  
 [39] G. Rucinskaitė, S. A. Thompson, S. Paterson, R. de la Rica, *Nanoscale* **2017**, *9*, 5404.  
 [40] Y. Tu, F. Peng, P. B. White, D. A. Wilson, *Angew. Chem., Int. Ed.* **2017**, *56*, 7620.  
 [41] Y. Tu, F. Peng, X. Sui, Y. Men, P. B. White, J. C. M. Van Hest, D. A. Wilson, *Nat. Chem.* **2016**, *9*, 480.  
 [42] Y. Tu, F. Peng, A. A. M. André, Y. Men, M. Srinivas, D. A. Wilson, *ACS Nano* **2017**, *11*, 1957.  
 [43] F. Tang, L. Li, D. Chen, *Adv. Mater.* **2012**, *24*, 1504.

- [44] X. Ma, H. Feng, C. Liang, X. Liu, F. Zeng, Y. Wang, *J. Mater. Sci. Technol.* **2017**, *44*, 1067.
- [45] X. Ma, S. Sanchez, *Chem. Commun.* **2015**, *51*, 5467.
- [46] X. Ma, S. Sánchez, *Tetrahedron* **2017**, *73*, 4883.
- [47] W. Stober, A. Fink, *J. Colloid Interface Sci.* **1968**, *26*, 62.
- [48] J. B. Sumner, D. B. Hand, *J. Am. Chem. Soc.* **1929**, *149*, 1925.
- [49] P. K. Smith, R. I. Krohn, G. T. Hermanson, A. K. Mallia, F. H. Gartner, M. D. Provenzano, E. K. Fujimoto, N. M. Goeke, B. J. Olson, D. C. Klenk, *Anal. Biochem.* **1985**, *150*, 76.
- [50] K. K. Dey, X. Zhao, B. M. Tansi, W. J. Méndez-Ortiz, U. M. Córdova-Figueroa, R. Golestanian, A. Sen, *Nano Lett.* **2015**, *15*, 8311.
- [51] P. Gaspard, R. Kapral, **2017**, arXiv:1706.05691v1.
- [52] P. Illien, R. Golestanian, A. Sen, *Chem. Soc. Rev.* **2017**, *46*, 5508.
- [53] G. Dunderdale, S. Ebbens, P. Fairclough, J. Howse, *Langmuir* **2012**, *28*, 10997.
- [54] J. R. Howse, R. A. L. Jones, A. J. Ryan, T. Gough, R. Vafabakhsh, R. Golestanian, *Phys. Rev. Lett.* **2007**, *99*, 8.
- [55] Z. Bajzer, E. E. Strehler, *Biochem. Biophys. Res. Commun.* **2012**, *417*, 982.
- [56] K. S. Mangaldas, Y. S. Rajput, R. Sharma, *J. Plant Biochem. Biotechnol.* **2010**, *19*, 73.
- [57] D. C. Prieve, *Adv. Colloid Interface Sci.* **1999**, *82*, 93.
- [58] N. Chen, C. Wu, C. Chung, Y. Hwu, S. Cheng, Y. Mou, L. Lo, *PLoS One* **2012**, *7*, 3.
- [59] X. Ma, S. Jang, M. N. Popescu, W. E. Uspal, A. Miguel-López, K. Hahn, D.-P. Kim, S. Sánchez, *ACS Nano* **2016**, *10*, 8751.
- [60] US Department of Health and Human Services FDA, *Use of International Standard ISO 10993-1, "Biological evaluation of medical devices—Part 1: Evaluation and testing within a risk management process", Guidance for Industry and Food and Drug Administration Staff*; **2016**.
- [61] C. J. Patton, S. R. Crouch, *Anal. Chem.* **1977**, *49*, 464.



# Chapter 4



**Targeting 3D Bladder Cancer Spheroids with Urease-Powered  
Nanomotors**

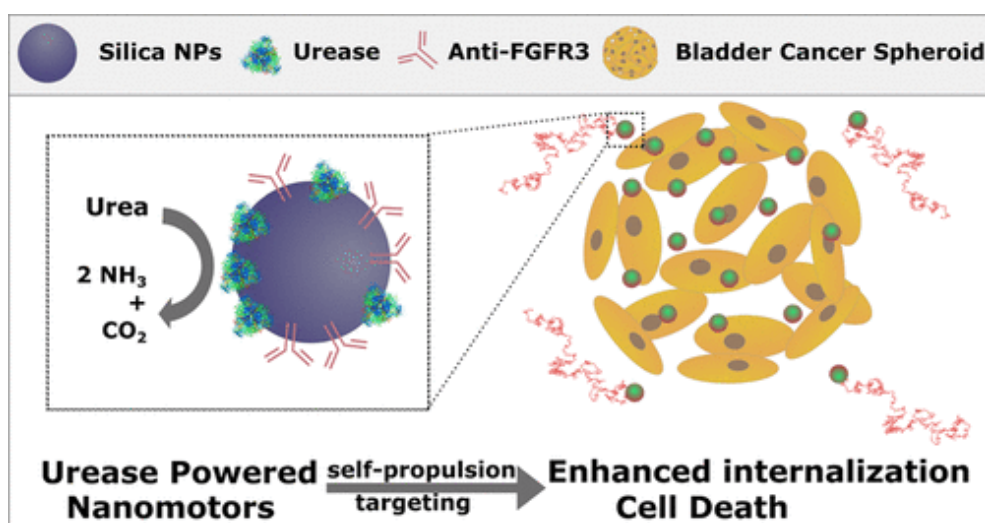




Bladder cancer is the 9<sup>th</sup> **most common cancer worldwide**, having very high relapse rates. The current treatments consist in tumor resection followed by intravesical administration of chemotherapy. However, these treatments have **low efficacy** due to brief drug residence time, low diffusivity of the drug in the urothelium, and degradation by the harsh environment within the bladder, thus urging the need for more effective therapeutic alternatives.

In this work, aiming at taking advantage of the high concentration of urea in the bladder, we designed urease powered nanomotors for **bladder cancer therapy**. For this, we modified the surface of the nanomotors with an **antibody** that targets the fibroblast growth factor 3 (anti-FGFR3), a receptor that is overexpressed in non-muscle invasive bladder cancer and was reported to have a therapeutic action against cancer, as it halts cell proliferation when bound to the receptor.

We studied the effect of self-propulsion in the **targeting and penetration capabilities** of the nanomotors, using **bladder cancer 3D spheroids** as model. We demonstrated that the **combination of self-propulsion with active targeting** significantly **enhanced internalization** of nanomotors into spheroids. Furthermore, thanks to the ability of anti-FGFR3 antibody to halt cell proliferation when bound to the receptor, we observed that spheroids showed **significantly lower cell proliferation** levels when treated with antibody-modified active nanomotors.



**Graphical Abstract 2.** Targeting of 3D bladder cancer spheroids using antibody-modified urease powered nanomotors.

# Targeting 3D Bladder Cancer Spheroids with Urease-Powered Nanomotors

Ana C. Hortelão,<sup>†</sup> Rafael Carrascosa,<sup>†</sup> Nerea Murillo-Cremaes,<sup>†</sup> Tania Patiño,<sup>\*,†</sup> and Samuel Sánchez<sup>\*,†,‡,§</sup>

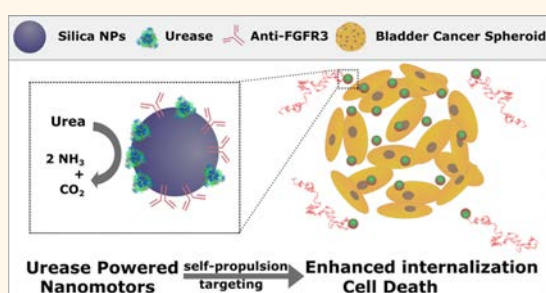
<sup>†</sup>Institute for Bioengineering of Catalonia (IBEC), The Barcelona Institute of Science and Technology (BIST), Baldori i Reixac 10-12, 08028 Barcelona Spain

<sup>‡</sup>Institució Catalana de Recerca i Estudis Avancats (ICREA), Passeig Lluís Companys 23, 08010 Barcelona, Spain

**S** Supporting Information

**ABSTRACT:** Cancer is one of the main causes of death around the world, lacking efficient clinical treatments that generally present severe side effects. In recent years, various nanosystems have been explored to specifically target tumor tissues, enhancing the efficacy of cancer treatment and minimizing the side effects. In particular, bladder cancer is the ninth most common cancer worldwide and presents a high survival rate but serious recurrence levels, demanding an improvement in the existent therapies. Here, we present urease-powered nanomotors based on mesoporous silica nanoparticles that contain both polyethylene glycol and anti-FGFR3 antibody on their outer surface to target bladder cancer cells in the form of 3D spheroids. The autonomous motion is promoted by urea, which acts as fuel and is inherently present at high concentrations in the bladder. Antibody-modified nanomotors were able to swim in both simulated and real urine, showing a substrate-dependent enhanced diffusion. The internalization efficiency of the antibody-modified nanomotors into the spheroids in the presence of urea was significantly higher compared with antibody-modified passive particles or bare nanomotors. Furthermore, targeted nanomotors resulted in a higher suppression of spheroid proliferation compared with bare nanomotors, which could arise from the local ammonia production and the therapeutic effect of anti-FGFR3. These results hold significant potential for the development of improved targeted cancer therapy and diagnostics using biocompatible nanomotors.

**KEYWORDS:** nanomotors, self-propulsion, nanomachines, enzymatic catalysis, targeting, 3D cell culture, bladder cancer



Cancer is the second leading cause of death worldwide, as reported by the World Health Organization (WHO).<sup>1</sup> Current clinical treatments of cancer include tumor resection surgery, radiotherapy and chemotherapy, which are often not effective and come at high cost in terms of the potential side effects.<sup>2</sup> Many efforts have been devoted to tackle these problems, especially using nanotechnology for the development of more efficient methods for diagnostics and therapy.<sup>3</sup> A wide range of nanosystems have been designed for delivering chemo-, radio-, gene-, photo-thermal-, and nanoassisted immunotherapy in the past decade to treat cancer in *in vitro* experiments.<sup>4</sup> Despite this, the majority of nanodevices do not translate into clinical use.<sup>5</sup> This might be due to the biological barriers present in the human body, such as the extracellular matrix, the interstitial flow pressure, phagocytic sequestration, or endosomal escape.<sup>6</sup> Researchers' endeavors to improve nanomedicine encompass the study of tumor heterogeneity and deeper investigation on

the interactions of nanodevices and biological interfaces as well as a better understanding on the influence of particle design.<sup>5,6</sup>

In addition, the field of active matter has devoted significant attention to the potential use of self-propelled particles as tools in nanomedicine because the continuous driving force provided by propulsion at the micro- and nanoscales may aid the conventional diffusive transport of drugs across biological barriers and assist in tissue penetration.<sup>7,8</sup> Furthermore, when used as drug-delivery vehicles, self-propelled particles have shown to enhance drug release rates as well as drug-delivery efficiency to cancer cells.<sup>9–11</sup> A plethora of approaches can be used to achieve propulsion at the micro- and nanoscale, such as external stimuli (e.g., light,<sup>12–15</sup> ultrasound waves,<sup>16,17</sup> and magnetic fields),<sup>18–20</sup> coupling motile cells to particles (e.g.,

**Received:** August 29, 2018

**Accepted:** December 27, 2018

**Published:** December 27, 2018

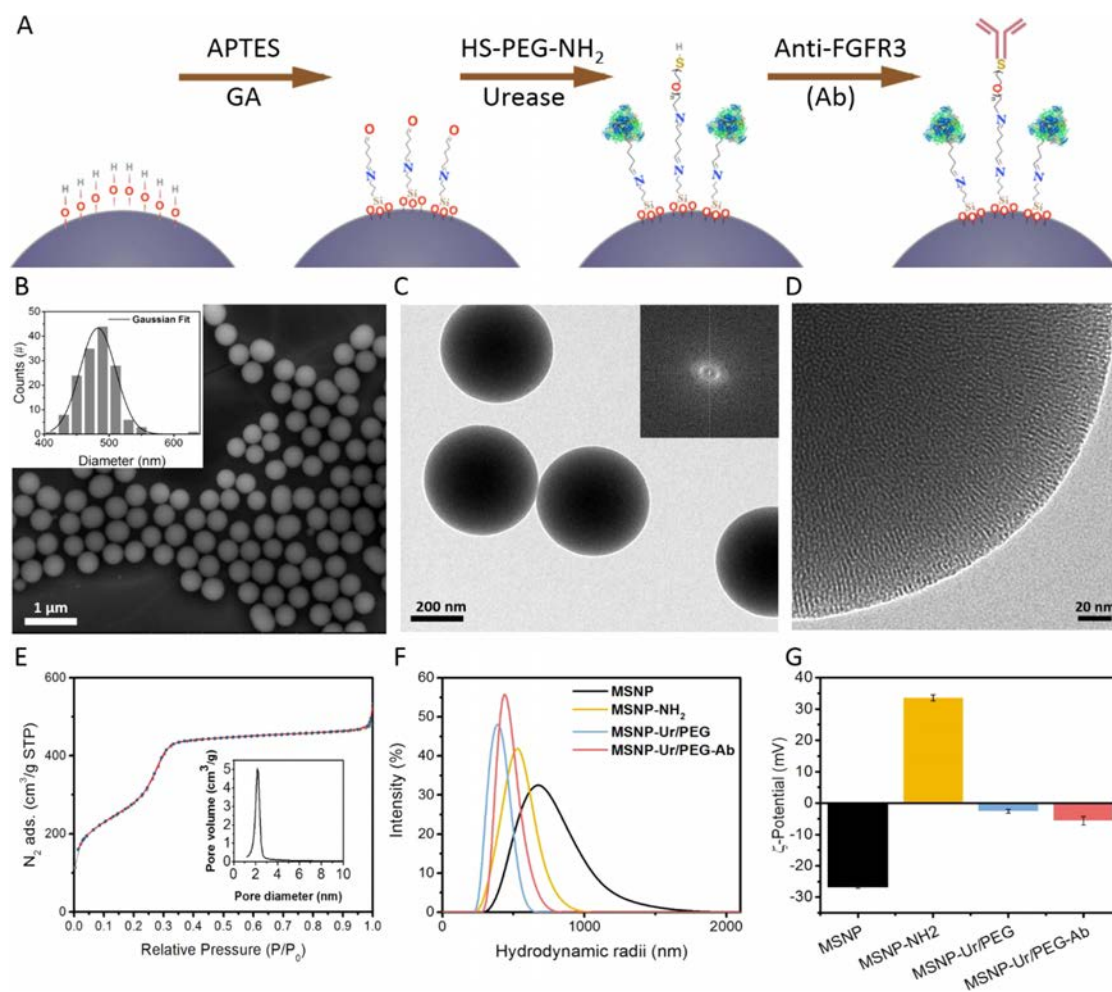


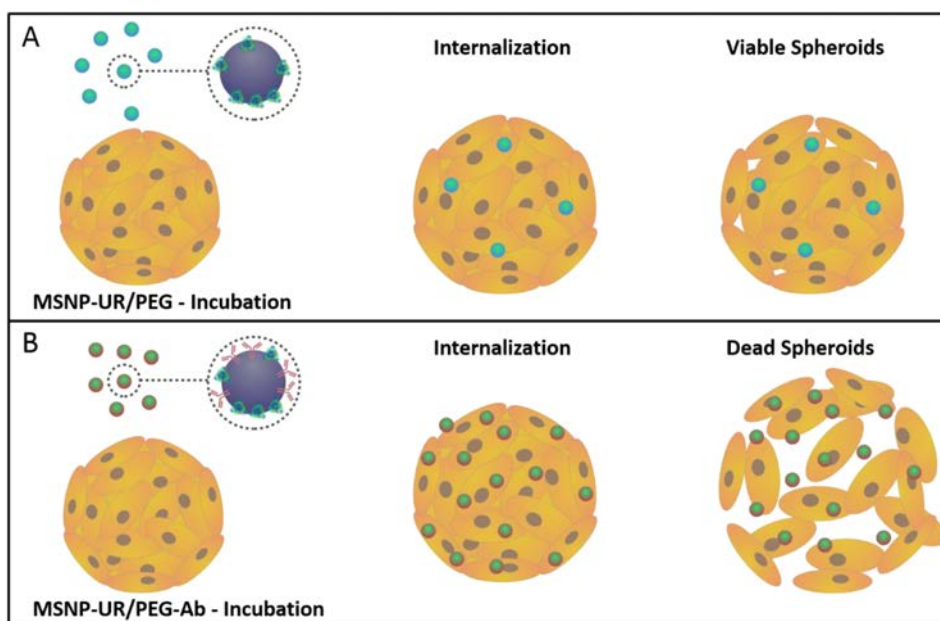
**Figure 1.** Fabrication and characterization of urease/polyethylene glycol nanomotors (MSNP-Ur/PEG) and antibody-modified urease nanomotors (MSNP-Ur/PEG-Ab). (A) Scheme illustrating the stepwise fabrication process to obtain the nanomotors. (B) SEM image of mesoporous silica nanoparticles (MSNPs). Inset: histogram of MSNPs size distribution evaluated by SEM. (C) TEM image of MSNPs. Inset: fast Fourier transform of MSNPs mesopores. (D) TEM image evidencing the porosity feature of the particles. (E) Nitrogen adsorption and desorption isotherms of the MSNPs. Inset: pore diameter distribution. (F) Hydrodynamic radii and (G) surface charge characterization of MSNPs and the subsequent stepwise modifications to obtain bare and antibody-modified nanomotors ( $N = 9$ ; results are shown as average plus or minus the standard error of the mean, SE).

sperm or bacteria),<sup>21–28</sup> or by incorporating catalytic units into the system as it is the case of catalytic micro- and nanomotors.<sup>29–31</sup> Catalytic motors were originally based on the decomposition of toxic fuels, for example hydrogen peroxide.<sup>32–34</sup> However, this hindered their applicability in biological environments, leading to the search of alternative safe fuel sources, such as propulsion based on magnesium's reaction with water.<sup>35,36</sup> Regarding biocompatibility, the use of enzymes as biocatalytic units to power the propulsion of micro- and nanomotors provides several advantages compared with other catalysts because they offer a wide choice of substrates or combination of substrates that are bioavailable and biocompatible, allowing us to tailor the motors on-demand of the target application.<sup>10,30,37–44</sup> Our group and others have previously reported the propulsion of different structures powered by the enzymatic conversion of glucose and urea,<sup>10,30,37–40,45–48</sup> which are substrates readily available in

the body. For instance, urea is present in considerable amount in the urinary bladder, where concentrations can reach 300 mM.<sup>49</sup> This feature allows for the design of urease-powered nanomotors, which become active in bladder due to urea conversion, and their use for the therapy of urinary tract diseases, such as bladder cancer.

Bladder cancer is the ninth most common cancer worldwide,<sup>50</sup> and despite having good survival rates, relapse is frequent (50%) and the treatment response is often poor in recurrence cases.<sup>51</sup> The current clinical treatments consist in tumor resection followed by intravesical chemotherapy, which has low effectiveness due to brief drug residence time in bladder, low permeability of the urothelium, and drug degradation by the harsh environment within the bladder.<sup>52,53</sup> This led to a demand for more-effective methods for bladder cancer therapy, capable of penetrating and delivering drugs to the tumor region.

**Scheme 1. Internalization of Urease-Powered Nanomotors (A) in the Absence and (B) in the Presence of the Anti-FGFR3 Antibody<sup>a</sup>**



<sup>a</sup>The interaction between antigen and the antibody in spheroids incubated with nanomotors composed of anti-FGFR3 leads to both a more-efficient internalization compared with bare nanomotors (panel B, left and middle panels) and to the blockage of the FGF pathway, resulting in cell death on 3D bladder cancer spheroids (panel B, right panel).

Herein, we present urease-powered nanomotors, coupled with an antibody (Figure 1A), for the active targeting of bladder cancer cells in 3D cultures (bladder cancer spheroids), which have been reported to better-mimic real tumor environments.<sup>54</sup> The enhanced diffusion provided by the biocatalytic conversion of urea at biologically relevant concentrations provides the nanomotors with a propulsion force and allows them to explore larger areas than passive diffusion, which could improve the chances of interaction between the antibody and the antigen. The antibody used in this work targets the fibroblast growth factor receptor 3 (FGFR3), a transmembrane protein that is over-expressed in bladder cancer cells and leads to the development of aggressive tumors, by up-regulating cell migration and proliferation.<sup>55–58</sup> The use of an antibody that actively binds to the FGFR3 antigen not only enables the targeting of bladder cancer cells but also allows us to achieve a therapeutic effect because it has been demonstrated that the interaction of FGFR3 with antibodies inhibits the fibroblast growth factor signaling pathway, thus blocking the proliferation of bladder cancer cell lines and ultimately leading to cell death (Scheme 1).<sup>55,57–59</sup>

## RESULTS AND DISCUSSION

Fully mesoporous silica nanoparticles (MSNPs) were prepared using sol–gel chemistry, in which cetyltrimethylammonium bromide (CTAB) was used as a porogenic agent and triethanolamine (TEOA) was used as base catalyst. The prepared MSNPs were characterized by scanning electron microscopy (SEM), as displayed in Figure 1B. SEM analysis revealed good monodispersity of the sample (polydispersity index of 0.114) and a mean diameter of  $481 \pm 2$  nm ( $N = 150$ , average size  $\pm$  SE), as depicted in the inset of Figure 1B.

Furthermore, the porous structure of the MSNPs was evaluated by transmission electron microscopy (TEM, Figure 1C,D). A clear radial porosity is evidenced by the TEM in Figure 1D. This crystalline configuration was further confirmed by the fast Fourier transform (inset of Figure 1C), which indicated the periodicity of the porous pattern. The surface area of the nanoparticles was studied by performing nitrogen adsorption and desorption using the Brunauer–Emmett–Teller analysis (BET) method. The MSNPs showed a type IV isotherm (Figure 1E), typical of mesoporous silica structures,<sup>60</sup> and a BET-specific surface area of  $1184.8$  m<sup>2</sup>/g, with an average pore size of 2 nm (inset of Figure 1E).

The produced particles were then functionalized with amine groups using aminopropyltriethoxysilane (APTES). The amine groups on the surface of the MSNP were later activated with glutaraldehyde (GA), which acted as a linker between the particle and the urease and heterobifunctional polyethylene glycol (PEG) molecules (Figure 1A). The terminal thiol group of PEG allowed for the coupling of the targeting moiety, antifibroblast growth factor 3 (anti-FGFR3).

The functionalization steps were followed by dynamic light scattering (DLS) and electrophoretic mobility analysis to obtain the hydrodynamic radii and surface charge, respectively (Figure 1E,F). The DLS analysis of the as-synthesized MSNPs showed a broad peak (Figure 1E, black), suggesting the presence of aggregates in the suspension. Electrophoretic mobility analysis of MSNPs indicated a surface charge of  $-26.81 \pm 0.35$  mV ( $N = 9$ , average  $\pm$  SE), typical for silica nanoparticles. The successful functionalization with amines was evidenced by the pronounced change in surface charge to a strongly positive value ( $33.6 \pm 1.0$  mV,  $N = 9$ , average  $\pm$  SE), characteristic of the presence of free amine groups on the surface. The hydrodynamic radii of amine functionalized



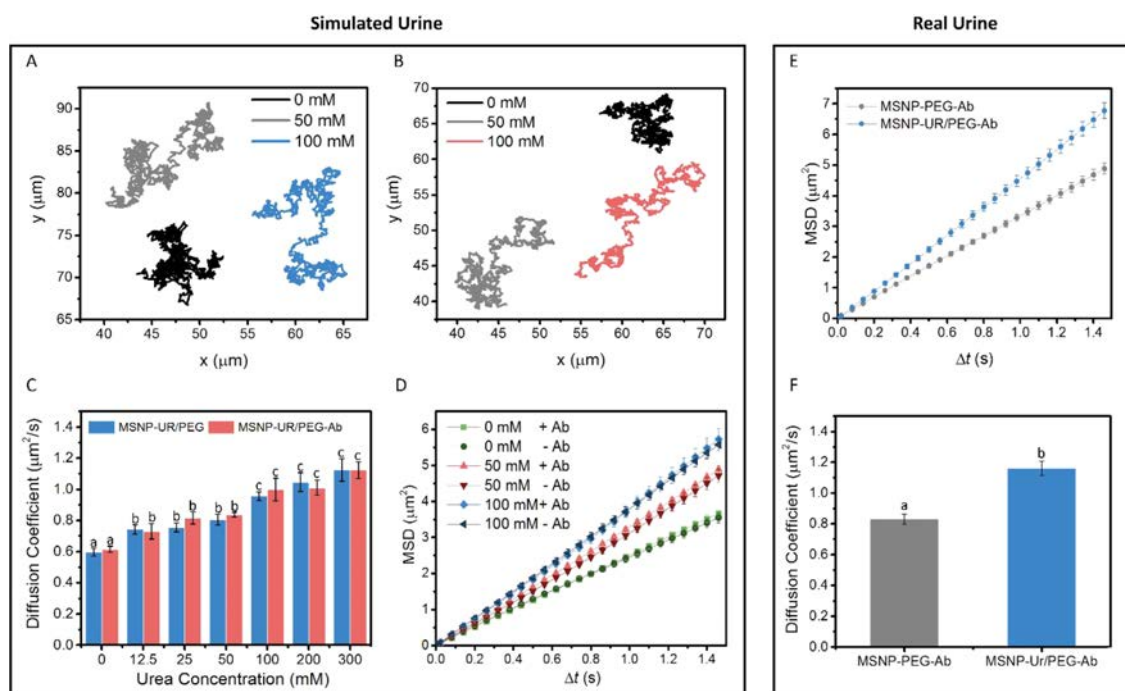
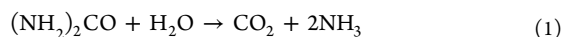


**Figure 2.** Motion analysis of MSNP-Ur/PEG and MSNP-Ur/PEG-Ab. Representative tracked trajectories of (A) MSNP-Ur/PEG nanomotors and (B) MSNP-Ur/PEG-Ab nanomotors at 0, 50, and 100 mM urea and (C) mean-squared displacements (MSDs) of both types of nanomotors at 0, 50, and 100 mM. (D) Effective diffusion coefficients obtained by MSD analysis at different urea concentrations (different superscripts denote significant differences among groups with  $P < 0.05$ ,  $N = 20$ ; results are shown as mean  $\pm$  SE). (E) Mean-squared displacements (MSDs) of particles modified with PEG and antibody (MSNP-PEG-Ab) and antibody-modified nanomotors (MSNP-Ur/PEG-Ab) in rat urine. (F) Effective diffusion coefficients for MSNP-PEG-Ab and MSNP-Ur/PEG-Ab in rat urine, obtained by MSD analysis (different superscripts denote significant differences among groups,  $P < 0.05$ ,  $N = 20$ , error bars represent SE).

MSNPs (MSNP-NH<sub>2</sub>) indicated a sharper peak that can be due to a stabilization of the particles by both surface charge and surface chemistry.<sup>61</sup>

The subsequent functionalization step concerned the coupling of both urease enzyme and heterobifunctional PEG. Typically, PEG is used as a spacer or as a means of preventing aggregation in suspension by providing steric hindrance between particles. We confirmed this effect on the colloidal stability of MSNP-Ur/PEG by DLS analysis, in which a sharp single population peak was observed (Figure 1F, blue). Furthermore, the PEG molecules allowed for the conjugation of the antibodies to the nanoparticles by linking the free thiol group at the outer end of the PEG to the antibodies' cysteine residues. This approach provides more specificity on the binding of IgG antibodies due to the high content of cysteine residues present on the constant region of the heavy chain (Figure 1A).<sup>62</sup> The conjugation of MSNP-Ur/PEG with anti-FGFR3 antibody (MSNP-Ur/PEG-Ab) was also analyzed by DLS, and the observed single peak (Figure 1F, red) showed that the presence of the antibody did not affect the stability of the particles in solution. We have confirmed the presence of both, as well as the antibody on the surface of the MSNPs using a kit that quantifies proteins based on the reduction of copper by proteins' peptide bonds (Figure S1)<sup>63</sup> and evaluated the urease enzymatic activity while bound to the nanomotors (Figure S2).

The urease present on the surface of the MSNP-Ur/PEG and MSNP-Ur/PEG-Ab allows for the biocatalytic conversion of urea into ammonia and carbon dioxide, following eq 1:



Typically, a geometrical asymmetry is induced on the micro- and nanostructures (e.g., Janus particles) to achieve an asymmetrical generation of forces,<sup>37,64</sup> which is an important requirement to produce motion at low Reynolds number. However, recently, our group reported that for the motors propelled via biocatalytic conversion, a molecular unbalanced distribution of enzymes is sufficient for the generation of the asymmetry necessary to generate net motion.<sup>45</sup> However, that previous study was reported for micron-sized motors. The MSNP-Ur/PEG and MSNP-Ur/PEG-Ab nanomotors reported in this work rely on such inherent asymmetries for self-propulsion in nanoscaled motors. The motion profiles of MSNP-Ur/PEG and MSNP-Ur/PEG-Ab were evaluated in the presence of a range of urea concentrations (0, 12.5, 25, 50, 100, 200, and 300 mM) in simulated urine. We have used optical tracking technique to obtain the tracked trajectories of the nanomotors (Figure 2A,B and Videos S1 and S2), which were then used to calculate the mean-squared displacement (MSD). Figure 2C displays the typical MSD of urease/PEG nanomotors and antibody-modified nanomotors in simulated urine. We observed that the MSD increases linearly with time, which is characteristic of diffusive motion<sup>64,65</sup> and obtained the effective diffusion coefficient for each given condition by fitting the MSDs to eq 2:

$$\text{MSD}(\Delta t) = 4D_e\Delta t \quad (2)$$

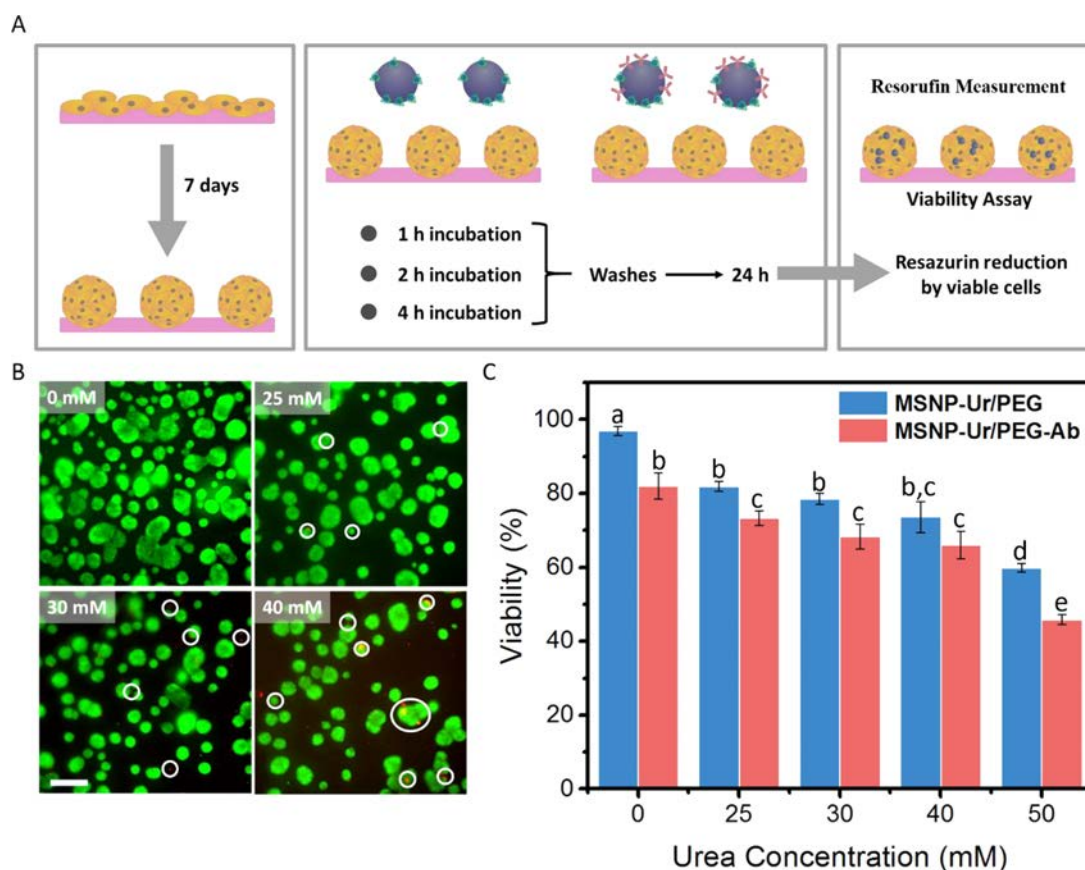


**Figure 3.** Effect of nanomotors with and without antibody on spheroids' viability in the presence of different concentrations of urea. (A) Experimental approach to investigate the effect of nanomotors on spheroids' viability. (B) Live/dead assay of spheroids after 4 h of incubation with nanomotors at 0, 25, 30, and 40 mM urea (scale bar is 200  $\mu\text{m}$ ). (C) Quantification of spheroids' viability after 4 h of incubation with MSNP-Ur/PEG (blue) and MSNP-Ur/PEG-Ab (red) at different urea concentrations; different superscripts denote significant differences among groups with  $P < 0.05$ ,  $N = 3$ , and results shown as mean  $\pm$  SE.

where  $D_e$  represents the effective diffusion coefficient, and  $\Delta t$  represents the time interval.<sup>64,65</sup>

Figure 2D shows the calculated effective diffusion coefficients for both MSNP-Ur/PEG and MSNP-Ur/PEG-Ab, evidencing that a significant increase in diffusion was achieved at 50 mM urea concentration. The diffusion coefficient further increased with increasing urea concentrations in simulated urine, reaching a plateau. The increase in diffusion with respect to increasing urea concentrations can be related with urease enzyme Michaelis–Menten kinetics, which obey eq 3:

$$v = \frac{V_{\max}[S]}{K_m + [S]} \quad (3)$$

where  $V_{\max}$  represents the maximum reaction rate,  $S$  represents substrate concentration, and  $K_m$  represents the Michaelis–Menten constant. As displayed in Figure 2D, no significant differences were found between the motion profiles of MSNP-Ur/PEG and MSNP-Ur/PEG-Ab, indicating that the presence of this targeting moiety does not hinder the motion abilities of the nanomotors. Furthermore, we have investigated the motion profile in real urine samples obtained from rats and observed similar results to the study performed using simulated urine (Figure 2 E,F and Video S3).

We studied the *in vitro* biocompatibility of the substrate required for nanomotors' motion (urea) and the byproduct of the biocatalysis (ammonia) by using 3D cultures (spheroids) of human urinary bladder transitional cell papilloma RT4 cells. The spheroids were obtained by seeding RT4 cells in dishes coated with Matrigel (Figure S3A), which resembles the extracellular matrix and provides a 3D environment for cell growth.<sup>66</sup> Then, the cultures were allowed to proliferate for 7 days, and spheroid growth was monitored every day (Figure S3B–E). We investigated the effect of a range of concentrations of urea (0, 25, 50, and 100 mM) and ammonia (0, 20, 30, 40, and 50 mM), by incubating the spheroids for 24 h at each condition. After that, the cultures were washed with medium and cell viability and proliferation was assessed using the alamarBlue assay. This assay is based on the reduction of resazurin into the fluorescent compound resorufin by metabolically active cells.

Urea exhibited good biocompatibility, not affecting spheroid viability even at the highest concentration we studied (Figure S4A), while ammonia, the product of the biocatalytic conversion of urea, revealed an increased cytotoxic trend with increasing concentrations (Figure S4B). Nevertheless, the spheroids remained viable (>70% viability)<sup>67</sup> at all ammonia

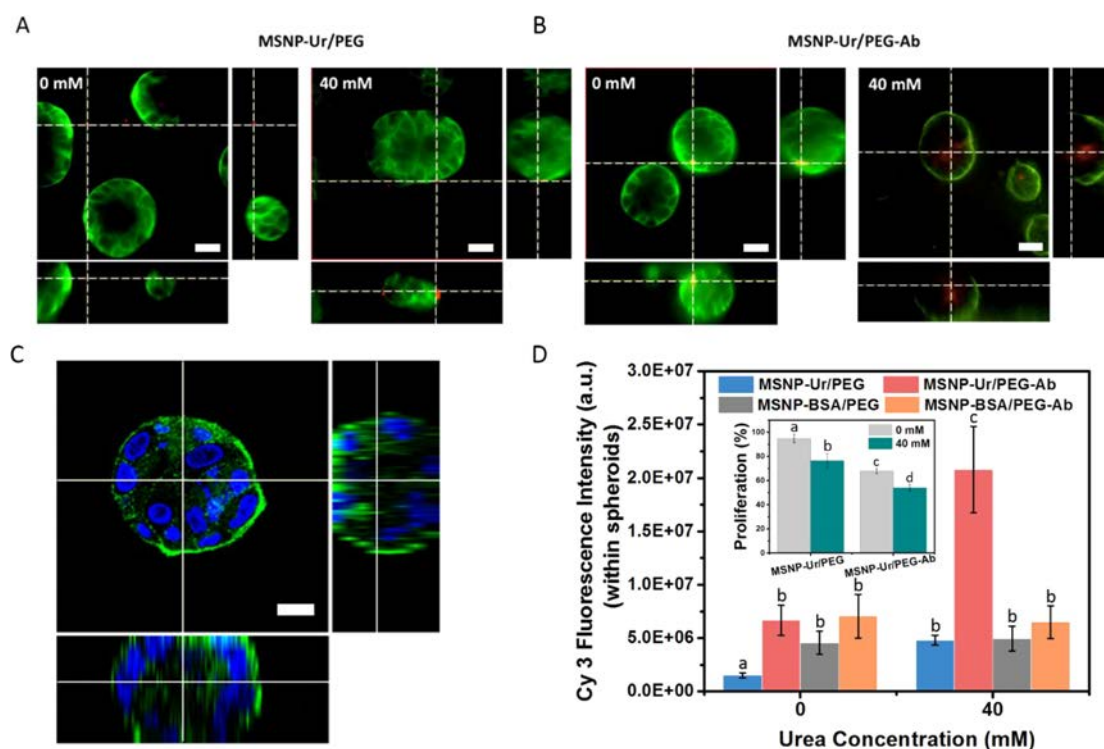


**Figure 4.** Targeting and penetration abilities of antibody-modified nanomotors into bladder cancer spheroids. (A) Fluorescence image of MSNP-Ur/PEG incubated with spheroids at 0 and 40 mM urea. (B) Fluorescence image of MSNP-Ur/PEG-Ab incubated with spheroids at 0 and 40 mM urea (scale bars are 50  $\mu\text{m}$ ). (C) Immunocytochemistry of FGFR3 antigen on the membrane of bladder cancer spheroids (scale bar is 10  $\mu\text{m}$ ). (D) Quantification of the internalization of antibody-modified nanomotors into bladder cancer spheroids in the presence (40 mM) and absence of urea after 4 h of incubation (different superscripts denote significant differences among groups with  $P < 0.05$ ,  $N = 30$ ; results are shown as mean  $\pm$  SE). Inset: quantification of the proliferation of spheroids incubated with MSNP-Ur/PEG and MSNP-Ur/PEG-Ab for 4 h in the presence (40 mM) and the absence of urea measured after a 48 h resting period incubation (different superscripts denote significant differences among groups with  $P < 0.05$ ,  $N = 3$ ; results are shown as mean  $\pm$  SE).

concentrations tested, which are in the range of the concentrations produced by the nanomotors (Figure S6).

We further investigated the viability of the spheroids when exposed to the nanomotors (MSNP-Ur/PEG), under a range of concentrations of urea and at different incubation periods. The spheroids were incubated with 12.5  $\mu\text{g}/\text{mL}$  of bare nanomotors or antibody-modified nanomotors at 0, 25, 30, and 40 mM of urea, for 1, 2, and 4 h (Figure S5). Next, the cultures were thoroughly washed with medium to remove nanomotors and uncatalyzed urea and kept for 24 h before analysis (Figure 3A). The effect of the nanomotors on bladder cancer spheroids' viability was visualized using the live/dead viability kit (Figure 3B) and quantified using the alamarBlue assay (Figure 3C). We observed that the nanomotors were not toxic in the absence of urea (Figure 3B,C), which indicates the good biocompatibility of the nanomotors' chassis (mesoporous silica, type MCM-41), as well as the PEG and enzyme. Upon the presence of increasing concentrations of urea, a cytotoxic effect is denoted for both nanomotors, being more pronounced on antibody-modified nanomotors (Figure 3C). The toxicity observed for bare nanomotors is due to the production of ammonia originated from the biocatalytic conversion of urea. However, the higher cytotoxic effect observed for nanomotors carrying the antibody can arise from the interaction between the anti-FGFR3 and the antigen present on the spheroids' membranes. The interaction between

these moieties has been reported to block the FGF signaling pathway, which is involved on cell growth and proliferation.<sup>55,57–59</sup>

To better understand the contribution of ammonia to the cytotoxic effect observed on the spheroids, we have studied the effective concentration of ammonia produced by the nanomotors for defined periods at different concentrations of urea. We incubated 12.5  $\mu\text{g}/\text{mL}$  of nanomotors with a range of concentrations of urea (0, 12.5, 25, 50, 100, 200, and 300 mM) and used *p*-nitrophenol as an indicator for pH (Figure S6). Because the conversion of urea into ammonia and carbon dioxide by nanomotors generates a sharp rise in pH, the solution containing nanomotors turns yellow due to the presence of *p*-nitrophenol and can be titrated with HCl to quantify the amount of ammonia present, according to eq 4:



We have found that at this concentration of nanomotors, the maximum ammonia output reached was 17 mM (Figure S6), which was found to be biocompatible toward bladder cancer spheroids (>70% viability for 20 mM ammonia, Figure S4B). Nevertheless, upon incubation with nanomotors and urea, the cytotoxic effect observed is stronger than with free ammonia. This outcome may emerge from the production of a locally higher concentration of ammonia by the nanomotors in the vicinity of the spheroids, thus leading to higher cytotoxicity.



Taking in consideration the nanomotors' enhanced diffusion capabilities and biocompatibility, we subsequently investigated their potential to target and penetrate into bladder cancer spheroids (Figure 4). First, we verified the expression of the targeted antigen (FGFR3) on the surface of the bladder cancer spheroids by immunocytochemistry, a technique used to visually detect the location of specific proteins on a sample by means of fluorescently labeled antibodies. Figure 4C displays an immunocytochemistry of a bladder cancer spheroid, where green fluorescence on the cell membranes confirms the presence of the transmembrane protein FGFR3, and blue represents the cell nuclei stained with Hoechst.

We then investigated the ability of nanomotors to penetrate the bladder cancer spheroids and the effect of the presence of the targeting moiety on internalization efficiency. Furthermore, we evaluated the influence of active motion in internalization efficiency by incubating the spheroids with bare nanomotors or antibody-modified nanomotors in the presence of 40 mM urea. For this, we labeled urease with the fluorescent marker cyanine3 (Cy3) prior to its functionalization onto the MSNP-NH<sub>2</sub> to precisely localize the nanomotors using fluorescence microscopy. Then, we functionalized the nanomotors with both nonlabeled urease and labeled urease (5%) and verified that the motion capabilities were retained despite the presence of labeled enzyme (Figure S7). Next, we incubated the 3D cultures with 12.5  $\mu\text{g}/\text{mL}$  of MSNP-Ur/PEG-Ab or MSNP-Ur/PEG as negative control for targeting for 4 h in the absence and the presence of urea (40 mM). Afterward, the cultures were washed, and cell membranes were labeled with wheat germ agglutinin (WGA) (Figure 4A,B). Quantification of fluorescence intensity of Cy3 within spheroids (50–100  $\mu\text{m}$  in diameter) revealed that active motors present a 3-fold higher internalization efficiency than in the absence of urea.

The urea present in the medium acts as a fuel for the urease-powered nanomotors. When antibody-modified nanomotors are actively moving (*i.e.*, in the presence of urea), the internalization efficiency is 3-fold higher than in the absence of urea (Figure 4D). This effect arises not only from the propulsion force generated by motion but also from the higher probability of interaction between the antibody and the target antigen, compared to when only Brownian diffusion is taking place.

In our case, a nanomotor propelling at 40 mM urea covers 53% more area in one second than a nanomotor merely experiencing Brownian diffusion, as evidenced by the MSDs (Figure S8), which improves the chances of the antibody to contact with the antigen, thus improving penetration into the spheroid. The combined effect of active motion and the presence of an antibody is confirmed by the control experiments, where spheroids were incubated with bare nanomotors (*i.e.*, without antibody, Figure 4A) or with antibody-modified nanomotors in the absence of urea (Figure 4B). We have observed a 4-fold increase in the internalization efficiency of passive nanomotors when they carry the targeting moiety. Moreover, the internalization is greatly improved by combining both the targeting and motion capabilities, being almost 14 times higher than in the case of passive particles without antibody (Figure 4D).

Additionally, we performed a control experiment functionalizing the particles with a catalytically inert protein (bovine serum albumin, BSA). We fabricated particles with and without anti-FGFR3 antibody (MSNP-BSA/PEG-Ab and MSNP-BSA/PEG, respectively) and incubated them with spheroids in the

presence (40 mM) and the absence of urea (0 mM). As expected, the lack of self-propulsion led to no significant differences in the internalization of the BSA coated particles by spheroids when urea was present in the medium (Figures 4D and S9).

Considering that the anti-FGFR3 antibody has shown to inhibit cell proliferation by blocking the FGF signaling pathway,<sup>55,57–59</sup> we studied the potential therapeutic effect by analyzing proliferation profiles of spheroids (see the inset of Figure 4D). For this, the bladder cancer spheroids were incubated with MSNP-Ur/PEG-Ab for 4 h, with and without urea, using nanomotors without antibody as a control. Then, the spheroids were washed to remove the uncatalyzed urea and noninternalized nanomotors, and the cultures were allowed to sit in repose for 48 h. After this period, the proliferation of the bladder cancer spheroids was evaluated using the alamarBlue assay. We observed that spheroids incubated with bare nanomotors (without antibody) retained the proliferation abilities (inset of Figure 4D), whereas spheroids incubated with antibody-modified nanomotors decreased the proliferation levels, indicating that the interaction between anti-FGFR3 antibody and the antigen present in the spheroids led to the inhibition of cell proliferation. These results point toward the applicability of nanomotors carrying the anti-FGFR3 antibody as tools for targeted bladder cancer therapy.

## CONCLUSIONS

We have developed urease-powered nanomotors composed of PEG, where the PEG acts both as a steric impediment to prevent aggregation and as a linker to connect a specific bladder cancer antibody on the nanomotors' surface (anti-FGFR3). The nanomotors, with and without antibody, present enhanced diffusion in simulated and real urine, which eventually could enable their use in biomedical applications in bladder. We demonstrated the substrate-dependent induced toxicity of these enzymatic nanomotors using spheroids derived from human bladder cancer cells (3D cultures), which are considered to better mimic tumor environments compared with conventional 2D cultures. We monitored internalization phenomena at a time period similar to bladder-voiding intervals and observed that active motion enhances nanomotors penetration by 3-fold. Furthermore, active antibody-modified nanomotors exhibited 4-fold higher internalization efficiency than active nanomotors without the antibody, reflecting the influence of self-propulsion and targeting on the ability of active particles to penetrate spheroids. Cell proliferation studies on spheroids indicated that targeted nanomotors induce a higher loss of viability than bare nanomotors (without antibody), indicating the therapeutic effect of the anti-FGFR3 that could arise from both the suppression of cell proliferation and higher nanomotor internalization rates. These results point toward the potentials of such antibody-modified nanomotors as tools in targeted bladder cancer therapy because the targeting capabilities of the particles are enhanced with active motion, resulting in the improvement of the therapeutic effect of the anti-FGFR3 antibody.

Future studies on the use of targeted nanomotors as a means of enhancing disease detection and simultaneous treatment using antibody-modified nanomotors that carry an imaging agent may offer the development of more-efficient cancer theranostic systems.

## METHODS

**Materials.** Ethanol (EtOH, 99%), methanol (MeOH, 99%), hydrochloric acid (37% in water), ammonium hydroxide (25% in water), tetraethylorthosilicate (TEOS, 99%), triethanolamine (TEOA, 99%), cetyltrimethylammonium bromide (CTAB, 99%), 3-aminopropyltriethoxysilane (APTES, 99%), glutaraldehyde (GA, 25% in water), urease (from *Canavalia ensiformis*, type IX, powder, 50 000–100 000 units per gram of solid), Urease Activity Assay Kit (Sigma-Aldrich), urea (99.9%), glycerol (99%), sodium borohydride powder ( $\text{NaBH}_4$ , 98.0%), formaldehyde solution (37% in water), bovine serum albumin (lyophilized powder), 4-nitrophenol solution (10 mM), sodium chloride puriss. (NaCl), potassium chloride anhydrous (KCl), sodium phosphate monobasic ( $\text{NaH}_2\text{PO}_4$ ), sodium bicarbonate BioXtra (99.5–100.5%,  $\text{NaHCO}_3$ ), dimethyl sulfoxide (DMSO, 99.9%), and HS-PEG5K-NH<sub>2</sub> (HCl salt) were purchased from Sigma-Aldrich. Pierce BCA Protein Assay Kit, Wheat Germ Agglutinin (WGA AlexaFluor 647 conjugate), Goat anti-mouse IgG (H+L) Alexa FluorTM 488 conjugate, 3-(4,5-dimethylthiazol-2-yl)-2,5-diphenyltetrazolium bromide (MTT), and phosphate-buffered saline (PBS) were purchased from Thermo Fisher Scientific. Matrigel basement matrix was purchased from Corning. Anti-FGFR3 antibody (ab89660) was purchased from Abcam. Hoechst 33342 was purchased from Life Sciences. Spectra/Por 7 Standard RC pretreated Dialysis Tubing (3.5 kDa) was purchased from Spectrum. Cyanine3 NHS ester was purchased from Lumiprobe. McCoy's 5A (modified) medium, penicillin–streptomycin solution, fetal bovine serum (FBS), and trypsin 0.5% EDTA were purchased from Gibco. A live/dead viability and cytotoxicity Kit was purchased from Invitrogen. Human urinary bladder transitional cell papilloma RT4 cells were obtained from ATCC (Rockville, MA).

**Instruments.** TEM images were captured using a JEOL JEM-2100 microscope. SEM images were captured using a FEI NOVA NanoSEM 230 at 10 kV. Hydrodynamic radii and electrophoretic mobility measurements were performed using a Wyatt Möbius coupled with an Atlas cell pressurization system. The Brunauer–Emmett–Teller (BET) analysis was carried out using a Micromeritics Tristar II Plus automated analyzer. Optical videos as well as cell culture imaging were performed using an inverted optical microscope (Leica DMi8) equipped with a 63× water objective, a galvo stage and filter cubes for FITC, rhodamine, DAPI, and CY5. Protein quantification and enzymatic activity assays were carried out using an Infinite M200 PRO Multimode Microplate Reader. The confocal microscopy analysis was performed using a LSM 800–Zeiss equipped with a 63× oil objective.

**Synthesis of Mesoporous Silica Nanoparticles.** The MSNPs were prepared using a sol–gel method. Briefly, a solution containing CTAB (570 mg), TEOA (35 g), and water (20 mL) was heated to 95 °C in a silicon oil bath. This mixture was stirred for 30 min, and subsequently, TEOS (1.5 mL) was added drop-wise. The mixture was further stirred at 95 °C for 2 h. The produced particles were collected by centrifugation and washed with ethanol (3 times, 1350g, 10 min). Then, the particles were suspended in a MeOH:HCl mixture (30 mL, 10:0.6) and refluxed at 80 °C for 24 h, for removal of CTAB from the MSNP pores. Finally, the particles are collected by centrifugation and washed in ethanol (3 times, 1350g, 10 min), with sonicating for 20 min between each centrifugation. Aliquots (0.5 mL) were collected, centrifuged, and air-dried to determine the concentration of the MSNPs suspension.

**Amine Functionalization of MSNPs.** The previously synthesized MSNPs were suspended in EtOH (2 mg/mL). Then, APTES was added to the suspension (10 μL/mg of MSNP), and it was shaken for 24 h at room temperature using an end-to-end rotary shaker. Finally, the particles were collected by centrifugation and washed in ethanol (3 times, 1350g, 10 min) and in water (3 times, 1928 g 10 min), with sonicating for 20 min between each centrifugation. Aliquots (0.5 mL) were collected, centrifuged, and air-dried to determine the concentration of the MSNPs suspension.

**Functionalization of MSNP-NH<sub>2</sub> with Urease and Heterobifunctional H<sub>2</sub>N-PEG-SH.** MSNP-NH<sub>2</sub> were centrifuged at 1340g

for 10 min, suspended in 900 μL of PBS (2 mg/mL), and sonicated for 20 min. After this, 100 μL of glutaraldehyde was added, and the mixture was vortexed for 30 s to obtain a good dispersion. The mixture was placed on an end-to-end rotary shaker for 2.5 h at room temperature. The nanoparticles were then collected and washed three times with PBS (1340g, 10 min) and sonicated for 20 min between each wash. Next, the GA-activated nanoparticles were suspended in solution of PBS containing urease (3 mg/mL) and H<sub>2</sub>N-PEG-SH (1 μg/mg of MSNP-NH<sub>2</sub>). The mixture was then placed on an end-to-end rotary shaker overnight, at room temperature. The resulting nanomotors were washed three times with PBS by centrifugation (1340g, 10 min), intercalating the washes with 3 min of sonication.

**Functionalization of PEGylated Urease Nanomotors with Anti-FGFR3 Antibody.** The nanomotors were suspended in PBS (2 mg/mL) and anti-FGFR3 antibody (30 μg of antibody per milligram of nanomotors) was added. The mixture was then incubated overnight in the rotary shaker at room temperature. Finally, the antibody-modified nanomotors were collected by centrifugation (1340g, 10 min) and washed three times with PBS, intercalating the washes with 3 min of sonication.

**Hydrodynamic Radii and Surface Charge Analysis.** A Wyatt Möbius DLS, coupled to an ATLAS pressurizer was used to characterize the size distribution and surface charge of MSNP, MSNP-NH<sub>2</sub>, MSNP-Ur/PEG, and MSNP-Ur/PEG-Ab. The equipment uses a 532 nm wavelength laser and a detector angle of 163.5°. The samples analyzed were diluted to a concentration 0.3 mg/mL and analyzed for light scattering and electrophoretic mobility simultaneously, with an acquisition time of 5 s, performing 3 runs per measurement. A total of 9 measurements were performed to obtain statistical relevant data.

**Quantification of Urease and Antibody Amounts on MSNP.** The concentration of urease present on MSNP-Ur/PEG was measured using the BCA Protein Assay Kit from Thermo Fisher Scientific according to the manufacturer's instructions. This kit correlates the quantity of proteins with the reduction of copper by peptide bonds.<sup>63</sup> The same procedure was repeated for MSNP-Ur/PEG-Ab to quantify the amount of antibody bound to the nanomotors.

**Urease Activity Assay.** Enzymatic activity of urease while bound to MSNPs was evaluated using a commercial kit that determines the concentration of ammonia generated by Berthelot's method.<sup>68</sup> The nanomotors were at a concentration of 0.5 mg/mL, and the experiment was performed according to the manufacturer's instructions.

**Urease Labeling with Cy3.** Urease (22 mg) was dissolved in 1 mL of sodium bicarbonate buffer (100 mM). Next, 7 μL of a Cy 3 solution in DMSO (5 mM) were added to the urease solution, and the mixture was incubated for 4 h at room temperature and shaking in the dark. The solution of labeled urease was then dialyzed (3.5 kDa pore membrane) for 24 h to eliminate nonreacted Cy3 molecules.

**Quantification of Ammonia Production by MSNP-Ur/PEG.** The ammonia produced by nanomotors was quantified using a titration method. For this, the nanomotors were incubated with different urea concentrations (12.5, 25, 50, 100, 200, and 300 mM), and the samples were analyzed at different time points (5, 15, 60, 120, and 240 min and at 24 h). At each time point, the suspensions of nanomotors was centrifuged and the supernatant was titrated with HCl (10 mM) using *p*-nitrophenol as indicator.

**Optical Video Recording of Nanomotors and MSD Analysis.** An inverted microscope equipped with a 63× water objective was used to observe and record videos of the nanomotors movement. Samples of aqueous solutions of simulated urine containing nanomotors were placed in a glass slide and mixed well with simulated urine at a range of urea concentrations (12.5, 25, 50, 100, 200, and 300 mM). The samples were then covered with a glass slide to avoid artifacts caused by drifting and videos of 30 s were recorded. For the real urine experiment, urine excreted from rats was immediately collected into a 1.5 mL eppendorf tube, centrifuged at 8000 rpm for 5 min, and syringe-filtered using a 0.22 μm filter. Filtered samples were kept at 4 °C up to their use. The nanomotors

were then suspended in filtered real urine aliquots, placed in a glass slide with a cover, and imaged for 30 s. The videos were acquired using a Hamamatsu camera, at a frame rate of 50 fps, in a bright field. At least 20 nanomotors are analyzed per condition. The videos were analyzed using a Python-based code to obtain the trajectories of the nanomotors, and compute the mean-squared displacement (MSD) following:

$$\text{MSD}(\Delta t) = \langle [x_i(t + \Delta t) - x_i(t)]^2 \rangle \quad i = 2 \text{ for 2D analysis} \quad (5)$$

After this, the diffusion coefficient ( $D_e$ ) was obtained by fitting the MSD data to eq 2, which is valid at short time intervals for small particles, with low rotational diffusion.<sup>65</sup>

**3D Cell Culture.** Human urinary bladder transitional cell papilloma RT4 cells were cultured in McCoy's 5A (modified) Medium, supplemented with FBS (10%) and penicillin–streptomycin solution (1%), in a 37 °C and 5% CO<sub>2</sub> atm. The cells were split every 4 days at a 1:2 ratio. To obtain 3D RT4 cell cultures, 8-well ibidi dishes were precoated with 23 μL of Matrigel (5 mg/mL) and incubated at 37 °C for 30 min, allowing the gel to form. Next, 30 μL of a suspension of RT4 cells at a density of 5 × 10<sup>6</sup> cells per milliliter was spread evenly in each well, and the dishes were incubated for 30 min at 37 °C. Finally, 150 μL of RT4 McCoy's medium containing 10% Matrigel was added. The cultures were allowed to grow for 7 days before the experiments, with the medium changed every 2 days.

**Immunostaining of FGFR3 Transmembrane Protein in 3D RT4 Cell Cultures.** The 3D cultures described above were washed 3 times with PBS 1×. Then, the surface of the wells was gently scratched with a pipet tip, and the culture was suspended in McCoy's medium in a tube. The tubes were briefly spun, and the supernatant was removed. Next, the cells were suspended in formaldehyde (3.7%), placed in an 8-well dish, and incubated for 15 min at room temperature. Following, the culture was washed with PBS 1×, a solution of PBS-BSA (5%) was added, and the dish was incubated for 40 min at room temperature. Then, the anti-FGFR3 was added to the culture at a proportion of 1:50, and the dish was incubated for 24 h, at 37 °C, in a 5% CO<sub>2</sub> atmosphere. After, the culture was washed 3 times with PBS 1×, the secondary antibody (labeled with AlexaFluor 488) was added in a proportion of 1:500, and the dish was incubated for 40 min, at room temperature in the dark. Finally, the culture was washed 3 times with PBS 1×, the nuclei were labeled with Hoechst, and a solution of glycerol in PBS (70%) was added. The culture was observed using confocal microscopy.

**Cytotoxicity Assays.** The viability of RT4 3D cultures was quantified using the alamarBlue assay and visualized using the live/dead viability kit. For this, RT4 cells were culture as mentioned above and at day 7 were incubated with each treatment: ammonia (1, 1.5, 3, 5, 10, and 20 mM for 24 h), urea (25, 30, 40, and 50 mM for 24 h), and MSNP-Ur/PEG (12.5 μg/mL at a range of urea concentrations of 25, 30, 40, and 50 mM, for 1, 2, and 4 h). Afterward, the cultures were washed with medium and kept resting for 24 h, and viability was investigated according to the manufacturer's instructions. Furthermore, viability was also assessed at the 48 h time point.

**Imaging of RT4 3D Cultures and Nanomotors.** At day 7, the 3D cell cultures were incubated with each treatment (MSNP-Ur/PEG or MSNP-Ur/PEG-Ab, 12.5 μg/mL) for 4 h. At each time point, the cultures were washed and kept in a 37 °C and 5% CO<sub>2</sub> atm for 24 h. Then, the cultures were labeled WGA 647 (membranes) and imaged using an inverted fluorescence microscope equipped with a 63× objective and a galvo stage as well as filter cubes for Rhodamine, FITC, DAPI, and Cy5.

## ASSOCIATED CONTENT

### Supporting Information

The Supporting Information is available free of charge on the ACS Publications website at DOI: 10.1021/acsnano.8b06610.

Figures showing the quantification of compounds bound to the MSNPs, enzymatic activity, 3D culture, effect of

urea and ammonia on the viability of bladder cancer spheroids, the effect of compounds at different urea concentrations, quantification of ammonia, diffusion coefficients, motion profiles, and targeting and penetration abilities (PDF)

A video showing urease-powered nanomotors in simulated urine (AVI)

A video showing antibody-modified urease-powered nanomotors in simulated urine (AVI)

A video showing PEG-Ab-modified mesoporous silica nanoparticles and antibody-modified urease-powered nanomotors in real urine (AVI)

## AUTHOR INFORMATION

### Corresponding Authors

\*E-mail: [tpatino@ibebarcelona.eu](mailto:tpatino@ibebarcelona.eu).

\*E-mail: [ssanchez@ibebarcelona.eu](mailto:ssanchez@ibebarcelona.eu).

### ORCID

Samuel Sánchez: 0000-0002-5845-8941

### Author Contributions

S.S., A.C.H., and T.P. designed the experiments. A.C.H. and R.C. performed the experiments and analyzed the data. N.M.-C. contributed to the fabrication of the particles. S.S. and T.P. initiated the idea and supervised the work. All authors discussed the results and commented on the manuscript.

### Notes

The authors declare no competing financial interest.

## ACKNOWLEDGMENTS

The research leading to these results has received funding from the Spanish MINECO (CTQ2015-68879-R (MICRODIA) and CTQ2015-72471-EXP (Enzwim)). S.S. acknowledges Foundation BBVA for the MEDIROBOTS project and the CERCA program by the Generalitat de Catalunya. A.C.H. thanks MINECO for the Severo Ochoa fellowship, and T.P. thanks MINECO for the Juan de la Cierva fellowship. The authors thank A. M. López for developing the Python code for motion analysis.

## REFERENCES

- (1) Ferlay, J.; Soerjomataram, I.; Ervik, M.; Dikshit, R.; Eser, S.; Mathers, C.; Rebelo, M.; Parkin, D. M.; Forman, D.; Bray, F. GLOBOCAN 2012 v1.0, *Cancer Incidence and Mortality Worldwide*; International Agency for Research on Cancer: Lyon, France; 2013.
- (2) Shi, J.; Kantoff, P. W.; Wooster, R.; Farokhzad, O. C. Cancer Nanomedicine: Progress, Challenges and Opportunities. *Nat. Rev. Cancer* **2017**, *17*, 20–37.
- (3) Ferrari, M. Cancer Nanotechnology: Opportunities and Challenges. *Nat. Rev. Cancer* **2005**, *5*, 161–171.
- (4) Mirkin, C. A.; Meade, T. J.; Petrosko, S. H.; Stegh, A. H. *Nanotechnology-Based Precision Tools for the Detection and Treatment of Cancer*; Mirkin, C. A., Meade, T. J., Petrosko, S. H., Stegh, A. H., Eds.; Springer International Publishing: Cham, Switzerland, 2015; Vol. 166.
- (5) Wilhelm, S.; Tavares, A. J.; Dai, Q.; Ohta, S.; Audet, J.; Dvorak, H. F.; Chan, W. C. W. Analysis of Nanoparticle Delivery to Tumours. *Nat. Rev. Mater.* **2016**, *1*, 16014.
- (6) Blanco, E.; Shen, H.; Ferrari, M. Principles of Nanoparticle Design for Overcoming Biological Barriers to Drug Delivery. *Nat. Biotechnol.* **2015**, *33*, 941–951.
- (7) Peng, F.; Tu, Y.; Adhikari, A.; Hintzen, J. C. J.; Lowik, D. W. P. M.; Wilson, D. A. A Peptide Functionalized Nanomotor as an Efficient Cell Penetrating Tool. *Chem. Commun.* **2017**, *53*, 1088–1091.



- (8) Wang, J.; Gao, W. Nano/microscale Motors: Biomedical Opportunities and Challenges. *ACS Nano* **2012**, *6*, 5745–5751.
- (9) Díez, P.; de Ávila, B. E.-F.; Ramírez-Herrera, D. E.; Villalonga, R.; Wang, J. Biomedical Nanomotors: Efficient Glucose-Mediated Insulin Release. *Nanoscale* **2017**, *9*, 14307–14311.
- (10) Hortelão, A. C.; Patiño, T.; Perez-Jiménez, A.; Blanco, À.; Sánchez, S. Enzyme-Powered Nanobots Enhance Anticancer Drug Delivery. *Adv. Funct. Mater.* **2018**, *28*, 1705086.
- (11) Li, J.; Esteban-Fernández de Ávila, B.; Gao, W.; Zhang, L.; Wang, J. Micro/nanorobots for Biomedicine: Delivery, Surgery, Sensing, and Detoxification. *Sci. Robot.* **2017**, *2*, No. eaam6431.
- (12) Kong, L.; Mayorga-Martinez, C. C.; Guan, J.; Pumera, M. Fuel-Free Light-Powered TiO<sub>2</sub>/Pt Janus Micromotors for Enhanced Nitroaromatic Explosives Degradation. *ACS Appl. Mater. Interfaces* **2018**, *10*, 22427–22434.
- (13) Chen, C.; Tang, S.; Teymourian, H.; Karshalev, E.; Zhang, F.; Li, J.; Mou, F.; Liang, Y.; Guan, J.; Wang, J. Chemical/Light-Powered Hybrid Micromotors with “On-the-Fly” Optical Brakes. *Angew. Chem., Int. Ed.* **2018**, *57*, 8110–8114.
- (14) Wang, X.; Sridhar, V.; Guo, S.; Talebi, N.; Miguel-López, A.; Hahn, K.; van Aken, P. A.; Sánchez, S. Fuel-Free Nanocap-Like Motors Actuated Under Visible Light. *Adv. Funct. Mater.* **2018**, *28*, 1705862.
- (15) Xuan, M.; Mestre, R.; Gao, C.; Zhou, C.; He, Q.; Sanchez, S. Noncontinuous Super-Diffusive Dynamics of a Light-Activated Nanobottle Motor. *Angew. Chem., Int. Ed.* **2018**, *57*, 6838–6842.
- (16) Esteban-Fernández de Ávila, B.; Ramírez-Herrera, D. E.; Campuzano, S.; Angsantikul, P.; Zhang, L.; Wang, J. Nanomotor-Enabled pH-Responsive Intracellular Delivery of Caspase-3: Toward Rapid Cell Apoptosis. *ACS Nano* **2017**, *11*, 5367–5374.
- (17) Hansen-Bruhn, M.; de Ávila, B. E.; Beltrán-Gastélum, M.; Zhao, J.; Ramírez-Herrera, D. E.; Angsantikul, P.; Vesterager Gothelf, K.; Zhang, L.; Wang, J. Active Intracellular Delivery of a Cas9/sgRNA Complex Using Ultrasound-Propelled Nanomotors. *Angew. Chem., Int. Ed.* **2018**, *57*, 2657–2661.
- (18) Chen, X.; Hoop, M.; Mushtaq, F.; Siringil, E.; Hu, C.; Nelson, B. J.; Pané, S. Recent Developments in Magnetically Driven Micro- and Nanorobots. *Appl. Mater. Today* **2017**, *9*, 37–48.
- (19) Li, T.; Li, J.; Morozov, K. I.; Wu, Z.; Xu, T.; Rozen, I.; Leshansky, A. M.; Li, L.; Wang, J. Highly Efficient Freestyle Magnetic Nanoswimmer. *Nano Lett.* **2017**, *17*, 5092–5098.
- (20) Walker, D.; Kasdorf, B. T.; Jeong, H.-H.; Lieleg, O.; Fischer, P. Enzymatically Active Biomimetic Micropropellers for the Penetration of Mucin Gels. *Sci. Adv.* **2015**, *1*, No. e1500501.
- (21) Medina-Sánchez, M.; Schwarz, L.; Meyer, A. K.; Hebenstreit, F.; Schmidt, O. G. Cellular Cargo Delivery: Toward Assisted Fertilization by Sperm-Carrying Micromotors. *Nano Lett.* **2016**, *16*, 555–561.
- (22) Di Leonardo, R.; Angelani, L.; Dell’arciprete, D.; Ruocco, G.; Iebba, V.; Schippa, S.; Conte, M. P.; Mecarini, F.; De Angelis, F.; Di Fabrizio, E. Bacterial Ratchet Motors. *Proc. Natl. Acad. Sci. U. S. A.* **2010**, *107*, 9541–9545.
- (23) Stanton, M. M.; Simmchen, J.; Ma, X.; Miguel-López, A.; Sánchez, S. Biohybrid Janus Motors Driven by Escherichia Coli. *Adv. Mater. Interfaces* **2016**, *3*, 1–8.
- (24) Mostaghaci, B.; Yasa, O.; Zhuang, J.; Sitti, M. Bioadhesive Bacterial Microswimmers for Targeted Drug Delivery in the Urinary and Gastrointestinal Tracts. *Adv. Sci.* **2017**, *4*, 1700058.
- (25) Stanton, M. M.; Park, B.-W.; Miguel-López, A.; Ma, X.; Sitti, M.; Sanchez, S. Biohybrid Microtube Swimmers Driven by Single Captured Bacteria. *Small* **2017**, *13*, 1603679.
- (26) Martel, S.; Mohammadi, M.; Felfoul, O.; Lu, Z.; Pouponneau, P. Flagellated Magnetotactic Bacteria as Controlled MRI-Trackable Propulsion and Steering Systems for Medical Nanorobots Operating in the Human Microvasculature. *Int. J. Rob. Res.* **2009**, *28*, 571–582.
- (27) Stanton, M. M.; Park, B.-W.; Vilela, D.; Bente, K.; Faivre, D.; Sitti, M.; Sánchez, S. Magnetotactic Bacteria Powered Biohybrids Target E. Coli Biofilms. *ACS Nano* **2017**, *11*, 9968–9978.
- (28) Felfoul, O.; Mohammadi, M.; Taherkhani, S.; de Lanauze, D.; Zhong Xu, Y.; Loghin, D.; Essa, S.; Jancik, S.; Houle, D.; Lafleur, M.; Gaboury, L.; Tabrizian, M.; Kaou, N.; Atkin, M.; Vuong, T.; Batist, G.; Beauchemin, N.; Radzioch, D.; Martel, S. Magneto-Aerotactic Bacteria Deliver Drug-Containing Nanoliposomes to Tumour Hypoxic Regions. *Nat. Nanotechnol.* **2016**, *11*, 941–947.
- (29) Sánchez, S.; Soler, L.; Katuri, J. Chemically Powered Micro- and Nanomotors. *Angew. Chem., Int. Ed.* **2015**, *54*, 1414–1444.
- (30) Ma, X.; Hortelão, A. C.; Patiño, T.; Sánchez, S. Enzyme Catalysis To Power Micro/Nanomachines. *ACS Nano* **2016**, *10*, 9111–9122.
- (31) Katuri, J.; Ma, X.; Stanton, M. M.; Sanchez, S. Designing Micro- and Nanoswimmers for Specific Applications. *Acc. Chem. Res.* **2017**, *50*, 2–11.
- (32) Magdanz, V.; Stoychev, G.; Ionov, L.; Sanchez, S.; Schmidt, O. G. Stimuli-Responsive Microjets with Reconfigurable Shape. *Angew. Chem., Int. Ed.* **2014**, *53*, 2673–2677.
- (33) Solovev, A. A.; Xi, W.; Gracias, D. H.; Harazim, S. M.; Deneke, C.; Sanchez, S.; Schmidt, O. G. Self-Propelled Nanotools. *ACS Nano* **2012**, *6*, 1751–1756.
- (34) Solovev, A. A.; Sanchez, S.; Pumera, M.; Mei, Y. F.; Schmidt, O. G. Magnetic Control of Tubular Catalytic Microbots for the Transport, Assembly, and Delivery of Micro-Objects. *Adv. Funct. Mater.* **2010**, *20*, 2430–2435.
- (35) de Ávila, B. E.-F.; Angsantikul, P.; Li, J.; Angel Lopez-Ramirez, M.; Ramírez-Herrera, D. E.; Thamphiwatana, S.; Chen, C.; Delezuk, J.; Samakapiruk, R.; Ramez, V.; Obonyo, M.; Zhang, L.; Wang, J. Micromotor-Enabled Active Drug Delivery for *in Vivo* Treatment of Stomach Infection. *Nat. Commun.* **2017**, *8*, 272.
- (36) Karshalev, E.; Esteban-Fernández de Ávila, B.; Beltrán-Gastélum, M.; Angsantikul, P.; Tang, S.; Mundaca-Urbe, R.; Zhang, F.; Zhao, J.; Zhang, L.; Wang, J. Micromotor Pills as a Dynamic Oral Delivery Platform. *ACS Nano* **2018**, *12*, 8397–8405.
- (37) Ma, X.; Jannasch, A.; Albrecht, U.-R.; Hahn, K.; Miguel-López, A.; Schäffer, E.; Sanchez, S. Enzyme-Powered Hollow Mesoporous Janus Nanomotors. *Nano Lett.* **2015**, *15*, 7043–7050.
- (38) Ma, X.; Wang, X.; Hahn, K.; Sánchez, S. Motion Control of Urea-Powered Biocompatible Hollow Microcapsules. *ACS Nano* **2016**, *10*, 3597–3605.
- (39) Nijemeisland, M.; Abdelmohsen, L. K. E. A.; Huck, W. T. S.; Wilson, D. A.; van Hest, J. C. M. A Compartmentalized Out-of-Equilibrium Enzymatic Reaction Network for Sustained Autonomous Movement. *ACS Cent. Sci.* **2016**, *2*, 843–849.
- (40) Abdelmohsen, L. K. E. A.; Nijemeisland, M.; Pawar, G. M.; Janssen, G. A.; Nolte, R. J. M.; van Hest, J. C. M.; Wilson, D. A. Dynamic Loading and Unloading of Proteins in Polymeric Stomatocytes: Formation of an Enzyme-Loaded Supramolecular Nanomotor. *ACS Nano* **2016**, *10*, 2652–2660.
- (41) Patiño, T.; Arqué, X.; Mestre, R.; Palacios, L.; Sánchez, S. Fundamental Aspects of Enzyme-Powered Micro- and Nanoswimmers. *Acc. Chem. Res.* **2018**, *51*, 2662–2671.
- (42) Zhao, X.; Gentile, K.; Mohajerani, F.; Sen, A. Powering Motion with Enzymes. *Acc. Chem. Res.* **2018**, *51*, 2373–2381.
- (43) Zhang, Y.; Tsitkov, S.; Hess, H. Complex Dynamics in a Two-Enzyme Reaction Network with Substrate Competition. *Nat. Catal.* **2018**, *1*, 276–281.
- (44) Bunea, A.-I.; Pavel, I.-A.; David, S.; Gáspár, S. Sensing Based on the Motion of Enzyme-Modified Nanorods. *Biosens. Bioelectron.* **2015**, *67*, 42–48.
- (45) Patiño, T.; Feiner-Gracia, N.; Arqué, X.; Miguel-López, A.; Jannasch, A.; Stumpp, T.; Schäffer, E.; Albertazzi, L.; Sánchez, S. Influence of Enzyme Quantity and Distribution on the Self-Propulsion of Non-Janus Urease-Powered Micromotors. *J. Am. Chem. Soc.* **2018**, *140*, 7896–7903.
- (46) Dey, K. K.; Zhao, X.; Tansi, B. M.; Méndez-Ortiz, W. J.; Córdova-Figueroa, U. M.; Golestanian, R.; Sen, A. Micromotors Powered by Enzyme Catalysis. *Nano Lett.* **2015**, *15*, 8311–8315.
- (47) Joseph, A.; Contini, C.; Cecchin, D.; Nyberg, S.; Ruiz-Perez, L.; Gaitzsch, J.; Fullstone, G.; Tian, X.; Azizi, J.; Preston, J.; Volpe, G.

- Battaglia, G. Chemotactic Synthetic Vesicles: Design and Applications in Blood-Brain Barrier Crossing. *Sci. Adv.* **2017**, *3*, No. e1700362.
- (48) Ma, X.; Hortelao, A. C.; Miguel-López, A.; Sánchez, S. Bubble-Free Propulsion of Ultrasmall Tubular Nanojets Powered by Biocatalytic Reactions. *J. Am. Chem. Soc.* **2016**, *138*, 13782–13785.
- (49) Liu, L.; Mo, H.; Wei, S.; Rafferty, D. Quantitative Analysis of Urea in Human Urine and Serum by <sup>1</sup>H Nuclear Magnetic Resonance. *Analyst* **2012**, *137*, 595–600.
- (50) Antoni, S.; Ferlay, J.; Soerjomataram, I.; Znaor, A.; Jemal, A.; Bray, F. Bladder Cancer Incidence and Mortality: A Global Overview and Recent Trends. *Eur. Urol.* **2017**, *71*, 96–108.
- (51) Berdik, C. Unlocking Bladder Cancer. *Nature* **2017**, *551*, S34.
- (52) Janicki, J. J.; Gruber, M. A.; Chancellor, M. B. Intravesical Liposome Drug Delivery and IC/BPS. *Transl. Androl. Urol. Vol 4, No 5 (October 2015) Transl. Androl. Urol. (Interstitial Cystitis/Painful Bl. Syndr. Part I)* **2015**, *5*, 572–578.
- (53) Tyagi, P.; Wu, P.-C.; Chancellor, M.; Yoshimura, N.; Huang, L. Recent Advances in Intravesical Drug/Gene Delivery. *Mol. Pharmaceutics* **2006**, *3*, 369–379.
- (54) Edmondson, R.; Broglie, J. J.; Adcock, A. F.; Yang, L. Three-Dimensional Cell Culture Systems and Their Applications in Drug Discovery and Cell-Based Biosensors. *Assay Drug Dev. Technol.* **2014**, *12*, 207–218.
- (55) Martínez-Torrecuadrada, J.; Cifuentes, G.; López-Serra, P.; Saenz, P.; Martínez, A.; Casal, J. I. Targeting the Extracellular Domain of Fibroblast Growth Factor Receptor 3 with Human Single-Chain Fv Antibodies Inhibits Bladder Carcinoma Cell Line Proliferation. *Clin. Cancer Res.* **2005**, *11*, 6280–6290.
- (56) Iyer, G.; Milowsky, M. I. Fibroblast Growth Factor Receptor-3 in Urothelial Tumorigenesis. *Urol. Oncol. Semin. Orig. Investig.* **2013**, *31*, 303–311.
- (57) Guancial, E. A.; Werner, L.; Bellmunt, J.; Bamias, A.; Choueiri, T. K.; Ross, R.; Schutz, F. A.; Park, R. S.; O'Brien, R. J.; Hirsch, M. S.; Barletta, J. A.; Berman, D. M.; Lis, R.; Loda, M.; Stack, E. C.; Garraway, L. A.; Riestter, M.; Michor, F.; Kantoff, P. W.; Rosenberg, J. E. FGFR3 Expression in Primary and Metastatic Urothelial Carcinoma of the Bladder. *Cancer Med.* **2014**, *3*, 835–844.
- (58) Qing, J.; Du, X.; Chen, Y.; Chan, P.; Li, H.; Wu, P.; Marsters, S.; Stawicki, S.; Tien, J.; Totpal, K.; Ross, S.; Stinson, S.; Dornan, D.; French, D.; Wang, Q.-R.; Stephan, J.-P.; Wu, Y.; Wiesmann, C.; Ashkenazi, A. Antibody-Based Targeting of FGFR3 in Bladder Carcinoma and t(4;14)-Positive Multiple Myeloma in Mice. *J. Clin. Invest.* **2009**, *119*, 1216–1229.
- (59) Hadari, Y.; Schlessinger, J. FGFR3-Targeted mAb Therapy for Bladder Cancer and Multiple Myeloma. *J. Clin. Invest.* **2009**, *119*, 1077–1079.
- (60) Han, B.-H.; Antonietti, M. One-Step Synthesis of Copper Nanoparticles Containing Mesoporous Silica by Nanocasting of Binuclear Copper(II) Complexes with Cyclodextrins. *J. Mater. Chem.* **2003**, *13*, 1793–1796.
- (61) Xiang, C.; Yang, F.; Li, M.; Jaridi, M.; Wu, N. Experimental and Statistical Analysis of Surface Charge, Aggregation and Adsorption Behaviors of Surface-Functionalized Titanium Dioxide Nanoparticles in Aquatic System. *J. Nanopart. Res.* **2013**, *15*, 1293.
- (62) Jazayeri, M. H.; Amani, H.; Pourfatollah, A. A.; Pazoki-Toroudi, H.; Sedighimoghaddam, B. Various Methods of Gold Nanoparticles (GNPs) Conjugation to Antibodies. *Sens. Bio-Sensing Res.* **2016**, *9*, 17–22.
- (63) Smith, P. K.; Krohn, R. I.; Hermanson, G. T.; Mallia, A. K.; Gartner, F. H.; Provenzano, M. D.; Fujimoto, E. K.; Goeke, N. M.; Olson, B. J.; Klenk, D. C. Measurement of Protein Using Bicinchoninic Acid. *Anal. Biochem.* **1985**, *150*, 76–85.
- (64) Howse, J. R.; Jones, R. A. L.; Ryan, A. J.; Gough, T.; Vafabakhsh, R.; Golestanian, R. Self-Motile Colloidal Particles: From Directed Propulsion to Random Walk. *Phys. Rev. Lett.* **2007**, *99*, 8–11.
- (65) Dunderdale, G.; Ebbens, S.; Fairclough, P.; Howse, J. Importance of Particle Tracking and Calculating the Mean-Squared Displacement in Distinguishing Nanopropulsion from Other Processes. *Langmuir* **2012**, *28*, 10997–11006.
- (66) Elia, N.; Lippincott-Schwartz, J. Culturing MDCK Cells in Three Dimensions for Analyzing Intracellular Dynamics. In *Current Protocols in Cell Biology*; John Wiley & Sons, Inc.: Hoboken, NJ, 2009; Vol. 43, pp 4.22.1–4.22.18.
- (67) ISO 10993-1. *Biological Evaluation of Medical Devices - Part 1: Evaluation and Testing within a Risk Management Process*. 2016. <https://www.iso.org/standard/68936.html>
- (68) Patton, C. J.; Crouch, S. R. Spectrophotometric and Kinetics Investigation of the Berthelot Reaction for the Determination of Ammonia. *Anal. Chem.* **1977**, *49*, 464–469.

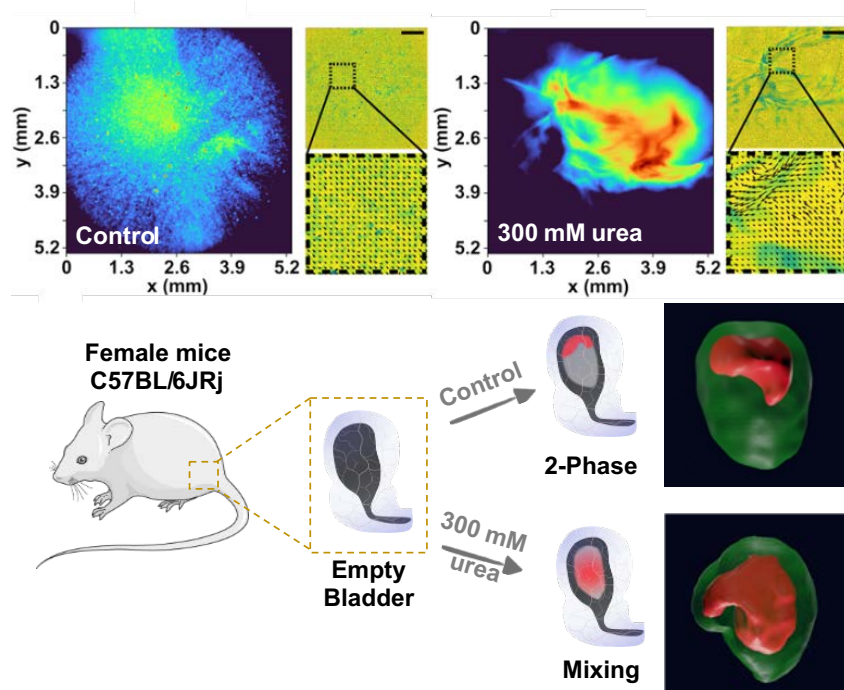
# Chapter 5



**Swarming behavior and in vivo monitoring of enzymatic  
nanomotors within the bladder**



The advances in nanomedicine led researchers to understand that studying nanomedicines at a single-particle level is not sufficient to fully understand and predict their outcome *in vivo*. This opened new investigation of the behavior of nanoparticle swarms, taking advantage of emergent collective behavior phenomena to amplify nanomedicines response *in vivo*. In this work, we investigated the swarming of gold nanoparticles (AuNPs) decorated urease powered nanomotors. For this, we used image processing methods and observed that, when in large populations, the nanomotors exhibited **swarming behavior** and that their collective motility led to the generation of **fluid flows and enhanced mixing**. We **collaborated with Dr. Jordi Llop's group** at the Radiology Department of CICBiomaGUNE used **nuclear medical imaging techniques** to further study the collective phenomena of the nanomotors, both *in vitro* and *in vivo*. We studied two radiolabeling strategies to visualize the nanomotors by PET-CT: (i) adsorbing iodine-124 isotope to the AuNPs or (ii) directly radiolabeling the enzymes using fluorine-18. Our results for the **biodistribution of radiolabeled nanomotors in mice** using PET-CT imaging showed that not only this is a suitable technique to track nanomotors *in vivo*, but also that the direct labeling of enzymes yields more **radiochemically stable constructs**. Following the current clinical method of chemotherapy administration in bladder cancer, we **intravesically instilled** the nanomotors in mice's bladders. PET-CT images showed that after nanomotors injection, the entrance of urine led to the formation a two-phased system, where nanomotors dispersion and fresh urine are separated. However, when injected in a urea suspension, nanomotors **collective motility and enhanced fluid mixing *in vivo*** provoked a progressive cancelling of the two phases, resulting in the nanomotors **uniform distribution** within the bladder in a **single-phase system**. This feature could be highly beneficial in the design of nanomedicines for bladder diseases, where ensuring that the active drug nanocarriers spread across the whole volume of the bladder is paramount to increase the efficiency of the treatment.



**Graphical Abstract 3.** Swarming behavior of urease powered nanomotors, monitored *in vitro* by optical microscopy, and *in vivo* within mice's bladders using PET-CT.



## NANOROBOTS

## Swarming behavior and in vivo monitoring of enzymatic nanomotors within the bladder

Ana C. Hortelao<sup>1\*</sup>, Cristina Simó<sup>2\*</sup>, Maria Guix<sup>1</sup>, Sandra Guallar-Garrido<sup>3</sup>, Esther Julián<sup>3</sup>, Diana Vilela<sup>1</sup>, Luka Rejc<sup>2†</sup>, Pedro Ramos-Cabrer<sup>2,4</sup>, Unai Cossío<sup>2</sup>, Vanessa Gómez-Vallejo<sup>2</sup>, Tania Patiño<sup>1,5‡</sup>, Jordi Llop<sup>2‡</sup>, Samuel Sánchez<sup>1,6‡</sup>

Enzyme-powered nanomotors are an exciting technology for biomedical applications due to their ability to navigate within biological environments using endogenous fuels. However, limited studies into their collective behavior and demonstrations of tracking enzyme nanomotors in vivo have hindered progress toward their clinical translation. Here, we report the swarming behavior of urease-powered nanomotors and its tracking using positron emission tomography (PET), both in vitro and in vivo. For that, mesoporous silica nanoparticles containing urease enzymes and gold nanoparticles were used as nanomotors. To image them, nanomotors were radiolabeled with either <sup>124</sup>I on gold nanoparticles or <sup>18</sup>F-labeled prosthetic group to urease. In vitro experiments showed enhanced fluid mixing and collective migration of nanomotors, demonstrating higher capability to swim across complex paths inside microfabricated phantoms, compared with inactive nanomotors. In vivo intravenous administration in mice confirmed their biocompatibility at the administered dose and the suitability of PET to quantitatively track nanomotors in vivo. Furthermore, nanomotors were administered directly into the bladder of mice by intravesical injection. When injected with the fuel, urea, a homogeneous distribution was observed even after the entrance of fresh urine. By contrast, control experiments using nonmotile nanomotors (i.e., without fuel or without urease) resulted in sustained phase separation, indicating that the nanomotors' self-propulsion promotes convection and mixing in living reservoirs. Active collective dynamics, together with the medical imaging tracking, constitute a key milestone and a step forward in the field of biomedical nanorobotics, paving the way toward their use in theranostic applications.

## INTRODUCTION

Self-propelled particles hold potential to overcome the biological barriers that limit current cancer nanomedicines, where only 0.7% of the administered dose reaches the target in vivo (1). In this regard, micro- and nanomotors have demonstrated enhanced targeting properties (2–5) and superior drug delivery efficiency compared with passive particles (6–9). In addition, they outperform traditional nanoparticles in terms of penetration into biological material, such as mucus (10–13), cells (14–16), or spheroids (4, 17). Using enzymes as biocatalysts is emerging as a particularly elegant approach when designing self-propelled particles, due to the use of endogenous fuels, which enables nanomotors' on-site activation and the design of fully biocompatible motor-fuel complexes. Moreover, the library of enzyme/substrate combinations permits the design of application-tailored enzymatic nanomotors, as is the case of urease-powered nanomotors for bladder cancer therapy (4).

Yet, the large number of nanoparticles required to treat tumors (18) demands better understanding, control, and visualization of

nanoparticle swarms to aid in the evaluation of motile nanomedicines and facilitate the eventual translation into clinics. Collective phenomena commonly observed in nature [active filaments (19); bacteria quorum sensing (20); cell migration (21); and swarms of fish, ants, and birds (22)] also occur in micro/nanomotors, which have demonstrated collective migration (23–26), assembly (27–30), and aggregation/diffusion behaviors in vitro (31–38). Ex vivo, swarms of magnetic micropellers have displayed long-range propulsion through porcine eyes to the retina, suggesting potential as active ocular delivery devices (39, 40). In vivo, controlled swimming of micromotor swarms has been observed in mouse peritoneal cavities (41), and micromotor swarms have been tracked in the stomach (24) and intestines (26) of rodents using magnetic resonance imaging and photoacoustic computed tomography, respectively. The sensitivity of these imaging techniques, however, is too low, and they fail to provide quantitative information.

Positron emission tomography (PET), a noninvasive nuclear imaging technique widely used in clinics, offers certain key advantages to address the aforementioned limitations. First, it is fully quantitative and allows whole-body image acquisition. Second, it relies on gamma-ray detection, which has no tissue-penetration limit, turning this imaging modality into a fully translational tool. Last, it is extremely sensitive, thus providing high-quality images by administering subpharmacological dosages of the radiolabeled entity (42, 43). Unexpectedly, its application for in vivo tracking of micro/nanomotors has barely been explored (44).

Here, we investigate the swarm behavior of enzyme-powered nanomotors in vitro and in vivo, using PET in combination with computed tomography (CT). We prepared enzyme-powered nanomotors based on a mesoporous silica chassis and labeled them with iodine-124 (<sup>124</sup>I; half-life = 4.2 days) and fluorine-18

<sup>1</sup>Institute for Bioengineering of Catalonia (IBEC), Barcelona Institute of Science and Technology (BIST), Baldori i Reixac 10-12, 08028 Barcelona Spain. <sup>2</sup>CIC biomaGUNE, Basque Research and Technology Alliance (BRTA), 20014 San Sebastian, Guipúzcoa, Spain. <sup>3</sup>Departament de Genètica i de Microbiologia, Facultat de Biociències, Universitat Autònoma de Barcelona, 08193 Bellaterra, Barcelona, Spain. <sup>4</sup>Ikerbasque, Basque Foundation for Science, Bilbao 48009, Spain. <sup>5</sup>Chemistry Department, University of Rome, Tor Vergata, Via della Ricerca Scientifica, 00133 Rome, Italy. <sup>6</sup>Institució Catalana de Recerca i Estudis Avançats (ICREA), Passeig Lluís Companys 23, 08010 Barcelona, Spain.

\*These authors contributed equally to this work.

†Present address: University of Ljubljana, Faculty of Chemistry and Chemical Technology, Večna pot 113, 1000 Ljubljana, Slovenia.

‡Corresponding author. Email: jllop@cicbiomagune.es (J.L.); ssanchez@ibecbarcelona.eu (S.S.); tpatino@ibecbarcelona.eu (T.P.)

( $^{18}\text{F}$ ; half-life = 119.7 min). The suitability of PET imaging to investigate the swarm behavior of labeled nanomotors in the presence of the fuel was first demonstrated *in vitro* using tailored phantoms. Stability of the label and whole-body biodistribution were then investigated *in vivo* after intravenous administration into mice. Last, time-resolved evidence of the motile properties of the nanomotors in the bladder was obtained after intravesical instillation.

## RESULTS

Nanomotors were prepared by synthesizing mesoporous silica nanoparticles (MSNPs) using a modification of the Stöber method (see experimental section for details) (45), and their surface was modified with amine groups by attaching aminopropyltriethoxysilane (APTES) (46). The amine groups were subsequently activated with glutaraldehyde (GA) to enable the covalent binding of the enzymes and the heterobifunctional polyethylene glycol ( $\text{NH}_2$ -PEG-SH). Last, gold nanoparticles (AuNPs) were anchored to the surface of the nanomotors by attachment to  $\text{NH}_2$ -PEG-SH via thiol-gold chemistry (Fig. 1A).

The hydrodynamic radii and stability of nanoparticles along the different fabrication steps were monitored by dynamic light scattering (DLS) analysis. The single population peak corresponding to MSNPs became sharper upon addition of  $\text{NH}_2$ -PEG-SH, suggesting that PEG provides steric stabilization to the nanomotors in solution (47). The single population peak was conserved after attachment of AuNPs, confirming that the final synthetic step of the process did not induce aggregation.

Electrophoretic mobility analysis was performed to characterize the surface properties of the particles after each functionalization step. Z-potential values for MSNP- $\text{NH}_2$  were found to be  $37.1 \pm 1.4$  mV. The trend toward a negatively charged surface in subsequent synthetic steps confirms the successful activation of the MSNP- $\text{NH}_2$  with GA (Z-potential =  $-2.2 \pm 0.2$  mV) and incorporation of  $\text{NH}_2$ -PEG-SH and urease enzymes (Z-potential =  $-32.0 \pm 0.6$  mV). The final negative value can be explained by urease's isoelectric point ( $\sim 5$ ), such that at  $\text{pH} > 5$ , the net charge of urease is negative, and by the negative charge of the AuNPs (48). The spherical nanoparticles had an average diameter of  $507.8 \pm 3.4$  nm and a stochastic distribution of the AuNPs on the surface, as shown in the transmission electron microscopy (TEM) image (Fig. 1B and fig. S1).

Next, to enable the visualization of the nanomotors by PET, we radiolabeled them with the positron emitters  $^{18}\text{F}$  and  $^{124}\text{I}$  (Fig. 1C). For the radiofluorination, a straightforward strategy based on the use of the pre-labeled prosthetic group 6- $^{18}\text{F}$ fluoronicotinic acid 2,3,5,6-tetrafluorophenyl ester ( $^{18}\text{F}$ -PyTFP) was developed (49). Taking advantage of the free amino groups on the enzyme, sufficient labeling yield (30% with respect to  $^{18}\text{F}$ -PyTFP, decay corrected) was achieved by incubation (35 min at room temperature) of the nanomotors with the prosthetic group. Radioiodination was achieved by direct absorption of  $^{124}\text{I}$  on AuNPs on the nanomotors (50). The radiochemical yield was  $71 \pm 2\%$ , due to the high-affinity binding between gold and iodine. Radiochemical purity after purification was  $\geq 99\%$  for both cases, as determined by instant thin layer chromatography (Fig. 1D).

The self-propulsion of urease-modified micro/nanomotors (4, 51–53) is caused by the asymmetric release of ionic species from the particles to the solution (54), which stems from the catalytic decomposition of urea into carbon dioxide and ammonia (fig. S2 and

movie S1). Despite the recent advances in the field, enzyme nanomotors have only been studied from a single-particle point of view and, in some cases, a few particles. However, their collective swarming behavior has yet to be investigated.

The motion dynamics and swarming behavior of nanomotors *in vitro* were first investigated by optical microscopy. A 2- $\mu\text{l}$  droplet of nanomotors suspension was placed onto a petri dish containing either pure water or 300 mM urea water (urea concentration was chosen on the basis of a known upper limit concentration in the bladder) (55), and videos were recorded over 2 min (Fig. 2, A and B; figs. S3 and S4; and movie S2). Figure 2A suggests that after addition of the droplet in water, the nanomotors mainly stayed at the seeding point following a stochastic distribution, which remained unaltered over time as observed in the histograms of pixel intensity distributions obtained for the selected region of interest (ROI) (Fig. 2C). Preferential tracks were observed immediately after seeding due to the motion of the nanomotors in urea, resulting in an anisotropic distribution of the nanomotors throughout the dish. This distribution also evolved over time, as observed in Fig. 2B and evidenced by the dynamic changes in the histograms (Fig. 2D). The same experiment was performed using phosphate-buffered saline (PBS) as solvent, yielding similar results (figs. S5 to S7 and movie S3). Moreover, we studied the nanomotor swarming phenomena by incorporating tracer particles into the system. For this, we codropped 5- $\mu\text{m}$  polystyrene (PS) particles with the nanomotors into the petri dish and monitored the PS tracers' behavior. We observed that when dropped in water or PBS, the swarms and tracers did not exhibit any displacement. However, in the presence of 300 mM urea, the nanomotors exhibited collective motion, dragging along the PS tracers, as evidenced by their trajectories (figs. S9 and S10). This was also denoted in the parabolic shape of the mean-squared displacement of the tracers, indicating their effective displacement.

To gain further insight into swarm dynamics, we then generated density maps. These were obtained by representing sum pixel intensity values of video frames within preestablished time ranges (0 to 40 s, 40 to 80 s, and 80 to 120 s) using a color map (Fig. 2E and figs. S3 to S5 and S7). In absence of urea, density maps did not substantially vary with time, and pixel intensity values for most of the population were around 60 (Fig. 2E, top). On the other hand, the density maps for nanomotors in urea show multiple paths followed by the nanomotors immediately after droplet addition (Fig. 2E, bottom). This is shown as a fast change in the color of the density maps, where the intensity of the overall field of view and nanomotor flocks rapidly increase, indicating high mobility and low residence time.

To investigate whether the activity of the nanomotors and the swarming behavior were associated with fluid flow generation, we carried out particle image velocimetry (PIV) analyses on the optical microscopy videos (Fig. 2E, inserts). PIV is an optical technique that allows the visualization of fluid flow associated with particle motility, indicating fluid and particle displacements in the form of vector fields. Under the control condition (Fig. 2E, top), the quiver plots show velocity vectors with low magnitude and in scarce amount (small panels). Conversely, the quiver plots obtained for nanomotors in urea show dispersed vector fields emerging not only from the swarms but also from the surrounding fluid. The evolution of the vector fields in time denotes the formation of vortices and fronts that promptly dissociate. Together, these results demonstrate that the activity of the nanomotors and their emergent collective behavior induce enhanced convection and fluid mixing, similar to what

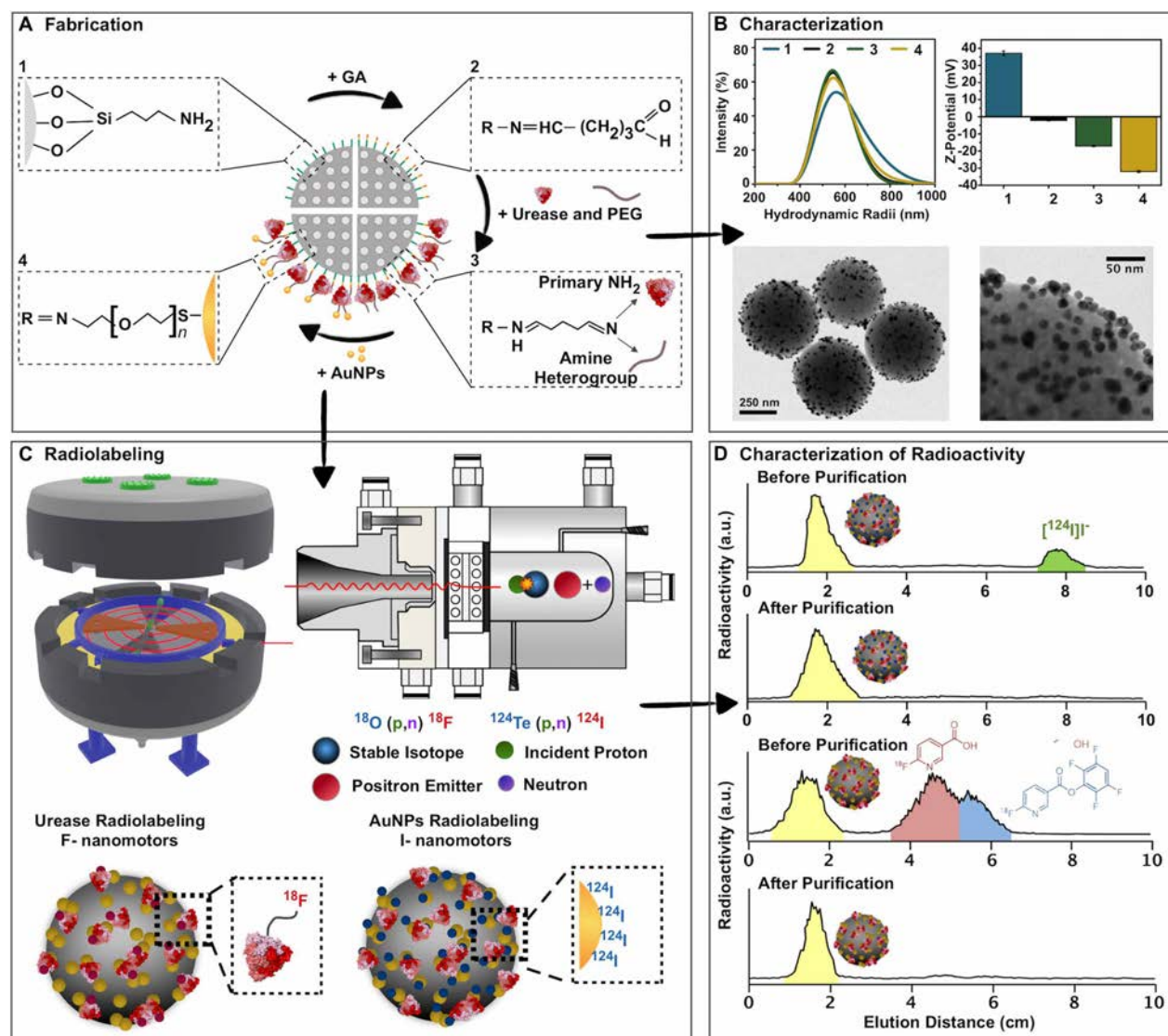


**Fig. 1. Preparation and characterization of radiolabeled urease-powered, AuNP-decorated nanomotors.** (A) Process flow of nanomotors fabrication steps. (B) Characterization of the nanomotors by DLS, Z-potential, and TEM. (C) Nanomotors radiolabeling using either  $^{18}\text{F}$  or  $^{124}\text{I}$  to yield  $^{18}\text{F}$ -nanomotors or  $^{124}\text{I}$ -nanomotors, respectively. (D) Labeling efficiency and radiochemical purity monitored by iTLC.

has been observed with catalytic micromotors (56–58). We hypothesize that these convective fluid flows arise from differences in the densities of enzymes’ substrates and products, in a similar manner to that observed enzymatic micropumps (59–62).

To corroborate these results and assess the feasibility of PET imaging to track swarm dynamics, we carried out parallel experiments with radiolabeled nanomotors. PET images obtained at different times after droplet addition confirmed that the nanomotors remained at the seeding point in water (Fig. 3A) and uniformly distributed over the whole volume of the petri dish in the presence of urea (Fig. 3B and movie S6). This behavior could also be visualized in three-dimensional (3D) histograms, which represent the concentration

of radioactivity throughout the petri dish (Fig. 3, C and D). Overall, these experiments demonstrated the suitability of PET imaging to obtain time-resolved quantitative information about the nanomotor swarming dynamics in vitro.

The in vitro swarming behavior of the nanomotors was investigated in four polydimethylsiloxane phantoms with increasing degrees of complexity (Fig. 4, A (top) and B to E, and fig. S11). The selected phantoms comprise different path shapes: (i) straight, (ii) rectangular, (iii) curved, and (iv) a curved path with longer straight trenches. Phantoms were positioned horizontally, and in each phantom, one channel was filled with water and another channel with 300 mM urea solution in water. The nanomotors (either  $^{124}\text{I}$ - or  $^{18}\text{F}$ -labeled)



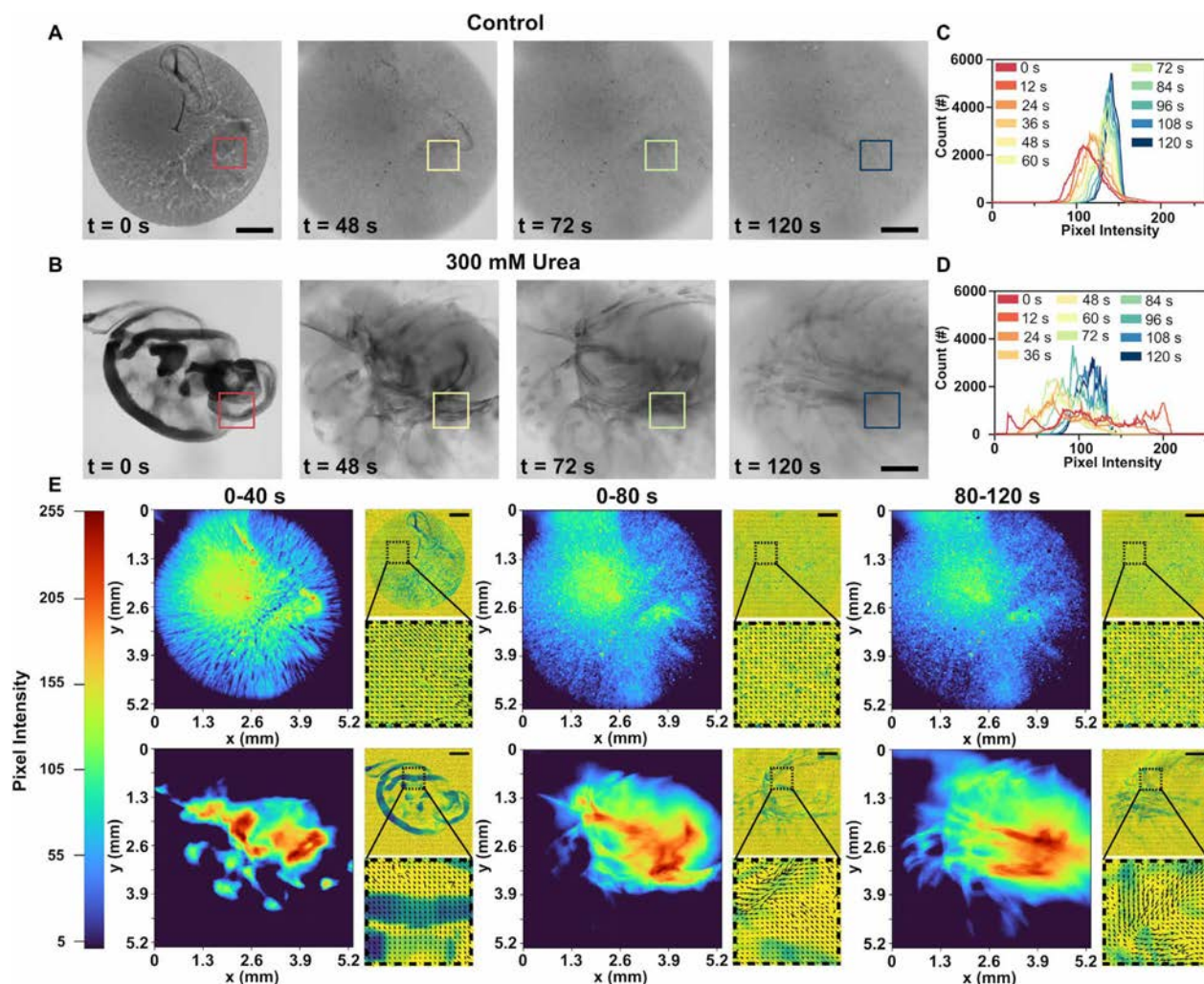


**Fig. 2. In vitro imaging of urease-powered nanomotor swarms by optical microscopy.** Snapshots of a population of urease-powered nanomotors in (A) water and (B) 300 mM urea in water. Scale bar, 1 mm. Corresponding pixel intensity distribution histograms within the ROIs noted in the images of nanomotors in (C) water and (D) 300 mM urea in water. Density maps (large panels) obtained by calculating the sum pixel intensity over periods of 40 s of the videos and PIV (small panels and zoom out) of (E) nanomotors in water (top) and in 300 mM urea in water (bottom); scale bar in small panels, 1 mm.

were seeded at the edge of each channel, and dynamic PET images were immediately acquired for 25 min.

The images obtained at  $t = 0.5, 7,$  and  $25$  min after seeding the  $^{18}\text{F}$ -nanomotors (Fig. 4, B and E, and movie S7) show that urea has a prominent effect on the motion dynamics of the nanomotors throughout the paths. Irrespective of the path shape, the nanomotors reached the end of the channel at  $t = 25$  min in the presence of the fuel, whereas most nanomotors remained close to the seeding point in water, where only minimal movement could be detected.

To get quantitative data, dynamic PET images were analyzed by dividing the phantoms in sectors (Fig. 4A, bottom right), and the concentration of radioactivity in each sector (normalized to the total amount of radioactivity in the channel) was determined as a function of time. Differences were evident even in the less restrictive phantom (straight shape), in which free diffusion of nonactivated

nanomotors is more favored. Curves with higher slope were obtained in sectors A to D in urea (Fig. 4B), confirming that the speed at which the nanomotors reach the different sectors is higher than in water. In addition, the fraction of nanomotors that reached the second half of the phantom (sectors B to D) at  $t = 25$  min was higher in the presence of urea (24%) than in water (18%). A similar trend was observed for  $^{124}\text{I}$ -nanomotors (fig. S11).

These differences increased when the mobility was limited by introducing complex paths (phantoms ii to iv). Figure 4 (C to E) shows that nanomotors reach sectors B to D much faster in urea than in water, which was confirmed by the amount of nanomotors reaching the second half of the phantom at the end of the imaging session. Values of 34.2, 17.1, and 17.0% were obtained for phantoms ii to iv in urea, whereas values in water were as low as 8.5, 4.2, and 2.1%. Equivalent results were obtained for  $^{124}\text{I}$ -nanomotors (fig. S12),

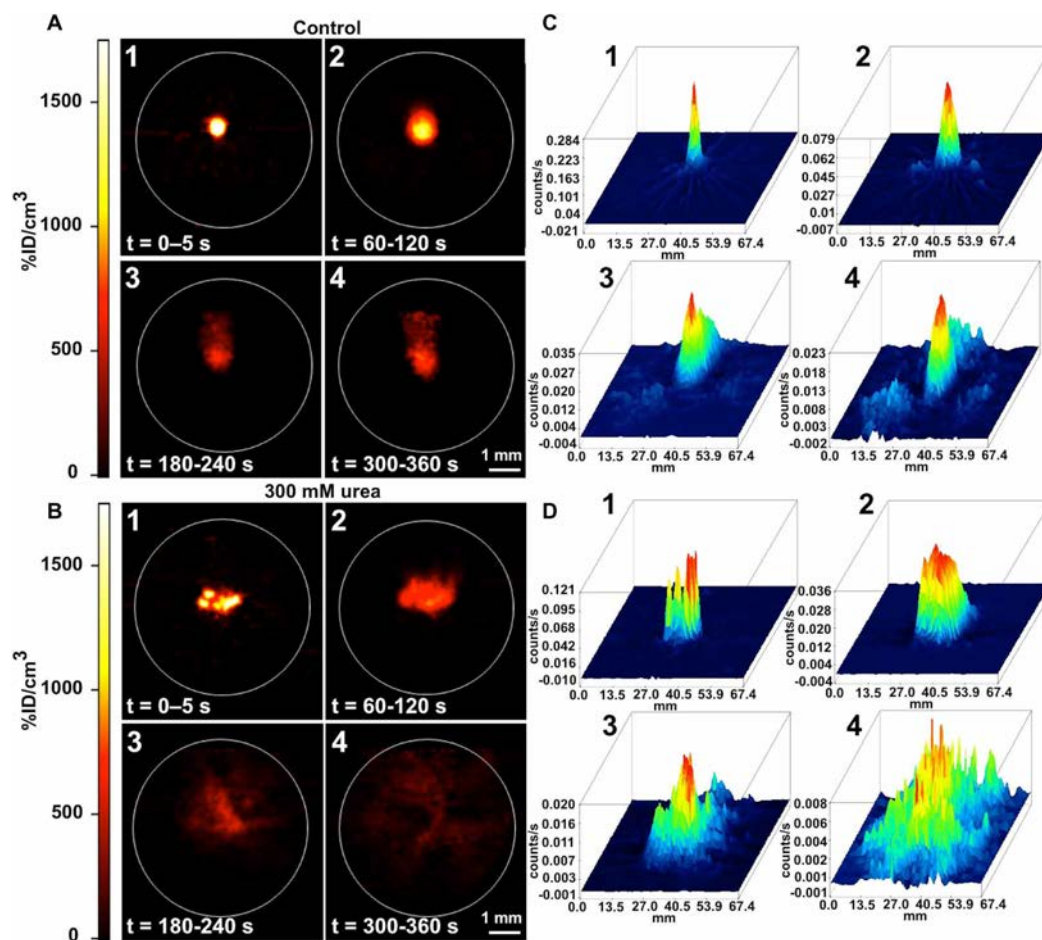


**Fig. 3.** In vitro imaging of urease-powered  $^{18}\text{F}$ -nanomotor swarms by PET. Snapshots of a population of urease-powered nanomotors in (A) water and (B) 300 mM urea imaged by PET. Pixel intensity distribution histograms of the population of nanomotors in the field of view in (C) water and (D) 300 mM urea.

where the fractions of radioactivity in the second half of the phantom at the end of the study were 7.4, 4.2, and 2.0% for phantoms ii to iv in water, whereas values in urea were 38.2, 20.6, and 27.0%, respectively. Small differences in the values obtained using the two radionuclides might be due to inherent limitations of PET imaging. The diameter of the channels is very close to the spatial resolution of our PET imaging system, which is 1.2-mm full-width half maximum for  $^{18}\text{F}$ , and notably lower for  $^{124}\text{I}$ , which has less favorable emission properties (63). This, together with the presence of a high concentration of radioactivity in small volumes, can lead to a partial volume effect, thus causing some error in the absolute quantification values. Despite this limitation, PET imaging results unambiguously confirmed the enhanced mobility of enzyme-powered nanomotors in urea, with an effect that becomes more relevant when the complexity of the path increases.

A biodistribution study of  $^{18}\text{F}$ -nanomotors and  $^{124}\text{I}$ -nanomotors in female mice after intravenous administration was carried out to (i) demonstrate the suitability of in vivo PET imaging to quantitatively track the nanomotors at the whole-body level and (ii) evaluate their radiochemical stability in vivo. Images obtained after administration

of  $^{18}\text{F}$ -nanomotors (Fig. 5A and movie S8) show a biodistribution profile with an initial accumulation in the lungs and the liver and a progressive elimination of the radioactivity via urine, as confirmed by image quantification (Fig. 5, B and C). These results suggest a rapid uptake by the mononuclear phagocyte system, as typically observed with intravenously administered nanoparticles of this size (64). Because the nanomotors are above the estimated size threshold for glomerular filtration ( $\sim 8$  nm) (65), the increase in radioactivity in urine indicates a slow detachment of the radiolabel from the nanomotors.

$^{124}\text{I}$ -nanomotors also show initial accumulation in the liver and the lungs (fig. S13 and movie S8). The concentration of radioactivity in both organs progressively decreases afterward, paralleled by an increase in the thyroid gland, stomach, and urine (fig. S13, B to D). The thyroid gland and bladder are the metabolic sites of free iodine, and hence, this suggests fast nanomotor deiodination, explained by the desorption of  $^{124}\text{I}$  from the gold surface.

Together, these results demonstrate that positron emitter-labeled nanomotors can be tracked in vivo after administration into living organisms using PET and that  $^{18}\text{F}$ -radiolabeling yields higher

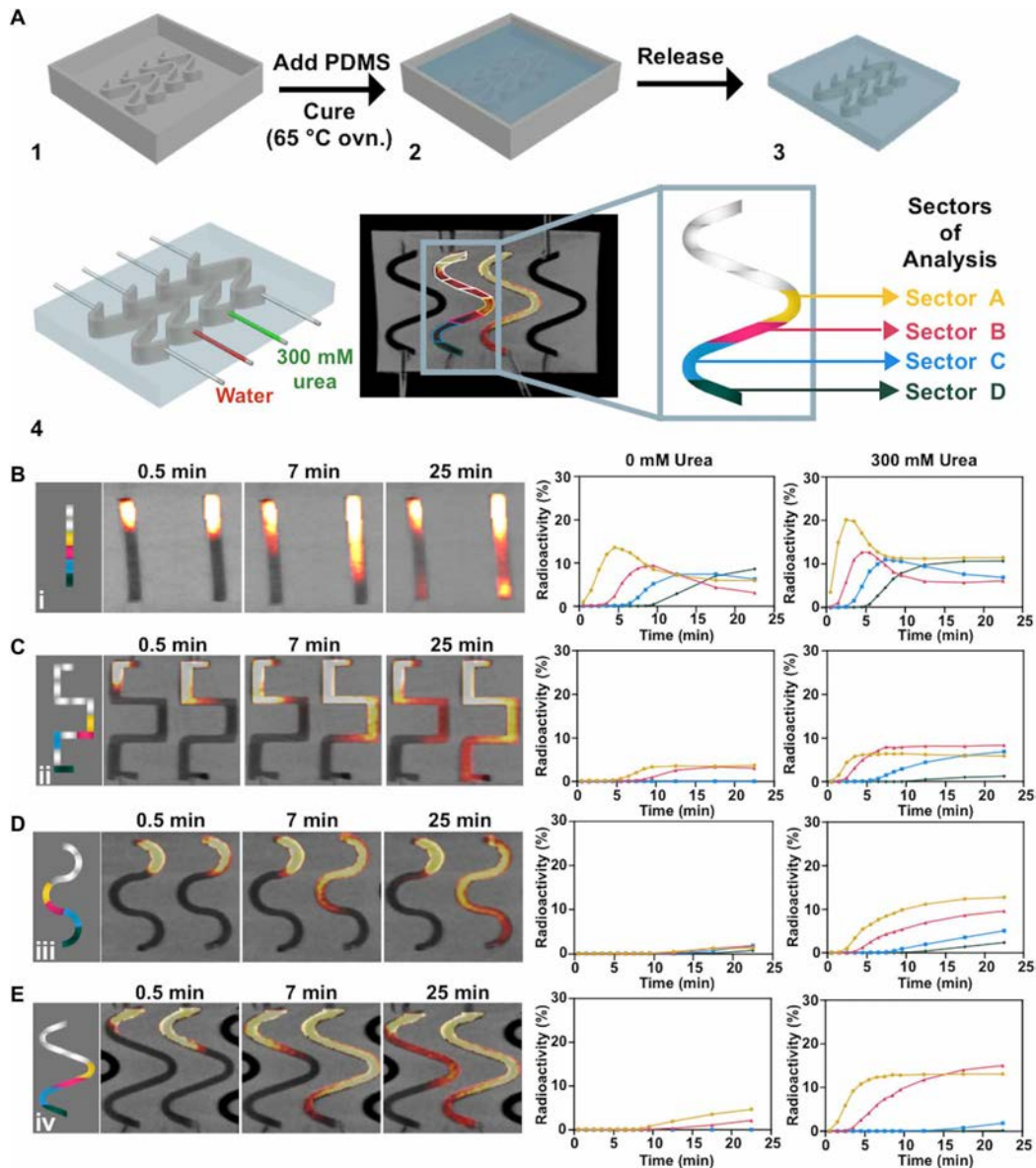


**Fig. 4. Effect of complex paths on the in vitro motion of  $^{18}\text{F}$ -radiolabeled urease-powered nanomotors studied by PET-CT imaging.** (A) Scheme depicting the fabrication process of 3D phantoms with different complex geometries (steps 1 to 4) and the corresponding method of analysis; (B to E) on the left, PET images (coronal projections) obtained at 0.5, 7, and 25 min after seeding of the nanomotors in different-shaped phantoms [(i) straight, (ii) rectangular, (iii) curved, and (iv) a curved path with longer straight trenches]. Scale bars, 3 mm. For each phantom, one of the channels was filled with water (left), and another channel was filled with 300 mM urea solution (right). The channels were positioned horizontally. Quantitative results of the normalized concentration of radioactivity for each sector as a function of time are shown on the right.

radiochemical stability in vivo than  $^{124}\text{I}$ -radiolabeling, because the detachment of the radiolabel is almost negligible over the duration of the study. No adverse effects were observed in the animals for 2 weeks after imaging sessions, thus suggesting that the administered dose is below the maximum tolerated dose.

Envisioning bladder cancer imaging and therapy and because the nanomotors' size prevents accumulation in the bladder after intravenous

injection, we studied their behavior after intravesical instillation (Fig. 6). This administration route is well established in bladder cancer therapy, because it maximizes the concentration of the drug in the target organ, resulting in improved efficacy and fewer side effects (66).

Owing to the stability of the  $^{18}\text{F}$ -radiolabel, demonstrated during the biodistribution study, only  $^{18}\text{F}$ -nanomotors were used in these experiments. In addition, the use of  $^{18}\text{F}$  should facilitate clinical



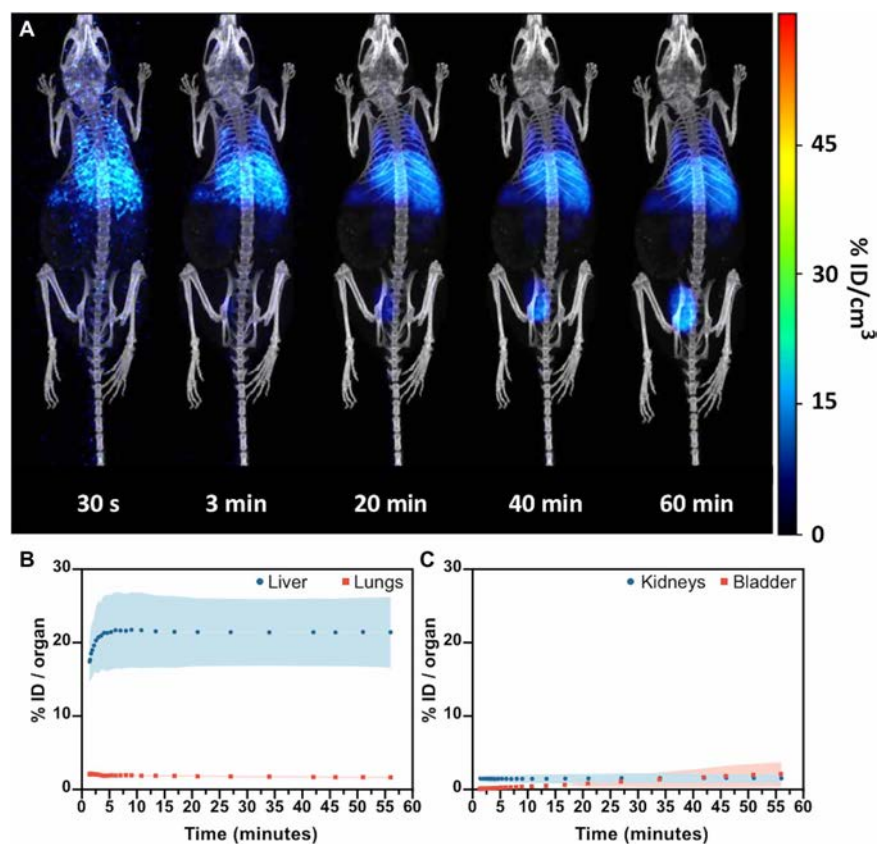


**Fig. 5. Analysis of the biodistribution of <sup>18</sup>F-labeled urease-AuNP nanomotors injected intravenously in female mice.** (A) PET-CT images (maximum intensity projections, coronal views) obtained at different time points after intravenous administration of <sup>18</sup>F-labeled urease-AuNP nanomotors; (B) time-activity curves in the liver and lungs and (C) kidneys and bladder, as determined by PET imaging. Results are expressed as percentage of injected dose per organ (mean ± SD, N = 2).

translation, because it can be easily produced in biomedical cyclotrons and presents superior physical properties. When <sup>18</sup>F-nanomotors were intravesically instilled using 300 mM urea in water as the vehicle, we observed a uniform distribution of the radioactivity immediately after instillation, followed by a two-phase formation at  $t = 15$  min [Fig. 6B(1) and movie S9]. Unexpectedly, a progressive cancelation of the difference between the two phases was observed at longer times, leading to a uniform distribution of radioactivity at  $t = 45$  min. On the contrary, when administered in water, the phase separation was maintained [Fig. 6B(2)]. These observations were further confirmed by analysis of the concentration of radioactivity in two volumes of interest (VOIs) drawn within the two phases observed. For <sup>18</sup>F-nanomotors injected in urea, the time-activity profile [Fig. 6C(1)] shows that the concentration of radioactivity in both regions was close to 50% immediately after instillation (homogeneous distribution). The value in VOI 1 progressively increased to reach a maximum at ~1000 s and decreased afterward to recover starting values at  $t > 2000$  s, confirming that the concentration of radioactivity within the bladder had regained homogeneity. In contrast, time-activity curves obtained under the control condition

show a progressively divergent trend [Fig. 6C(2)], confirming that the concentration of radioactivity in the bladder was not homogeneous by the end of the study. We hypothesize that immediately after nanomotor instillation into the empty bladders, fresh urine starts entering. This (radioactivity-free) urine displaces the solution present in the bladder (containing the labeled nanomotors) and two different phases are formed. Because <sup>18</sup>F-nanomotor swarms can actively move and enhance mixing in urea, they reverse the phase separation. However, when instilled in water, the separation of the two phases prevents the nanomotors from being in close contact with the urea (present only in the fresh urine), and consequently, the nanomotors lack motility, thus maintaining the phase separation. The observed phenomenon is potentially advantageous in the design of active drug delivery systems, where homogeneous distribution of the delivery vehicles is required to ensure they reach the target site.

As an additional proof of our hypothesis, we administered <sup>18</sup>F-labeled bovine serum albumin (BSA)-modified particles (MSNP-<sup>18</sup>F-BSA), which do not show self-propelling properties in urea or water. In this case, the time-activity curves followed the same trend as for <sup>18</sup>F-nanomotors instilled in water (Fig. 6, B and C) (3, 4), confirming that the lack of particle motility in nonhomogenization of the two phases had formed in the bladder cavity.

## DISCUSSION

We designed AuNP-decorated enzyme-powered nanomotors and investigated their swarming behavior in vitro, both using optical microscopy and by PET-CT. When swimming without boundaries, we observed that the nanomotor swarms lead to the formation of vortices and unstable fronts and that this emergent collective behavior induces enhanced fluid convection and mixing. Moreover, when the nanomotors are subjected to boundaries in the form of complex geometries, the collective motion allows them to overcome the hurdles encountered, i.e., the turns and angles present on the paths and reach the end of the track.

We studied the suitability of PET-CT to image nanomotors in vivo and at the whole-body level, using two different radiolabeling strategies: (i) attach <sup>124</sup>I isotope to the AuNPs and (ii) directly label the enzymes with <sup>18</sup>F isotope. We not only demonstrated that PET-CT is a highly adequate technique to image nanomotors but also that the direct labeling of enzymes affords a radiochemically stable structure.

Envisioning the application of urease-powered nanomotors in the treatment of bladder diseases, we studied their motility within the bladder of mice, verifying that the swarming behavior and



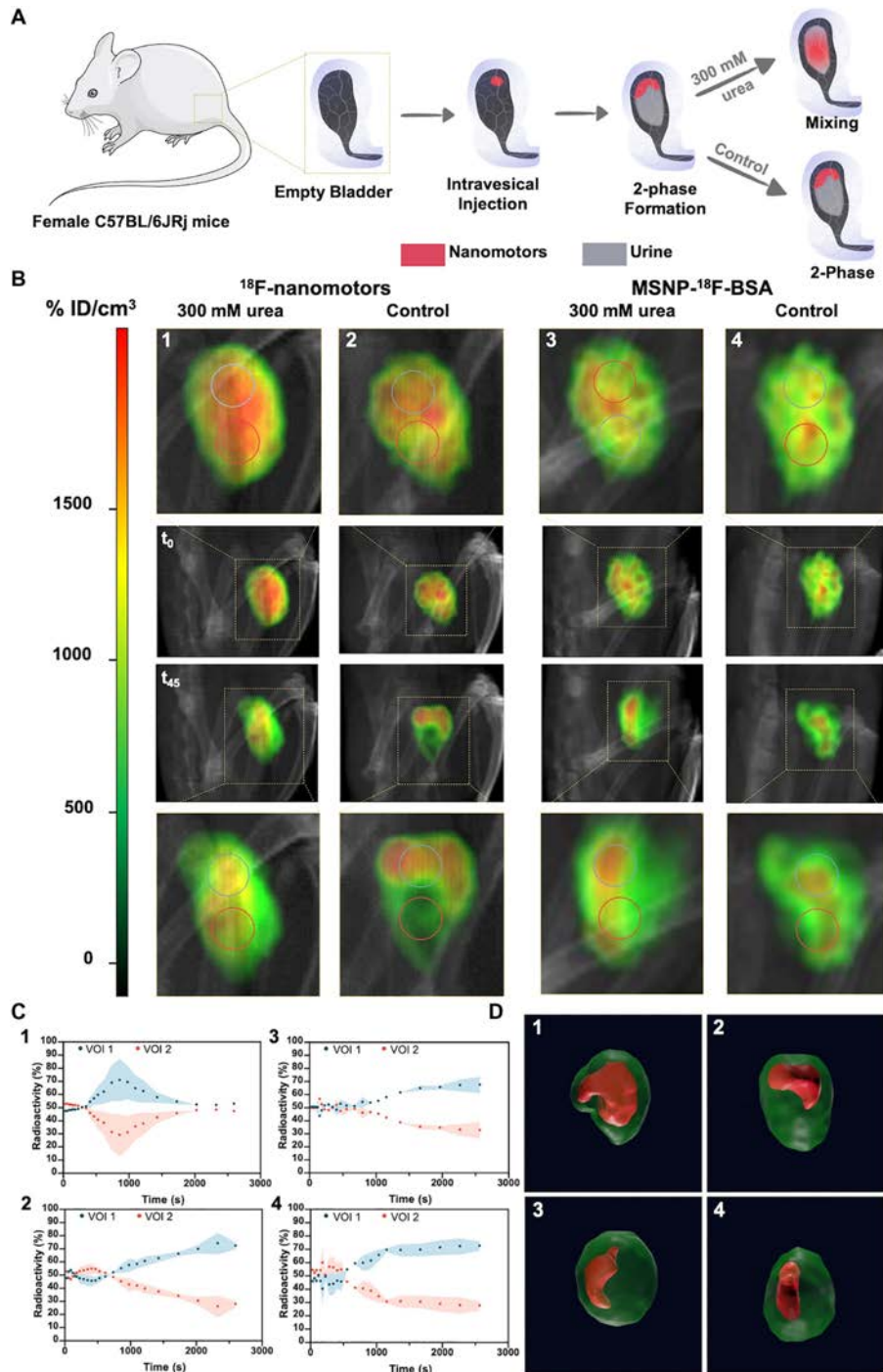


**Fig. 6.** PET-CT analysis of the biodistribution in the bladder of  $^{18}\text{F}$ -nanomotors and MSNP- $^{18}\text{F}$ -BSA administered via intravesical instillation. (A) Scheme depicting the administration method and phenomena observed. (B) PET-CT images (maximum intensity projections) obtained at different time points after the intravesical instillation of  $^{18}\text{F}$ -labeled urease nanomotors in urea (1) and water (2), and control BSA- $^{18}\text{F}$ -MSNP in urea (3) and water (4). (C) Quantification analysis of the radioactivity detected within the VOIs indicated in the PET-CT images. (D) 3D-reconstructed rendering of PET images of bladders showing the contour of the bladder (as a semitransparent green layer) and the regions of high intensity in PET images (as rendered red surfaces) at  $t = 45$  min after administration. Same threshold levels have been set for all images.

dynamic distribution of enzymatic nanomotors also occurred in vivo. When intravesically instilled in mice, the nanomotors were able to move in swarms and exhibit enhanced fluid mixing, which led to their homogeneous distribution in the whole bladder cavity. In contrast, passive particles resulted in a nonhomogeneous distribution, where a two-phase distribution was observed.

In conclusion, we studied the collective behavior of enzymatic nanomotors in vitro and in vivo by a combination of optical microscopy and PET-CT imaging techniques. The swarming behavior and fluid mixing of enzyme nanobots observed upon intravesical injection hold great potential toward biomedical applications, where their active homogeneous distribution and enhanced fluid mixing could be exploited for targeting and drug delivery purposes. Further understanding on the mechanism of swarming formation should be addressed in the near future, from a fundamental point of view and toward a better control of pattern formation.

## MATERIALS AND METHODS

### Materials

Ethanol (99%), methanol (99%), hydrochloric acid (37% in water), ammonium hydroxide (25% in water), tetraethylorthosilicate (TEOS; 99%), triethanolamine (TEOA; 99%), cetyltrimethylammonium bromide (CTAB; 99%), 3-APTES (99%), GA (25% in water), urease (from *Canavalia ensiformis*, type IX, powder, 50,000 to 100,000 U/g of solid), urea (99.9%), BSA (lyophilized powder) gold(III) chloride trihydrate ( $\text{HauCl}_4$ ), sodium citrate (NaCit), and HS-PEG5K-NH<sub>2</sub> (HCl salt) were purchased from Sigma-Aldrich. PBSs were purchased from Thermo Fisher Scientific. Standard Grey V4 resin (FLGPGR04) for the 3D printing of rigid molds was purchased from FormLabs. SYLGARD 184 Silicone Elastomer was purchased from Ellsworth Adhesives Ibérica.

### Instruments

TEM images were captured using a JEOL JEM-2100 microscope. Hydrodynamic radii and electrophoretic mobility measurements were performed using a Wyatt Möbius. Optical videos were recorded using an inverted optical microscope (Leica DMi8) equipped with a 2.5× objective. The molds for the phantoms were fabricated by using a stereolithography 3D printer FormLabs 2 (FormLabs). The fluorine radionucleotide was synthesized using a TRACERlab FX-FN from GE Healthcare. The molecular imaging experiments were performed using a MOLECUBES β-CUBE (PET) and the MOLECUBES X-CUBE (CT) scanner.

### Animals

Female mice (C57BL/6J), 8 weeks old, Janvier Labs; 16 animals, see below for number of animals under different experimental scenarios) weighing  $20 \pm 3$  g were used to conduct the biodistribution studies. The animals were maintained and handled in accordance with the Guidelines for Accommodation and Care of Animals (European Convention for the Protection of Vertebrate Animals Used for Experimental and Other Scientific Purposes) and internal guidelines. All experimental procedures were approved by the ethical committee and the local authorities before conducting experimental work (code: PRO-AE-SS-059).

### Synthesis of MSNPs

The MSNPs that serve as chassis for the fabrication of the nanomotors were synthesized by sol-gel chemistry using a modification

of the Stöber method (45). Briefly, a mixture of TEOA (35 g), Milli-Q water (20 ml), and CTAB (570 mg) was placed in a three-mouthed round-bottom flask and heated up to 95°C in a silicon oil bath, under reflux and stirring, for 30 min. After this, TEOS (1.5 ml) was added dropwise. The reaction took place for 2 hours, under stirring and reflux at 95°C, and then the resulting MSNPs were collected by centrifugation (three times, 1350g, 5 min). The CTAB was then removed by reflux in acidic methanol. For this, the MSNPs were suspended in a methanol (30 ml) and hydrochloric acid (1.8 ml) mixture, placed in a one-mouthed round-bottom flask in a silicon oil bath at 80°C, and refluxed for 24 hours. Last, the MSNPs were collected by centrifugation and washed thrice in ethanol and thrice in Milli-Q water (three times, 1350g, 5 min). The concentration of the final dispersion was evaluated by dry weighing.

### Amine modification of MSNPs

The surface of the MSNPs was then modified to carry free amine groups, using a modification of a reported method (46). Briefly, a suspension of MSNPs (2 mg/ml) in water was placed in a round-bottom flask and heated up to 50°C under vigorous stirring. Then, APTES was added to the dispersion to a final concentration of 5 mM. The reaction took place under reflux, at 50°C, for 24 hours, after which point the MSNP-NH<sub>2</sub>s were collected and washed thrice in water by centrifugation (three times, 1350g, 5 min). The concentration of the final dispersion was evaluated by dry weighing.

### Synthesis of AuNPs

The AuNPs were synthesized according to a previously reported method (67, 68). Briefly, all necessary materials were cleaned using freshly prepared aqua regia and then rinsed extensively with water and dried in air. Then, a solution of 1 mM HAuCl<sub>4</sub> was heated up to a boil under stirring, in a round-bottom flask integrated in a reflux system. After this, 10 ml of a NaCit solution (38.8 mM) were added, and the solution was boiled for 20 min, turning red in color. The solution was stirred without heating for 1 hour, reaching room temperature. The resulting AuNP dispersion was stored at room temperature in the dark. The Z-potential of the synthesized AuNPs in water was  $-40.26 \pm 2.23$  mV, and their hydrodynamic radii were  $10.4 \pm 0.1$  nm ( $n = 10$ ).

### Fabrication of nanomotors

The MSNP-NH<sub>2</sub>s were resuspended in PBS 1× at a concentration of 1 mg/ml and a total volume of 900 μl and activated with GA (100 μl). The reaction took place for 2.5 hours, at room temperature, under mixing in an end-to-end shaker. After this, the activated MSNP-NH<sub>2</sub>s were collected and washed in PBS 1× thrice by centrifugation (1350g, 5 min), lastly being resuspended in a solution of urease (3 mg/ml) and heterobifunctional PEG (1 μg PEG/mg of MSNP-NH<sub>2</sub>) in PBS 1×. This mixture was left reacting in an end-to-end shaker for 24 hours at room temperature. The resulting nanomotors were then collected and washed three times in PBS 1× by centrifugation (1350g, 5 min). Then, these nanomotors were resuspended in a dispersion of AuNPs and left rotating in an end-to-end shaker for 10 min, followed by thorough washing by centrifugation (five times, 1350g, 5 min).

### DLS and electrophoretic mobility characterization of nanomotors

A Wyatt Möbius DLS was used to characterize the hydrodynamic size distribution and surface charge of the MSNPs, MSNP-NH<sub>2</sub>, GA-activated MSNP-NH<sub>2</sub>, nanomotors, and AuNP-decorated nanomotors.

The equipment comprises a 532-nm wavelength and a detector angle of 163.5°, and it is able to analyze for light scattering and electrophoretic mobility simultaneously. We analyzed each of the particle types at a concentration of 20 µg/ml, with an acquisition time of 5 s and three runs per experiment. A total of nine measurements per type of particle were performed to obtain statistically relevant data.

### TEM imaging of the nanomotors

The AuNP-decorated nanomotors were diluted to a final concentration of 20 µg/ml in water, and the TEM images were captured.

### Synthesis of [<sup>18</sup>F]F-PyTFP

[<sup>18</sup>F]F-PyTFP was synthesized following a previously described procedure, with modifications (69). Briefly, aqueous [<sup>18</sup>F]fluoride was first trapped in an ion-exchange resin (Sep-Pak Accell Plus QMA Light) and subsequently eluted to the reactor vessel with a solution of Kryptofix K<sub>2,2,2</sub>/K<sub>2</sub>CO<sub>3</sub> in a mixture of water and acetonitrile. After azeotropic drying of the solvent, a solution of F-PyTFP (10 mg) in a mixture of *tert*-butanol and acetonitrile (4:1) was added and heated at 40°C for 15 min. The reaction mixture was then diluted with 1 ml of acetonitrile and 1 ml of water and purified by high-performance liquid chromatography (HPLC) using a Nucleosil 100-7 C18 column (Machery-Nagel, Düren, Germany) as the stationary phase and 0.1% trifluoroacetic acid (TFA)/acetonitrile (25:75) as the mobile phase at a flow rate of 3 ml/min. The desired fraction (retention time = 22 to 23 min; [<sup>18</sup>F]F-PyTFP) was collected, diluted with water (25 ml) and flushed through a C18 cartridge (Sep-Pak Light, Waters) to selectively retain [<sup>18</sup>F]F-PyTFP. The desired labeled species was lastly eluted with acetonitrile (1 ml). Radiochemical purity was determined by radio-HPLC using a Mediterranean C18 column (4.6 mm by 150 mm, 5 µm) as the stationary phase and 0.1% TFA/acetonitrile (0 to 1 min 25% acetonitrile, 9 to 12 min 90% acetonitrile, and 13 to 15 min 25% acetonitrile) as the mobile phase at a flow rate of 1.5 ml/min (retention time = 7.5 min).

### Radiolabeling of AuNP-decorated nanomotors with [<sup>18</sup>F]F-PyTFP

The radiofluorination of urease-gold nanomotors with <sup>18</sup>F was carried out by the reaction between the free amine groups of urease (e.g., present in lysine residues) contained at the surface of the nanomotors and [<sup>18</sup>F]F-PyTFP. Briefly, 200 µl of AuNP-decorated nanomotor solution (1 mg/ml) was centrifuged during 10 min at 14,800 rpm, resuspended in PBS (10 µl, 10 mM, pH 8), and mixed with 4 µl of [<sup>18</sup>F]F-PyTFP in acetonitrile (about 74 MBq). The reaction mixture was incubated at room temperature for 35 min. After incubation, the crude was diluted with water (100 µl) and purified by centrifugation (5 min, 14,800 rpm). The resulting precipitate was washed three times with water. The amounts of radioactivity in the supernatant and the precipitate were determined in a dose calibrator (CPCRC-25R, Capintec Inc., NJ, USA) and analyzed with radio-thin-layer chromatography (radio-TLC) using an iTLC-SG chromatography paper (Agilent Technologies, CA, USA) and dichloromethane and methanol (2:1) as the stationary and mobile phases, respectively. TLC plates were analyzed using a TLC reader (MiniGITA, Raytest).

### Radiolabeling of BSA-MSNP with [<sup>18</sup>F]F-PyTFP

The radiofluorination of BSA-AuNPs with <sup>18</sup>F was carried out following the same procedure described for AuNP-decorated nanomotors above.

### Radiolabeling of AuNP-decorated nanomotors with <sup>124</sup>I

The radioiodination of urease-AuNPs was performed by incubation with [<sup>124</sup>I]NaI. Briefly, 200 µl of urease-AuNP solution (1 mg/ml) diluted in 100 µl of water and 8 µl of [<sup>124</sup>I]NaI (about 1L MBq) were incubated at room temperature for 30 min. After incubation, the reaction mixture was purified by centrifugation (5 min, 14,800 rpm). The resulting precipitate was washed three times with water (100 µl). The amounts of radioactivity in the supernatant and the precipitate were determined in a dose calibrator (CPCRC-25R, Capintec Inc., NJ, USA) and analyzed with radio-TLC, using an iTLC-SG chromatography paper (Agilent Technologies, CA, USA) and dichloromethane and methanol (2:1) as the stationary and mobile phases, respectively. TLC plates were analyzed using a TLC reader (MiniGITA, Raytest).

### Optical video recording

The optical videos of the swarms of nanomotors were acquired using a Leica DMi8 microscope, coupled with a Hamamatsu high-speed cooled charge-coupled device camera and a 2.5× objective. For this, the AuNP-decorated nanomotors were centrifuged and resuspended in 200 µl of either water or PBS 1×. Then, a Petri dish was filled with 3 ml of either pure water, PBS, or a 300 mM solution of urea (in water or PBS) and placed in the microscope. A drop of 5 µl of the nanomotors was then added to the liquid-filled Petri dish, and 2-min videos were acquired at a frame rate of 25 frames per second.

### Histogram analysis

The acquired videos were then analyzed for pixel intensity distribution. For this, an ROI was selected, satisfying conditions such that it enclosed both a part of the nanomotor population but also a portion of the background and a dimension of 300 pixels by 300 pixels. After this, the pixel intensity distribution within the ROI was analyzed at 12-s intervals, using ImageJ software.

### Density map analysis

The density maps of the optical videos were obtained using a custom-made Python code. Before this, the videos were treated to remove the background using ImageJ software, and the grayscale images were inverted. Then, the sum of pixel intensity of blocks of 1000 frames was calculated, and the resulting images were loaded in the Python code, applying the look-up table turbo (70).

### PIV analysis

The PIV analysis of the optical videos was performed using a custom-made Python code based on the OpenPIV library. Before loading the images in the code, the frames of the videos were treated to remove the background using ImageJ software. After this, the resulting images were loaded in the Python code, with a window size of 24 pixels, a window overlap of 3 pixels, a search size of 25 pixels, and a frame rate of 0.4 s. Spurious vectors were removed by applying local, global, and signal-to-noise ratio filters.

### Phantom fabrication

To analyze the effect of complex paths on the motility of passive nanoparticles and active nanomotor swarms, phantoms with different shapes were fabricated. To obtain the desired channels' geometry, a 3D design was prepared by using autoCAD software and posttreated with PreForm Software to be later 3D printed by stereolithography. The rigid mold containing the inverse design of the desired channels was printed, followed by the required postprocessing steps: (i)

removal of the nonpolymerized resin by two sequential washing steps in an isopropanol bath, (ii) hardening of the photopolymerized resin by 15 min of ultraviolet exposure, and (iii) removal of support structures. To fabricate the flexible and transparent polydimethylsiloxane (PDMS)-based channels, the catalyzer and the monomer were first mixed at a ratio of 1:10, and the solution was degassed for 15 min to avoid the bubble presence on the final chip. The solution was poured onto the rigid mold, followed by the curing process at 65°C overnight. The polymerized PDMS was then removed from the rigid mold, containing the desired channels. At this stage, the tubing was implemented in the system, removing any debris that would fall into the channels. To close the system and obtain the phantom, a 2-mm-thick layer of flat PDMS was bound to the open side of the channels using a 2-min plasma treatment.

**PET-CT image acquisition**

In vitro imaging studies were conducted using PET-CT as molecular imaging techniques. All the phantoms were filled with either 300 mM urea solution in water or ultrapure water (one channel with each medium) and positioned in the center of the field of view of the MOLECUBES β-CUBE (PET) scanner. The field of view was selected to cover the whole length of the phantom. For each type of nanomotor, two samples (10 μl, about 1 MBq each) were seeded simultaneously in one of the edges of the phantom, one in the channel filled with urea solution and the other one in the channel filled with ultrapure water. Immediately after, a dynamic PET scan was acquired for 25 min, followed by a CT acquisition.

**Phantom PET-CT imaging analysis**

PET images were reconstructed and analyzed using PMOD image processing tool. With that aim, the whole channel was divided in sectors with the same length over the coronal view, and the concentration of activity in each section was determined as a function on time. The values of activity concentration were lastly normalized to the whole amount of radioactivity in the channel.

**Intravenous administration**

Anesthesia was induced by inhalation of 3% isoflurane in pure O<sub>2</sub> and maintained by 1.5 to 2% isoflurane in 100% O<sub>2</sub>. With the animal under anesthesia, the F-nanomotors or I-nanomotors were injected via one of the lateral tail veins using PBS (pH 7.4) as the vehicle (N = 2 for each type of radiolabeling; see Table 1 for details). Dynamic, whole-body 60-min PET imaging sessions were immediately started after administration of the labeled compounds using a MOLECUBES β-CUBE scanner. After the PET scan, whole-body

high-resolution CT acquisitions were performed on the MOLECUBES X-CUBE scanner to provide anatomical information of each animal and the attenuation map for the later reconstruction of the PET images.

**Intravesical administration**

Anesthesia was induced by inhalation of 3% isoflurane in pure O<sub>2</sub> and maintained by 1.5 to 2% isoflurane in 100% O<sub>2</sub>. With the animal under anesthesia, the animals were positioned in supine position, and the bladder was emptied by massaging the abdominal region. Immediately after, the F-nanomotors and MSNP-F-BSA were introduced in the bladder (through a catheter) by intravesical administration using 300 mM urea or water as the vehicle (N = 2 for each type of radiolabeling and vehicle; see Table 1 for details). Administration was followed by 45-min PET imaging sessions and whole-body high-resolution CT acquisitions as above. PET images were reconstructed using 3D OSEM (ordered subset expectation maximization) reconstruction algorithm and applying random, scatter, and attenuation corrections. PET-CT images of the same mouse were coregistered and analyzed using PMOD image processing tool.

**Biodistribution analysis**

VOIs were placed on selected organs (namely, brain, thyroid, lungs, liver, stomach, kidneys, spleen, and bladder), as well as the heart to get an estimation of the concentration of radioactivity in blood. Time-activity curves (decay corrected) were obtained as cps/cm<sup>3</sup> in each organ. Curves were transformed into real activity (Bq/cm<sup>3</sup>) curves by using a calibration factor, obtained from previous scans performed on a phantom (Micro Deluxe, Data Spectrum Corp.) under the same experimental conditions (isotope, reconstruction algorithm, and energetic window).

**Bladder distribution analysis**

PET images were reconstructed using 3D OSEM reconstruction algorithm and applying random, scatter, and attenuation corrections. PET-CT images of the same mouse were coregistered and analyzed using PMOD image processing tool. Two VOIs were placed on the upper and lower regions of the bladder (namely, VOI 1 and VOI 2) to obtain the concentration of radioactivity in both VOIs over time. The values were normalized to the maximum values for each frame.

For the generation of 3D-rendered images of the bladder, raw 16-bit PET images (pixel values from 0 to 65,546) were imported into ImageJ software and color coded. Images were resized by a factor of 3 in all three dimensions using bilinear interpolation. Pixels with a value below 5000 were removed as noise, and orthogonal cuts through the object (axial, coronal, and sagittal) were created using

**Table 1. Summary of the in vivo studies performed with the different types of nanomotors and administration routes.**

Group	Number of animals	Particle	Administration route	Vehicle	Activity (MBq)	Mass of particles (μg)
1	2	F-nanomotors	Intravenous	PBS	2.2 ± 0.10	73
2	2	I-nanomotors	Intravenous	PBS	1.6 ± 0.10	73
3	2	F-nanomotors	Intravesical	Water	1.6 ± 0.10	33
4	2	F-nanomotors	Intravesical	Urea	1.9 ± 0.15	33
5	2	MSNP-F-BSA	Intravesical	Water	0.5 ± 0.06	33
6	2	MSNP-F-BSA	Intravesical	Urea	0.4 ± 0.05	33



the Orthogonal Views function of ImageJ. For 3D rendering, raw 16-bit PET images (pixel values from 0 to 65,546) were opened in ImageJ and resized threefold (bilinear interpolation), and two copies of each image were created, one including all pixels above a value of 5000 (all but noise, corresponding to the whole bladder contour) and another with pixels with values above 45,000 (high-intensity regions in PET). Both images were transformed in binary masks, rendered as surfaces, and exported as STL (Standard Triangle Language) files using ImageJ 3D-viewer plug-in. STL files were imported into Blender 2.8 and beautified by giving a semitransparent aspect to image 1 (bladder contour) and a solid aspect to image 2 (high-intensity regions). Point of view and illumination of the scene were manually selected for each set of images, and 2D images presented here were rendered.

### SUPPLEMENTARY MATERIALS

robotics.sciencemag.org/cgi/content/full/6/52/eabd2823/DC1

Fig. S1. Characterization of the AuNP-decorated nanomotors.

Fig. S2. Motion analysis of single urease-powered nanomotors.

Fig. S3. In vitro imaging of urease-powered nanomotor swarms by optical microscopy.

Fig. S4. In vitro imaging of urease-powered nanomotor swarms by optical microscopy.

Fig. S5. In vitro imaging of urease-powered nanomotor swarms by optical microscopy.

Fig. S6. In vitro analysis of the motion of swarms of urease-powered AuNP-decorated nanomotors by optical microscopy.

Fig. S7. Motion analysis of the nanomotor swarms by optical microscopy.

Fig. S8. Analysis of large passive MSNP (without enzymes) populations.

Fig. S9. Motion analysis of the nanomotor swarms codropped with 5- $\mu$ m PS tracer microparticles [0.01% (w/v)] in water.

Fig. S10. Motion analysis of the nanomotor swarms codropped with 5- $\mu$ m PS tracer microparticles [0.01% (w/v)] in PBS.

Fig. S11. Fabrication of the molds for the complex paths phantoms.

Fig. S12. PET-CT coronal images obtained a 0.5, 7, and 25 min for each phantom, which was filled with either Milli-Q water or 300 mM urea solution.

Fig. S13. Analysis of the biodistribution of l-nanomotors injected intravenously.

Fig. S14. Image sets showing the PET images of the different bladders just after injection of nanomotors ( $t = 0$ ) and 45 min later.

Movie S1. Motion of single nanomotor in water and in PBS.

Movie S2. In vitro imaging of enzyme-powered nanomotor swarms in water by optical microscopy.

Movie S3. In vitro imaging of enzyme-powered nanomotor swarms in PBS by optical microscopy.

Movie S4. In vitro imaging of passive MSNPs dropped onto water and water-based urea solutions by optical microscopy.

Movie S5. In vitro imaging of enzyme-powered nanomotor swarms and tracer microparticles in water and in PBS by optical microscopy.

Movie S6. In vitro imaging of enzyme-powered nanomotor swarms by PET.

Movie S7. Effect of complex paths on the in vitro motion of  $^{18}$ F-radiolabeled urease-powered nanomotors studied by PET-CT imaging.

Movie S8. Study of the biodistribution of enzyme-powered nanomotors by PET-CT.

Movie S9. PET-CT analysis of the distribution of  $^{18}$ F-nanomotors and MSNP- $^{18}$ F-BSA in the bladder administered via intravesical instillation.

### REFERENCES AND NOTES

1. S. Wilhelm, A. J. Tavares, Q. Dai, S. Ohta, J. Audet, H. F. Dvorak, W. C. W. Chan, Analysis of nanoparticle delivery to tumours. *Nat. Rev. Mater.* **1**, 16014 (2016).
2. Z. Wu, X. Lin, Y. Wu, T. Si, J. Sun, Q. He, Near-infrared light-triggered "on/off" motion of polymer multilayer rockets. *ACS Nano* **8**, 6097–6105 (2014).
3. S. M. Douglas, I. Bachelet, G. M. Church, A logic-gated nanorobot for targeted transport of molecular payloads. *Science* **335**, 831–834 (2012).
4. A. C. Hortelão, R. Carrasqueira, N. Murillo-Cremaes, T. Patiño, S. Sánchez, Targeting 3D bladder cancer spheroids with urease-powered nanomotors. *ACS Nano* **13**, 429–439 (2019).
5. F. Hallouard, N. Anton, P. Choquet, A. Constantinesco, T. Vandamme, Iodinated blood pool contrast media for preclinical X-ray imaging applications—A review. *Biomaterials* **31**, 6249–6268 (2010).
6. A. C. Hortelão, T. Patiño, A. Perez-Jiménez, À. Blanco, S. Sánchez, Enzyme-powered nanobots enhance anticancer drug delivery. *Adv. Funct. Mater.* **28**, 1705086 (2018).
7. F. Peng, Y. Tu, D. A. Wilson, Micro/nanomotors towards: In vivo application: Cell, tissue and biofluid. *Chem. Soc. Rev.* **46**, 5289–5310 (2017).
8. A. Llopis-Lorente, A. García-Fernández, N. Murillo-Cremaes, A. C. Hortelão, T. Patiño, R. Villalonga, F. Sancción, R. Martínez-Máñez, S. Sánchez, Enzyme-powered gated

mesoporous silica nanomotors for on-command intracellular payload delivery. *ACS Nano* **13**, 12171–12183 (2019).

9. S. Tang, F. Zhang, H. Gong, F. Wei, J. Zhuang, E. Karshalev, B. Esteban-Fernández de Ávila, C. Huang, Z. Zhou, Z. Li, L. Yin, H. Dong, R. H. Fang, X. Zhang, L. Zhang, J. Wang, Enzyme-powered Janus platelet cell robots for active and targeted drug delivery. *Sci. Robot.* **5**, eaba6137 (2020).
10. W. Gao, R. Dong, S. Thamphiwatana, J. Li, W. Gao, L. Zhang, J. Wang, Artificial micromotors in the mouse's stomach: A step toward in vivo use of synthetic motors. *ACS Nano* **9**, 117–123 (2015).
11. D. Schamel, A. G. Mark, J. G. Gibbs, C. Miksch, K. I. Morozov, A. M. Leshansky, P. Fischer, Nanopropellers and their actuation in complex viscoelastic media. *ACS Nano* **8**, 8794–8801 (2014).
12. H. Choi, S. H. Cho, S. K. Hahn, Urease-powered polydopamine nanomotors for intravesical therapy of bladder diseases. *ACS Nano* **14**, 6683–6692 (2020).
13. D. Walker, B. T. Kasdorf, H.-H. Jeong, O. Lieleq, P. Fischer, Enzymatically active biomimetic micropellers for the penetration of mucin gels. *Sci. Adv.* **1**, e1500501 (2015).
14. J. Wang, B. J. Toebes, A. S. Plachokova, Q. Liu, D. Deng, J. A. Jansen, F. Yang, D. A. Wilson, Self-propelled PLGA micromotor with chemotactic response to inflammation. *Adv. Healthc. Mater.* **9**, 1901710 (2020).
15. F. Peng, Y. Tu, A. Adhikari, J. C. J. Hintzen, D. W. P. M. Löwik, D. A. Wilson, A peptide functionalized nanomotor as efficient cell penetrating tool. *Chem. Commun.* **53**, 1088–1091 (2016).
16. J. Sun, M. Mathesh, W. Li, D. A. Wilson, Enzyme-powered nanomotors with controlled size for biomedical applications. *ACS Nano* **13**, 10191–10200 (2019).
17. M. A. Ramos-Docampo, M. Fernández-Medina, E. Taipaleenmäki, O. Hovorka, V. Salgueirinho, B. Städler, Microswimmers with heat delivery capacity for 3D cell spheroid penetration. *ACS Nano* **13**, 12192–12205 (2019).
18. G. von Maltzahn, J.-H. Park, K. Y. Lin, N. Singh, C. Schwöppe, R. Mesters, W. E. Berdel, E. Ruoslahti, M. J. Sailor, S. N. Bhatia, Nanoparticles that communicate in vivo to amplify tumour targeting. *Nat. Mater.* **10**, 545–552 (2011).
19. D. Needleman, Z. Dogic, Active matter at the interface between materials science and cell biology. *Nat. Rev. Mater.* **2**, 17048 (2017).
20. M. Whiteley, S. P. Diggle, E. P. Greenberg, Progress in and promise of bacterial quorum sensing research. *Nature* **551**, 313–320 (2017).
21. K. Kawabata, M. Nagayama, H. Haga, T. Sambongi, Mechanical effects on collective phenomena of biological systems: Cell locomotion. *Curr. Appl. Phys.* **1**, 66–71 (2001).
22. Z.-M. Qian, S. H. Wang, X. E. Cheng, Y. Q. Chen, An effective and robust method for tracking multiple fish in video image based on fish head detection. *BMC Bioinformatics* **17**, 251 (2016).
23. Z. Deng, F. Mou, S. Tang, L. Xu, M. Luo, J. Guan, Swarming and collective migration of micromotors under near infrared light. *Appl. Mater. Today* **13**, 45–53 (2018).
24. X. Yan, Q. Zhou, M. Vincent, Y. Deng, J. Yu, J. Xu, T. Xu, T. Tang, L. Bian, Y.-X. J. Wang, K. Kostarelos, L. Zhang, Multifunctional biobrid magnetite microrobots for imaging-guided therapy. *Sci. Robot.* **2**, eaq1155 (2017).
25. A. Somasundar, S. Ghosh, F. Mohajerani, L. N. Massenbun, T. Yang, P. S. Cremer, D. Velegol, A. Sen, Positive and negative chemotaxis of enzyme-coated liposome motors. *Nat. Nanotechnol.* **14**, 1129–1134 (2019).
26. Z. Wu, L. Li, Y. Yang, P. Hu, Y. Li, S.-Y. Yang, L. V. Wang, W. Gao, A microrobotic system guided by photoacoustic computed tomography for targeted navigation in intestines in vivo. *Sci. Robot.* **4**, eaax0613 (2019).
27. A. Aubret, M. Youssef, S. Sacanna, J. Palacci, Targeted assembly and synchronization of self-spinning microgears. *Nat. Phys.* **14**, 1114–1118 (2018).
28. C. Zhou, N. J. Suematsu, Y. Peng, Q. Wang, X. Chen, Y. Gao, W. Wang, Coordinating an ensemble of chemical micromotors via spontaneous synchronization. *ACS Nano* **14**, 5360–5370 (2020).
29. X. Chen, C. Zhou, Y. Peng, Q. Wang, W. Wang, Temporal light modulation of photochemically active, oscillating micromotors: Dark pulses, mode switching, and controlled clustering. *ACS Appl. Mater. Interfaces* **12**, 11843–11851 (2020).
30. X. Cao, E. Panizon, A. Vanossi, N. Manini, C. Bechinger, Orientational and directional locking of colloidal clusters driven across periodic surfaces. *Nat. Phys.* **15**, 776–780 (2019).
31. D. Zhou, Y. Gao, J. Yang, Y. C. Li, G. Shao, G. Zhang, T. Li, L. Li, Light-ultrasound driven collective "firework" behavior of nanomotors. *Adv. Sci.* **5**, 1800122 (2018).
32. F. Mou, X. Li, Q. Xie, J. Zhang, K. Xiong, L. Xu, J. Guan, Active micromotor systems built from passive particles with biomimetic predator-prey interactions. *ACS Nano* **14**, 406–414 (2020).
33. T. Xu, F. Soto, W. Gao, R. Dong, V. Garcia-Gradilla, E. Magaña, X. Zhang, J. Wang, Reversible swarming and separation of self-propelled chemically powered nanomotors under acoustic fields. *J. Am. Chem. Soc.* **137**, 2163–2166 (2015).
34. M. Ibele, T. E. Mallouk, A. Sen, Schooling behavior of light-powered autonomous micromotors in water. *Angew. Chemie Int. Ed.* **48**, 3308–3312 (2009).
35. J. Yan, M. Han, J. Zhang, C. Xu, E. Luijten, S. Granick, Reconfiguring active particles by electrostatic imbalance. *Nat. Mater.* **15**, 1095–1099 (2016).

36. I. Buttinoni, J. Bialké, F. Kümmel, H. Löwen, C. Bechinger, T. Speck, Dynamical clustering and phase separation in suspensions of self-propelled colloidal particles. *Phys. Rev. Lett.* **110**, 238301 (2013).
37. T. Bäuerle, A. Fischer, T. Speck, C. Bechinger, Self-organization of active particles by quorum sensing rules. *Nat. Commun.* **9**, 3232 (2018).
38. J. Palacci, S. Sacanna, A. P. Steinberg, D. J. Pine, P. M. Chaikin, Living crystals of light-activated colloidal surfers. *Science* **339**, 936–940 (2013).
39. J. Yu, D. Jin, K.-F. Chan, Q. Wang, K. Yuan, L. Zhang, Active generation and magnetic actuation of microbotic swarms in bio-fluids. *Nat. Commun.* **10**, 5631 (2019).
40. Z. Wu, J. Troll, H.-H. Jeong, Q. Wei, M. Stang, F. Ziemssen, Z. Wang, M. Dong, S. Schnichels, T. Qiu, P. Fischer, A swarm of slippery micropellers penetrates the vitreous body of the eye. *Sci. Adv.* **4**, eaat4388 (2018).
41. A. Servant, F. Qiu, M. Mazza, K. Kostarelos, B. J. Nelson, Controlled in vivo swimming of a swarm of bacteria-like microbotic flagella. *Adv. Mater.* **27**, 2981–2988 (2015).
42. M. Bauer, C. C. Wagner, O. Langer, Microdosing studies in humans. *Drugs R D* **9**, 73–81 (2008).
43. M. Bergstrom, The use of microdosing in the development of small organic and protein therapeutics. *J. Nucl. Med.* **58**, 1188–1195 (2017).
44. D. Vilela, U. Cossio, J. Parmar, A. M. Martínez-Villacorta, V. Gómez-Vallejo, J. Llop, S. Sánchez, Medical imaging for the tracking of micromotors. *ACS Nano* **12**, 1220–1227 (2018).
45. Q. He, X. Cui, F. Cui, L. Guo, J. Shi, Size-controlled synthesis of monodispersed mesoporous silica nano-spheres under a neutral condition. *Microporous Mesoporous Mater.* **117**, 609–616 (2009).
46. Y. Wang, Y. Sun, J. Wang, Y. Yang, Y. Li, Y. Yuan, C. Liu, Charge-reversal APTES-modified mesoporous silica nanoparticles with high drug loading and release controllability. *ACS Appl. Mater. Interfaces* **8**, 17166–17175 (2016).
47. H. Xu, F. Yan, E. E. Monson, R. Kopelman, Room-temperature preparation and characterization of poly (ethylene glycol)-coated silica nanoparticles for biomedical applications. *J. Biomed. Mater. Res. A* **66A**, 870–879 (2003).
48. M. R. Ivanov, H. R. Bednar, A. J. Haes, Investigations of the mechanism of gold nanoparticle stability and surface functionalization in capillary electrophoresis. *ACS Nano* **3**, 386–394 (2009).
49. Z. Liu, Y. Yan, F. T. Chin, F. Wang, X. Chen, Dual integrin and gastrin-releasing peptide receptor targeted tumor imaging using 18F-labeled PEGylated RGD-bombesin heterodimer 18F-FB-PEG3-Glu-RGD-BBN. *J. Med. Chem.* **52**, 425–432 (2009).
50. K. R. Pulagam, K. B. Gona, V. Gómez-Vallejo, J. Meijer, C. Zilberfain, I. Estrela-Lopis, Z. Baz, U. Cossio, J. Llop, Gold nanoparticles as boron carriers for boron neutron capture therapy: Synthesis, radiolabelling and in vivo evaluation. *Molecules* **24**, 3609 (2019).
51. X. Ma, A. Jannasch, U.-R. Albrecht, K. Hahn, A. Miguel-López, E. Schäffer, S. Sánchez, Enzyme-powered hollow mesoporous janus nanomotors. *Nano Lett.* **15**, 7043–7050 (2015).
52. X. Arqué, A. Romero-Rivera, F. Feixas, T. Patiño, S. Osuna, S. Sánchez, Intrinsic enzymatic properties modulate the self-propulsion of micromotors. *Nat. Commun.* **10**, 2826 (2019).
53. T. Patiño, N. Feiner-Gracia, X. Arqué, A. Miguel-López, A. Jannasch, T. Stumpp, E. Schäffer, L. Albertazzi, S. Sánchez, Influence of enzyme quantity and distribution on the self-propulsion of non-janus urease-powered micromotors. *J. Am. Chem. Soc.* **140**, 7896–7903 (2018).
54. M. De Corato, X. Arqué, T. Patiño, M. Arroyo, S. Sánchez, I. Pagonabarraga, Self-propulsion of active colloids via ion release: Theory and experiments. *Phys. Rev. Lett.* **124**, 108001 (2020).
55. L. Liu, H. Mo, S. Wei, D. Raftery, Quantitative analysis of urea in human urine and serum by 1H nuclear magnetic resonance. *Analyst* **137**, 595–600 (2012).
56. L. Soler, V. Magdanz, V. M. Fomin, S. Sanchez, O. G. Schmidt, Self-propelled micromotors for cleaning polluted water. *ACS Nano* **7**, 9611–9620 (2013).
57. J. Orozco, B. Jurado-Sánchez, G. Wagner, W. Gao, R. Vazquez-Duhalt, S. Sattayasamitsathit, M. Galarnyk, A. Cortés, D. Saintillan, J. Wang, Bubble-propelled micromotors for enhanced transport of passive tracers. *Langmuir* **30**, 5082–5087 (2014).
58. E. Morales-Narváez, M. Guix, M. Medina-Sánchez, C. C. Mayorga-Martinez, A. Merkoçi, Micromotor enhanced microarray technology for protein detection. *Small* **10**, 2542–2548 (2014).
59. L. Valdez, H. Shum, I. Ortiz-Rivera, A. C. Balazs, A. Sen, Solutal and thermal buoyancy effects in self-powered phosphatase micropumps. *Soft Matter* **13**, 2800–2807 (2017).
60. I. Ortiz-Rivera, H. Shum, A. Agrawal, A. Sen, A. C. Balazs, Convective flow reversal in self-powered enzyme micropumps. *Proc. Natl. Acad. Sci. U.S.A.* **113**, 2585–2590 (2016).
61. S. Maiti, O. E. Shklyav, A. C. Balazs, A. Sen, Self-organization of fluids in a multienzymatic pump system. *Langmuir* **35**, 3724–3732 (2019).
62. M. Alarcón-Correa, J.-P. Günther, J. Troll, V. M. Kadiri, J. Bill, P. Fischer, D. Rothenstein, Self-assembled phage-based colloids for high localized enzymatic activity. *ACS Nano* **13**, 5810–5815 (2019).
63. H. W. A. M. de Jong, L. Perk, G. W. M. Visser, R. Boellaard, G. A. M. S. van Dongen, A. A. Lammertsma, High resolution PET imaging characteristics of <sup>68</sup>Ga, <sup>124</sup>I and <sup>89</sup>Zr compared to <sup>18</sup>F, in *IEEE Nuclear Science Symposium Conference Record, 2005* (Puerto Rico, 23 to 29 October 2005), vol. 3, pp. 1624–1627.
64. N. Hoshyar, S. Gray, H. Han, G. Bao, The effect of nanoparticle size on in vivo pharmacokinetics and cellular interaction. *Nanomedicine* **11**, 673–692 (2016).
65. B. Du, X. Jiang, A. Das, Q. Zhou, M. Yu, R. Jin, J. Zheng, Glomerular barrier behaves as an atomically precise bandpass filter in a sub-nanometre regime. *Nat. Nanotechnol.* **12**, 1096–1102 (2017).
66. S. H. Kim, S. H. Choo, *Bladder Cancer*, J. H. Ku, Ed. (Elsevier, ed. 1, 2018), pp. 263–276.
67. K. Ai, Y. Liu, L. Lu, Hydrogen-bonding recognition-induced color change of gold nanoparticles for visual detection of melamine in raw milk and infant formula. *J. Am. Chem. Soc.* **131**, 9496–9497 (2009).
68. D. Vilela, A. C. Hortelao, R. Balderas-Xicohtencatl, M. Hirscher, K. Hahn, X. Ma, S. Sánchez, Facile fabrication of mesoporous silica micro-jets with multi-functionalities. *Nanoscale* **9**, 13990–13997 (2017).
69. D. E. Olberg, J. M. Arukwe, D. Grace, O. K. Hjelstuen, M. Solbakken, G. M. Kindberg, A. Cuthbertson, One step radiosynthesis of 6-[18F]fluoronicotinic acid 2,3,5,6-tetrafluorophenyl ester ([18F]F-Py-TFP): A new prosthetic group for efficient labeling of biomolecules with fluorine-18. *J. Med. Chem.* **53**, 1732–1740 (2010).
70. A. Mikhailov, *Turbo, An Improved Rainbow Colormap for Visualization* (Google AI Blog, 2019).

#### Acknowledgments

**Funding:** The research leading to these results has received funding from the Spanish MINECO (BOTSinFluids project), the Foundation BBVA (MEDIROBOTS project), the CERCA program by the Generalitat de Catalunya, and the Caixaimpulse program by La Caixa Foundation (TERANOBOOTS project). This project has received funding from the European Research Council (ERC) under the European Union's Horizon 2020 research and innovation program (grant agreement no. 866348; iNanoSwarms). A.C.H. thanks MINECO for the Severo Ochoa PhD fellowship. M.G. thanks MINECO for the Juan de la Cierva fellowship (IJCI2016-30451), the Beatriz de Pinós Programme (2018-BP-00305), and the Ministry of Business and Knowledge of the Government of Catalonia. D.V. acknowledges financial support provided by the European Commission under Horizon 2020 Marie Skłodowska-Curie Actions COFUND scheme (grant agreement no. 712754) and by the Severo Ochoa program of the Spanish Ministry of Economy and Competitiveness [grant SEV-2014-0425 (2015–2019)]. T.P. thanks the European Union's Horizon 2020 research and innovation program, under the Marie Skłodowska-Curie Individual Fellowship (H2020-MSCA-IF2018, DNA-bots). J.L. thanks the Spanish Ministry of Economy and Competitiveness (grants CTQ2017-87637-R, SAF2017-87670-R) for financial support. Part of the work was conducted under the María de Maeztu Units of Excellence Programme (grant no. MDM-2017-0720). **Author contributions:** A.C.H. synthesized the nanomotors, performed their characterization, optical tracking, corresponding image processing, and data analysis. C.S. performed radiolabeling, PET-CT experiments, and data analysis. M.G. fabricated the phantoms and helped with graphic design and video editing. S.G.-G. and E.J. helped set up the intravesical administration model. D.V. synthesized the AuNPs and performed their characterization. L.R. developed the <sup>18</sup>F-radiolabeling protocol. P.R.-C. provided graphic design of the radiochemical facility and contributed in image analysis after intravesical instillation. U.C. performed reconstruction, analysis, and quantification of PET images. V.G.-V. contributed to the in vivo experimental design. T.P., J.L., and S.S. conceived the idea, designed, and supervised the work. The manuscript was written through contributions of all authors. All authors have given approval to the final version of the manuscript. **Competing interests:** The authors declare that they have no competing interests. **Data and materials availability:** All data needed to support the conclusions of this paper are available in the paper or the Supplementary Materials.

Submitted 12 June 2020

Accepted 16 February 2021

Published 17 March 2021

10.1126/scirobotics.abd2823

**Citation:** A. C. Hortelao, C. Simó, M. Guix, S. Guallar-Garrido, E. Julián, D. Vilela, L. Rejc, P. Ramos-Cabrer, U. Cossio, V. Gómez-Vallejo, T. Patiño, J. Llop, S. Sánchez, Swarming behavior and in vivo monitoring of enzymatic nanomotors within the bladder. *Sci. Robot.* **6**, eabd2823 (2021).

# Chapter 6

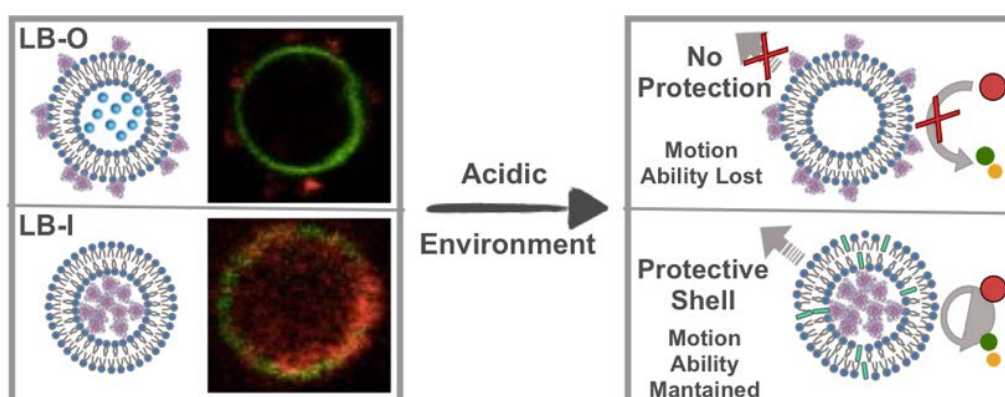


**LipoBots: using liposomal vesicles as protective shell of  
urease-based nanomotors**





The use of nanotechnology in biomedical applications requires attention to several features beyond biocompatibility and biodegradability, such as withstanding the harsh environments they may face in vivo. Aiming at expanding our library of chassis for the fabrication of nanomotors, as well as develop a nanomotors capable of protecting itself from harsh conditions, we **teamed up with Prof. Daniel Maspoch's group at ICN2** to investigate liposomes as protective shells of urease powered nanomotors. In this work, we fabricated urease powered nanomotors based where the **enzymes were either encapsulated in liposomes (LB-I)** or attached electrostatically to the outer surface of the liposomes (LB-O). We verified that while LB-O showed a concentration-dependent enhanced diffusion in the presence of urea, LB-I required the **addition of a component of the bile salts** to percolate the liposomes bilayer, thus triggering **LB-I's self-propulsion**. We explored the protective capabilities of the liposome chassis by exposing the liposome motors to harsh acidic conditions. We observed that LB-O lost both motion and catalytic abilities, while LB-I **maintained their ability to catalyze** the decomposition of urea and **exhibit self-propulsion**, thus evidencing the **protective features** of the liposome shells.



**Graphical Abstract 4.** Protective features of liposomes chassis for the fabrication of enzyme powered nanomotors.

# LipoBots: Using Liposomal Vesicles as Protective Shell of Urease-Based Nanomotors

Ana C. Hortelão, Sonia García-Jimeno, Mary Cano-Sarabia, Tania Patiño,\*  
Daniel MasPOCH,\* and Samuel Sanchez\*

Developing self-powered nanomotors made of biocompatible and functional components is of paramount importance in future biomedical applications. Herein, the functional features of LipoBots (LBs) composed of a liposomal carrier containing urease enzymes for propulsion, including their protective properties against acidic conditions and their on-demand triggered activation, are reported. Given the functional nature of liposomes, enzymes can be either encapsulated or coated on the surface of the vesicles. The influence of the location of urease on motion dynamics is first studied, finding that the surface-urease LBs undergo self-propulsion whereas the encapsulated-urease LBs do not. However, adding a percolating agent present in the bile salts to the encapsulated-urease LBs triggers active motion. Moreover, it is found that when both types of nanomotors are exposed to a medium of similar pH found in the stomach, the surface-urease LBs lose activity and motion capabilities, while the encapsulated-urease LBs retain activity and mobility. The results for the protection enzyme activity through encapsulation within liposomes and in situ triggering of the motion of LBs upon exposure to bile salts may open new avenues for the use of liposome-based nanomotors in drug delivery, for example, in the gastrointestinal tract, where bile salts are naturally present in the intestine.

## 1. Introduction

Over the past decade, scientists inspired by nature have developed nanoscale motors, known as catalytic nanomotors, that harvest chemical energy from their surrounding microenvironment and subsequently convert it into motion for various practical applications. Such devices have been reported to swim,<sup>[1–4]</sup> transport,<sup>[5–8]</sup> drill,<sup>[9–11]</sup> clean,<sup>[12–18]</sup> sense, and actuate in fluids.<sup>[19–22]</sup> Accordingly, they demonstrate great potential for biomedical applications.<sup>[23–28]</sup> Indeed, compared to their passive counterparts, these actively propelled devices can cover larger areas/volumes, thus increasing potential interactions with a target;<sup>[29,30]</sup> penetrate tissue to a greater degree;<sup>[29,31,32]</sup> and perform superior drug delivery.<sup>[33,34]</sup>

An especially appealing aspect of using catalytic nanomotors for biomedical applications is the possibility of actuating them in situ using various biomolecules as fuels. In this regard, enzymes are an attractive source of catalytic power for

nanomotors, as they are highly diverse, substrate-specific and ubiquitous in the body. Thus, entire libraries of enzyme/biomolecule (engine/fuel) combinations could be designed for specific on-demand applications.<sup>[35–37]</sup> Enzymes used in catalytic nanomotors include urease,<sup>[38–44]</sup> acetylcholine esterase,<sup>[44]</sup> glucose-oxidase,<sup>[39,44,45]</sup> lipase,<sup>[46]</sup> catalase,<sup>[39,42,47–50]</sup> and combinations thereof, all which can induce propulsion of various nano- and/or microparticles. Nevertheless, the use of enzyme-powered nanomotors in vivo demands additional application requirements beyond biocompatibility and fuel bioavailability. For instance, inside living organisms, such devices could be exposed to harsh conditions (e.g., other enzymes and changes in pH) that can degrade and consequently inactivate the enzymatic motor.<sup>[51]</sup>

An intriguing but scarcely explored strategy for improving the stability of enzyme-powered nanomotors under harsh conditions is to protect the enzymes by encapsulating them into functional nanostructures: in other words, by using nanomaterials as both functional and protective chassis. In this study, we chose liposomes as preliminary chassis for three reasons: first, for their well-known capacity for encapsulation and protection of various actives, ranging from small

A. C. Hortelão, Dr. T. Patiño, Prof. S. Sánchez  
Institute for Bioengineering of Catalonia (IBEC)  
The Barcelona Institute of Science and Technology (BIST)  
Baldri i Reixac 10-12, Barcelona 08028, Spain  
E-mail: tpatino@ibecbarcelona.eu; ssanchez@ibecbarcelona.eu

Dr. S. García-Jimeno, Dr. M. Cano-Sarabia, Prof. D. MasPOCH  
Catalan Institute of Nanoscience and Nanotechnology (ICN2)  
CSIC and The Barcelona Institute of Science and Technology  
Universitat Autònoma de Barcelona  
Bellaterra, Barcelona 08193, Spain  
E-mail: daniel.masPOCH@icn2.cat

Dr. T. Patiño  
Chemistry Department  
University of Rome  
Tor Vergata  
Via della Ricerca Scientifica  
Rome 00133, Italy

Prof. D. MasPOCH, Prof. S. Sánchez  
Institució Catalana de Recerca i Estudis Avançats (ICREA)  
Passeig Lluís Companys 23, Barcelona 08010, Spain

The ORCID identification number(s) for the author(s) of this article can be found under <https://doi.org/10.1002/adfm.202002767>.

DOI: 10.1002/adfm.202002767

drug molecules to larger biomolecules (e.g., proteins and enzymes);<sup>[52]</sup> secondly, for their permeable membrane, which enables bidirectional transport of substances in and out of them; and finally, for their excellent biocompatibility and safety.<sup>[53]</sup> To date, very little work has been done in this field. In a very recent and pioneering example, Sen and co-workers coupled enzymes onto the outer layer of liposomes, observing self-propulsion and chemotactic behavior in the resultant conjugates.<sup>[41,42]</sup> The surface enzymes were sensitive to surrounding ionic gradients, and the direction of motion of the resultant nanomotors depended on the Hoffmeister series. The work by Sen and co-workers provided a foundation for using liposomes as chassis for enzyme-nanomotors; however, they did not explore encapsulation as an enzyme-protection strategy.

In our study, we demonstrate a new type of enzyme-powered nanomotors, called LipoBots (LBs), which are powered by urease. In these LBs, the urease is encapsulated into the inner liposomal compartment, named LipoBots-Inside (LB-I). For comparison purposes, we also synthesized a second prototype of LBs, LipoBots-Outside (LB-O), in which the urease enzymes are attached to the liposomes' surface by physisorption.<sup>[54]</sup> This salt acts as an edge activator, causing disruption and permeabilization of the lipid bilayer<sup>[55–57]</sup> and therefore, enabling exchange of substrates and products. Accordingly, exposure of LB-I to sodium deoxycholate triggers motion of the nanomotor. As proof of concept, we exploited the protective effects of the lipid bilayer on the encapsulated enzymes, demonstrating that the enzymatic activity of these liposomal motors can be retained after incubation in harsh acidic conditions and their motion can be triggered by posterior addition of sodium deoxycholate at neutral pH.

## 2. Results and Discussion

LipoBots were prepared using the thin-film hydration and extrusion method,<sup>[58,59]</sup> where LBs were either hydrated under vigorous stirring with a urease solution (LB-I) or with phosphate buffer saline (PBS), followed by incubation with urease solution (LB-O) (see the Experimental Section for details).

The morphology and size of both LBs was investigated using cryo-transmission electron microscopy (cryoTEM), which revealed the formation of a mixture of unilamellar and multivesicular vesicles with a mean radius of  $105.7 \pm 0.8$  and  $100.7 \pm 0.5$  nm (average  $\pm$  standard deviation, SD) for LB-O and LB-I, respectively (Figure 1b,c). The LBs were also characterized using dynamic light scattering (DLS), where we observed that LB-O presented a broader peak than bare liposomes, which could be attributed to aggregation caused by the presence of enzymes on the surface of the liposomes.

Enzyme localization and distribution was investigated using nonextruded micrometer-sized liposomes, due to the ease of visualization of the structures, by confocal laser scanning microscopy (CLSM), as displayed in Figure 1d,e. For this, we labeled urease enzymes with cyanine5 (Cy5) and used Oregon Green 488 to mark the lipidic bilayer. We observed that, for LB-I, urease (in red) was mainly located inside the liposomes (in green), whereas in LB-O, urease (in red) was located on the outer layer. We also observed that the stochastic binding of the

enzyme leads to the formation of asymmetric patches similar to those reported for silica-based micromotors using glutaraldehyde crosslinker.<sup>[43]</sup> This positioning of the enzymes on the external surface of the liposome may be crucial for breaking the symmetry in the generation of biocatalytic reaction products, thus leading to self-propulsion. Further studies on the effect of enzyme mobility in soft scaffolds on the motion will be the focus of future research.<sup>[43]</sup> We expect these observations to extrapolate to the smaller liposomes used in this work; however, to further confirm the successful attachment of urease on the outer surface of liposomes in LB-O and encapsulation in LB-I, we investigated the surface charge of both LBs by studying their electrophoretic mobility (Figure 1g). LB-I were positively charged ( $18.6 \pm 1.0$  mV, average  $\pm$  Standard error of the mean (SEM)), as they are composed of cationic  $3\beta$ -[N-(N',N'-dimethylaminoethane)-carbonyl]cholesterol hydrochloride (Chol+).<sup>[60]</sup> Nevertheless, even though LB-O were also composed of Chol+, they displayed a negative surface charge ( $-11.8 \pm 0.4$  mV, average  $\pm$  SEM), which could be attributed to the urease negative charges at neutral pH (isoelectric point of urease  $\approx 5.1$ ).<sup>[61]</sup> Altogether, these results confirm that the urease molecules are mainly confined into the inner compartment in LB-I, and that urease molecules are physisorbed on the external surface in LB-O.

We further characterized urease powered LBs by quantifying their total protein content (Figure 1h), using the bicinchoninic acid (BCA) assay, which relies on the reduction of copper by proteins and the colorimetric detection of the cuprous cation by BCA.<sup>[62]</sup> The total amount protein was determined to be slightly higher in the case of LB-O ( $\approx 51\%$  binding yield) compared to LB-I ( $\approx 46\%$  encapsulation yield), nevertheless it was not statistically different ( $P < 0.06$ ). Moreover, we studied how enzyme location affected its activity. Figure 1i shows urease activity of both types of LBs, evidencing that LB-I presents lower catalytic activity than LB-O ( $P < 0.05$ , unpaired *t*-test). This could be explained not only by the lower amount of urease molecules on the LB-I, but also by the fuel availability. Even though urea is a small water-soluble polar molecule,<sup>[63]</sup> it relies on passive transport to cross lipid membranes,<sup>[64]</sup> thus its access to urease in LB-O is much more facilitated than in the case of LB-I, leading to lower urease activity.

We then investigated the motion capabilities of the urease-powered LBs by DLS. Figure 2a displays the diffusion coefficients of LB-O and LB-I when exposed to a range of urea concentrations ( $25 \times 10^{-3}$ ,  $50 \times 10^{-3}$ , and  $100 \times 10^{-3}$  M), evidencing an increase in the diffusion coefficient of LB-O with increasing urea concentrations. However, as shown in Figure 2b, the diffusion coefficient of LB-I did not increase in the presence of urea, but rather showed a slight decrease.

This could be attributed to the fact that, despite urea can be catalyzed by urease, the release of the reaction's products from the inner compartment of the liposomes is not efficient enough to generate motion or the release of products does not occur in an asymmetric manner. Furthermore, the slight decrease in diffusion coefficient could be explained by the possible accumulation of CO<sub>2</sub> inside of the LB-I, leading to its swelling, which in turn increases the hydrodynamic radii detected by DLS, translated into a smaller diffusion. Figure 2c,d shows the shifts in hydrodynamic radii for LB-O and LB-I, respectively. For LB-O,

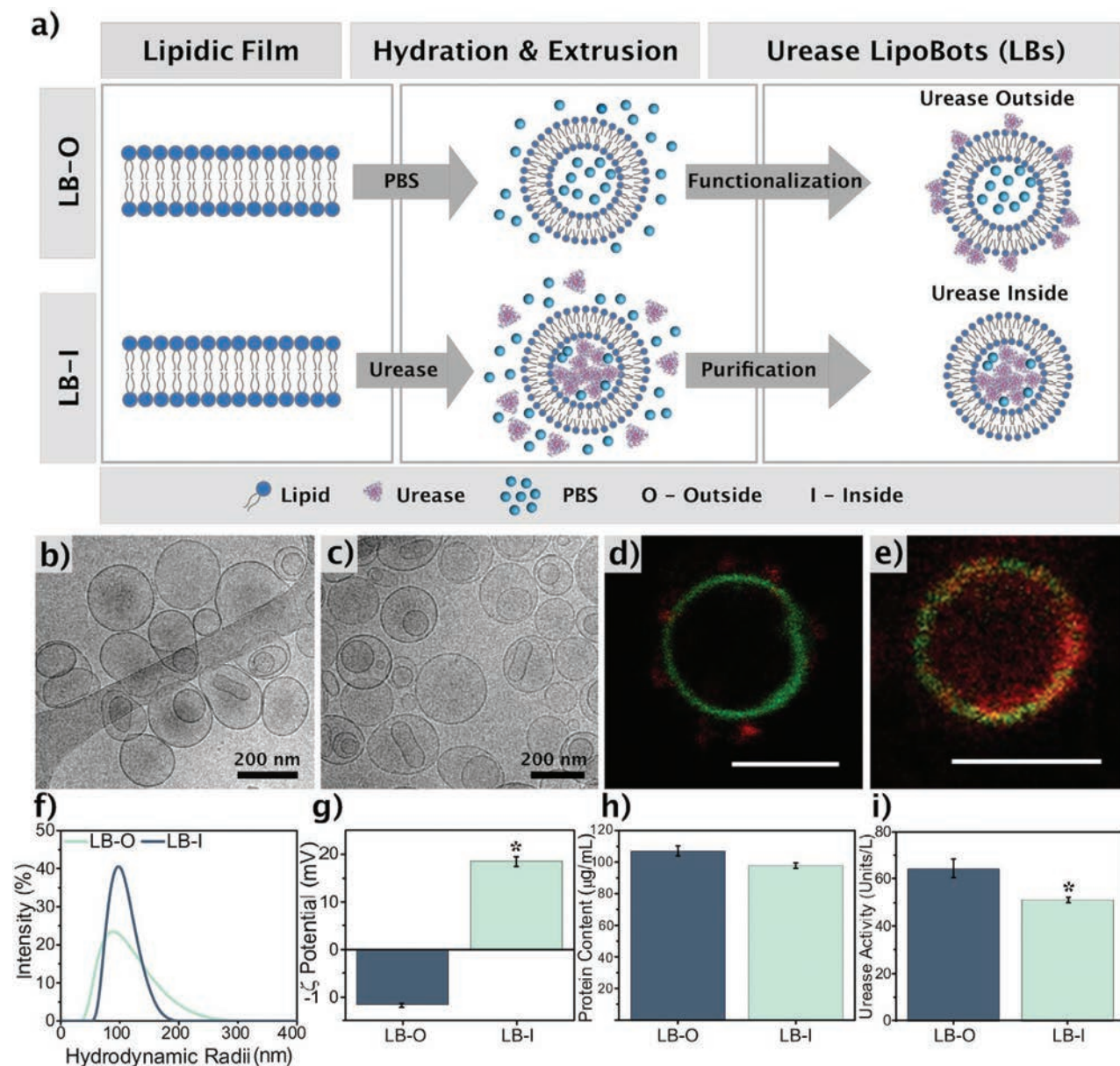


**Figure 1.** Fabrication and characterization of the LipoBots (LBs), comprising urease enzyme on the outer surface (LB-O), or into the inner compartment (LB-I). a) Scheme illustrating the fabrication process of LB-O and LB-I. CryoTEM images of b) LB-O and c) LB-I. Confocal laser scanning microscopy images of urease (red) in d) micrometer-sized LB-O (green) and e) micrometer-sized LB-I (green). Scale bars are 2 μm. f) Hydrodynamic radii characterization by DLS. g) Surface charge evaluation of the LB given by electrophoretic mobility measurements. h) Quantification of the total protein content present on the LBs. i) Enzymatic activity of the urease present on the LBs. Results are shown as the mean ± standard error of the mean (SEM),  $N = 10$ , asterisks denote a significant difference between LB-O and LB-I, with  $P < 0.05$ .

a shift towards smaller hydrodynamic radii was observed with increasing concentrations of urea, evidencing also a narrower peak than the control without urea, suggesting a uniformity in the self-propulsion. Oppositely, no shift was observed for the LB-I sample, indicating no self-propulsion. Furthermore, when LB-I were exposed to  $100 \times 10^{-3}$  M urea, the observed peak was broader than the control without urea, which could be explained by the retention of products within the inner cavity of the LBs.

As we previously observed, the absence of motion in LB-I could be explained because of the inefficient entrance of fuel

into the liposomes and/or to the inefficient release of substances ( $\text{CO}_2$  and  $\text{NH}_3$ ) resulting from the enzymatic reaction. For this reason, we hypothesized that enhancement of the permeability of LB-I should facilitate the bidirectional transport of urea into the liposome and of  $\text{CO}_2$  and  $\text{NH}_3$  out of the liposome, opening a way for triggering their motion. In this respect, a well-known strategy to enhance the permeability of liposomes is by the use of bile salts. For instance, the bile salt sodium deoxycholate can act as an edge activator and disruptor of lipid bilayers by solubilization, causing an increase on bilayer flexibility and



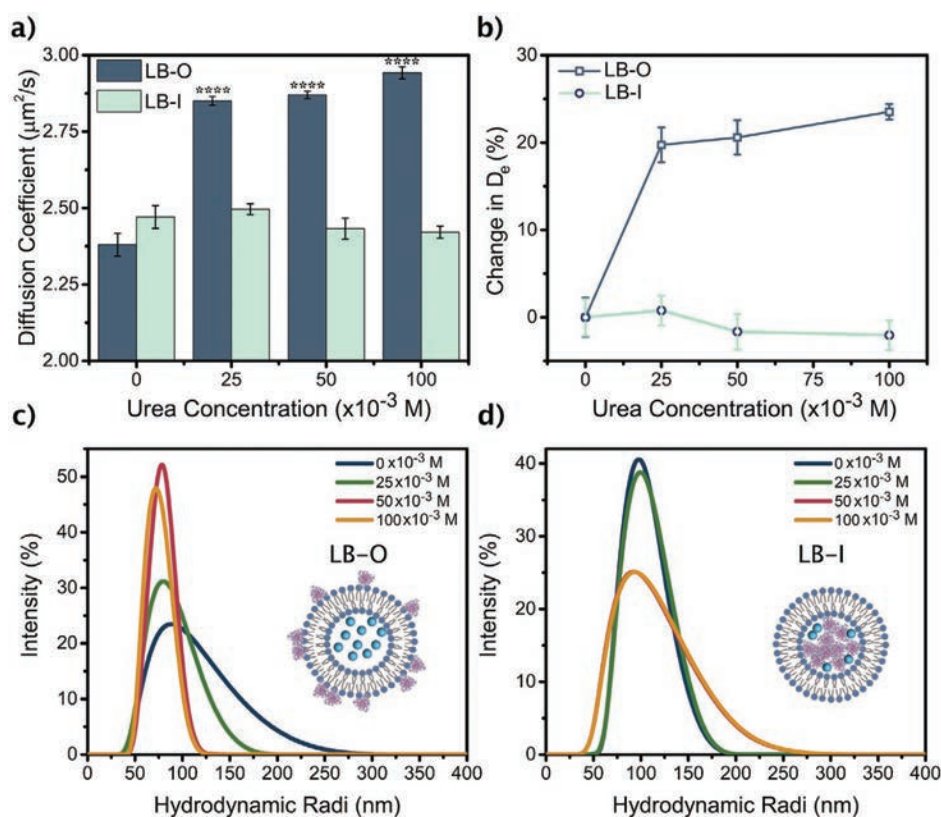


**Figure 2.** Motion profile of LB-O and LB-I. a) Diffusion coefficient of both LBs in the presence of increasing urea concentrations. Asterisks denote a significant difference from the control ( $0 \times 10^{-3}$  M) with  $P < 0.0001$ , results are shown as mean  $\pm$  SEM,  $N = 10$ . b) Percentage of change in the diffusion coefficient in relation to the control ( $0 \times 10^{-3}$  M urea) for LB-O and LB-I. Hydrodynamic radii shift for c) LB-O and for d) LB-I.

permeability.<sup>[65,66]</sup> To study the effect of sodium deoxycholate on the permeability and self-propulsion capabilities of LB-I, we exposed them to different concentrations of sodium deoxycholate and investigated their motion capability by DLS.

**Figure 3a** and **Figure S2** (Supporting Information) show the DLS study of the diffusion coefficient of LB-I in the presence of the different sodium deoxycholate concentrations, both in the absence and presence of urea ( $100 \times 10^{-3}$  M). We found that, at a sodium deoxycholate concentration of 0.05%, the LB-I still showed a low diffusion coefficient, meaning that urea did not induce self-propulsion. This fact could be explained because LB-I were not enriched with enough deoxycholate molecules to increase the lipid bilayer permeability. Nonetheless, upon increasing the concentration of sodium deoxycholate up to 0.075%, a higher diffusion coefficient was clearly observed, being it significantly higher when exposed to urea. At higher concentrations of sodium deoxycholate (0.1%), however, we observed a decrease of the diffusion coefficient, both in the absence and presence of urea. We attributed this to the fact that, when the cholate concentration increases, the increase in fluidity and deformability of the bilayer leads to the liposome elongation, and subsequent excision, as well as formation of smaller mixed micelles.<sup>[57,67]</sup>

Being confirmed the possibility to in situ trigger the active motion of urease-encapsulated LB-I upon exposure to sodium deoxycholate and taking 0.075% as the optimal concentration

of this bile salt, we then investigated the self-propulsion of LB-I with respect to fuel concentration (**Figure 3b,c**). To this end, LB-I were incubated with increasing concentrations of urea, ranging from 0 to  $100 \times 10^{-3}$  M, where a concentration-dependent increase of the diffusion coefficient was observed. Since sodium deoxycholate alters the fluidity and permeability of the lipid bilayer, we studied the integrity of LB-I upon exposure to sodium deoxycholate by cryoTEM (**Figure 3d-f**). **Figure 3e,f** reveals the presence of liposomes with a mean radius of  $107.7 \pm 3.6$  nm (average  $\pm$  SEM), thus confirming the stability of LB-I under motion-triggering conditions. Moreover, a comparison of LB-I incubated in PBS containing urea in the presence and absence of sodium deoxycholate showed that liposomes were more elongated in presence of sodium deoxycholate, further suggesting a higher flexibility (and thus, permeability) of LB-I under these conditions, as reported in literature.<sup>[55]</sup>

The possibility to fabricate enzyme-encapsulated nanomotors which motion is activated under certain conditions opens new avenues for using this class of nanomotors in conditions in which the enzymes can degrade. As proof-of-concept, we evaluated whether the liposomal chassis can be used to protect the enzymes when crossing adverse conditions, making them still active when the motion triggering conditions are found or applied. For this, LB-I (and also LB-O for comparison purposes) were exposed to an acidic medium of the same pH as stomach



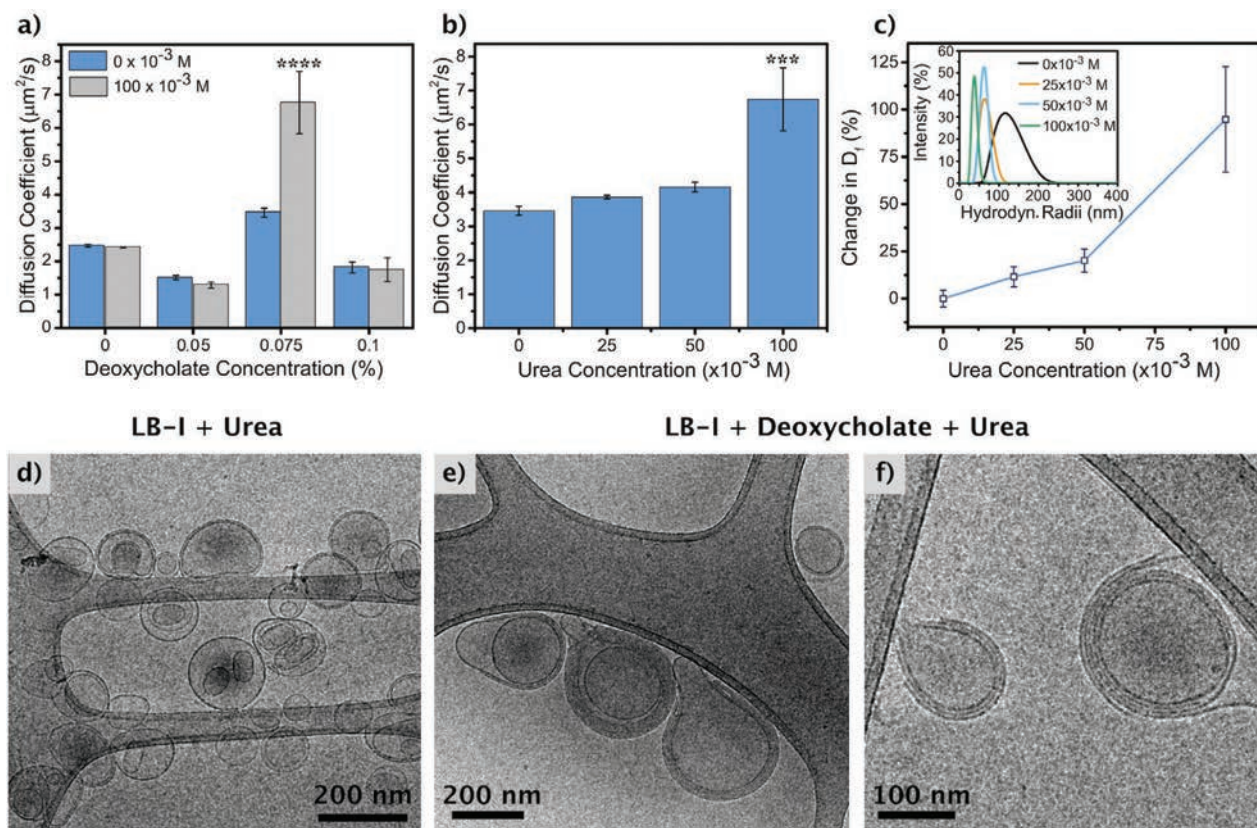


**Figure 3.** Motion profile of LB-I in the presence of sodium deoxycholate. a) Diffusion coefficient of the LB-I in the presence of different sodium deoxycholate concentrations. Asterisks denote a significant difference from control ( $0 \times 10^{-3}$  M) with  $P < 0.001$ , results are shown as mean  $\pm$  SEM,  $N = 10$ . b) Diffusion coefficient of LB-I in the presence of 0.075% sodium deoxycholate and increasing concentrations of urea. Asterisks denote a significant difference from control ( $0 \times 10^{-3}$  M) with  $P < 0.01$ , results are shown as mean  $\pm$  SEM,  $N = 10$ . c) Percentage of change in the diffusion coefficient of LB-I in relation to the control (0.075% sodium deoxycholate,  $0 \times 10^{-3}$  M urea); inset: hydrodynamic radii of LB-I in the presence of 0.075% sodium deoxycholate and increasing concentrations of urea. CryoTEM images of d) LB-I and e, f) LB-I in the presence of both deoxycholate and urea ( $100 \times 10^{-3}$  M).

for 1 h (Figures 4). The literature on stomach acidity levels shows that there is a high intersubject variability.<sup>[68]</sup> Moreover, the pH of the stomach is variable throughout the day and dependent on the food intake, with pH values ranging from 2 to 6.7.<sup>[54]</sup> The pH values chosen (pH = 3 and pH = 5) were chosen to mimic different acidity levels of the stomach and are in accordance with the regulatory guidelines of the Food and Drug Administration.<sup>[54,68,69]</sup>

After 1 h incubation at pH 3 and 5, both LB-I and LB-O solutions were neutralized (final pH = 7.2) by adding PBS, PBS containing urea ( $100 \times 10^{-3}$  M), PBS containing 0.075% sodium deoxycholate, or PBS containing both urea and sodium deoxycholate (Figure 4a; see the Experimental Section for further details) and analyzed by DLS to investigate their ability to retain motility and enzymatic activity after incubation in acidic conditions. To investigate the effect of harsh environments on the liposome chassis, we characterized their morphology by CryoTEM (Figure 4b,c). The images obtained showed that the lipid bilayers maintained its structural integrity after exposure to acidic medium, as reported in literature for liposomes designed for GI tract delivery.<sup>[70]</sup> We then studied the protective effect of the lipid shell on the urease by analyzing the LBs motion abilities and enzyme activity after acidic incubation. Figure 4d,e

displays the change in diffusion coefficient in the presence of urea ( $100 \times 10^{-3}$  M), in relation to control ( $0 \times 10^{-3}$  M urea), and the enzymatic activity of both types of LBs when exposed to pH 3 and 5. For comparison purposes, they also show the change in diffusion coefficient and enzymatic activity of both LBs directly exposed to pH = 7.4. We observed that, unlike at pH = 7.4, the enzymatic activity and ability to self-propel of LB-O are completely lost after incubation at both pH 3 and 5, which can be due to the denaturalization of the urease placed on the external surface of the liposomes, or even to the detachment of the enzyme from the liposome's surface since it is bound by electrostatic interactions and the acidic environment causes its surface charge to turn positive.

The enzymatic activity of LB-O was also measured, from which a complete loss of activity was detected. Remarkably, LB-I displayed a slight increase in diffusion coefficient in the presence of urea after incubation in acidic conditions, even without addition of sodium deoxycholate. This can be due to an effect of acidic conditions in the permeability of the lipid bilayer, allowing for a more efficient exchange of substrate and catalytic products.<sup>[71]</sup> Nevertheless, in the presence of both urea and sodium deoxycholate, LB-I presented a higher increase in diffusion coefficient, indicating retention of their self-propulsion

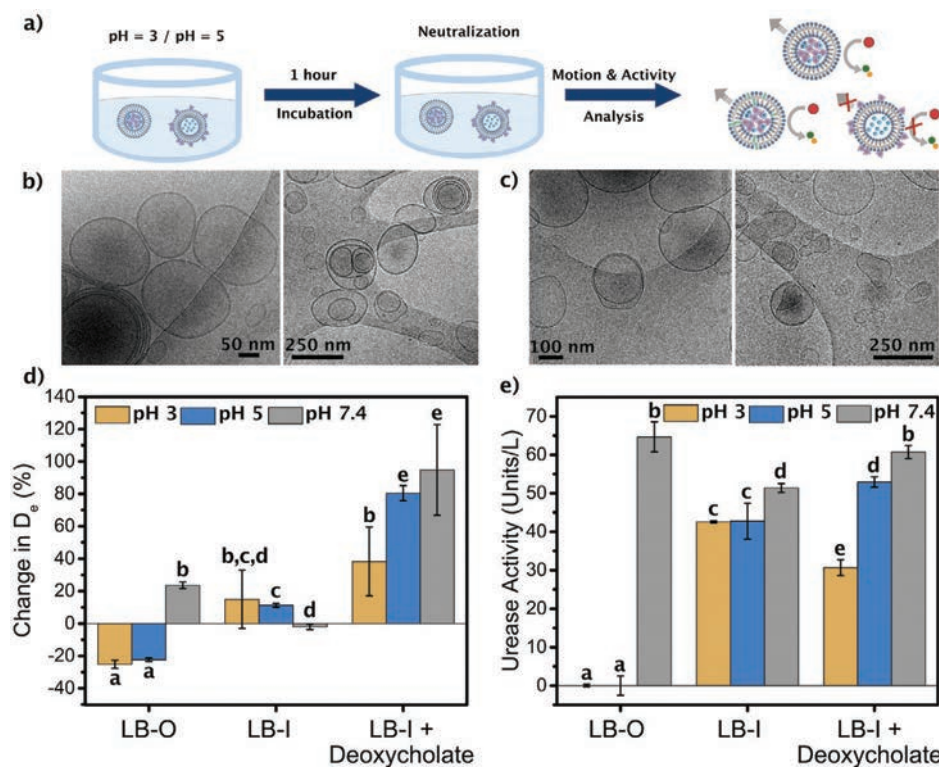


**Figure 4.** Stability in acidic conditions and recovery of the motion capabilities of LBs. a) Scheme illustrating the experimental approach: LB incubation in acidic conditions for 1 h, followed by neutralization and investigation of their motion abilities. CryoTEM images of b) LB-O and c) LB-I after incubation in acidic conditions. d) Percentage change in the diffusion coefficient in relation to control, for LB-O, LB-I and LB-I in the presence of 0.075% of sodium deoxycholate, results are shown as mean  $\pm$  SEM,  $N = 5$ . e) Enzymatic activity of urease present in the LBs after neutralization, results are shown as mean  $\pm$  SEM,  $N = 3$ . Different superscripts denote groups of significance ( $P < 0.05$ ).

abilities and the protection of urease from denaturalization inside the liposomes after incubation in acidic conditions. This protection was also confirmed by measuring the enzymatic activity of LB-I after incubation in acidic conditions, observing that urease enzymes remained active (Figure 4e).

### 3. Conclusion

In summary, we have developed two different liposome-based nanomotors powered by urease enzymes, which were either encapsulated or electrostatically bound to the outer surface of the liposome. We verified that the stochastic electrostatic binding of urease on the outer surface of the liposomes is sufficient to generate an asymmetric distribution that can lead to motion. Upon the presence of the sodium deoxycholate to act as an edge activator, the fluidity of the lipid bilayer is modulated, and this enhances the motility of the LBs containing encapsulated urease. Moreover, the lipid bilayer surrounding the encapsulated enzymes exerts a protective effect against harsh conditions such as acidic pH, allowing the liposomal nanomotors to recover motility after a 1 h incubation period in these conditions. Further studies focusing on the *in vivo* kinetics of these liposomal based nanomotors and in the presence of gradients of enzymatic substrate and sodium deoxycholate are required. Nevertheless, these findings can pave the way to the

development of new active drug delivery systems for applications in different *in vivo* locations, such as in GI tract, comprising enzyme-powered nanomotors.

### 4. Experimental Section

**Materials:** 1,2-Dimyristoyl-*sn*-glycero-3-phosphocholine (DMPC) was purchased from Lipoid GmbH (Switzerland).  $3\beta$ -[*N,N'*-Dimethylaminoethane]-carbamoyl]cholesterol hydrochloride (Chol+) cholesterol (CH), urease (from *Canavalia ensiformis*, type IX, powder, 50 000–100 000 units per gram of solid), Urease Activity Assay Kit, urea, and sodium deoxycholate were acquired from Sigma Aldrich (USA). Oregon Green 488 DHPE dye, BCA Protein Assay Kit, and phosphate-buffered saline (PBS) were supplied by Thermo Fisher Scientific (USA). Spectra/Por 7 Standard RC pretreated Dialysis Tubing (3.5 kDa) was purchased from Spectrum. Cyanine5 NHS ester (Cy5) was purchased from Lumiprobe.

**Instruments:** The liposomes were prepared using an extruder from Lipex Biomembranes, Canada. Protein quantification and enzymatic activity assays were carried out using an Infinite M200 PRO Multimode Microplate Reader. CryoTEM images were obtained using a JEOL-JEM 1400 microscope (Jeol Ltd., Tokyo, Japan). Confocal laser scanning microscope (CLSM) images were obtained using a Leica TCS SP5 confocal laser scanning microscope (Leica Microsystems, Germany). Hydrodynamic radii and electrophoretic mobility measurements were performed using a Wyatt Möbius and a Malvern Zetasizer.

**Preparation of the LBs:** Liposomal-based nanomotors (LBs) were prepared using the thin-film hydration method. Two LB prototypes

with different enzyme position, inside (LB-I) and outside (LB-O) were developed. Briefly, DMPC, Chol<sup>+</sup> and Chol were dissolved in chloroform solutions and mixed at 1:0.5:0.5 molar ratio, respectively. Total lipid concentration was  $30 \times 10^{-3}$  M. The organic solvent was removed under vacuum and nitrogen to afford a dry lipid film, which was hydrated under vigorous stirring with a solution of urease dissolved in PBS ( $3 \text{ mg mL}^{-1}$ ) for LB-I, or PBS for LB-O. Under these conditions, the stacks of liquid crystalline lipid bilayers become fluid and swell, which led to detachment during agitation and self-closure to yield multilamellar large vesicles (MLV). After, the MLV were homogenized using an extruder and a polycarbonate membrane (pore size 200 nm). For LB-I, the nonencapsulated urease was eliminated washing by centrifugation at 50 000 rpm and 10 °C for 30 min and resuspending the precipitated pellet with PBS thrice. For LB-O, the PBS-hydrated liposomes were incubated overnight with a  $3 \text{ mg mL}^{-1}$  urease PBS solution in the rotary shaker at 25 °C. Finally, the unbound urease was eliminated washing by centrifugation as described above.

The micrometer-sized LBs were prepared using the same protocol described above, omitting the extrusion step.

**Characterization of Size Distribution, Surface Charge, and Morphology of LBs:** Particle size distributions of the liposomes were determined using a dynamic light scattering (DLS) analyzer combined with noninvasive backscatter technology. The stability of the liposomes was examined by measuring their electrophoretic mobility using a Malvern Zetasizer. For this, the liposome-based nanomotors were diluted 50 times and placed in a cuvette for analysis. Liposome morphology was examined using CryoTEM in a JEOL-JEM 1400 microscope (Jeol Ltd., Tokyo, Japan). For this, LB-I in each condition before being placed in the TEM grid and cryogenized for observation.

**Functionalization of Urease with Cy5:** A solution of urease ( $20 \text{ mg mL}^{-1}$ ) in sodium bicarbonate buffer ( $100 \times 10^{-3}$  M) was prepared. Next,  $7 \mu\text{L}$  of a Cy 5 solution in DMSO ( $5 \times 10^{-3}$  M) were added, and the mixture was incubated for 4 h at 25 °C and shaking in the dark. The solution of labeled urease was then dialyzed in PBS (3.5 kDa pore membrane) for 24 h to eliminate nonreacted Cy5 molecules.

**Evaluation of Urease Distribution on the LBs:** Evaluation of the distribution of urease in liposomes was done by CLSM, using a Leica TCS SP5 confocal microscope (Leica Microsystems, Germany). For that, fluorescently labelled urease was encapsulated in liposomes for LB-I or incubated with liposomes for LB-O, with the lipid bilayer previously labelled with Oregon Green 488 DHPE. The resulting nonextruded liposomal formulations were examined by CLSM.

**Total Protein Content Quantification Assays:** The concentration of urease present on the LBs was measured using the BCA Protein Assay Kit from Thermo Fisher Scientific according to the manufacturer's instructions. This kit correlates the quantity of proteins with the reduction of copper by peptide bonds.<sup>[62]</sup> For this, the total protein content present on the supernatants from liposome washings, as well as in the urease stock solutions used for incubation was measured. The total protein content bound or encapsulated in the liposomes was calculated as the difference between the content of the stock solutions and the content of the supernatants. The results were analyzed statistically by performing an unpaired *t*-test.

**Urease Enzymatic Activity Assays:** Enzymatic activity of urease present on the LBs was evaluated using a commercial kit from Sigma Aldrich that determines the concentration of ammonia generated by Berthelot's method.<sup>[72]</sup> The liposomal nanomotors were diluted 50 times, and the experiment was performed according to the manufacturer's instructions.

**Motion Behavior Analysis:** The motion behavior of the LipoBots was analyzed by DLS, a technique that correlates the intensity of scattered light with the translational diffusion coefficient of the particles.

The purified LB-O were diluted 100 times prior to analysis by DLS, yielding dispersions containing liposomes and urea, at concentrations of 0,  $25 \times 10^{-3}$ ,  $50 \times 10^{-3}$ , and  $100 \times 10^{-3}$  M. Each condition was measured at least ten times. Regarding the LB-I, first they were analyzed in the absence of sodium deoxycholate using the methodology described above. For the analysis in the presence of sodium deoxycholate, this edge activator was added to the dispersions containing LB-I and urea

before analysis, at concentrations of 0%, 0.05%, 0.075%, and 0.1% (w/w). Each condition was measured at least ten times. The results were analyzed statistically by performing an ANOVA followed by Tukey's test.

**Motion Behavior after GI tract Simulation:** The LBs were diluted 50 times in acidic solutions of pH 3 and pH 5 and incubated for 1 h, in order to simulate the harsh stomach conditions. Following this, the liposomal dispersions were neutralized using PBS or PBS containing urea ( $100 \times 10^{-3}$  M) for LNM-O, and with PBS, PBS containing sodium deoxycholate (0.075% (w/w)), or PBS containing both urea ( $100 \times 10^{-3}$  M) and sodium deoxycholate (0.075% (w/w)) for LB-I. The neutralized dispersions were analyzed by DLS to evaluate their motion profiles. The results were analyzed statistically by performing an ANOVA followed by Tukey's test.

## Supporting Information

Supporting Information is available from the Wiley Online Library or from the author.

## Acknowledgements

The research leading to these results was funded by the Spanish MINECO (BOTSinFluids project), the Foundation BBVA (MEDIROBOTS project), the CERCA program by the Generalitat de Catalunya, and the CaixaImpulse program by La Caixa Foundation (TERANOBOTS project). A.C.H. thanks MINECO for the Severo Ochoa PhD fellowship, and T.P. thanks the European Union's Horizon 2020 research and innovation program under the Marie Skłodowska-Curie Individual Fellowship (H2020-MSCA-IF2018, DNA-bots). This work was also supported by the Catalan AGAUR (project 2017 SGR 238). It was also funded by the CERCA Program/Generalitat de Catalunya. ICN2 was supported by the Severo Ochoa program from the Spanish MINECO (Grant No. SEV-2017-0706).

## Conflict of Interest

The authors declare no conflict of interest.

## Author Contributions

M.C.-S. and S.G.-J. synthesized the liposome vesicles and encapsulated the enzymes. S.G.-J. performed the CLSM experiments. A.C.H. and S.G.-J. performed the TEM characterization and the motility experiments. A.C.H. performed the protein quantification and enzymatic activity experiments and analyzed the data. D.M., S.S., and T.P. designed and supervised the work. The manuscript was written through contributions of all authors. All authors have given approval to the final version of the manuscript.

## Keywords

enzyme catalysis, liposomes, nanomotors, self-propulsion

Received: March 27, 2020

Revised: June 22, 2020

Published online: August 14, 2020

- [1] A. C. Balazs, P. Fischer, A. Sen, *Acc. Chem. Res.* **2018**, *51*, 2979.
- [2] H. Wang, M. Pumera, *Chem. Rev.* **2015**, *115*, 8704.
- [3] J. Katuri, X. Ma, M. M. Stanton, S. Sanchez, *Acc. Chem. Res.* **2017**, *50*, 2.
- [4] Y. Ji, X. Lin, Z. Wu, Y. Wu, W. Gao, Q. He, *Angew. Chem., Int. Ed.* **2019**, *58*, 12200.
- [5] T. Kroupa, S. Hermanová, C. C. Mayorga-Martinez, F. Novotný, Z. Sofer, M. Pumera, *Langmuir* **2019**, *35*, 10618.



- [6] Y. Yoshizumi, K. Okubo, M. Yokokawa, H. Suzuki, *Langmuir* **2016**, 32, 9381.
- [7] J. Orozco, B. Jurado-Sánchez, G. Wagner, W. Gao, R. Vazquez-Duhalt, S. Sattayasamitsathit, M. Galarnyk, A. Cortés, D. Saintillan, J. Wang, *Langmuir* **2014**, 30, 5082.
- [8] L. Baraban, M. Tasinkevych, M. N. Popescu, S. Sanchez, S. Dietrich, O. G. Schmidt, *Soft Matter* **2012**, 8, 48.
- [9] W. Xi, A. A. Solovov, A. N. Ananth, D. H. Gracias, S. Sanchez, O. G. Schmidt, *Nanoscale* **2013**, 5, 1294.
- [10] A. A. Solovov, W. Xi, D. H. Gracias, S. M. Harazim, C. Deneke, S. Sanchez, O. G. Schmidt, *ACS Nano* **2012**, 6, 1751.
- [11] S. K. Srivastava, M. Medina-Sánchez, B. Koch, O. G. Schmidt, *Adv. Mater.* **2016**, 28, 832.
- [12] Y. Ying, M. Pumera, *Chem. – Eur. J.* **2019**, 25, 106.
- [13] S. Wang, Z. Jiang, S. Ouyang, Z. Dai, T. Wang, *ACS Appl. Mater. Interfaces* **2017**, 9, 23974.
- [14] M. Zarei, M. Zarei, *Small* **2018**, 14, 1800912.
- [15] M. Safdar, J. Simmchen, J. Jänis, *Environ. Sci.: Nano* **2017**, 4, 1602.
- [16] J. Parmar, D. Vilela, K. Villa, J. Wang, S. Sánchez, *J. Am. Chem. Soc.* **2018**, 140, 9317.
- [17] M. Safdar, S. U. Khan, J. Jänis, *Adv. Mater.* **2018**, 30, 1703660.
- [18] F. Mushtaq, X. Chen, S. Staufert, H. Torlakcik, X. Wang, M. Hoop, A. Gerber, X. Li, J. Cai, B. J. Nelson, S. Pané, *J. Mater. Chem. A* **2019**, 7, 24847.
- [19] T. Patino, A. Porchetta, A. Jannasch, A. Lladó, T. Stumpp, E. Schäffer, F. Ricci, S. Sánchez, *Nano Lett.* **2019**, 19, 3440.
- [20] J. Orozco, V. García-Gradilla, M. D'Agostino, W. Gao, A. Cortés, J. Wang, *ACS Nano* **2013**, 7, 818.
- [21] V. V. Singh, K. Kaufmann, J. Orozco, J. Li, M. Galarnyk, G. Arya, J. Wang, *Chem. Commun.* **2015**, 51, 11190.
- [22] L. Kong, J. Guan, M. Pumera, *Curr. Opin. Electrochem.* **2018**, 10, 174.
- [23] J. Li, B. Esteban-Fernández de Ávila, W. Gao, L. Zhang, J. Wang, *Sci. Rob.* **2017**, 2, eaam6431.
- [24] F. Peng, Y. Tu, D. A. Wilson, *Chem. Soc. Rev.* **2017**, 46, 5289.
- [25] C. Gao, Z. Lin, X. Lin, Q. He, *Adv. Ther.* **2018**, 1, 1800056.
- [26] Z. Lin, X. Fan, M. Sun, C. Gao, Q. He, H. Xie, *ACS Nano* **2018**, 12, 2539.
- [27] B. Esteban-Fernández de Ávila, P. Angsantikul, J. Li, W. Gao, L. Zhang, J. Wang, *Adv. Funct. Mater.* **2018**, 28, 1705640.
- [28] Z. Wu, L. Li, Y. Yang, P. Hu, Y. Li, S.-Y. Yang, L. V. Wang, W. Gao, *Sci. Rob.* **2019**, 4, eaax0613.
- [29] A. C. Hortelao, R. Carrascosa, N. Murillo-Cremaes, T. Patino, S. Sánchez, *ACS Nano* **2019**, 13, 429.
- [30] X. Wang, X.-Z. Chen, C. C. J. Alcântara, S. Sevim, M. Hoop, A. Terzopoulou, C. de Marco, C. Hu, A. J. de Mello, P. Falcaro, S. Furukawa, B. J. Nelson, J. Puigmartí-Luis, S. Pané, *Adv. Mater.* **2019**, 31, 1970192.
- [31] F. Peng, Y. Men, Y. Tu, Y. Chen, D. A. Wilson, *Adv. Funct. Mater.* **2018**, 28, 1706117.
- [32] J. Min, Y. Yang, Z. Wu, W. Gao, *Adv. Ther.* **2019**, 3, 1900125.
- [33] A. C. Hortelão, T. Patiño, A. Perez-Jiménez, A. Blanco, S. Sánchez, *Adv. Funct. Mater.* **2018**, 28, 1705086.
- [34] A. Llopis-Lorente, A. García-Fernández, N. Murillo-Cremaes, A. C. Hortelão, T. Patinõ, R. Villalonga, F. Sancenón, R. Martínez-Máñez, S. Sánchez, *ACS Nano* **2019**, 13, 12171.
- [35] X. Ma, A. C. Hortelão, T. Patiño, S. Sánchez, *ACS Nano* **2016**, 10, 9111.
- [36] T. Patiño, X. Arqué, R. Mestre, L. Palacios, S. Sánchez, *Acc. Chem. Res.* **2018**, 51, 2662.
- [37] M. Nijemeisland, L. K. E. A. Abdelmohsen, W. T. S. Huck, D. A. Wilson, J. C. M. van Hest, *ACS Cent. Sci.* **2016**, 2, 843.
- [38] X. Ma, X. Wang, K. Hahn, S. Sánchez, *ACS Nano* **2016**, 10, 3597.
- [39] X. Ma, A. Jannasch, U.-R. Albrecht, K. Hahn, A. Miguel-López, E. Schäffer, S. Sánchez, *Nano Lett.* **2015**, 15, 7043.
- [40] X. Ma, A. C. Hortelao, A. Miguel-López, S. Sánchez, *J. Am. Chem. Soc.* **2016**, 138, 13782.
- [41] S. Ghosh, F. Mohajerani, S. Son, D. Velegol, P. J. Butler, A. Sen, *Nano Lett.* **2019**, 19, 6019.
- [42] A. Somasundar, S. Ghosh, F. Mohajerani, L. N. Massenbourg, T. Yang, P. S. Cremer, D. Velegol, A. Sen, *Nat. Nanotechnol.* **2019**, 14, 1129.
- [43] T. Patiño, N. Feiner-Gracia, X. Arqué, A. Miguel-López, A. Jannasch, T. Stumpp, E. Schäffer, L. Albertazzi, S. Sánchez, *J. Am. Chem. Soc.* **2018**, 140, 7896.
- [44] X. Arqué, A. Romero-Rivera, F. Feixas, T. Patiño, S. Osuna, S. Sánchez, *Nat. Commun.* **2019**, 10, 2826.
- [45] L. K. E. A. Abdelmohsen, M. Nijemeisland, G. M. Pawar, G. A. Janssen, R. J. M. Nolte, J. C. M. van Hest, D. A. Wilson, *ACS Nano* **2016**, 10, 2652.
- [46] L. Wang, A. C. Hortelão, X. Huang, S. Sánchez, *Angew. Chem., Int. Ed.* **2019**, 58, 7992.
- [47] J. Sun, M. Mathesh, W. Li, D. A. Wilson, *ACS Nano* **2019**, 13, 10191.
- [48] B. J. Toebes, F. Cao, D. A. Wilson, *Nat. Commun.* **2019**, 10, 5308.
- [49] B. J. Toebes, L. K. E. A. Abdelmohsen, D. A. Wilson, *Polym. Chem.* **2018**, 9, 3190.
- [50] Y. Wu, X. Lin, Z. Wu, H. Möhwald, Q. He, *ACS Appl. Mater. Interfaces* **2014**, 6, 10476.
- [51] S. K. Srivastava, G. Clergeaud, T. L. Andresen, A. Boisen, *Adv. Drug Delivery Rev.* **2019**, 138, 41.
- [52] M. T. Hussain, N. Forbes, Y. Perrie, K. P. Malik, C. Duru, P. Matejtschuk, *Int. J. Pharm.* **2020**, 573, 118722.
- [53] Y. S. Youn, Y. H. Bae, *Adv. Drug Delivery Rev.* **2018**, 130, 3.
- [54] D. M. Mudie, G. L. Amidon, G. E. Amidon, *Mol. Pharmaceutics* **2010**, 7, 1388.
- [55] A. De La Maza, A. M. Manich, J. L. Parra, *J. Microsc.* **1997**, 186, 75.
- [56] H. Ahyayauch, M. Bennouna, A. Alonso, F. M. Goñi, *Langmuir* **2010**, 26, 7307.
- [57] L. G. Hermida, M. Sabés-Xamaní, R. Barnadas-Rodríguez, *Soft Matter* **2014**, 10, 6677.
- [58] A. D. Bangham, M. W. Hill, N. G. A. Miller, E. D. Korn, *Ion Channel Reconstitution* (Ed: C. Miller), Springer US, Boston, MA **1974**, pp. 1–68.
- [59] F. Szoka, D. Papahadjopoulos, *Annu. Rev. Biophys. Bioeng.* **1980**, 9, 467.
- [60] Y. Maitani, S. Igarashi, M. Sato, Y. Hattori, *Int. J. Pharm.* **2007**, 342, 33.
- [61] J. B. Sumner, D. B. Hand, *J. Am. Chem. Soc.* **1929**, 149, 1925.
- [62] P. K. Smith, R. I. Krohn, G. T. Hermanson, A. K. Mallia, F. H. Gartner, M. D. Provenzano, E. K. Fujimoto, N. M. Goeke, B. J. Olson, D. C. Klenk, *Anal. Biochem.* **1985**, 150, 76.
- [63] L. A. Pinck, M. A. Kelly, *J. Am. Chem. Soc.* **1925**, 47, 2170.
- [64] J. D. Harvey Lodish, A. Berk, S. Lawrence Zipursky, P. Matsudaira, D. Baltimore, in *Molecular Cell Biology* (Ed: W. H. Freeman), New York **2000**, Chap. 15.
- [65] E. P. O. Silva, L. P. Franchi, A. C. Tedesco, *RSC Adv.* **2016**, 6, 79631.
- [66] E. H. Lee, A. Kim, Y. K. Oh, C. K. Kim, *Biomaterials* **2005**, 26, 205.
- [67] M. Cano-Sarabia, A. Angelova, N. Ventosa, S. Lesieur, J. Veciana, *J. Colloid Interface Sci.* **2010**, 350, 10.
- [68] L. Kalantzi, K. Goumas, V. Kalioras, B. Abrahamsson, J. B. Dressman, C. Reppas, *Pharm. Res.* **2006**, 23, 165.
- [69] FDA Administration, Guidance for Industry Bioavailability and Bioequivalence Studies for Orally Administered Drug Products—General Guidance for Industry Bioavailability and Bioequivalence, FDA Guidelines, FDA, Silver Spring, MD **2002**, pp. 1–24.
- [70] M. Manconi, F. Marongiu, I. Castangia, M. L. Manca, C. Caddeo, C. I. G. Tuberoso, G. D'hallewin, G. Bacchetta, A. M. Fadda, *Colloids Surf., B* **2016**, 146, 910.
- [71] A. S. Kaviratna, R. Banerjee, *Colloids Surf. A* **2009**, 345, 155.
- [72] C. J. Patton, S. R. Crouch, *Anal. Chem.* **1977**, 49, 464.



# Chapter 7



## General Discussion





Nano- and micromotors are devices capable of swimming in fluids, and perform diverse tasks with applications in sensing,<sup>145,146,321,446–448</sup> environmental remediation,<sup>137–139,142,143,147,292</sup> and active delivery of nanomedicines.<sup>148,149,152,155,156,181</sup> These devices can harness energy from external sources (e.g. ultrasounds,<sup>183,249,255,256,449,450</sup> magnetic fields,<sup>127,129,182,184,185,241,362,451–454</sup> or light<sup>144,181,185,188–190,207,217,408,455–459</sup>), or by transducing free energy from their surrounding environment via chemical reactions.<sup>193,194,199,460</sup> Particularly for biomedical applications, the use of external actuators to power the nano- and micromotors can bring some constraints. Apart from the expensive setups required for the actuation of these devices, other limitations also may arise, such as limitations on control of motors by the penetration-depth of the external power source (light or magnetic fields) or unspecific damage to the tissues surrounding the target location due to light exposure.<sup>148,428,429,461,462</sup>

Alternatively, catalytic motors do not require external actuation since they convert chemical energy into mechanical work by turning over substrates that may be available within the organism. This aspect is one of the main features to take into account when designing catalytic motors. Initially, this type of motors relied mostly on Pt as catalyst, using high concentrations of hydrogen peroxide as fuel, which led to toxicity in biological environments.

Using enzymes as the power engine for the propulsion of synthetic nano- and micromotors emerged as an elegant alternative to the use of inorganic catalysts, opening new and exciting design possibilities due to the wide variety of enzyme/substrate available. Moreover, this approach to achieve propulsion by means of biocatalysis allows not only the development of multiple fully biocompatible chassis-engine-fuel combinations, but also the opportunity to activate these machines *in situ*, avoiding the need for external actuation.

A myriad of materials were reported as chassis for the fabrications of enzymatic nano- and micromotors, such as mesoporous silica,<sup>316,320,324</sup> stomatocytes,<sup>325,339,463</sup> polymersomes,<sup>342</sup> and liposomes.<sup>329,342</sup> In addition, aiming at tailoring the motors to specific biomedical, several enzymes and cascades of enzymatic reactions have been tested as engines to power the propulsion of biocatalytic motors.<sup>325,380,464</sup> In this regard, Arqué *et al* combined experimental and molecular dynamics simulations approaches to investigate how intrinsic enzymatic properties modulate self-propulsion, using urease, aldolase, acetylcholine esterase and glucose oxidase in the study.<sup>320</sup> The authors reported that urease and acetylcholine esterase were the only enzymes capable of producing active motion of the microcapsules used, denoting a correlation with the enzymatic turnover number. They also showed that the propulsion obtained when using urease was significantly more efficient than when acetylcholine esterase was used. Moreover, urease has been shown to efficiently power the propulsion of various types of chassis, with different materials and ranging from the nanometer to the micrometer scale in size.<sup>316,317,320,329,348,465,466</sup> Considering this, and the availability of urea substrate in biological fluids, urease is an ideal candidate for the development of nano-micro motors for biomedical applications and, therefore, was the enzyme used for the studies presented on this thesis.

Despite the significant growth of the nanomedicine field, the amount of research that translates into clinical is still limited, in fact a recent meta-analysis study reports that only 0.7% of the injected dose actually reaches the target site.<sup>105</sup> This limitation is in part due to the presence of biological barriers, that hinder the

diffusivity of the nanocarriers *in vivo*.<sup>104,108,112</sup> In this regard, enzyme-powered micro- and nanomotors could bring several potential advantages, since their propulsion allows them to explore greater areas than traditional passive particles, and their continuous momentum may help overcoming tissue and cell penetration, leading to more effective drug delivery.<sup>148,152</sup>

In our **first work**, we explored urease-powered nanomotors as active anticancer drug delivery vehicles, using core-shell mesoporous silica nanomotors loaded with the anticancer model drug doxorubicin, and demonstrated that in the presence of urea, the substrate for urease enzyme, these motors exhibited an enhanced drug release profile and cytotoxic effect towards human epithelial cervix adenocarcinoma cells (HeLa). For this, firstly we tackled the fabrication of the nanomotors and the analysis of their motion behavior and showed that urea biocatalysis led to an increase of the effective diffusion of the nanomotors in both ultrapure water and in PBS solutions. This finding is of key importance in the development of nanomotors for biomedical applications, as one of the major drawbacks of chemically powered nanomotors is that their motility can be affected by the presence of ionic species in the medium,<sup>350</sup> with several reports of reduced or arrested propulsion.<sup>294,347,348,350,467</sup> However, these reports mostly concern microparticles with inorganic catalysts, or microparticles powered by enzymatic reactions.<sup>320,350</sup> In our work, we use a nanosized chassis to fabricate the enzymatic nanomotors, and their enhanced motility in salt solutions may be due to the presence of a different motion and/or mechanism from those mentioned above, and further research is needed to elucidate the mechanism for this type of motor.

Next, we investigated the drug loading and release capabilities of the nanomotors. Mesoporous silica has been widely investigated for drug delivery purposes, due to its biocompatibility and high cargo loading capacity within the mesopores.<sup>468-471</sup> Taking advantage of this feature, we were able to load *ca.* 10 % (w/w) of doxorubicin into the nanomotors, which is considerably high amount and within the order of magnitude reported in literature for the loading of doxorubicin into mesoporous silica nanoparticles.<sup>472-476</sup>

We then evaluated the *in vitro* drug release kinetics from the nanomotors, denoting a urea-dependent enhancement on doxorubicin release profiles, where active nanomotors achieved almost four times higher drug release than passive nanoparticles. The enhanced release profiles could be attributed to an increase in pH due to the conversion of urea into ammonia and carbon dioxide, which in turn would lead to changes in the electrostatic interactions between the surface of the mesoporous silica and the doxorubicin resulting in enhanced release of drug from the pores. Considering this, we further evaluated the release profiles of the nanomotors when placed in buffer solutions at pH 9, both in the presence and absence of urea. We found that even when the initial pH of the medium is high, doxorubicin release was significantly enhanced by active nanomotors. Considering this, we attributed the enhancement in drug release by active nanomotors to the catalytic activity and consequent local change in the electrostatic interactions between the drug and the nanomotor surface.

Doxorubicin is a benchmark anticancer drug that leads to cell death via apoptosis due to its ability to intercalate within DNA base pairs and cause breakage of strands, as well as inhibition of nucleic acid synthesis. The mechanism of action of this drug relies on its entrance into the cell, therefore the intracellular delivery efficiency of the nanocarriers is of high importance to ensure maximum therapeutic effect with minimum off-

target complications. Given the capability of nanomotors to enhance drug release, we studied their efficacy in delivering doxorubicin to cancer cells, observing that active nanomotors were much more efficient to cause toxicity to cancer cells, requiring a 10-fold lower concentration than passive particles to obtain the same effect. Moreover, we observed that when cells were incubated with active nanomotors, the doxorubicin fluorescence signal within the cytoplasm was higher than the passive nanoparticles control. Altogether, these findings indicate that in active drug-loaded nanomotors present higher delivery efficacy than their traditional counterparts, which could be attributed to synergistic effects from the faster drug release kinetics, increased transport to the vicinity or to the inside of the cell and simultaneous production of ammonia.

Drug release profiles can be improved by the use of active nanomotors; however, this release is uncontrolled and can be enhanced in any given location in presence of urea. One long-standing goal of nanomedicine has been the targeted and controlled delivery of actives in site-specific locations, and researchers developed several strategies to achieve it, such as the integration of features sensitive to external triggers (*e.g.* light<sup>451,477–479</sup> or heat<sup>480–483</sup> stimuli), triggered disintegration of the carrier,<sup>463,484–486</sup> or the use of molecular gates to cap the carrier's pores. In a collaborative work with Martínez-Mañez group from UPV, we took a further step on the investigation of urease-powered nanomotors as active drug delivery vehicles adding molecular gates to achieve controlled intracellular delivery (see annex II). In this work, mesoporous silica nanoparticles were loaded with doxorubicin model drug, posteriorly gated with molecules sensitive to pH changes and, finally, functionalized with urease enzymes. In this way, the nanomotors exhibited propulsion in the presence of urea fuel, and upon cellular uptake, the acidic environment in the lysosomes led to the opening of the molecular gates, thus allowing for controlled intracellular delivery of the chemotherapy drug.

Another strategy to diminish off-target effects of nanomedicines is to functionalize nanocarriers with targeting moieties.<sup>487–490</sup> We functionalized urease-powered nanomotors with anti-FGFR3 antibody, which targets a transmembrane protein that is over-expressed in bladder cancer cells and leads to the development of aggressive tumors, by up-regulating cell migration and proliferation.<sup>491–493</sup>

We evaluated the motility of the antibody-modified nanomotors in both simulated urine and in real urine collected from rats, and compared it with the motility of bare nanomotors, observing that the presence of the antibody did not cause a reduction in motion abilities.

Then, we assessed both the ability of the nanomotors to enhance targeting of bladder cancer cells, using spheroids, since three-dimensional cell cultures are known to better mimic the tumor microenvironments, as they possess several features that resemble *in vivo* scenarios, such as physiologically relevant cell-cell and cell-ECM interactions, hypoxia and central necrosis.<sup>494,495</sup> We found a 4-fold increase in the internalization efficiency of passive nanomotors when they carry the targeting moiety, evidencing the targeting ability of the antibody chosen. More importantly, we denoted that spheroid penetration was greatly improved by combining both the targeting and motion capabilities, where a *ca.* 14-fold increase was detected in comparison to bare passive particles. Since the interaction of anti-FGFR3 with the antigen has been reported to inhibit the fibroblast growth signaling pathway, thus blocking cell proliferation and ultimately leading to cell death,<sup>491–493</sup> we examined spheroids' viability after incubation with the nanomotors, showing that antibody-modified nanomotors decreased the proliferation levels of the spheroids.

These results point towards the potential of nanomotors in bladder cancer, where antibody-functionalized nanomotors could have implications as drug-free therapy tools, reducing the proliferation of tumor masses with high specificity, thus leading to more effective treatments with fewer side-effects and lower relapse rates. In addition, these nanomotors could also be suitable as diagnostic tools, due to the fact that they efficiently target bladder cancer cells.

Any realistic biomedical application of nano- and micromotors must take in consideration that high concentrations of nanomedicines are required to achieve a therapeutic effect *in vivo*, and for this it is of the utmost importance that researchers investigate the collective behaviors of the active nano- and micromachines and exploit them to improve their efficacy. Despite being a behavior ubiquitous in nature, the study of swarms is still in its infancy in the nano- and micromotors community, and the vast majority of the works related to this topic rely on magnetic motors,<sup>237,413,437</sup> (external stimuli such as light or ultrasounds,<sup>408,432,496–499</sup> or gradients of substrates to trigger collective behaviors.<sup>328,409</sup> In addition, monitoring the collective behavior of nano- and micromotors *in vivo* is a challenge in itself, since most current medical imaging techniques have insufficient resolution and/or sensitivity.<sup>500</sup> Even so, researchers have used several medical imaging techniques to localize motors *in vivo*, such as Wu *et al* that showed the displacement of motors in intestines using photoacoustic computerized tomography.<sup>442</sup> However, the collective dynamics were not investigated in-depth. In other works, researchers have visualized the collective behavior of magnetic motors *ex vivo*. For instance, Yu *et al* demonstrated the magnetic actuation of microrobotic swarms in porcine eyes using ultrasound feedback,<sup>437</sup> and Wu *et al* showed a swarm of slippery helicoidal motors penetrating the vitreous body of porcine eyes using optical coherence tomography.<sup>237</sup>

In our **third work** we investigated the collective behavior of large populations of urease-powered nanomotors *in vitro* using optical microscopy, and *in vivo* within mice's bladders using PET-CT, which presents several advantages as medical imaging technique, such as high detection sensitivity, quantifiability, limitless depth of penetration.<sup>501</sup> We showed that the nanomotors exhibited swarming behavior and that their ensemble motility led to the generation of fluid flows and enhanced fluid mixing. We then investigated the swarming behavior of the nanomotors in confined complex geometries, observing that the active motion allowed the swarms to overcome the hurdles encountered along the paths (*i.e.* sharp turns and subsequent angles), enabling them to reach the end of the geometries, while their passive counterparts were conditioned by the barriers presented and did not manage to overcome them. Following this, we assessed the feasibility of using PET-CT to image nanomotors *in vivo*. To this end, we administered nanomotors intravenously to mice, noting that PET is a suitable technique to image and quantify the distribution of the nanomotors *in vivo*. Moreover, we investigated the stability of the radioactive labeling of the nanomotors using two distinct strategies: i) using the <sup>124</sup>I isotope to label the gold nanoparticles, ii) directly label the urease enzymes with <sup>18</sup>F isotope and demonstrated that direct enzyme labeling leads to higher *in vivo* radiostability and, thus, more reliable results. Importantly, no adverse effects were observed in the mice for two weeks following the imaging sessions, which suggested that the administered dose was below the maximum tolerated dose.

Since PET imaging has good spatial and temporal resolutions, and virtually no penetration depth limitations, in comparison to medical imaging techniques such as MRI and ultrasound, it allows the evaluation

of collective motility in living organisms. We administered the nanomotors intravesically in the bladders of living mice, and observed for the first time the collective behavior of enzyme-powered nanomotors *in vivo*, and demonstrated that the active and collective motion of the nanomotors led to their homogeneous distribution within the bladder, contrarily to passive particles that fail to spread across the cavity. This phenomenon could be potentially advantageous in the design of active drug delivery systems for bladder diseases, where homogeneous distribution of the delivery vehicles would ensure that the active systems reach the target sites.

The application of enzyme-powered nanomotors could potentially expand further than bladder diseases, however for this several challenges must be met, such as the protection of the enzymatic engine towards the degradability that it could face *in vivo* (*i.e.* proteases, harsh pHs, etc.). In our **fourth work**, we developed enzyme-powered nanomotors using liposome vesicles as chassis, where the urease enzyme was either encapsulated in the inner compartment of the vesicles for protection, or coated on the outer layer for comparison purposes.

Even though the spatial control over the positioning of the catalyst in nanomotors was previously reported,<sup>327</sup> the effect of this aspect in relation to the motion abilities of the motor was not investigated further. In this work, we investigated how the location of the enzyme relative to the vesicle influenced the motility and catalytic activity of each liposome nanomotor under different conditions, such as harsh acidic pHs. We observed that while the liposomes containing urease on the outer layer exhibited an increasing trend in diffusion coefficient when exposed to increasing urea concentrations, the liposome nanomotors with encapsulated enzyme did not exhibit any motility. We attributed this to an inefficient exchange of substrates and reaction products between the inner compartment of the liposome and the surrounding medium. However, by using sodium deoxycholate as an edge activator to cause an increase on bilayer flexibility and permeability,<sup>502</sup> the liposome nanomotors with encapsulated enzyme showed enhanced motility capabilities, with an increase in diffusion coefficient *ca.* 100% in the presence of 100 mM urea fuel.

Liposomes have been widely explored as nanocarriers in nanomedicine, and are in fact the main nanotechnological component of Doxil®, the first anticancer nanomedicine approved by FDA.<sup>49</sup> Nevertheless, this multifunctional nanocarrier has scarcely been explored as chassis for the fabrication of motors.<sup>328,329</sup> As proof-of-concept, we evaluated whether the liposomal chassis could be used to protect the enzymes when the nanomotors face adverse conditions, keeping them active till the motion triggering conditions are found or applied. We verified that while the nanomotors based on encapsulated enzymes within the liposome compartment retained the catalytic activity and were still able to self-propel after facing acidic environments, the nanomotors with enzymes in the outer shell of the liposomes could sustain enzymatic activity and thus lost motility after acidic incubation. These results indicate that liposomes are ideal candidates for chassis of enzyme-powered nanomotors, providing not only biocompatibility and biodegradability, but also protecting the engine of the motor from harsh degrading conditions.



Apart from studying a different architecture as chassis for the development of enzyme powered nanomotors, we also investigated other enzymes capable of propelling nanostructures. In this regard, in a collaborative work with Dr. L. Wang and Dr. X. Huang from Harbin Institute of Technology, we developed lipase-powered nanomotors (see annex V). We showed that lipase was able to act as an engine for the propulsion of mesoporous silica nanoparticles through the degradation of triglycerides. Moreover, we demonstrated that not only these motors were able to perform long-lasting motility (up to 40 minutes), but also were capable of efficiently degrade oil droplets, which could be promising for applications in nanomedicine and environmental applications.

Taken together, the results obtained during the course of this thesis provide significant advances regarding the potential applicability of urease-powered nanomotors as nanomedicines, in particular for bladder cancer therapy. Prior to this thesis work, it was only hypothesized that active drug delivery vehicles could bring several advantages compared to traditional nanomedicines, and the study of enzyme-powered nanomotors from *in vitro* models to *in vivo* monitoring had not been reported. The results presented in this thesis work verify the hypothesis and experimentally demonstrate advantages of active drug delivery vehicles such as improved drug release profiles and more efficient anticancer drug delivery to cells, ability to penetrate into complex 3D structures like cancer spheroids, improve active targeting due to self-propulsion and exhibit swarming behavior *in vivo*, which can be highly beneficial to achieve efficient tumor targeting and drug delivery. Thus, it is of paramount importance to further study these nanomotors as potential active nanomedicines, stepping forward pre-clinical studies where their performance as adjuvant or alternative therapies is investigated in regards to safety, stability and efficiency.

# Chapter 8



## Conclusion and Outlook



The advances in nanoscience and biotechnology paved the way for the development of numerous tools in biomedicine, such as nanodiagnostics and drug delivery. However, the efficacy of such tools is often hindered by several biological barriers, which limit the ability of nanomedicines to reach the desired target-site. In this regard, the use of motile particles as nanomedicines has emerged as an attractive alternative to traditional nanosystems, since their continuous propulsion force could aid in overcoming the aforementioned barriers.

The work presented on this thesis focuses on the development of enzyme-powered nanomotors and their applicability in nanomedicine, concluding:

- I. Urease-powered nanomotors efficiently load the anticancer drug doxorubicin and exhibit enhanced drug release profile in the presence of urea compared to passive nanoparticles. In addition these nanomotors are able to propel in phosphate buffer saline solutions in the presence of urea.
- II. Active urease-powered nanomotors present an enhanced anticancer activity towards HeLa cells. This effect arises not only from the enhanced drug release provided by the nanomotors activity, but also from the localized increase on ammonia concentration, which is toxic to cells. These results hint that enzymatic nanomotors are promising candidates for active nanomedicines.
- III. Antibody-functionalized urease-powered nanomotors demonstrate self-propulsion in simulated urine and urine from mice.
- IV. The combination of self-propulsion and targeting abilities leads these nanomotors to exhibited higher penetration efficiency of 3D bladder cancer spheroids than passive particles. These nanomotors are able to reduce spheroid proliferation due to the action of anti-FGFR3 antibody on inhibition of the FGF pathway.
- V. Urease-powered nanomotors show collective swarming behavior, which induces enhanced fluid convection and mixing, and allows the nanomotor swarms to overcome hurdles such as turns and angles in confined paths.
- VI. Nanomotors labeled with radioisotopes are able to be visualized by PET-CT, both *in vitro* and *in vivo* at the whole-body level. When instilled intravesically, the nanomotors move in swarms and exhibit fluid mixing, leading to their homogenous distribution within the whole bladder cavity.
- VII. Liposomes can serve as biodegradable and functional chassis for the development of enzyme-powered nanomotors.
- VIII. The encapsulation of urease enzymes within the inner cavity of liposomes allows for their protection from harsh environments (e.g. acidic medium) and the presence of bile salts triggers the motion abilities by permeabilizing the lipidic bilayer.

Future work regarding enzyme-powered nanomotors as biomedical tools for bladder cancer therapy includes the study of the urease nanomotors developed in this thesis settings closer to the clinics. For instance, using patient-derived cells to fabricate three-dimensional spheroids and study the ability of antibody-modified nanomotors to penetrate and arrest their proliferation. The validation of the results obtained *in vitro* must be translated to *in vivo* scenarios, where the nanomotors' capabilities as active drug delivery devices to target and

irradiate cancer in live subjects such as mice is investigated. In addition, the study of targeted nanomotors as novel diagnostic tools for cancer should be investigated, given the potential accumulation of targeted nanomotors in tumor regions.

In addition, the potential of enzyme-powered nanomotors in biomedicine spans beyond bladder cancer, having several other interesting and challenging diseases to target, such as lung cancer or pancreatic cancer, where a nearly impenetrable stroma presents as critical biological barrier for modern medicines. Joint injuries, where the highly viscous environment hinders the diffusivity of pharmaceutical actives, is another case study where nanomotors could be of use. The study of enzymatic nanomotors' collective behavior in complex media (i.e., synovial fluid, lung lining mucosa, stomach lining mucosa, etc.) must be evaluated in order to make nanomotors applicable in such scenarios.

# Chapter 9



## References





- (1) Feynman, R. P. There's Plenty of Room at the Bottom. *Resonance* **2011**, *16* (9), 890. <https://doi.org/10.1007/s12045-011-0109-x>.
- (2) "Plenty of Room" Revisited. *Nat. Nanotechnol.* **2009**, *4* (12), 781–781. <https://doi.org/10.1038/nnano.2009.356>.
- (3) Zhao, H.; Lee, Y.; Han, M.; Sharma, B. K.; Chen, X.; Ahn, J.-H.; Rogers, J. A. Nanofabrication Approaches for Functional Three-Dimensional Architectures. *Nano Today* **2020**, *30*, 100825. <https://doi.org/10.1016/j.nantod.2019.100825>.
- (4) Cheng, L.; Wang, X.; Gong, F.; Liu, T.; Liu, Z. 2D Nanomaterials for Cancer Theranostic Applications. *Adv. Mater.* **2020**, *32* (13), 1902333. <https://doi.org/10.1002/adma.201902333>.
- (5) Smith, B. R.; Gambhir, S. S. Nanomaterials for In Vivo Imaging. *Chem. Rev.* **2017**, *117* (3), 901–986. <https://doi.org/10.1021/acs.chemrev.6b00073>.
- (6) Nagamune, T. Biomolecular Engineering for Nanobio/Bionanotechnology. *Nano Converg.* **2017**, *4* (1), 9. <https://doi.org/10.1186/s40580-017-0103-4>.
- (7) Frey, S.; Castro, A.; Arsiwala, A.; Kane, R. S. Bionanotechnology for Vaccine Design. *Curr. Opin. Biotechnol.* **2018**, *52*, 80–88. <https://doi.org/10.1016/j.copbio.2018.03.003>.
- (8) Wang, X.; Hu, Y.; Wei, H. Nanozymes in Bionanotechnology: From Sensing to Therapeutics and Beyond. *Inorg. Chem. Front.* **2016**, *3* (1), 41–60. <https://doi.org/10.1039/C5QI00240K>.
- (9) van der Meel, R.; Sulheim, E.; Shi, Y.; Kiessling, F.; Mulder, W. J. M.; Lammers, T. Smart Cancer Nanomedicine. *Nat. Nanotechnol.* **2019**, *14* (11), 1007–1017. <https://doi.org/10.1038/s41565-019-0567-y>.
- (10) Shi, J.; Kantoff, P. W.; Wooster, R.; Farokhzad, O. C. Cancer Nanomedicine: Progress, Challenges and Opportunities. *Nat. Rev. Cancer* **2017**, *17*, 20–37. <https://doi.org/10.1038/nrc.2016.108>.
- (11) Youn, Y. S.; Bae, Y. H. Perspectives on the Past, Present, and Future of Cancer Nanomedicine. *Adv. Drug Deliv. Rev.* **2018**, *130*, 3–11. <https://doi.org/10.1016/j.addr.2018.05.008>.
- (12) Chan, W. C. W. Nanomedicine 2.0. *Acc. Chem. Res.* **2017**, *50* (3), 627–632. <https://doi.org/10.1021/acs.accounts.6b00629>.
- (13) Salvioni, L.; Rizzuto, M. A.; Bertolini, J. A.; Pandolfi, L.; Colombo, M.; Prosperi, D. Thirty Years of Cancer Nanomedicine: Success, Frustration, and Hope. *Cancers* **2019**, *11* (12). <https://doi.org/10.3390/cancers11121855>.
- (14) Zingg, R.; Fischer, M. The Consolidation of Nanomedicine. *Wiley Interdiscip. Rev. Nanomed. Nanobiotechnol.* **2019**, *11* (6), 1–6. <https://doi.org/10.1002/wnan.1569>.
- (15) Irvine, D. J.; Dane, E. L. Enhancing Cancer Immunotherapy with Nanomedicine. *Nat. Rev. Immunol.* **2020**, *20* (5), 321–334. <https://doi.org/10.1038/s41577-019-0269-6>.
- (16) Wagner, V.; Dullaart, A.; Bock, A. K.; Zweck, A. The Emerging Nanomedicine Landscape. *Nat. Biotechnol.* **2006**, *24* (10), 1211–1217. <https://doi.org/10.1038/nbt1006-1211>.
- (17) Hauert, S.; Bhatia, S. N. Mechanisms of Cooperation in Cancer Nanomedicine: Towards Systems Nanotechnology. *Trends Biotechnol.* **2014**, *32* (9), 448–455. <https://doi.org/10.1016/j.tibtech.2014.06.010>.
- (18) Wagner, V.; Husing, B.; Gaisser, S.; Bock, A.-K. Nanomedicine: Drivers for Development and Possible Impacts. *Eur. Comm. Jt. Res. Cent. Rep. No 46744* **2006**, 1–116.
- (19) Martins, J. P.; das Neves, J.; de la Fuente, M.; Celia, C.; Florindo, H.; Günday-Türeli, N.; Popat, A.; Santos, J. L.; Sousa, F.; Schmid, R.; Wolfram, J.; Sarmiento, B.; Santos, H. A. The Solid Progress of Nanomedicine. *Drug Deliv. Transl. Res.* **2020**, 9–12. <https://doi.org/10.1007/s13346-020-00743-2>.
- (20) Wolfram, J.; Ferrari, M. Clinical Cancer Nanomedicine. *Nano Today* **2019**, *25*, 85–98. <https://doi.org/10.1016/j.nantod.2019.02.005>.
- (21) Ramos, A. P.; Cruz, M. A. E.; Tovani, C. B.; Ciancaglini, P. Biomedical Applications of Nanotechnology. *Biophys. Rev.* **2017**, *9* (2), 79–89. <https://doi.org/10.1007/s12551-016-0246-2>.
- (22) Wang, C.; Fan, W.; Zhang, Z.; Wen, Y.; Xiong, L.; Chen, X. Advanced Nanotechnology Leading the Way to Multimodal Imaging-Guided Precision Surgical Therapy. *Adv. Mater.* **2019**, *31* (49), 1904329–1904329. <https://doi.org/10.1002/adma.201904329>.
- (23) Arca-Lafuente, S.; Martínez-Román, P.; Mate-Cano, I.; Madrid, R.; Briz, V. Nanotechnology: A Reality for Diagnosis of HCV Infectious Disease. *J. Infect.* **2020**, *80* (1), 8–15. <https://doi.org/10.1016/j.jinf.2019.09.010>.
- (24) Kashaninejad, N.; Yaghoobi, M.; Pourhassan-Moghaddam, M.; Bazaz, S. R.; Jin, D.; Warkiani, M. E. Biological Diagnosis Based on Microfluidics and Nanotechnology. In *Nanotechnology and Microfluidics*; John Wiley & Sons, Ltd, 2020; pp 211–238. <https://doi.org/10.1002/9783527818341.ch7>.
- (25) Moelenbroek, G. T. van; Patiño, T.; Llop, J.; Sánchez, S. Engineering Intelligent Nanosystems for Enhanced Medical Imaging. *Adv. Intell. Syst.* **2020**, *2* (10), 2000087. <https://doi.org/10.1002/aisy.202000087>.
- (26) Yarlagadda, T.; Sharma, S.; Yarlagadda, P. K. D. V.; Sharma, J. Recent Developments in the Field of Nanotechnology for Development of Medical Implants. *Procedia Manuf.* **2019**, *30*, 544–551. <https://doi.org/10.1016/j.promfg.2019.02.077>.
- (27) Mendonça Munhoz, A.; Santanelli di Pompeo, F.; De Mezerville, R. Nanotechnology, Nanosurfaces and Silicone Gel Breast Implants: Current Aspects. *Case Rep. Plast. Surg. Hand Surg.* **2017**, *4* (1), 99–113. <https://doi.org/10.1080/23320885.2017.1407658>.
- (28) Wakaskar, R. R. Promising Effects of Nanomedicine in Cancer Drug Delivery. *J. Drug Target.* **2018**, *26* (4), 319–324. <https://doi.org/10.1080/1061186X.2017.1377207>.
- (29) Ganipineni, L. P.; Danhier, F.; Prétat, V. Drug Delivery Challenges and Future of Chemotherapeutic Nanomedicine for Glioblastoma Treatment. *J. Controlled Release* **2018**, *281*, 42–57. <https://doi.org/10.1016/j.jconrel.2018.05.008>.
- (30) Tran, S.; DeGiovanni, P.-J.; Piel, B.; Rai, P. Cancer Nanomedicine: A Review of Recent Success in Drug Delivery. *Clin. Transl. Med.* **2017**, *6* (1), 44. <https://doi.org/10.1186/s40169-017-0175-0>.
- (31) Curley, P.; Liptrott, N. J.; Owen, A. Advances in Nanomedicine Drug Delivery Applications for HIV Therapy. *Future Sci. OA* **2017**, *4* (1), FSO230. <https://doi.org/10.4155/foa-2017-0069>.
- (32) Rabolli, V.; Thomassen, L. C. J.; Princen, C.; Napierska, D.; Gonzalez, L.; Kirsch-Volders, M.; Hoet, P. H.; Huaux, F.; Kirschhock, C. E. A.; Martens, J. A.; Lison, D. Influence of Size, Surface Area and Microporosity on the in Vitro Cytotoxic Activity of Amorphous Silica Nanoparticles in Different Cell Types. *Nanotoxicology* **2010**, *4* (3), 307–318. <https://doi.org/10.3109/17435390.2010.482749>.

- (33) Rossmannith, R.; Weiss, C. K.; Geserick, J.; Hüsing, N.; Hörmann, U.; Kaiser, U.; Landfester, K. Porous Anatase Nanoparticles with High Specific Surface Area Prepared by Miniemulsion Technique. *Chem. Mater.* **2008**, *20* (18), 5768–5780. <https://doi.org/10.1021/cm800533a>.
- (34) Duffin, R.; Tran, L.; Brown, D.; Stone, V.; Donaldson, K. Proinflammatory Effects of Low-Toxicity and Metal Nanoparticles In Vivo and In Vitro: Highlighting the Role of Particle Surface Area and Surface Reactivity. *Inhal. Toxicol.* **2007**, *19* (10), 849–856. <https://doi.org/10.1080/08958370701479323>.
- (35) Almeida, J. P. M.; Chen, A. L.; Foster, A.; Drezek, R. In Vivo Biodistribution of Nanoparticles. *Nanomed.* **2011**, *6* (5), 815–835. <https://doi.org/10.2217/nmm.11.79>.
- (36) Duan, X.; Li, Y. Physicochemical Characteristics of Nanoparticles Affect Circulation, Biodistribution, Cellular Internalization, and Trafficking. *Small* **2013**, *9* (9–10), 1521–1532. <https://doi.org/10.1002/sml.201201390>.
- (37) Torchilin, V. P. Multifunctional, Stimuli-Sensitive Nanoparticulate Systems for Drug Delivery. *Nat. Rev. Drug Discov.* **2014**, *13* (11), 813–827. <https://doi.org/10.1038/nrd4333>.
- (38) Kim, D.; Shin, K.; Kwon, S. G.; Hyeon, T. Synthesis and Biomedical Applications of Multifunctional Nanoparticles. *Adv. Mater.* **2018**, *30* (49), 1802309. <https://doi.org/10.1002/adma.201802309>.
- (39) Bao, G.; Mitragotri, S.; Tong, S. Multifunctional Nanoparticles for Drug Delivery and Molecular Imaging. *Annu. Rev. Biomed. Eng.* **2013**, *15* (1), 253–282. <https://doi.org/10.1146/annurev-bioeng-071812-152409>.
- (40) Jin, Y.; Jia, C.; Huang, S.-W.; O'Donnell, M.; Gao, X. Multifunctional Nanoparticles as Coupled Contrast Agents. *Nat. Commun.* **2010**, *1* (1), 41. <https://doi.org/10.1038/ncomms1042>.
- (41) Lee, D.-E.; Koo, H.; Sun, I.-C.; Ryu, J. H.; Kim, K.; Kwon, I. C. Multifunctional Nanoparticles for Multimodal Imaging and Theragnosis. *Chem. Soc. Rev.* **2012**, *41* (7), 2656–2672. <https://doi.org/10.1039/C2CS15261D>.
- (42) Bobo, D.; Robinson, K. J.; Islam, J.; Thurecht, K. J.; Corrie, S. R. Nanoparticle-Based Medicines: A Review of FDA-Approved Materials and Clinical Trials to Date. *Pharm. Res.* **2016**, *33* (10), 2373–2387. <https://doi.org/10.1007/s11095-016-1958-5>.
- (43) Hare, J. I.; Lammers, T.; Ashford, M. B.; Puri, S.; Storm, G.; Barry, S. T. Challenges and Strategies in Anti-Cancer Nanomedicine Development: An Industry Perspective. *Adv. Drug Deliv. Rev.* **2017**, *108*, 25–38. <https://doi.org/10.1016/j.addr.2016.04.025>.
- (44) Farjadian, F.; Ghasemi, A.; Gohari, O.; Roojintan, A.; Karimi, M.; Hamblin, M. R. Nanopharmaceuticals and Nanomedicines Currently on the Market: Challenges and Opportunities. *Nanomed.* **2019**, *14* (1). <https://doi.org/10.2217/nmm-2018-0120>.
- (45) Etheridge, M. L.; Campbell, S. A.; Erdman, A. G.; Haynes, C. L.; Wolf, S. M.; McCullough, J. The Big Picture on Nanomedicine: The State of Investigational and Approved Nanomedicine Products. *Nanomedicine Nanotechnol. Biol. Med.* **2013**, *9* (1), 1–14. <https://doi.org/10.1016/j.nano.2012.05.013>.
- (46) Yingchoncharoen, P.; Kalinowski, D. S.; Richardson, D. R. Lipid-Based Drug Delivery Systems in Cancer Therapy: What Is Available and What Is Yet to Come. *Pharmacol. Rev.* **2016**, *68* (3), 701 LP – 787. <https://doi.org/10.1124/pr.115.012070>.
- (47) Rideau, E.; Dimova, R.; Schwille, P.; Wurm, F. R.; Landfester, K. Liposomes and Polymersomes: A Comparative Review towards Cell Mimicking. *Chem. Soc. Rev.* **2018**, *47* (23), 8572–8610. <https://doi.org/10.1039/C8CS00162F>.
- (48) Zylberberg, C.; Matosevic, S. Pharmaceutical Liposomal Drug Delivery: A Review of New Delivery Systems and a Look at the Regulatory Landscape. *Drug Deliv.* **2016**, *23* (9), 3319–3329. <https://doi.org/10.1080/10717544.2016.1177136>.
- (49) Barenholz, Y. (Chezy). Doxil® — The First FDA-Approved Nano-Drug: Lessons Learned. *J. Controlled Release* **2012**, *160* (2), 117–134. <https://doi.org/10.1016/j.jconrel.2012.03.020>.
- (50) Ponzoni, M. Liposomal Chemotherapy. In *Encyclopedia of Cancer*; Schwab, M., Ed.; Springer Berlin Heidelberg: Berlin, Heidelberg, 2015; pp 1–5. [https://doi.org/10.1007/978-3-642-27841-9\\_3387-2](https://doi.org/10.1007/978-3-642-27841-9_3387-2).
- (51) Chen, H.; Zhang, W.; Zhu, G.; Xie, J.; Chen, X. Rethinking Cancer Nanotheranostics. *Nat. Rev. Mater.* **2017**, *2* (7), 17024. <https://doi.org/10.1038/natrevmats.2017.24>.
- (52) Pinel, S.; Thomas, N.; Boura, C.; Barberi-Heyob, M. Approaches to Physical Stimulation of Metallic Nanoparticles for Glioblastoma Treatment. *Adv. Drug Deliv. Rev.* **2019**, *138*, 344–357. <https://doi.org/10.1016/j.addr.2018.10.013>.
- (53) Baranwal, A.; Mahato, K.; Srivastava, A.; Kumar Maurya, P.; Chandra, P. Phytomimetic Metallic Nanoparticles and Their Clinical Applications. *RSC Adv.* **2016**, *6* (107), 105996–106010. <https://doi.org/10.1039/C6RA23411A>.
- (54) Ahmad, M. Z.; Akhter, S.; Jain, G. K.; Rahman, M.; Pathan, S. A.; Ahmad, F. J.; Khar, R. K. Metallic Nanoparticles: Technology Overview & Drug Delivery Applications in Oncology. *Expert Opin. Drug Deliv.* **2010**, *7* (8), 927–942. <https://doi.org/10.1517/17425247.2010.498473>.
- (55) Penon, O.; Marín, M. J.; Amabilino, D. B.; Russell, D. A.; Pérez-García, L. Iron Oxide Nanoparticles Functionalized with Novel Hydrophobic and Hydrophilic Porphyrins as Potential Agents for Photodynamic Therapy. *J. Colloid Interface Sci.* **2016**, *462*, 154–165. <https://doi.org/10.1016/j.jcis.2015.09.060>.
- (56) Yan, L.; Amirshaghghi, A.; Huang, D.; Miller, J.; Stein, J. M.; Busch, T. M.; Cheng, Z.; Tsourkas, A. Protoporphyrin IX (PpIX)-Coated Superparamagnetic Iron Oxide Nanoparticle (SPION) Nanoclusters for Magnetic Resonance Imaging and Photodynamic Therapy. *Adv. Funct. Mater.* **2018**, *28* (16), 1707030–1707030. <https://doi.org/10.1002/adfm.201707030>.
- (57) Quinto, C. A.; Mohindra, P.; Tong, S.; Bao, G. Multifunctional Superparamagnetic Iron Oxide Nanoparticles for Combined Chemotherapy and Hyperthermia Cancer Treatment. *Nanoscale* **2015**, *7* (29), 12728–12736. <https://doi.org/10.1039/C5NR02718G>.
- (58) Yang, Y.; Huang, M.; Qian, J.; Gao, D.; Liang, X. Tunable Fe<sub>3</sub>O<sub>4</sub> Nanorods for Enhanced Magnetic Hyperthermia Performance. *Sci. Rep.* **2020**, *10* (1), 8331–8331. <https://doi.org/10.1038/s41598-020-65095-w>.
- (59) Jose, J.; Kumar, R.; Harilal, S.; Mathew, G. E.; Parambi, D. G. T.; Prabhu, A.; Uddin, Md. S.; Aleya, L.; Kim, H.; Mathew, B. Magnetic Nanoparticles for Hyperthermia in Cancer Treatment: An Emerging Tool. *Environ. Sci. Pollut. Res.* **2020**, *27* (16), 19214–19225. <https://doi.org/10.1007/s11356-019-07231-2>.
- (60) Kaur, A.; Preet, S.; Kumar, V.; Kumar, R.; Kumar, R. Synergetic Effect of Vancomycin Loaded Silver Nanoparticles for Enhanced Antibacterial Activity. *Colloids Surf. B Biointerfaces* **2019**, *176*, 62–69. <https://doi.org/10.1016/j.colsurfb.2018.12.043>.

- (61) Tang, S.; Zheng, J. Antibacterial Activity of Silver Nanoparticles: Structural Effects. *Adv. Healthc. Mater.* **2018**, *7* (13), 1701503. <https://doi.org/10.1002/adhm.201701503>.
- (62) Patra, J. K.; Baek, K.-H. Antibacterial Activity and Synergistic Antibacterial Potential of Biosynthesized Silver Nanoparticles against Foodborne Pathogenic Bacteria along with Its Anticandidal and Antioxidant Effects. *Front. Microbiol.* **2017**, *08*. <https://doi.org/10.3389/fmicb.2017.00167>.
- (63) Choudhury, H.; Gorain, B.; Pandey, M.; Khurana, R. K.; Kesharwani, P. Strategizing Biodegradable Polymeric Nanoparticles to Cross the Biological Barriers for Cancer Targeting. *Int. J. Pharm.* **2019**, *565*, 509–522. <https://doi.org/10.1016/j.ijpharm.2019.05.042>.
- (64) Karlsson, J.; Vaughan, H. J.; Green, J. J. Biodegradable Polymeric Nanoparticles for Therapeutic Cancer Treatments. *Annu. Rev. Chem. Biomol. Eng.* **2018**, *9* (1), 105–127. <https://doi.org/10.1146/annurev-chembioeng-060817-084055>.
- (65) Begines, B.; Ortiz, T.; Pérez-Aranda, M.; Martínez, G.; Merinero, M.; Argüelles-Arias, F.; Alcudia, A. Polymeric Nanoparticles for Drug Delivery: Recent Developments and Future Prospects. *Nanomaterials* **2020**, *10* (7), 1403. <https://doi.org/10.3390/nano10071403>.
- (66) Wong, C. K.; Stenzel, M. H.; Thordarson, P. Non-Spherical Polymersomes: Formation and Characterization. *Chem. Soc. Rev.* **2019**, *48* (15), 4019–4035. <https://doi.org/10.1039/C8CS00856F>.
- (67) Iqbal, S.; Blenner, M.; Alexander-Bryant, A.; Larsen, J. Polymersomes for Therapeutic Delivery of Protein and Nucleic Acid Macromolecules: From Design to Therapeutic Applications. *Biomacromolecules* **2020**, *21* (4), 1327–1350. <https://doi.org/10.1021/acs.biomac.9b01754>.
- (68) Balasubramanian, V.; Herranz-Blanco, B.; Almeida, P. V.; Hirvonen, J.; Santos, H. A. Multifaceted Polymersome Platforms: Spanning from Self-Assembly to Drug Delivery and Protocells. *Prog. Polym. Sci.* **2016**, *60*, 51–85. <https://doi.org/10.1016/j.progpolymsci.2016.04.004>.
- (69) Hu, X.; Zhang, Y.; Xie, Z.; Jing, X.; Bellotti, A.; Gu, Z. Stimuli-Responsive Polymersomes for Biomedical Applications. *Biomacromolecules* **2017**, *18* (3), 649–673. <https://doi.org/10.1021/acs.biomac.6b01704>.
- (70) Vhora, I.; Patil, S.; Bhatt, P.; Misra, A. Chapter One - Protein- and Peptide-Drug Conjugates: An Emerging Drug Delivery Technology. In *Protein and Peptide Nanoparticles for Drug Delivery*; Donev, R. B. T., Ed.; Academic Press, 2015; Vol. 98, pp 1–55. <https://doi.org/10.1016/bs.apcsb.2014.11.001>.
- (71) Functional Validation of Drug Nanoconjugates in Vivo. In *Frontiers in Nanomedicine*; Abasolo, I., Fernández, Y., Schwartz, S., Eds.; Bentham Science Publishers, 2017; Vol. 2, pp 184–198. <https://doi.org/10.2174/9781681084930117020010>.
- (72) Kumar, S.; Ali, J.; Baboota, S. Polysaccharide Nanoconjugates for Drug Solubilization and Targeted Delivery; Maiti, S., Jana, S. B. T., Eds.; Woodhead Publishing, 2019; pp 443–475. <https://doi.org/10.1016/B978-0-08-102553-6.00016-7>.
- (73) Munir, I.; Ajmal, S.; Shah, M. R.; Ahmad, A.; Hameed, A.; Ali, S. A. Protein-Drug Nanoconjugates: Finding the Alternative Proteins as Drug Carrier. *Int. J. Biol. Macromol.* **2017**, *101*, 131–145. <https://doi.org/10.1016/j.ijbiomac.2017.03.095>.
- (74) Mohammad, I. S.; Hu, H.; Yin, L.; He, W. Drug Nanocrystals: Fabrication Methods and Promising Therapeutic Applications. *Int. J. Pharm.* **2019**, *562*, 187–202. <https://doi.org/10.1016/j.ijpharm.2019.02.045>.
- (75) Lu, Y.; Lv, Y.; Li, T. Hybrid Drug Nanocrystals. *Adv. Drug Deliv. Rev.* **2019**, *143*, 115–133. <https://doi.org/10.1016/j.addr.2019.06.006>.
- (76) Yang, X.; Hu, C.; Tong, F.; Liu, R.; Zhou, Y.; Qin, L.; Ouyang, L.; Gao, H. Tumor Microenvironment-Responsive Dual Drug Dimer-Loaded PEGylated Bilirubin Nanoparticles for Improved Drug Delivery and Enhanced Immune-Chemotherapy of Breast Cancer. *Adv. Funct. Mater.* **2019**, *29* (32), 1901896. <https://doi.org/10.1002/adfm.201901896>.
- (77) Zhang, L.; Zhang, M.; Zhou, L.; Han, Q.; Chen, X.; Li, S.; Li, L.; Su, Z.; Wang, C. Dual Drug Delivery and Sequential Release by Amphiphilic Janus Nanoparticles for Liver Cancer Theranostics. *Biomaterials* **2018**, *181*, 113–125. <https://doi.org/10.1016/j.biomaterials.2018.07.060>.
- (78) Nozohouri, S.; Salehi, R.; Ghanbarzadeh, S.; Adibkia, K.; Hamishehkar, H. A Multilayer Hollow Nanocarrier for Pulmonary Co-Drug Delivery of Methotrexate and Doxorubicin in the Form of Dry Powder Inhalation Formulation. *Mater. Sci. Eng. C* **2019**, *99*, 752–761. <https://doi.org/10.1016/j.msec.2019.02.009>.
- (79) Zununi Vahed, S.; Salehi, R.; Davaran, S.; Sharifi, S. Liposome-Based Drug Co-Delivery Systems in Cancer Cells. *Mater. Sci. Eng. C* **2017**, *71*, 1327–1341. <https://doi.org/10.1016/j.msec.2016.11.073>.
- (80) Guo, Y.; Li, S.; Wang, Y.; Zhang, S. Diagnosis–Therapy Integrative Systems Based on Magnetic RNA Nanoflowers for Co-Drug Delivery and Targeted Therapy. *Anal. Chem.* **2017**, *89* (4), 2267–2274. <https://doi.org/10.1021/acs.analchem.6b03346>.
- (81) Zhang, Y.; Yang, C.; Wang, W.; Liu, J.; Liu, Q.; Huang, F.; Chu, L.; Gao, H.; Li, C.; Kong, D.; Liu, Q.; Liu, J. Co-Delivery of Doxorubicin and Curcumin by PH-Sensitive Prodrug Nanoparticle for Combination Therapy of Cancer. *Sci. Rep.* **2016**, *6* (1), 21225. <https://doi.org/10.1038/srep21225>.
- (82) Yin, Y.; Hu, Q.; Xu, C.; Qiao, Q.; Qin, X.; Song, Q.; Peng, Y.; Zhao, Y.; Zhang, Z. Co-Delivery of Doxorubicin and Interferon- $\gamma$  by Thermosensitive Nanoparticles for Cancer Immunotherapy. *Mol. Pharm.* **2018**, *15* (9), 4161–4172. <https://doi.org/10.1021/acs.molpharmaceut.8b00564>.
- (83) Senapati, S.; Mahanta, A. K.; Kumar, S.; Maiti, P. Controlled Drug Delivery Vehicles for Cancer Treatment and Their Performance. *Signal Transduct. Target. Ther.* **2018**, *3* (1), 7. <https://doi.org/10.1038/s41392-017-0004-3>.
- (84) Brudno, Y.; Mooney, D. J. On-Demand Drug Delivery from Local Depots. *J. Controlled Release* **2015**, *219*, 8–17. <https://doi.org/10.1016/j.jconrel.2015.09.011>.
- (85) Wang, Y.; Kohane, D. S. External Triggering and Triggered Targeting Strategies for Drug Delivery. *Nat. Rev. Mater.* **2017**, *2* (6), 17020. <https://doi.org/10.1038/natrevmats.2017.20>.
- (86) Zhang, P.; Gao, D.; An, K.; Shen, Q.; Wang, C.; Zhang, Y.; Pan, X.; Chen, X.; Lyv, Y.; Cui, C.; Liang, T.; Duan, X.; Liu, J.; Yang, T.; Hu, X.; Zhu, J.-J.; Xu, F.; Tan, W. A Programmable Polymer Library That Enables the Construction of Stimuli-Responsive Nanocarriers Containing Logic Gates. *Nat. Chem.* **2020**, *12* (4), 381–390. <https://doi.org/10.1038/s41557-020-0426-3>.



- (87) Juneja, R.; Lyles, Z.; Vadarevu, H.; Afonin, K. A.; Vivero-Escoto, J. L. Multimodal Polysilsesquioxane Nanoparticles for Combinatorial Therapy and Gene Delivery in Triple-Negative Breast Cancer. *ACS Appl. Mater. Interfaces* **2019**, *11* (13), 12308–12320. <https://doi.org/10.1021/acsami.9b00704>.
- (88) Muhanna, N.; Cui, L.; Chan, H.; Burgess, L.; Jin, C. S.; MacDonald, T. D.; Huynh, E.; Wang, F.; Chen, J.; Irish, J. C.; Zheng, G. Multimodal Image-Guided Surgical and Photodynamic Interventions in Head and Neck Cancer: From Primary Tumor to Metastatic Drainage. *Clin. Cancer Res.* **2015**. <https://doi.org/10.1158/1078-0432.CCR-15-1235>.
- (89) Paris, J. L.; Villaverde, G.; Gómez-Graña, S.; Vallet-Regí, M. Nanoparticles for Multimodal Antivascular Therapeutics: Dual Drug Release, Photothermal and Photodynamic Therapy. *Acta Biomater.* **2020**, *101*, 459–468. <https://doi.org/10.1016/j.actbio.2019.11.004>.
- (90) Park, S. M.; Aalipour, A.; Vermesh, O.; Yu, J. H.; Gambhir, S. S. Towards Clinically Translatable in Vivo Nanodiagnosics. *Nat. Rev. Mater.* **2017**, *2* (May). <https://doi.org/10.1038/natrevmats.2017.14>.
- (91) Hansen, A. E.; Petersen, A. L.; Henriksen, J. R.; Boerresen, B.; Rasmussen, P.; Elema, D. R.; Rosenschöld, P. M. af; Kristensen, A. T.; Kjær, A.; Andresen, T. L. Positron Emission Tomography Based Elucidation of the Enhanced Permeability and Retention Effect in Dogs with Cancer Using Copper-64 Liposomes. *ACS Nano* **2015**, *9* (7), 6985–6995. <https://doi.org/10.1021/acs.nano.5b01324>.
- (92) Karathanasis, E.; Suryanarayanan, S.; Balusu, S. R.; McNeeley, K.; Sechopoulos, I.; Karellas, A.; Annapragada, A. V.; Bellamkonda, R. V. Imaging Nanoprobe for Prediction of Outcome of Nanoparticle Chemotherapy by Using Mammography. *Radiology* **2009**, *250* (2), 398–406. <https://doi.org/10.1148/radiol.2502080801>.
- (93) Guo, J.; Guo, N.; Lang, L.; Kiesewetter, D. O.; Xie, Q.; Li, Q.; Eden, H. S.; Niu, G.; Chen, X. 18F-Alfatide II and 18F-FDG Dual-Tracer Dynamic PET for Parametric, Early Prediction of Tumor Response to Therapy. *J. Nucl. Med.* **2014**, *55* (1), 154–160. <https://doi.org/10.2967/jnumed.113.122069>.
- (94) Di Corato, R.; Béalle, G.; Kolosnjaj-Tabi, J.; Espinosa, A.; Clément, O.; Silva, A. K. A.; Ménager, C.; Wilhelm, C. Combining Magnetic Hyperthermia and Photodynamic Therapy for Tumor Ablation with Photoresponsive Magnetic Liposomes. *ACS Nano* **2015**, *9* (3), 2904–2916. <https://doi.org/10.1021/nn506949t>.
- (95) Toy, R.; Hayden, E.; Camann, A.; Berman, Z.; Vicente, P.; Tran, E.; Meyers, J.; Pansky, J.; Peiris, P. M.; Wu, H.; Exner, A.; Wilson, D.; Ghaghada, K. B.; Karathanasis, E. Multimodal In Vivo Imaging Exposes the Voyage of Nanoparticles in Tumor Microcirculation. *ACS Nano* **2013**, *7* (4), 3118–3129. <https://doi.org/10.1021/nn3053439>.
- (96) Notohamiprodo, M.; Staehler, M.; Steiner, N.; Schwab, F.; Sourbron, S. P.; Michaely, H. J.; Helck, A. D.; Reiser, M. F.; Nikolaou, K. Combined Diffusion-Weighted, Blood Oxygen Level-Dependent, and Dynamic Contrast-Enhanced MRI for Characterization and Differentiation of Renal Cell Carcinoma. *Acad. Radiol.* **2013**, *20* (6), 685–693. <https://doi.org/10.1016/j.acra.2013.01.015>.
- (97) Sun, X.; Yan, Y.; Liu, S.; Cao, Q.; Yang, M.; Neamati, N.; Shen, B.; Niu, G.; Chen, X. 18F-FPPRGD2 and 18F-FDG PET of Response to Abraxane Therapy. *J. Nucl. Med.* **2011**, *52* (1), 140–146. <https://doi.org/10.2967/jnumed.110.080606>.
- (98) Kim, T. H.; Lee, S.; Chen, X. Nanotheranostics for Personalized Medicine. *Expert Rev. Mol. Diagn.* **2013**, *13* (3), 257–269. <https://doi.org/10.1586/erm.13.15>.
- (99) Mura, S.; Couvreur, P. Nanotheranostics for Personalized Medicine. *Adv. Drug Deliv. Rev.* **2012**, *64* (13), 1394–1416. <https://doi.org/10.1016/j.addr.2012.06.006>.
- (100) Schork, N. J. Personalized Medicine: Time for One-Person Trials. *Nature* **2015**, *520* (7549), 609–611. <https://doi.org/10.1038/520609a>.
- (101) Ventola, C. L. Progress in Nanomedicine: Approved and Investigational Nanodrugs. *P T Peer-Rev. J. Formul. Manag.* **2017**, *42* (12), 742–755.
- (102) He, H.; Liu, L.; Morin, E. E.; Liu, M.; Schwendeman, A. Survey of Clinical Translation of Cancer Nanomedicines - Lessons Learned from Successes and Failures. *Acc. Chem. Res.* **2019**, *52* (9), 2673–2683. <https://doi.org/10.1021/acs.accounts.9b00228>.
- (103) Sanhai, W. R.; Sakamoto, J. H.; Canady, R.; Ferrari, M. Seven Challenges for Nanomedicine. *Nat. Nanotechnol.* **2008**, *3* (5), 242–244. <https://doi.org/10.1038/nnano.2008.114>.
- (104) Anchordoquy, T. J.; Barenholz, Y.; Boraschi, D.; Chorny, M.; Decuzzi, P.; Dobrovolskaia, M. A.; Farhangrazi, Z. S.; Farrell, D.; Gabizon, A.; Ghandehari, H.; Godin, B.; La-Beck, N. M.; Ljubimova, J.; Moghimi, S. M.; Pagliaro, L.; Park, J.-H.; Peer, D.; Ruoslahti, E.; Serkova, N. J.; Simberg, D. Mechanisms and Barriers in Cancer Nanomedicine: Addressing Challenges, Looking for Solutions. *ACS Nano* **2017**, *11* (1), 12–18. <https://doi.org/10.1021/acs.nano.6b08244>.
- (105) Wilhelm, S.; Tavares, A. J.; Dai, Q.; Ohta, S.; Audet, J.; Dvorak, H. F.; Chan, W. C. W. Analysis of Nanoparticle Delivery to Tumours. *Nat. Rev. Mater.* **2016**, *1* (5), 16014. <https://doi.org/10.1038/natrevmats.2016.14>.
- (106) Wu, L. P.; Wang, D.; Li, Z. Grand Challenges in Nanomedicine. *Mater. Sci. Eng. C* **2020**, *106* (October 2019). <https://doi.org/10.1016/j.msec.2019.110302>.
- (107) Hoshyar, N.; Gray, S.; Han, H.; Bao, G. The Effect of Nanoparticle Size on in Vivo Pharmacokinetics and Cellular Interaction. *Nanomed.* **2016**, *11* (6), 673–692. <https://doi.org/10.2217/nnm.16.5>.
- (108) Nia, H. T.; Munn, L. L.; Jain, R. K. Physical Traits of Cancer. *Science* **2020**, *370* (6516). <https://doi.org/10.1126/science.aaz0868>.
- (109) Zhou, Y.; Dai, Z. New Strategies in the Design of Nanomedicines to Oppose Uptake by the Mononuclear Phagocyte System and Enhance Cancer Therapeutic Efficacy. *Chem. – Asian J.* **2018**, *13* (22), 3333–3340. <https://doi.org/10.1002/asia.201800149>.
- (110) Mowat, A. M.; Scott, C. L.; Bain, C. C. Barrier-Tissue Macrophages: Functional Adaptation to Environmental Challenges. *Nat. Med.* **2017**, *23* (11), 1258–1270. <https://doi.org/10.1038/nm.4430>.
- (111) Parmar, K.; Patel, J. K. Surface Modification of Nanoparticles to Oppose Uptake by the Mononuclear Phagocyte System. In *Surface Modification of Nanoparticles for Targeted Drug Delivery*; Springer International Publishing: Cham, 2019; pp 221–236. [https://doi.org/10.1007/978-3-030-06115-9\\_12](https://doi.org/10.1007/978-3-030-06115-9_12).
- (112) Blanco, E.; Shen, H.; Ferrari, M. Principles of Nanoparticle Design for Overcoming Biological Barriers to Drug Delivery. *Nat. Biotechnol.* **2015**, *33* (9), 941–951. <https://doi.org/10.1038/nbt.3330>.

- (113) Zhou, Q.; Dong, C.; Fan, W.; Jiang, H.; Xiang, J.; Qiu, N.; Piao, Y.; Xie, T.; Luo, Y.; Li, Z.; Liu, F.; Shen, Y. Tumor Extravasation and Infiltration as Barriers of Nanomedicine for High Efficacy: The Current Status and Transcytosis Strategy. *Biomaterials* **2020**, *240*, 119902. <https://doi.org/10.1016/j.biomaterials.2020.119902>.
- (114) Papademetriou, I.; Vedula, E.; Charest, J.; Porter, T. Effect of Flow on Targeting and Penetration of Angiopep-Decorated Nanoparticles in a Microfluidic Model Blood-Brain Barrier. *PLoS ONE* **2018**, *13* (10), e0205158.
- (115) Han, X.; Xu, Y.; Geranpayehvaghei, M.; Anderson, G. J.; Li, Y.; Nie, G. Emerging Nanomedicines for Anti-Stromal Therapy against Desmoplastic Tumors. *Biomaterials* **2020**, *232*, 119745. <https://doi.org/10.1016/j.biomaterials.2019.119745>.
- (116) Singh, A. P.; Guo, L.; Verma, A.; Wong, G. G.-L.; Thurber, G. M.; Shah, D. K. Antibody Coadministration as a Strategy to Overcome Binding-Site Barrier for ADCs: A Quantitative Investigation. *AAPS J.* **2020**, *22* (2), 28. <https://doi.org/10.1208/s12248-019-0387-x>.
- (117) Miao, L.; Newby, J. M.; Lin, C. M.; Zhang, L.; Xu, F.; Kim, W. Y.; Forest, M. G.; Lai, S. K.; Milowsky, M. I.; Wobker, S. E.; Huang, L. The Binding Site Barrier Elicited by Tumor-Associated Fibroblasts Interferes Disposition of Nanoparticles in Stroma-Vessel Type Tumors. *ACS Nano* **2016**, *10* (10), 9243–9258. <https://doi.org/10.1021/acsnano.6b02776>.
- (118) Degors, I. M. S.; Wang, C.; Rehman, Z. U.; Zuhorn, I. S. Carriers Break Barriers in Drug Delivery: Endocytosis and Endosomal Escape of Gene Delivery Vectors. *Acc. Chem. Res.* **2019**, *52* (7), 1750–1760. <https://doi.org/10.1021/acs.accounts.9b00177>.
- (119) Pei, D.; Buyanova, M. Overcoming Endosomal Entrapment in Drug Delivery. *Bioconj. Chem.* **2019**, *30* (2), 273–283. <https://doi.org/10.1021/acs.bioconjchem.8b00778>.
- (120) Bar-Zeev, M.; Livney, Y. D.; Assaraf, Y. G. Targeted Nanomedicine for Cancer Therapeutics: Towards Precision Medicine Overcoming Drug Resistance. *Drug Resist. Updat.* **2017**, *31*, 15–30. <https://doi.org/10.1016/j.drup.2017.05.002>.
- (121) Lepeltier, E.; Rijo, P.; Rizzolio, F.; Popovtzer, R.; Petrikaite, V.; Assaraf, Y. G.; Passirani, C. Nanomedicine to Target Multidrug Resistant Tumors. *Drug Resist. Updat.* **2020**, *52*, 100704. <https://doi.org/10.1016/j.drup.2020.100704>.
- (122) Barui, A. K.; Oh, J. Y.; Jana, B.; Kim, C.; Ryu, J.-H. Cancer-Targeted Nanomedicine: Overcoming the Barrier of the Protein Corona. *Adv. Ther.* **2020**, *3* (1), 1900124. <https://doi.org/10.1002/adtp.201900124>.
- (123) Cai, R.; Chen, C. The Crown and the Scepter: Roles of the Protein Corona in Nanomedicine. *Adv. Mater.* **2019**, *31* (45), 1805740. <https://doi.org/10.1002/adma.201805740>.
- (124) Corbo, C.; Molinaro, R.; Tabatabaei, M.; Farokhzad, O. C.; Mahmoudi, M. Personalized Protein Corona on Nanoparticles and Its Clinical Implications. *Biomater. Sci.* **2017**, *5* (3), 378–387. <https://doi.org/10.1039/C6BM00921B>.
- (125) Ke, P. C.; Lin, S.; Parak, W. J.; Davis, T. P.; Caruso, F. A Decade of the Protein Corona. *ACS Nano* **2017**, *11* (12), 11773–11776. <https://doi.org/10.1021/acsnano.7b08008>.
- (126) Nguyen, V. H.; Lee, B.-J. Protein Corona: A New Approach for Nanomedicine Design. *Int. J. Nanomedicine* **2017**, *Volume 12*, 3137–3151. <https://doi.org/10.2147/IJN.S129300>.
- (127) Gao, W.; Kagan, D.; Pak, O. S.; Clawson, C.; Campuzano, S.; Chuluun-Erdene, E.; Shipton, E.; Fullerton, E. E.; Zhang, L.; Lauga, E.; Wang, J. Cargo-Towing Fuel-Free Magnetic Nanoswimmers for Targeted Drug Delivery. *Small* **2012**, *8* (3), 460–467. <https://doi.org/10.1002/sml.201101909>.
- (128) Archer, R. A.; Howse, J. R.; Fujii, S.; Kawashima, H.; Buxton, G. A.; Ebbens, S. J. PH-Responsive Catalytic Janus Motors with Autonomous Navigation and Cargo-Release Functions. *Adv. Funct. Mater.* **2020**, *30* (19), 1–9. <https://doi.org/10.1002/adfm.202000324>.
- (129) Li, J.; Li, X.; Luo, T.; Wang, R.; Liu, C.; Chen, S.; Li, D.; Yue, J.; Cheng, S. H.; Sun, D. Development of a Magnetic Microrobot for Carrying and Delivering Targeted Cells. *Sci. Robot.* **2018**, *3* (19), 1–12. <https://doi.org/10.1126/scirobotics.aat8829>.
- (130) Kojima, M.; Miyamoto, T.; Nakajima, M.; Homma, M.; Arai, T.; Fukuda, T. Bacterial Sheet-Powered Rotation of a Micro-Object. *Sens. Actuators B Chem.* **2016**, *222*, 1220–1225. <https://doi.org/10.1016/j.snb.2015.07.071>.
- (131) Xu, H.; Medina-Sánchez, M.; Maitz, M. F.; Werner, C.; Schmidt, O. G. Sperm Micromotors for Cargo Delivery through Flowing Blood. *ACS Nano* **2020**, *14* (3), 2982–2993. <https://doi.org/10.1021/acsnano.9b07851>.
- (132) Xi, W.; Solovev, A. A.; Ananth, A. N.; Gracias, D. H.; Sanchez, S.; Schmidt, O. G. Rolled-up Magnetic Microdrillers: Towards Remotely Controlled Minimally Invasive Surgery. *Nanoscale* **2013**, *5* (4), 1294–1297. <https://doi.org/10.1039/C2NR32798H>.
- (133) Gultepe, E.; Randhawa, J. S.; Kadam, S.; Yamanaka, S.; Selaru, F. M.; Shin, E. J.; Kalloo, A. N.; Gracias, D. H. Biopsy with Thermally-Responsive Untethered Microtools. *Adv. Mater.* **2013**, *25* (4), 514–519. <https://doi.org/10.1002/adma.201203348>.
- (134) Srivastava, S. K.; Medina-Sánchez, M.; Koch, B.; Schmidt, O. G. Medibots: Dual-Action Biogenic Microdaggers for Single-Cell Surgery and Drug Release. *Adv. Mater.* **2016**, *28* (5), 832–837. <https://doi.org/10.1002/adma.201504327>.
- (135) Balasubramanian, S.; Kagan, D.; Jack Hu, C.-M.; Campuzano, S.; Lobo-Castañón, M. J.; Lim, N.; Kang, D. Y.; Zimmerman, M.; Zhang, L.; Wang, J. Micromachine-Enabled Capture and Isolation of Cancer Cells in Complex Media. *Angew. Chem. Int. Ed.* **2011**, *50* (18), 4161–4164. <https://doi.org/10.1002/anie.201100115>.
- (136) Simmchen, J.; Baeza, A.; Ruiz, D.; Esplandiú, M. J.; Vallet-Regí, M. Asymmetric Hybrid Silica Nanomotors for Capture and Cargo Transport: Towards a Novel Motion-Based DNA Sensor. *Small* **2012**, *8* (13), 2053–2059. <https://doi.org/10.1002/sml.201101593>.
- (137) Maric, T.; Nasir, M. Z. M.; Rosli, N. F.; Budanović, M.; Webster, R. D.; Cho, N. J.; Pumera, M. Microrobots Derived from Variety Plant Pollen Grains for Efficient Environmental Clean Up and as an Anti-Cancer Drug Carrier. *Adv. Funct. Mater.* **2020**, *30* (19), 1–13. <https://doi.org/10.1002/adfm.202000112>.
- (138) Villa, K.; Parmar, J.; Vilela, D.; Sánchez, S. Metal-Oxide-Based Microjets for the Simultaneous Removal of Organic Pollutants and Heavy Metals. *ACS Appl. Mater. Interfaces* **2018**, *10* (24), 20478–20486. <https://doi.org/10.1021/acsami.8b04353>.
- (139) Vilela, D.; Parmar, J.; Zeng, Y.; Zhao, Y.; Sánchez, S. Graphene-Based Microbots for Toxic Heavy Metal Removal and Recovery from Water. *Nano Lett.* **2016**, *16* (4), 2860–2866. <https://doi.org/10.1021/acs.nanolett.6b00768>.



- (140) Ying, Y.; Pumera, M. Micro/Nanomotors for Water Purification. *Chem. - Eur. J.* **2019**, *25* (1), 106–121. <https://doi.org/10.1002/chem.201804189>.
- (141) Zeng, M.; Yuan, S.; Huang, D.; Cheng, Z. Accelerated Design of Catalytic Water-Cleaning Nanomotors via Machine Learning. *ACS Appl. Mater. Interfaces* **2019**, *11* (43), 40099–40106. <https://doi.org/10.1021/acsami.9b14792>.
- (142) Parmar, J.; Vilela, D.; Villa, K.; Wang, J.; Sánchez, S. Micro- and Nanomotors as Active Environmental Microcleaners and Sensors. *J. Am. Chem. Soc.* **2018**, *140* (30), 9317–9331. <https://doi.org/10.1021/jacs.8b05762>.
- (143) Soler, L.; Sanchez, S. Catalytic Nanomotors for Environmental Monitoring and Water Remediation. *Nanoscale* **2014**, *6* (13), 7175–7182. <https://doi.org/10.1039/c4nr01321b>.
- (144) Safdar, M.; Simmchen, J.; Jänis, J. Light-Driven Micro- and Nanomotors for Environmental Remediation. *Environ. Sci. Nano* **2017**, *4* (8), 1602–1616. <https://doi.org/10.1039/c7en00367f>.
- (145) Kagan, D.; Calvo-Marzal, P.; Balasubramanian, S.; Sattayasamitsathit, S.; Manesh, K. M.; Flechsig, G. U.; Wang, J. Chemical Sensing Based on Catalytic Nanomotors: Motion-Based Detection of Trace Silver. *J. Am. Chem. Soc.* **2009**, *131* (34), 12082–12083. <https://doi.org/10.1021/ja905142q>.
- (146) Kong, L.; Guan, J.; Pumera, M. Micro- and Nanorobots Based Sensing and Biosensing. *Curr. Opin. Electrochem.* **2018**, *10*, 174–182. <https://doi.org/10.1016/j.coelec.2018.06.004>.
- (147) Zarei, M.; Zarei, M. Self-Propelled Micro/Nanomotors for Sensing and Environmental Remediation. *Small* **2018**, *14* (30), 1–17. <https://doi.org/10.1002/sml.201800912>.
- (148) Gao, C.; Wang, Y.; Ye, Z.; Lin, Z.; Ma, X.; He, Q. Biomedical Micro-/Nanomotors: From Overcoming Biological Barriers to In Vivo Imaging. *Adv. Mater.* **2020**, *n/a* (n/a), 2000512. <https://doi.org/10.1002/adma.202000512>.
- (149) Wang, Z.; Tu, Y.; Chen, Y.; Peng, F. Emerging Micro/Nanomotor-Based Platforms for Biomedical Therapy. *Adv. Intell. Syst.* **2020**, *2* (5), 1900081. <https://doi.org/10.1002/aisy.201900081>.
- (150) Wang, S.; Liu, K.; Wang, F.; Peng, F.; Tu, Y. The Application of Micro- and Nanomotors in Classified Drug Delivery. *Chem. - Asian J.* **2019**, *14* (14), 2336–2347. <https://doi.org/10.1002/asia.201900274>.
- (151) Peng, F.; Tu, Y.; Wilson, D. A. Micro/Nanomotors towards in Vivo Application: Cell, Tissue and Biofluid. *Chem. Soc. Rev.* **2017**, *46* (17), 5289–5310. <https://doi.org/10.1039/C6CS00885B>.
- (152) Ou, J.; Liu, K.; Jiang, J.; Wilson, D. A.; Liu, L.; Wang, F.; Wang, S.; Tu, Y.; Peng, F. Micro-/Nanomotors toward Biomedical Applications: The Recent Progress in Biocompatibility. *Small* **2020**, *1906184*, 1–16. <https://doi.org/10.1002/sml.201906184>.
- (153) Wang, J.; Dong, R.; Wu, H.; Cai, Y.; Ren, B. A Review on Artificial Micro/Nanomotors for Cancer-Targeted Delivery, Diagnosis, and Therapy. *Nano-Micro Lett.* **2020**, *12* (1). <https://doi.org/10.1007/s40820-019-0350-5>.
- (154) Li, J.; Esteban-Fernández de Ávila, B.; Gao, W.; Zhang, L.; Wang, J. Micro/Nanorobots for Biomedicine: Delivery, Surgery, Sensing, and Detoxification. *Sci. Robot.* **2017**, *2* (4), eaam6431. <https://doi.org/10.1126/scirobotics.aam6431>.
- (155) Wang, J.; Gao, W. Nano/Microscale Motors: Biomedical Opportunities and Challenges. *ACS Nano* **2012**, *6* (7), 5745–5751.
- (156) Abdelmohsen, L. K. E. A.; Peng, F.; Tu, Y.; Wilson, D. A. Micro- and Nano-Motors for Biomedical Applications. *J Mater Chem B* **2014**, *2* (17), 2395–2408. <https://doi.org/10.1039/C3TB21451F>.
- (157) Purcell, E. M.; Purcell, E. M. Life at Low Reynolds Number. *Am. J. Phys.* **1977**, *45* (1), 3–11. <https://doi.org/10.1119/1.10903>.
- (158) Akin, D.; Sturgis, J.; Ragheb, K.; Sherman, D.; Burkholder, K.; Robinson, J. P.; Bhunia, A. K.; Mohammed, S.; Bashir, R. Bacteria-Mediated Delivery of Nanoparticles and Cargo into Cells. *Nat. Nanotechnol.* **2007**, *2* (7), 441–449. <https://doi.org/10.1038/nnano.2007.149>.
- (159) Park, S. J.; Park, S.-H.; Cho, S.; Kim, D.-M.; Lee, Y.; Ko, S. Y.; Hong, Y.; Choy, H. E.; Min, J.-J.; Park, J.-O.; Park, S. New Paradigm for Tumor Theranostic Methodology Using Bacteria-Based Microrobot. *Sci. Rep.* **2013**, *3* (1), 3394. <https://doi.org/10.1038/srep03394>.
- (160) Banskota, S.; Yousefpour, P.; Chilkoti, A. Cell-Based Biohybrid Drug Delivery Systems: The Best of the Synthetic and Natural Worlds. *Macromol. Biosci.* **2017**, *17* (1), 1600361. <https://doi.org/10.1002/mabi.201600361>.
- (161) Zhuang, J.; Sitti, M. Chemotaxis of Bio-Hybrid Multiple Bacteria-Driven Microswimmers. *Sci. Rep.* **2016**, *6* (1), 32135. <https://doi.org/10.1038/srep32135>.
- (162) Park, B.-W.; Zhuang, J.; Yasa, O.; Sitti, M. Multifunctional Bacteria-Driven Microswimmers for Targeted Active Drug Delivery. *ACS Nano* **2017**, *11* (9), 8910–8923. <https://doi.org/10.1021/acsnano.7b03207>.
- (163) Viznyiczai, G.; Frangipane, G.; Maggi, C.; Saglimbeni, F.; Bianchi, S.; Di Leonardo, R. Light Controlled 3D Micromotors Powered by Bacteria. *Nat. Commun.* **2017**, *8* (1), 15974. <https://doi.org/10.1038/ncomms15974>.
- (164) Singh, A. V.; Hosseini-Doust, Z.; Park, B.-W.; Yasa, O.; Sitti, M. Microemulsion-Based Soft Bacteria-Driven Microswimmers for Active Cargo Delivery. *ACS Nano* **2017**, *11* (10), 9759–9769. <https://doi.org/10.1021/acsnano.7b02082>.
- (165) Stanton, M. M.; Sánchez, S. Pushing Bacterial Biohybrids to In Vivo Applications. *Trends Biotechnol.* **2017**, *35* (10), 910–913. <https://doi.org/10.1016/j.tibtech.2017.04.008>.
- (166) Stanton, M. M.; Park, B.-W.; Vilela, D.; Bente, K.; Faivre, D.; Sitti, M.; Sánchez, S. Magnetotactic Bacteria Powered Biohybrids Target E. Coli Biofilms. *ACS Nano* **2017**, *11* (10), 9968–9978. <https://doi.org/10.1021/acsnano.7b04128>.
- (167) Stanton, M. M.; Simmchen, J.; Ma, X.; Miguel-López, A.; Sánchez, S. Biohybrid Janus Motors Driven by Escherichia Coli. *Adv. Mater. Interfaces* **2016**, *3*, 1–8. <https://doi.org/10.1002/admi.201500505>.
- (168) Stanton, M. M.; Park, B.-W.; Miguel-López, A.; Ma, X.; Sitti, M. Biohybrid Microtube Swimmers Driven by Single Captured Bacteria. *Small* **2017**, *13* (19), 1–10. <https://doi.org/10.1002/sml.201603679>.
- (169) Weibel, D. B.; Garstecki, P.; Ryan, D.; DiLuzio, W. R.; Mayer, M.; Seto, J. E.; Whitesides, G. M. Microoxen: Microorganisms to Move Microscale Loads. *Proc. Natl. Acad. Sci.* **2005**, *102* (34), 5. <https://doi.org/10.1073/pnas.0505481102>.
- (170) Choi, M.-R.; Stanton-Maxey, K. J.; Stanley, J. K.; Levin, C. S.; Bardhan, R.; Akin, D.; Badve, S.; Sturgis, J.; Robinson, J. P.; Bashir, R.; Halas, N. J.; Clare, S. E. A Cellular Trojan Horse for Delivery of Therapeutic Nanoparticles into Tumors. *Nano Lett.* **2007**, *7* (12), 3759–3765. <https://doi.org/10.1021/nl072209h>.

- (171) Hu, C.-M. J.; Fang, R. H.; Zhang, L. Erythrocyte-Inspired Delivery Systems. *Adv. Healthc. Mater.* **2012**, *1* (5), 537–547. <https://doi.org/10.1002/adhm.201200138>.
- (172) Magdanz, V.; Sanchez, S.; Schmidt, O. G. Development of a Sperm-Flagella Driven Micro-Bio-Robot. *Adv. Mater.* **2013**, *25* (45), 6581–6588. <https://doi.org/10.1002/adma.201302544>.
- (173) Medina-Sánchez, M.; Schwarz, L.; Meyer, A. K.; Hebenstreit, F.; Schmidt, O. G. Cellular Cargo Delivery: Toward Assisted Fertilization by Sperm-Carrying Micromotors. *Nano Lett.* **2016**, *16* (1), 555–561. <https://doi.org/10.1021/acs.nanolett.5b04221>.
- (174) Chen, C.; Chang, X.; Angsantikul, P.; Li, J.; Esteban-Fernández de Ávila, B.; Karshalev, E.; Liu, W.; Mou, F.; He, S.; Castillo, R.; Liang, Y.; Guan, J.; Zhang, L.; Wang, J. Chemotactic Guidance of Synthetic Organic/Inorganic Payloads Functionalized Sperm Micromotors. *Adv. Biosyst.* **2018**, *2* (1), 1700160. <https://doi.org/10.1002/adbi.201700160>.
- (175) Magdanz, V.; Medina-Sánchez, M.; Schwarz, L.; Xu, H.; Elgeti, J.; Schmidt, O. G. Spermatozoa as Functional Components of Robotic Microswimmers. *Adv. Mater.* **2017**, *29* (24), 1606301. <https://doi.org/10.1002/adma.201606301>.
- (176) Shao, J.; Xuan, M.; Zhang, H.; Lin, X.; Wu, Z.; He, Q. Chemotaxis-Guided Hybrid Neutrophil Micromotors for Targeted Drug Transport. *Angew. Chem.* **2017**, *129* (42), 13115–13119. <https://doi.org/10.1002/ange.201706570>.
- (177) Xu, H.; Medina-Sánchez, M.; Magdanz, V.; Schwarz, L.; Hebenstreit, F.; Schmidt, O. G. Sperm-Hybrid Micromotor for Targeted Drug Delivery. *ACS Nano* **2018**, *12* (1), 327–337. <https://doi.org/10.1021/acsnano.7b06398>.
- (178) Striggow, F.; Medina-Sánchez, M.; Auernhammer, G. K.; Magdanz, V.; Friedrich, B. M.; Schmidt, O. G. Sperm-Driven Micromotors Moving in Oviduct Fluid and Viscoelastic Media. *Small* **2020**, *16* (24), 2000213. <https://doi.org/10.1002/sml.202000213>.
- (179) Magdanz, V.; Medina-Sánchez, M.; Chen, Y.; Guix, M.; Schmidt, O. G. How to Improve SpermBot Performance. *Adv. Funct. Mater.* **2015**, *25* (18), 2763–2770. <https://doi.org/10.1002/adfm.201500015>.
- (180) Xu, T.; Gao, W.; Xu, L.-P.; Zhang, X.; Wang, S. Fuel-Free Synthetic Micro-/Nanomachines. *Adv. Mater.* **2017**, *29* (9), 1603250. <https://doi.org/10.1002/adma.201603250>.
- (181) Wang, J.; Xiong, Z.; Zheng, J.; Zhan, X.; Tang, J. Light-Driven Micro/Nanomotor for Promising Biomedical Tools: Principle, Challenge, and Prospect. *Acc. Chem. Res.* **2018**, *51* (9), 1957–1965. <https://doi.org/10.1021/acs.accounts.8b00254>.
- (182) Chen, X.; Hoop, M.; Mushtaq, F.; Siringil, E.; Hu, C.; Nelson, B. J.; Pané, S. Recent Developments in Magnetically Driven Micro- and Nanorobots. *Appl. Mater. Today* **2017**, *9*, 37–48. <https://doi.org/10.1016/j.apmt.2017.04.006>.
- (183) Xu, T.; Xu, L. P.; Zhang, X. Ultrasound Propulsion of Micro-/Nanomotors. *Appl. Mater. Today* **2017**, *9*, 493–503. <https://doi.org/10.1016/j.apmt.2017.07.011>.
- (184) Qiu, F.; J. Nelson, B. Magnetic Helical Micro- and Nanorobots: Toward Their Biomedical Applications. *Engineering* **2015**, *1* (1), 21. <https://doi.org/10.15302/J-ENG-2015005>.
- (185) Mandal, P.; Patil, G.; Kakoty, H.; Ghosh, A. Magnetic Active Matter Based on Helical Propulsion. *Acc. Chem. Res.* **2018**, *51* (11), 2689–2698. <https://doi.org/10.1021/acs.accounts.8b00315>.
- (186) Khalil, I. S. M.; Fatih Tabak, A.; Klingner, A.; Sitti, M. Magnetic Propulsion of Robotic Sperms at Low-Reynolds Number. *Appl. Phys. Lett.* **2016**, *109* (3), 33701. <https://doi.org/10.1063/1.4958737>.
- (187) Yu, H.; Tang, W.; Mu, G.; Wang, H.; Chang, X.; Dong, H.; Qi, L.; Zhang, G.; Li, T. Micro-/Nanorobots Propelled by Oscillating Magnetic Fields. *Micromachines* **2018**, *9* (11). <https://doi.org/10.3390/mi9110540>.
- (188) Šipová-Jungová, H.; Andrén, D.; Jones, S.; Käll, M. Nanoscale Inorganic Motors Driven by Light: Principles, Realizations, and Opportunities. *Chem. Rev.* **2020**, *120* (1), 269–287. <https://doi.org/10.1021/acs.chemrev.9b00401>.
- (189) Palagi, S.; Singh, D. P.; Fischer, P. Light-Controlled Micromotors and Soft Microrobots. *Adv. Opt. Mater.* **2019**, *7* (16), 1–18. <https://doi.org/10.1002/adom.201900370>.
- (190) Villa, K.; Pumbera, M. Fuel-Free Light-Driven Micro/Nanomachines: Artificial Active Matter Mimicking Nature. *Chem. Soc. Rev.* **2019**, *48* (19), 4966–4978. <https://doi.org/10.1039/c9cs00090a>.
- (191) Dong, R.; Cai, Y.; Yang, Y.; Gao, W.; Ren, B. Photocatalytic Micro/Nanomotors: From Construction to Applications. *Acc. Chem. Res.* **2018**, *51* (9), 1940–1947. <https://doi.org/10.1021/acs.accounts.8b00249>.
- (192) Lu, X.; Shen, H.; Zhao, K.; Wang, Z.; Peng, H.; Liu, W. Micro-/Nanomachines Driven by Ultrasonic Power Sources. *Chem. - Asian J.* **2019**, *14* (14), 2406–2416. <https://doi.org/10.1002/asia.201900281>.
- (193) Sánchez, S.; Soler, L.; Katuri, J. Chemically Powered Micro- and Nanomotors. *Angew. Chem. Int. Ed.* **2015**, *54* (5), 1414–1444. <https://doi.org/10.1002/anie.201406096>.
- (194) Katuri, J.; Ma, X.; Stanton, M. M.; Sánchez, S. Designing Micro-and Nanoswimmers for Specific Applications. *Acc. Chem. Res.* **2017**, *50* (1), 2–11. <https://doi.org/10.1021/acs.accounts.6b00386>.
- (195) Dey, K. K.; Sen, A. Chemically Propelled Molecules and Machines. *J. Am. Chem. Soc.* **2017**, *139* (23), 7666–7676. <https://doi.org/10.1021/jacs.7b02347>.
- (196) Robertson, B.; Huang, M. J.; Chen, J. X.; Kapral, R. Synthetic Nanomotors: Working Together through Chemistry. *Acc. Chem. Res.* **2018**, *51* (10), 2355–2364. <https://doi.org/10.1021/acs.accounts.8b00239>.
- (197) Wong, F.; Dey, K. K.; Sen, A. Synthetic Micro/Nanomotors and Pumps: Fabrication and Applications. *Annu. Rev. Mater. Res.* **2016**, *46* (1), 407–432. <https://doi.org/10.1146/annurev-matsci-070115-032047>.
- (198) Patiño, T.; Arqué, X.; Mestre, R.; Palacios, L.; Sánchez, S. Fundamental Aspects of Enzyme-Powered Micro- and Nanoswimmers. *Acc. Chem. Res.* **2018**, *51* (11), 2662–2671. <https://doi.org/10.1021/acs.accounts.8b00288>.
- (199) Dey, K. K.; Wong, F.; Altemose, A.; Sen, A. Current Opinion in Colloid & Interface Science Catalytic Motors — Quo Vadimus? *Curr. Opin. Colloid Interface Sci.* **2016**, *21*, 4–13. <https://doi.org/10.1016/j.cocis.2015.12.001>.
- (200) Esplandiú, M. J.; Zhang, K.; Fraxedas, J.; Sepulveda, B.; Reguera, D. Unraveling the Operational Mechanisms of Chemically Propelled Motors with Micropumps. *Acc. Chem. Res.* **2018**, *51* (9), 1921–1930. <https://doi.org/10.1021/acs.accounts.8b00241>.
- (201) Taherkhani, S.; Mohammadi, M.; Daoud, J.; Martel, S.; Tabrizian, M. Covalent Binding of Nanoliposomes to the Surface of Magnetotactic Bacteria for the Synthesis of Self-Propelled Therapeutic Agents. *ACS Nano* **2014**, *8* (5), 5049–5060. <https://doi.org/10.1021/nn5011304>.

- (202) Alapan, Y.; Yasa, O.; Schauer, O.; Giltinan, J.; Tabak, A. F.; Sourjik, V.; Sitti, M. Soft Erythrocyte-Based Bacterial Microswimmers for Cargo Delivery. *Sci. Robot.* **2018**, *3* (17), eaar4423. <https://doi.org/10.1126/scirobotics.aar4423>.
- (203) Di Leonardo, R.; Angelani, L.; Dell'arciprete, D.; Ruocco, G.; Iebba, V.; Schippa, S.; Conte, M. P.; Mecerini, F.; De Angelis, F.; Di Fabrizio, E. Bacterial Ratchet Motors. *Proc. Natl. Acad. Sci. U. S. A.* **2010**, *107* (21), 9541–9545. <https://doi.org/10.1073/pnas.0910426107>.
- (204) Behkam, B.; Sitti, M. Bacterial Flagella-Based Propulsion and on/off Motion Control of Microscale Objects. *Appl. Phys. Lett.* **2007**, *90* (2), 023902. <https://doi.org/10.1063/1.2431454>.
- (205) Xu, L.; Mou, F.; Gong, H.; Luo, M.; Guan, J. Light-Driven Micro/Nanomotors: From Fundamentals to Applications. *Chem. Soc. Rev.* **2017**, *46* (22), 6905–6926. <https://doi.org/10.1039/c7cs00516d>.
- (206) Mou, F.; Kong, L.; Chen, C.; Chen, Z.; Xu, L.; Guan, J. Light-Controlled Propulsion, Aggregation and Separation of Water-Fuelled TiO<sub>2</sub>/Pt Janus Submicromotors and Their “on-the-Fly” Photocatalytic Activities. *Nanoscale* **2016**, *8* (9), 4976–4983. <https://doi.org/10.1039/C5NR06774J>.
- (207) Dong, R.; Zhang, Q.; Gao, W.; Pei, A.; Ren, B. Highly Efficient Light-Driven TiO<sub>2</sub>-Au Janus Micromotors. *ACS Nano* **2016**, *10* (1), 839–844. <https://doi.org/10.1021/acsnano.5b05940>.
- (208) Dai, B.; Wang, J.; Xiong, Z.; Zhan, X.; Dai, W.; Li, C.-C.; Feng, S.-P.; Tang, J. Programmable Artificial Phototactic Microswimmer. *Nat. Nanotechnol.* **2016**, *11* (12), 1087–1092. <https://doi.org/10.1038/nnano.2016.187>.
- (209) Ibele, M.; Mallouk, T. E.; Sen, A. Schooling Behavior of Light-Powered Autonomous Micromotors in Water. *Angew. Chem. Int. Ed.* **2009**, *48* (18), 3308–3312. <https://doi.org/10.1002/anie.200804704>.
- (210) Kline, T. R.; Sen, A. Reversible Pattern Formation through Photolysis. *Langmuir* **2006**, *22* (17), 7124–7127. <https://doi.org/10.1021/la061165+>.
- (211) Anderson, J. L. Colloid Transport by Interfacial Forces. *Annu. Rev. Fluid Mech.* **1989**, *21* (1), 61–99. <https://doi.org/10.1146/annurev.fl.21.010189.000425>.
- (212) Simmchen, J.; Baeza, A.; Miguel-Lopez, A.; Stanton, M. M.; Vallet-Regi, M.; Ruiz-Molina, D.; Sánchez, S. Dynamics of Novel Photoactive AgCl Microstars and Their Environmental Applications. *ChemNanoMat* **2017**, *3* (1), 65–71. <https://doi.org/10.1002/cnma.201600300>.
- (213) Duan, W.; Ibele, M.; Liu, R.; Sen, A. Motion Analysis of Light-Powered Autonomous Silver Chloride Nanomotors. *Eur. Phys. J. E* **2012**, *35* (8), 77. <https://doi.org/10.1140/epje/i2012-12077-x>.
- (214) Sen, A.; Ibele, M.; Hong, Y.; Velegol, D. Chemo and Phototactic Nano/Microbots. *Faraday Discuss.* **2009**, *143* (0), 15–27. <https://doi.org/10.1039/B900971J>.
- (215) Hong, Y.; Diaz, M.; Córdova-Figueroa, U. M.; Sen, A. Light-Driven Titanium-Dioxide-Based Reversible Microfireworks and Micromotor/Micropump Systems. *Adv. Funct. Mater.* **2010**, *20* (10), 1568–1576. <https://doi.org/10.1002/adfm.201000063>.
- (216) Jang, B.; Hong, A.; Kang, H. E.; Alcantara, C.; Charreyron, S.; Mushtaq, F.; Pellicer, E.; Büchel, R.; Sort, J.; Lee, S. S.; Nelson, B. J.; Panè, S. Multiwavelength Light-Responsive Au/B-TiO<sub>2</sub> Janus Micromotors. *ACS Nano* **2017**, *11* (6), 6146–6154. <https://doi.org/10.1021/acsnano.7b02177>.
- (217) Wang, X.; Sridhar, V.; Guo, S.; Talebi, N.; Miguel-López, A.; Hahn, K.; van Aken, P. A.; Sánchez, S. Fuel-Free Nanocap-Like Motors Actuated Under Visible Light. *Adv. Funct. Mater.* **2018**, *28* (25), 1705862. <https://doi.org/10.1002/adfm.201705862>.
- (218) Dong, R.; Hu, Y.; Wu, Y.; Gao, W.; Ren, B.; Wang, Q.; Cai, Y. Visible Light-Driven BiOI-Based Janus Micromotor in Pure Water. *J. Am. Chem. Soc.* **2017**, *139* (5), 1722–1725. <https://doi.org/10.1021/jacs.6b09863>.
- (219) Wu, Y.; Si, T.; Shao, J.; Wu, Z.; He, Q. Near-Infrared Light-Driven Janus Capsule Motors: Fabrication, Propulsion, and Simulation. *Nano Res.* **2016**, *9* (12), 3747–3756. <https://doi.org/10.1007/s12274-016-1245-0>.
- (220) Jiang, H.-R.; Yoshinaga, N.; Sano, M. Active Motion of a Janus Particle by Self-Thermophoresis in a Defocused Laser Beam. *Phys. Rev. Lett.* **2010**, *105* (26), 268302. <https://doi.org/10.1103/PhysRevLett.105.268302>.
- (221) Qian, B.; Montiel, D.; Bregulla, A.; Cichos, F.; Yang, H. Harnessing Thermal Fluctuations for Purposeful Activities: The Manipulation of Single Micro-Swimmers by Adaptive Photon Nudging. *Chem. Sci.* **2013**, *4* (4), 1420–1429. <https://doi.org/10.1039/C2SC21263C>.
- (222) Li, Y.; Mou, F.; Chen, C.; You, M.; Yin, Y.; Xu, L.; Guan, J. Light-Controlled Bubble Propulsion of Amorphous TiO<sub>2</sub>/Au Janus Micromotors. *RSC Adv.* **2016**, *6* (13), 10697–10703. <https://doi.org/10.1039/C5RA26798F>.
- (223) Xuan, M.; Wu, Z.; Shao, J.; Dai, L.; Si, T.; He, Q. Near Infrared Light-Powered Janus Mesoporous Silica Nanoparticle Motors. *J. Am. Chem. Soc.* **2016**, *138* (20), 6492–6497. <https://doi.org/10.1021/jacs.6b00902>.
- (224) Xuan, M.; Mestre, R.; Gao, C.; Zhou, C.; He, Q.; Sanchez, S. Noncontinuous Super-Diffusive Dynamics of a Light-Activated Nanobottle Motor. *Angew. Chem. Int. Ed.* **2018**, *57* (23), 6838–6842.
- (225) Wu, Z.; Si, T.; Gao, W.; Lin, X.; Wang, J.; He, Q. Superfast Near-Infrared Light-Driven Polymer Multilayer Rockets. *Small* **2016**, *12* (5), 577–582. <https://doi.org/10.1002/sml.201502605>.
- (226) Mou, F.; Li, Y.; Chen, C.; Li, W.; Yin, Y.; Ma, H.; Guan, J. Single-Component TiO<sub>2</sub> Tubular Microengines with Motion Controlled by Light-Induced Bubbles. *Small* **2015**, *11* (21), 2564–2570. <https://doi.org/10.1002/sml.201403372>.
- (227) Giudicatti, S.; M. Marz, S.; Soler, L.; Madani, A.; R. Jorgensen, M.; Sanchez, S.; G. Schmidt, O. Photoactive Rolled-up TiO<sub>2</sub> Microtubes: Fabrication, Characterization and Applications. *J. Mater. Chem. C* **2014**, *2* (29), 5892–5901. <https://doi.org/10.1039/C4TC00796D>.
- (228) Wu, Z.; Lin, X.; Wu, Y.; Si, T.; Sun, J.; He, Q. Near-Infrared Light-Triggered “On/Off” Motion of Polymer Multilayer Rockets. *ACS Nano* **2014**, *8* (6), 6097–6105. <https://doi.org/10.1021/nn501407r>.
- (229) Zhang, L.; Abbott, J. J.; Dong, L.; Kratochvil, B. E.; Bell, D.; Nelson, B. J. Artificial Bacterial Flagella: Fabrication and Magnetic Control. *Appl. Phys. Lett.* **2009**, *94* (6), 064107. <https://doi.org/10.1063/1.3079655>.
- (230) Schamel, D.; Mark, A. G.; Gibbs, J. G.; Miksch, C.; Morozov, K. I.; Leshansky, A. M.; Fischer, P. Nanopropellers and Their Actuation in Complex Viscoelastic Media. *ACS Nano* **2014**, *8* (9), 8794–8801. <https://doi.org/10.1021/nn502360t>.
- (231) Ghosh, A.; Paria, D.; Rangarajan, G.; Ghosh, A. Velocity Fluctuations in Helical Propulsion: How Small Can a Propeller Be. *J. Phys. Chem. Lett.* **2014**, *5* (1), 62–68. <https://doi.org/10.1021/jz402186w>.



- (232) Ghosh, A.; Fischer, P. Controlled Propulsion of Artificial Magnetic Nanostructured Propellers. *Nano Lett.* **2009**, *9* (6), 2243–2245. <https://doi.org/10.1021/nl900186w>.
- (233) Tottori, S.; Zhang, L.; Qiu, F.; Krawczyk, K. K.; Franco-Obregón, A.; Nelson, B. J. Magnetic Helical Micromachines: Fabrication, Controlled Swimming, and Cargo Transport. *Adv. Mater.* **2012**, *24* (6), 811–816. <https://doi.org/10.1002/adma.201103818>.
- (234) Magdanz, V.; Khalil, I. S. M.; Simmchen, J.; Furtado, G. P.; Mohanty, S.; Gebauer, J.; Xu, H.; Klingner, A.; Aziz, A.; Medina-Sánchez, M.; Schmidt, O. G.; Misra, S. IRONSperm: Sperm-Templated Soft Magnetic Microrobots. *Sci. Adv.* **2020**, *6* (28), eaba5855. <https://doi.org/10.1126/sciadv.aba5855>.
- (235) Zhang, L.; Petit, T.; Lu, Y.; Kratochvil, B. E.; Peyer, K. E.; Pei, R.; Lou, J.; Nelson, B. J. Controlled Propulsion and Cargo Transport of Rotating Nickel Nanowires near a Patterned Solid Surface. *ACS Nano* **2010**, *4* (10), 6228–6234. <https://doi.org/10.1021/nn101861n>.
- (236) Hu, N.; Wang, L.; Zhai, W.; Sun, M.; Xie, H.; Wu, Z.; He, Q. Magnetically Actuated Rolling of Star-Shaped Hydrogel Microswimmer. *Macromol. Chem. Phys.* **2018**, *219* (5), 1700540. <https://doi.org/10.1002/macp.201700540>.
- (237) Wu, Z.; Troll, J.; Jeong, H.-H.; Wei, Q.; Stang, M.; Ziemssen, F.; Wang, Z.; Dong, M.; Schnichels, S.; Qiu, T.; Fischer, P. A Swarm of Slippery Micropropellers Penetrates the Vitreous Body of the Eye. *Sci. Adv.* **2018**, *4* (11), eaat4388–eaat4388. <https://doi.org/10.1126/sciadv.aat4388>.
- (238) Walker, D.; Kasdorf, B. T.; Jeong, H.-H.; Lieleg, O.; Fischer, P. Enzymatically Active Biomimetic Micropropellers for the Penetration of Mucin Gels. *Sci. Adv.* **2015**, *1* (11), e1500501–e1500501. <https://doi.org/10.1126/sciadv.1500501>.
- (239) Dreyfus, R.; Baudry, J.; Roper, M. L.; Fermigier, M.; Stone, H. A.; Bibette, J. Microscopic Artificial Swimmers. *Nature* **2005**, *437* (7060), 862–865. <https://doi.org/10.1038/nature04090>.
- (240) Liu, Y.; Ge, D.; Cong, J.; Piao, H.-G.; Huang, X.; Xu, Y.; Lu, G.; Pan, L.; Liu, M. Magnetically Powered Annelid-Worm-Like Microswimmers. *Small* **2018**, *14* (17), 1704546. <https://doi.org/10.1002/smll.201704546>.
- (241) Li, T.; Zhang, A.; Shao, G.; Wei, M.; Guo, B.; Zhang, G.; Li, L.; Wang, W. Janus Microdimer Surface Walkers Propelled by Oscillating Magnetic Fields. *Adv. Funct. Mater.* **2018**, *28* (25), 1–9. <https://doi.org/10.1002/adfm.201706066>.
- (242) Kim, K.; Xu, X.; Guo, J.; Fan, D. L. Ultrahigh-Speed Rotating Nanoelectromechanical System Devices Assembled from Nanoscale Building Blocks. *Nat. Commun.* **2014**, *5*, 1–9. <https://doi.org/10.1038/ncomms4632>.
- (243) Boymelgreen, A. M.; Balli, T.; Miloh, T.; Yossifon, G. Active Colloids as Mobile Microelectrodes for Unified Label-Free Selective Cargo Transport. *Nat. Commun.* **2018**, *9* (1), 760. <https://doi.org/10.1038/s41467-018-03086-2>.
- (244) Calvo-Marzal, P.; Sattayasamitsathit, S.; Balasubramanian, S.; Windmiller, J. R.; Dao, C.; Wang, J. Propulsion of Nanowire Diodes. *Chem. Commun.* **2010**, *46* (10), 1623–1624. <https://doi.org/10.1039/B925568K>.
- (245) Loget, G.; Kuhn, A. Electric Field-Induced Chemical Locomotion of Conducting Objects. *Nat. Commun.* **2011**, *2* (1). <https://doi.org/10.1038/ncomms1550>.
- (246) Ni, S.; Marini, E.; Buttinoni, I.; Wolf, H.; Isa, L. Hybrid Colloidal Microswimmers through Sequential Capillary Assembly. *Soft Matter* **2017**, *13* (23), 4252–4259. <https://doi.org/10.1039/C7SM00443E>.
- (247) Chang, S. T.; Paunov, V. N.; Petsev, D. N.; Velev, O. D. Remotely Powered Self-Propelling Particles and Micropumps Based on Miniature Diodes. *Nat. Mater.* **2007**, *6* (3), 235–240. <https://doi.org/10.1038/nmat1843>.
- (248) Garcia-Gradilla, V.; Sattayasamitsathit, S.; Soto, F.; Kuralay, F.; Yardımcı, C.; Wiitala, D.; Galarnyk, M.; Wang, J. Ultrasound-Propelled Nanoporous Gold Wire for Efficient Drug Loading and Release. *Small* **2014**, *10* (20), 4154–4159. <https://doi.org/10.1002/smll.201401013>.
- (249) Kagan, D.; Benchimol, M. J.; Claussen, J. C.; Chuluun-Erdene, E.; Esener, S.; Wang, J. Acoustic Droplet Vaporization and Propulsion of Perfluorocarbon-Loaded Microbullets for Targeted Tissue Penetration and Deformation. *Angew. Chem. Int. Ed.* **2012**, *51* (30), 7519–7522. <https://doi.org/10.1002/anie.201201902>.
- (250) Wang, W.; Castro, L. A.; Hoyos, M.; Mallouk, T. E. Autonomous Motion of Metallic Microrods Propelled by Ultrasound. *ACS Nano* **2012**, *6* (7), 6122–6132. <https://doi.org/10.1021/nn301312z>.
- (251) Ahmed, S.; Wang, W.; Mair, L. O.; Fraleigh, R. D.; Li, S.; Castro, L. A.; Hoyos, M.; Huang, T. J.; Mallouk, T. E. Steering Acoustically Propelled Nanowire Motors toward Cells in a Biologically Compatible Environment Using Magnetic Fields. *Langmuir* **2013**, *29* (52), 16113–16118. <https://doi.org/10.1021/la403946j>.
- (252) Wang, D.; Gao, C.; Wang, W.; Sun, M.; Guo, B.; Xie, H.; He, Q. Shape-Transformable, Fusible Rodlike Swimming Liquid Metal Nanomachine. *ACS Nano* **2018**, *12* (10), 10212–10220. <https://doi.org/10.1021/acsnano.8b05203>.
- (253) Wang, W.; Li, S.; Mair, L.; Ahmed, S.; Huang, T. J.; Mallouk, T. E. Acoustic Propulsion of Nanorod Motors Inside Living Cells. *Angew. Chem. Int. Ed.* **2014**, *53* (12), 3201–3204. <https://doi.org/10.1002/anie.201309629>.
- (254) Garcia-Gradilla, V.; Orozco, J.; Sattayasamitsathit, S.; Soto, F.; Kuralay, F.; Pourazary, A.; Katzenberg, A.; Gao, W.; Shen, Y.; Wang, J. Functionalized Ultrasound-Propelled Magnetically Guided Nanomotors: Toward Practical Biomedical Applications. *ACS Nano* **2013**, *7* (10), 9232–9240. <https://doi.org/10.1021/nn403851v>.
- (255) de Ávila, B. E.-F.; Angell, C.; Soto, F.; Lopez-Ramirez, M. A.; Báez, D. F.; Xie, S.; Wang, J.; Chen, Y. Acoustically Propelled Nanomotors for Intracellular siRNA Delivery. *ACS Nano* **2016**, *10* (5), 4997–5005. <https://doi.org/10.1021/acsnano.6b01415>.
- (256) Hansen-Bruhn, M.; de Ávila, B. E.-F.; Beltrán-Gastélum, M.; Zhao, J.; Ramírez-Herrera, D. E.; Angsantikul, P.; Vesterager Gothelf, K.; Zhang, L.; Wang, J. Active Intracellular Delivery of a Cas9/SgRNA Complex Using Ultrasound-Propelled Nanomotors. *Angew. Chem. Int. Ed.* **2018**, *57* (10), 2657–2661. <https://doi.org/10.1002/anie.201713082>.
- (257) Díez, P.; de Ávila, B. E.-F.; Ramírez-Herrera, D. E.; Villalonga, R.; Wang, J. Biomedical Nanomotors: Efficient Glucose-Mediated Insulin Release. *Nanoscale* **2017**, *9* (38), 14307–14311.
- (258) Esteban-Fernández de Ávila, B.; Ramírez-Herrera, D. E.; Campuzano, S.; Angsantikul, P.; Zhang, L.; Wang, J. Nanomotor-Enabled PH-Responsive Intracellular Delivery of Caspase-3: Toward Rapid Cell Apoptosis. *ACS Nano* **2017**, *11* (6), 5367–5374. <https://doi.org/10.1021/acsnano.7b01926>.
- (259) Wu, Z.; Li, T.; Li, J.; Gao, W.; Xu, T.; Christianson, C.; Gao, W.; Galarnyk, M.; He, Q.; Zhang, L.; Wang, J. Turning Erythrocytes into Functional Micromotors. *ACS Nano* **2014**, *8* (12), 12041–12048. <https://doi.org/10.1021/nn506200x>.

- (260) Sabrina, S.; Tasinkevych, M.; Ahmed, S.; Brooks, A. M.; Olvera de la Cruz, M.; Mallouk, T. E.; Bishop, K. J. M. Shape-Directed Microspinners Powered by Ultrasound. *ACS Nano* **2018**, *12* (3), 2939–2947. <https://doi.org/10.1021/acsnano.8b00525>.
- (261) McNeill, J. M.; Nama, N.; Braxton, J. M.; Mallouk, T. E. Wafer-Scale Fabrication of Micro- to Nanoscale Bubble Swimmers and Their Fast Autonomous Propulsion by Ultrasound. *ACS Nano* **2020**, *14* (6), 7520–7528. <https://doi.org/10.1021/acsnano.0c03311>.
- (262) Ren, L.; Nama, N.; McNeill, J. M.; Soto, F.; Yan, Z.; Liu, W.; Wang, W.; Wang, J.; Mallouk, T. E. 3D Steerable, Acoustically Powered Microswimmers for Single-Particle Manipulation. *Sci. Adv.* **2019**, *5* (10), eaax3084. <https://doi.org/10.1126/sciadv.aax3084>.
- (263) Gao, W.; Pei, A.; Wang, J. Water-Driven Micromotors. *ACS Nano* **2012**, *6* (9), 8432–8438. <https://doi.org/10.1021/nn303309z>.
- (264) Gao, W.; Uygun, A.; Wang, J. Hydrogen-Bubble-Propelled Zinc-Based Microrockets in Strongly Acidic Media. *J. Am. Chem. Soc.* **2012**, *134* (2), 897–900. <https://doi.org/10.1021/ja210874s>.
- (265) Sattayasamitsathit, S.; Kou, H.; Gao, W.; Thavarajah, W.; Kaufmann, K.; Zhang, L.; Wang, J. Fully Loaded Micromotors for Combinatorial Delivery and Autonomous Release of Cargoes. *Small* **2014**, *10* (14), 2830–2833. <https://doi.org/10.1002/smll.201303646>.
- (266) Gao, W.; Feng, X.; Pei, A.; Gu, Y.; Li, J.; Wang, J. Seawater-Driven Magnesium Based Janus Micromotors for Environmental Remediation. *Nanoscale* **2013**, *5* (11), 4696–4700. <https://doi.org/10.1039/C3NR01458D>.
- (267) Mou, F.; Chen, C.; Ma, H.; Yin, Y.; Wu, Q.; Guan, J. Self-Propelled Micromotors Driven by the Magnesium–Water Reaction and Their Hemolytic Properties. *Angew. Chem.* **2013**, *125* (28), 7349–7353. <https://doi.org/10.1002/ange.201300913>.
- (268) Mou, F.; Chen, C.; Zhong, Q.; Yin, Y.; Ma, H.; Guan, J. Autonomous Motion and Temperature- Controlled Drug Delivery of Mg / Pt-Poly (N- Isopropylacrylamide ) Janus Micromotors Driven by Simulated Body Fluid and Blood Plasma. *ACS Appl. Mater. Interfaces* **2014**, *6* (12), 9897–9903. <https://doi.org/10.1021/am502729y>.
- (269) Chen, C.; Karshalev, E.; Li, J.; Soto, F.; Castillo, R.; Campos, I.; Mou, F.; Guan, J.; Wang, J. Transient Micromotors That Disappear When No Longer Needed. *ACS Nano* **2016**, *10* (11), 10389–10396. <https://doi.org/10.1021/acsnano.6b06256>.
- (270) Zhou, M.; Hou, T.; Li, J.; Yu, S.; Xu, Z.; Yin, M.; Wang, J.; Wang, X. Self-Propelled and Targeted Drug Delivery of Poly(Aspartic Acid)/Iron–Zinc Microrocket in the Stomach. *ACS Nano* **2019**, *13* (2), 1324–1332. <https://doi.org/10.1021/acsnano.8b06773>.
- (271) Jia, Y.; Dong, W.; Feng, X.; Li, J.; Li, J. A Self-Powered Kinesin-Microtubule System for Smart Cargo Delivery. *Nanoscale* **2014**, *7* (1), 82–85. <https://doi.org/10.1039/C4NR04454A>.
- (272) Guix, M.; Meyer, A. K.; Koch, B.; Schmidt, O. G. Carbonate-Based Janus Micromotors Moving in Ultra-Light Acidic Environment Generated by HeLa Cells in Situ. *Sci. Rep.* **2016**, *6* (1), 21701–21701. <https://doi.org/10.1038/srep21701>.
- (273) Ismagilov, R. F.; Schwartz, A.; Bowden, N.; Whitesides, G. M. Autonomous Movement and Self-Assembly. *Angew. Chem. Int. Ed.* **2002**, *41* (4), 652–654. [https://doi.org/10.1002/1521-3773\(20020215\)41:4<652::AID-ANIE652>3.0.CO;2-U](https://doi.org/10.1002/1521-3773(20020215)41:4<652::AID-ANIE652>3.0.CO;2-U).
- (274) Paxton, W. F.; Kistler, K. C.; Olmeda, C. C.; Sen, A.; St. Angelo, S. K.; Cao, Y.; Mallouk, T. E.; Lammert, P. E.; Crespi, V. H. Catalytic Nanomotors: Autonomous Movement of Striped Nanorods. *J. Am. Chem. Soc.* **2004**, *126* (41), 13424–13431. <https://doi.org/10.1021/ja047697z>.
- (275) Fournier-Bidoz, S.; Arsenaault, A. C.; Manners, I.; Ozin, G. A. Synthetic Self-Propelled Nanorotors. *Chem. Commun.* **2005**, No. 4, 441–443. <https://doi.org/10.1039/B414896G>.
- (276) Lee, T. C.; Alarcón-Correa, M.; Miksch, C.; Hahn, K.; Gibbs, J. G.; Fischer, P. Self-Propelling Nanomotors in the Presence of Strong Brownian Forces. *Nano Lett.* **2014**, *14* (5), 2407–2412. <https://doi.org/10.1021/nl500068n>.
- (277) Di Leonardo, R. Controlled Collective Motions. *Nat. Mater.* **2016**, *15* (10), 1057–1058. <https://doi.org/10.1038/nmat4761>.
- (278) Zhou, L.; Zhang, H.; Bao, H.; Wei, Y.; Fu, H.; Cai, W. Monodispersed Snowman-Like Ag-MoS<sub>2</sub> Janus Nanoparticles as Chemically Self-Propelled Nanomotors. *ACS Appl. Nano Mater.* **2020**, *3* (1), 624–632. <https://doi.org/10.1021/acsnm.9b02159>.
- (279) Xing, Y.; Zhou, M.; Du, X.; Li, X.; Li, J.; Xu, T.; Zhang, X. Hollow Mesoporous Carbon@Pt Janus Nanomotors with Dual Response of H<sub>2</sub>O<sub>2</sub> and Near-Infrared Light for Active Cargo Delivery. *Appl. Mater. Today* **2019**, *17*, 85–91. <https://doi.org/10.1016/j.apmt.2019.07.017>.
- (280) Katuri, J.; Uspal, W. E.; Simmchen, J.; Miguel-López, A.; Sánchez, S. Cross-Stream Migration of Active Particles. *Sci. Adv.* **2018**, *4* (1), eaao1755. <https://doi.org/10.1126/sciadv.aao1755>.
- (281) Katuri, J.; Caballero, D.; Voituriez, R.; Samitier, J.; Sanchez, S. Directed Flow of Micromotors through Alignment Interactions with Micropatterned Ratchets. *ACS Nano* **2018**, *12* (7), 7282–7291. <https://doi.org/10.1021/acsnano.8b03494>.
- (282) Palacios, L. S.; Katuri, J.; Pagonabarraga, I.; Sánchez, S. Guidance of Active Particles at Liquid–Liquid Interfaces near Surfaces. *Soft Matter* **2019**, *15* (32), 6581–6588. <https://doi.org/10.1039/C9SM01016E>.
- (283) Gomez-Solano, J. R.; Blokhuis, A.; Bechinger, C. Dynamics of Self-Propelled Janus Particles in Viscoelastic Fluids. *Phys. Rev. Lett.* **2016**, *116* (13), 138301. <https://doi.org/10.1103/PhysRevLett.116.138301>.
- (284) Popescu, M. N.; Uspal, W. E.; Bechinger, C.; Fischer, P. Chemotaxis of Active Janus Nanoparticles. *Nano Lett.* **2018**, *18* (9), 5345–5349. <https://doi.org/10.1021/acs.nanolett.8b02572>.
- (285) Berthier, L.; Flenner, E.; Szamel, G. Glassy Dynamics in Dense Systems of Active Particles. *J. Chem. Phys.* **2019**, *150* (20), 200901. <https://doi.org/10.1063/1.5093240>.
- (286) Lavergne, F. A.; Wendehenne, H.; Bäuerle, T.; Bechinger, C. Group Formation and Cohesion of Active Particles with Visual Perception-Dependent Motility. *Science* **2019**, *364* (6435), 70–74. <https://doi.org/10.1126/science.aau5347>.
- (287) Simmchen, J.; Katuri, J.; Uspal, W. E.; Popescu, M. N.; Tasinkevych, M.; Sánchez, S. Topographical Pathways Guide Chemical Microswimmers. *Nat. Commun.* **2016**, *7* (1), 10598. <https://doi.org/10.1038/ncomms10598>.
- (288) Volpe, G.; Buttinoni, I.; Vogt, D.; Kümmerer, H.-J.; Bechinger, C. Microswimmers in Patterned Environments. *Soft Matter* **2011**, *7* (19), 8810–8815. <https://doi.org/10.1039/C1SM05960B>.

- (289) Solovev, A. A.; Xi, W.; Gracias, D. H.; Harazim, S. M.; Deneke, C.; Sanchez, S.; Schmidt, O. G. Self-Propelled Nanotools. *ACS Nano* **2012**, *6* (2), 1751–1756.
- (290) Magdanz, V.; Stoychev, G.; Ionov, L.; Sanchez, S.; Schmidt, O. G. Stimuli-Responsive Microjets with Reconfigurable Shape. *Angew. Chem.* **2014**, *53*, 2673–2677. <https://doi.org/10.1002/anie.201308610>.
- (291) Solovev, A. A.; Sanchez, S.; Mei, Y.; Schmidt, O. G. Tunable Catalytic Tubular Micro-Pumps Operating at Low Concentrations of Hydrogen Peroxide. *Phys. Chem. Chem. Phys.* **2011**, *13* (21), 10131–10135. <https://doi.org/10.1039/C1CP20542K>.
- (292) Parmar, J.; Vilela, D.; Pellicer, E.; Esqué-de los Ojos, D.; Sort, J.; Sánchez, S. Reusable and Long-Lasting Active Microcleaners for Heterogeneous Water Remediation. *Adv. Funct. Mater.* **2016**, *26* (23), 4152–4161. <https://doi.org/10.1002/adfm.201600381>.
- (293) Paxton, W. F.; Kistler, K. C.; Olmeda, C. C.; Sen, A.; St. Angelo, S. K.; Cao, Y.; Mallouk, T. E.; Lammert, P. E.; Crespi, V. H. Catalytic Nanomotors: Autonomous Movement of Striped Nanorods. *J. Am. Chem. Soc.* **2004**, *126* (41), 13424–13431. <https://doi.org/10.1021/ja047697z>.
- (294) Paxton, W. F.; Baker, P. T.; Kline, T. R.; Wang, Y.; Mallouk, T. E.; Sen, A. Catalytically Induced Electrokinetics for Motors and Micropumps. *J. Am. Chem. Soc.* **2006**, *128* (46), 14881–14888. <https://doi.org/10.1021/ja0643164>.
- (295) Wang, Y.; Hernandez, R. M.; Bartlett, D. J.; Bingham, J. M.; Kline, T. R.; Sen, A.; Mallouk, T. E. Bipolar Electrochemical Mechanism for the Propulsion of Catalytic Nanomotors in Hydrogen Peroxide Solutions. *Langmuir* **2006**, *22* (25), 10451–10456. <https://doi.org/10.1021/la0615950>.
- (296) Liu, R.; Sen, A. Autonomous Nanomotor Based on Copper–Platinum Segmented Nanobattery. *J. Am. Chem. Soc.* **2011**, *133* (50), 20064–20067. <https://doi.org/10.1021/ja2082735>.
- (297) Laocharoensuk, R.; Burdick, J.; Wang, J. Carbon-Nanotube-Induced Acceleration of Catalytic Nanomotors. *ACS Nano* **2008**, *2* (5), 1069–1075. <https://doi.org/10.1021/nm800154g>.
- (298) Demirok, U. K.; Laocharoensuk, R.; Manesh, K. M.; Wang, J. Ultrafast Catalytic Alloy Nanomotors. *Angew. Chem. Int. Ed.* **2008**, *47* (48), 9349–9351. <https://doi.org/10.1002/anie.200803841>.
- (299) Solovev, A. A.; Sanchez, S.; Pumera, M.; Mei, Y. F.; Schmidt, O. G. Magnetic Control of Tubular Catalytic Microbots for the Transport, Assembly, and Delivery of Micro-Objects. *Adv. Funct. Mater.* **2010**, *20*, 2430–2435. <https://doi.org/10.1002/adfm.200902376>.
- (300) Sanchez, S.; Solovev, A. A.; Schulze, S.; Schmidt, O. G. Controlled Manipulation of Multiple Cells Using Catalytic Microbots. *Chem. Commun.* **2010**, *47* (2), 698–700. <https://doi.org/10.1039/C0CC04126B>.
- (301) Wilson, D. A.; Nolte, R. J. M.; van Hest, J. C. M. Autonomous Movement of Platinum-Loaded Stomatocytes. *Nat. Chem.* **2012**, *4* (4), 268–274. <https://doi.org/10.1038/nchem.1281>.
- (302) Pijpers, I. A. B.; Cao, S.; Llopis-Lorente, A.; Zhu, J.; Song, S.; Joosten, R. R. M.; Meng, F.; Friedrich, H.; Williams, D. S.; Sánchez, S.; van Hest, J. C. M.; Abdelmohsen, L. K. E. A. Hybrid Biodegradable Nanomotors through Compartmentalized Synthesis. *Nano Lett.* **2020**, *20* (6), 4472–4480. <https://doi.org/10.1021/acs.nanolett.0c01268>.
- (303) Wu, Z.; Wu, Y.; He, W.; Lin, X.; Sun, J.; He, Q. Self-Propelled Polymer-Based Multilayer Nanorockets for Transportation and Drug Release. *Angew. Chem. Int. Ed.* **2013**, *52* (27), 7000–7003. <https://doi.org/10.1002/anie.201301643>.
- (304) Tu, Y.; Peng, F.; Sui, X.; Men, Y.; White, P. B.; van Hest, J. C. M.; Wilson, D. A. Self-Propelled Supramolecular Nanomotors with Temperature-Responsive Speed Regulation. *Nat. Chem.* **2017**, *9* (5), 480–486. <https://doi.org/10.1038/nchem.2674>.
- (305) Peng, F.; Tu, Y.; Men, Y.; Hest, J. C. M. van; Wilson, D. A. Supramolecular Adaptive Nanomotors with Magnetotaxis Behavior. *Adv. Mater.* **2017**, *29* (6), 1604996. <https://doi.org/10.1002/adma.201604996>.
- (306) Peng, F.; Tu, Y.; van Hest, J. C. M.; Wilson, D. A. Self-Guided Supramolecular Cargo-Loaded Nanomotors with Chemotactic Behavior towards Cells. *Angew. Chem. Int. Ed.* **2015**, *54* (40), 11662–11665. <https://doi.org/10.1002/anie.201504186>.
- (307) Tu, Y.; Peng, F.; André, A. A. M.; Men, Y.; Srinivas, M.; Wilson, D. A. Biodegradable Hybrid Stomatocyte Nanomotors for Drug Delivery. *ACS Nano* **2017**, *11* (2), 1957–1963. <https://doi.org/10.1021/acsnano.6b08079>.
- (308) Tu, Y.; Peng, F.; White, P. B.; Wilson, D. A. Redox-Sensitive Stomatocyte Nanomotors: Destruction and Drug Release in the Presence of Glutathione. *Angew. Chem. Int. Ed.* **2017**, *56* (26), 7620–7624. <https://doi.org/10.1002/anie.201703276>.
- (309) Ortiz-Rivera, I.; Mathesh, M.; Wilson, D. A. A Supramolecular Approach to Nanoscale Motion: Polymersome-Based Self-Propelled Nanomotors. *Acc. Chem. Res.* **2018**, *51* (9), 1891–1900. <https://doi.org/10.1021/acs.accounts.8b00199>.
- (310) Parmar, J.; Villa, K.; Vilela, D.; Sánchez, S. Platinum-Free Cobalt Ferrite Based Micromotors for Antibiotic Removal. *Appl. Mater. Today* **2017**, *9*, 605–611. <https://doi.org/10.1016/j.apmt.2017.11.002>.
- (311) Butler, P. J.; Dey, K. K.; Sen, A. Impulsive Enzymes: A New Force in Mechanobiology. *Cell. Mol. Bioeng.* **2015**, *8* (1), 106–118. <https://doi.org/10.1007/s12195-014-0376-1>.
- (312) Ma, X.; Hortelão, A. C.; Patiño, T.; Sánchez, S. Enzyme Catalysis To Power Micro/Nanomachines. *ACS Nano* **2016**, *10* (10), 9111–9122. <https://doi.org/10.1021/acsnano.6b04108>.
- (313) Zhao, X.; Gentile, K.; Mohajerani, F.; Sen, A. Powering Motion with Enzymes. *Acc. Chem. Res.* **2018**, *51* (10), 2373–2381. <https://doi.org/10.1021/acs.accounts.8b00286>.
- (314) Wang, J.; Toebes, B. J.; Plachokova, A. S.; Liu, Q.; Deng, D.; Jansen, J. A.; Yang, F.; Wilson, D. A. Self-Propelled PLGA Micromotor with Chemotactic Response to Inflammation. *Adv. Healthc. Mater.* **2020**, *9* (7), 1901710. <https://doi.org/10.1002/adhm.201901710>.
- (315) Poddar, A.; Bandopadhyay, A.; Chakraborty, S. Activated Micromotor Propulsion by Enzyme Catalysis in a Biofluid Medium. *Appl. Phys. Lett.* **2019**, *114* (5). <https://doi.org/10.1063/1.5081751>.
- (316) Patiño, T.; Feiner-Gracia, N.; Arqué, X.; Miguel-López, A.; Jannasch, A.; Stumpp, T.; Schäffer, E.; Albertazzi, L.; Sánchez, S. Influence of Enzyme Quantity and Distribution on the Self-Propulsion of Non-Janus Urease-Powered Micromotors. *J. Am. Chem. Soc.* **2018**, *140* (25), 7896–7903. <https://doi.org/10.1021/jacs.8b03460>.
- (317) Ma, X.; Wang, X.; Hahn, K.; Sánchez, S.; Xing, M.; Wang, X.; Hahn, K.; Sa, S. Motion Control of Urea-Powered Biocompatible Hollow Microcapsules. *ACS Nano* **2016**, *10* (3), 3597–3605. <https://doi.org/10.1021/acsnano.5b08067>.



- (318) You, Y.; Xu, D.; Pan, X.; Ma, X. Self-Propelled Enzymatic Nanomotors for Enhancing Synergetic Photodynamic and Starvation Therapy by Self-Accelerated Cascade Reactions. *Appl. Mater. Today* **2019**, *16*, 508–517. <https://doi.org/10.1016/j.apmt.2019.07.008>.
- (319) Dey, K. K.; Zhao, X.; Tansi, B. M.; Méndez-Ortiz, W. J.; Córdova-Figueroa, U. M.; Golestanian, R.; Sen, A. Micromotors Powered by Enzyme Catalysis. *Nano Lett.* **2015**, *15* (12), 8311–8315. <https://doi.org/10.1021/acs.nanolett.5b03935>.
- (320) Arqué, X.; Romero-Rivera, A.; Feixas, F.; Patiño, T.; Osuna, S.; Sánchez, S. Intrinsic Enzymatic Properties Modulate the Self-Propulsion of Micromotors. *Nat. Commun.* **2019**, *10* (1), 1–12. <https://doi.org/10.1038/s41467-019-10726-8>.
- (321) Patino, T.; Porchetta, A.; Jannasch, A.; Lladó, A.; Stumpp, T.; Schäffer, E.; Ricci, F.; Sánchez, S. Self-Sensing Enzyme-Powered Micromotors Equipped with PH-Responsive DNA Nanoswitches. *Nano Lett.* **2019**, *19* (6), 3440–3447. <https://doi.org/10.1021/acs.nanolett.8b04794>.
- (322) Sun, J.; Mathesh, M.; Li, W.; Wilson, D. A. Enzyme-Powered Nanomotors with Controlled Size for Biomedical Applications. *ACS Nano* **2019**, *13* (9), 10191–10200. <https://doi.org/10.1021/acs.nano.9b03358>.
- (323) Toebes, B. J.; Abdelmohsen, L. K. E. A.; Wilson, D. A. Enzyme-Driven Biodegradable Nanomotor Based on Tubular-Shaped Polymeric Vesicles. *Polym. Chem.* **2018**, *9* (23), 3190–3194. <https://doi.org/10.1039/C8PY00559A>.
- (324) Ma, X.; Jannasch, A.; Albrecht, U.-R.; Hahn, K.; Miguel-López, A.; Schäffer, E.; Sánchez, S. Enzyme-Powered Hollow Mesoporous Janus Nanomotors. *Nano Lett.* **2015**, *15* (10), 7043–7050. <https://doi.org/10.1021/acs.nanolett.5b03100>.
- (325) Abdelmohsen, L. K. E. A.; Nijemeisland, M.; Pawar, G. M.; Janssen, G.-J. A.; Nolte, R. J. M.; van Hest, J. C. M.; Wilson, D. A. Dynamic Loading and Unloading of Proteins in Polymeric Stomatocytes: Formation of an Enzyme-Loaded Supramolecular Nanomotor. *ACS Nano* **2016**, *10* (2), 2652–2660. <https://doi.org/10.1021/acs.nano.5b07689>.
- (326) Rucinskaite, G.; Thompson, S.; Paterson, S.; de la Rica, R. Enzyme-Coated Janus Nanoparticles That Selectively Bind Cell Receptors as a Function of the Concentration of Glucose. *Nanoscale* **2017**. <https://doi.org/10.1039/C7NR00298J>.
- (327) Toebes, B. J.; Cao, F.; Wilson, D. A. Spatial Control over Catalyst Positioning on Biodegradable Polymeric Nanomotors. *Nat. Commun.* **2019**, *10* (1), 1–6. <https://doi.org/10.1038/s41467-019-13288-x>.
- (328) Somasundar, A.; Ghosh, S.; Mohajerani, F.; Massenbun, L. N.; Yang, T.; Cremer, P. S.; Velegol, D.; Sen, A. Positive and Negative Chemotaxis of Enzyme-Coated Liposome Motors. *Nat. Nanotechnol.* **2019**, *14* (December). <https://doi.org/10.1038/s41565-019-0578-8>.
- (329) Ghosh, S.; Mohajerani, F.; Son, S.; Velegol, D.; Butler, P. J.; Sen, A. Motility of Enzyme-Powered Vesicles. *Nano Lett.* **2019**, *19* (9), 6019–6026. <https://doi.org/10.1021/acs.nanolett.9b01830>.
- (330) Sanchez, S.; Solovev, A. A.; Mei, Y.; Schmidt, O. G. Dynamics of Biocatalytic Microengines Mediated by Variable Friction Control. *J. Am. Chem. Soc.* **2010**, *132* (38), 13144–13145. <https://doi.org/10.1021/ja104362r>.
- (331) SCOGS (Select Committee on GRAS Substances) <https://www.cfsanappsexternal.fda.gov/scripts/fdc/?set=SCOGS&sort=Sortsubstance&order=ASC&startrow=1&type=basic&search=silica> (accessed May 2, 2021).
- (332) Schattling, P.; Thingholm, B.; Städler, B. Enhanced Diffusion of Glucose-Fueled Janus Particles. *Chem. Mater.* **2015**, *27* (21), 7412–7418. <https://doi.org/10.1021/acs.chemmater.5b03303>.
- (333) Guo, Z.; Liu, J.; Li, Y.; McDonald, J. A.; Bin Zulkifli, M. Y.; Khan, S. J.; Xie, L.; Gu, Z.; Kong, B.; Liang, K. Biocatalytic Metal–Organic Framework Nanomotors for Active Water Decontamination. *Chem. Commun.* **2020**, *56* (94), 14837–14840. <https://doi.org/10.1039/D0CC06429G>.
- (334) Pavel, I.-A.; Bunea, A.-I.; David, S.; Gáspár, S. Nanorods with Biocatalytically Induced Self-Electrophoresis. *ChemCatChem* **2014**, *6* (3), 866–872. <https://doi.org/10.1002/cctc.201301016>.
- (335) Bunea, A.-I.; Pavel, I.-A.; David, S.; Gaspar, S. Modification with Hemeproteins Increases the Diffusive Movement of Nanorods in Dilute Hydrogen Peroxide Solutions. *Chem. Commun.* **2013**, *49* (78), 8803–8805. <https://doi.org/10.1039/C3CC44614J>.
- (336) Mano, N.; Heller, A. Bioelectrochemical Propulsion. *J. Am. Chem. Soc.* **2005**, *127* (33), 11574–11575. <https://doi.org/10.1021/ja053937e>.
- (337) Pantarotto, D.; Browne, W. R.; Feringa, B. L. Autonomous Propulsion of Carbon Nanotubes Powered by a Multienzyme Ensemble. *Chem. Commun.* **2008**, No. 13, 1533–1535. <https://doi.org/10.1039/B715310D>.
- (338) Nijemeisland, M.; Abdelmohsen, L. K. E. A.; Huck, W. T. S.; Wilson, D. A.; van Hest, J. C. M. A Compartmentalized Out-of-Equilibrium Enzymatic Reaction Network for Sustained Autonomous Movement. *ACS Cent. Sci.* **2016**, *2* (11), 843–849. <https://doi.org/10.1021/acscentsci.6b00254>.
- (339) Che, H.; Zhu, J.; Song, S.; Mason, A. F.; Cao, S.; Pijpers, I. A. B.; Abdelmohsen, L. K. E. A.; Hest, J. C. M. van. ATP-Mediated Transient Behavior of Stomatocyte Nanosystems. *Angew. Chem. Int. Ed.* **2019**, *58* (37), 13113–13118. <https://doi.org/10.1002/anie.201906331>.
- (340) Kumar, B. V. V. S. P.; Patil, A. J.; Mann, S. Enzyme-Powered Motility in Buoyant Organoclay/DNA Protocells. *Nat. Chem.* **2018**, *10* (11), 1154–1163. <https://doi.org/10.1038/s41557-018-0119-3>.
- (341) Schattling, P. S.; Ramos-Docampo, M. A.; Salgueiriño, V.; Städler, B. Double-Fueled Janus Swimmers with Magnetotactic Behaviour. *ACS Nano* **2017**, *11* (4), 3973–3983. <https://doi.org/10.1021/acs.nano.7b00441>.
- (342) Joseph, A.; Contini, C.; Cecchin, D.; Nyberg, S.; Ruiz-Perez, L.; Gaitzsch, J.; Fullstone, G.; Tian, X.; Azizi, J.; Preston, J.; Volpe, G.; Battaglia, G. Chemotactic Synthetic Vesicles: Design and Applications in Blood-Brain Barrier Crossing. *Sci. Adv.* **2017**, *3* (8), e1700362–e1700362. <https://doi.org/10.1126/sciadv.1700362>.
- (343) Li, H.; Sun, Z.; Jiang, S.; Lai, X.; Böckler, A.; Huang, H.; Peng, F.; Liu, L.; Chen, Y. Tadpole-like Unimolecular Nanomotor with Sub-100 Nm Size Swims in a Tumor Microenvironment Model. *Nano Lett.* **2019**, *19* (12), 8749–8757. <https://doi.org/10.1021/acs.nanolett.9b03456>.
- (344) Wu, Y.; Lin, X.; Wu, Z.; Möhwald, H.; He, Q. Self-Propelled Polymer Multilayer Janus Capsules for Effective Drug Delivery and Light-Triggered Release. *ACS Appl. Mater. Interfaces* **2014**, *6* (13), 10476–10481. <https://doi.org/10.1021/am502458h>.
- (345) Wu, Z.; Lin, X.; Zou, X.; Sun, J.; He, Q. Biodegradable Protein-Based Rockets for Drug Transportation and Light-Triggered Release. *ACS Appl. Mater. Interfaces* **2015**, *7* (1), 250–255. <https://doi.org/10.1021/am507680u>.

- (346) Tang, S.; Zhang, F.; Gong, H.; Wei, F.; Zhuang, J.; Karshalev, E.; Esteban-Fernández de Ávila, B.; Huang, C.; Zhou, Z.; Li, Z.; Yin, L.; Dong, H.; Fang, R. H.; Zhang, X.; Zhang, L.; Wang, J. Enzyme-Powered Janus Platelet Cell Robots for Active and Targeted Drug Delivery. *Sci. Robot.* **2020**, *5* (43), eaba6137–eaba6137. <https://doi.org/10.1126/scirobotics.aba6137>.
- (347) Brown, A.; Poon, W. Ionic Effects in Self-Propelled Pt-Coated Janus Swimmers. *Soft Matter* **2014**, *10* (22), 4016–4027. <https://doi.org/10.1039/C4SM00340C>.
- (348) De Corato, M.; Arqué, X.; Patiño, T.; Arroyo, M.; Sánchez, S.; Pagonabarraga, I. Self-Propulsion of Active Colloids via Ion Release: Theory and Experiments. *Phys. Rev. Lett.* **2020**, *124* (10), 108001. <https://doi.org/10.1103/PhysRevLett.124.108001>.
- (349) Gibbs, J. G.; Zhao, Y.-P. Autonomously Motile Catalytic Nanomotors by Bubble Propulsion. *Appl. Phys. Lett.* **2009**, *94* (16), 163104. <https://doi.org/10.1063/1.3122346>.
- (350) Arqué, X.; Andrés, X.; Mestre, R.; Ciraulo, B.; Ortega Arroyo, J.; Quidant, R.; Patiño, T.; Sánchez, S. Ionic Species Affect the Self-Propulsion of Urease-Powered Micromotors. *Research* **2020**, *2020*, 1–14. <https://doi.org/10.34133/2020/2424972>.
- (351) Ramos-Docampo, M. A.; Fernández-Medina, M.; Taipaleenmäki, E.; Hovorka, O.; Salgueiriño, V.; Städler, B. Microwimmers with Heat Delivery Capacity for 3D Cell Spheroid Penetration. *ACS Nano* **2019**, *13* (10), 12192–12205. <https://doi.org/10.1021/acsnano.9b06869>.
- (352) Peng, F.; Tu, Y.; Adhikari, A.; Hintzen, J. C. J.; Lowik, D. W. P. M.; Wilson, D. A. Peptide Functionalized Nanomotor as Efficient Cell Penetrating Tool. *Chem. Commun.* **2016**, *53* (6), 1088–1091. <https://doi.org/10.1039/C6CC09169E>.
- (353) Peng, F.; Men, Y.; Tu, Y.; Chen, Y.; Wilson, D. A. Nanomotor-Based Strategy for Enhanced Penetration across Vasculature Model. *Adv. Funct. Mater.* **2018**, *28* (25), 1706117. <https://doi.org/10.1002/adfm.201706117>.
- (354) Erkoc, P.; Yasa, I. C.; Ceylan, H.; Yasa, O.; Alapan, Y.; Sitti, M. Mobile Microrobots for Active Therapeutic Delivery. *Adv. Mater.* **2019**, *2* (1), 1800064. <https://doi.org/10.1002/admp.201800064>.
- (355) Llopis-Lorente, A.; García-Fernández, A.; Lucena-Sánchez, E.; Díez, P.; Sancenón, F.; Villalonga, R.; Wilson, D. A.; Martínez-Mañez, R. Stimulus-Responsive Nanomotors Based on Gated Enzyme-Powered Janus Au–Mesoporous Silica Nanoparticles for Enhanced Cargo Delivery. *Chem. Commun.* **2019**, *55* (87), 13164–13167. <https://doi.org/10.1039/C9CC07250K>.
- (356) Llopis-Lorente, A.; García-Fernández, A.; Murillo-Cremaes, N.; Hortela, A. C.; Patiño, T.; Villalonga, R.; Sancenón, F.; Martínez-Mañez, R.; Sánchez, S. Enzyme-Powered Gated Mesoporous Silica Nanomotors for on-Command Intracellular Payload Delivery. *ACS Nano* **2019**, *13* (10), 12171–12183. <https://doi.org/10.1021/acsnano.9b06706>.
- (357) Orozco, J.; Jurado-Sánchez, B.; Wagner, G.; Gao, W.; Vazquez-Duhalt, R.; Sattayasamitsathit, S.; Galarnyk, M.; Cortés, A.; Saintillan, D.; Wang, J. Bubble-Propelled Micromotors for Enhanced Transport of Passive Tracers. *Langmuir* **2014**, *30* (18), 5082–5087. <https://doi.org/10.1021/la500819r>.
- (358) Ju, G.; Cheng, M.; Xiao, M.; Xu, J.; Pan, K.; Wang, X.; Zhang, Y.; Shi, F. Smart Transportation Between Three Phases Through a Stimulus-Responsive Functionally Cooperating Device. *Adv. Mater.* **2013**, *25* (21), 2915–2919. <https://doi.org/10.1002/adma.201205240>.
- (359) Baraban, L.; Tasinkevych, M.; Popescu, M. N.; Sanchez, S.; Dietrich, S.; Schmidt, O. G. Transport of Cargo by Catalytic Janus Micro-Motors. *Soft Matter* **2012**, *8* (1), 48–52. <https://doi.org/10.1039/C1SM06512B>.
- (360) Sanchez, S.; Solovev, A. A.; Harazim, S. M.; Schmidt, O. G. Microbots Swimming in the Flowing Streams of Microfluidic Channels. *J. Am. Chem. Soc.* **2011**, *133* (4), 701–703. <https://doi.org/10.1021/ja109627w>.
- (361) Burdick, J.; Laocharoensuk, R.; Wheat, P. M.; Posner, J. D.; Wang, J. Synthetic Nanomotors in Microchannel Networks: Directional Microchip Motion and Controlled Manipulation of Cargo. *J. Am. Chem. Soc.* **2008**, *130* (26), 8164–8165. <https://doi.org/10.1021/ja803529u>.
- (362) Kim, S.; Qiu, F.; Kim, S.; Ghanbari, A.; Moon, C.; Zhang, L.; Nelson, B. J.; Choi, H. Fabrication and Characterization of Magnetic Microrobots for Three-Dimensional Cell Culture and Targeted Transportation. *Adv. Mater.* **2013**, *25* (41), 5863–5868. <https://doi.org/10.1002/adma.201301484>.
- (363) Hu, N.; Zhang, B.; Gai, M.; Zheng, C.; Frueh, J.; He, Q. Forecastable and Guidable Bubble-Propelled Microplate Motors for Cell Transport. *Macromol. Rapid Commun.* **2017**, *38* (11), 1600795. <https://doi.org/10.1002/marc.201600795>.
- (364) Yoshizumi, Y.; Okubo, K.; Yokokawa, M.; Suzuki, H. Programmed Transport and Release of Cells by Self-Propelled Micromotors. *Langmuir* **2016**, *32* (37), 9381–9388. <https://doi.org/10.1021/acs.langmuir.5b04206>.
- (365) Gao, W.; Wang, J. Synthetic Micro/Nanomotors in Drug Delivery. *Nanoscale* **2014**, *6* (18), 10486–10494. <https://doi.org/10.1039/C4NR03124E>.
- (366) Medina-Sánchez, M.; Xu, H.; Schmidt, O. G. Micro- and Nano-Motors: The New Generation of Drug Carriers. *Ther. Deliv.* **2018**, *9* (4), 303–316. <https://doi.org/10.4155/tde-2017-0113>.
- (367) Alapan, Y.; Bozuyuk, U.; Erkoc, P.; Karacakol, A. C.; Sitti, M. Multifunctional Surface Microrollers for Targeted Cargo Delivery in Physiological Blood Flow. *Sci. Robot.* **2020**, *5* (42), eaba5726–eaba5726. <https://doi.org/10.1126/scirobotics.aba5726>.
- (368) Li, J.; Thamphiwatana, S.; Liu, W.; Esteban-Fernández de Ávila, B.; Angsantikul, P.; Sandraz, E.; Wang, J.; Xu, T.; Soto, F.; Ramez, V.; Wang, X.; Gao, W.; Zhang, L.; Wang, J. Enteric Micromotor Can Selectively Position and Spontaneously Propel in the Gastrointestinal Tract. *ACS Nano* **2016**, *10* (10), 9536–9542. <https://doi.org/10.1021/acsnano.6b04795>.
- (369) Díez, P.; Lucena-Sánchez, E.; Escudero, A.; Llopis-Lorente, A.; Villalonga, R.; Martínez-Mañez, R. Ultrafast Directional Janus Pt–Mesoporous Silica Nanomotors for Smart Drug Delivery. *ACS Nano* **2021**, *15* (3), 4467–4480. <https://doi.org/10.1021/acsnano.0c08404>.
- (370) Vyskočil, J.; Mayorga-Martinez, C. C.; Jablonská, E.; Novotný, F.; Ruml, T.; Pumera, M. Cancer Cells Microsurgery via Asymmetric Bent Surface Au/Ag/Ni Microrobotic Scalpels Through a Transversal Rotating Magnetic Field. *ACS Nano* **2020**, *14* (7), 8247–8256. <https://doi.org/10.1021/acsnano.0c01705>.
- (371) Diller, E.; Sitti, M. Three-Dimensional Programmable Assembly by Untethered Magnetic Robotic Micro-Grippers. *Adv. Funct. Mater.* **2014**, *24* (28), 4397–4404. <https://doi.org/10.1002/adfm.201400275>.

- (372) Chatzipirpiridis, G.; Ergeneman, O.; Pokki, J.; Ullrich, F.; Fusco, S.; Ortega, J. A.; Sivaraman, K. M.; Nelson, B. J.; Pané, S. Electroforming of Implantable Tubular Magnetic Microrobots for Wireless Ophthalmologic Applications. *Adv. Healthc. Mater.* **2015**, *4* (2), 209–214. <https://doi.org/10.1002/adhm.201400256>.
- (373) Mazur, F.; Fernández-Medina, M.; Gal, N.; Hovorka, O.; Chandrawati, R.; Städler, B. Locomotion of Micromotors Due to Liposome Disintegration. *Langmuir* **2020**. <https://doi.org/10.1021/acs.langmuir.9b03509>.
- (374) Gao, W.; Dong, R.; Thamphiwatana, S.; Li, J.; Gao, W.; Zhang, L.; Wang, J. Artificial Micromotors in the Mouse's Stomach: A Step toward in Vivo Use of Synthetic Motors. *ACS Nano* **2015**, *9* (1), 117–123. <https://doi.org/10.1021/nn507097k>.
- (375) Esteban-Fernández de Ávila, B.; Angsantikul, P.; Li, J.; Angel Lopez-Ramirez, M.; Ramirez-Herrera, D. E.; Thamphiwatana, S.; Chen, C.; Delezuk, J.; Samakapiruk, R.; Ramez, V.; Obonyo, M.; Zhang, L.; Wang, J. Micromotor-Enabled Active Drug Delivery for in Vivo Treatment of Stomach Infection. *Nat. Commun.* **2017**, *8* (1), 272–272. <https://doi.org/10.1038/s41467-017-00309-w>.
- (376) von Maltzahn, G.; Park, J.-H. H.; Lin, K. Y.; Singh, N.; Schwöppe, C.; Mesters, R.; Berdel, W. E.; Ruoslahti, E.; Sailor, M. J.; Bhatia, S. N. Nanoparticles That Communicate in Vivo to Amplify Tumour Targeting. *Nat. Mater.* **2011**, *10* (7), 545–552. <https://doi.org/10.1038/nmat3049>.
- (377) Hong, Y.; Blackman, N. M. K.; Kopp, N. D.; Sen, A.; Velegol, D. Chemotaxis of Nonbiological Colloidal Rods. *Phys. Rev. Lett.* **2007**, *99* (17), 178103. <https://doi.org/10.1103/PhysRevLett.99.178103>.
- (378) Baraban, L.; Harazim, S. M.; Sanchez, S.; Schmidt, O. G. Chemotactic Behavior of Catalytic Motors in Microfluidic Channels. *Angew. Chem. Int. Ed.* **2013**, *52* (21), 5552–5556. <https://doi.org/10.1002/anie.201301460>.
- (379) Dey, K. K.; Das, S.; Poyton, M. F.; Sengupta, S.; Butler, P. J.; Cremer, P. S.; Sen, A. Chemotactic Separation of Enzymes. **2014**, No. 12, 11941–11949.
- (380) Zhao, X.; Palacci, H.; Yadav, V.; Spiering, M. M.; Gilson, M. K.; Butler, P. J.; Hess, H.; Benkovic, S. J.; Sen, A. Substrate-Driven Chemotactic Assembly in an Enzyme Cascade. *Nat. Chem.* **2018**, *10* (3), 311–317. <https://doi.org/10.1038/nchem.2905>.
- (381) Gao, W.; Pei, A.; Feng, X.; Hennessy, C.; Wang, J. Organized Self-Assembly of Janus Micromotors with Hydrophobic Hemispheres. *J. Am. Chem. Soc.* **2013**, *135* (3), 998–1001. <https://doi.org/10.1021/ja311455k>.
- (382) Wang, W.; Duan, W.; Sen, A.; Mallouk, T. E. Catalytically Powered Dynamic Assembly of Rod-Shaped Nanomotors and Passive Tracer Particles. *Proc. Natl. Acad. Sci.* **2013**, *110* (44), 17744–17749. <https://doi.org/10.1073/pnas.1311543110>.
- (383) Aubret, A.; Youssef, M.; Sacanna, S.; Palacci, J. Targeted Assembly and Synchronization of Self-Spinning Microgears. *Nat. Phys.* **2018**, *14* (11), 1114–1118. <https://doi.org/10.1038/s41567-018-0227-4>.
- (384) Dong, B.; Zhou, T.; Zhang, H.; Li, C. Y. Directed Self-Assembly of Nanoparticles for Nanomotors. *ACS Nano* **2013**, *7* (6), 5192–5198. <https://doi.org/10.1021/nn400925q>.
- (385) Liu, C.; Xu, T.; Xu, L. P.; Zhang, X. Controllable Swarming and Assembly of Micro/Nanomachines. *Micromachines* **2017**, *9* (1). <https://doi.org/10.3390/mi9010010>.
- (386) Snezhko, A.; Aranson, I. S. Magnetic Manipulation of Self-Assembled Colloidal Asters. *Nat. Mater.* **2011**, *10* (9), 698–703. <https://doi.org/10.1038/nmat3083>.
- (387) Wang, W.; Duan, W.; Ahmed, S.; Sen, A.; Mallouk, T. E. From One to Many: Dynamic Assembly and Collective Behavior of Self-Propelled Colloidal Motors. **2015**. <https://doi.org/10.1021/acs.accounts.5b00025>.
- (388) Ahmed, S.; Gentekos, D. T.; Fink, C. A.; Mallouk, T. E. Self-Assembly of Nanorod Motors into Geometrically Regular Multimers and Their Propulsion by Ultrasound. *ACS Nano* **2014**, *8* (11), 11053–11060. <https://doi.org/10.1021/nn5039614>.
- (389) Ma, F.; Wang, S.; Wu, D. T.; Wu, N. Electric-Field-Induced Assembly and Propulsion of Chiral Colloidal Clusters. *Proc. Natl. Acad. Sci.* **2015**, *112* (20), 6307–6312. <https://doi.org/10.1073/pnas.1502141112>.
- (390) Martinez-Pedrero, F.; Tierno, P. Magnetic Propulsion of Self-Assembled Colloidal Carpets: Efficient Cargo Transport via a Conveyor-Belt Effect. *Phys. Rev. Appl.* **2015**, *3* (5), 051003. <https://doi.org/10.1103/PhysRevApplied.3.051003>.
- (391) Yan, J.; Han, M.; Zhang, J.; Xu, C.; Luijten, E.; Granick, S. Reconfiguring Active Particles by Electrostatic Imbalance. *Nat. Mater.* **2016**, *15* (10), 1095–1099. <https://doi.org/10.1038/nmat4696>.
- (392) Massana-Cid, H.; Meng, F.; Matsunaga, D.; Golestanian, R.; Tierno, P. Tunable Self-Healing of Magnetically Propelling Colloidal Carpets. *Nat. Commun.* **2019**, *10* (1), 2444. <https://doi.org/10.1038/s41467-019-10255-4>.
- (393) Hwang, G.; Paula, A. J.; Hunter, E. E.; Liu, Y.; Babeer, A.; Karabucak, B.; Stebe, K.; Kumar, V.; Steager, E.; Koo, H. Catalytic Antimicrobial Robots for Biofilm Eradication. *Sci. Robot.* **2019**, *4* (29). <https://doi.org/10.1126/scirobotics.aaw2388>.
- (394) Li, Z.; Zhang, H.; Wang, D.; Gao, C.; Sun, M.; Wu, Z.; He, Q. Reconfigurable Assembly of Active Liquid Metal Colloidal Cluster. *Angew. Chem. Int. Ed.* **2020**, *59* (45), 19884–19888. <https://doi.org/10.1002/anie.202007911>.
- (395) Vach, P. J.; Walker, D.; Fischer, P.; Fratzl, P.; Faivre, D. Pattern Formation and Collective Effects in Populations of Magnetic Microswimmers. *J. Phys. Appl. Phys.* **2017**, *50* (11), 11LT03. <https://doi.org/10.1088/1361-6463/aa5d36>.
- (396) Li, J.; Li, T.; Xu, T.; Kiristi, M.; Liu, W.; Wu, Z.; Wang, J. Magneto-Acoustic Hybrid Nanomotor. *Nano Lett.* **2015**, *15* (7), 4814–4821. <https://doi.org/10.1021/acs.nanolett.5b01945>.
- (397) Wang, W.; Duan, W.; Zhang, Z.; Sun, M.; Sen, A.; Mallouk, T. E. A Tale of Two Forces: Simultaneous Chemical and Acoustic Propulsion of Bimetallic Micromotors. *Chem. Commun.* **2014**, *51* (6), 1020–1023. <https://doi.org/10.1039/C4CC09149C>.
- (398) Ahmed, D.; Baasch, T.; Blondel, N.; Läubli, N.; Dual, J.; Nelson, B. J. Neutrophil-Inspired Propulsion in a Combined Acoustic and Magnetic Field. *Nat. Commun.* **2017**, *8* (1), 770. <https://doi.org/10.1038/s41467-017-00845-5>.
- (399) Ibele, M. E.; Lammert, P. E.; Crespi, V. H.; Sen, A. Emergent, Collective Oscillations of Self-Mobile Particles and Patterned Surfaces under Redox Conditions. *ACS Nano* **2010**, *4* (8), 4845–4851. <https://doi.org/10.1021/nn101289p>.
- (400) Bricard, A.; Caussin, J.-B.; Desreumaux, N.; Dauchot, O.; Bartolo, D. Emergence of Macroscopic Directed Motion in Populations of Motile Colloids. *Nature* **2013**, *503* (7474), 95–98. <https://doi.org/10.1038/nature12673>.
- (401) Duan, W.; Liu, R.; Sen, A. Transition between Collective Behaviors of Micromotors in Response to Different Stimuli. *J. Am. Chem. Soc.* **2013**, *135* (4), 1280–1283. <https://doi.org/10.1021/ja3120357>.



- (402) Hernández-Navarro, S.; Tierno, P.; Farrera, J. A.; Ignés-Mullol, J.; Sagués, F. Reconfigurable Swarms of Nematic Colloids Controlled by Photoactivated Surface Patterns. *Angew. Chem.* **2014**, *126* (40), 10872–10876. <https://doi.org/10.1002/ange.201406136>.
- (403) Ren, L.; Zhou, D.; Mao, Z.; Xu, P.; Huang, T. J.; Mallouk, T. E. Rheotaxis of Bimetallic Micromotors Driven by Chemical–Acoustic Hybrid Power. *ACS Nano* **2017**, *11* (10), 10591–10598. <https://doi.org/10.1021/acsnano.7b06107>.
- (404) Wang, X.; Hu, C.; Schurz, L.; De Marco, C.; Chen, X.; Pané, S.; Nelson, B. J. Surface–Chemistry-Mediated Control of Individual Magnetic Helical Microswimmers in a Swarm. *ACS Nano* **2018**, *12* (6), 6210–6217. <https://doi.org/10.1021/acsnano.8b02907>.
- (405) Yu, J.; Yang, L.; Zhang, L. Pattern Generation and Motion Control of a Vortex-like Paramagnetic Nanoparticle Swarm. *Int. J. Robot. Res.* **2018**, *37* (8), 912–930. <https://doi.org/10.1177/0278364918784366>.
- (406) Zhang, Y.; Yan, K.; Ji, F.; Zhang, L. Enhanced Removal of Toxic Heavy Metals Using Swarming Biohybrid Adsorbents. *Adv. Funct. Mater.* **2018**, *28* (52), 1806340. <https://doi.org/10.1002/adfm.201806340>.
- (407) Yu, J.; Wang, B.; Du, X.; Wang, Q.; Zhang, L. Ultra-Extensible Ribbon-like Magnetic Microswarm. *Nat. Commun.* **2018**, *9* (1), 3260. <https://doi.org/10.1038/s41467-018-05749-6>.
- (408) Deng, Z.; Mou, F.; Tang, S.; Xu, L.; Luo, M.; Guan, J. Swarming and Collective Migration of Micromotors under near Infrared Light. *Appl. Mater. Today* **2018**, *13*, 45–53. <https://doi.org/10.1016/j.apmt.2018.08.004>.
- (409) Ji, Y.; Lin, X.; Wu, Z.; Wu, Y.; Gao, W.; He, Q. Macroscale Chemotaxis from a Swarm of Bacteria-Mimicking Nanoswimmers. *Angew. Chem. Int. Ed.* **2019**, *58* (35), 12200–12205. <https://doi.org/10.1002/anie.201907733>.
- (410) Baker, R.; Kauffman, J. E.; Laskar, A.; Shklyaev, O. E.; Potomkin, M.; Dominguez-Rubio, L.; Shum, H.; Cruz-Rivera, Y.; Aranson, I. S.; Balazs, A. C.; Sen, A. Fight the Flow: The Role of Shear in Artificial Rheotaxis for Individual and Collective Motion. *Nanoscale* **2019**, *11* (22), 10944–10951. <https://doi.org/10.1039/C8NR10257K>.
- (411) Mou, F.; Zhang, J.; Wu, Z.; Du, S.; Zhang, Z.; Xu, L.; Guan, J. Phototactic Flocking of Photochemical Micromotors. *iScience* **2019**, *19*, 415–424. <https://doi.org/10.1016/j.isci.2019.07.050>.
- (412) Yu, J.; Wang, Q.; Li, M.; Liu, C.; Wang, L.; Xu, T.; Zhang, L. Characterizing Nanoparticle Swarms With Tuneable Concentrations for Enhanced Imaging Contrast. *IEEE Robot. Autom. Lett.* **2019**, *4* (3), 2942–2949. <https://doi.org/10.1109/LRA.2019.2924055>.
- (413) Xie, H.; Sun, M.; Fan, X.; Lin, Z.; Chen, W.; Wang, L.; Dong, L.; He, Q. Reconfigurable Magnetic Microrobot Swarm: Multimode Transformation, Locomotion, and Manipulation. *Sci. Robot.* **2019**, *4* (28), eaav8006. <https://doi.org/10.1126/scirobotics.aav8006>.
- (414) Yigit, B.; Alapan, Y.; Sitti, M. Programmable Collective Behavior in Dynamically Self-Assembled Mobile Microbotic Swarms. *Adv. Sci.* **2019**, *6* (6), 1801837. <https://doi.org/10.1002/advs.201801837>.
- (415) Tang, S.; Zhang, F.; Zhao, J.; Talaat, W.; Soto, F.; Karshalev, E.; Chen, C.; Hu, Z.; Lu, X.; Li, J.; Lin, Z.; Dong, H.; Zhang, X.; Nourhani, A.; Wang, J. Structure-Dependent Optical Modulation of Propulsion and Collective Behavior of Acoustic/Light-Driven Hybrid Microbowls. *Adv. Funct. Mater.* **2019**, *29* (23), 1809003. <https://doi.org/10.1002/adfm.201809003>.
- (416) Schuerle, S.; Soleimany, A. P.; Yeh, T.; Anand, G. M.; Häberli, M.; Fleming, H. E.; Mirkhani, N.; Qiu, F.; Hauert, S.; Wang, X.; Nelson, B. J.; Bhatia, S. N. Synthetic and Living Micropropellers for Convection-Enhanced Nanoparticle Transport. *Sci. Adv.* **2019**, *5* (4), eaav4803. <https://doi.org/10.1126/sciadv.aav4803>.
- (417) Jin, D.; Yu, J.; Yuan, K.; Zhang, L. Mimicking the Structure and Function of Ant Bridges in a Reconfigurable Microswarm for Electronic Applications. *ACS Nano* **2019**, *13* (5), 5999–6007. <https://doi.org/10.1021/acsnano.9b02139>.
- (418) Dong, X.; Sitti, M. Controlling Two-Dimensional Collective Formation and Cooperative Behavior of Magnetic Microrobot Swarms. *Int. J. Robot. Res.* **2020**, *39* (5), 617–638. <https://doi.org/10.1177/0278364920903107>.
- (419) Petrichenko, O.; Kitenbergs, G.; Brics, M.; Dubois, E.; Perzynski, R.; Cēbers, A. Swarming of Micron-Sized Hematite Cubes in a Rotating Magnetic Field – Experiments. *J. Magn. Magn. Mater.* **2020**, *500*, 166404. <https://doi.org/10.1016/j.jmmm.2020.166404>.
- (420) Wang, Q.; Wang, B.; Yu, J.; Schweizer, K.; Nelson, B. J.; Zhang, L. Reconfigurable Magnetic Microswarm for Thrombolysis under Ultrasound Imaging. In *2020 IEEE International Conference on Robotics and Automation (ICRA)*; 2020; pp 10285–10291. <https://doi.org/10.1109/ICRA40945.2020.9197432>.
- (421) Yigit, B.; Alapan, Y.; Sitti, M. Cohesive Self-Organization of Mobile Microbotic Swarms. *Soft Matter* **2020**, *16* (8), 1996–2004. <https://doi.org/10.1039/C9SM01284B>.
- (422) Liang, X.; Mou, F.; Huang, Z.; Zhang, J.; You, M.; Xu, L.; Luo, M.; Guan, J. Hierarchical Microswarms with Leader–Follower-Like Structures: Electrohydrodynamic Self-Organization and Multimode Collective Photoresponses. *Adv. Funct. Mater.* **2020**, *30* (16), 1–10. <https://doi.org/10.1002/adfm.201908602>.
- (423) Wu, C.; Dai, J.; Li, X.; Gao, L.; Wang, J.; Liu, J.; Zheng, J.; Zhan, X.; Chen, J.; Cheng, X.; Yang, M.; Tang, J. Ion-Exchange Enabled Synthetic Swarm. *Nat. Nanotechnol.* **2021**, *16* (3), 288–295. <https://doi.org/10.1038/s41565-020-00825-9>.
- (424) Wang, B.; Chan, K. F.; Yu, J.; Wang, Q.; Yang, L.; Chiu, P. W. Y.; Zhang, L. Reconfigurable Swarms of Ferromagnetic Colloids for Enhanced Local Hyperthermia. *Adv. Funct. Mater.* **2018**, *28* (25), 1705701. <https://doi.org/10.1002/adfm.201705701>.
- (425) Kagan, D.; Balasubramanian, S.; Wang, J. Chemically Triggered Swarming of Gold Microparticles. *Angew. Chem. Int. Ed.* **2011**, *50* (2), 503–506. <https://doi.org/10.1002/anie.201005078>.
- (426) Palacci, J.; Sacanna, S.; Steinberg, A. P.; Pine, D. J.; Chaikin, P. M. Living Crystals of Light-Activated Colloidal Surfers. *Science* **2013**, *339* (6122), 936–940. <https://doi.org/10.1126/science.1230020>.
- (427) Liu, J. F.; Jang, B.; Issadore, D.; Tsourkas, A. Use of Magnetic Fields and Nanoparticles to Trigger Drug Release and Improve Tumor Targeting. *WIREs Nanomedicine Nanobiotechnology* **2019**, *11* (6), e1571. <https://doi.org/10.1002/wnan.1571>.
- (428) Rotariu, O.; Strachan, N. J. C. Modelling Magnetic Carrier Particle Targeting in the Tumor Microvasculature for Cancer Treatment. *J. Magn. Magn. Mater.* **2005**, *293* (1), 639–646. <https://doi.org/10.1016/j.jmmm.2005.01.081>.

- (429) Bertrand, N.; Leroux, J.-C. The Journey of a Drug-Carrier in the Body: An Anatomico-Physiological Perspective. *J. Controlled Release* **2012**, *161* (2), 152–163. <https://doi.org/10.1016/j.jconrel.2011.09.098>.
- (430) Gibbs, J. G.; Zhao, Y. Self-Organized Multiconstituent Catalytic Nanomotors. *Small* **2010**, *6* (15), 1656–1662. <https://doi.org/10.1002/sml.201000415>.
- (431) Shklyaev, O. E.; Shum, H.; Sen, A.; Balazs, A. C. Harnessing Surface-Bound Enzymatic Reactions to Organize Microcapsules in Solution. *Sci. Adv.* **2016**, *2* (3).
- (432) Mou, F.; Li, X.; Xie, Q.; Zhang, J.; Xiong, K.; Xu, L.; Guan, J. Active Micromotor Systems Built from Passive Particles with Biomimetic Predator–Prey Interactions. *ACS Nano* **2020**, *14* (1), 406–414. <https://doi.org/10.1021/acsnano.9b05996>.
- (433) Theurkauff, I.; Cottin-Bizonne, C.; Palacci, J.; Ybert, C.; Bocquet, L. Dynamic Clustering in Active Colloidal Suspensions with Chemical Signaling. *Phys. Rev. Lett.* **2012**, *108* (26), 268303. <https://doi.org/10.1103/PhysRevLett.108.268303>.
- (434) Buttinoni, I.; Bialké, J.; Kümmel, F.; Löwen, H.; Bechinger, C.; Speck, T. Dynamical Clustering and Phase Separation in Suspensions of Self-Propelled Colloidal Particles. *Phys. Rev. Lett.* **2013**, *110* (23), 238301. <https://doi.org/10.1103/PhysRevLett.110.238301>.
- (435) Wang, Y.; Fei, S.; Byun, Y.-M.; Lammert, P. E.; Crespi, V. H.; Sen, A.; Mallouk, T. E. Dynamic Interactions between Fast Microscale Rotors. *J. Am. Chem. Soc.* **2009**, *131* (29), 9926–9927. <https://doi.org/10.1021/ja904827j>.
- (436) Zhou, C.; Suematsu, N. J.; Peng, Y.; Wang, Q.; Chen, X.; Gao, Y.; Wang, W. Coordinating an Ensemble of Chemical Micromotors via Spontaneous Synchronization. *ACS Nano* **2020**. <https://doi.org/10.1021/acsnano.9b08421>.
- (437) Yu, J.; Jin, D.; Chan, K.-F.; Wang, Q.; Yuan, K.; Zhang, L. Active Generation and Magnetic Actuation of Microbotic Swarms in Bio-Fluids. *Nat. Commun.* **2019**, *10* (1), 5631–5631. <https://doi.org/10.1038/s41467-019-13576-6>.
- (438) Wang, Q.; Yang, L.; Yu, J.; Chiu, P. W. Y.; Zheng, Y.-P.; Zhang, L. Real-Time Magnetic Navigation of a Rotating Colloidal Microswarm Under Ultrasound Guidance. *IEEE Trans. Biomed. Eng.* **2020**, *67* (12), 3403–3412. <https://doi.org/10.1109/TBME.2020.2987045>.
- (439) Wang, Q.; Yu, J.; Yuan, K.; Yang, L.; Jin, D.; Zhang, L. Disassembly and Spreading of Magnetic Nanoparticle Clusters on Uneven Surfaces. *Appl. Mater. Today* **2020**, *18*, 100489. <https://doi.org/10.1016/j.apmt.2019.100489>.
- (440) Servant, A.; Qiu, F.; Mazza, M.; Kostarelos, K.; Nelson, B. J. Controlled In Vivo Swimming of a Swarm of Bacteria-Like Microbotic Flagella. *Adv. Mater.* **2015**, *27* (19), 2981–2988. <https://doi.org/10.1002/adma.201404444>.
- (441) Wei, X.; Beltrán-Gastélum, M.; Karshalev, E.; Esteban-Fernández de Ávila, B.; Zhou, J.; Ran, D.; Angsantikul, P.; Fang, R. H.; Wang, J.; Zhang, L. Biomimetic Micromotor Enables Active Delivery of Antigens for Oral Vaccination. *Nano Lett.* **2019**, *19* (3), 1914–1921. <https://doi.org/10.1021/acs.nanolett.8b05051>.
- (442) Wu, Z.; Li, L.; Yang, Y.; Hu, P.; Li, Y.; Yang, S.-Y.; Wang, L. V.; Gao, W. A Microbotic System Guided by Photoacoustic Computed Tomography for Targeted Navigation in Intestines in Vivo. *Sci. Robot.* **2019**, *4* (32), eaax0613. <https://doi.org/10.1126/scirobotics.aax0613>.
- (443) Yan, X.; Zhou, Q.; Vincent, M.; Deng, Y.; Yu, J.; Xu, J.; Xu, T.; Tang, T.; Bian, L.; Wang, Y.-X. J.; Kostarelos, K.; Zhang, L. Multifunctional Biohybrid Magnetite Microrobots for Imaging-Guided Therapy. *Sci. Robot.* **2017**, *2* (12), eaaq1155. <https://doi.org/10.1126/scirobotics.aaq1155>.
- (444) Cheng, R.; Huang, W.; Huang, L.; Yang, B.; Mao, L.; Jin, K.; ZhuGe, Q.; Zhao, Y. Acceleration of Tissue Plasminogen Activator-Mediated Thrombolysis by Magnetically Powered Nanomotors. *ACS Nano* **2014**, *8* (8), 7746–7754. <https://doi.org/10.1021/nn5029955>.
- (445) Xie, L.; Pang, X.; Yan, X.; Dai, Q.; Lin, H.; Ye, J.; Cheng, Y.; Zhao, Q.; Ma, X.; Zhang, X.; Liu, G.; Chen, X. Photoacoustic Imaging-Trackable Magnetic Microswimmers for Pathogenic Bacterial Infection Treatment. *ACS Nano* **2020**, *14* (3), 2880–2893. <https://doi.org/10.1021/acsnano.9b06731>.
- (446) Esteban-Fernández de Ávila, B.; Martín, A.; Soto, F.; Lopez-Ramirez, M. A.; Campuzano, S.; Vázquez-Machado, G. M.; Gao, W.; Zhang, L.; Wang, J. Single Cell Real-Time miRNAs Sensing Based on Nanomotors. *ACS Nano* **2015**, *9* (7), 6756–6764. <https://doi.org/10.1021/acsnano.5b02807>.
- (447) Bunea, A.-I.; Pavel, I.-A.; David, S.; Gáspár, S. Sensing Based on the Motion of Enzyme-Modified Nanorods. *Biosens. Bioelectron.* **2015**, *67*, 42–48. <http://dx.doi.org/10.1016/j.bios.2014.05.062>.
- (448) Yang, X.; Tang, Y.; Mason, S. D.; Chen, J.; Li, F. Enzyme-Powered Three-Dimensional DNA Nanomachine for DNA Walking, Payload Release, and Biosensing. *ACS Nano* **2016**, *10* (2), 2324–2330. <https://doi.org/10.1021/acsnano.5b07102>.
- (449) Ahmed, S.; Wang, W.; Bai, L.; Gentekos, D. T.; Hoyos, M.; Mallouk, T. E. Density and Shape Effects in the Acoustic Propulsion of Bimetallic Nanorod Motors. *ACS Nano* **2016**, *10* (4), 4763–4769. <https://doi.org/10.1021/acsnano.6b01344>.
- (450) Qualliotine, J. R.; Bolat, G.; Beltrán-Gastélum, M.; de Ávila, B. E. F.; Wang, J.; Califano, J. A. Acoustic Nanomotors for Detection of Human Papillomavirus–Associated Head and Neck Cancer. *Otolaryngol. - Head Neck Surg. U. S.* **2019**, *161* (5), 814–822. <https://doi.org/10.1177/0194599819866407>.
- (451) Bozuyuk, U.; Yasa, O.; Yasa, I. C.; Ceylan, H.; Kizilel, S.; Sitti, M. Light-Triggered Drug Release from 3D-Printed Magnetic Chitosan Microswimmers. *ACS Nano* **2018**, *12* (9), 9617–9625. <https://doi.org/10.1021/acsnano.8b05997>.
- (452) Khalil, I. S. M.; Dijkslag, H. C.; Abelman, L.; Misra, S. MagnetoSperm: A Microbot That Navigates Using Weak Magnetic Fields. *Appl. Phys. Lett.* **2014**, *104* (22), 223701. <https://doi.org/10.1063/1.4880035>.
- (453) Li, T.; Li, J.; Morozov, K. I.; Wu, Z.; Xu, T.; Rozen, I.; Leshansky, A. M.; Li, L.; Wang, J. Highly Efficient Freestyle Magnetic Nanoswimmer. *Nano Lett.* **2017**, *17* (8), 5092–5098. <https://doi.org/10.1021/acs.nanolett.7b02383>.
- (454) Lin, Z.; Fan, X.; Sun, M.; Gao, C.; He, Q.; Xie, H. Magnetically Actuated Peanut Colloid Motors for Cell Manipulation and Patterning. *ACS Nano* **2018**, *12* (3), 2539–2545. <https://doi.org/10.1021/acsnano.7b08344>.
- (455) Chen, C.; Mou, F.; Xu, L.; Wang, S.; Guan, J.; Feng, Z.; Wang, Q.; Kong, L.; Li, W.; Wang, J.; Zhang, Q. Light-Steered Isotropic Semiconductor Micromotors. *Adv. Mater.* **2017**, *29* (3), 1603374. <https://doi.org/10.1002/adma.201603374>.
- (456) Choi, H.; Lee, G.-H.; Kim, K. S.; Hahn, S. K. Light-Guided Nanomotor Systems for Autonomous Photothermal Cancer Therapy. *ACS Appl. Mater. Interfaces* **2018**, *10* (3), 2338–2346. <https://doi.org/10.1021/acsnami.7b16595>.
- (457) Du, S.; Wang, H.; Zhou, C.; Wang, W.; Zhang, Z. Motor and Rotor in One: Light-Active ZnO/Au Twinned Rods of Tunable Motion Modes. *J. Am. Chem. Soc.* **2020**, *142* (5), 2213–2217. <https://doi.org/10.1021/jacs.9b13093>.

- (458) Esplandiú, M. J.; Afshar Farniya, A.; Bachtold, A. Silicon Based Chemical Motors: An Efficient Pump for Triggering and Guiding Fluid Motion Using Visible Light. *ACS Nano* **2015**, No. 11, 150908143923005. <https://doi.org/10.1021/acsnano.5b04830>.
- (459) Pacheco, M.; Jurado-Sánchez, B.; Escarpa, A. Visible-Light-Driven Janus Microvehicles in Biological Media. *Angew. Chem. Int. Ed.* **2019**, *58* (50), 18017–18024. <https://doi.org/10.1002/anie.201910053>.
- (460) Ebbens, S. J.; Gregory, D. A. Catalytic Janus Colloids: Controlling Trajectories of Chemical Microswimmers. *Acc. Chem. Res.* **2018**, *51* (9), 1931–1939. <https://doi.org/10.1021/acs.accounts.8b00243>.
- (461) Chen, H.; Zhao, Q.; Du, X. Light-Powered Micro/Nanomotors. *Micromachines* **2018**, *9* (2). <https://doi.org/10.3390/mi9020041>.
- (462) Tong, R.; Kohane, D. S. Shedding Light on Nanomedicine. *WIREs Nanomedicine Nanobiotechnology* **2012**, *4* (6), 638–662. <https://doi.org/10.1002/wnan.1188>.
- (463) Tu, Y.; Peng, F.; White, P. B.; Wilson, D. A. Self-Destroyed Redox-Sensitive Stomatocyte Nanomotor. *Angew. Chem.* **2017**, *56* (26), n/a-n/a. <https://doi.org/10.1002/ange.201703276>.
- (464) Lv, R.; Lin, S.; Sun, S.; He, H.; Zheng, F.; Tan, D.; Ma, B.; He, M. Cascade Cycling of Nicotinamide Cofactor in a Dual Enzyme Microsystem. *Chem. Commun.* **2020**, *56* (18), 2723–2726. <https://doi.org/10.1039/c9cc10031h>.
- (465) Choi, H.; Cho, S. H.; Hahn, S. K. Urease-Powered Polydopamine Nanomotors for Intravesical Therapy of Bladder Diseases. *ACS Nano* **2020**. <https://doi.org/10.1021/acsnano.9b09726>.
- (466) Ma, X.; Hortelao, A. C.; Miguel-López, A.; Sánchez, S. Bubble-Free Propulsion of Ultrasmall Tubular Nanojets Powered by Biocatalytic Reactions. *J. Am. Chem. Soc.* **2016**, *138* (42), 13782–13785. <https://doi.org/10.1021/jacs.6b06857>.
- (467) T. Brown, A.; K. Poon, W. C.; Holm, C.; Graaf, J. de. Ionic Screening and Dissociation Are Crucial for Understanding Chemical Self-Propulsion in Polar Solvents. *Soft Matter* **2017**, *13* (6), 1200–1222. <https://doi.org/10.1039/C6SM01867J>.
- (468) Li, Z.; Barnes, J. C.; Bosoy, A.; Stoddart, J. F.; Zink, J. I. Mesoporous Silica Nanoparticles in Biomedical Applications. *Chem. Soc. Rev.* **1390**, *41* (7), 2590–2605. <https://doi.org/10.1039/C1CS15246G>.
- (469) Mamaeva, V.; Sahlgren, C.; Lindén, M. Mesoporous Silica Nanoparticles in Medicine—Recent Advances. *Adv. Drug Deliv. Rev.* **2013**, *65* (5), 689–702. <https://doi.org/10.1016/j.addr.2012.07.018>.
- (470) Yang, P.; Gai, S.; Lin, J. Functionalized Mesoporous Silica Materials for Controlled Drug Delivery. *Chem. Soc. Rev.* **2012**, *41* (9), 3679–3698. <https://doi.org/10.1039/C2CS15308D>.
- (471) Slowing, I. I.; Vivero-Escoto, J. L.; Wu, C.; Lin, V. S. Mesoporous Silica Nanoparticles as Controlled Release Drug Delivery and Gene Transfection Carriers ☆. *Adv. Drug Deliv. Rev.* **2008**, *60* (11), 1278–1288. <https://doi.org/10.1016/j.addr.2008.03.012>.
- (472) Xie, M.; Shi, H.; Li, Z.; Shen, H.; Ma, K.; Li, B.; Shen, S.; Jin, Y. A Multifunctional Mesoporous Silica Nanocomposite for Targeted Delivery, Controlled Release of Doxorubicin and Bioimaging. *Colloids Surf. B Biointerfaces* **2013**, *110*, 138–147. <https://doi.org/10.1016/j.colsurfb.2013.04.009>.
- (473) Zheng, H.; Wang, Y.; Che, S. Coordination Bonding-Based Mesoporous Silica for PH-Responsive Anticancer Drug Doxorubicin Delivery. *J. Phys. Chem. C* **2011**, *115* (34), 16803–16813. <https://doi.org/10.1021/jp203799n>.
- (474) Qu, Q.; Ma, X.; Zhao, Y. Targeted Delivery of Doxorubicin to Mitochondria Using Mesoporous Silica Nanoparticle Nanocarriers. *Nanoscale* **2015**, *7* (40), 16677–16686. <https://doi.org/10.1039/C5NR05139H>.
- (475) Rahmani, S.; Durand, J.-O.; Charnay, C.; Lichon, L.; Férid, M.; Garcia, M.; Gary-Bobo, M. Synthesis of Mesoporous Silica Nanoparticles and Nanorods: Application to Doxorubicin Delivery. *Solid State Sci.* **2017**, *68*, 25–31. <https://doi.org/10.1016/j.solidstatesciences.2017.04.003>.
- (476) Meng, H.; Xue, M.; Xia, T.; Ji, Z.; Tarn, D. Y.; Zink, J. I.; Nel, A. E. Use of Size and a Copolymer Design Feature To Improve the Biodistribution and the Enhanced Permeability and Retention Effect of Doxorubicin-Loaded Mesoporous Silica Nanoparticles in a Murine Xenograft Tumor Model. *ACS Nano* **2011**, *5* (5), 4131–4144. <https://doi.org/10.1021/nn200809t>.
- (477) Tsai, M.-F.; Lo, Y.-L.; Soorni, Y.; Su, C.-H.; Sivasoorian, S. S.; Yang, J.-Y.; Wang, L.-F. Near-Infrared Light-Triggered Drug Release from Ultraviolet- and Redox-Responsive Polymersome Encapsulated with Core-Shell Upconversion Nanoparticles for Cancer Therapy. *ACS Appl. Bio Mater.* **2021**, *4* (4), 3264–3275. <https://doi.org/10.1021/acsbm.0c01621>.
- (478) Li, H.; Yang, X.; Zhou, Z.; Wang, K.; Li, C.; Qiao, H.; Oupicky, D.; Sun, M. Near-Infrared Light-Triggered Drug Release from a Multiple Lipid Carrier Complex Using an All-in-One Strategy. *J. Controlled Release* **2017**, *261*, 126–137. <https://doi.org/10.1016/j.jconrel.2017.06.029>.
- (479) Zhao, T.; Chen, L.; Li, Q.; Li, X. Near-Infrared Light Triggered Drug Release from Mesoporous Silica Nanoparticles. *J. Mater. Chem. B* **2018**, *6* (44), 7112–7121. <https://doi.org/10.1039/C8TB01548A>.
- (480) Moros, M.; Idiago-López, J.; Asín, L.; Moreno-Antolín, E.; Beola, L.; Grazú, V.; Fratila, R. M.; Gutiérrez, L.; de la Fuente, J. M. Triggering Antitumoural Drug Release and Gene Expression by Magnetic Hyperthermia. *Adv. Drug Deliv. Rev.* **2019**, *138*, 326–343. <https://doi.org/10.1016/j.addr.2018.10.004>.
- (481) Malekigorji, M.; Alfahad, M.; Lin, P. K. T.; Jones, S.; Curtis, A.; Hoskins, C. Thermally Triggered Theranostics for Pancreatic Cancer Therapy. *Nanoscale* **2017**, *9* (34), 12735–12745. <https://doi.org/10.1039/C7NR02751F>.
- (482) Gray, M. D.; Lyon, P. C.; Mannaris, C.; Folkes, L. K.; Stratford, M.; Campo, L.; Chung, D. Y. F.; Scott, S.; Anderson, M.; Goldin, R.; Carlisle, R.; Wu, F.; Middleton, M. R.; Gleeson, F. V.; Coussios, C. C. Focused Ultrasound Hyperthermia for Targeted Drug Release from Thermosensitive Liposomes: Results from a Phase I Trial. *Radiology* **2019**, *291* (1), 232–238. <https://doi.org/10.1148/radiol.2018181445>.
- (483) Jiang, K.; Zhang, L.; Hu, Q.; Zhang, Q.; Lin, W.; Cui, Y.; Yang, Y.; Qian, G. Thermal Stimuli-Triggered Drug Release from a Biocompatible Porous Metal–Organic Framework. *Chem. – Eur. J.* **2017**, *23* (42), 10215–10221. <https://doi.org/10.1002/chem.201701904>.
- (484) Zhou, Y.; Chen, R.; Yang, H.; Bao, C.; Fan, J.; Wang, C.; Lin, Q.; Zhu, L. Light-Responsive Polymersomes with a Charge-Switch for Targeted Drug Delivery. *J. Mater. Chem. B* **2020**, *8* (4), 727–735. <https://doi.org/10.1039/C9TB02411E>.



- (485) Polat, H.; Kutluay, G.; Polat, M. Analysis of Dilution Induced Disintegration of Micellar Drug Carriers in the Presence of Inter and Intra Micellar Species. *Colloids Surf. Physicochem. Eng. Asp.* **2020**, *601*, 124989. <https://doi.org/10.1016/j.colsurfa.2020.124989>.
- (486) Miao, Y.; Qiu, Y.; Yang, W.; Guo, Y.; Hou, H.; Liu, Z.; Zhao, X. Charge Reversible and Biodegradable Nanocarriers Showing Dual PH-/Reduction-Sensitive Disintegration for Rapid Site-Specific Drug Delivery. *Colloids Surf. B Biointerfaces* **2018**, *169*, 313–320. <https://doi.org/10.1016/j.colsurfb.2018.05.026>.
- (487) Tabayoyong, W. B.; Kamat, A. M.; O'Donnell, M. A.; McKiernan, J. M.; Ray-Zack, M. D.; Palou, J.; Brausi, M.; Black, P. C.; Williams, S. B. Systematic Review on the Utilization of Maintenance Intravesical Chemotherapy in the Management of Non-Muscle-Invasive Bladder Cancer. *Eur. Urol. Focus* **2018**, *4* (4), 512–521. <https://doi.org/10.1016/j.euf.2018.08.019>.
- (488) GuhaSarkar, S.; Banerjee, R. Intravesical Drug Delivery: Challenges, Current Status, Opportunities and Novel Strategies. *J. Controlled Release* **2010**, *148* (2), 147–159. <https://doi.org/10.1016/j.jconrel.2010.08.031>.
- (489) Kim, S. I.; Choo, S. H. Intravesical Chemotherapy. In *Bladder Cancer*; Ku, J. H., Ed.; Elsevier, 2018; pp 263–276. <https://doi.org/10.1016/B978-0-12-809939-1.00019-9>.
- (490) Weintraub, M. D.; Li, Q. Q.; Agarwal, P. K. Advances in Intravesical Therapy for the Treatment of Non-muscle Invasive Bladder Cancer (Review). *Mol. Clin. Oncol.* **2014**, *2* (5), 656–660. <https://doi.org/10.3892/mco.2014.314>.
- (491) Guancial, E. A.; Werner, L.; Bellmunt, J.; Bamias, A.; Choueiri, T. K.; Ross, R.; Schutz, F. A.; Park, R. S.; O'Brien, R. J.; Hirsch, M. S.; Barletta, J. A.; Berman, D. M.; Lis, R.; Loda, M.; Stack, E. C.; Garraway, L. A.; Riester, M.; Michor, F.; Kantoff, P. W.; Rosenberg, J. E. FGFR3 Expression in Primary and Metastatic Urothelial Carcinoma of the Bladder. *Cancer Med.* **2014**, *3* (4), 835–844. <https://doi.org/10.1002/cam4.262>.
- (492) Qing, J.; Du, X.; Chen, Y.; Chan, P.; Li, H.; Wu, P.; Marsters, S.; Stawicki, S.; Tien, J.; Totpal, K.; Ross, S.; Stinson, S.; Dorman, D.; French, D.; Wang, Q.-R.; Stephan, J.-P.; Wu, Y.; Wiesmann, C.; Ashkenazi, A. Antibody-Based Targeting of FGFR3 in Bladder Carcinoma and t(4;14)-Positive Multiple Myeloma in Mice. *J. Clin. Invest.* **2009**, *119* (5), 1216–1229. <https://doi.org/10.1172/JCI38017>.
- (493) Hadari, Y.; Schlessinger, J. FGFR3-Targeted MAb Therapy for Bladder Cancer and Multiple Myeloma. *J. Clin. Invest.* **2009**, *119* (5), 1077–1079. <https://doi.org/10.1172/JCI38948>.
- (494) Edmondson, R.; Broglie, J. J.; Adcock, A. F.; Yang, L. Three-Dimensional Cell Culture Systems and Their Applications in Drug Discovery and Cell-Based Biosensors. *ASSAY Drug Dev. Technol.* **2014**, *12* (4), 207–218. <https://doi.org/10.1089/adt.2014.573>.
- (495) Wang, S.; Gao, D.; Chen, Y. The Potential of Organoids in Urological Cancer Research. *Nat. Rev. Urol.* **2017**, *14* (7), 401–414. <https://doi.org/10.1038/nrurol.2017.65>.
- (496) Lu, X.; Shen, H.; Wei, Y.; Ge, H.; Wang, J.; Peng, H.; Liu, W. Ultrafast Growth and Locomotion of Dandelion-Like Microswarms with Tubular Micromotors. *Small* **2020**, *16* (38), 2003678. <https://doi.org/10.1002/smll.202003678>.
- (497) Hu, Y.; Liu, W.; Sun, Y. Multiwavelength Phototactic Micromotor with Controllable Swarming Motion for “Chemistry-on-the-Fly.” *ACS Appl. Mater. Interfaces* **2020**, *12* (37), 41495–41505. <https://doi.org/10.1021/acsami.0c11443>.
- (498) Wang, J.; Xiong, Z.; Tang, J. The Encoding of Light-Driven Micro/Nanorobots: From Single to Swarming Systems. *Adv. Intell. Syst.* **2021**, *3* (4), 2000170. <https://doi.org/10.1002/aisy.202000170>.
- (499) Lin, Z.; Si, T.; Wu, Z.; Gao, C.; Lin, X.; He, Q. Light-Activated Active Colloid Ribbons. *Angew. Chem.* **2017**, *129* (43), 13702–13705. <https://doi.org/10.1002/ange.201708155>.
- (500) Medina-Sánchez, M.; Schmidt, O. G. Medical Microbots Need Better Imaging and Control. *Nat. News* **2017**, *545* (7655), 406. <https://doi.org/10.1038/545406a>.
- (501) Goel, S.; England, C. G.; Chen, F.; Cai, W. Positron Emission Tomography and Nanotechnology: A Dynamic Duo for Cancer Theranostics. *Adv. Drug Deliv. Rev.* **2017**, *113*, 157–176. <https://doi.org/10.1016/j.addr.2016.08.001>.
- (502) Kokkona, M.; Kallinteri, P.; Fatouros, D.; Antimisiaris, S. G. Stability of SUV Liposomes in the Presence of Cholates Salts and Pancreatic Lipases: Effect of Lipid Composition. *Eur. J. Pharm. Sci.* **2000**, *9* (3), 245–252. [https://doi.org/10.1016/S0928-0987\(99\)00064-0](https://doi.org/10.1016/S0928-0987(99)00064-0).

# **Chapter 10**



## **Annexes**



Given the advantages regarding biocompatibility and use of bioavailable substrates, the use of enzymes to power the motion of nano- and microstructures gathered significant interest from the active matter community. Considering this, and the pioneering works of the Smart Nano-bio-devices group on the development of enzymatic motors, in the early stages of my PhD we reviewed the literature on the topic, collecting reports of the propulsion of several small-scaled structures powered by enzyme catalysis (see annex I).

As denoted in annex I, our group reported the use of enzymes to power the motion of nano- and microparticles based on silica. Apart from that, we also reported the use of urease as engine of bubble-free biocatalytic tubular nanomotors (see annex II). In this work, we developed nanosized silica tubes and explored the biocatalytic decomposition of urea into ammonia and carbon dioxide to power the bubble-free propulsion of silica-based nanojets. These nanojets propelled due to the generation of an internal fluid flow, that extends from the inner cavity to the surrounding fluid. Moreover, we investigated the effect of the biocatalyst positioning on the nanojets' motion profiles, showing that placing the enzymes both on the outer surface and in the inner cavity of the nanojets led to a more efficient displacement.

In the first work reported on this thesis, we showed that nanomotors can enhance the delivery of drugs to cancer cells. However, in this work, doxorubicin had a sustained release from the nanomotors. To achieve further control and avoid off-target effects, in a collaborative work with Martínez-Mañez group from UPV, we incorporated molecular gates into the urease-powered nanomotors, as an additional functionality to achieve controlled intracellular drug delivery (see annex III). In that work, we observed that upon cell uptake of the active nanomotors, the acidic intracellular environment within lysosomes provoked the opening of the molecular gates and, in consequence, the controlled delivery of the drug.

Aiming at further expanding the library of engines, our group devoted efforts to test the ability of several enzymes to power the propulsion of nano- and microstructures. In collaborative work with researchers from the Harbin Institute of Technology, we developed lipase powered nanomotors based on mesoporous silica (see annex IV). These nanomotors consume triglycerides to harness energy for propulsion and are capable of degrading oil droplets and could have potential applications regarding diseases related with triglyceride accumulation or degradation of oil spills.

- I. Enzyme catalysis to power micro/nanomachines. X. Ma<sup>§\*</sup>, **A. C. Hortelão**<sup>§</sup>, T. Patiño, S. Sanchez<sup>\*</sup>. *ACS Nano*. 2016, *10*, 9111–9122 .
- II. Bubble-free propulsion of ultrasmall tubular nanojets powered by biocatalytic reactions. X. Ma, **A. C. Hortelão**, A. Migue-Lopez, S. Sanchez<sup>\*</sup>. *J. Am. Chem. Soc.* 2016, *138*, 13782–13785
- III. Enzyme-powered gated mesoporous silica nanomotors for on-command intracellular payload delivery. A. Llopis-Lorente, A. García-Fernandez, N. Murillo-Cremaes, **A. C. Hortelão**, T. Patiño, R. Villalonga, F. Sancenón, R. Martínez-Mañez<sup>\*</sup>, S. Sanchez<sup>\*</sup>. *ACS Nano*. 2019, *13*, 12171–12183
- IV. Lipase-powered mesoporous silica nanomotors for triglyceride degradation. L. Wang<sup>§</sup>, **A. C. Hortelão**<sup>§</sup>, X. Huang, S. Sánchez<sup>\*</sup>. *Angew. Chem. Int. Ed.* 2019, *58*, 7992–7996



# Enzyme Catalysis To Power Micro/Nanomachines

Xing Ma,<sup>†,‡,⊥</sup> Ana C. Hortelão,<sup>†,||,⊥</sup> Tania Patiño,<sup>||</sup> and Samuel Sánchez<sup>\*,†,§,||</sup>

<sup>†</sup>Max Planck Institute for Intelligent Systems, Heisenbergstraße 3, 70569 Stuttgart, Germany

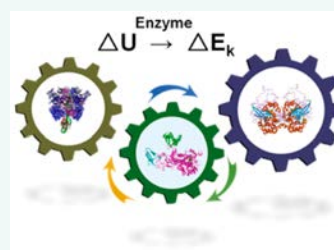
<sup>‡</sup>School of Materials Science and Engineering, Shenzhen Graduate School, Harbin Institute of Technology, 518055 Shenzhen, China

<sup>§</sup>Institució Catalana de Recerca i Estudis Avançats (ICREA), Pg. Lluís Companys 23, 08010 Barcelona, Spain

<sup>||</sup>Institut de Bioenginyeria de Catalunya (IBEC), Baldiri i Reixac 10-12, 08028 Barcelona, Spain

**ABSTRACT:** Enzymes play a crucial role in many biological processes which require harnessing and converting free chemical energy into kinetic forces in order to accomplish tasks. Enzymes are considered to be molecular machines, not only because of their capability of energy conversion in biological systems but also because enzymatic catalysis can result in enhanced diffusion of enzymes at a molecular level. Enlightened by nature's design of biological machinery, researchers have investigated various types of synthetic micro/nanomachines by using enzymatic reactions to achieve self-propulsion of micro/nanoarchitectures. Yet, the mechanism of motion is still under debate in current literature. Versatile proof-of-concept applications of these enzyme-powered micro/nanodevices have been recently demonstrated. In this review, we focus on discussing enzymes not only as stochastic swimmers but also as nanoengines to power self-propelled synthetic motors. We present an overview on different enzyme-powered micro/nanomachines, the current debate on their motion mechanism, methods to provide motion and speed control, and an outlook of the future potentials of this multidisciplinary field.

**KEYWORDS:** enzyme catalysis, micro/nanomachines, self-propulsion, nanomotors, synthetic motors



The harnessing of chemically free energy for conversion into mechanical work is ubiquitous in nature and crucial for survival of organisms from all levels of complexity. Tasks such as phagocytosis, vesicle transportation within the cells, locomotion, and cell division are based on mechanical work achieved through surrounding substrate decomposition.<sup>1</sup> In biological systems, enzymes are workhorse proteins that act as catalysts, being able to turnover substrates with high specificity and efficiency that power biological machinery. Examples include synthesis of DNA molecules by DNA polymerase, hydrolysis of proteins by endopeptidase, and using energy by ATP hydrolysis.<sup>2</sup> Effectively, enzymes are themselves considered to be nanomachines because fundamental studies on enzymes revealed that catalytic activity enhances diffusion at the single-molecule level.<sup>3–5</sup>

Synthetic micro/nanomachines arose from endeavors to mimic biological counterparts abundant in nature, in order to understand its fundamentals and to develop functional and well-controlled tools with applications in a wide range of fields.<sup>6</sup> Synthetic machines controllable at such a tiny scale may power devices for applications in environmental sciences,<sup>7</sup> biomedicine,<sup>8</sup> or diagnostics<sup>9</sup> to name a few.

In this review, we focus on enzymes as molecular machines, as well as their driving force when combined with synthetic micro/nanomachines. These synthetic molecular machines can be based in a myriad of structures.<sup>10</sup> One example is nucleic-

acid-based motors, where enzymatic activity controls the hybridization and hydrolysis of DNA and/or RNA strands, promoting motion of structures based in nucleic acids.<sup>11–13</sup> Recently, enzymatic catalysis was also reported to power the motion of various structures at the micro/nanoscale, such as polymeric<sup>14</sup> and inorganic particles.<sup>15,16</sup> By coupling enzymes onto the surfaces of these structures, enzymatic turnover of substrates provides necessary energy to overcome random Brownian motion and achieve active motion. Moreover, by functionalizing fixed surfaces with enzymes, the driving force produced by enzymatic catalysis is transferred to the surrounding environment, giving rise to fluid flow (Scheme 1).<sup>17</sup>

Researchers have carried out in-depth studies on enzymes as swimmers and as engines for active synthetic matter. In order to use biocatalytic energy, investigation on the fundamental mechanism of enzymatic reactions has been performed, aiming at understanding the conversion of enzyme catalysis into propulsion power, including on the mechanism of single enzymes as active motors (Scheme 1).<sup>3,5,18,19</sup>

Although this field is still in its infancy, it can have an impact in fields such as smart drug delivery, bio-nanotechnology for

**Received:** June 21, 2016

**Accepted:** September 25, 2016

**Published:** September 25, 2016

Scheme 1. Schematic Illustration of Enzyme-Powered Micro/Nanomachines

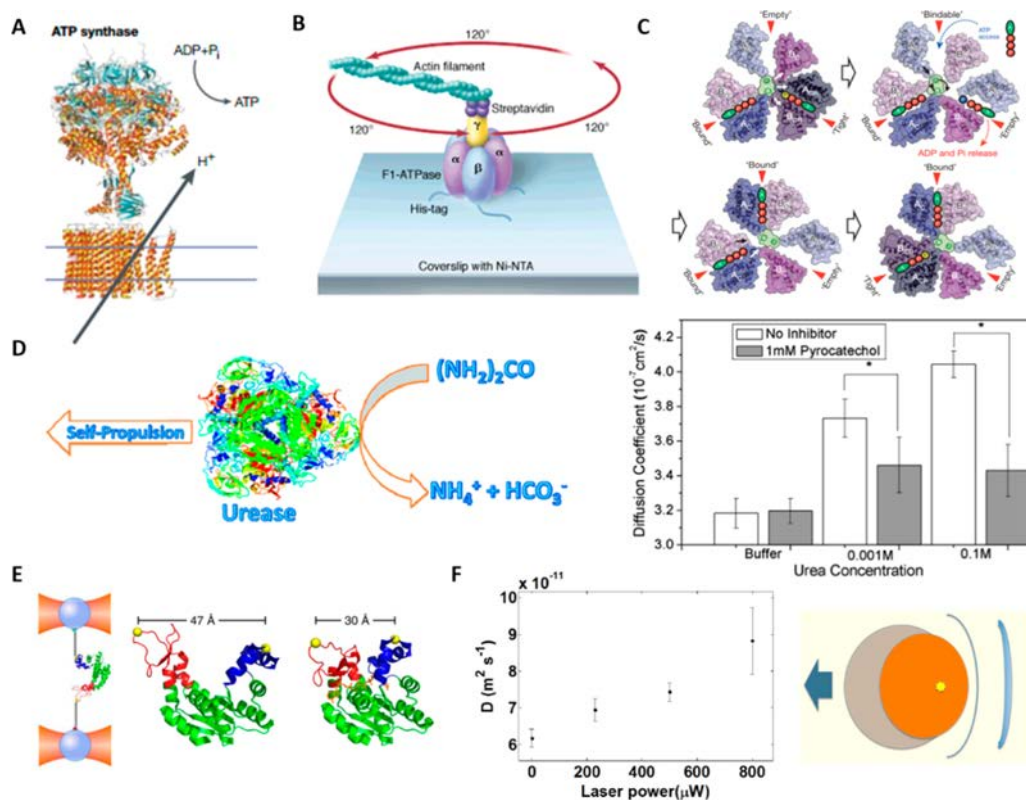
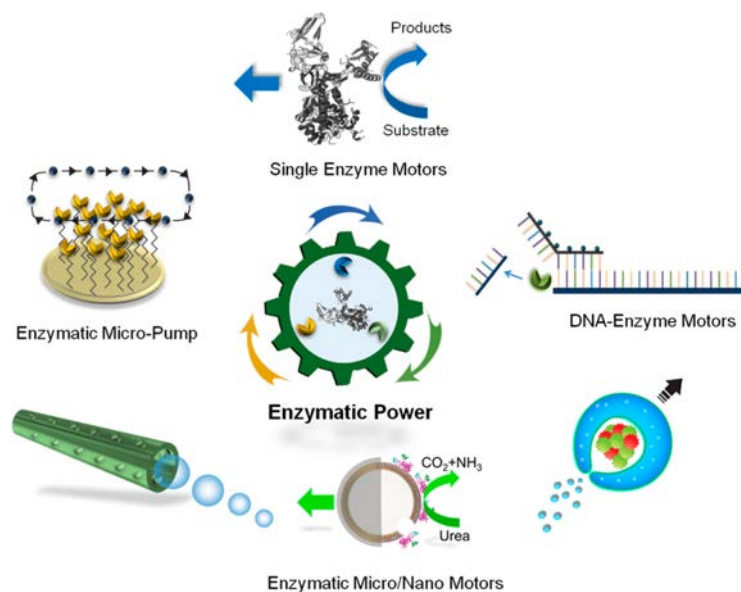


Figure 1. (A) ATP synthase 3D structure. Reprinted with permission from ref 31. Copyright 2001 Nature Publishing Group. (B) Direct observation of F1-ATPase rotation movement by coupling a fluorescence actin filament. Reprinted with permission from ref 35. Copyright 1998 American Association for the Advancement of Science. (C) Conformational changes during ATP synthesis. Reprinted with permission from ref 39. Copyright 2013 Nature Publishing Group. (D) Schematic representation of urease self-diffusion enhancement by catalysis and diffusion coefficients of urease when exposed to increasing substrate concentrations. Reprinted from ref 3. Copyright 2010 American Chemical Society. (E) Conformational changes of adenylate cyclase measured by single-molecule force spectroscopy. Reprinted with permission from ref 49. Copyright 2016 Nature Publishing Group. (F) Diffusion coefficient of catalase as a function of the laser power (402 nm) and schematic representation of enzyme motion driven by chemoacoustic effect. Reprinted with permission from ref 5. Copyright 2014 Nature Publishing Group.



medical purposes, environmental remediation, among others. Therefore, it is important to investigate enzymes, not only understanding the basic knowledge of the biocatalytic process but also carrying out in-depth studies on enzymes as swimmers. Furthermore, it is crucial to unravel the mechanism underlying the motion/swimming when enzymes are conjugated onto more complex structures. Deeper insights on enzymatic propulsion may affect the development of advanced and more versatile types of synthetic micro/nanomachines. Herein, we review the study of enzymes as molecular machines and used as engines to power motion of other structures. We expect that comprehensive studies on this type of propulsion at the micro/nanoscale will help to develop micro/nanomachines, providing insights for future development of this field.

**Enzymes as Motors.** Enzymes are proteins capable of efficiently catalyzing the conversion of a substrate into products,<sup>20–23</sup> including most forms of biological motion at the cellular level.<sup>24</sup> In this sense, myosins, which move along actin filaments,<sup>25,26</sup> and kinesins and dyneins, which move along microtubule tracks,<sup>27</sup> are the three main types of molecular motors within the cells. These molecular motors generate energy to move from the hydrolysis of ATP ( $\text{ATP} + \text{H}_2\text{O} \rightarrow \text{ADP} + \text{inorganic phosphate (Pi)}$ ) by enzymes, e.g., ATPase,<sup>26,28</sup> with forces that vary between 1 and 10 pN.<sup>24,29,30</sup>

Other types of intracellular motion can be achieved through single enzymes, as in ATPase rotation. These proteins are motor complexes anchored to organelle membranes and are involved in either the synthesis of ATP coupled to the electrochemical proton gradient formed by electron transfer chains (F-ATPase)<sup>31</sup> (Figure 1A) or the acidification of intra- or extracellular compartments (V-ATPase).<sup>32,33</sup> Although the rotary mechanism of ATPases was hypothesized by Boyer in 1979,<sup>34</sup> it was empirically observed by Noji and collaborators<sup>35,36</sup> for the first time in 1997, through the conjugation of a fluorescent actin filament to the immobilized enzyme (Figure 1B).<sup>36</sup> The rotation movement of ATPases is triggered by changes in the conformation of the different subunits (Figure 1C) following substrate binding or release.<sup>37–40</sup> Moreover, in 2002, Montemagno and co-workers<sup>41</sup> discovered that ATPases are capable of generating forces and also move nickel rotors.

Apart from these well-known intracellular motion mechanisms, the self-diffusion of cytoplasm-located enzymes has been hypothesized to play a vital role for transduction of intracellular signals.<sup>42</sup> However, there was no empirical demonstration of these nontraditional enzymatic motions until very recently. In this respect, Muddana and co-workers reported in 2010 a catalysis-enhanced diffusion of urease enzyme,<sup>3</sup> which was shown to be highly reliant upon substrate concentration (Figure 1D). The same authors further confirmed these results using both urease and catalase enzymes, where they observed that the diffusion of free urease and catalase enzymes was not only significantly enhanced by the turnover of their substrates [ $(\text{NH}_2)_2\text{CO} + \text{H}_2\text{O} \rightarrow \text{CO}_2 + 2\text{NH}_3$ ,  $\text{H}_2\text{O}_2 \rightarrow \text{H}_2\text{O} + 1/2\text{O}_2$ , respectively] but also displayed preferential movement toward increasing substrate concentrations, which should be regarded as a different form of molecular chemotaxis.<sup>4</sup>

These findings have led to the harnessing of chemical energy released by enzymes as a source of power for micro- and nanomotors. Yet, the exact mechanism that underlies enzymatic motion in fluids is not completely understood. Golestanian suggested that the enhanced diffusion of enzymes could be explained by a self-diffusiophoresis mechanism triggered by the asymmetric release of products involved in the catalytic

reaction, creating interfacial forces depending on osmotic gradients, charges, or other properties.<sup>18,43</sup> This theory has been further confirmed by Colberg *et al.*,<sup>19</sup> who reported that self-propulsion forces of ångström-sized molecules are generated by different interactions of the enzyme with the local gradient of products released. On the other hand, the enhanced diffusion of single enzymes could also be attributed to the conformational changes that play a critical role in catalysis. This phenomenon could result in stochastic swimming.<sup>18,44–48</sup> Recently, Pelz and co-workers<sup>49</sup> performed a direct measurement of the energetic drive of substrate-dependent lid closing in the enzyme adenylate kinase ( $\text{ATP} + \text{AMP} \rightarrow 2\text{ADP}$ ) by using a single-molecule force spectroscopy approach based on optical tweezers (Figure 1E).

The increase of temperature during catalysis is involved in single-enzyme-enhanced diffusion. In this sense, Riedel *et al.*<sup>5</sup> recently reported that the enhanced diffusion of enzymes is related to the heat released during substrate turnover. Based on their observations through fluorescence correlation spectroscopy analyzed within the framework of stochastic theory, these researchers proposed a motion mechanism based on the generation of an asymmetric pressure wave by the transient displacement of the center-of-mass of the enzyme (chemoacoustic effect, Figure 1F). However, this is a topic of current debate. In this regard, Golestanian has examined the role of four different mechanisms (*i.e.*, self-thermophoresis, boost in kinetic energy, stochastic swimming, and collective heating) in the temperature-driven enhanced diffusion of enzymes observed by Riedel *et al.* In this work, it is concluded that there is not enough evidence to assume that either self-thermophoresis or a boost in kinetic energy is responsible for the experimentally obtained values of effective diffusion. As an alternative, he also proposes that the enhanced diffusion of enzymes that catalyze exothermic reactions could be attributed to a combination of (a) global temperature increase in the sample container and (b) enhanced conformational changes that can lead to a hydrodynamic enhancement of effective diffusion coefficient.<sup>18</sup> Although at present there is no conclusive answer to this controversial discussion, fully understanding the fundamental mechanism of the motion of single enzyme is still rather critical for the development of enzyme-powered micro/nanomachines. Sophisticated experimental design will be highly desired in order to distinguish those different effects described before, which will be helpful for the future design and use of these enzymes as “nanoengines” to power artificial systems.

**DNA–Enzyme Motors.** Biological functions are performed by highly complex and hierarchical nanomachineries, namely, motor proteins<sup>26,27</sup> and nucleic acids.<sup>50</sup> Based on these molecular machines, researchers developed DNA-based motors that can process information and execute transport over considerable distances powered by enzymatic reactions. Typically, these motors consist of single-stranded DNA or RNA that is complementary to domains present along the patterned tracks. The motion is controlled by cyclic reactions of hybridization and hydrolysis between the DNA-based motor and the track, recurring to restriction enzymes that comprehend specific recognition sites in the hybridized motor–track complex.<sup>11–13,51–54</sup>

These motors may have applications as cargo transportation devices or biosensors for highly sensitive and sequence-specific nucleic acid assays. Despite their programmability and precise control over the motion along a track,<sup>51,53</sup> DNA-based

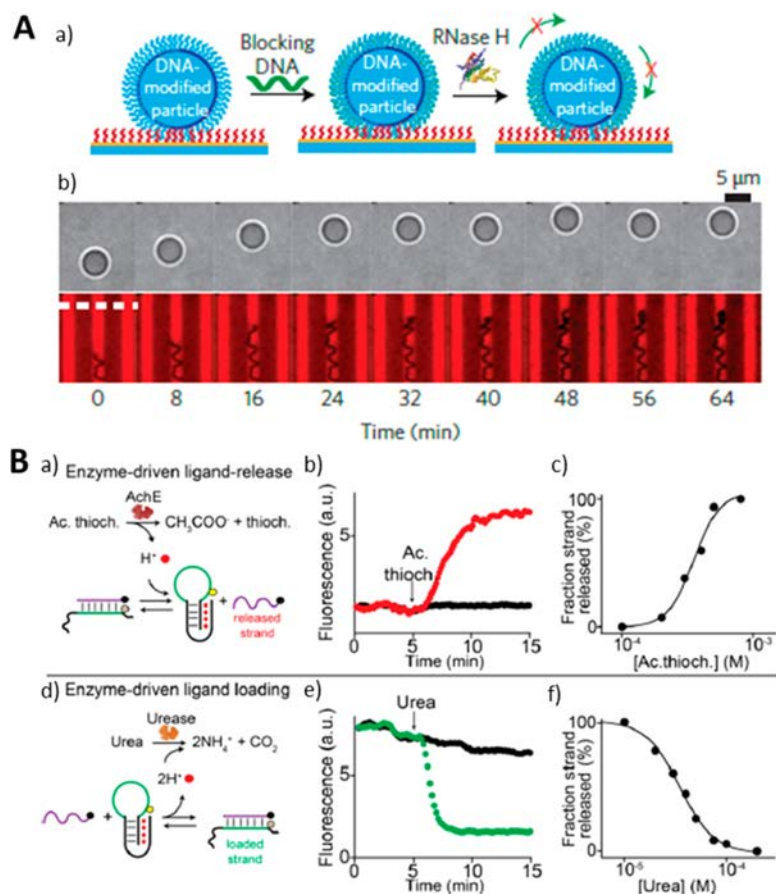


**Figure 2.** DNA-based micro/nanomotors powered and controlled by different classes of enzymes. (A) DNA rolling motor (a) with motion powered by RNase H (b). Reprinted with permission from ref 13. Copyright 2015 Nature Publishing Group. (B) Control of cargo loading and release by a pH-sensitive DNA switch using proton-producing/proton-consuming enzymes. Reprinted from ref 55. Copyright 2015 American Chemical Society.

molecular machines' velocity is limited to rates around 1 nm/min due to compromises between its endurance and speed. To tackle these problems, Salaita and co-workers<sup>13</sup> designed a DNA-based walker that moves through a cog-and-wheel mechanism (Figure 2A), which overcomes trade-off issues of multivalent DNA motors and improves their velocity. Its motion is due to a similar mechanism as referred to above, and it is powered by the addition of RNase H. Its directionality is based on a sequence of reactions of DNA complementary RNA hybridization, hydrolysis by RNase H, and rehybridization with new ssRNA, occurring with consumption of substrate (ssRNA) as the motor rolls upon the track.

Li and co-workers<sup>54</sup> engineered a patterned track and DNA walker conjugated onto the same spherical particle, which increased local effective concentrations of DNA. This motor achieves motion through the hybridization of the walker with the DNA substrate, followed by hydrolysis by a nicking endonuclease.

The majority of DNA-based nanomachines are powered by enzymes with nucleic acid affinity, such as nucleases, ligases, polymerases, or nicking enzymes, but those represent only a small fraction of the enzymes used to catalyze reactions in nature. Recently, Ricci and co-workers<sup>55,56</sup> employed different classes of non-DNA-recognizing enzymes, namely, proton-producing and proton-consuming enzymes, to control DNA-

based nanodevices through pH-dependent DNA reactions. The researchers demonstrated that a DNA switch could be reversibly triggered into opening or closing states by reactions catalyzed by non-DNA-recognizing enzymes. To do so, they used a pH-dependent labeled switch<sup>56</sup> and engineered the protonation and deprotonation of the switch using glutathione transferase (GST) ( $\text{GSH} + \text{CDNB} \rightarrow \text{GS-DNB} + \text{HCl}$ ) and urease, respectively. Furthermore, they utilized enzymatic reactions as a way to control the load and release of ligands using urease to prompt cargo loading and trigger its release (Figure 2B),<sup>55</sup> proving that enzymes can be a wide toolkit to power biostructures.

**Enzyme-Powered Micro/Nanomotors.** Enzymes have been used to power the motion of biologically occurring structures. The ability of enzymes to provide sufficient driving force to propel larger synthetic structures has been reported.<sup>14,15,57–59</sup> Sánchez and co-workers<sup>60</sup> fabricated 400 nm diameter Janus hollow mesoporous silica nanoparticles (HMSNPs, Figure 3A(a,b)), by coating either silica or metallic element (Ni) onto one side of a monolayer of the particles through electron beam evaporation (Figure 3A(c)). Three different enzymes, catalase, urease, or glucose oxidase (GOx) ( $\beta\text{-D-glucose} + \text{O}_2 + \text{H}_2\text{O} \rightarrow \text{gluconic acid} + \text{H}_2\text{O}_2$ ), were conjugated onto one face of the particles. Upon addition of corresponding substrates  $\text{H}_2\text{O}_2$ , urea, or glucose, all nano-

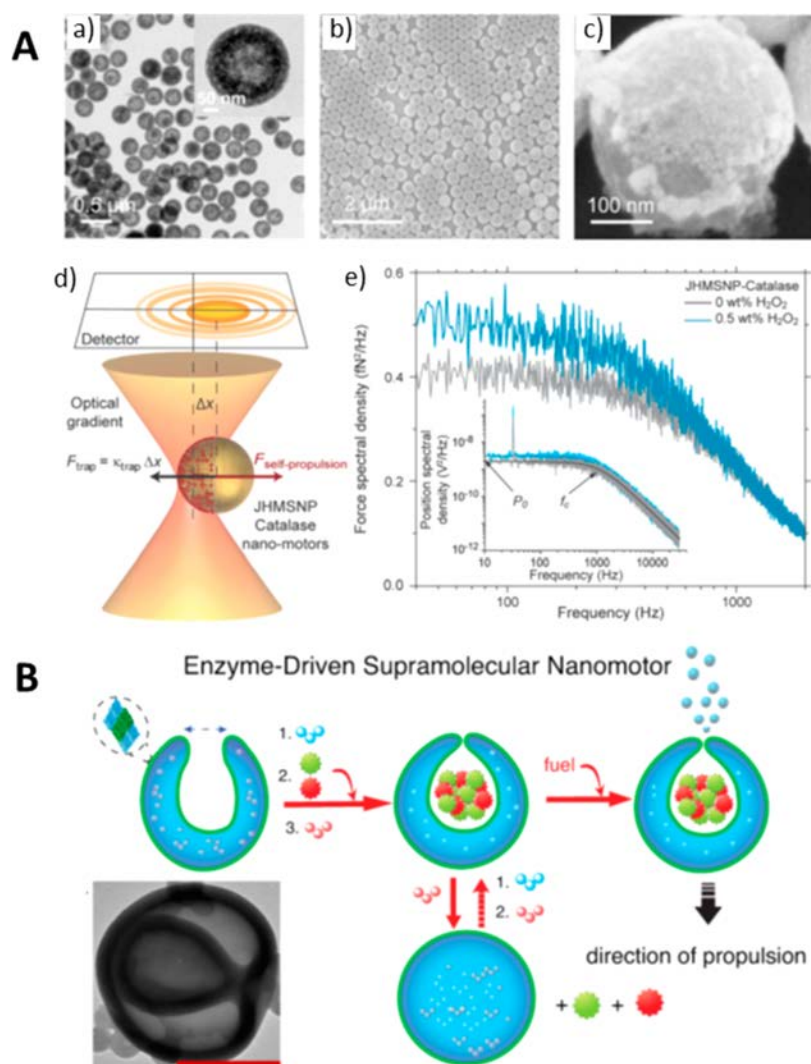


**Figure 3.** Enzyme-powered nanomotors. (A) Janus hollow mesoporous silica nanomotors powered by individual enzymes: (a) TEM and (b) SEM images of HMSNPs; (c) SEM image of JHMSNP-catalase; (d) schematic illustration of the force measurement by optical tweezers and (e) force spectral density as a function of frequency for JHMSNP-catalase nanomotors. Reprinted from ref 60. Copyright 2015 American Chemical Society. (B) Supramolecular assembly of the enzyme-driven polymeric stomatocyte nanomotors; inset is the TEM image of the polymeric stomatocytes (scale bar: 200 nm). Reprinted from ref 14. Copyright 2016 American Chemical Society.

motors exhibited enhanced diffusion that the authors claim to be generated by a chemophoretic mechanism. By utilizing an optical trapping technique (Figure 3A(d)), the authors measured a driving force around 60 fN applied on a catalase-powered nanomotor (Figure 3A(e)).

Wilson and co-workers<sup>14</sup> loaded enzymes, such as catalase or catalase and GOx combination, into 500 nm supramolecular stomatocytes (Figure 3B), achieving self-propulsion by gas expulsion from a very small opening of these structures. Enzymes were also employed to drive one-dimensional nanoarchitectures. Feringa and co-workers<sup>59</sup> claimed bubble propulsion of glucose oxidase/catalase conjugated carbon nanotubes (diameter = 20 nm) with addition of glucose and oxygen. Gáspár and co-workers<sup>61,62</sup> conjugated several enzymes, including GOx, glutamate oxidase, xanthine oxidase, horseradish peroxidase, and catalase, onto polypyrrole-gold nanorods whose fuel-dependent enhanced diffusion behavior was explained by self-electrophoresis based on a bioelectro-

chemical mechanism ( $2\text{H}^+ + 2\text{e}^- + \text{H}_2\text{O}_2 \rightarrow 2\text{H}_2\text{O}$ ;  $2\text{O}_2 \rightarrow 2\text{O}_2^{\bullet-} + 2\text{e}^-$ ). Such behavior was further utilized for substrate sensing applications.<sup>63</sup> Mano and Heller<sup>64</sup> coupled another two-enzyme system: glucose oxidase and bilirubin oxidase, onto a macroscale carbon fiber, which moved by bioelectrochemical propulsion at the air-liquid interface when fueled with glucose, resulting in the net bioelectrochemomechanical power-generating reaction ( $\beta\text{-D-glucose} + 1/2 \text{O}_2 \rightarrow \delta\text{-glucono-1,5-lactone} + \text{H}_2\text{O}$ ).

Sen and co-workers<sup>16</sup> immobilized two individual enzymes, catalase and urease, onto the whole surface of polystyrene particles. The enhanced diffusion of these particles was explained by a thermal effect due to exothermic enzymatic reactions (Figure 4A(a)). Nevertheless, such a hypothesis needs further investigation as pointed out by the authors. Städler and co-workers<sup>65</sup> also immobilized two enzymes, catalase and GOx, onto one face of Janus silica particles, which also showed enhanced diffusion properties (Figure 4A(b)). A long-standing



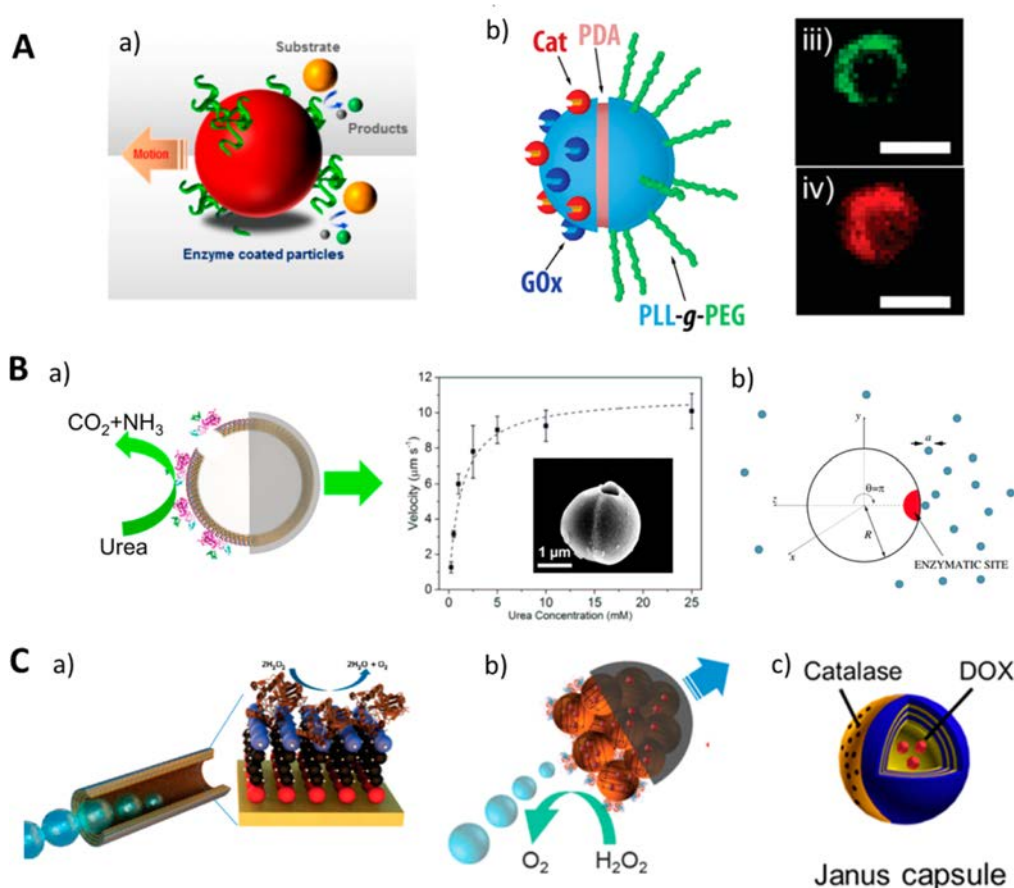


**Figure 4.** Enzyme-powered micromotors. (A) (a) Enzymatic micromotor fully coated with catalase or urease. Reprinted from ref 16. Copyright 2015 American Chemical Society. (b) Janus microparticle half-coated with (iii) catalase/(iv) GOx (scale bar: 1  $\mu\text{m}$ ). Reprinted from ref 65. Copyright 2015 American Chemical Society. (B) (a) Schematic illustration and urea-dependent velocity of biocompatible Janus microcapsule motors. Inset is a SEM image of a single Janus microcapsule motor. Reprinted from ref 66. Copyright 2016 American Chemical Society. (b) Schematic illustration of a phoretic micromotor driven by asymmetric enzymatic reactions. Reprinted with permission from ref 43. Copyright 2005 American Physical Society. (C) Enzyme catalase-based bubble propulsion of (a) rolling up microtubular motor (reprinted from ref 67; copyright 2010 American Chemical Society); (b) Janus mesoporous silica cluster motor (reprinted with permission from ref 57; copyright 2015 Royal Society of Chemistry), and (c) Janus self-assembled polymeric capsule motor (reprinted from ref 72; copyright 2014 American Chemical Society).

challenge for utilizing micro/nanomotors as drug delivery carriers is biocompatibility of the whole self-propelled system, which encourages researchers to design enzymatic motors consuming nontoxic fuels.<sup>14–16,65</sup> Although the above-mentioned works successfully proved the feasibility of using these biocompatible fuels to power micro/nanomotors, the drawback of randomized movement due to Brownian activation makes it hard to meet realistic applications. Very recently, Sánchez and co-workers managed to construct a fully biocompatible microcapsule motor based on Janus hollow mesoporous silica spheres with an average diameter of 2.3  $\mu\text{m}$  (Figure 4B(a)). The capability of long-range movement ( $>100 \mu\text{m}$ ), with considerable velocity ( $>10 \mu\text{m s}^{-1}$ ) for long time at physiological concentration of urea, makes it a promising candidate for potential biomedical applications.<sup>66</sup> The urea-powered hollow microcapsule motor demonstrated directional self-propulsion driven by a phoretic mechanism, which provided experimental evidence for the theoretical hypothesis given by Golestanian and co-workers that asymmetric distribution of enzymatic reaction products could lead to

phoretic motion (electrophoresis, diffusiophoresis, or osmophoresis) of enzyme-conjugated Janus micro/nanoparticles (Figure 4B(b)).<sup>43</sup> However, for the self-propulsion behavior in the form of enhanced diffusion, in addition to the phoretic mechanism, other effects of enzymatic reactions, such as global temperature increase and conformational changes, might also increase the inherent Brownian motion, leading to enhancement of the effective diffusion coefficient of the motors.

Following the classic self-propulsion system based on Pt/ $\text{H}_2\text{O}_2$ , researchers initially used catalase to replace Pt. For instance, Sánchez and co-workers first immobilized catalase into the tubular micromotor (length of 25  $\mu\text{m}$ ) by covalent linkage and achieved ultrafast movement by bubble propulsion (Figure 4C(a)).<sup>67</sup> They improved self-propulsion efficiency by utilizing enzymatic reactions compared to Pt/ $\text{H}_2\text{O}_2$  system. Similar strategy was employed by other research groups, including He and Wang, to fabricate bubble propulsion tubular micromotors,<sup>68–71</sup> where they demonstrated proof-of-concept applications, including active drug delivery toward cells,<sup>68</sup> water quality testing,<sup>69</sup> toxin sensing,<sup>70</sup> and decontamination.<sup>71</sup>

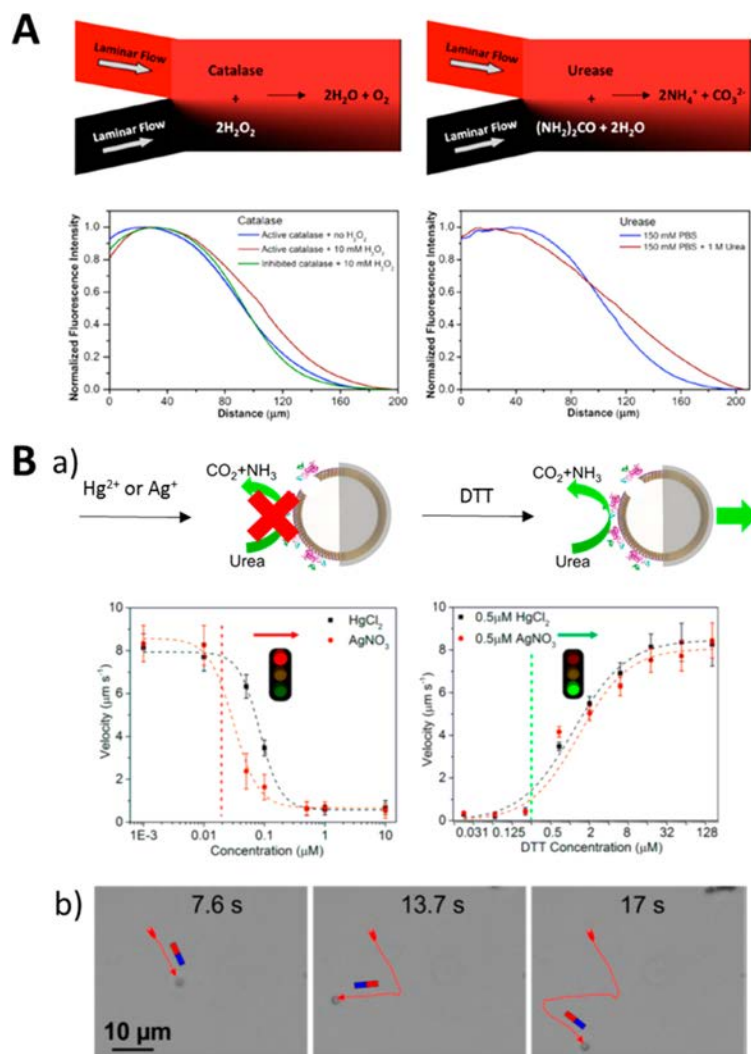


**Figure 5.** Motion control of enzymatic micro/nanomotors. (A) Schematic of microfluidic setup showing corresponding chemotaxis shifting of catalase and urease motors toward the high concentration area of corresponding fuels. Reprinted from ref 4. Copyright 2013 American Chemical Society. (B) (a) Schematic illustration and plots of motion control on urea-powered microcapsule motors by inhibiting and reactivating the enzymatic activity; (b) directional guidance on the microcapsule motors by remote magnetic control. Reproduced from ref 66. Copyright 2016 American Chemical Society.

applications. Besides tubular micromotors, which can generate bubbles through one-dimensional confinement, catalase was conjugated onto one side of Janus particles, as well. With a rough surface (Figure 4C(b))<sup>57</sup> or a relatively large size ( $>10 \mu\text{m}$ ) (Figure 4C(c))<sup>72,73</sup> at the biocatalytic face, oxygen bubbles could generate quickly and push the motors toward the non-enzyme side. Catalase-based enzymatic motors by a bubble propulsion mechanism can achieve directional movement with extremely high velocity up to hundreds of micrometers per second, more than 10 times higher than the phoretic motion of micromotors such as urea-powered microcapsule motors, but biotoxicity and high oxidative activity of  $\text{H}_2\text{O}_2$  fuel limited these motors' realistic applications, especially in the biomedical field.

Enzyme-based nano/micromotors have shown, for catalase enzyme, high efficiency compared to that with Pt-based counterparts. That effect was observed in tubular microjets<sup>67</sup> and in stomatocyte nanocapsules.<sup>14</sup> The high efficiency of enzyme-based micro/nanomotors could be attributed to the

high catalytic rate of the catalase enzyme and the fact that enzymes were confined into the cavities of the micro/nanomotors, where products accumulate and are thereafter expelled through the openings of the motors as nozzles or jets.

To achieve external control on the movement of micro/nanomotors, Sen and co-workers demonstrated one-dimensional guidance of single-enzyme motors (catalase, urease)<sup>4</sup> and enzyme-conjugated micromotors in a microfluidic setup (Figure 5A).<sup>16</sup> The enzymatic motors prefer to move toward the high concentration region of the substrate through collective behavior of chemotaxis. Furthermore, computational models have been developed using surface-bound enzymatic reactions to organize structures in solution.<sup>74</sup> Another common strategy is remote magnetic guidance. Researchers accomplished directional guidance by incorporating magnetic element, such as Fe or Ni, into the motors' structure. Remote control on the orientation of the enzymatic micromotors was readily available by applying a magnetic field (Figure 5B-

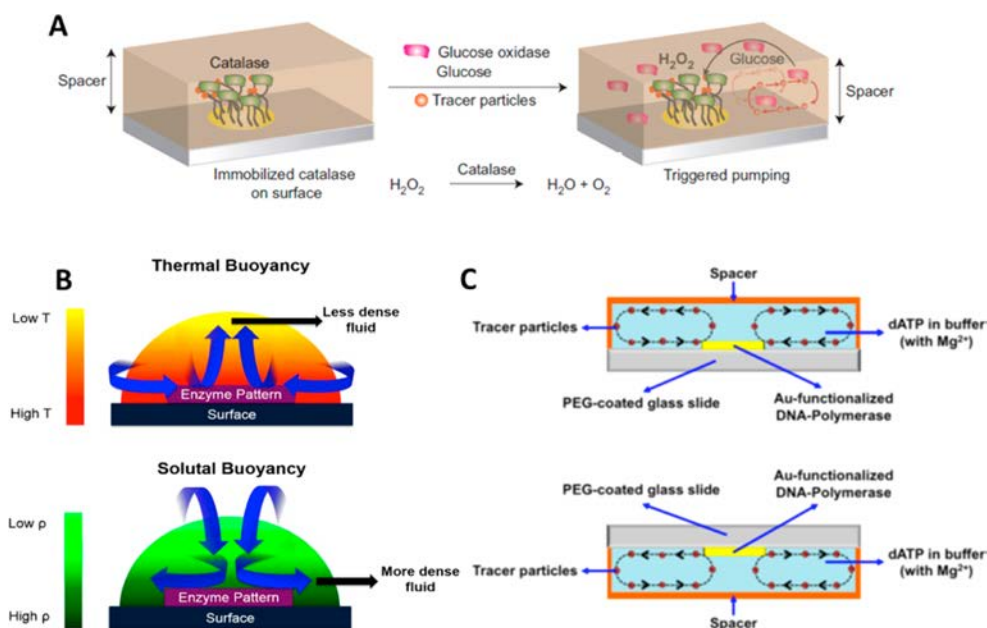


**Figure 6.** Fluid flow induced by enzymatic pumping and enzymatic pumps as environmental sensors. (A) Schematic design of an enzymatic pump setup is presented: the enzyme is conjugated onto a gold pattern through a SAM, and tracer particles of a known size are used to determine the fluid flow. Reprinted with permission from ref 17. Copyright 2014 Nature Publishing Group. (B) Proposed mechanisms of fluid convection in enzyme-powered micropumps. Reprinted with permission from ref 80. Copyright 2016 Proceedings of the National Academy of Sciences of the United States of America. (C) Inverted setup is presented, giving insight into the pumping mechanism. Reprinted from ref 78. Copyright 2014 American Chemical Society with permission.

B(b)).<sup>57,66,72</sup> In addition to directional guidance, Sánchez and co-workers<sup>66</sup> realized velocity manipulation by tuning the enzymatic activity of urease with addition of enzyme inhibitors, such as  $Hg^{2+}$  or  $Ag^+$  ions (Figure 5B(a)). Enzyme inhibition property was also utilized for water quality sensing through direct observation of the inhibited motion behavior of bubble propulsion microtubular motors.<sup>69,71</sup>

**Enzymatic Micropumps.** Nonmechanical micropumps that can function without the need for an external power source have great potential as active biosystems, but the use of nonbiocompatible fuels hinders their applicability. Sánchez and co-workers developed a nonmechanical, tunable, catalytic micropump that operates by decomposing low concentrations of hydrogen peroxide into water and oxygen, generating bubbles that provoke fluid flow.<sup>75</sup> A myriad of catalysts can trigger hydrogen peroxide decomposition, among which are most transition metals and enzyme catalase. However, it is a toxic fuel, hindering this micropump's applicability.

As discussed previously, single enzymes' diffusion increases in a concentration-dependent manner.<sup>3,4,76</sup> Tethering enzymes to a fixed surface permits the transfer of this force to the surrounding environment, moving fluid as well as particles in a directed fashion. In addition, these micropumps are activated by the presence of specific compounds, such as substrate molecules and cofactors, thus enabling the use of such devices both as sensors and triggered micropumps.<sup>17,77</sup>

Sen and co-workers designed multiple triggered micropumps with the flow rate tunable by analyte concentration.<sup>17,78</sup> First, they used the wild-type of the enzyme T4 DNA polymerase, which can switch the mode of action from polymerase to exonuclease. In the case of the presence of a single nucleotide, T4 DNA polymerase action is restricted and the primer strand

is shifted back and forth while the enzyme incorporates and removes nucleotides. By immobilizing this enzyme onto a self-assembled monolayer (SAM), the researchers developed a micropump with energy conversion efficiency ( $10^{-7}$ )<sup>79</sup> comparable to that in previously reported synthetic systems.<sup>78</sup> Later, they made use of a similar approach with ATP-independent enzymes of distinct classes—catalase, urease, lipase, and GOx, demonstrating the first examples of ATP-independent enzyme-based pumps.<sup>17</sup> The pumping ability of each enzyme was assessed by injecting a substrate solution in a sealed system containing tracer particles (Figure 6C),<sup>17,78</sup> which were used to monitor the speed and directionality of fluid flow. Interestingly, the convective flow in urease micropump is reversed, contrary to that in the other micropumps tested. Researchers pointed out that urea decomposition products by urease catalysis are ionic, which can increase the density of the fluid near the patterned surface, causing it to spread along the glass and driving it away from the pattern.<sup>80</sup> They hypothesize catalysis-induced density-driven convective flow as a mechanism for the directional fluid pumping (Figure 6B). Furthermore, the same group proved the applicability of such pumps as biomedical devices, demonstrating the triggered release of insulin in response to glucose (Figure 6A).<sup>17</sup>

The applications of a self-powered enzyme-based micropump go beyond the biomedical field. Recently, Sen's group demonstrated the use of urease and catalase pumps as sensors for toxic substances. Enzymatic activity can be severely affected in the presence of sufficient concentration of inhibitors, which in enzyme-based micropumps affects the fluid flow, thus translating into a signal of contamination. This demonstrates



Table 1. Summary of Enzymatic Micro/Nanomachines

	material (size)	enzymes	mechanism	ref
single-enzyme motors	NA	ATPase	rotation induced by conformational changes	36–38,40
		urease	catalysis-enhanced diffusion by phoretic mechanism (plausible)	3
		urease, catalase		4
		catalase, urease, alkaline phosphatase, and triose phosphate isomerase	chemoacoustic effect by exothermic catalytic reactions	5
DNA–enzyme nanomachines/motors	single-stranded DNA (ssDNA)	glutathione transferase/urease	pH-sensitive switch activated by proton-producing/proton-consuming enzymes	55
	ssDNA	restriction enzyme (Nt.AlwI)	hybridization/cleavage cycles	52
	DNA template	T4 DNA polymerase (wild-type)	nonreciprocal conformational changes	78
	DNA origami tile (100 nm × 70 nm) + ssDNA	restriction enzyme Nt.BbvCI	hybridization/cleavage cycles	12
	gold nanoparticle coated with ssDNA	restriction enzyme Nb.BvCI	hybridization/cleavage cycles	54
enzyme-powered nanomotors	DNA-coated spherical particle (Ø = 5 or 0.5 µm)	RNase H	hybridization/hydrolysis cycles	13
	Janus HMSNP (389 nm)	catalase/urease/GOx	phoretic mechanism	15
	supramolecular stomatocytes (500 nm)	catalase/catalase+GOx	gas expelling	14
	MWCNT (20 nm × 1 µm)	catalase+GOx	bubble propulsion	59
	polypyrrole–gold (PPy–Au; 200 nm × 1.5–2 µm) nanorods	GOx, glutamate oxidase (GluOx), xanthine oxidase (XOD); horseradish peroxidase (HRP) + catalase; HRP	self-electrophoresis	61–63
enzyme-powered micromotors	polystyrene particles (0.79 µm)	catalase/urease	collective heating	16
	Janus silica particles (0.8 µm)	catalase+GOx	buoyancy effect (Archimedes law)	65
	Janus mesoporous silica microcapsule (2.3 µm)	urease	phoretic mechanism	66
	rolling up microtube (Au/Ni, 3 × 25 µm)	catalase	bubble propulsion	67
	bovine serum albumin/poly-L-lysine (PLL/BSA) multilayer tube (5 µm × 20 µm)	catalase	bubble propulsion	68
	PEDOT/Au tube (2 µm × 20 µm)	catalase	bubble propulsion	69,70
	Janus poly(styrenesulfonate)/poly(allylamine hydrochloride) (PSS/PAH) polymer capsule (8 µm)	catalase	bubble propulsion	72
	Janus silica particles	catalase	bubble propulsion	73
enzyme-powered macromotors	plant (radish) tissue tube (1 mm × 7 mm)	catalase+peroxidase	bubble propulsion	71
	carbon fiber (7 µm × 0.5–1 cm)	GOx+bilirubin oxidase (BO)	bioelectrochemical propulsion	64
enzyme-powered micropumps	SAM/gold pattern in PEG-coated glass surface (Ø = 6 mm)	catalase/urease/lipase/GOx	catalysis-induced density-driven convective flow	17
	SAM/gold pattern in PEG-coated glass surface (Ø = 6 mm)	T4 DNA polymerase (wild-type)	nonreciprocal conformational changes/catalysis-induced density-driven convective flow	78
	SAM/gold pattern in PEG-coated glass surface (Ø = 6 mm)	catalase/urease	catalysis-induced density-driven convective flow	81

the possibility of using these devices not only as drug delivery systems but also as sensors and actuators for bioremediation.<sup>81</sup>

## CONCLUSIONS AND OUTLOOK

Enzymes are naturally presented as biological “engines” of molecular machines in biological systems, which convert chemical energy into mechanical motion in order to accomplish different kinds of biofunctions. Enzymatic biocatalysis plays a critical role in the energy conversion process, and therefore, researchers have explored the fundamental mechanism of these biocatalytic reactions and contributed considerable efforts to unveil the motion mechanism of enzyme-powered molecular motors. Recent results suggest that single enzymes have been investigated as nanomotors exhibiting enhanced diffusion by turning over corresponding substrate, but debate on their motion mechanism is still under discussion. Through combination with biological molecules (*e.g.*, DNA) or organic and inorganic micro/nanoarchitectures (*e.g.*, silica particles, carbon fibers, metallic nanorods, microfluidic setup, *etc.*), enzymes have been utilized to power micro/nanosystems as self-propelled motors or pumps. Apart from catalase/H<sub>2</sub>O<sub>2</sub>-based bubble propulsion, there is still a scientific need for understanding the motion mechanism of enzyme-powered

synthetic micro/nanomotors, in particular, enhanced diffusion of nanomotors and directional/phoretic motion of micromotors. Current achievements of enzyme-powered micro/nanomachines, both biological and synthetic, are summarized in Table 1.

At present, enzyme-powered micro/nanomachines have been proven to be useful tools in various proof-of-concept applications, presenting possible solutions for many engineering problems from different fields, such as environmental protection, biosensing, and nanomedicine. Compared to conventional inorganic catalyst-based catalytic motors, micro/nanomotors powered by enzyme-based biocatalytic reactions are advantageous considering the biocompatibility of enzymes as well as versatile choices of enzymes/fuels in nature, which allows for future development of biocompatible propulsion micro/nanosystems. Especially, the recent achievement of biocompatible fuel-powered micro/nanomotors has aroused significant attention for the potential of using natural substrate-powered micro/nanomotors as active drug delivery systems in physiological conditions. However, the stability and sensitivity of enzymes toward the environment conditions, such as pH, temperature, and poisonous chemicals, are disadvantages for enzyme-powered micro/nanomotors. Moreover, other chal-

lenges in a biological environment, including high viscosity, strong flow, and component complexity of biological fluids, need to be overcome in the near future. Nevertheless, the field of enzyme-powered micro/nanomachines has been undergoing a quick growth and attracted increasing interests, wherein further advancement requires collaboration from multiple disciplines, including physics, biology, chemistry, and engineering.

## AUTHOR INFORMATION

### Corresponding Author

\*E-mail: [sanchez@is.mpg.de](mailto:sanchez@is.mpg.de) or [ssanchez@ibecbarcelona.eu](mailto:ssanchez@ibecbarcelona.eu).

### Author Contributions

<sup>†</sup>X.M. and A.C.H. contributed equally.

### Notes

The authors declare no competing financial interest.

## ACKNOWLEDGMENTS

The research leading to these results has received funding from the European Research Council under the European Union's Seventh Framework Program (FP7/2007/2013)/ERC Grant Agreement No. 311529 (LT-NRBS), the Alexander von Humboldt Foundation, and the Spanish MINECO under Grants CTQ2015-72471-EXP (Enzwim) and CTQ2015-68879-R (MICRODIA).

## VOCABULARY

**synthetic micro/nanomachines**, man-made micro- and nanoscale devices capable of performing assigned tasks; **molecular machines**, molecular components assembled to produce mechanical work in response to specific stimuli; **biocatalytic energy**, energy obtained through biological conversion of chemically free energy; **propulsion**, force that provokes motion; **enzymatic catalysis**, increase on the rate of a given reaction caused by the active site of a protein; **micro/nanomotors**, micro- and nanoscale devices capable of converting energy into active motion

## REFERENCES

- (1) Alberts, B.; Johnson, A.; Lewis, J.; Morgan, D.; Raff, M.; Roberts, K.; Walter, P. *Molecular Biology of the Cell*, 6th ed.; Garland Science: New York, 2014.
- (2) Lehninger, A. L.; Nelson, D. L.; Cox, M. M. *Principles of Biochemistry*, 6th ed.; Worth Publishers: New York, 2013.
- (3) Muddana, H. S.; Sengupta, S.; Mallouk, T. E.; Sen, A.; Butler, P. J. Substrate Catalysis Enhances Single-Enzyme Diffusion. *J. Am. Chem. Soc.* **2010**, *132*, 2110–2111.
- (4) Sengupta, S.; Dey, K. K.; Muddana, H. S.; Tabouillot, T.; Ibele, M. E.; Butler, P. J.; Sen, A. Enzyme Molecules as Nanomotors. *J. Am. Chem. Soc.* **2013**, *135*, 1406–1414.
- (5) Riedel, C.; Gabizon, R.; Wilson, C. A. M.; Hamadani, K.; Tsekouras, K.; Marqusee, S.; Pressé, S.; Bustamante, C. The Heat Released during Catalytic Turnover Enhances the Diffusion of an Enzyme. *Nature* **2014**, *517*, 227–230.
- (6) Wang, J. *Nanomachines: Fundamentals and Applications*; Wiley-VCH: Weinheim, Germany, 2013.
- (7) Soler, L.; Sanchez, S. Catalytic Nanomotors for Environmental Monitoring and Water Remediation. *Nanoscale* **2014**, *6*, 7175–7182.
- (8) Abdelmohsen, L. K. E. A.; Peng, F.; Tu, Y.; Wilson, D. A. Micro- and Nano-Motors for Biomedical Applications. *J. Mater. Chem. B* **2014**, *2*, 2395–2408.
- (9) Chalupniak, A.; Morales-Narváez, E.; Merkoçi, A. Micro and Nanomotors in Diagnostics. *Adv. Drug Delivery Rev.* **2015**, *95*, 104–116.

(10) Wang, H.; Pumera, M. Fabrication of Micro/Nanoscale Motors. *Chem. Rev.* **2015**, *115*, 8704–8735.

(11) Bath, J.; Green, S. J.; Turberfield, A. J. A Free-Running DNA Motor Powered by a Nicking Enzyme. *Angew. Chem., Int. Ed.* **2005**, *44*, 4358–4361.

(12) Wickham, S. F. J.; Bath, J.; Katsuda, Y.; Endo, M.; Hidaka, K.; Sugiyama, H.; Turberfield, A. J. A DNA-Based Molecular Motor That Can Navigate a Network of Tracks. *Nat. Nanotechnol.* **2012**, *7*, 169–173.

(13) Yehl, K.; Mugler, A.; Vivek, S.; Liu, Y.; Zhang, Y.; Fan, M.; Weeks, E. R.; Salaita, K. High-Speed DNA-Based Rolling Motors Powered by RNase H. *Nat. Nanotechnol.* **2015**, *11*, 184–190.

(14) Abdelmohsen, L. K. E. A.; Nijemeisland, M.; Pawar, G. M.; Janssen, G.-J. A.; Nolte, R. J. M.; van Hest, J. C. M.; Wilson, D. A. Dynamic Loading and Unloading of Proteins in Polymeric Stomatocytes: Formation of an Enzyme-Loaded Supramolecular Nanomotor. *ACS Nano* **2016**, *10*, 2652–2660.

(15) Ma, X.; Jannasch, A.; Albrecht, U.-R.; Hahn, K.; Miguel-López, A.; Schäffer, E.; Sánchez, S. Enzyme-Powered Hollow Mesoporous Janus Nanomotors. *Nano Lett.* **2015**, *15*, 7043–7050.

(16) Dey, K. K.; Zhao, X.; Tansi, B. M.; Méndez-Ortiz, W. J.; Córdova-Figueroa, U. M.; Golestanian, R.; Sen, A. Micromotors Powered by Enzyme Catalysis. *Nano Lett.* **2015**, *15*, 8311–8315.

(17) Sengupta, S.; Patra, D.; Ortiz-Rivera, I.; Agrawal, A.; Shklyav, S.; Dey, K. K.; Córdova-Figueroa, U.; Mallouk, T. E.; Sen, A. Self-Powered Enzyme Micropumps. *Nat. Chem.* **2014**, *6*, 415–422.

(18) Golestanian, R. Enhanced Diffusion of Enzymes That Catalyze Exothermic Reactions. *Phys. Rev. Lett.* **2015**, *115*, 108102.

(19) Colberg, P. H.; Kapral, R. Nanoconfined Catalytic Ångström-Size Motors. *J. Chem. Phys.* **2015**, *143*, 184906.

(20) Knowles, J. R. Enzyme Catalysis: Not Different, Just Better. *Nature* **1991**, *350*, 121–124.

(21) Albery, W. J.; Knowles, J. R. Efficiency and Evolution of Enzyme Catalysis. *Angew. Chem., Int. Ed. Engl.* **1977**, *16*, 285–293.

(22) Neet, K. E. Enzyme Catalytic Power Minireview Series. *J. Biol. Chem.* **1998**, *273*, 25527–25528.

(23) Agarwal, P. K. Enzymes: An Integrated View of Structure, Dynamics and Function. *Microb. Cell Fact.* **2006**, *5*, 2.

(24) Schliwa, M.; Woehlke, G. Molecular Motors. *Nature* **2003**, *422*, 759–765.

(25) Tyska, M. J.; Warsaw, D. M. The Myosin Power Stroke. *Cell Motil. Cytoskeleton* **2002**, *51*, 1–15.

(26) Tsao, D. S.; Diehl, M. R. Molecular Motors: Myosins Move ahead of the Pack. *Nat. Nanotechnol.* **2014**, *9*, 9–10.

(27) Hancock, W. O. Bidirectional Cargo Transport: Moving beyond Tug of War. *Nat. Rev. Mol. Cell Biol.* **2014**, *15*, 615–628.

(28) Brokaw, C. J. Mechanical Components of Motor Enzyme Function. *Biophys. J.* **1997**, *73*, 938–951.

(29) Butler, P. J.; Dey, K. K.; Sen, A. Impulsive Enzymes: A New Force in Mechanobiology. *Cell. Mol. Bioeng.* **2015**, *8*, 106–118.

(30) Spudich, J. A.; Rice, S. E.; Rock, R. S.; Purcell, T. J.; Warrick, H. M. Optical Traps to Study Properties of Molecular Motors. *Cold Spring Harbor Protocols* **2011**, *2011*, 1305–1318.

(31) Yoshida, M.; Muneyuki, E.; Hisabori, T. ATP Synthase—a Marvellous Rotary Engine of the Cell. *Nat. Rev. Mol. Cell Biol.* **2001**, *2*, 669–677.

(32) Nishi, T.; Forgac, M. The Vacuolar(H<sup>+</sup>)-ATPases—Nature's Most Versatile Proton Pumps. *Nat. Rev. Mol. Cell Biol.* **2002**, *3*, 94–103.

(33) Forgac, M. Vacuolar ATPases: Rotary Proton Pumps in Physiology and Pathophysiology. *Nat. Rev. Mol. Cell Biol.* **2007**, *8*, 917–929.

(34) Boyer, P. D. The Binding-Change Mechanism of ATP Synthesis. In *Membrane Bioenergetics*; Addison-Wesley: Reading, MA, 1979; pp 461–479.

(35) Noji, H. AMERSHAM PHARMACIA BIOTECH & SCIENCE PRIZE: The Rotary Enzyme of the Cell: The Rotation of F<sub>1</sub>-ATPase. *Science* **1998**, *282*, 1844–1845.

- (36) Noji, H.; Yasuda, R.; Yoshida, M.; Kinoshita, K. Direct Observation of the Rotation of F1-ATPase. *Nature* **1997**, *386*, 299–302.
- (37) Nakanishi-Matsui, M.; Sekiya, M.; Nakamoto, R. K.; Futai, M. The Mechanism of Rotating Proton Pumping ATPases. *Biochim. Biophys. Acta, Bioenerg.* **2010**, *1797*, 1343–1352.
- (38) Itoh, H.; Takahashi, A.; Adachi, K.; Noji, H. Mechanically Driven ATP Synthesis by F1-ATPase. *Nature* **2004**, *427*, 465–468.
- (39) Arai, S.; Saijo, S.; Suzuki, K.; Mizutani, K.; Kakinuma, Y.; Ishizuka-Katsura, Y.; Ohsawa, N.; Terada, T.; Shirouzu, M.; Yokoyama, S.; Iwata, S.; Yamato, I.; Murata, T. Rotation Mechanism of *Enterococcus hirae* V1-ATPase Based on Asymmetric Crystal Structures. *Nature* **2013**, *493*, 703–707.
- (40) Martin, J. L.; Ishmukhametov, R.; Hornung, T.; Ahmad, Z.; Frasch, W. D. Anatomy of F1-ATPase Powered Rotation. *Proc. Natl. Acad. Sci. U. S. A.* **2014**, *111*, 3715–3720.
- (41) Montemagno, C.; Bachand, G. Constructing Nanomechanical Devices Powered by Biomolecular Motors. *Nanotechnology* **1999**, *10*, 225–231.
- (42) Takahashi, K.; Arjunan, S. N. V.; Tomita, M. Space in Systems Biology of Signaling Pathways - towards Intracellular Molecular Crowding in Silico. *FEBS Lett.* **2005**, *579*, 1783–1788.
- (43) Golestanian, R.; Liverpool, T. B.; Ajdari, A. Propulsion of a Molecular Machine by Asymmetric Distribution of Reaction Products. *Phys. Rev. Lett.* **2005**, *94*, 220801.
- (44) Golestanian, R.; Ajdari, A. Mechanical Response of a Small Swimmer Driven by Conformational Transitions. *Phys. Rev. Lett.* **2008**, *100*, 38101.
- (45) Hammes-Schiffer, S. Impact of Enzyme Motion on Activity. *Biochemistry* **2002**, *41*, 13335–13343.
- (46) Eisenmesser, E. Z.; Millet, O.; Labeikovsky, W.; Korzhnev, D. M.; Wolf-Watz, M.; Bosco, D. A.; Skalicky, J. J.; Kay, L. E.; Kern, D. Intrinsic Dynamics of an Enzyme Underlies Catalysis. *Nature* **2005**, *438*, 117–121.
- (47) Osuna, S.; Jiménez-Osés, G.; Noey, E. L.; Houk, K. N. Molecular Dynamics Explorations of Active Site Structure in Designed and Evolved Enzymes. *Acc. Chem. Res.* **2015**, *48*, 1080–1089.
- (48) Luk, L. Y. P.; Loveridge, E. J.; Allemann, R. K. Protein Motions and Dynamic Effects in Enzyme Catalysis. *Phys. Chem. Chem. Phys.* **2015**, *17*, 30817–30827.
- (49) Pelz, B.; Žoldák, G.; Zeller, F.; Zacharias, M.; Rief, M. Subnanometre Enzyme Mechanics Probed by Single-Molecule Force Spectroscopy. *Nat. Commun.* **2016**, *7*, 10848.
- (50) Taylor, J. H. Nucleic Acid Synthesis in Relation to the Cell Division Cycle. *Ann. N. Y. Acad. Sci.* **1960**, *90*, 409–421.
- (51) Wickham, S. F. J.; Endo, M.; Katsuda, Y.; Hidaka, K.; Bath, J.; Sugiyama, H.; Turberfield, A. J. Direct Observation of Stepwise Movement of a Synthetic Molecular Transporter. *Nat. Nanotechnol.* **2011**, *6*, 166–169.
- (52) Chen, Y.; Xiang, Y.; Yuan, R.; Chai, Y. A Restriction Enzyme-Powered Autonomous DNA Walking Machine: Its Application for a Highly Sensitive Electrochemiluminescence Assay of DNA. *Nanoscale* **2015**, *7*, 981–986.
- (53) von Delius, M.; Geertsema, E. M.; Leigh, D. A. A Synthetic Small Molecule That Can Walk down a Track. *Nat. Chem.* **2010**, *2*, 96–101.
- (54) Yang, X.; Tang, Y.; Mason, S. D.; Chen, J.; Li, F. Enzyme-Powered Three-Dimensional DNA Nanomachine for DNA Walking, Payload Release, and Biosensing. *ACS Nano* **2016**, *10*, 2324–2330.
- (55) Del Grosso, E.; Dallaire, A.-M.; Vallée-Bélisle, A.; Ricci, F. Enzyme-Operated DNA-Based Nanodevices. *Nano Lett.* **2015**, *15*, 8407–8411.
- (56) Idili, A.; Vallée-Bélisle, A.; Ricci, F. Programmable pH-Triggered DNA Nanoswitches. *J. Am. Chem. Soc.* **2014**, *136*, 5836–5839.
- (57) Ma, X.; Sanchez, S. A Bio-Catalytically Driven Janus Mesoporous Silica Cluster Motor with Magnetic Guidance. *Chem. Commun.* **2015**, *51*, 5467–5470.
- (58) Ma, X.; Hahn, K.; Sanchez, S. Catalytic Mesoporous Janus Nanomotors for Active Cargo Delivery. *J. Am. Chem. Soc.* **2015**, *137*, 4976–4979.
- (59) Pantarotto, D.; Browne, W. R.; Feringa, B. L. Autonomous Propulsion of Carbon Nanotubes Powered by a Multienzyme Ensemble. *Chem. Commun.* **2008**, 1533–1535.
- (60) Ma, X.; Jannasch, A.; Albrecht, U.-R.; Hahn, K.; Miguel-López, A.; Schäffer, E.; Sánchez, S. Enzyme-Powered Hollow Mesoporous Janus Nanomotors. *Nano Lett.* **2015**, *15*, 7043–7050.
- (61) Pavel, I.-A.; Bunea, A.-I.; David, S.; Gáspár, S. Nanorods with Biocatalytically Induced Self-Electrophoresis. *ChemCatChem* **2014**, *6*, 866–872.
- (62) Bunea, A.-I.; Pavel, I.-A.; David, S.; Gaspar, S. Modification with Hemeproteins Increases the Diffusive Movement of Nanorods in Dilute Hydrogen Peroxide Solutions. *Chem. Commun.* **2013**, *49*, 8803–8805.
- (63) Bunea, A.-I.; Pavel, I.-A.; David, S.; Gáspár, S. Sensing Based on the Motion of Enzyme-Modified Nanorods. *Biosens. Bioelectron.* **2015**, *67*, 42–48.
- (64) Mano, N.; Heller, A. Bioelectrochemical Propulsion. *J. Am. Chem. Soc.* **2005**, *127*, 11574–11575.
- (65) Schattling, P.; Thingholm, B.; Städler, B. Enhanced Diffusion of Glucose-Fueled Janus Particles. *Chem. Mater.* **2015**, *27*, 7412–7418.
- (66) Ma, X.; Wang, X.; Hahn, K.; Sánchez, S. Motion Control of Urea-Powered Biocompatible Hollow Microcapsules. *ACS Nano* **2016**, *10*, 3597–3605.
- (67) Sanchez, S.; Solovev, A. A.; Mei, Y.; Schmidt, O. G. Dynamics of Biocatalytic Microengines Mediated by Variable Friction Control. *J. Am. Chem. Soc.* **2010**, *132*, 13144–13145.
- (68) Wu, Z.; Lin, X.; Zou, X.; Sun, J.; He, Q. Biodegradable Protein-Based Rockets for Drug Transportation and Light-Triggered Release. *ACS Appl. Mater. Interfaces* **2015**, *7*, 250–255.
- (69) Orozco, J.; García-Gradilla, V.; D'Agostino, M.; Gao, W.; Cortés, A.; Wang, J. Artificial Enzyme-Powered Microfish for Water-Quality Testing. *ACS Nano* **2013**, *7*, 818–824.
- (70) Singh, V. V.; Kaufmann, K.; Esteban-Fernandez de Avila, B.; Uygün, M.; Wang, J. Nanomotors Responsive to Nerve-Agent Vapor Plumes. *Chem. Commun.* **2016**, *52*, 3360–3363.
- (71) Sattayasamitsathit, S.; Kaufmann, K.; Galarnyk, M.; Vazquez-Duhalt, R.; Wang, J. Dual-Enzyme Natural Motors Incorporating Decontamination and Propulsion Capabilities. *RSC Adv.* **2014**, *4*, 27565–27570.
- (72) Wu, Y.; Lin, X.; Wu, Z.; Möhwald, H.; He, Q. Self-Propelled Polymer Multilayer Janus Capsules for Effective Drug Delivery and Light-Triggered Release. *ACS Appl. Mater. Interfaces* **2014**, *6*, 10476–10481.
- (73) Simmchen, J.; Baeza, A.; Ruiz, D.; Esplandiú, M. J.; Vallet-Regí, M. Asymmetric Hybrid Silica Nanomotors for Capture and Cargo Transport: Towards a Novel Motion-Based DNA Sensor. *Small* **2012**, *8*, 2053–2059.
- (74) Shklyav, O. E.; Shum, H.; Sen, A.; Balazs, A. C. Harnessing Surface-Bound Enzymatic Reactions to Organize Microcapsules in Solution. *Sci. Adv.* **2016**, *2*, e1501835.
- (75) Solovev, A. A.; Sanchez, S.; Mei, Y.; Schmidt, O. G. Tunable Catalytic Tubular Micro-Pumps Operating at Low Concentrations of Hydrogen Peroxide. *Phys. Chem. Chem. Phys.* **2011**, *13*, 10131–10135.
- (76) Yu, H.; Jo, K.; Kounovsky, K. L.; Pablo, J. J. de; Schwartz, D. C. Molecular Propulsion: Chemical Sensing and Chemotaxis of DNA Driven by RNA Polymerase. *J. Am. Chem. Soc.* **2009**, *131*, 5722–5723.
- (77) Yadav, V.; Duan, W.; Butler, P. J.; Sen, A. Anatomy of Nanoscale Propulsion. *Annu. Rev. Biophys.* **2015**, *44*, 77–100.
- (78) Sengupta, S.; Spiering, M. M.; Dey, K. K.; Duan, W.; Patra, D.; Butler, P. J.; Astumian, R. D.; Benkovic, S. J.; Sen, A. DNA Polymerase as a Molecular Motor and Pump. *ACS Nano* **2014**, *8*, 2410–2418.
- (79) Wang, W.; Chiang, T.-Y.; Velegol, D.; Mallouk, T. E. Understanding the Efficiency of Autonomous Nano- and Microscale Motors. *J. Am. Chem. Soc.* **2013**, *135*, 10557–10565.

(80) Ortiz-Rivera, I.; Shum, H.; Agrawal, A.; Sen, A.; Balazs, A. C. Convective Flow Reversal in Self-Powered Enzyme Micropumps. *Proc. Natl. Acad. Sci. U. S. A.* **2016**, *113*, 2585–2590.

(81) Ortiz-Rivera, I.; Courtney, T. M.; Sen, A. Enzyme Micropump-Based Inhibitor Assays. *Adv. Funct. Mater.* **2016**, *26*, 2135–2142.





## Bubble-Free Propulsion of Ultrasmall Tubular Nanojets Powered by Biocatalytic Reactions

Xing Ma,<sup>‡, #</sup> Ana C. Hortelao,<sup>‡, ||</sup> Albert Miguel-López,<sup>||</sup> and Samuel Sánchez<sup>\*, ‡, ||, §</sup>

<sup>‡</sup>Max-Planck Institute for Intelligent Systems Institution, Heisenbergstraße 3, 70569 Stuttgart, Germany

<sup>#</sup>School of Materials Science and Engineering, Harbin Institute of Technology Shenzhen Graduate School, 518055 Shenzhen, China

<sup>||</sup>Institut de Bioenginyeria de Catalunya (IBEC), Baldri i Reixac 10-12, 08028 Barcelona, Spain

<sup>§</sup>Institució Catalana de Recerca i Estudis Avançats (ICREA), Pg. Lluís Companys 23, 08010 Barcelona, Spain

### Supporting Information

**ABSTRACT:** The motion of self-propelled tubular micro- and nanojets has so far been achieved by bubble propulsion, e.g., O<sub>2</sub> bubbles formed by catalytic decomposition of H<sub>2</sub>O<sub>2</sub>, which renders future biomedical applications inviable. An alternative self-propulsion mechanism for tubular engines on the nanometer scale is still missing. Here, we report the fabrication and characterization of bubble-free propelled tubular nanojets (as small as 220 nm diameter), powered by an enzyme-triggered biocatalytic reaction using urea as fuel. We studied the translational and rotational dynamics of the nanojets as functions of the length and location of the enzymes. Introducing tracer nanoparticles into the system, we demonstrated the presence of an internal flow that extends into the external fluid via the cavity opening, leading to the self-propulsion. One-dimensional nanosize, longitudinal self-propulsion, and biocompatibility make the tubular nanojets promising for future biomedical applications.

Researchers have fabricated multiple micro/nanomotors that mimic natural systems<sup>1</sup> and are capable of converting chemical energy into kinetic energy for self-propulsion.<sup>2</sup> Tubular catalytic motors have been demonstrated as versatile “on-the-fly” microsystems for various proof-of-concept applications, such as heavy metal capture<sup>3</sup> or water remediation,<sup>4</sup> cargo loading and transportation,<sup>5</sup> drug delivery,<sup>6</sup> sensing,<sup>7</sup> and as microdrillers for minimally invasive surgery.<sup>8</sup> Almost all the current tubular motors are driven by a bubble propulsion mechanism on the micrometer scale. Usually, an inorganic catalytic component, such as platinum,<sup>6,9</sup> silver,<sup>10</sup> or MnO<sub>2</sub>,<sup>11</sup> is included inside the tubes to trigger decomposition of hydrogen peroxide (H<sub>2</sub>O<sub>2</sub> → H<sub>2</sub>O + <sup>1</sup>/<sub>2</sub>O<sub>2</sub>). Alternatively, catalase enzyme has been used as an organic catalyst to efficiently provide self-propulsion by decomposing much lower concentrations of H<sub>2</sub>O<sub>2</sub>.<sup>7b,12</sup> The underlying mechanism involves the formation and continuous ejection of oxygen bubbles from the tubular confinement, provoking motion in the opposite direction.

Before now, there have been two major strategies for the fabrication of tubular motors. One is the “rolling-up” method based on clean-room photolithography and electron-beam evaporation techniques, which can produce tubular structures with sizes from sub-micrometer up to 30 μm diameter and from

25 μm to 1 mm length.<sup>8a,9b,13</sup> Clean-room-free “rolling-up” methods have been also reported.<sup>14</sup> The other method is electrochemical deposition on porous membranes (Al<sub>2</sub>O<sub>3</sub> or polycarbonate),<sup>3,7b,9a</sup> which produces microtubes from 2 to 5 μm diameter. Until now, only a very few works have reported nanotubular motors, all of them using high concentrations of H<sub>2</sub>O<sub>2</sub> as fuel and surfactant to reduce the surface tension.<sup>8a,14,15</sup> A cheap and facile fabrication method that could be scaled-up, enabling a metal-free nanoarchitecture, is sought. Biofriendly processes such as enzyme catalysis can provide mechanical force to drive micro/nanostructures, with great potential for biocompatible self-powered systems.<sup>16</sup> We previously demonstrated that enzyme-based silica micromotors show biocompatibility against HeLa cells.<sup>16e</sup> Additionally, a bubble-free propulsion mechanism would avoid accumulation of gas bubbles in the fluidic environment, which is advantageous for future *in vivo* biomedical use.

Herein, we present ultrasmall tubular silica nanojets (220 nm diameter on average) that are self-propelled by enzymatic reactions. The nanojets are powered by the turnover of urea substrate (at physiological concentrations) triggered by enzyme urease (urea → NH<sub>3(aq)</sub> + CO<sub>2(aq)</sub>). The reaction products, ammonia and carbon dioxide, are formed inside the nanotubes (NTs), generating internal flows that extend into the external space via the tube opening. This generates a thrust longitudinally that maintains the directional movement of the nanojets by a “jetting effect”.<sup>17</sup> The existence of a flow was supported by analyzing tracer nanoparticles (NPs) expelled from the back side of the nanojets.

The silica nanotubes (SNTs) were fabricated by using silver nanowires (AgNWs, 115 nm × 50 μm) as the templates on which a thin layer of silica was grown by sol-gel chemistry.<sup>18</sup> The silica-coated AgNWs (AgNW@SiO<sub>2</sub>) (Figure S1a) were then broken down into shorter segments by sonication for 3 h (see details in the Supporting Information (SI)). After removal of the AgNW templates by etching in *aqua regia* overnight, the SNTs were obtained (Figure S1b,c). We functionalized the SNTs with amine groups (-NH<sub>2</sub>) by grafting, yielding SNT-NH<sub>2</sub>. The amine groups on SNT-NH<sub>2</sub> were detected by fluorescamine, which upon reaction with primary -NH<sub>2</sub> exhibit fluorescent emission at 477 nm (Figure S2a). Zeta-potential measurement showed that the

Received: July 3, 2016

Published: October 9, 2016



surface charge of the SNTs changed from  $-39 \pm 11$  to  $44 \pm 11$  mV for SNT-NH<sub>2</sub>, proving the success of surface functionalization with amine groups (Figure S2b). We further conjugated enzyme (urease) onto the surface of the SNTs by using glutaraldehyde as a linker molecule,<sup>16e,f</sup> yielding SNT-urease (Figure 1a). We

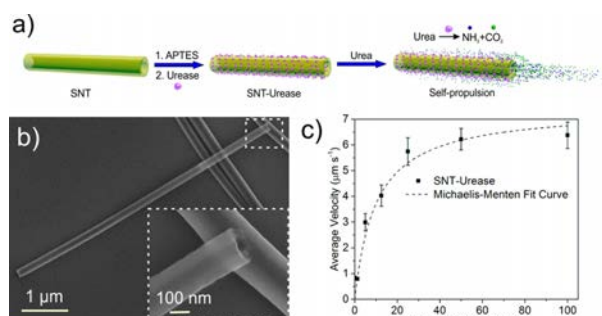


**Figure 1.** (a) Schematic illustration of the fabrication of urease-conjugated silica tubular (SNT-urease) nanojets. (b) Typical SEM image of the SNTs. (c) Fuel-dependent average velocity of SNT-urease with an average length of 10 μm. Error bars indicate standard error of the mean,  $N = 10$ .

confirmed the enzyme conjugation by using a protein staining kit to visualize the presence of urease on the SNT-urease, as indicated by red fluorescence color in Figure S3.<sup>16e</sup> A typical scanning electron microscopy (SEM) image of a SNT is presented in Figure 1b, and its quasi-transparent tubular structure in the inset image. The average diameter of the SNTs, determined from SEM images, is  $D = 220 \pm 24$  nm (average  $\pm$  standard deviation,  $N = 30$ ). The length of the NTs ranges from 3 to 40 μm and can be controlled by using different templates, centrifugation, and variable sonication times. When the enzymatic nanojets were placed in solution containing urea, we observed directional self-propulsion along the longitudinal axis (Video S1). The average velocity of tubular nanojets with an average length of  $\sim 10$  μm (9–13 μm) showed a fuel-dependent increasing trend, which fits well with the Michaelis–Menten enzymatic kinetics, reaching a plateau at 25 mM (Figure 1c). The close correlation between velocity and enzymatic activity suggests that the biocatalytic reaction provides mechanical power for the motion of the nanojets.

In the absence of urea, the nanojets exhibited only Brownian motion (Figure S4 and Video S2). The translational diffusion coefficient ( $D_t$ ) retrieved from a mean-square displacement (MSD) plot ( $\text{MSD} = 4D_t\Delta t$  for two-dimensional case) fits well with the theoretical calculation (inset of Figure 2b).<sup>19</sup> Upon addition of urea (100 mM), the nanojets showed longitudinal self-propulsion. Snapshots of tracking trajectories of the self-propelled nanojets of three different lengths (3.17, 5.42, and 18.03 μm) are presented in Figure 2a (Video S3). We characterized the motion of the nanojets by quantifying the velocity ( $V$ ), measuring the longitudinal displacement ( $\Delta L$ ) within a given time ( $\Delta t$ ), as  $V = \Delta L/\Delta t$ . We found a decreasing trend of the velocity with increasing length of the nanojets (Figure 2b). We further analyzed the rotational diffusion of the nanojets by automatic tracking of the orientation angle ( $\theta$ ) of the nanojets, as shown in Video S1 and Figure S5a. The plot of mean square angular displacement (MSAD) was calculated to retrieve the effective rotational diffusion coefficient  $D_r(\text{eff})$  by the equation  $\text{MSAD} = 2D_r(\text{eff})\Delta t$  in the one-dimensional case, as shown in Figure S5c.

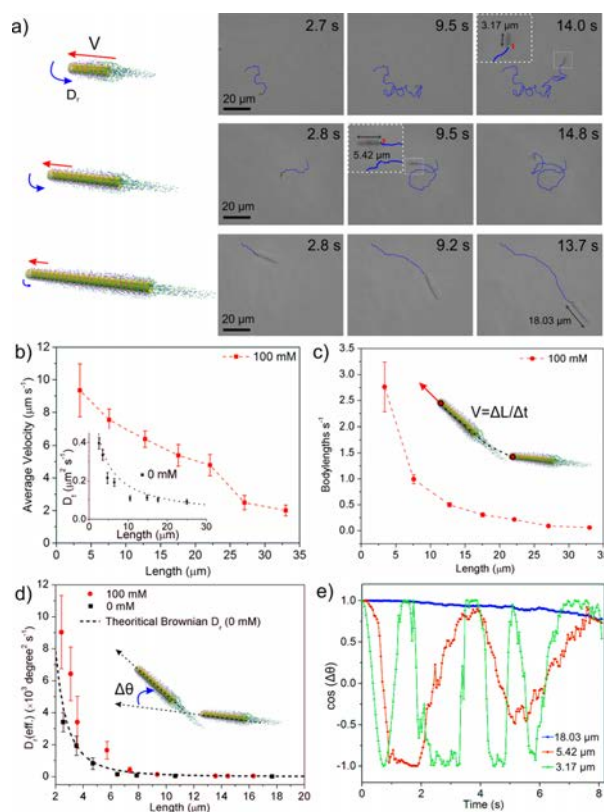


**Figure 2.** Dynamics of urease-powered tubular nanojets. (a) Schematic illustration and tracking trajectories of the tubular nanojets with varied lengths. Variation with tubular nanojet length of (b) longitudinal average velocity in  $\mu\text{m s}^{-1}$  (inset is Brownian translational diffusion coefficient,  $D_t$ , of the nanojets without fuel; dashed line is theoretical value of  $D_t$ ), (c) body lengths in  $\text{s}^{-1}$ , and (d) effective rotational diffusion coefficient ( $D_r(\text{eff})$ ) with (100 mM) and without (0 mM) fuel (dashed line is theoretical value of Brownian  $D_r$ ). (e) Angular autocorrelation of the three nanojets shown in (a). Error bars indicate standard error of the mean,  $N = 10$ .

In the absence of fuel, the rotational diffusion of the nanojets was only due to Brownian motion, consistent with the theoretical calculation (dashed line, Figure 2d).<sup>19</sup> In the presence of urea, the tubular nanojets showed enhanced rotational diffusion, in particular when their length was  $< 10$  μm. However, the rotational behavior was stabilized and angular changes decreased when the length of the tubular motors was  $> 10$  μm. To learn more details about the orientation change with time of three distinct nanojets, we analyzed their angular autocorrelation ( $\cos(\Delta\theta)$ ) for a period of 8 s, where  $\Delta\theta$  is the angular change compared to their initial orientation,<sup>20</sup> as plotted in Figure 2e. A quickly changing autocorrelation value indicates a fast rotation of the nanojets, whereas a constant value close to 1 is associated with a stable orientation. The frequency of angular change for the nanojet of length 3.17 μm is substantially higher than that for the 5.42 μm one (green and red lines, respectively). A nanojet of  $\sim 18$  μm (blue line) maintains an undisturbed angular correlation for the represented time.

To identify the driving force of the nanojets, we selectively functionalized urease inside (SNT-Urease-I), outside (SNT-Urease-O), or all over the nanotube (SNT-Urease-A), as presented in Figure 3a (see experimental procedures in the SI).

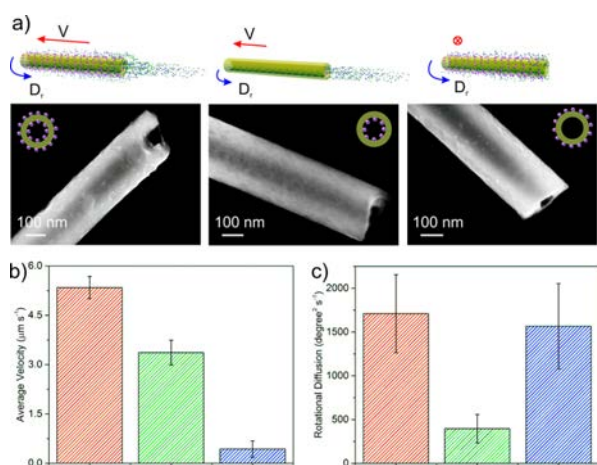


**Figure 3.** Enzyme location-dependent motion behavior. (a) Schematic illustration of SNT-urease with enzyme all over (SNT-urease-A), inside (SNT-urease-I), and outside (SNT-urease-O) the nanotube, and corresponding SEM images. (b) Longitudinal average velocity of the three nanotubular motors with average length of 20 μm. (c) Rotational diffusion of the three nanotubular motors with average length of 5.5 μm. Error bars indicate standard error of the mean,  $N = 10$ .

The presence of urease on the external surface of the samples of SNT-Urease-A and SNT-Urease-O was seen in the SEM images (Figure 3a), while smooth bare silica was observed for SNT-Urease-I. The protein concentration conjugated to the different types of NTs was evaluated using a Coomassie Brilliant Blue-based protein quantification kit (Figure S10a). Furthermore, the enzymatic activity of the three urease-conjugated tubular nanojets was evaluated according to a previously reported method,<sup>16f</sup> indicating that the immobilized enzymes on all three nanojets were active (Figure S10b).

The effect of enzyme location on the dynamics of the three types of nanojets with average length of 20 μm was analyzed (Figure 3b). Although all three nanojets were biocatalytically active, only SNT-Urease-A and SNT-Urease-I demonstrated longitudinal self-propulsion (Video S4). In contrast, SNT-Urease-O showed only Brownian motion. These results evidence that the longitudinal self-propulsion of the tubular nanojets should be attributed to the enzymatic reaction taking place inside the NTs. SNT-Urease-A has the highest velocity among the three tubular nanojets, implying that the enzymatic reactions on the external surface might contribute to enhancing the longitudinal velocity. The change from silica/H<sub>2</sub>O molecules on a nonactive surface into a much more complex situation, where interactions between multiple molecules (e.g., biocatalytic products) and the enzymatically active surface of SNT-Urease-A were taking place, might alter the interfacial tension and possibly decrease resistance to self-propulsion, leading to velocity enhancement. We tracked tracer NPs located near the nanojets and found that those were “attracted” toward the outer surface, implying a flow field on the surface of the nanojet. Similarly to the enzymatic micropumps reported by Sen et al.,<sup>21</sup> the enzymatically active outer surface would create density-driven convective flows that can be indirectly observed by the “trapping” effect of tracer NPs along the tube surface (see details in Figure S11 and discussion in the SI). Such an external flow field might also contribute to the velocity enhancement for the SNT-Urease-All. However, further

in-depth investigation is needed before reaching a conclusive understanding of this phenomenon.

We further analyzed the rotational behavior of the three kinds of nanojets with an average length of 5.5 μm, at which an obvious nonbalance effect was observed. SNT-Urease-A and SNT-Urease-O showed 3 times higher rotational diffusion coefficients compared to SNT-Urease-I (Figure 3c), suggesting that the enzymatic reaction on the external surface of the tubular nanojets indeed enhanced their rotational diffusion.

The biocatalytic nanojets act as jet engines as they generate thrust from their cavity, releasing a jet of fluid backward (in this case the products of the enzymatic reaction). Before now, this jetting force provided by catalytic microjets has been caused by bubble generation. In the current work, the products do not generate visible bubbles, yet they induce enough propelling force to move the nanojets forward. This jet of liquid has been studied using a suspension of tracer NPs with the nanojets (Figure 4 and

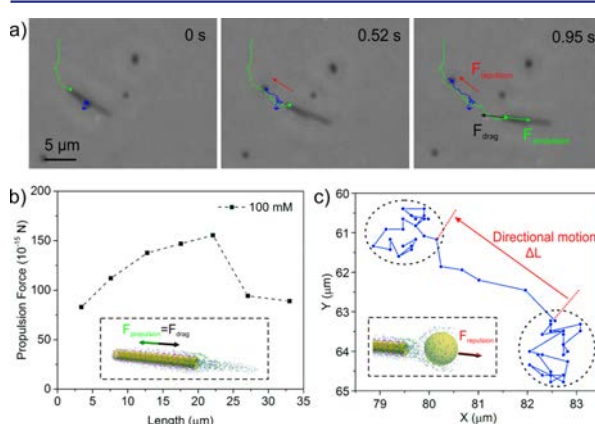


**Figure 4.** Nanopropulsion from internal flows. (a) Video snapshot of a self-propelled nanojet (green track) expelling a tracer NP (blue tracking trajectory). (b) Propulsion force of the nanojets calculated by eq 2, based on the velocity value in Figure 2b. (c) Tracking trajectory of the tracer NP indicates the directional motion of the tracer NP instantly pushed by the repulsion force originated from the internal flow.

Video S5). The tracking trajectory is presented in Figure 4a. At low Reynolds numbers, the propulsion force ( $F_{prop}$ ) is equal to the drag force ( $F_{drag}$ ) applied on the tubular nanojets,<sup>22</sup> as indicated in Figure 4a. We approximated the dynamics of the tubular nanojets by using the Stokes’ drag equation for nanorods,<sup>9a,23</sup>

$$F_{drag} = \frac{2\pi\mu LV}{\ln(2L/R) - 0.72} \quad (1)$$

where  $\mu$  is viscosity and  $R$ ,  $L$ , and  $V$  are radius, length, and velocity of the nanorods, and we calculated the drag force applied on the tubular nanojets based on the velocity results presented in Figure 2c. As shown in Figure 4b, the drag force ranges from 80 to 150 fN. When the NPs were not affected by the flow field of the active nanojets, they demonstrated only randomized Brownian motion (blue trajectory) without any given directionality. The tracer NPs, once in the vicinity of the rear opening of nanojets, were repelled and pushed away, which clearly evidenced the internal flow of the biocatalytic products (Figure 4c). We measured the length ( $\Delta L = 4.07 \mu\text{m}$ ) and time interval ( $\Delta t = 0.21 \text{ s}$ ) of the directional motion range of the specific tracer NP in Figure 4a and calculated the instantaneous velocity of the tracer NP as  $V = \Delta L / \Delta t = 19.38 \mu\text{m s}^{-1}$ . By Stokes’ drag law for an active spherical particle in fluid,

$$F = 6\pi\mu RV \quad (2)$$

where  $\mu$  is viscosity and  $R$  and  $V$  are radius and velocity of the particle, we calculated the drag force ( $F_{\text{drag}}(\text{NP}) = 124 \text{ fN}$ ) during the directional motion range, which can be used to approximate the repulsion force  $F_{\text{rep}}(\text{NP})$  applied on the tracer NP. The length and the longitudinal velocity of the specific tubular nanojet shown in Figure 4a are  $L = 6.93 \mu\text{m}$  and  $V = 9.58 \mu\text{m s}^{-1}$ . Thus, the drag force (propulsion force) for the specific tubular nanojet was found to be  $F_{\text{drag}}(\text{jet}) = F_{\text{prop}}(\text{jet}) = 134 \text{ fN}$  (by eq 1), which agrees with the repulsion force (or drag force) of the tracer NP found experimentally. These results prove that the motion of the tubular nanojets can be attributed to active flow of the enzymatic reaction products, providing a new mechanism for tubular motors besides the current bubble propulsion mechanism.

In summary, we fabricated a self-propelled tubular nanojet driven by a bubble-free propulsion mechanism. In contrast to most tubular motors based on bubble propulsion by decomposition of  $\text{H}_2\text{O}_2$ , the mechanical power is generated by enzymatic decomposition of biofriendly urea substrate that does not generate visible bubbles. We observed that not only enzymes inside but also those located outside the nanojets contribute to the self-propulsion. Considering the small dimension and biofriendly motors and fuel, these nanojets hold great potential for use in biomedical fields. To control their motion, the use of external sources will be necessary as well as the study of the collective behavior of nanojets. Further experimental and theoretical studies will be performed to better understand the non-bubble propulsion mechanism.

## ■ ASSOCIATED CONTENT

### ■ Supporting Information

The Supporting Information is available free of charge on the ACS Publications website at DOI: 10.1021/jacs.6b06857.

Experimental details of protocols, methods, and characterization, including Figures S1–S11 (PDF)

Video S1, self-propulsion of SNT-urease; Video S2, SNT-urease at 0 mM urea; Video S3, SNT-urease of varied length at 1000 mM urea; Video S4, SNT-urease with enzyme all over, inside, and outside; and Video S5, moving SNT-urease with tracer NPs (AVI)

## ■ AUTHOR INFORMATION

### Corresponding Author

\*sanchez@is.mpg.de; sanchez@ibebarcelona.eu

### Notes

The authors declare no competing financial interest.

## ■ ACKNOWLEDGMENTS

The research leading to these results has received funding from the European Research Council under the European Union's Seventh Framework Program (FP7/20072013)/ERC grant agreement no. 311529 (LT-NRBS) and the Alexander von Humboldt Foundation (to X.M.). S.S. thanks the Spanish MINECO for grants CTQ2015-68879-R (MICRODIA) and CTQ2015-72471-EXP (Enzwim).

## ■ REFERENCES

(1) (a) Sánchez, S.; Soler, L.; Katuri, J. *Angew. Chem., Int. Ed.* **2015**, *54*, 1414. (b) Wang, H.; Pumera, M. *Chem. Rev.* **2015**, *115*, 8704. (c) Wang, J. *Nanomachines: Fundamentals and Applications*; Wiley-VCH: Weinheim, 2013. (d) Lin, X.; Wu, Z.; Wu, Y.; Xuan, M.; He, Q. *Adv. Mater.* **2016**, *28*, 1060.

(2) (a) Sengupta, S.; Ibele, M. E.; Sen, A. *Angew. Chem., Int. Ed.* **2012**, *51*, 8434. (b) Ozin, G. A.; Manners, I.; Fournier-Bidoz, S.; Arsenault, A. *Adv. Mater. (Weinheim, Ger.)* **2005**, *17*, 3011. (c) Paxton, W. F.; Sundararajan, S.; Mallouk, T. E.; Sen, A. *Angew. Chem., Int. Ed.* **2006**, *45*, 5420.

(3) Vilela, D.; Parmar, J.; Zeng, Y.; Zhao, Y.; Sánchez, S. *Nano Lett.* **2016**, *16*, 2860.

(4) (a) Soler, L.; Magdanz, V.; Fomin, V. M.; Sánchez, S.; Schmidt, O. G. *ACS Nano* **2013**, *7*, 9611. (b) Parmar, J.; Vilela, D.; Pellicer, E.; Esqué-de los Ojos, D.; Sort, J.; Sánchez, S. *Adv. Funct. Mater.* **2016**, *26*, 4152.

(5) (a) Solovev, A. A.; Sánchez, S.; Pumera, M.; Mei, Y. F.; Schmidt, O. G. *Adv. Funct. Mater.* **2010**, *20*, 2430. (b) Restrepo-Perez, L.; Soler, L.; Martínez-Cisneros, C.; Sánchez, S.; Schmidt, O. G. *Lab Chip* **2014**, *14*, 2914.

(6) Wu, Z.; Wu, Y.; He, W.; Lin, X.; Sun, J.; He, Q. *Angew. Chem., Int. Ed.* **2013**, *52*, 7000.

(7) (a) Wu, J.; Balasubramanian, S.; Kagan, D.; Manesh, K. M.; Campuzano, S.; Wang, J. *Nat. Commun.* **2010**, *1*, 36. (b) Singh, V. V.; Kaufmann, K.; Esteban-Fernandez de Avila, B.; Uygun, M.; Wang, J. *Chem. Commun.* **2016**, *52*, 3360. (c) Orozco, J.; García-Gradilla, V.; D'Agostino, M.; Gao, W.; Cortés, A.; Wang, J. *ACS Nano* **2013**, *7*, 818.

(8) (a) Solovev, A. A.; Xi, W.; Gracias, D. H.; Harazim, S. M.; Deneke, C.; Sánchez, S.; Schmidt, O. G. *ACS Nano* **2012**, *6*, 1751. (b) Gao, W.; Dong, R.; Thamphiwatana, S.; Li, J.; Gao, W.; Zhang, L.; Wang, J. *ACS Nano* **2015**, *9*, 117.

(9) (a) Gao, W.; Sattayasamitsathit, S.; Orozco, J.; Wang, J. *J. Am. Chem. Soc.* **2011**, *133*, 11862. (b) Solovev, A. A.; Mei, Y. F.; Urena, E. B.; Huang, G. S.; Schmidt, O. G. *Small* **2009**, *5*, 1688.

(10) Mei, Y. F.; Huang, G. S.; Solovev, A. A.; Urena, E. B.; Moench, I.; Ding, F.; Reindl, T.; Fu, R. K. Y.; Chu, P. K.; Schmidt, O. G. *Adv. Mater. (Weinheim, Ger.)* **2008**, *20*, 4085.

(11) Safdar, M.; Wani, O. M.; Jänis, J. *ACS Appl. Mater. Interfaces* **2015**, *7*, 25580.

(12) Sánchez, S.; Solovev, A. A.; Mei, Y.; Schmidt, O. G. *J. Am. Chem. Soc.* **2010**, *132*, 13144.

(13) Harazim, S. M.; Xi, W.; Schmidt, C. K.; Sánchez, S.; Schmidt, O. G. *J. Mater. Chem.* **2012**, *22*, 2878.

(14) (a) Yao, K.; Manjare, M.; Barrett, C. A.; Yang, B.; Salguero, T. T.; Zhao, Y. *J. Phys. Chem. Lett.* **2012**, *3*, 2204. (b) Zhao, G. J.; Ambrosi, A.; Pumera, M. *J. Mater. Chem. A* **2014**, *2*, 1219. (c) Li, J.; Liu, Z.; Huang, G.; An, Z.; Chen, G.; Zhang, J.; Li, M.; Liu, R.; Mei, Y. *NPG Asia Mater.* **2014**, *6*, e94.

(15) Sánchez, S.; Solovev, A. A.; Harazim, S. M.; Deneke, C.; Feng Mei, Y.; Schmidt, O. G. *Chem. Rec.* **2011**, *11*, 367.

(16) (a) Schattling, P.; Thingholm, B.; Städler, B. *Chem. Mater.* **2015**, *27*, 7412. (b) Dey, K. K.; Zhao, X.; Tansi, B. M.; Méndez-Ortiz, W. J.; Córdova-Figueroa, U. M.; Golestanian, R.; Sen, A. *Nano Lett.* **2015**, *15*, 8311. (c) Bunea, A.-I.; Pavel, I.-A.; David, S.; Gáspár, S. *Biosens. Bioelectron.* **2015**, *67*, 42. (d) Abdelmohsen, L. K. E. A.; Nijemeisland, M.; Pawar, G. M.; Janssen, G.-J. A.; Nolte, R. J. M.; van Hest, J. C. M.; Wilson, D. A. *ACS Nano* **2016**, *10*, 2652. (e) Ma, X.; Wang, X.; Hahn, K.; Sánchez, S. *ACS Nano* **2016**, *10*, 3597. (f) Ma, X.; Jannasch, A.; Albrecht, U.-R.; Hahn, K.; Miguel-López, A.; Schäffer, E.; Sánchez, S. *Nano Lett.* **2015**, *15*, 7043. (g) Pantarotto, D.; Browne, W. R.; Feringa, B. L. *Chem. Commun.* **2008**, *10*, 1533.

(17) Spagnolie, S. E.; Lauga, E. *Phys. Fluids* **2010**, *22*, 081902.

(18) Yin, Y.; Lu, Y.; Sun, Y.; Xia, Y. *Nano Lett.* **2002**, *2*, 427.

(19) Tirado, M. M.; Martínez, C. L.; de la Torre, J. G. *J. Chem. Phys.* **1984**, *81*, 2047.

(20) Wang, X.; In, M.; Blanc, C.; Nobili, M.; Stocco, A. *Soft Matter* **2015**, *11*, 7376.

(21) Sengupta, S.; Patra, D.; Ortiz-Rivera, I.; Agrawal, A.; Shklyae, S.; Dey, K. K.; Córdova-Figueroa, U.; Mallouk, T. E.; Sen, A. *Nat. Chem.* **2014**, *6*, 415.

(22) Happel, J.; Brenner, H. *Low Reynolds Number Hydrodynamics*, 2nd ed.; Martinus Nijhoff Publishers: The Hague, 1983.

(23) Wang, W.; Castro, L. A.; Hoyos, M.; Mallouk, T. E. *ACS Nano* **2012**, *6*, 6122.



# Enzyme-Powered Gated Mesoporous Silica Nanomotors for On-Command Intracellular Payload Delivery

Antoni Llopis-Lorente,<sup>†,‡,§</sup> Alba García-Fernández,<sup>†,‡,§</sup> Nerea Murillo-Cremaes,<sup>||</sup> Ana C. Hortelão,<sup>||</sup> Tania Patiño,<sup>||,∇</sup> Reynaldo Villalonga,<sup>⊥,Ⓜ</sup> Félix Sancenón,<sup>†,‡,§</sup> Ramón Martínez-Mañez,<sup>\*,†,‡,§,Ⓜ</sup> and Samuel Sánchez<sup>\*,||,#,Ⓜ</sup>

<sup>†</sup>Instituto Interuniversitario de Investigación de Reconocimiento Molecular y Desarrollo Tecnológico (IDM), Universitat Politècnica de València, Universitat de València, Spain, Universitat Politècnica de València, Camino de Vera s/n, 46022 València, Spain

<sup>‡</sup>Unidad Mixta UPV-CIPF de Investigación en Mecanismos de Enfermedades y Nanomedicina, Valencia, Universitat Politècnica de València, Centro de Investigación Príncipe Felipe, 46012 València, Spain

<sup>§</sup>CIBER de Bioingeniería, Biomateriales y Nanomedicina (CIBER-BBN), 28029 Madrid, Spain

<sup>||</sup>Institute for Bioengineering of Catalonia (IBEC), The Barcelona Institute of Science and Technology (BIST), Baldri Reixac 10-12, 08028 Barcelona, Spain

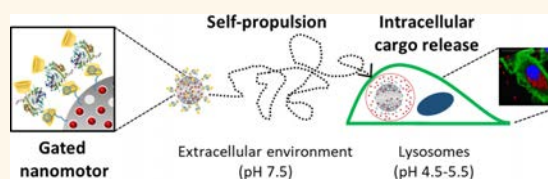
<sup>⊥</sup>Department of Analytical Chemistry, Faculty of Chemistry, Complutense University of Madrid, 28040 Madrid, Spain

<sup>#</sup>Institució Catalana de Recerca i Estudis Avançats (ICREA), Pg. Lluís Companys 23, 08010 Barcelona, Spain

## Supporting Information

**ABSTRACT:** The introduction of stimuli-responsive cargo release capabilities on self-propelled micro- and nanomotors holds enormous potential in a number of applications in the biomedical field. Herein, we report the preparation of mesoporous silica nanoparticles gated with pH-responsive supramolecular nanovalves and equipped with urease enzymes which act as chemical engines to power the nanomotors. The nanoparticles are loaded with different cargo molecules ( $[\text{Ru}(\text{bpy})_3]\text{Cl}_2$  ( $\text{bpy} = 2,2'$ -bipyridine) or doxorubicin), grafted with benzimidazole groups on the outer surface, and capped by the formation of inclusion complexes between benzimidazole and cyclodextrin-modified urease. The nanomotor exhibits enhanced Brownian motion in the presence of urea. Moreover, no cargo is released at neutral pH, even in the presence of the biofuel urea, due to the blockage of the pores by the bulky benzimidazole:cyclodextrin-urease caps. Cargo delivery is only triggered on-command at acidic pH due to the protonation of benzimidazole groups, the dethreading of the supramolecular nanovalves, and the subsequent uncapping of the nanoparticles. Studies with HeLa cells indicate that the presence of biofuel urea enhances nanoparticle internalization and both  $[\text{Ru}(\text{bpy})_3]\text{Cl}_2$  or doxorubicin intracellular release due to the acidity of lysosomal compartments. Gated enzyme-powered nanomotors shown here display some of the requirements for ideal drug delivery carriers such as the capacity to self-propel and the ability to “sense” the environment and deliver the payload on demand in response to predefined stimuli.

**KEYWORDS:** nanomotors, drug delivery, controlled release, nanocarriers, enzymatic catalysis, stimuli-responsive nanomaterials, gatekeepers



Development of micro- and nanobots is an ambitious and multidisciplinary research topic that may lead to revolutionary advancements in different areas such as medicine, sensing, and environmental science.<sup>1–5</sup> Researchers have developed microscale motors capable of *in vivo* treatment of stomach infection,<sup>6</sup> targeted navigation in intestines,<sup>7</sup> penetration of the vitreous body of the eye,<sup>8</sup> cell manipulation,<sup>9</sup> and drug loading and delivery.<sup>10</sup> In the field of drug delivery, the

design of advanced nanoparticles able to self-propel in an aqueous environment and to deliver the drug on-command holds great potential to improve classical treatments. Propulsion

**Received:** August 23, 2019

**Accepted:** October 3, 2019

**Published:** October 3, 2019

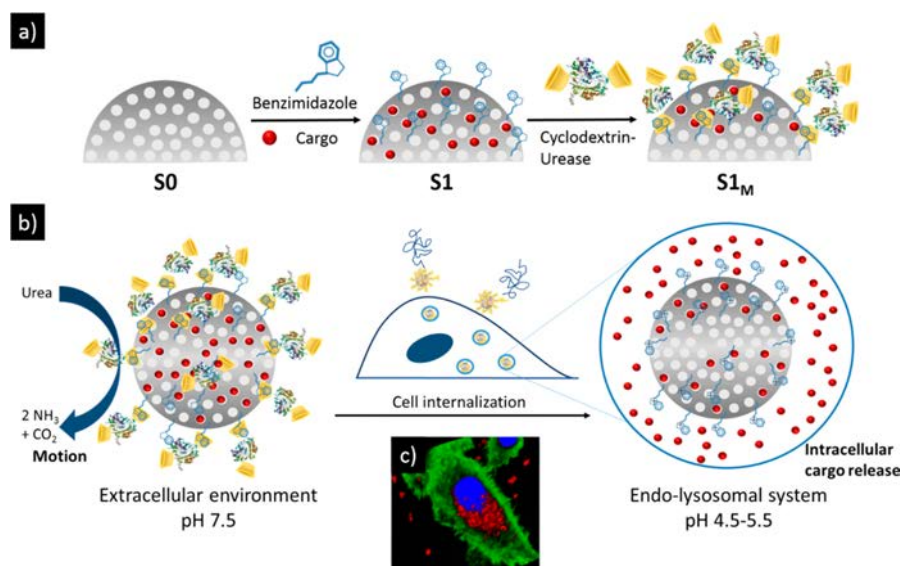


**Figure 1.** Schematic illustration of the fabrication and performance of enzyme-powered stimuli-responsive nanomotors. (a) Schematic of the fabrication process. Nanomotors consist of mesoporous silica nanoparticles loaded with a cargo (a dye or a drug), functionalized with benzimidazole groups on the outer surface, and capped with cyclodextrin-modified urease. (b) These biocatalytic nanomotors exhibit enhanced Brownian motion due to the enzymatic conversion of urea and release their cargo at acidic pH through the dethreading of the supramolecular nanovalve. (c) 3D confocal microscopy reconstruction of a cell with internalized nanomotors. Different signals corresponding to WGA membrane marker (green), DNA-marker Hoechst 33342 (blue), and dox (red).

can be achieved using different approaches such as the use of light,<sup>11,12</sup> magnetic fields,<sup>13,14</sup> and ultrasounds<sup>15,16</sup> or by catalysis.<sup>17,18</sup> In recent years, several proof-of-concept studies regarding the use of nanoscale motors in drug delivery have been conducted.<sup>19,20</sup> Wang and co-workers reported porous gold nanowires of 1.8  $\mu\text{m}$  in length that were propelled by ultrasounds and released doxorubicin (dox) around cells upon light irradiation.<sup>21</sup> Ultrasound-propelled nanorod motors have also been used to deliver therapeutic caspase-3 and Cas9 proteins.<sup>22,23</sup> He's team developed layer-by-layer chitosan-alginate-Pt nanotubes with a length of 8–10  $\mu\text{m}$  that propelled in 3%  $\text{H}_2\text{O}_2$ , attached to the outer surface of HeLa cells and released dox upon sonication.<sup>24</sup> Additionally,  $\text{H}_2\text{O}_2$ -fueled Janus platinum-mesoporous silica nanomotors loaded with model cargos have also been reported.<sup>25</sup> On the other hand, Wilson's group developed Pt-nanoparticle loaded stomatocytes that propelled by converting  $\text{H}_2\text{O}_2$  and released dox upon degradation.<sup>26,27</sup> Notwithstanding, the employment of toxic fuels such as  $\text{H}_2\text{O}_2$  or hydrazine limits the use of these systems in realistic biological environments.<sup>28,29</sup> In the quest for alternative fuels and catalysts, the use of enzymes that can act as engines<sup>30</sup> to propel micro- and nanostructures has been regarded as an excellent and versatile alternative,<sup>31–33</sup> and several studies have reported autonomous motion of enzyme-driven micro-objects,<sup>34–41</sup> metallic nanorods,<sup>42</sup> nanoparticles,<sup>43–45</sup> and polymeric structures.<sup>46–49</sup>

Another important issue when designing drug delivery systems is the possibility of “reading” information from the environment and delivering the cargo at-will upon the presence or application of a specific stimulus.<sup>50–52</sup> This contrasts with passive delivery systems in which cargo release is achieved by simple diffusion and/or by the slow degradation of the carrier. Among potential nanocarriers, mesoporous silicas are highly appealing since they offer advantageous properties such as easy synthesis, large specific surface area, high loading capacity, and

biocompatibility.<sup>53</sup> Moreover, the possibility of attaching “molecular gates” (also known as nanovalves or gatekeepers) on the external surface allows designing gated materials that ideally show “zero” release until an external stimulus is present.<sup>54–56</sup> A wide variety of gated materials able to respond to different stimuli (such as light, temperature, magnetic fields, pH, molecules, and biomolecules)<sup>57–59</sup> have been developed and applied in controlled drug delivery<sup>60–63</sup> and communication protocols.<sup>64–67</sup>

Mesoporous silica has already been tested as a scaffold for the preparation of enzyme-powered microcapsules,<sup>36,37</sup> tubular jets,<sup>38</sup> Janus Pt-based motors,<sup>25,68</sup> and enzyme-powered nanoparticles.<sup>43,44</sup> Recently, light-propelled Janus mesoporous silica nanomotors modified with macrophage cell membrane have been shown to percolate into cancer cells.<sup>69</sup> Mesoporous silica-based nanomotors have also been loaded with drugs and presented enhanced diffusion when exposed to fuel, resulting in enhanced drug release kinetics.<sup>45</sup> However, in previously reported examples, the pores of mesoporous silica were not gated and a sustained unspecific cargo release was observed, limiting somehow their potential application since a non-negligible amount of drug would be released before reaching the target location. In this scenario, it is apparent from the literature that enzyme-powered gated mesoporous silica nanomotors able to deliver the payload at-will have not yet been developed. In fact, the advantages of combining self-propulsion abilities and stimuli-responsive delivery systems, when compared to passive drug carriers, are immediately obvious; this constitutes the basis of vehicles with a continuous driving force able to “read” information (*i.e.*, the stimulus) from environment and act accordingly, for instance releasing on-demand a certain drug.

Herein, we present the design, preparation, and characterization of enzymatic nanomotors based on mesoporous silica gated with pH-responsive supramolecular nanovalves. The design of the nanomotor is depicted in Figure 1. It consists of



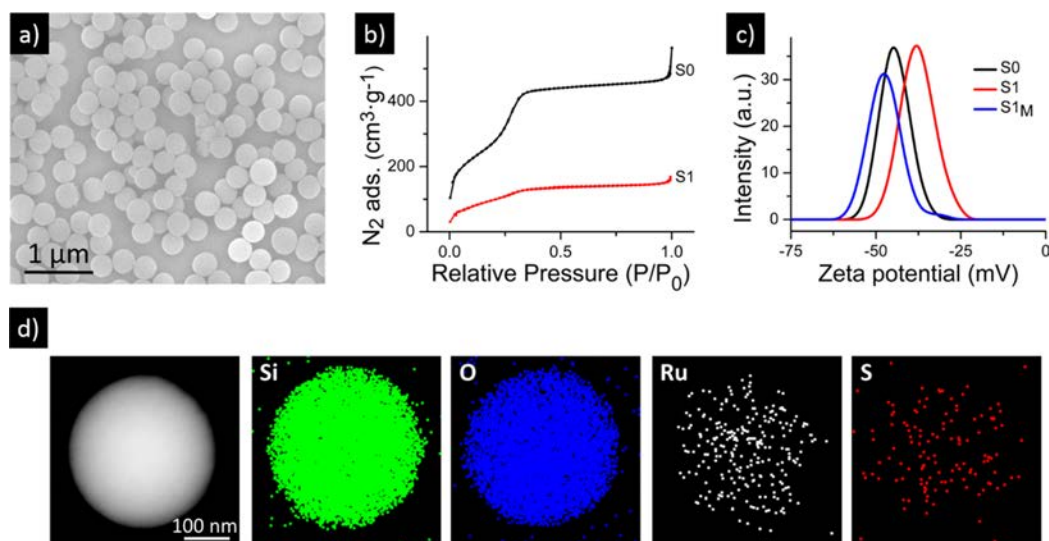


**Figure 2. Materials characterization.** (a) SEM image of the starting mesoporous nanoparticles (S0). (b)  $N_2$  adsorption–desorption isotherms of S0 and dye-loaded nanoparticles (S1). (c) The  $\zeta$  potential distribution for each preparation step: initial S0, loaded and functionalized S1, and capped S1<sub>M</sub>. (d) STEM-EDX mapping of different atoms for S1<sub>M</sub>: Si and O attributed to the silica scaffold, Ru corresponding to the cargo, and S ascribed to enzymes.

mesoporous silica nanoparticles, functionalized with benzimidazole groups, loaded with a dye or a model drug (*i.e.*,  $[Ru(bpy)_3]Cl_2$ ,  $bpy = 2,2'$ -bipyridine, or dox) and capped with cyclodextrin-modified urease (CD-U) *via* the formation of inclusion complexes between CD-U and the benzimidazole moieties. Urease units allow the enhanced Brownian motion of nanoparticles in the presence of urea as biofuel. At the same time, the benzimidazole:CD-U nanovalves act as bulky caps that prevent cargo release at physiological pH, whereas cargo delivery is observed at acidic pH due to protonation of the benzimidazole groups and the subsequent dethreading of the benzimidazole:CD-U inclusion complexes. Studies with HeLa cells show that the nanomotors enhance internalization in the presence of the urea biofuel and the payload is released upon cellular uptake due to the acidic environment of the lysosomes.

## RESULTS AND DISCUSSION

**Nanoparticles Synthesis and Characterization.** MCM-41-type mesoporous silica nanoparticles were synthesized by hydrolysis and condensation of tetraethyl orthosilicate (TEOS) in aqueous media basified with triethanolamine and using cetyltrimethylammonium bromide (CTAB) as structure-directing agent (see [Methods](#) section for details). The CTAB surfactant was then removed by acidic extraction in methanol, which yielded the starting mesoporous nanoparticles (S0). Then, the process of nanomotor assembly proceeded as schematized in [Figure 1a](#). First, the nanoparticles were suspended in an acetonitrile solution containing the dye  $[Ru(bpy)_3]Cl_2$ , in order to load the pores by stirring overnight. Next, 3-iodopropyltrimethoxysilane was anchored on the outer silica surface by reaction with silanol groups. In a further step, nucleophilic substitution between the grafted iodopropyl moieties and benzimidazole yielded the benzimidazole-functionalized solid S1. Finally, cyclodextrin-modified urease (CD-U) (prepared following a previously reported procedure)<sup>70</sup> was added to an aqueous dispersion of S1 nanoparticles at pH 7.5 in order to cap the pores *via* the formation of inclusion complexes between benzimidazole and cyclodextrin groups. The

solid was collected by centrifugation and thoroughly washed with phosphate buffer, yielding the final enzyme-powered gated mesoporous silica nanomotors S1<sub>M</sub>.

Scanning electron microscopy (SEM) images of S0 ([Figure 2a](#) and [Figure SI-1](#)) confirmed the formation of the nanoparticles with good monodispersity in size and a spherical shape. From statistical analysis of SEM images, a diameter of  $418 \pm 21$  nm was determined (average size  $\pm$  standard error of mean (s.e.m.)),  $N = 200$ ) for the starting mesoporous nanoparticles. Such nanomotor size was selected since it allows reliable motion tracking by optical microscopy, avoiding the challenges of observation of smaller nanoparticles. Notwithstanding, the fabrication of sub-100 nm nanomotors with stimuli-responsive cargo release is appealing for drug delivery and will be investigated in future works. The powder X-ray diffraction (PXRD) pattern of S0 showed the typical (100) reflection peak around  $2.3^\circ$  characteristic of MCM-41-type mesoporous materials ([Figure SI-2](#)).<sup>71</sup> The preservation of this characteristic peak in the PXRD pattern of S1 confirmed that loading and functionalization processes did not damage the three-dimensional (3D) mesoporous structure. Furthermore, from  $N_2$  adsorption–desorption isotherms ([Figure 2b](#)), a specific surface area of  $1195 \text{ cm}^2\cdot\text{g}^{-1}$  for S0 was calculated by applying the Brunauer–Emmett–Teller (BET)<sup>72</sup> model. Pore diameter and pore volume were found to be 2.44 nm ([Figure SI-3](#)) and  $0.80 \text{ cm}^3\cdot\text{g}^{-1}$ , respectively, by using the Barret–Joyner–Halenda (BJH)<sup>73</sup> model on the adsorption branch of the isotherm. For S1 nanoparticles, volume of adsorbed  $N_2$  decreased due to the filling of pores with the dye, and the specific surface area and pore volume reduced to  $392 \text{ cm}^2\cdot\text{g}^{-1}$  and  $0.26 \text{ cm}^3\cdot\text{g}^{-1}$ , respectively. We also monitored the fabrication process by  $\zeta$  potential and hydrodynamic diameter using electrophoretic mobility and dynamic light scattering (DLS) measurements. The  $\zeta$  potential changed from  $-40$  mV for S0 to  $-10$  mV for the benzimidazole-functionalized solid S1, due to the attachment of organic groups to the surface ([Figure 2c](#)). For the final nanomotor S1<sub>M</sub>, the surface charge changed from  $-10$  to  $-50$  mV. Urease has an isoelectric point of *ca.* 5.1 (pH at which the

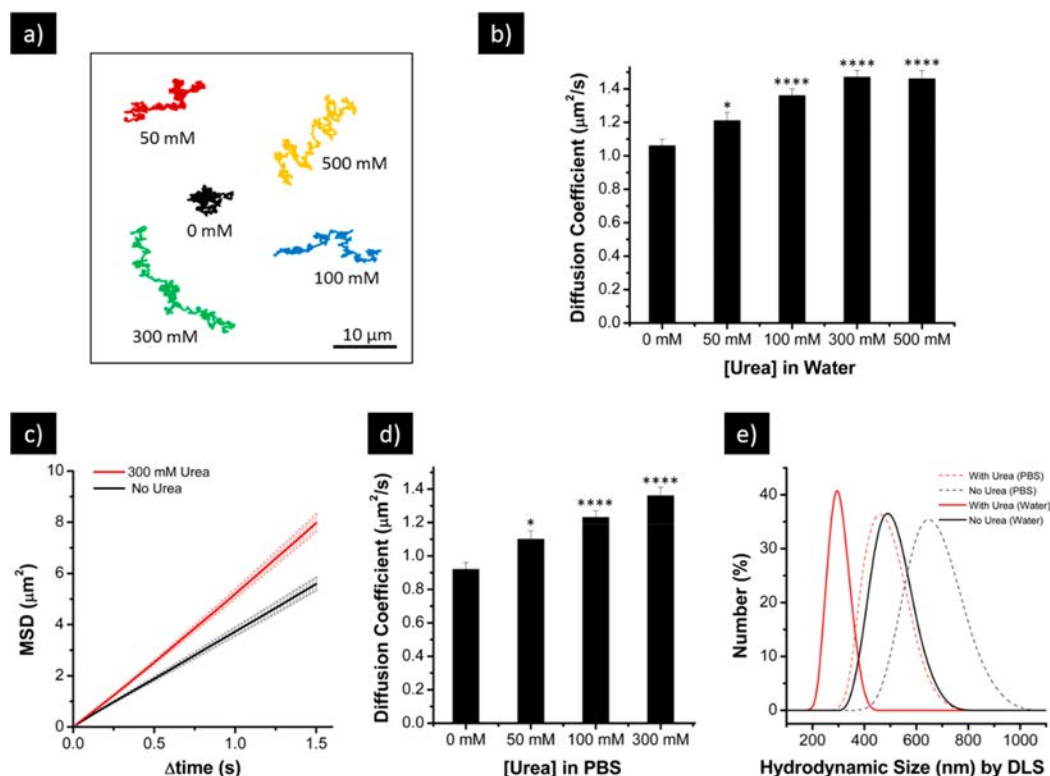


**Figure 3.** Analysis of the motion capability of the stimuli-responsive nanomotors ( $S1_M$ ). (a) Representative tracking trajectories of the nanomotors during 15 s with different urea concentrations. (b) Diffusion coefficient of nanomotors obtained by optical tracking at different urea concentrations ( $N = 20$ , error bars represent s.e.m.). Superscripts denote statistically significant differences compared to diffusion at 0 mM of urea, with (\*)  $p < 0.05$  and (\*\*\*\*)  $p < 0.0001$  (ANOVA test). (c) MSD of nanomotors in PBS without and with urea (300 mM) in PBS ( $N = 20$ , error bars represent s.e.m.). (d) Diffusion coefficient in PBS ( $N = 20$ , error bars represent s.e.m.). Superscripts indicate statistically significant differences compared to diffusion at 0 mM of urea, with (\*)  $p < 0.05$  and (\*\*\*\*)  $p < 0.0001$  (ANOVA test). (e) Apparent hydrodynamic diameter of nanomotors obtained by DLS without (black) and with urea (red, 300 mM) in water (continuous lines) and in PBS (dashed lines).

net charge of the protein is zero), and therefore it is negatively charged at neutral pH. Thus, the change in  $\zeta$  potential to a more negative value is consistent with a successful coordination of the negatively charged enzyme to the benzimidazole-functionalized silica surface. Moreover, the hydrodynamic diameter increased after each preparation step (445, 468, and 494 nm for  $S0$ ,  $S1$ , and  $S1_M$ , respectively) (Figure SI-4). In all cases, a single population distribution was observed indicating that the particles were not aggregated, even after the functionalization with the benzimidazol groups and capping process with the cyclodextrin-modified urease.

From elemental and thermogravimetric analyses, the content of  $[Ru(bpy)_3]Cl_2$  and 1-propyl-1-*H*-benzimidazole on  $S1$  was determined as 220 mg, which corresponds to 22% of dye loading and 32 mg per g of nanoparticle, respectively.  $S1_M$  was also characterized by TEM (Figure SI-5). The mesopores were clearly observed, confirming the preservation of the morphology and porous structure in the final  $S1_M$  nanomotor. Additionally, scanning transmission electron microscopy coupled with energy dispersive X-ray spectroscopy (STEM-EDX) mapping of  $S1_M$  clearly indicated the presence of Si and O from the silica matrix, Ru atoms (attributed to the cargo), and S (characteristic of enzymes) (Figure 2d). Finally, the amount of protein on the final nanomotor was quantified using the Bradford method<sup>74</sup> as 108 mg per g of solid.

**Motion Behavior.** In a first step, the catalytic activity of the enzyme-powered gated nanomotors  $S1_M$  was evaluated using a colorimetric urease-specific assay kit based on the Berthelot's method.<sup>75</sup> One unit (U) of urease is defined as the amount of enzyme that catalyzes the hydrolysis of 1  $\mu$ mol of urea (formation of 2  $\mu$ mol of ammonia) per minute [i.e.,  $(NH_2)_2CO + 3H_2O \rightarrow CO_2 + 2NH_4OH$ ]. In this assay, ammonia produced by the enzymatic process reacts with Berthelot's reagent (alkaline solution of phenol and hypochlorite) to form a blue indophenol product that is measured using a spectrophotometer ( $\lambda_{max} = 670$  nm). A calibration curve was obtained from the absorbance of ammonium standards (Figure SI-6), which was used for determining the urease activity on  $S1_M$  as 120 U per g of nanoparticles (by applying supplementary eq 1 in the Supporting Information). This corresponds to 1.1 U per mg of enzyme (according to the protein quantification by the Bradford assay) and represents a 78 % of enzymatic activity compared to the free enzyme (1.4 U  $mg^{-1}$ , measured by Berthelot's method).

Once the activity of urease on the gated nanomotors  $S1_M$  was demonstrated, motion analysis was performed using optical microscopy. Nanomotors' trajectory was tracked in the absence and in the presence of different concentrations of urea in water (see representative trajectories in Figure 3a). From the trajectories, an in-house developed python code was used to

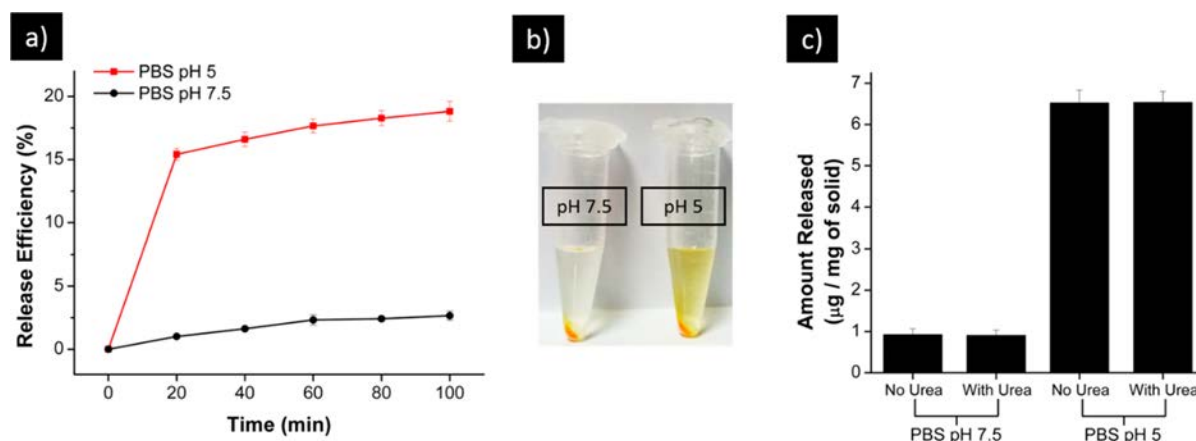


**Figure 4.** Cargo release experiments. (a) Cargo release profile from stimuli-responsive nanomotors  $S1_M$  in PBS at physiological pH (7.5, black curve) and at lysosomal pH (5, red curve). (b) Visualization of  $[Ru(bpy)_2]Cl_2$  released from  $S1_M$  at pH 7.5 and at pH 5 to the solution, after 100 min of incubation. (c) Amount of cargo released from  $S1_M$  in PBS at pH 7.5 and at pH 5 in the absence and presence of urea (100 mM), quantified by measuring  $[Ru(bpy)_2]Cl_2$  absorbance at 453 nm. Error bars represent s.e.m. from three independent experiments.

compute the mean squared displacement (MSD) as a function of time for each condition. MSD always increased linearly with time, which corresponds to typical diffusive motion (Figure SI-7). The resulting MSD was then fitted to  $MSD = 4D_e\Delta t$ , where  $D_e$  represents the effective diffusion coefficient and  $\Delta t$  represents the time interval.<sup>76,77</sup> The diffusion coefficient for  $S1_M$  in the absence of urea (Brownian motion) was found to be  $1.06 \pm 0.04 \mu m^2/s$ , which is very close to the theoretical value for 418 nm nanoparticles ( $D = TK_B/3\pi\eta d = 1.2 \mu m^2/s$ , where  $T$  is the temperature,  $K_B$  the Boltzmann constant,  $\eta$  the viscosity, and  $d$  the diameter). As depicted in Figure 3b, the enzymatic nanomotors showed a significant increase in the diffusion coefficient dependent on urea concentration, reaching a maximum of  $1.47 \pm 0.04 \mu m^2/s$  at 300 mM of urea.

Bearing in mind that a realistic application of the nanomotors should take place in the presence of salts in a physiological media, we evaluated the self-propulsion capabilities in a physiological buffer (PBS, 1×) at different urea concentrations (0 mM, 50 mM, 100 mM, and 300 mM). Representative trajectories in PBS are depicted in Figure SI-8. From the MSD plots (Figure 3c and SI-9), a significant increase in diffusion coefficient from  $0.90 \pm 0.04 \mu m^2/s$  (in the absence of urea) to  $1.36 \pm 0.05 \mu m^2/s$  (in the presence of 300 mM urea) in PBS was determined (Figure 3d). Despite the decrease in the diffusion coefficients found for  $S1_M$  in PBS (statistically significant with  $p < 0.02$ ), the relative increase in the presence of fuel was higher in PBS (48 %) than in water (39 %), which is in agreement to previously reported urease-powered motors.<sup>45</sup> Additionally, the apparent hydrodynamic diameter determined by DLS decreased in the presence of urea in water and in PBS (Figure 3e). Smaller hydrodynamic diameter ( $d$ ) in the presence of fuel correlates with a higher diffusion coefficient ( $D$ ), according to the Stokes–Einstein equation ( $D = TK_B/3\pi\eta d$ ), thus confirming the enhanced diffusion observed by optical microscopy. Although we are aware that the nanomotor enhanced diffusion may become negligible in the blood flow, we believe that enhanced diffusion can be advantageous in certain tissues or organs (e.g., in tumor tissues or in the bladder),<sup>78</sup> where enhanced diffusion may increment internalization in cells (*vide infra*). Regarding enzymatic motors, a recent study has demonstrated by stochastically optical reconstruction microscopy (STORM)

that enzyme molecules are nonhomogeneously distributed onto the surface of non-Janus spherical micromotors,<sup>41</sup> which explains the self-propulsion observed in non-Janus spherical particles.<sup>31,41,45</sup>

**On-Command Controlled Release Studies.** Once demonstrated that the nanomotor  $S1_M$  displays enhanced Brownian motion in the presence of urea, cargo release from  $S1_M$  suspensions in different conditions was evaluated. In these experiments,  $S1_M$  was brought to a concentration of 2.5 mg mL<sup>-1</sup> in phosphate buffer at physiological pH (7.5) and at lysosomal pH (5). At scheduled times (each 20 min), aliquots were taken and centrifuged to sediment the nanoparticles, and cargo release was determined by measuring the  $[Ru(bpy)_2]Cl_2$  absorbance in the supernatant. As can be observed in Figure 4a, at pH 7.5, the release was negligible after 100 min (ca. 2.5% of release efficiency), which indicates the correct capping of the material by the bulky cyclodextrin-modified urease. In contrast, a notable release occurred at pH 5 (ca. 20% of release efficiency), which could be appreciated even with the naked eye (Figure 4b). This was attributed to the protonation of benzimidazole groups ( $pK_a = 5.5$ )<sup>79</sup> and the subsequent rupture of the inclusion complexes between the protonated benzimidazole groups and  $\beta$ -cyclodextrin from the cyclodextrin-modified urease, which induced the dethreading of the caps allowing payload release.

In additional experiments, the amount of protein detached from  $S1_M$  (corresponding to the CD-U caps) was quantified by the Bradford assay. No protein release was detected after  $S1_M$  incubation at pH 7.5. In contrast, the amount of free protein in solution after  $S1_M$  incubation at pH 5 was measured to be 145  $\mu g$  mL<sup>-1</sup>. On the other hand, release experiments with  $S1$  (without capping with CD-U) were also conducted. In this case, a marked cargo release from  $S1$  was observed at both physiological (7.5) and at lysosomal pH (5) (Figure SI-10), which confirms the advantage of blocking the pores with the cyclodextrin-modified urease for releasing the payload on-command. Finally, we also evaluated whether the presence of the urea fuel induced any premature cargo leakage from  $S1_M$  in buffer at neutral pH. For this, similar experiments to those explained above with  $S1_M$  were carried out. Cargo delivery from  $S1_M$  (concentration of 2.5 mg mL<sup>-1</sup>) in phosphate buffer at pH 7.5 containing urea at a concentration of 100 mM was studied. The amount of cargo



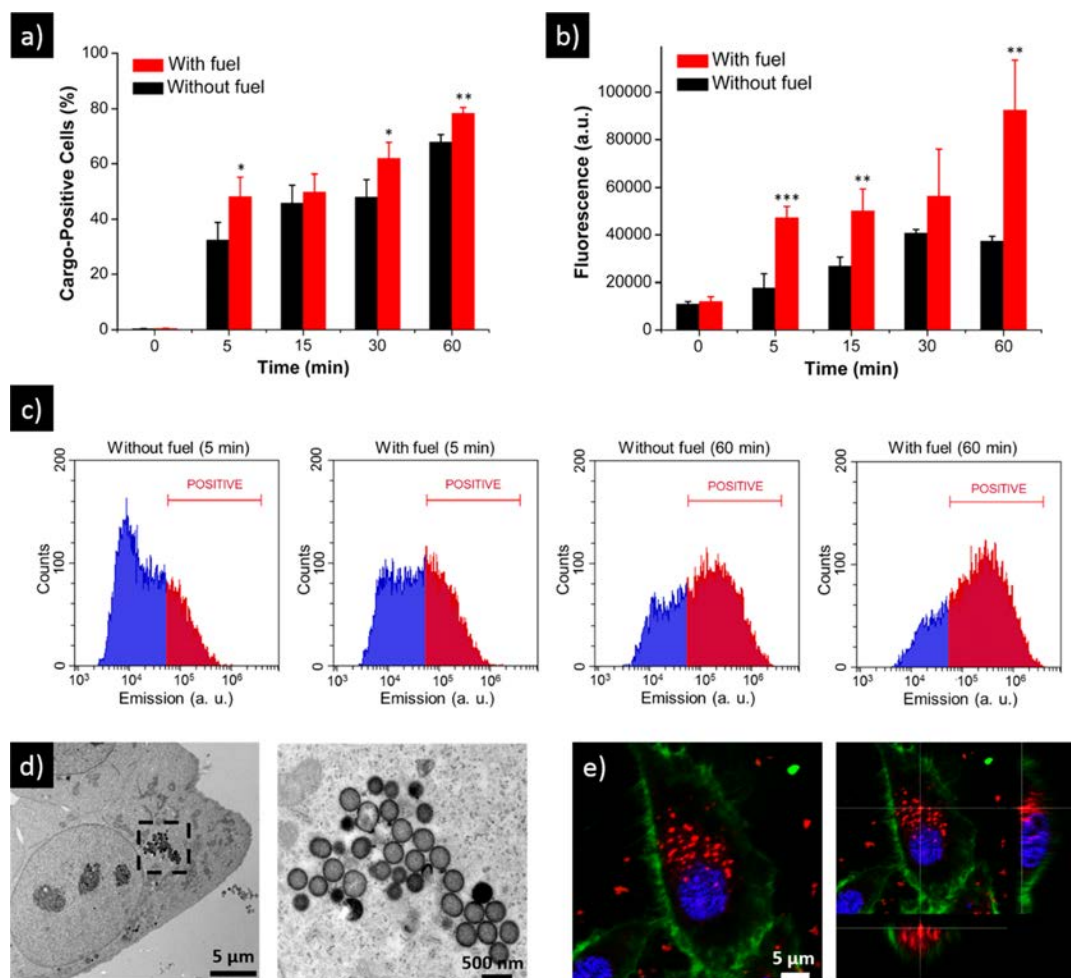


**Figure 5.** Flow cytometry and internalization studies. (a) Analysis of the percentage of cargo-positive HeLa cells at different times. Cells were treated with  $50 \mu\text{g mL}^{-1}$  of  $\text{S1}_\text{M}$  in the absence and presence of urea (50 mM). (b) Analysis of  $[\text{Ru}(\text{bpy})_3]\text{Cl}_2$  associated-fluorescence of HeLa cells treated with  $50 \mu\text{g mL}^{-1}$  of  $\text{S1}_\text{M}$  in the absence and presence of urea (50 mM) at different times. (c) Representative population distributions (nonpositive/cargo-positive cells) obtained in a flow cytometry experiment using the CytoFLEX S instrument after 5 and 60 min. Error bars represent s.e.m. from three independent experiments. Superscripts mark that the effect of fuel was statistically significant with (\*)  $p < 0.05$ , (\*\*)  $p < 0.02$ , and (\*\*\*)  $p < 0.005$ , respectively. (d) TEM image showing  $\text{S1}_\text{M}$  internalization in HeLa cells. (e) High-resolution confocal image a HeLa cell (right) and orthogonal sectioning of the cell (left), showing nanomotor internalization ( $\text{S1}_{\text{MDOX}}$ ). Different signals corresponding to WGA membrane marker (green), DNA-marker Hoechst 33342 (blue), and dox (red).

release was quantified from absorbance values, by applying Beer–Lambert’s law, and the results are shown in Figure 4c. No significant cargo release was observed for  $\text{S1}_\text{M}$  in media at neutral pH in the absence or presence of urea, which confirms the correct blockage of the pores in physiological buffer even in the presence of the fuel. In previous reports, nongated catalytic nanomotors exhibited a large payload release in the presence of fuel due to motion.<sup>25,45</sup> This can produce the release of a non-negligible amount of cargo before reaching the target area/cells. In contrast, the gated nanomotors we report here do not show this effect, which can be an advantage for future therapeutic applications. Furthermore, we also tested the effect of urea in cargo delivery from  $\text{S1}_\text{M}$  in media at pH 5 and found no significant difference between the amount released in the absence or presence of urea.

These *in vitro* studies demonstrated that (i) nanomotor  $\text{S1}_\text{M}$  displays self-propulsion ability, (ii) no cargo delivery is observed in a competitive media such as phosphate buffer at physiological

pH when the nanomotor is neither off (in the absence of urea) nor on (in the presence of urea), and (iii) cargo delivery is triggered at acidic pH (simulating a lysosomal environment). Therefore,  $\text{S1}_\text{M}$  fulfills some requirements of an ideal drug delivery vehicle and shows clear enhanced properties, in terms of autonomous mobility and controlled release, when compared with classical passive delivery systems.

**Cargo Delivery in Cells.** Encouraged by the above-mentioned results, that is, the selective delivery of the cargo (*i.e.*,  $[\text{Ru}(\text{bpy})_3]\text{Cl}_2$ ) at acidic pH and the enhanced Brownian motion showed by the nanomotor, we tested the short-term cytotoxicity of  $\text{S1}_\text{M}$  and cargo delivery, in the absence and the presence of urea, in human epithelial cervix adenocarcinoma HeLa cells. Short-term cytotoxicity of the urea-powered gated  $\text{S1}_\text{M}$  nanomotor was assessed by means of WST-1 cell viability assays (Figure SI-11). The data indicated that  $\text{S1}_\text{M}$  did not affect cell viability at concentrations as high as  $100 \mu\text{g mL}^{-1}$  in the absence of urea after the 24 h incubation period. In fact, a *ca.*

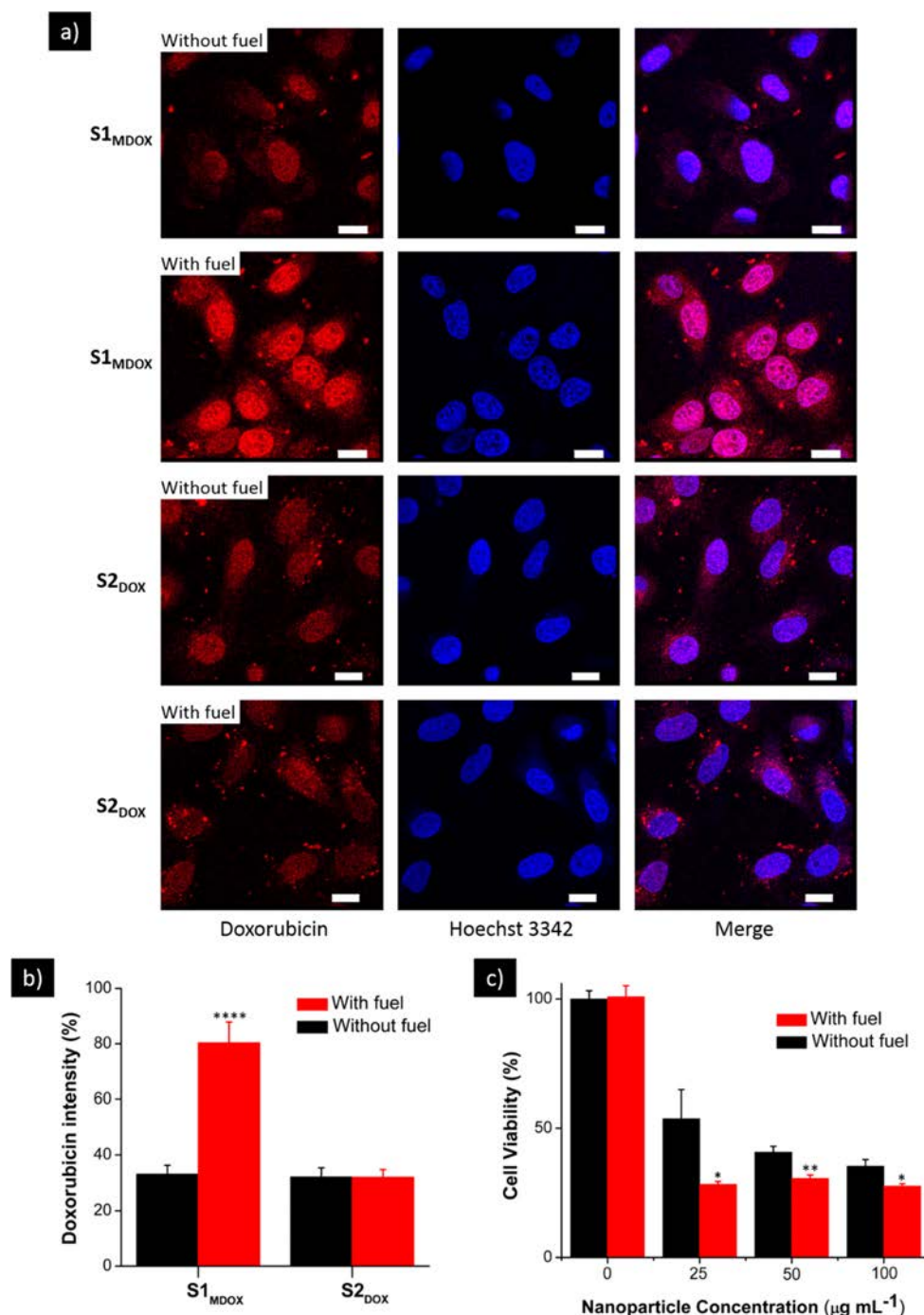


**Figure 6.** Delivery of dox in HeLa cells. (a) Confocal microscopy images of HeLa cells treated with S1<sub>MDOX</sub> nanomotors and with “control” S2<sub>DOX</sub> (without urease) in the absence and presence of urea (50 mM). From left to right: dox fluorescence, DNA-marker (Hoechst 3342) fluorescence, and combined (merge). Scale bars: 5 µm. (b) Doxorubicin intensity quantification in cells from confocal images using the ImageJ software. (c) Viability of HeLa cancer cells after 24 h of incubation with different concentrations of S1<sub>MDOX</sub> nanomotors in the absence and presence of urea (50 mM). Error bars represent s.e.m. from three independent experiments containing triplicates. Superscripts indicate statistically significant differences compared to absence of urea; with (\*)  $p < 0.05$ , (\*\*)  $p < 0.005$ , and (\*\*\*)  $p < 0.0001$  (ANOVA test).

100% cell viability was found for the nanomotor in the 0–100 µg mL<sup>-1</sup> concentration range, which covers the relevant concentrations recommended for the study of mesoporous silica nanoparticles toxicity.<sup>54</sup> A very similar cell viability was

observed in the presence of nanomotor and urea at a concentration of 50 mM, indicating that neither the biofuel urea nor S1<sub>M</sub> with enhanced diffusion was toxic for HeLa cells. This urea concentration was selected to be in the range of that



found in the serum of patients suffering from conditions such as kidney disease, liver dysfunction, chemotherapy-induced renal damage, or gastrointestinal problems.<sup>80–82</sup>

Internalization of  $S1_M$  in HeLa cells in the absence and the presence of urea was studied by flow cytometry (FC). Despite the good performance of this technique,<sup>83</sup> its use to study the interaction of nanomotors with cells has not been previously reported. In these experiments,  $50 \mu\text{g mL}^{-1}$  of  $S1_M$  was added to the cell culture media in the absence or presence of urea (50 mM). At scheduled times, cells were injected in the FC instrument in order to measure cell fluorescence at 590 nm (which is associated with  $[\text{Ru}(\text{bpy})_3]\text{Cl}_2$ ,  $\lambda_{\text{exc}} = 453 \text{ nm}$ ).

The FC results showed that the number of cargo-positive cells increased with time in both cases (in the presence and in the absence of the fuel), although a larger percentage of positive cells was found in the presence of urea (Figure 5a). For instance, after 5 min of incubation, 32% of cargo-positive HeLa cells were found in the absence of urea, whereas this value increased to 48% in the presence of the biofuel. Moreover, when the cargo intensity in cells was measured (which is related with the amount of  $S1_M$  internalized in cells), more evident differences with and without urea were found (Figure 5b). In fact, Figure 5b shows that the intensity of fluorescence in cells increased with time and that a larger intensity was found at any time (except at time zero) for the nanomotors incubated with urea. For instance, after 5 min of incubation, emission intensity at 590 nm was 2.7 times larger with urea when compared with the same results in the absence of the fuel (average fluorescence was 17,751 au without fuel and 47,242 au with fuel). After an incubation time of 60 min, the intensity ratio in the absence and presence of urea was *ca.* 1.2 to 3 (average fluorescence was 37,328 au without fuel and 92,398 au with fuel). Representative cell population distributions (where the *x*-axis represents the emission of a cell and the *y*-axis represents the number of cells with that emission) obtained in a typical FC experiment are showed in Figure 5c, where the cells with a higher emission (red area) than the control (untreated cells) are determined as positive (red area). Additionally, we also prepared control nanoparticles ( $S1_{\text{CD}}$ ) capped with  $\beta$ -cyclodextrin but lacking the enzyme and confirmed that in this case no enhancement in cell fluorescence was observed in the presence of urea (Figure SI-12). In further control experiments, we determined that the pH of the cell media remained buffered after incubation with nanomotors  $S1_M$  and urea. Moreover, the successful internalization of nanomotors in HeLa cells was confirmed by TEM (Figure 5d) and by 3D confocal imaging (Figures 5e and 1c).

In order to complete the studies shown above, we also prepared the nanomotors  $S1_{\text{MDOX}}$  which are similar to  $S1_M$  but loaded with the drug dox. The profiles of dox release can be observed in Figure SI-13. In this case, the release efficiency of dox from  $S1_{\text{MDOX}}$  was 40% at pH 5, whereas it was negligible (only 1.6%) in phosphate buffer at neutral pH. Additionally, we confirmed that the particles remained capped (no dox was prematurely released) in cell culture media (DMEM supplemented with 10% FBS). To directly visualize intracellular cargo release, and since dox is fluorescent, we carried out experiments of  $S1_{\text{MDOX}}$  uptake by HeLa cells using confocal microscopy. For this, HeLa cells were incubated with  $50 \mu\text{g mL}^{-1}$  of  $S1_{\text{MDOX}}$  for 1 h in the absence and in the presence of urea (50 mM) and then washed to remove noninternalized nanoparticles. Cells were also stained with the DNA marker Hoechst 3342. Confocal images (Figure 6a) showed a clear increase in dox-associated fluorescence ( $\lambda_{\text{exc}} = 480 \text{ nm}$ ,  $\lambda_{\text{em}} = 550 \text{ nm}$ ) for cells treated

with  $S1_{\text{MDOX}}$  incubated with the biofuel urea when compared with the control (absence of urea). A quantification of this increase in fluorescence was carried out using the ImageJ software to measure the emission inside cells. The fluorescence associated with dox for cells treated with  $S1_{\text{MDOX}}$  in the presence of urea was 2.4 times larger compared with  $S1_{\text{MDOX}}$  without urea (Figure 6b). These results (in terms of enhanced internalization and emission intensity) agree with those found in flow cytometry studies for  $S1_M$  (*vide ante*). As additional control experiments, we prepared dox-loaded nanoparticles  $S2_{\text{DOX}}$  (capped with  $\beta$ -cyclodextrin without urease) and confirmed that no increase in cell fluorescence was observed in the presence of urea (Figure 6a,b).

Finally, we also carried out studies of HeLa cell viability after treatment of HeLa cells with  $S1_{\text{MDOX}}$ . In the absence of fuel, a  $S1_{\text{MDOX}}$  concentration-dependent decrease of living cells was observed (cell viability was 54% at  $25 \mu\text{g mL}^{-1}$  of  $S1_{\text{MDOX}}$ , 41% at  $50 \mu\text{g mL}^{-1}$ , and 35.2% at  $100 \mu\text{g mL}^{-1}$ ) (Figure 6c). In contrast, a larger cell viability reduction to about *ca.* 28% was observed when  $S1_{\text{MDOX}}$  was incubated with cells in the presence of urea (50 mM) even at nanomotor concentrations as low as  $25 \mu\text{g mL}^{-1}$ . In fact, compared with the minimum of 35.2% viability in the absence of fuel at a  $S1_{\text{MDOX}}$  concentration of  $100 \mu\text{g mL}^{-1}$ , urea-fueled nanomotor produced even a larger viability decrease (to *ca.* 28% viability) using 4 times less nanoparticle concentration. Moreover, at the same nanoparticle concentration of  $25 \mu\text{g mL}^{-1}$ , the presence of fuel resulted in a relative increase in cell death (reduction of cell viability) of 47% when compared with cells treated with  $S1_{\text{MDOX}}$  at the same concentration. From another point of view, taking into account that the total amount of dox in  $25 \mu\text{g mL}^{-1}$  of  $S1_{\text{MDOX}}$  is  $0.030 \mu\text{M}$  and that it reduces viability to 28% in the presence of fuel, the nanomotor has a considerably enhanced efficacy compared to free dox, since  $0.374 \mu\text{M}$  of free dox has been reported to decrease HeLa cells viability to 50%.<sup>84</sup>

Altogether, these results indicate that an enhanced cell uptake due to the enhanced Brownian motion of the nanomotor and a larger cargo release inside cells is observed, when urea is present in the medium. Note that, because of the design of the nanosystem, there is no cargo delivery in the cellular medium neither in the absence nor in the presence of urea (Figure 4), yet cargo delivery only occurs after nanomotor internalization in cells due to the pH-triggered dethreading of the nanovalve.

## CONCLUSIONS

In summary, we report here the design, preparation, and characterization of biocatalytic nanomotors based on mesoporous silica nanoparticles capped with supramolecular nanovalves for active cargo transport and pH-responsive release. In particular, mesoporous silica nanoparticles functionalized with benzimidazole groups and capped by the formation of inclusion complexes with cyclodextrin-modified urease (CD-U) were prepared. The nanomotors exhibit enhanced Brownian motion in the presence of urea thanks to enzymatic catalysis in water and in ionic media (PBS). At physiological pH, the supramolecular benzimidazole:CD-U nanovalve acts as a bulky stopper and prevents cargo release both in the absence and in the presence of urea. In contrast, a notable delivery occurs at lysosomal acidic pH due to protonation of benzimidazole groups and dethreading of the supramolecular ensemble. Cell studies show that the presence of the fuel enhances both nanomotor internalization and intracellular cargo delivery. This has been demonstrated for both  $S1_M$  and  $S1_{\text{MDOX}}$  loaded with the dye  $[\text{Ru}(\text{bpy})_3]\text{Cl}_2$  and

dox, respectively. For the nanomotors loaded with dox, the presence of urea allowed to obtain a similar viability to that found in the absence of urea, but using 4 times less nanoparticle concentration. Studies with the nanomotor loaded with  $[\text{Ru}(\text{bpy})_3]\text{Cl}_2$  demonstrated that the system has no short-term cytotoxicity, a highly desired characteristic for biomedical applications. The improvement in drug delivery properties, in terms of enhanced effectiveness by gated enzyme-powered nanomotors, holds potential use in different biomedical settings, such as the active transport of a drug into a specific tissue or cell without drug leaking before reaching the target location and payload delivery at-will using endogenous or exogenous stimuli. These findings may further motivate and inspire the development of micro- and nanomotors for the transport and stimulus-responsive controlled release of drugs.

## METHODS

**Chemicals.** Tetraethylorthosilicate (TEOS, >99%), triethanolamine (TEOA, 99%), cetyltrimethylammonium bromide (CTAB, 99%), ethanol (>99%), hydrochloric acid (37%), (3-iodopropyl)trimethoxysilane (>95%), tris(2,2'-bipyridyl)dichlororuthenium(II) hexahydrate ( $[\text{Ru}(\text{bpy})_3]\text{Cl}_2$ , benzimidazole (98%), triethylamine (TEA, 98%), sodium dihydrogen phosphate monohydrate (>99%), urease from *Canavalia ensiformis* (type IX), urea (99.9%), *N*-(3-(dimethylamino)propyl)-*N'*-ethylcarbodiimide hydrochloride (EDC, >99%), *N*-hydroxysuccinimide (NHS, 98%), and urease activity assay kit were acquired from Sigma-Aldrich. Toluene (99%), acetonitrile (99.5%), and disodium hydrogen phosphate heptahydrate (99%) were provided by Scharlau. Doxorubicin hydrochloride was purchased from Carbosynth. For cells experiments, Dulbecco's phosphate buffered saline (PBS), Dulbecco's modified Eagle's medium (DMEM) - high glucose, and fetal bovine serum (FBS) were purchased from Sigma-Aldrich. Cell proliferation reagent WST-1 was obtained from Roche Applied Science (Madrid, Spain). All reagents were used as received.

**Instruments.** SEM images were acquired using a FEI NOVA NanoSEM 230 microscope working at 5 kV. TEM and STEM-EDX imaging was carried out using a JEOL JEM-2100 LaB6 electron microscope working at 200 kV accelerating voltage and equipped with an Oxford Instruments INCA x-sight (Si(Li) detector) and a Zeiss SESAM microscope (200 kV) equipped with an energy dispersive X-ray (EDX) spectroscopy system from ThermoFisher. PXRD measurements were performed on a Seifert 3000TT diffractometer using  $\text{Cu K}\alpha$  radiation.  $\text{N}_2$  adsorption-desorption isotherms were recorded on a Micromeritics TriStar II Plus automated analyzer. The  $\zeta$  potential and hydrodynamic diameter experiments were performed with a ZetaSizer Nano ZS (Malvern). Elemental analysis was performed using a LECO CHNS-932 Elemental Analyzer. Enzymatic activity assay was carried out using an Infinite M200 PRO Multimode Microplate Reader. Optical videos were recorded using a Leica DMI8 inverted microscope equipped with a 63 $\times$  water objective and a Hamamatsu Camera. Absorbance measurements were performed with a JASCO V-650 spectrophotometer. Cell viability measurements were taken with a Wallac 1420 workstation. Flow cytometry studies were carried out using a CytoFLEX S instrument (Beckman-Coulter, USA). Confocal microscopy imaging was performed with a Leica TCS SP8 AOBS inverted laser scanning confocal microscope (Leica Microsystems Heidelberg GmbH).

**Synthesis and Characterization of  $\beta$ -Cyclodextrin-Modified Urease.**  $\beta$ -cyclodextrin-modified urease (CD-U) was prepared following a procedure previously reported.<sup>70,85,86</sup> Briefly, a mixture of 10 mg of urease, 10 mg of EDC, 10 mg of NHS, and 5 mg of aminated  $\beta$ -cyclodextrin in 2.5 mL of phosphate buffer (50 mM) was incubated for 24 h at 4 °C under stirring. After this, the modified enzyme was isolated by centrifugation using Amicon Ultra-05 centrifugal filter units with Ultracel-10 membranes and dialyzed in phosphate buffer at pH 7.5. The resulting CD-U was characterized by phenol-sulfuric acid method revealing a cyclodextrin content of 3 wt % (see Supporting Information

for details)<sup>87</sup> and by urease activity assay revealing an activity of 1.4 U  $\text{mg}^{-1}$ .

**Synthesis of Mesoporous Silica Nanoparticles (S0).** CTAB (570 mg) and TEOA (35 g) were dissolved in a flask contain 20 mL of DI water. The mixture was subsequently heated in an oil bath at 95 °C for 30 min. Then, 1.5 mL of TEOS was added to the mixture dropwise. The reaction was allowed to proceed for 2 h under magnetic stirring. Then, the particles were collected and rinsed three times by centrifuging and redispersing in ethanol. To obtain the mesoporous structure, the as-prepared particles were dispersed in a solution containing 30 mL of methanol and 1.8 mL of HCl for 24 h reflux at 80 °C. Finally, the material was washed three times with ethanol and labeled as S0.

**Preparation of S1.** 100 mg of mesoporous nanoparticles (S0) was suspended in 8 mL of acetonitrile containing 60 mg of  $[\text{Ru}(\text{bpy})_3]\text{Cl}_2$ , and the mixture was stirred overnight. Then, 100  $\mu\text{L}$  of (3-iodopropyl)trimethoxysilane was added and further stirred for 5.5 h. Afterward, the solid was isolated by centrifugation, washed with acetonitrile and toluene, and let to dry at room temperature for 3 days. Next, we prepared a saturated solution of benzimidazole in toluene (500 mg in 30 mL of toluene mixed with 1485  $\mu\text{L}$  of TEA and stirred for 20 min at 70 °C). Twenty mL of this solution was added over the nanoparticles, and the mixture was stirred for 3 days at 80 °C. Finally, the S1 material was isolated by centrifugation, washed with toluene and acetonitrile, and dried at room temperature.

**Preparation of S1<sub>M</sub>.** Eight mg of S1 and 3 mg of CD-U were stirred in 1 mL of sodium phosphate buffer overnight at 4 °C. Afterward, the capped material S1<sub>M</sub> was exhaustively washed by centrifugation with fresh buffer. The resulting material was kept refrigerated in phosphate buffer at a concentration of 10  $\text{mg mL}^{-1}$  until use.

**Optical Video Acquisition and MSD Analysis.** An aqueous solution of nanomotors S1<sub>M</sub> (0.02  $\text{mg mL}^{-1}$ ) was placed on a glass slide containing an aqueous solution of urea at the desired concentration. Then, a coverslip was used to cover the mixture in order to avoid any drifting artifact. Bright-field videos of 30 s were recorded using a Hamamatsu camera working at a frame rate of 50 fps. Tracking of the nanomotors was performed by using an in-house developed Python code. After obtaining the tracked trajectories with corresponding coordinates ( $x$ ,  $y$ ), MSD was calculated using the formula:

$$\text{MSD}(\Delta t) = \langle (r(t + \Delta t) - r(t))^2 \rangle$$

where  $r$  is the position of nanomotor at the initial time,  $t$  represents time,  $\Delta t$  is the elapsed time, and  $\langle \cdot \rangle$  represents the time and ensemble average. The diffusion coefficient ( $D$ ) is obtained by fitting the data of 20 particles per condition to  $\text{MSD} = 4D\Delta t$ , according to previous studies.<sup>76,77</sup>

**Triggered Release Experiments.** S1<sub>M</sub> stock was washed with deionized water at pH 7.5, divided into fractions, and brought to a concentration of 2.5  $\text{mg mL}^{-1}$  in sodium phosphate buffer (10 mM) adjusted at the corresponding pH (7.5 or 5). At scheduled times, aliquots were taken and centrifuged at 12,000 rpm for 2 min to precipitate the nanoparticles. Then, the supernatant absorbance at 453 nm was measured using a spectrophotometer in order to evaluate  $[\text{Ru}(\text{bpy})_3]\text{Cl}_2$  release. From absorbance, the amount of released cargo was directly calculated by applying the Beer-Lambert's law:

$$\text{absorbance}(453\text{nm}) = \epsilon_{453} \times L \times C$$

where  $\epsilon_{453}$  is the molar extinction of  $[\text{Ru}(\text{bpy})_3]\text{Cl}_2$  at 453 nm (14,600  $\text{M}^{-1} \text{cm}^{-1}$ ),  $L$  is the optical path of the cuvette (1 cm), and  $C$  is  $[\text{Ru}(\text{bpy})_3]\text{Cl}_2$  concentration. Furthermore, the maximum release efficiency was calculated by treating the solid with 20% NaOH for 1 h, which dissolved the silica scaffold.

**Cell Culture Conditions.** HeLa human cervix adenocarcinoma cells were purchased from the German Resource Centre for Biological Materials (DSMZ) and were grown in DMEM supplemented with 10% FBS. Cells were incubated at 37 °C in an atmosphere of 5% carbon dioxide and 95% air and underwent passage twice a week.

**Short-Term Cytotoxicity Studies.** The short-term cytotoxicity of the system was tested *in vitro* in the HeLa cells. For this purpose, HeLa

cells were seeded in a 96-well plate at 3500 cells/well and treated with different  $S1_M$  concentrations (0, 25, 50, 100  $\mu\text{g mL}^{-1}$ ; aliquots were taken from a stock of 2 mg  $\text{mL}^{-1}$  of  $S1_M$  and added the corresponding amount to cell culture media in order to obtain the desired concentration) in the absence or presence of urea at 50 mM in the media. Cells were incubated for 24 h, and the viability was determined by the WST-1 cell proliferation assay. Finally, absorbance was measured at 595 nm in the Wallac Workstation. Three independent experiments containing triplicates were carried out.

**Internalization Kinetics Studies Using Flow Cytometry.** HeLa cells were seeded at 300,000 cells  $\text{mL}^{-1}$  in 6-well plate and incubated at 37 °C for 24 h. Then,  $S1_M$  was added at 50  $\mu\text{g mL}^{-1}$  concentration in the absence or presence of urea (50 mM). At different times (0, 5, 15, 30, and 60 min), cells were washed with PBS to remove non-internalized nanoparticles and collected for analysis by the cytometer. Three independent experiments were carried out.

**TEM Imaging of HeLa Cells.** Cell uptake of nanoparticles was confirmed by TEM. HeLa cells were seeded in chamber slides at 35,000 cell  $\text{mL}^{-1}$  in DMEM (10% FBS) for 24 h. Then,  $S1_M$  was added to HeLa cell culture at 50  $\mu\text{g mL}^{-1}$ . After incubation for 1 h, cells were washed and fixed with 3% of glutaraldehyde in sodium phosphate buffer (0.1 M), dehydrated in ethanol, and stained with uranyl acetate (1%) and osmium tetroxide (1%). The samples were included in epoxy resin (Araldite) and sectioned for TEM analysis. TEM images were acquired using a microscope FEI Tecnai Spirit G2 operating at 80 kV with a digital camera (Soft Image System, Morada).

**Confocal Microscopy Imaging of Drug Delivery.** In order to test the potential use of enzyme-powered nanomotors equipped with pH-responsive nanovalves for the delivery of anticancer drugs, solid  $S1_{MDOX}$  was prepared (like  $S1_M$  but loaded with the cytotoxic drug dox). The amount of loaded dox was determined as 1.2  $\mu\text{mol per g}$  of solid by UV-visible spectrophotometry. For visualization of dox delivery in a cancer cell line, HeLa cells were seeded over glass coverslips at 300,000 cells  $\text{mL}^{-1}$  in a 6-well plate and incubated at 37 °C for 24 h. Then,  $S1_{MDOX}$  was added to HeLa cell culture media at a concentration of 50  $\mu\text{g mL}^{-1}$  in the absence or presence of urea (50 mM). After incubation for 1 h, cells were washed several times with PBS, and finally, slides were visualized using a confocal microscope Leica TCS SP8 AOBs. Furthermore, the fluorescence intensity associated with dox was quantified using the ImageJ software.

**Confirmation of  $S1_{MDOX}$  Internalization by 3D Confocal Imaging.** HeLa cells were seeded in glass coverslips in 6-well plates at 350,000 cells/mL in DMEM supplemented with 10% FBS for 24 h. Then,  $S1_{MDOX}$  (50  $\mu\text{g mL}^{-1}$ ) was added and incubated for 1 h. Afterward, cells were washed, and wheat germ agglutinin (WGA, 5  $\mu\text{g mL}^{-1}$ ) and Hoechst 33342 (2  $\mu\text{g mL}^{-1}$ ) were added for confocal microscopy analysis. Serial optical slices were obtained of the samples from up to down (z-sections) to analyze the entirety of the cells and to confirm the nanoparticles uptake. Finally, the images were stacked, creating a 3D reconstruction of the cell. Moreover, orthogonal sectioning was applied to determine the cellular localization of the nanoparticles.

**Cell Viability after Treatment with  $S1_{MDOX}$ .** For these experiments, HeLa cells were seeded in a 96-well plate at 3500 cells per well and treated with different  $S1_{MDOX}$  concentrations (0, 25, 50, and 100  $\mu\text{g mL}^{-1}$  in PBS) in the absence and in the presence of urea at 50 mM. Cells were incubated for 24 h, and the viability was determined by the WST-1 cell proliferation assay. Absorbance was measured at 595 nm in the Wallac Workstation. Three independent experiments containing triplicates were carried out.

**Preparation of Control Nanoparticles without the Urease Enzyme.** Control dye-loaded nanoparticles and control dox-loaded nanoparticles (lacking urease enzyme) were prepared by incubating 8 mg of the loaded solids with 1.2 mg  $\text{mL}^{-1}$  of  $\beta$ -cyclodextrin solution (without urease) overnight (sodium phosphate buffer, pH 7.5). Afterward, the capped materials were exhaustively washed with fresh buffer and isolated by centrifugation.

## ASSOCIATED CONTENT

### Supporting Information

The Supporting Information is available free of charge on the ACS Publications website at DOI: 10.1021/acsnano.9b06706.

Video S1: Nanomotor tracking in water at 0 mM urea concentration (AVI)

Video S2: Nanomotor tracking in water at 300 mM urea concentration (AVI)

Video S3: Nanomotor tracking in PBS at 0 mM urea concentration (AVI)

Video S4: Nanomotor tracking in PBS at 300 mM urea concentration (AVI)

Figures showing SEM images, PXRD patterns, pore distribution, hydrodynamic diameter, TEM images, enzymatic assay, MSD in water, trajectories in buffer, MSD in buffer, release from uncapped nanoparticles, cell viability, cell fluorescence upon treatment with nanoparticles without enzyme, and dox release kinetics; and phenol-sulfuric and Bradford assays methodology (PDF)

## AUTHOR INFORMATION

### Corresponding Authors

\*E-mail: rmaez@qim.upv.es.

\*E-mail: ssanchez@ibecbarcelona.eu.

### ORCID

Reynaldo Villalonga: 0000-0002-5227-7891

Ramón Martínez-Máñez: 0000-0001-5873-9674

Samuel Sánchez: 0000-0002-5845-8941

### Present Address

<sup>†</sup>Laboratory of Biosensors and Nanomachines, Department of Chemistry, University of Rome Tor Vergata, Via della Ricerca Scientifica, 1, Rome 00133, Italy

### Notes

The authors declare no competing financial interest.

## ACKNOWLEDGMENTS

A.L.-L. is grateful to “La Caixa” Banking Foundation for his Ph.D. grant. A.G.-F. thanks the Spanish government for her FPU fellowship. The authors are grateful to the Spanish Government (MINECO Projects MAT2015-64139-C4-1, CTQ2014-58989-PCTQ2015-71936-REDT, CTQ2015-68879-R (MICRODIA) and CTQ2015-72471-EXP (Enzwin)), the BBVA foundation (MEDIROBOTS), the CERCA Programme by the Generalitat de Catalunya, and the Generalitat Valenciana (Project PROMETEO/2018/024 and PROMETEOII/2014/061) for support. T.P. thanks MINECO for the Juan de la Cierva postdoctoral fellowship and the European Union’s Horizon 2020 research and innovation program, under the Marie Skłodowska-Curie Individual Fellowship (H2020-MSCA-IF-2018, DNA-bots). A.C.H. thanks MINECO for the Severo Ochoa fellowship. The authors would like to thank A. Miguel-Lopez for the development of the python code for motion analysis.

## REFERENCES

- (1) Wang, J.; *Nanomachines: Fundamentals and Applications*; John Wiley & Sons: New York, 2013.
- (2) Mavroidis, C.; Ferreira, A. *Nanorobotics: Current Approaches and Techniques*; Springer: New York, 2013.
- (3) Wang, H.; Pumera, M. Fabrication of Micro/Nanoscale Motors. *Chem. Rev.* **2015**, *115*, 8704–8735.



- (4) Li, J.; Esteban-Fernández de Ávila, B.; Gao, W.; Zhang, L.; Wang, J. Micro/Nanorobots for Biomedicine: Delivery, Surgery, Sensing, and Detoxification. *Sci. Robot.* **2017**, *2*, No. eaam6431.
- (5) Parmar, J.; Vilela, D.; Villa, K.; Wang, J.; Sánchez, S. Micro- and Nanomotors as Active Environmental Microcleaners and Sensors. *J. Am. Chem. Soc.* **2018**, *140*, 9317–9331.
- (6) de Avila, B. E.-F.; Angsantikul, P.; Li, J.; Angel Lopez-Ramirez, M.; Ramirez-Herrera, D. E.; Thamphiwatana, S.; Chen, C.; Delezuk, J.; Samakapiruk, R.; Ramez, V.; Obonyo, M.; Zhang, L.; Wang, J. Micromotor-Enabled Active Drug Delivery for *In Vivo* Treatment of Stomach Infection. *Nat. Commun.* **2017**, *8*, 272.
- (7) Wu, Z.; Li, L.; Yang, Y.; Hu, P.; Li, Y.; Yang, S.-Y.; Wang, L. V.; Gao, W. A Microrobotic System Guided by Photoacoustic Computed Tomography for Targeted Navigation in Intestines *In Vivo*. *Sci. Rob.* **2019**, *4*, No. eaax0613.
- (8) Wu, Z.; Troll, J.; Jeong, H.-H.; Wei, Q.; Stang, M.; Ziemssen, F.; Wang, Z.; Dong, M.; Schnichels, S.; Qiu, T.; Fischer, P. A Swarm of Slippery Micropellers Penetrates the Vitreous Body of the Eye. *Sci. Adv.* **2018**, *4*, No. eaat4388.
- (9) Villa, K.; Krejcova, L.; Novotny, F.; Heger, Z.; Sofer, Z.; Pumera, M. Cooperative Multifunctional Self-Propelled Paramagnetic Micro-robots with Chemical Handles for Cell Manipulation and Drug Delivery. *Adv. Funct. Mater.* **2018**, *28*, 1804343.
- (10) Lee, S.; Kim, S.; Kim, S.; Kim, J.-Y.; Moon, C.; Nelson, B. J.; Choi, H. A Capsule-Type Microrobot with Pick-and-Drop Motion for Targeted Drug and Cell Delivery. *Adv. Healthcare Mater.* **2018**, *7*, 1700985.
- (11) Xuan, M.; Wu, Z.; Shao, J.; Dai, L.; Si, T.; He, Q. Near Infrared Light-Powered Janus Mesoporous Silica Nanoparticle Motors. *J. Am. Chem. Soc.* **2016**, *138*, 6492–6497.
- (12) Wang, J.; Xiong, Z.; Zheng, J.; Zhan, X.; Tang, J. Light-Driven Micro/Nanomotors for Promising Biomedical Tools: Principle, Challenge and Prospect. *Acc. Chem. Res.* **2018**, *51*, 1957–1965.
- (13) Mandal, P.; Patil, G.; Kakoty, H.; Ghosh, A. Magnetic Active Matter Based on Helical Propulsion. *Acc. Chem. Res.* **2018**, *51*, 2689–2698.
- (14) Mushtaq, F.; Torlakcik, H.; Hoop, M.; Jang, B.; Carlson, F.; Grunow, T.; Läubli, N.; Ferreira, A.; Chen, X.-Z.; Nelson, B. J.; Pané, S. Motile Piezoelectric Nanoels for Targeted Drug Delivery. *Adv. Funct. Mater.* **2019**, *29*, 1808135.
- (15) Wang, W.; Li, S.; Mair, L.; Ahmed, S.; Huang, T. J.; Mallouk, T. E. Acoustic Propulsion of Nanorod Motors Inside Living Cells. *Angew. Chem.* **2014**, *126*, 3265–3268.
- (16) Melde, K.; Mark, A. G.; Qiu, T.; Fischer, P. Holograms for Acoustics. *Nature* **2016**, *537*, 518–522.
- (17) Dey, K. K.; Sen, A. Chemically Propelled Molecules and Machines. *J. Am. Chem. Soc.* **2017**, *139*, 7666–7676.
- (18) Sánchez, S.; Soler, S.; Katuri, K. Chemically Powered Micro- and Nanomotors. *Angew. Chem., Int. Ed.* **2015**, *54*, 1414–1444.
- (19) Peng, F.; Tu, Y.; Wilson, D. A. Micro/Nanomotors Towards *In Vivo* Application. *Chem. Soc. Rev.* **2017**, *46*, 5289–5310.
- (20) Wang, S.; Liu, X.; Wang, Y.; Xu, D.; Liang, C.; Guo, J.; Ma, X. Biocompatibility of Artificial Micro/Nanomotors for Use in Biomedicine. *Nanoscale* **2019**, *11*, 14099–14112.
- (21) García-Gradilla, V.; Sattayasamitsathit, S.; Soto, F.; Kuralay, F.; Yardimci, C.; Wiitala, D.; Galarnyk, M.; Wang, J. Ultrasound-Propelled Nanoporous Gold Wire for Efficient Drug Loading and Release. *Small* **2014**, *10*, 4154–4159.
- (22) Esteban-Fernández de Ávila, B.; Ramírez-Herrera, D. E.; Campuzano, S.; Angsantikul, P.; Zhang, L.; Wang, J. Nanomotor-Enabled pH-Responsive Intracellular Delivery of Caspase-3: Toward Rapid Cell Apoptosis. *ACS Nano* **2017**, *11*, 5367–5374.
- (23) Hansen-Bruhn, M.; de Avila, B. E.-F.; Beltran-Gastelum, M.; Zhao, J.; Ramirez-Herrera, D. E.; Angsantikul, P.; Vesterager Gothelf, K.; Zhang, L.; Wang, J. Active Intracellular Delivery of a Cas9/sgRNA Complex Using Ultrasound-Propelled Nanomotors. *Angew. Chem., Int. Ed.* **2018**, *57*, 2657–2661.
- (24) Wu, Z.; Wu, Y.; He, W.; Lin, X.; Sun, J.; He, Q. Self-Propelled Polymer-Based Multilayer Nanorockets for Transportation and Drug Release. *Angew. Chem., Int. Ed.* **2013**, *52*, 7000–7003.
- (25) Ma, X.; Hahn, K.; Sánchez, S. Catalytic Mesoporous Janus Nanomotors for Active Cargo Delivery. *J. Am. Chem. Soc.* **2015**, *137*, 4976–4979.
- (26) Tu, Y.; Peng, F.; André, A. A. M.; Men, Y.; Srinivas, Y.; Wilson, D. A. Biodegradable Hybrid Stomatocyte Nanomotors for Drug Delivery. *ACS Nano* **2017**, *11*, 1957–1963.
- (27) Tu, Y.; Peng, F.; White, P. B.; Wilson, D. A. Redox-Sensitive Stomatocyte Nanomotors: Destruction and Drug Release in the Presence of Glutathione. *Angew. Chem., Int. Ed.* **2017**, *56*, 7620–7624.
- (28) Gao, W.; Pei, A.; Dong, R.; Wang, J. Catalytic Iridium-Based Janus Micromotors Powered by Ultralow Levels of Chemical Fuels. *J. Am. Chem. Soc.* **2014**, *136*, 2276–2279.
- (29) Solovev, A. A.; Xi, W.; Gracias, D. H.; Harazim, S. M.; Deneke, C.; Sánchez, S.; Schmidt, O. G. Self-Propelled Nanotools. *ACS Nano* **2012**, *6*, 1751–1756.
- (30) Zhang, Y.; Hess, H. Enhanced Diffusion of Catalytically Active Enzymes. *ACS Cent. Sci.* **2019**, *5*, 939–948.
- (31) Dey, K. K.; Zhao, X.; Tansi, B. M.; Mendez-Ortiz, W. J.; Cordova-Figueroa, U. M.; Golestanian, R.; Sen, A. Micromotors Powered by Enzyme Catalysis. *Nano Lett.* **2015**, *15*, 8311–8315.
- (32) Patiño, T.; Arqué, X.; Mestre, R.; Palacios, L.; Sánchez, S. Fundamental Aspects of Enzyme-Powered Micro- and Nanoswimmers. *Acc. Chem. Res.* **2018**, *51*, 2662–2671.
- (33) Zhao, X.; Gentile, K.; Mohajerani, F.; Sen, A. Powering Motion with Enzymes. *Acc. Chem. Res.* **2018**, *51*, 2373–2381.
- (34) Schattling, P. S.; Ramos-Docampo, M. A.; Salgueirino, V.; Stadler, B. Double-Fueled Janus Swimmers with Magnetotactic Behaviour. *ACS Nano* **2017**, *11*, 3973–3983.
- (35) Schattling, P. S.; Thingholm, B.; Städler, B. Enhanced Diffusion of Glucose-Fueled Janus Particles. *Chem. Mater.* **2015**, *27*, 7412–7418.
- (36) Ma, X.; Wang, X.; Hahn, K.; Sánchez, S. Motion Control of Urea-Powered Biocompatible Hollow Microcapsules. *ACS Nano* **2016**, *10*, 3597–3605.
- (37) Arqué, X.; Romero-Rivera, A.; Feixas, F.; Patiño, T.; Osuna, S.; Sánchez, S. Intrinsic Enzymatic Properties Modulate the Self-Propulsion of Micromotors. *Nat. Commun.* **2019**, *10*, 2826.
- (38) Ma, X.; Hortelao, A. C.; Miguel-López, A.; Sánchez, S. Bubble-Free Propulsion of Ultrasmall Tubular Nanojets Powered by Biocatalytic Reactions. *J. Am. Chem. Soc.* **2016**, *138*, 13782–13785.
- (39) Jang, W.-S.; Kim, J. H.; Gao, C.; Lee, D.; Hammer, D. A. Enzyme-Powered Surface-Associated Self-Motile Protocells. *Small* **2018**, *14*, 1801715.
- (40) Simmchen, J.; Baeza, A.; Ruiz-Molina, D.; Vallet-Regí, M. Improving Catalase-Based Propelled Motor Endurance by Enzyme Encapsulation. *Nanoscale* **2014**, *6*, 8907–8913.
- (41) Patiño, T.; Feiner-Gracia, N.; Arqué, X.; Miguel-López, A.; Jannasch, A.; Stumpp, T.; Schäffer, E.; Albertazzi, L.; Sánchez, S. Influence of Enzyme Quantity and Distribution on the Self-Propulsion of Non-Janus Urease-Powered Micromotors. *J. Am. Chem. Soc.* **2018**, *140*, 7896–7903.
- (42) Bunea, A.-I.; Pavel, I.-A.; David, S.; Gáspár, S. Sensing Based on the Motion of Enzyme-Modified Nanorods. *Biosens. Bioelectron.* **2015**, *67*, 42–48.
- (43) Ma, X.; Jannasch, A.; Albrecht, U.-R.; Hahn, K.; Miguel-López, A.; Schäffer, E.; Sánchez, S. Enzyme-Powered Hollow Mesoporous Janus Nanomotors. *Nano Lett.* **2015**, *15*, 7043–7050.
- (44) Wang, L.; Hortelao, A. C.; Huang, X.; Sánchez, S. Lipase-Powered Mesoporous Silica Nanomotors for Triglyceride Degradation. *Angew. Chem., Int. Ed.* **2019**, *58*, 7992–7996.
- (45) Hortelao, A. C.; Patiño, T.; Perez-Jiménez, A.; Blanco, A.; Sánchez, S. Enzyme-Powered Nanobots Enhance Anticancer Drug Delivery. *Adv. Funct. Mater.* **2018**, *28*, 1705086.
- (46) Abdelmohsen, L. K. E. A.; Nijemeisland, M.; Pawar, G. M.; Janssen, G. E. A.; Nolte, R. J. M.; van Hest, J. C.; Wilson, D. A. Dynamic Loading and Unloading of Proteins in Polymeric Stomatocytes:

Formation of an Enzyme-Loaded Supramolecular Nanomotor. *ACS Nano* **2016**, *10*, 2652–2660.

(47) Nijemeisland, M.; Abdelmohsen, L. K. E. A.; Huck, W. T. S.; Wilson, D. A.; van Hest, J. C. M. A Compartmentalized Out-of-Equilibrium Enzymatic Reaction Network for Sustained Autonomous Movement. *ACS Cent. Sci.* **2016**, *2*, 843–849.

(48) Wu, Z.; Lin, X.; Si, T.; He, Q. Recent Progress on Bioinspired Self-Propelled Micro/Nanomotors via Controlled Molecular Self-Assembly. *Small* **2016**, *12*, 3080–3093.

(49) Joseph, A.; Contini, C.; Cecchin, D.; Nyberg, S.; Ruiz-Perez, L.; Gaitzsch, J.; Fullstone, G.; Tian, X.; Azizi, J.; Preston, J.; Volpe, G.; Battaglia, G. Chemotactic Synthetic Vesicles: Design and Applications in Blood-Brain Barrier Crossing. *Sci. Adv.* **2017**, *3*, No. e1700362.

(50) Mura, S.; Nicolas, J.; Couvreur, P. Stimuli-Responsive Nanocarriers for Drug Delivery. *Nat. Mater.* **2013**, *12*, 991–1003.

(51) Llopis-Lorente, A.; de Luis, B.; García-Fernández, A.; Jimenez-Falcao, S.; Orzáez, M.; Sancenón, F.; Villalonga, R.; Martínez-Máñez, R. Hybrid Mesoporous Nanocarriers Act by Processing Logic Tasks: Toward the Design of Nanobots Capable of Reading Information from the Environment. *ACS Appl. Mater. Interfaces* **2018**, *10*, 26494–26500.

(52) Patiño, T.; Porchetta, A.; Jannasch, A.; Lladó, A.; Stumpp, T.; Schäffer, E.; Ricci, F.; Sánchez, S. Self-Sensing Enzyme-Powered Micromotors Equipped with pH-Responsive DNA Nanoswitches. *Nano Lett.* **2019**, *19*, 3440–3447.

(53) Croissant, J. G.; Fatiev, Y.; Almalik, A.; Khashab, N. Mesoporous Silica and Organosilica Nanoparticles: Physical Chemistry, Biosafety, Delivery Strategies, and Biomedical Applications. *Adv. Healthcare Mater.* **2018**, *7*, 1700831.

(54) Tarn, D.; Ashley, C. E.; Xue, M.; Carnes, E. C.; Zink, J. I.; Brinker, C. J. Mesoporous Silica Nanoparticle Nanocarriers: Biofunctionality and Biocompatibility. *Acc. Chem. Res.* **2013**, *46*, 792–801.

(55) Coll, C.; Bernardos, A.; Martínez-Máñez, R.; Sancenón, F. Gated Silica Mesoporous Supports for Controlled Release and Signaling Applications. *Acc. Chem. Res.* **2013**, *46*, 339–349.

(56) Wen, J.; Yang, K.; Liu, F.; Li, H.; Xu, Y.; Sun, S. Diverse Gatekeepers for Mesoporous Silica Nanoparticle Based Drug Delivery Systems. *Chem. Soc. Rev.* **2017**, *46*, 6024–6045.

(57) Aznar, E.; Oroval, M.; Pascual, L.; Murguía, J. R.; Martínez-Máñez, R.; Sancenón, F. Gated Materials for On-Command Release of Guest Molecules. *Chem. Rev.* **2016**, *116*, 561–718.

(58) Song, N.; Yang, Y.-W. Molecular and Supramolecular Switches on Mesoporous Silica Nanoparticles. *Chem. Soc. Rev.* **2015**, *44*, 3474–3504.

(59) Climent, E.; Mondragón, L.; Martínez-Máñez, R.; Sancenón, F.; Marcos, M. D.; Murguía, J. R.; Amorós, P.; Rurack, K.; Pérez-Payá, E. Selective, Highly Sensitive, and Rapid Detection of Genomic DNA by Using Gated Materials: Mycoplasma Detection. *Angew. Chem., Int. Ed.* **2013**, *52*, 8938–8942.

(60) Hernández-Montoto, A.; Montes, R.; Samadi, A.; Gorbe, M.; Terrés, J. M.; Cao-Milán, R.; Aznar, E.; Ibáñez, J.; Masot, R.; Marcos, M. D.; Orzáez, M.; Sancenón, F.; Oddershede, L. B.; Martínez-Máñez, R. Gold Nanostars Coated with Mesoporous Silica Are Effective and Nontoxic Photothermal Agents Capable of Gate Keeping and Laser-Induced Drug Release. *ACS Appl. Mater. Interfaces* **2018**, *10*, 27644–27656.

(61) de la Torre, C.; Casanova, I.; Acosta, G.; Coll, C.; Moreno, M. J.; Albericio, F.; Aznar, E.; Mangues, R.; Royo, M.; Sancenón, F.; Martínez-Máñez, R. Gated Mesoporous Silica Nanoparticles Using a Double-Role Circular Peptide for the Controlled and Target-Preferential Release of Doxorubicin in CXCR4-Expressing Lymphoma Cells. *Adv. Funct. Mater.* **2015**, *25*, 687–695.

(62) Agostini, A.; Mondragón, L.; Bernardos, A.; Martínez-Máñez, R.; Marcos, M. D.; Sancenón, F.; Soto, J.; Costero, A.; Manguan-García, C.; Perona, R.; Moreno-Torres, M.; Aparicio-Sanchis, R.; Murguía, J. R. Targeted Cargo Delivery in Senescent Cells Using Capped Mesoporous Silica Nanoparticles. *Angew. Chem., Int. Ed.* **2012**, *51*, 10556–10560.

(63) Pascual, L.; Cerqueira-Coutinho, C.; Garcia-Fernandez, A.; de Luis, B.; Bernardes, E. S.; Albernaz, M. S.; Missailidis, S.; Martínez-Máñez, R.; Santos-Oliveira, R.; Orzaez, M.; Sancenon, F. MUC1

Aptamer-Capped Mesoporous Silica Nanoparticles for Controlled Drug Delivery and Radio-Imaging Applications. *Nanomedicine* **2017**, *13*, 2495–2505.

(64) Llopis-Lorente, A.; Díez, P.; Sánchez, A.; Marcos, M. D.; Sancenón, F.; Martínez-Ruiz, P.; Villalonga, R.; Martínez-Máñez, R. Interactive Models of Communication at the Nanoscale Using Nanoparticles that Talk to One Another. *Nat. Commun.* **2017**, *8*, 15511.

(65) De Luis, B.; Llopis-Lorente, A.; Rincón, P.; Gadea, J.; Sancenón, F.; Aznar, E.; Villalonga, R.; Murguía, J. R.; Martínez-Máñez, R. An Interactive Model of Communication between Abiotic Nanodevices and Microorganisms. *Angew. Chem., Int. Ed.* **2019**, DOI: 10.1002/anie.201908867.

(66) Giménez, C.; Climent, E.; Aznar, E.; Martínez-Máñez, R.; Sancenón, F.; Marcos, M. D.; Amorós, P.; Rurack, K. Toward Chemical Communication between Gated Nanoparticles. *Angew. Chem., Int. Ed.* **2014**, *53*, 12629–12633.

(67) Llopis-Lorente, A.; Díez, P.; Sánchez, A.; Marcos, M. D.; Sancenón, F.; Martínez-Ruiz, P.; Villalonga, R.; Martínez-Máñez, R. Toward Chemical Communication between Nanodevices. *Nano Today* **2018**, *18*, 8–11.

(68) Ma, X.; Jang, S.; Popescu, M. N.; Uspal, W. E.; Miguel-López, A.; Hahn, K.; Kim, D.-P.; Sánchez, S. Reversed Janus Micro/Nanomotors with Internal Chemical Engine. *ACS Nano* **2016**, *10*, 8751–8759.

(69) Xuan, M.; Shao, J.; Gao, C.; Wang, W.; Dai, L.; He, Q. Self-Propelled Nanomotors for Thermomechanically Percolating Cell Membranes. *Angew. Chem., Int. Ed.* **2018**, *57*, 12463–12467.

(70) Holzinger, M.; Bouffier, L.; Villalonga, R.; Cosnier, S. Adamantane/ $\beta$ -Cyclodextrin Affinity Biosensors Based on Single-Walled Carbon Nanotubes. *Biosens. Bioelectron.* **2009**, *24*, 1128–1134.

(71) García-Fernández, A.; García-Laínez, G.; Ferrándiz, M. L.; Aznar, E.; Sancenón, F.; Alcaraz, M. J.; Murguía, J. R.; Marcos, M. D.; Martínez-Máñez, R.; Costero, A. M.; Orzáez, M. Targeting Inflammation by the Inhibition of Caspase-1 Activity using Capped Mesoporous Silica Nanoparticles. *J. Controlled Release* **2017**, *248*, 60–70.

(72) Brunauer, S.; Emmett, P. H.; Teller, E. Adsorption of Gases in Multimolecular Layers. *J. Am. Chem. Soc.* **1938**, *60*, 309–319.

(73) Barrett, E. P.; Joyner, L. G.; Halenda, P. P. The Determination of Pore Volume and Area Distributions in Porous Substances. I. Computations from Nitrogen Isotherms. *J. Am. Chem. Soc.* **1951**, *73*, 373–380.

(74) Bradford, M. A. Rapid and Sensitive Method for the Quantitation of Microgram Quantities of Protein Utilizing the Principle of Protein-Dye Binding. *Anal. Biochem.* **1976**, *72*, 248–254.

(75) Moliner-Martínez, Y.; Herráez-Hernández, R.; Campíns-Falcó, P. Improved Detection Limit for Ammonium/Ammonia Achieved by Berthelot's Reaction by Use of Solid-Phase Extraction Coupled to Diffuse Reflectance Spectroscopy. *Anal. Chim. Acta* **2005**, *534*, 327–334.

(76) Howse, J. R.; Jones, R. A. L.; Ryan, A. J.; Gough, T.; Vafabakhsh, R.; Golestanian, R. Self-Motile Colloidal Particles: From Directed Propulsion to Random Walk. *Phys. Rev. Lett.* **2007**, *99*, 048102.

(77) Dunderdale, G.; Ebbens, S.; Fairclough, P.; Howse, J. Importance of Particle Tracking and Calculating the Mean-Squared Displacement in Distinguishing Nanopropulsion from Other Processes. *Langmuir* **2012**, *28*, 10997–11006.

(78) Hortelao, A. C.; Carrascosa, R.; Murillo-Cremaes, N.; Patiño, T.; Sánchez, S. Targeting 3D Bladder Cancer Spheroids with Urease-Powered Nanomotors. *ACS Nano* **2019**, *13*, 429–439.

(79) Jerez, G.; Kaufman, G.; Prystai, M.; Schenkeveld, S.; Donkor, K. K. Determination of Thermodynamic  $pK_a$  Values of Benzimidazole and Benzimidazole Derivatives by Capillary Electrophoresis. *J. Sep. Sci.* **2009**, *32*, 1087–1095.

(80) Pundir, C. S.; Jakhar, S.; Narwal, V. Determination of Urea with Special Emphasis on Biosensors: A Review. *Biosens. Bioelectron.* **2019**, *123*, 36–50.

(81) Ansari, S. G.; Wahab, R.; Ansari, Z. A.; Kim, Y.-S.; Khang, G.; Al-Hajry, A.; Shin, H.-S. Effect of Nanostructure on the Urea Sensing



Properties of Sol-Gel Synthesized ZnO. *Sens. Actuators, B* **2009**, *137*, 566–573.

(82) Guo, Y.; Wang, N.; Mou, J.; Zhao, Z.; Yang, J.; Zhu, F.; Pei, G.; Zhu, H.; Wang, Y.; Xu, G.; et al. Pretreatment of Huaqihuang Extractum Protects against Cisplatin-Induced Nephrotoxicity. *Sci. Rep.* **2018**, *8*, 7333.

(83) Ibrahim, S. F.; van den Engh, G. Flow Cytometry and Cell Sorting. *Adv. Biochem. Eng./Biotechnol.* **2007**, *106*, 19–39.

(84) Sadeghi-Aliabadi, H.; Minaïyan, M.; Dabestan, A. Cytotoxic Evaluation of Doxorubicin in Combination with Simvastatin against Human Cancer Cells. *Res. Pharm. Sci.* **2010**, *5*, 127–133.

(85) Aznar, E.; Villalonga, R.; Giménez, C.; Sancenón, F.; Marcos, M. D.; Martínez-Mañez, R.; Díez, P.; Pingarrón, J. M.; Amorós, P. Glucose-Triggered Release Using Enzyme-Gated Mesoporous Silica Nanoparticles. *Chem. Commun.* **2013**, *49*, 6391–6393.

(86) Oroval, M.; Díez, P.; Aznar, E.; Coll, C.; Marcos, M. D.; Sancenón, F.; Villalonga, R.; Martínez-Manez, R. Self-Regulated Glucose-Sensitive Neoglycoenzyme-Capped Mesoporous Silica Nanoparticles for Insulin Delivery. *Chem. - Eur. J.* **2017**, *23*, 1353–1360.

(87) Dubois, M.; Gilles, K. A.; Hamilton, J. K.; Rebers, P. A.; Smith, F. Colorimetric Method for Determination of Sugars and Related Substances. *Anal. Chem.* **1956**, *28*, 350–356.

## Nanomotors

 International Edition: DOI: 10.1002/anie.201900697  
 German Edition: DOI: 10.1002/ange.201900697

## Lipase-Powered Mesoporous Silica Nanomotors for Triglyceride Degradation

 Lei Wang<sup>†</sup>, Ana C. Hortelão<sup>†</sup>, Xin Huang, and Samuel Sánchez\*

**Abstract:** We report lipase-based nanomotors that are capable of enhanced Brownian motion over long periods of time in triglyceride solution and of degrading triglyceride droplets that mimic “blood lipids”. We achieved about 40 min of enhanced diffusion of lipase-modified mesoporous silica nanoparticles (MSNPs) through a biocatalytic reaction between lipase and its corresponding water-soluble oil substrate (triacetin) as fuel, which resulted in an enhanced diffusion coefficient (ca. 50% increase) at low triacetin concentration (< 10 mM). Lipase not only serves as the power engine but also as a highly efficient cleaner for the triglyceride droplets (e.g., tributyrin) in PBS solution, which could yield potential biomedical applications, for example, for dealing with diseases related to the accumulation of triglycerides, or for environmental remediation, for example, for the degradation of oil spills.

Synthetic micro/nanomotors are active colloids that self-propel in fluids while performing complex tasks such as cargo pick-up and release,<sup>[1]</sup> sensing,<sup>[2]</sup> biomedical applications,<sup>[3]</sup> and environmental remediation.<sup>[4]</sup> There are several methods to trigger the propulsion of micro/nanomotors, including through catalytic reactions,<sup>[5]</sup> electric fields,<sup>[6]</sup> as well as ultrasonic,<sup>[7]</sup> magnetic,<sup>[8]</sup> and light excitation.<sup>[9]</sup> Particularly for in vivo applications, it is necessary to explore biocompatible and biomimetic designs that are capable of actuating in biological systems without side effects. Therefore, enzymes that carry out energy conversion in biological systems by using existing fuel sources, and without requiring an external power source, are good candidates to address these concerns.<sup>[10]</sup> Sen and co-workers provided experimental evidence of enhanced single-enzyme diffusion based on substrate turnover.<sup>[11]</sup> They also demonstrated molecular chemotaxis of urease and catalase towards a gradient of increasing

substrate concentrations,<sup>[11b]</sup> as well as the fabrication of enzymatic motors.<sup>[12]</sup> Our group extended this field by modifying Janus mesoporous silica micro/nanoparticles with different enzymes.<sup>[13]</sup> With urease, the hollow Janus silica micromotors achieved a directional propulsion with a high degree of controllability, either through the addition of salts or in the presence of a magnetic field.<sup>[13b]</sup> In addition, we reported how the stochastic binding of enzymes to the surface of the particles with a molecular asymmetry in enzyme distribution results in an asymmetric generation of forces, which in turn leads to self-propulsion.<sup>[14]</sup> This technique was also adopted for the fabrication of nanomotors based on mesoporous silica nanoparticles, which yielded a more efficient delivery and release system of anticancer drugs to cells in vitro, as well as for the fabrication of antibody-modified urease nanomotors for efficient penetration of bladder cancer spheroids.<sup>[15]</sup> Apart from spherical particles, enzymes have been reported to power various other structures, such as supramolecular stomatocytes,<sup>[16]</sup> polymersomes,<sup>[17]</sup> carbon nanotubes,<sup>[18]</sup> silica nanotubes,<sup>[19]</sup> PEDOT/Au microtubes,<sup>[20]</sup> polypyrrole/Au nanorods,<sup>[21]</sup> silk fibroin,<sup>[22]</sup> and macroscale carbon fibers.<sup>[23]</sup> Despite significant advances in the field of motors, only a few micro/nanomotors demonstrated motion in oily solution,<sup>[24]</sup> and enzymatic motors capable of navigating in oil solution or at the oil–water interface are still rarely explored.

Herein, we demonstrate that lipase-powered nanomotors (LNMs), with stochastic binding of lipase on mesoporous silica nanoparticles (MSNPs), can swim in dissolvable triglyceride solution, thus improving the degradation efficiency of slightly dissolvable triglyceride. Lipase (triacylglycerol ester hydrolases from *Candida rugosa*, EC 3.1.1.3) was chosen for the experiment as lipase can act as a catalyst for the decomposition of triglyceride substrates, both dissolvable (e.g., triacetin with a solubility of 61 mg mL<sup>-1</sup>) and slightly dissolvable (e.g., tributyrin with a solubility of 0.133 mg mL<sup>-1</sup>) ones. It offers two functionalities: 1) It acts as the power engine with triacetin as the fuel, and 2) it takes on the role of active cleaner for the tributyrin droplets. In addition to enhancing the motion of LNMs, the triacetin fuel is biocompatible (an FDA-approved food additive<sup>[25]</sup>) and thus suitable for biological and environmental applications. Furthermore, LNMs present a high efficiency in triglyceride degradation compared with free lipase and other enzymatic motors (see Figure 4).

The LNMs were fabricated using MSNPs as the substrate to immobilize lipase. MSNPs are biocompatible, and their porous structure is useful for drug loading.<sup>[26]</sup> The surface of the MSNPs was modified chemically using glutaraldehyde as a crosslinker between the amino groups of lipase and MSNPs,

[\*] Dr. L. Wang,<sup>[†]</sup> Prof. Dr. X. Huang  
 MIIT Key Laboratory of Critical Materials Technology for New Energy Conversion and Storage  
 School of Chemistry and Chemical Engineering  
 Harbin Institute of Technology, Harbin 150001 (China)  
 Dr. L. Wang,<sup>[†]</sup> A. C. Hortelão,<sup>[†]</sup> Prof. Dr. S. Sánchez  
 Institute for Bioengineering of Catalonia (IBEC)  
 The Barcelona Institute of Science and Technology (BIST)  
 Baldiri i Reixac 10–12, 08028 Barcelona (Spain)  
 E-mail: ssanchez@ibecbarcelona.eu  
 Prof. Dr. S. Sánchez  
 Institució Catalana de Recerca i Estudis Avançats (ICREA)  
 Pg. Lluís Companys 23, 08010 Barcelona (Spain)

[†] These authors contributed equally to this work.

Supporting information and the ORCID identification number(s) for the author(s) of this article can be found under:  
<https://doi.org/10.1002/anie.201900697>.

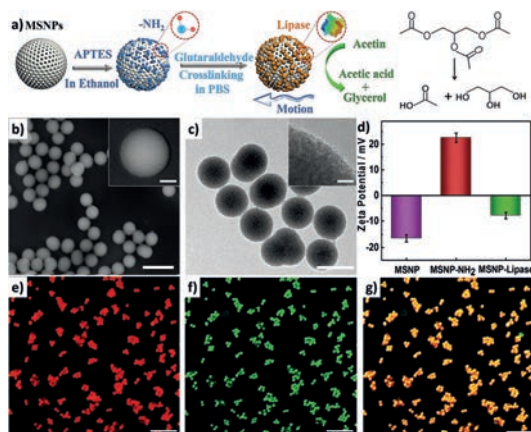


**Figure 1.** a) Schematic representation of the functionalization strategy for the preparation of the lipase-based nanomotors, whose motion is triggered by the catalytic reaction with triacetin. b) SEM and c) TEM microscopy images of MSNPs modified with lipase, with insets showing magnifications. Scale bars: b) 1  $\mu\text{m}$  (100 nm in the inset), and c) 500 nm (20 nm in the inset). d) Evolution of the surface charge after modifying the MSNP surfaces with amine functional groups, followed by lipase. All measurements were carried out in the same PBS (pH 7.4) solution. e–g) Confocal fluorescence (FL) images of lipase-modified MSNPs, scale bars are 5  $\mu\text{m}$ . The red FL is due to Rhodamine B (RB) loading of the MSNPs, while the green FL is generated by the Krypton-modified lipase. g) The corresponding merged image.

respectively (Figure 1 a), resulting in stable catalytic activity.<sup>[27]</sup> The MSNPs were characterized by transmission electron microscopy (TEM) and scanning electron microscopy (SEM; see the Supporting Information, Figure S1 a, b). They consisted of uniform spheres (Figure 1 b, c) with a porous structure (Figure S1 a, inset) and showed an average diameter of  $431.01 \pm 1.99$  nm ( $N=100$ , average diameter  $\pm$  standard error of the mean (SE), see Figure S2). They showed no aggregation, which was also confirmed through dynamic light scattering (DLS). After each modification step, there was only a single population distribution in the hydrodynamic radius plots (Figure S3 a), indicating that the MSNPs were still well dispersed. The increase in hydrodynamic radius and the broader peak can be attributed to the amination and lipase immobilization (Figure S3 a). Furthermore, the change in surface charge confirmed each modification step (Figure 1 d): The as-synthesized MSNPs had a negative surface charge of  $-16.43 \pm 1.36$  mV, which increased to  $22.57 \pm 1.79$  mV after amination. Lipase immobilization in PBS solution (phosphate-buffered saline, pH 7.4) caused the surface charge to drop to  $-7.68 \pm 1.21$  mV, which can be attributed to the isoelectric point of lipase of about pH 5.6–5.8.<sup>[28]</sup> Additionally, protein immobilization was characterized by fluorescence staining (Figure 1 e–g). Confocal FL microscopy images show the MSNPs loaded with Rhodamine B (RB) (Figure 1 e) and stained with Krypton (Figure 1 f). Immobilization of lipase on the surface of the MSNPs was also confirmed (Figure 1 g). These results were further corroborated by the presence of

a peak at 280 nm in the UV spectrum of the lipase-modified MSNPs (Figure S3 b).<sup>[29]</sup>

Enzyme assays were carried out to confirm that lipase remained active after its immobilization onto the MSNPs. In the studied motor concentration range of 0.1 to 1.0  $\text{mg mL}^{-1}$ , the active milliunits of lipase linearly increased with motor concentration (Figure S4 a), confirming the catalytic activity of the lipase-modified MSNPs. To investigate the motility of the lipase-modified MSNPs in PBS solution, we selected triacetin as the substrate because of its solubility in PBS. As the catalytic reaction of triacetin generates acetic acid [Eq. (1) in the Supporting Information], litmus ( $10 \text{ mg mL}^{-1}$ ) was added as a pH indicator to the triacetin ( $10 \text{ mM}$ )-containing PBS solution (pH 7.4, 10 mM) to further confirm the catalytic activity of the LNMs. This was followed by the collection of UV spectra. Initially, that is, prior to the addition of the LNMs, the triacetin PBS solution had a blue color (absorption at 580 nm; Figure S4 b, blue curve), which changed to pink within about 3 h after adding the LNMs (absorption at 500 nm; Figure S4 b, red curve). This further confirmed that lipase maintained its activity after being immobilized on the MSNPs (Figure S5).

We tested different concentrations of triacetin as fuel for the lipase-modified MSNPs. The mean squared displacement (MSD; Figure 2 a), calculated from the tracked trajectories

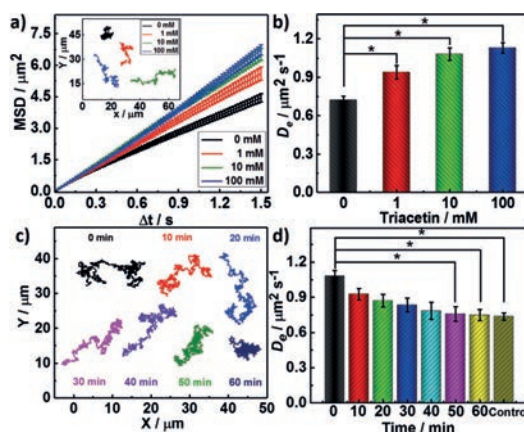


**Figure 2.** a) Representative trajectories (inset) of LNMs with different triacetin concentrations of 0 mM (black), 1 mM (red), 10 mM (green), and 100 mM (blue) and corresponding mean square displacements (MSDs;  $n \geq 20$ , error bars represent SE). b) Effective diffusion coefficients obtained by analyzing the MSD for different triacetin concentrations. c) Representative trajectories of LNMs at different times with sufficient fuel. d) Diffusion coefficients of LNMs as a function of time, with 100 mM of triacetin. Control experiment: LNMs in PBS solution without fuel.  $*p < 0.05$  when compared to the control group.

(Figure 2 a, inset), increased linearly with time and fuel concentration, indicating a fuel-concentration-dependent motility.<sup>[30]</sup> The effective diffusion coefficient ( $D_e$ ) was calculated from the MSD per time interval ( $\Delta t$ ) as  $D_e = 0.25 \text{ MSD} / \Delta t$ . During the studied time range, the  $D_e$  value of

the lipase-modified MSNPs was  $0.72 \pm 0.03 \mu\text{m}^2\text{s}^{-1}$  in PBS solution without adding fuel, increasing to  $0.94 \pm 0.05$ ,  $1.08 \pm 0.05$ , and  $1.13 \pm 0.04 \mu\text{m}^2\text{s}^{-1}$  (Figure 2b) when 1.0, 10, and 100 mM of fuel was added, respectively. This illustrates the increase in  $D_e$  with triacetin concentration. As  $D_e$  increased only marginally (by 4.6%) when adding 100 mM instead of 10 mM of fuel, we used 10 mM for all subsequent experiments. When adding 10 mM of fuel, the LNMs were capable of a sustained motion for about 40 min (Figure 2c). After 40 min, the  $D_e$  dropped again to the control value (sample without added fuel; Figure 2d).

To explore the ability of LNMs to degrade triglyceride, tributyrin was selected as the removal target as it is slightly dissolvable in PBS solution, thus resembling “blood lipid”. When LNMs ( $50 \mu\text{g mL}^{-1}$ ) were added to a PBS solution containing tributyrin droplets in suspension (Figure S6), the LNMs exhibited typical Brownian motion with  $D_e = 0.78 \pm 0.043 \mu\text{m}^2\text{s}^{-1}$  (Figure 3a–d). This suggests that low tributyrin concentrations ( $0.133 \text{ mg mL}^{-1}$ , saturated concentration) do not induce enhanced Brownian diffusion of LNMs. After adding fuel (triacetin, 10 mM), the LNMs moved more rapidly, resulting in  $D_e = 1.096 \pm 0.085 \mu\text{m}^2\text{s}^{-1}$  (Figure 3b–d). When

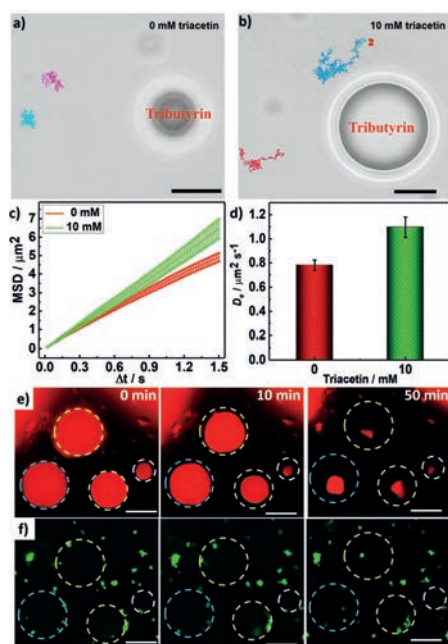


**Figure 3.** Representative trajectories of lipase motors surrounding tributyrin droplets with a) 0 and b) 10 mM of added triacetin. Scale bars are  $5 \mu\text{m}$ . c) MSDs of the LNMs with 0 and 10 mM triacetin ( $n \geq 16$ , error bars represent the SE). d) Effective diffusion coefficients obtained from the MSD at different triacetin concentrations (with tributyrin droplets present in the solution). e, f) FL microscopy images showing the interaction between the droplets (red FL from Nile Red in tributyrin oil phase) and motors (green FL from FITC loaded in MSNPs) at different times, with dashed circles showing the initial sizes.

the LNMs happened to reach the surface of the oil droplets, they were confined at the oil–water interface because of the inherent amphiphility of lipase,<sup>[31]</sup> but still maintained a diffusion coefficient of  $D_e = 0.174 \pm 0.038 \mu\text{m}^2\text{s}^{-1}$  (Figure S7), which is significantly smaller than that of Brownian motion in bulk solution. The confinement of LNMs to the oil droplets' surface is shown in Figures 3e, f and S8, where the interfacial catalysis between lipase and tributyrin occurred. Therefore, the tributyrin droplets were degraded ( $\leq 20 \mu\text{m}$  in diameter) within 1 h.

To dynamically explore the degradation process, we focused on a single representative tributyrin droplet. Litmus was used to illustrate the dynamic color change during the degradation of tributyrin by LNMs, which produces butyric acid [Figure 4a, Eq. (2) in the Supporting Information].

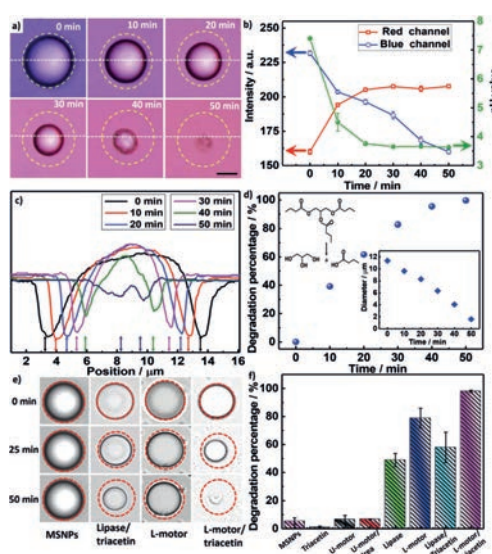


**Figure 4.** Demonstrating the dynamic degradation process of tributyrin droplets with lipase motors at different times. a) The color change of the surrounding medium is caused by the litmus, indicating the continuous generation of butyric acid. Round dashed circles indicate the initial size of the tributyrin droplets. The scale bar is  $5 \mu\text{m}$ . b) Corresponding RGB intensity and pH value in the surrounding solution. c) Size measurement of the tributyrin droplets according to the white dashed lines in (a). d) Degradation percentage of tributyrin droplets calculated from their diameters (see inset); the chemical equation shows the catalytic decomposition of tributyrin. e) Optical microscopy of the degradation processes of tributyrin droplets under different conditions. f) Corresponding histogram to (e), showing the degradation percentage of tributyrin droplets under different conditions after 1 h.

While the fuel-induced catalytic reaction can trigger an immediate local pH change, the color change may be delayed by up to 3 h because of the low fuel concentration (10 mM). However, tributyrin degradation significantly accelerated the acidification, producing a color change in just 30 min. The color of the surrounding solution was simultaneously ana-



lyzed by individual channel using Image J software (RGB intensity; see Figure 4b). Initially, the diameter of a representative tributyrin droplet was about 11.36  $\mu\text{m}$  (Figure 4d), and the solution exhibited a blueish color (blue intensity (BI): 231.6; red intensity (RI): 160) with a pH value of 7.4 (Figure 4b,  $t=0$  min). After 10 min, the diameter of the droplet had decreased to 9.65  $\mu\text{m}$ , and the surrounding solution turned purple (Figure 4a,b, BI: 203.5 and RI: 194.1, pH 4.5). As time progressed, the droplet size continued to decrease, while the surrounding solution turned increasingly red (decreasing BI and increasing RI values). Towards the end of the experiment (50 min), the tributyrin droplet had been degraded, and the solution had changed to pink (BI: 160.0; RI: 207.7) because of the continuous release of butyric acid into the surrounding solution. This represents a visible dynamic demonstration of the tributyrin degradation process (from 0% to 100%).

To further demonstrate the advantages of LNMs for the degradation of tributyrin, different control experiments were conducted (Figures 4e, f and S9), including with bare MSNPs, triacetin, urease-MSNPs nanomotors, urease-MSNPs nanomotors with urea fuel (20 mM), free lipase, free lipase with triacetin, LNMs without fuel, and LNMs with triacetin as fuel (10 mM). Urease nanomotors were chosen as controls because we needed to determine whether enhanced diffusion can improve the degradation. With bare MSNPs, there was only 5.2% degradation of the droplets after 1 h. This is mainly due to the low tributyrin solubility, indicating that bare MSNPs have almost no effect on tributyrin droplets. Pure triacetin (10 mM), urease-MSNPs motors with urea (20 mM), and urease-MSNPs motors without urea yielded degradations of 1%, 6.5%, and 6.7%, respectively. We can thus conclude that urease-MSNPs nanomotors, despite containing enzymes on the surface and presenting enhanced diffusion, cannot degrade tributyrin droplets. Additionally, we also compared the affinities of urease motors and LNMs for targeting the tributyrin droplets. The same concentration of MSNPs was later separated into two aliquots, which were loaded with fluorescein isothiocyanate (FITC), followed by the corresponding modification with urease and lipase, respectively. After these two types of FITC-loaded nanomotors had been added into the solution containing tributyrin droplets, we calculated the FL intensity on the tributyrin droplet area (see the Supporting Information and Figures S10 and S11 for details). Initially, both types of motors were distributed randomly in the solution (Figure S10) with a similar FL intensity within the droplet area. Within 1 h, the FL intensity surrounding the droplet area increased dramatically in the presence of fuel for the LNMs (Figure S11), confirming that LNMs tend to accumulate on the surface of tributyrin droplets, which leads to their highly efficient degradation. Besides, with free lipase ( $2 \mu\text{g mL}^{-1}$ ), the droplet degradation was 48.9%, which increased to 57.9% after adding triacetin, thus illustrating the enhanced degradation process in the presence of fuel due to the enhanced diffusion of free lipase. LNMs ( $50 \mu\text{g mL}^{-1}$ ) with  $2 \mu\text{g mL}^{-1}$  lipase (measured through bicinchoninic acid assay (BCA), details in the Supporting Information) can lead to a 78.8% degradation, which is higher than that with free lipase. This is due to the fact that

free lipase tends to form bimolecular aggregates that partially block the lipase active centers, which in turn results in a less active form.<sup>[32]</sup> The immobilization can be beneficial for cleaving these lipase dimers, thus improving their efficiency. Notably, more than 98% of the droplets can be degraded through the addition of triacetin, which demonstrates how lipase anchored to MSNPs increases the efficient propulsion and diffusion towards the target.

In conclusion, we have demonstrated that the lipase-based catalytic reaction can be utilized to provide MSNPs with enhanced motility in triglyceride-containing PBS solutions. Compared to free lipase and urease nanomotors, we showed that active lipase nanomotors can accelerate the degradation of tributyrin droplets to a very high degree (ca. 98% within 50 min). These results hint towards possible new applications of lipase-powered nanomotors, in biomedicine for high-triglyceride-related diseases or in environmental remediation for oil removal. However, it is necessary to understand the stability and activity of such motors in oil-polluted waters, as well as the interaction of these motors with adipocytes. Future work should be dedicated to improving the motion control, as well as their performance in biological fluids, such as serum or blood.

#### Acknowledgements

We thank Albert Miguel López and Lucas Santiago Palacios Ruiz for the development of the tracking and extracting software, respectively. L.W. thanks the NSFC (No. 51703043), the Marie Skłodowska-Curie fellowship (Grant No. 712754), and the Severo Ochoa programme (Grant SEV-2014-0425 (2015–2019)). A.C.H. thanks MINECO for a Severo Ochoa fellowship. X.H. thanks the NSFC (No. 21871069). S.S. thanks the Spanish MINECO for grants CTQ2015-68879-R (MICRODIA) and CTQ2015-72471-EXP (Enzwim).

#### Conflict of interest

The authors declare no conflict of interest.

**Keywords:** enzyme nanomotors · lipase · micromotors · oil removal · self-propulsion

**How to cite:** *Angew. Chem. Int. Ed.* **2019**, *58*, 7992–7996  
*Angew. Chem.* **2019**, *131*, 8076–8080

- [1] a) J. Wang, *Nanomachines: fundamentals and applications*, Wiley, Hoboken, **2013**; b) S. Balasubramanian, D. Kagan, C.-M. Jack Hu, S. Campuzano, M. J. Lobo-Castañon, N. Lim, D. Y. Kang, M. Zimmerman, L. Zhang, J. Wang, *Angew. Chem. Int. Ed.* **2011**, *50*, 4161–4164; *Angew. Chem.* **2011**, *123*, 4247–4250.
- [2] a) M. Moreno-Guzman, A. Jodra, M.-Á. López, A. Escarpa, *Anal. Chem.* **2015**, *87*, 12380–12386; b) X. Yang, Y. Tang, S. D. Mason, J. Chen, F. Li, *ACS Nano* **2016**, *10*, 2324–2330.
- [3] a) J. Shao, M. Xuan, H. Zhang, X. Lin, Z. Wu, Q. He, *Angew. Chem. Int. Ed.* **2017**, *56*, 12935–12939; *Angew. Chem.* **2017**, *129*, 13115–13119; b) M. Medina-Sánchez, H. Xu, O. G. Schmidt, *Ther. Delivery* **2018**, *9*, 303–316.



- [4] a) J. Orozco, D. Vilela, G. Ramírez, Y. Fedorak, A. Escarpa, R. Duhalt, J. Wang, *Chem. Eur. J.* **2014**, *20*, 2866–2871; b) J. Parmar, D. Vilela, K. Villa, J. Wang, S. Sánchez, *J. Am. Chem. Soc.* **2018**, *140*, 9317–9331.
- [5] a) W. Qin, T. Peng, Y. Gao, F. Wang, X. Hu, K. Wang, J. Shi, D. Li, J. Ren, C. Fan, *Angew. Chem. Int. Ed.* **2017**, *56*, 515–518; *Angew. Chem.* **2017**, *129*, 530–533; b) L. Wang, Y. Liu, J. He, M. J. Hourwitz, Y. Yang, J. T. Fourkas, X. Han, Z. Nie, *Small* **2015**, *11*, 3762–3767; c) Y. Wu, T. Si, C. Gao, M. Yang, Q. He, *J. Am. Chem. Soc.* **2018**, *140*, 11902–11905.
- [6] J. Guo, J. J. Gallegos, A. R. Tom, D. Fan, *ACS Nano* **2018**, *12*, 1179–1187.
- [7] a) T. Xu, F. Soto, W. Gao, V. Garcia-Gradilla, J. Li, X. Zhang, J. Wang, *J. Am. Chem. Soc.* **2014**, *136*, 8552–8555; b) D. Zhou, Y. Gao, J. Yang, Y. C. Li, G. Shao, G. Zhang, T. Li, L. Li, *Adv. Sci.* **2018**, 1800122.
- [8] a) M. Pal, N. Somalwar, A. Singh, R. Bhat, S. M. Eswarappa, D. K. Saini, A. Ghosh, *Adv. Mater.* **2018**, *30*, 1800429; b) T. Xu, J. Yu, X. Yan, H. Choi, L. Zhang, *Micromachines* **2015**, *6*, 1346–1364.
- [9] a) C. Chen, F. Mou, L. Xu, S. Wang, J. Guan, Z. Feng, Q. Wang, L. Kong, W. Li, J. Wang, Q. Zhang, *Adv. Mater.* **2017**, *29*, 1603374; b) M. Xuan, R. Mestre, C. Gao, C. Zhou, Q. He, S. Sánchez, *Angew. Chem. Int. Ed.* **2018**, *57*, 6838–6842; *Angew. Chem.* **2018**, *130*, 6954–6958; c) R. Dong, Q. Zhang, W. Gao, A. Pei, B. Ren, *ACS Nano* **2015**, *10*, 839–844; d) J. Wang, Z. Xiong, J. Zheng, X. Zhan, J. Tang, *Acc. Chem. Res.* **2018**, *51*, 1957–1965.
- [10] a) T. Patiño, X. Arqué, R. Mestre, L. Palacios, S. Sánchez, *Acc. Chem. Res.* **2018**, *51*, 2662–2671; b) X. Zhao, K. Gentile, F. Mohajerani, A. Sen, *Acc. Chem. Res.* **2018**, *51*, 2373–2381; c) X. Ma, A. C. Hortelão, T. Patiño, S. Sánchez, *ACS Nano* **2016**, *10*, 9111–9122.
- [11] a) H. S. Muddana, S. Sengupta, T. E. Mallouk, A. Sen, P. J. Butler, *J. Am. Chem. Soc.* **2010**, *132*, 2110–2111; b) S. Sengupta, K. K. Dey, H. S. Muddana, T. Tabouillot, M. E. Ibele, P. J. Butler, A. Sen, *J. Am. Chem. Soc.* **2013**, *135*, 1406–1414.
- [12] K. K. Dey, X. Zhao, B. M. Tansi, W. J. Méndez-Ortiz, U. M. Córdova-Figueroa, R. Golestanian, A. Sen, *Nano Lett.* **2015**, *15*, 8311–8315.
- [13] a) X. Ma, A. Jannasch, U.-R. Albrecht, K. Hahn, A. Miguel-López, E. Schäffer, S. Sánchez, *Nano Lett.* **2015**, *15*, 7043–7050; b) X. Ma, X. Wang, K. Hahn, S. Sánchez, *ACS Nano* **2016**, *10*, 3597–3605; c) X. Ma, S. Sánchez, *Tetrahedron* **2017**, *73*, 4883–4886.
- [14] a) T. Patiño, N. Gracia, X. Arqué, A. Miguel-López, A. Jannasch, T. Stumpp, E. Schäffer, L. Albertazzi, S. Sánchez, *J. Am. Chem. Soc.* **2018**, *140*, 7896–7903; b) T. Patiño, A. Porchetta, A. Jannasch, A. Lladó, T. Stumpp, E. Schäffer, F. Ricci, S. Sánchez, *Nano Lett.* **2019**, <https://doi.org/10.1021/acs.nanolett.8b04794>.
- [15] a) A. C. Hortelão, T. Patiño, A. Perez-Jiménez, À. Blanco, S. Sánchez, *Adv. Funct. Mater.* **2018**, *28*, 1705086; b) A. C. Hortelão, R. Carrascosa, N. Murillo-Cremaes, T. Patiño, S. Sánchez, *ACS Nano* **2019**, *13*, 429–439.
- [16] L. Abdelmohsen, M. Nijemeisland, G. Pawar, G. Janssen, R. J. Nolte, J. van Hest, D. Wilson, *ACS Nano* **2016**, *10*, 2652–2660.
- [17] A. Joseph, C. Contini, D. Cecchin, S. Nyberg, L. Ruiz-Perez, J. Gaitzsch, G. Fullstone, X. Tian, J. Azizi, J. Preston, G. Volpe, G. Battaglia, *Sci. Adv.* **2017**, *3*, e1700362.
- [18] D. Pantarotto, W. R. Browne, B. L. Feringa, *Chem. Commun.* **2008**, 1533–1535.
- [19] X. Ma, A. C. Hortelão, A. Miguel-López, S. Sánchez, *J. Am. Chem. Soc.* **2016**, *138*, 13782–13785.
- [20] J. Orozco, V. Garcia-Gradilla, M. D'Agostino, W. Gao, A. Cortés, J. Wang, *ACS Nano* **2013**, *7*, 818–824.
- [21] I.-A. Pavel, A.-I. Bunea, S. David, S. Gáspár, *ChemCatChem* **2014**, *6*, 866–872.
- [22] D. A. Gregory, Y. Zhang, P. J. Smith, X. Zhao, S. J. Ebbens, *Small* **2016**, *12*, 4048–4055.
- [23] N. Mano, A. Heller, *J. Am. Chem. Soc.* **2005**, *127*, 11574–11575.
- [24] a) M. Guix, J. Orozco, M. García, W. Gao, S. Sattayasamitsathit, A. Merkoçi, A. Escarpa, J. Wang, *ACS Nano* **2012**, *6*, 4445–4451; b) C. Liang, C. Zhan, F. Zeng, D. Xu, Y. Wang, W. Zhao, J. Zhang, J. Guo, H. Feng, X. Ma, *ACS Appl. Mater. Interfaces* **2018**, *10*, 35099–35107.
- [25] “Final report on the safety assessment of triacetin”: M. Z. Fiume, Cosmetic Ingredients Review Expert Panel, *Int. J. Toxicol.* **2003**, *22*, 1–10.
- [26] Y. Wang, Q. Zhao, N. Han, L. Bai, J. Li, J. Liu, E. Che, L. Hu, Q. Zhang, T. Jiang, *Nanomedicine* **2015**, *11*, 313–327.
- [27] W. Xie, X. Zang, *Food Chem.* **2016**, *194*, 1283–1292.
- [28] K. Veeraragavan, B. F. Gibbs, *Biotechnol. Lett.* **1989**, *11*, 345–348.
- [29] H. Edelhoch, *Biochemistry* **1967**, *6*, 1948–1954.
- [30] G. Dunderdale, S. Ebbens, P. Fairclough, J. Howse, *Langmuir* **2012**, *28*, 10997–11006.
- [31] L. Wang, Y. Lin, Y. Zhou, H. Xie, J. Song, M. Li, Y. Huang, X. Huang, S. Mann, *Angew. Chem. Int. Ed.* **2019**, *58*, 1067; *Angew. Chem.* **2019**, *131*, 1079.
- [32] R. C. Rodrigues, C. Ortiz, Á. Berenguer-Murcia, R. Torres, R. Fernández-Lafuente, *Chem. Soc. Rev.* **2013**, *42*, 6290–6307.

Manuscript received: January 17, 2019

Revised manuscript received: March 15, 2019

Accepted manuscript online: April 16, 2019

Version of record online: May 8, 2019